Subhasis Bhaumik
Subrata Chattopadhyay
Tanushyam Chattopadhyay
Srijan Bhattacharya   *Editors*

Proceedings of International Conference on Industrial Instrumentation and Control

ICI2C 2021

Springer

Lecture Notes in Electrical Engineering

Volume 815

The book series *Lecture Notes in Electrical Engineering* (LNEE) publishes the latest developments in Electrical Engineering - quickly, informally and in high quality. While original research reported in proceedings and monographs has traditionally formed the core of LNEE, we also encourage authors to submit books devoted to supporting student education and professional training in the various fields and applications areas of electrical engineering. The series cover classical and emerging topics concerning:

- Communication Engineering, Information Theory and Networks
- Electronics Engineering and Microelectronics
- Signal, Image and Speech Processing
- Wireless and Mobile Communication
- Circuits and Systems
- Energy Systems, Power Electronics and Electrical Machines
- Electro-optical Engineering
- Instrumentation Engineering
- Avionics Engineering
- Control Systems
- Internet-of-Things and Cybersecurity
- Biomedical Devices, MEMS and NEMS

For general information about this book series, comments or suggestions, please contact leontina.dicecco@springer.com.

To submit a proposal or request further information, please contact the Publishing Editor in your country:

China

Jasmine Dou, Editor (jasmine.dou@springer.com)

India, Japan, Rest of Asia

Swati Meherishi, Editorial Director (Swati.Meherishi@springer.com)

Southeast Asia, Australia, New Zealand

Ramesh Nath Premnath, Editor (ramesh.premnath@springernature.com)

USA, Canada:

Michael Luby, Senior Editor (michael.luby@springer.com)

All other Countries:

Leontina Di Cecco, Senior Editor (leontina.dicecco@springer.com)

** This series is indexed by EI Compendex and Scopus databases. **

More information about this series at https://link.springer.com/bookseries/7818

Subhasis Bhaumik · Subrata Chattopadhyay ·
Tanushyam Chattopadhyay · Srijan Bhattacharya
Editors

Proceedings of International Conference on Industrial Instrumentation and Control

ICI2C 2021

Springer

Editors
Subhasis Bhaumik
Department of Aerospace Engineering
and Applied Mechanics
Indian Institute of Engineering Science
and Technology, Shibpur
Howrah, West Bengal, India

Tanushyam Chattopadhyay
TCS Research and Innovation Lab
Kolkata, West Bengal, India

Subrata Chattopadhyay
Department of Electrical Engineering
National Institute of Technical Teachers'
Training & Research
Kolkata, West Bengal, India

Srijan Bhattacharya
Department of Applied Electronics
and Instrumentation Engineering
RCC Institute of Information Technology
Kolkata, West Bengal, India

Committee for ICI2C-2021

Conference Chief

Padma Shri Prof. Ajoy Kumar Ray, Ex-VC, BESU, Ex-Director IIEST, Ex-Chairman, RCCIIT

Honorary General Chair

Pranabesh Das, Director, Technical Education, Government of West Bengal, India, and Chairman, BOG, RCC Institute of Information Technology, India
Anirban Mukherjee, Principal (O), RCC Institute of Information Technology, India
Vincenzo Piuri, FIEEE, University of Milan, Italy

General Chair

Srijan Bhattacharya, SMIEEE, LMTRS, MIE(I), RCC Institute of Information Technology, India

Program Chair

Arijit Ghosh, MIE(I), RCC Institute of Information Technology, India

Organizing Chair

Avishek Paul, RCC Institute of Information Technology, India
Naiwrita Dey, MIEEE, LMTRS RCC Institute of Information Technology, India

Publication Chair

Debabrata Bhattacharya, RCC Institute of Information Technology, India
Kalyan Biswas, RCC Institute of Information Technology, India

Advisory Board

Padma Shri Prof. Ajoy Kumar Ray, Ex-VC, BESU, Ex-Director IIEST, Ex-Chairman, RCCIIT
Anton Nijholt, University of Twente, The Netherlands
Asokan Thondiyath, SMIEEE, Indian Institute of Technology, Madras, India
Anoop Kumar Mukhopadhyay, Manipal University, Jaipur, India (Ex-Chief Scientist at CSIR-CGCRI, Kolkata)
Anirban Chowdhury, University of Essex, UK
Bikash Bepari, Haldia Institute of Technology, Haldia, India
Debjani Ganguly, SMIEEE, Indian Institute of Engineering Science and Technology, Shibpur, India
Gautam Sarkar, Jadavpur University, India
Koushik Guha, SMIEEE, National Institute of Technology, Silchar, India
Kaushik Pal, Indian Institute of Technology, Roorkee, India
Md Zahidul Islam, SMIEEE, Islamic University, Bangladesh
Md. Atiqur Rahman Ahad, SMIEEE, University of Dhaka, Bangladesh
Nachappa Gopalsami, FIEEE, Argonne National Laboratory, USA
Prithwiraj Purkait, SMIEEE, Jadavpur University, India
Palash Kumar Kundu, MIEEE, Jadavpur University, India
Subhasis Bhaumik, Indian Institute of Engineering Science and Technology, Shibpur, India
Subrata Chattopadhyay, National Institute of Technical Teachers' Training & Research, Kolkata, India
Salah-ddine Krit, SMIEEE, Ibn Zohr University, Agadir, Morocco
Soumya Kanti Manna, Canterbury Christ Church University, UK
Vincenzo Piuri, FIEEE, University of Milan, Italy

International Program Committee

Alok Kole, SMIEEE, RCC Institute of Information Technology, India
Alokananda Dey, RCC Institute of Information Technology, India
Arup Kumar Bhattacharjee, RCC Institute of Information Technology, India
Ashok Mondal, RCC Institute of Information Technology, India
Abhijit Das, MIEEE, RCC Institute of Information Technology, India
Abhishek Basu, MIEEE, RCC Institute of Information Technology, India
Arpita Ghosh, MIEEE, RCC Institute of Information Technology, India
Abhijit Dutta, ArcelorMittal, Katowice, Poland
Arindam Mahanti, IOCL, Paradip, India
Avik Kumar Saha, Indira Gandhi Centre for Atomic Research, Kalpakkam, India
Anton Nijholt, University of Twente, Netherlands
Anup Kumar Kolya, MIEEE, RCC Institute of Information Technology, India
Anirban Chowdhury, University of Essex, UK
Anup Kumar Sharma, National Institute of Technology, Silchar, India
Asokan Thondiyath, SMIEEE, Indian Institute of Technology, Madras, India
Abantika Choudhury, RCC Institute of Information Technology, India
Arpan Deyasi, SMIEEE, RCC Institute of Information Technology, India
Apu Mistry, RCC Institute of Information Technology, India
Astha Sharma, MIEEE, IILM-AHL College of Engineering and Technology, Greater Noida, India
Amitava Das, MIEEE, NSHM Knowledge Campus, Durgapur, India
Bishnu Prasad De, KIIT University, India
Biswarup Mukherjee, Indian Institute of Technology, Delhi, India
Brojo Kishore Mishra, SMIEEE, GIET University, Gunupur, India
Debasish Mondal, MIEEE, RCC Institute of Information Technology, India
Debabrata Bhaskar, ONGC, India
Debjani Ganguly, SMIEEE, Indian Institute of Engineering Science and Technology, Shibpur, India
Dipankar Majumdar, RCC Institute of Information Technology, India
Eshan Samanta, Global Institute of Science and Technology, Haldia
Ganesh Roy, Central Institute of Technology, Kokrajhar, India
Gitosree Khan, B. P. Poddar Institute of Management and Technology Kolkata, India
Hiranmoy Mandal, Academy of Technology, India
Hiranmoy Roy, RCC Institute of Information Technology, India
Indrajit Pan, SMIEEE, RCC Institute of Information Technology, India
Jayanta Datta, RCC Institute of Information Technology, India
Joyeeta Basu Pal, RCC Institute of Information Technology, India
Kanchan Kr. Patra, RCC Institute of Information Technology, India
Koena Mukherjee, National Institute of Technology, Silchar, India
Koushik Dutta, Indian Institute of Information Technology, Design and Manufacturing, Jabalpur, India
Liton Chandra Paul, Pabna University of Science and Technology, Bangladesh

Institutional Core Committee

Abhishek Basu, MIEEE, FIC-Aca, ECE, RCCIIT
Srijibendu Bagchi, MIEEE, HOD-ECE, RCCIIT
Debasish Mondal, MIEEE, HOD-EE, RCCIIT
Indrajit Pan, SMIEEE, HOD-IT, RCCIIT
Abhijit Das, MIEEE, IT, RCCIIT
Minakshi Banerjee, Chairperson-R&D, CSE, RCCIIT
Soham Sarkar, MIEEE, Conv-R&D, ECE, RCCIIT
Rajib Saha, HOD-CSE, RCCIIT
Biswanath Chakraborty, HOD-CA, RCCIIT
Papia Datta, HOD-AS, RCCIIT
Nitai Banerjee, HOD-ESM, RCCIIT
Ashoke Mondal, EE, RCCIIT
Arpita Ghosh, MIEEE, ECE, RCCIIT
Tiya Dey Malakar, ECE, RCCIIT
Arpan Deyasi, SMIEEE, ECE, RCCIIT
Budhaditya Biswas, EE, RCCIIT
Anindya Basu, ECE, RCCIIT
Alok Kole, EE, RCCIIT
Parama Bagchi, CSE, RCCIIT
Anup Kumar Kolya, CSE, RCCIIT
Kanchan Kr. Patra, Applied Science, RCCIIT
Arup Kumar Bhattacharjee, CSE, RCCIIT
Soumen Mukherjee, CA, RCCIIT
Apu Mistry, ECE, RCCIIT
Goutam Bera, AEIE, RCCIIT
Arijit Majumder, System, RCCIIT
Chinmoy Ghosal, Finance, RCCIIT
Santasil Roy, Accounts, RCCIIT
Rimo Kumar Dey, AEIE, RCCIIT
Kuntal Ghosh, AEIE, RCCIIT
Dibyendu Datta, AEIE, RCCIIT
Subhasis Banerjee, EE, RCCIIT

Publicity Chairs

Anindya Basu, RCC Institute of Information Technology, India
Arijit Majumder, RCC Institute of Information Technology, India
Budhaditya Biswas, RCC Institute of Information Technology, India
Goutam Bera, RCC Institute of Information Technology, India

Finance Chairs

Chinmoy Ghosal, RCC Institute of Information Technology, India
Santasil Roy, RCC Institute of Information Technology, India

Hospitality Chairs

Rimo Kumar Dey, RCC Institute of Information Technology, India
Kuntal Ghosh, RCC Institute of Information Technology, India
Dibyendu Datta, RCC Institute of Information Technology, India

Preface

The ICI2C-2021 is organized by the Department of Applied Electronics and Instrumentation Engineering, RCC Institute of Information Technology, Kolkata, on 20–22 August 2021. This conference aims to bring together academicians, researchers, developers, industrial practitioners, scientists and engineers from academia and industry to discuss about their research, studies, findings, new ideas and concepts, contributions and developments related to the areas of measurement, control and its applications, communication techniques, robotics and signal processing, power and calibration.

This conference will create a platform to share, disseminate and address the recent trends in research and developments in these areas to the academic and research community. The event will also try to foster the engineers for contributing towards technology-based solutions for the benefit of human civilization for efficient and optimum utilization of resources to lead better life.

ICI2C-2021 Knowledge Partner—Institution of Engineers (India), and Technical Co Sponsors—IEEE Industry Applications Society (IAS)—Kolkata Chapter, The Robotics Society, India (TRS), Indian Ceramic Society—Karnataka Chapter.

In ICI2C-2021, total 11 keynote speakers delivered lectures from different academia and industry; the list of respected speakers is—

(1)   Padma Shri Prof. Ajoy Kumar Ray, Ex-VC, BESU, Ex-Director IIEST, Ex-Chairman, RCCIIT
(2)   Prof. Anton Nijholt, University of Twente, The Netherlands
(3)   Prof. Subir Kumar Saha, IIT Delhi, India
(4)   Prof. Subhasis Bhaumik, Indian Institute of Engineering Science and Technology, Shibpur, India
(5)   Dr. Nachappa Gopalsami, FIEEE, Argonne Associate, Sensors, Instrumentation, and NDE, Nuclear Science and Engineering Division, Argonne National Laboratory, USA
(6)   Prof. Asokan Thondiyath, IIT Madras, India
(7)   Prof. Bikash Bepari, HIT, Haldia, India
(8)   Prof. Prithwiraj Purkait, Jadavpur University, India

 (9)   Md. Atiqur Rahman Ahad, University of Dhaka, Bangladesh
(10)   Prof. Anirban Chowdhury, University of Essex, UK
(11)   Prof. Soumya Kanti Manna, Canterbury Christ Church University, UK

    Fifty-eight papers are accepted for this conference with nine tracks, one best paper awarded for each track. One special paper by Prof. Anton Nijholt, University of Twente, Netherlands, is introduced.

Kolkata, India   Prof. Subhasis Bhaumik
August 2021   Prof. Subrata Chattopadhyay
                                                        Dr. Tanushyam Chattopadhyay
                                                            Dr. Srijan Bhattacharya

Contents

About the Editors

Prof. Subhasis Bhaumik did B.E. in Mechanical Engineering and M.E. in Production Engineering. After post graduation he joined in TATA STEEL—Jadavpur University joint research project for development of a robotic system for steel plant application. He did Ph.D. in the area of robotics. He has served as faculty of Birla Institute of Technology (Deemed University) Mesra Ranchi, Thapar Institute of Engineering and Technology (Deemed University) Patiala and Regional Engineering College (NIT) Durgapur. Dr. Bhaumik is currently working as Professor in the Dept. of Aerospace Engineering, Indian Institute of Engineering Science and Technology Shibpur. He is also former Head of School of Mechatronics and Robotics in IIEST Shibpur. His research interest is Mechatronics, Robotics, Smart Material, CAD/CAM/Industrial Automation, Assistive Devices, Innovative Product Development and BCI/HMI and Rural Technology. Dr. Bhaumik is the principal investigator of sponsored projects of Indo-US Fabrionics, BRNS-BARC, DST, AICTE, UGC, Larsen & Toubro, IE(I), DST-FIST and MHRD—National Initiative on Design Innovation. He has guided 9 PhD thesis and presently guiding three Ph.D. work. He has published more than 80 research papers in SCI journals and International conferences. Two innovative products have been filed for patent. He is a Fellow of Institution of Engineers (I), Member of Association of Machines and Mechanism, Robotics Society of India and Expert Member—Rehabilitation Council of India. He was the Zonal Vice President of Association of Machines and Mechanism, editorial board member and member of Robotics Society of India. Dr. Bhaumik is presently acting as Dean (Research & Consultancy) and President, IIC, IIEST Shibpur.

Prof. Subrata Chattopadhyay was born in India in 1965. He received his Ph. D (Tech) in Instrumentation Engineering from the University of Calcutta, India in 2006, preceded by M.Tech. (Instrumentation), B.Tech. (Electrical) and B.Sc. (Hons) in Physics, in 1993, 1991 and 1987 respectively. He served as a Deputy Manager (Projects & Maintenance) in Electrical and Instrumentation Engineering of Chemical and Manufacturing Industries in India and then joined as an Assistant Professor in Electrical Engineering Department of National Institute of Technical Teachers' Training & Research, Kolkata, under Ministry of Human Resource Development,

Government of India in 2003. At present he is working as a Professor in Electrical Engineering and In-charge of NITTTR Kolkata Extension Centre, Bhubaneswar, India. He introduced, as head of Electrical Engineering Department, a new Post Graduate Programme (M.Tech. in Mechatronics Engineering), first of its kind in Eastern India at NITTTR Kolkata, with required development of the Department to accommodate the same. He is highly involved in Teaching and Research and his present investigation is on innovation of noble techniques of measurement and control based on Sensor and Transducer development, Process Automation, PLC and Distributed Control System, Mechatronics, Robotics etc. He has guided one research scholar who have been awarded with Ph.D. (Tech.) degree from the National Institute of Technology, Durgapur, India. Presently, five scholars are working under him for the Ph.D. degree. He has around 100 papers in international and national journals and conference proceedings.

Dr. Tanushyam Chattopadhyay is currently working as a Principal Scientist at TCS Research and Innovation Labs. He started his career as research in Indian Statistical Institute, Kolkata and later on, joined Tata Consultancy Services Limited in 2004. He awarded Ph.D. degree from Jadavpur University for the work done at ISI, Kolkata, in 2012. He has nearly 55+ patents got granted across the globe. He also authored a book and some book chapters. He has published nearly 70+ papers in peer reviewed journals and conferences. He is a member of International Machine Learning Society. Serving as a member of Board of Governor of several academic institutions. His current research is evolved around developing an analytics solution for TCS built IoT platform namely TCS Connected Universe Platform (TCUP) which involves both research and engineering in different areas of data science. He was awarded with many prizes like: Winner of the WWW 2011 Software Contest, Winner of Computer Society of India Young IT Professional Award in region level and awarded with special mention award in national level, Significant contribution award from CSI in 2012–2013, From TCS got the awards like Patent Champion (twice) for the years 2010–2011 and 2014–2015, Star of the month in January 2010 and November, 2005, Best team of TCS for the month in August 2010, Top 100 C Coder of TCS in March, 2009, Young Innovator in 2007. He was awarded with the University Gold (1st Class 1st) medal in MCA, First class Third in graduation (Physics as Major).

Dr. Srijan Bhattacharya is working as Assistant Professor and Head in Department of Applied Electronics and Instrumentation Engineering, (AEIE) in RCC Institute of Information Technology, Kolkata, India. He did B.E. in Electronics and Instrumentation Engineering from Gandhi Institute of Engineering and Technology (Presently GIET University), Orissa, India (2003) and M.Tech. in Electrical Engineering (Specialization Mechatronics) from National Institute of Technical Teachers Training and Research, Kolkata, India (2008) and Ph.D. from Indian Institute of Engineering Science and Technology, Shibpur, India (2017). He received Gold medal from West Bengal University of Technology, West Bengal [Presently Maulana Abul Kalam Azad University of Technology (MAKAUT)]. He had published book title—"Advancements in Instrumentation and Control in Applied System Applications" as single

editor with IGI Global, USA, and Presently one edited book is under process on "Ionic Polymer Metal Composite (IPMC)-Present Scenario and Next Generation Research" with CRC Press, Taylor and Francis Group. He is guest editor for Springer Journal of "The Institution of Engineers (India): Series B", He has published 30+ peer-reviewed journals/Book Chapter/conference papers and completed one Research project sponsored by—Institution of Engineers (India)—IE(I). He had served as keynote/invited speaker/Mentor-Judge in different events (AICTE, ISRO, University's, etc.). He has established several international / National MOU / collaborations. He had organized more than 35 events (International Conference, FDP, Workshop etc.) He has been involved with academic administration as, Board of Studies—Member (AEIE) MAKAUT, West Bengal. Coordinator of—Student Chapter RCCIIT—The Robotics Society (TRS)-India. He is senior member of IEEE (M'16, SM'20), His research interest is in Mechatronics system design, Sensors design and application, smart material—Ionic Polymer Metal Composite (IPMC).

Capturing Obstructed Nonverbal Cues in Augmented Reality Interactions: A Short Survey

Anton Nijholt

Abstract We present a short survey on recovering nonverbal communication cues that are hidden by head-mounted devices while interacting in augmented reality. The focus is on recovering facial expressions and gaze behavior by using various kinds of sensors that are attached to or integrated with these devices. The nonverbal cues can be made visible for other co-located or remote interactants on devices or avatars.

Keywords Augmented reality · Head-mounted devices · Nonverbal interaction · Facial expressions

1 Introduction

While in 1968, Ivan Sutherland's virtual reality device, hanging from the ceiling of its laboratory, could indeed be seen as a threatening "Sword of Damocles", nowadays we have headsets for augmented and virtual reality with a multitude of sensors and functions, almost resembling ordinary glasses, and also various ways to control the augmented environments and manipulate its virtual objects. We can make use of cheap sensors, powerful processors, and high-bandwidth networking. Head tracking takes care of providing a correct user's perspective of the world. Augmented reality (AR) cameras and computer vision make it possible to align virtual objects with the real world. Gaze, gestures, and voice commands, built-in or custom, can be used to interact with the environment. Techniques have become available for modeling and updating a user's spatial environment.

Head-mounted devices (HMDs) for AR and virtual reality (VR) have become well-known. Smart glasses, after a rather unfortunate start, are gaining attention again and are once again on the road to enter the consumer market. In AR video see-through, both the real and virtual scenes are available in digital form which allows detailed manipulation and alignment. In optical see-through (OST) AR, the user sees the real world directly with virtual objects superimposed on it. The HMDs are

A. Nijholt (✉)
Faculty EEMCS, Human Media Interaction, University of Twente, Enschede, The Netherlands
e-mail: a.nijholt@utwente.nl

bulky, uncomfortable, and sometimes weigh more than half a kilo. Less advanced AR is possible with smart (AR) glasses, head-up displays, sometimes hooked up to a smartphone or other handheld that is used as an additional head-down display and control.

Smooth human–human interaction requires the use and recognition of social signals, verbal and nonverbal cues that are used by partners in face-to-face and multiple-user interactions. These communication cues cannot always be detected when one or more interaction partners wear a head-mounted augmented reality device. Face regions are covered, eye and eyebrow movements are hidden, and facial expressions cannot be recognized. Moreover, users of these HMDs may have to deal with information that pops up during a task, and this may disrupt their communication and their exchange of communication cues with local or remote collaborators.

In this paper, we survey the research attempts that aim at recovering social signals, in particular those that can be detected from facial expressions, from AR devices that nowadays hide regions of the face that in unobstructed human–human interaction would provide information about the affective and cognitive state of an interaction partner. We aim at recovering those signals, maybe even enhance them, to design a more natural—not obstructed by technology—interaction between co-located partners or between partners, colleagues, collaborators, or instructors in remote locations.

2 Nonverbal Communication Cues

Nonverbal cues play an important role in social and other human–human interactions. We make gestures while speaking, we move our head and body, our facial expressions change, and our speech has nonverbal components. Listening has also many active components. Mimicry occurs naturally. While interacting, we can point at objects, pick up, manipulate, or assemble them, leaf through a book, use a tool, et cetera. Our attitude toward the interaction, for example, consent, approval, contempt, discomfort, impatience, confidence, interest, anxiousness, and especially focus of attention, is visible in our body language and facial expressions. It shows in movements of the eyes, eyebrows, and mouth, in our head orientation, body pose, and gaze, our gestures, and the proxemic distance we keep.

In AR, we will have situations where humans wearing AR HMDs communicate with each other, with people that do not wear them, and with avatars, visible in their HMD, that represent remote interactants. Besides, there can be virtual humans with their own algorithmic identity and intelligence. These latter interactants will not be considered here. Wearing AR devices disrupts the display and the detection of nonverbal communication cues. Can that be repaired, can they be translated to artificial signals, or can we even think of using the technology to enhance these cues?

AR research can profit from past human–computer interaction research done in the context of virtual reality, intelligent virtual agents, and affective computing.

Nonverbal interaction behavior has been studied in various large-scale European projects and networks of excellence on nonverbal augmented and multiparty (human–human, human-virtual agent) interaction such as augmented multi-part interaction (AMI) and social signal processing (SSPnet) [1]. Face-to-face interaction research is usually based on Sachs' turn-taking model of conversations [2]. This is a model with a speaker speaking, a listener providing nonverbal feedback, and continuous role switching. Within turns, there is also simultaneous expressive behavior that requires synchronization. Mimicking [3], for example, is a naturally occurring phenomenon. Gaze and facial expressions are sources of important nonverbal information.

Simultaneity and synchronization require timing and anticipation. In [4], more observations and examples of what we call "anticipatory synchronization" can be found. Performing joint tasks, for example, building a sandcastle, walking together, shaking hands, moving furniture, and cooperative and competitive game and sports activities require synchronization as well. In (future) AR where we deal with real and virtual objects, such activities require coordination and mutual adjustments as well.

In the next section, we will survey the many ways AR technology obstructs the communication of nonverbal cues during interactions and the attempts to reduce this obstruction. Many parameters need to be taken into account. Devices can obstruct the emitting and detection of social cues, causing problems with turn-taking, delay in responses, and keeping interpersonal distance. Lack of or reduced eye contact is another cause of poor and unbalanced communication. Interesting virtual content, not available to the non-user, can distract the AR user, and this can also lead to not emitting or paying attention to social cues in a conversation. Moreover, among the parameters are the different AR technologies. We have OST and video see-through devices. We can also look at hybrid AR devices, spatial AR, and handheld, eyes-down, AR. Moreover, we should take into account that AR technology is progressing, HMDs are becoming smaller, come to resemble ordinary glasses, and nevertheless have many sensors, that not only provide information about the environment but also about the users of AR devices and their interaction partner, whether or not this partner is using an AR or VR device. Our focus is on the use of HMDs that use OST AR.

3   Recovering Occluded Nonverbal Cues

Obstruction in perceiving nonverbal signals does not only occur while using AR or VR HMDs. For example, naturally occurring interaction supporting gestures are hindered by devices that must be operated simultaneously. But also darkened or mirrored glasses, ordinary glasses, scalp hair, beards, and mustaches, can make it difficult to recognize faces and facial expressions. Ear, nose, or lip piercings and make-up may have an impact too. A niqab only leaves the eyes uncovered. Face masks to prevent the spread of viruses cover the lower region of the face and confuse facial expression recognition software [5, 6]. Face masks that are decorated with

facial expressions using LEDs and partially transparent face masks that let people see your facial expressions are available on the consumer market. Face accessories that are meant to evade facial recognition have been designed as well, including IR LEDs embedded in glasses that are intended to confuse surveillance cameras.

In contrast to situations where a user is isolated in his task, revealing obstructed signals from face, body posture, and hand gestures while using AR or VR devices is a necessity if we want to convey the users' eye gaze and emotions during social and collaborative interactions. The focus here is on the face because facial regions are the most noticeable occlusions caused by AR and VR technology, that is, by wearable and head-attached devices. Not seeing the other person's face degrades the quality and the efficiency of the interaction. Moreover, the information from eye and facial movements can be integrated with other information, such as head and body pose, nonverbal speech, and physiological information. Also, for this latter information, we should ask how the technology that is used may prevent otherwise naturally occurring nonverbal behavior. Being able to disclose social signals leads to the question of how to communicate that now digitally available information and for whom. This depends on whether we have co-located AR-supported face-to-face communication or mediated communication between multiple users in distant locations and a mixed-reality collaboration space.

Below we will review the most important approaches to recover eye contact, gaze awareness, and facial expressions from occluded facial regions. We should take into account that head-attached VR and AR devices are getting smaller and come to resemble ordinary glasses. Nevertheless, eye and eyebrow movements will be difficult or not at all to detect. Capturing of social and attention signals should also be done when we need to represent remote interaction participants as avatars in collaborative AR and VR.

3.1 Private and Co-Located Use of Captured Behavior

An early example of capturing facial expressions of a user wearing special glasses is "expression glasses" [7]. Piezoelectric contact sensors (strain gauges) are used that sense facial muscle movement around the eyes. Applications in which the measurements are communicated to other devices and to have feedback on one's own emotions are mentioned in this paper. Optical (infrared photo-reflective) sensors do not require physical contact with the user's face. For example, [8] reports about smart eyewear that uses 17 integrated sensors that measure the distance between the sensors and the skin surface of the user's face. Movements of facial muscles cause three-dimensional deformations of the skin. Mainly based on information around the eyes, eight different facial expressions are distinguished. This information is meant to be used, among other things, to give the spectacle wearer information about his affective states during his social interactions in daily life. Hence, although this research provides approaches to capturing facial expressions, it has not been done in the context of AR or VR research. That would preferably also require information about the head pose and

gaze direction, for example, to have this information transmitted to other interactants, co-located or remote.

In a co-located situation, we can have interaction between a participant with HMD and collaborators or bystanders without HMD. VR HMDs have a longer history than AR HMDs, and several research papers have addressed this situation. That is, revealing an HMD user's face but also what she is looking at is useful knowledge for co-located partners that do not use an HMD. In the case of VR, the front of the HMD can be used to make information visible to bystanders. This is not possible with OST AR. If we can capture the face, it can be displayed elsewhere, visible to others. If the bystanders were to wear an HMD, it could appear more naturally in that HMD. We mention a few methods of face capturing in VR HMDs that are aimed at making the face visible to bystanders.

The face capturing methods are interesting for AR, but the display of the face should be done differently. For example, in [9], a 3D-face model of the user is rendered on the front of the VR HMD. Only the obscured area of the human face is displayed, giving the illusion of a transparent HMD. No eye-tracking of the HMD user is involved, just random movements of eyeballs, eyebrows, and eyelids. It is projected according to the bystander's head position which is tracked using a front-facing camera on the HMD. This method would conflict with the OST property of an AR device, and a different solution for the display should be designed. A similar observation can be made for the approach in [10]. Here a VR HMD has been given a front-facing screen displaying the scene the user is looking at, overlaid with a cartoon representation of the user's eyes and their movements. The latter, obtained with an eye-tracker, reveals the user's visual attention to nearby bystanders or collaborators. The HMD user is in control, but since a collaborator has the same view, they can discuss the scene and the next actions. Again, such a display cannot be realized on an OST HMD, and the display should be done somewhere else in the location or on a bystander's HMD.

In [11], the users wear OST HMDs with head pose detection and line-of-sight sensing. 3D face shape construction of a user's face with various eye expressions representing line-of-sights and eyelid motions takes place offline. The textures are overlaid in real time on the position and pose of the real faces wearing the HMDs. The system is used in a shared mixed-reality space where people share virtual objects and gaze awareness.

AR displays have become part of cross-device systems, distributed display environments, either for use by the AR user or by providing external observers or collaborators with a similar experience as the AR user. Smartphones and smartwatches can be combined with head-worn AR devices. The AAR system [12] uses a HoloLens AR HMD with an actuated head-mounted projector that shares the AR user's view with external users and that also allows view-dependent rendering of virtual objects on a nearby wall for an external user. In [13], the interaction between an AR HMD user and non-HMD users is also realized with an HMD combined with a dynamic projector that displays the augmented content onto planar surfaces.

Finally, in [14], a "headset removal" process is applied to a VR headset that incorporates eye-tracking. The HMD user performs in a virtual world and is observed

in a live stream by the audience. A personalized face model together with a set of textures indexed by eye gaze has been captured offline. It is aligned and blended with the visual portion of the face in the live stream. The eye-tracking information is used to search the gaze database for a corresponding gaze image which is then rendered as appearing behind a translucent part of the headset. A smooth merging is obtained by interpolating between successive gaze images. The translucency helps to hide small imperfections.

3.2 Transmitting and Displaying Captured Nonverbal Information

Head pose, gaze, and facial expressions need to be captured to have them displayed on an avatar in a co-located or remote mixed-reality interaction situation. There is a variety of research addressing these issues. In [15], the aim is to capture head motions and facial expressions of HMD users and to implement them on their avatars that can perform in face-to-face conversations. The inside of the HMD is augmented with ultra-thin strain gauges that make contact with the face to measure the movements of the occluded upper face regions. Also, there is a separate head-mounted camera to capture the movements in the visible lower face region. In a subsequent paper [16], to improve the quality of face-to-face communication, the focus is on tracking mouth movements with the camera attached to the HMD and regressing the images to the parameters that control the animations of the lip movements of an avatar. In [17], it is shown that also optical (photo-reflective) sensors attached inside an Oculus Rift HMD can be used to distinguish the five basic facial expressions of an HMD user. Capturing of deformations caused by mouth movement is, however, limited. In their case, the expressions are reproduced in real time on a cartoon avatar. In [18], the IR gaze-tracking camera within the Oculus Rift headset is used to infer facial expressions of captured images of the user's eyes.

Projecting a 3D face model into a video mimicking the head pose and facial expressions of an HMD user is the aim of [19]. The visual parts of the face are kept while replacing those hidden by the HMD. The system is trained to learn the facial expressions of the user from the lower part of the face only. In real time, the upper part of the face and its expression changes are recovered in synchrony with the movements of the lower (visible) part. The reconstructed face can be transmitted to remote conversational partners or collaborators. In Microsoft's Holoportation project [20], persons are captured in full 3D and virtually teleported into a remote participant's physical space. Also here, the lack of eye contact when users wear their headsets was experienced as a limitation of the mixed-reality interaction. In this case, tiny inward-looking cameras on the HoloLens have been used to capture the eye regions, and mesh blending and texture mapping are performed on the 3D face geometry and shown as appearing being behind the HoloLens visor in a translucent view.

Rekimoto's "face-through HMD" [21] uses an infrared cut filter (an IR mirror) that reflects infrared light and is transparent for visible light. This mirror is placed between the user's face and the lenses of the HMD. Side-attached IR cameras capture the reflection from the eye and eyebrow region on the filter. A normal camera mounted on the bottom of the HMD in front of the face captures the other face regions, and with colorization of the IR image, the three camera images are merged on a pre-scanned 3D face of the user in real time. Although presented for a VR device, it will be interesting to see the method applied to an AR device that requires optical see-through. In [22], an HMD with face capturing is presented where the HMD enclosure is made from transparent material covered by IR pass filters. The filters block visible light but transmit infrared light. Therefore, an IR camera, mounted on the HMD and in front of the user's eyes, can be used to capture the user's face behind the IR pass filters, while the user sees unobstructed VR images. The IR images have to be colorized. Infrared cameras in the HMD, that is, behind the lenses, are used in [23] for capturing the eye regions, while an RGB camera records the visible face regions. Offline, a personalized 3D head model is constructed, and various head poses are recorded in a reference image data set. Head poses are tracked, and queried images are retrieved and synthesized with the camera images with accurate tracking of head motion, facial expression, and eye movement.

For completeness, we mention a recent paper [24], where filling in the HMD-occluded face region is done by using the information from a subject's face represented in RGB-D images. However, only a subject's head pose is taken into account. Changes in facial expressions and gaze behavior are not modeled. This makes the approach not yet suitable for conveying social cues during communication.

4 Conclusions

We discussed the importance of nonverbal cues in human–human interaction, how their generation, display, and perception are hindered by AR technology. Many approaches to recover nonverbal communication cues can be distinguished. This is an ongoing research topic that is not only important in the context of AR technology but also in the more general context of wearables, whether they are handheld, head-worn, on the wrist, or in clothes. In the research that was discussed, we see the influence of advancing technology on how the problem can be tackled, from the maker and craft approaches to the use of advanced and miniature sensors integrated into HMDs. We also see the lack of attention to other, non-HMD-oriented technology to measure affective and cognitive states of the interactants and use that information in the repair of occluded nonverbal communication cues. This other technology includes the use of head-worn EEG scalp or ear sensors, headbands with pressure sensors, or physiological sensors that help to indicate stress or attention. Moreover, AR interactions take place in smart environments, and the users and their devices become part of the Internet of Things (IoT) so that more information about users and their activities is known and can be used to support them.

References

1. Brunet, P.M., Cowie, R., Heylen, D., Nijholt, A., Schröder, M. (eds.): Special issue on conceptual frameworks for multimodal social signal processing. J. Multimodal User Interfaces **6**(3–4), 95–99 (2012)
2. Sacks, H., Schegloff, E.A., Jefferson, G.: A simplest systematics for the organization of turn-taking for conversation. Language **50**(4), 696–735 (1974)
3. Sun, X., Lichtenauer, J., Valstar, M., Nijholt, A., Pantic, M.: A multimodal database for mimicry analysis. In: D'Mello, M. et al. (eds.) Affective Computing and Intelligent Interaction (ACII 2011), vol 6974, pp. 367–376. LNCS, Springer, Berlin, Germany (2011)
4. Nijholt, A., Reidsma, D., van Welbergen, H., op den Akker, R., Ruttkay, Z.: Mutually coordinated anticipatory multimodal interaction. In: Esposito, A. et al. (eds.) Verbal and Nonverbal Features of Human–Human and Human–Machine Interaction, vol 5042, pp. 70–89. LNCS, Springer, Berlin, Germany (2008)
5. Yang, B., Wu, J., Hattori, G.: Facial expression recognition with the advent of face masks. In: 19th International Conference on Mobile and Ubiquitous Multimedia, pp. 1–3. ACM, New York, USA (2020)
6. Carbon, C.-C.: Wearing face masks strongly confuses counterparts in reading emotions. Front. Psychol. **11**, 566886 (2020). https://doi.org/10.3389/fpsyg.2020.566886
7. Scheirer, J., Fernandez, R., Picard, R.W.: Expression glasses: a wearable device for facial expression recognition. In: CHI '99 Extended Abstracts on Human Factors in Computing Systems (CHI EA '99), pp. 262–263. ACM, New York, USA (1999)
8. Masai, K., Sugiura, Y., Ogata, M., Kunze, K., Inami, M., Sugimoto, M.: Facial expression recognition in daily life by embedded photo reflective sensors on smart eyewear. In: 21st Conference on Intelligent User Interfaces, pp. 317–326. ACM, New York, USA (2016)
9. Mai, C., Rambold, L., Khamis, M.: TransparentHMD: revealing the HMD user's face to bystanders. In: 16th International Conference on Mobile and Ubiquitous Multimedia (MUM '17), pp. 515–520. ACM, New York, USA (2017)
10. Chan, L., Minamizawa, K.: FrontFace: facilitating communication between HMD users and outsiders using front-facing-screen HMDs. In: 19th International Conference on Human-Computer Interaction with Mobile Devices and Services (MobileHCI '17). Article 22, pp. 1–5. ACM, New York, USA (2017)
11. Takemura, M., Ohta, Y.: Diminishing head-mounted display for shared mixed reality. In: Proceedings International Symposium on Mixed and Augmented Reality, pp. 149–156. Darmstadt, Germany (2002)
12. Hartmann, J., Yeh, Y.-T., Vogel, D.: AAR: augmenting a wearable augmented reality display with an actuated head-mounted projector. In: Proceedings of the 33rd Annual ACM Symposium on User Interface Software and Technology (UIST '20), pp. 445–458. ACM, New York, USA (2020)
13. Jansen, P., Fischbach, F., Gugenheimer, J., Stemasov, E., Frommel, J., Rukzio, E.: ShARe: enabling co-located asymmetric multi-user interaction for augmented reality head-mounted displays. In: 33rd Annual ACM Symposium on User Interface Software and Technology (UIST '20), pp. 459–471. ACM, New York, USA (2020)
14. Frueh, C., Sud, A., Kwatra, V.: Headset removal for virtual and mixed reality. In: ACM SIGGRAPH 2017 Talks (SIGGRAPH '17), Article 80. ACM, New York, USA (2017)
15. Li, H., Trutoiu, L., Olszewski, K., Wei, L., Trutna, T., Hsieh, P.-L., Nicholls, A., Ma, C.: Facial performance sensing head-mounted display. ACM Trans. Graph. **34**(4), 47 (2015)
16. Olszewski, K., Lim, J.J., Saito, S., Li, H.: High-fidelity facial and speech animation for VR HMDs. ACM Trans. Graph. **35**, 6, Article 221 (2016)
17. Suzuki, K., Nakamura, F., Otsuka, J., Masai, K., Itoh, Y., Sugiura, Y., Sugimoto, M.: Recognition and mapping of facial expressions to avatar by embedded photo reflective sensors in head-mounted display. In: IEEE Virtual Reality, pp. 177–185. Los Angeles, CA, USA (2017)

18. Hickson, S., Dufour, N., Sud, A., Kwatra, V., Essa, I.: Eyemotion: classifying facial expressions in VR using eye-tracking cameras. In: IEEE Winter Conference on Applications of Computer Vision, pp. 1626–1635. Waikoloa Village, HI, USA, (2019)
19. Burgos-Artizzu, X.P., Fleureau, J., Dumas, O., Tapie, T., LeClerc, F., Mollet, N.: Real-time expression-sensitive HMD face reconstruction. In: SIGGRAPH Asia 2015 Technical Briefs (SA '15). Article 9, pp. 1–4. ACM, New York, USA (2015)
20. Orts-Escolano, S. et al.: Holoportation: virtual 3D teleportation in real-time. In: Proceedings of the 29th Annual Symposium on User Interface Software and Technology (UIST '16), pp. 741–754. ACM, New York, USA (2016)
21. Rekimoto, J., Uragaki, K., Yamada, K.: Behind-the-mask: a face-through head-mounted display. In: Proceedings of the 2018 International Conference on Advanced Visual Interfaces (AVI '18), Article 32, pp. 1–5. ACM, New York, USA (2018)
22. Chiba, M., Yamada, W., Manabe, H.: Transparent mask: face-capturing head-mounted display with IR pass filters. In: The 31st Annual ACM Symposium on User Interface Software and Technology Adjunct Proceedings (UIST '18 Adjunct), pp. 149–151. ACM, New York, USA (2018)
23. Zhao, Y., Xu, Q., Chen, W., Du, C., Xing, J., Huang, X., Yang, R.: Mask-off: synthesizing face images in the presence of head-mounted displays. In: 2019 IEEE Conference on Virtual Reality and 3D User Interfaces (VR), pp. 267–276 (2019)
24. Numan, N., Haar, F., Cesar, P.: Generative RGB-D face completion for head-mounted display removal. In: IEEE Conference on Virtual Reality and 3D User Interfaces Abstracts and Workshops (VRW), pp. 109–116 (2021)

A Smart and Secure IoMT Tele-Neurorehabilitation Framework for Post-Stroke Patients

Soumya Kanti Manna [ORCID]**, M. A. Hannan Bin Azhar, and Mohamed Sakel**

Abstract COVID-19 pandemic adversely challenged the healthcare system in an unprecedented way. Access to neurorehabilitation programme for patients with stroke and other neurological disability was severely restricted including shutting down of most community-based and outpatient facilities. There is hardly any organised virtual programme of exploring any potential of stretching and exercising of muscles needed in a rehabilitation programme. There is an impetus to innovate service developments, while the risks and fear of contracting the coronavirus remain prevalent. We propose a framework for developing a novel tele-neurorehabilitation system that will guide the patients to perform therapeutic exercises, as proposed by the clinicians, remotely. The system will allow patients to directly interact with doctors through a secure audio–video online portal. Wearable motion tracking sensors will be integrated within a hardware-based home setting for gathering performance data live from patients while they are performing exercises. The paper describes the design components of the framework justifying the tools, hardware, and protocols required to implement a secure online portal for tele-neurorehabilitation. Specifications of the core architectural layers have been reported. Some preliminary work demonstrates how the framework specifies capturing and analysing of physiological data using wearable sensors, as well as displaying of gait parameters on a software dashboard.

Keywords Tele-neurorehabilitation · Stroke · Joint parameters · IoMT

S. K. Manna (✉) · M. A. H. Bin Azhar
School of Engineering, Technology and Design, Canterbury Christ Church University, Canterbury, UK
e-mail: soumyakanti.manna@canterbury.ac.uk

M. A. H. Bin Azhar
e-mail: hannan.azhar@canterbury.ac.uk

M. Sakel
East Kent Hospitals University NHS Foundation Trust, Kent, UK
e-mail: msakel@nhs.net

1 Introduction

COVID-19 pandemic adversely impacted post-stroke rehabilitation for a number of reasons including diverting clinicians to urgent COVID care, closure of outpatient and community-based programmes to reduce infections and fear of disabled patients to attend hospitals. World Health Organization (WHO) estimated the total number of new COVID-19 cases to be more than 1.3 billion with 27 million deaths worldwide [1]. Hospitals in UK prioritised care for COVID and emergency patients only [2]. Currently, there are 80 million stroke survivors in the world [3]. They require ongoing rehabilitation programme for reducing neuromotor disabilities. Such programmes were mostly shut down during the pandemic. Video-based consultations started quite early in the pandemic. However, there is no software tool to provide post-stroke therapies to patients remotely via telerehabilitation which would include rehabilitation exercises that are personalised, complex and interactive. The anticipated limitations and challenges for any apps to assist telerehabilitation would include design, usability, functionality and security features [4]. The scope of remote treatment using tele-medicine is widely accepted among healthcare professionals, as it facilitates real-time interaction between doctors and patients in a remote location [5]. During COVID pandemic, doctors and healthcare workers used several smartphone applications to provide diagnosis and instructions to patients virtually [6]. It reduces human contact and is safer, since it obviates the need for patients and carers to visit hospitals. Telerehabilitation could potentially enable doctors to provide patients with instructions, monitor the performance of patients and provide feedback quickly.

There are only a few projects so far to facilitate and explore telerehabilitation. Tan [7] conducted a telerehabilitation experiment on 52 stroke patients, where half of the patients experienced conventional in-person rehabilitation sessions, and the other half experienced telerehabilitation via video conferencing with a therapist. There was no difference in physical function and independence in movement among the two cohorts of patients, although the experiment only focused on one type of stroke and did not take severity into account. A study conducted by Sarsak [8] explored the effects of telerehabilitation on different sets of post-stroke patients with mobility impairments using videogame-based virtual reality rehabilitation system. They found that the therapist located 100 miles away could accurately assess the functional needs of patients and prescribe suitable devices for them. The system was conducted over the Internet with personal computer-based cameras. Another game-based telerehabilitation method was conducted using Kinect-based system (KiReS) [9]. The system could monitor patients, while they perform their assigned tasks using a Kinect sensor. Evaluations were carried out by an exercise recognition algorithm and presented to the user interface to allow feedback. However, all these telerehabilitation systems lack several necessary functionalities, such as assessing necessary joint parameters during an activity, e.g. gait, posture, spasticity, torques, stiffness, walking patterns, neuromotor functions and balances. These systems also lack storing and feeding real-time performance data to doctors and patients. None of these tools had proactive artificial intelligence (AI)-assisted prediction and guidance for estimating abnormalities

and recovery rate of users. A concern exists regarding full stack security at hardware and software levels. There is no such customised online guiding tool available for specific stroke-related therapy to influence joint spasticity and stiffness, which hinders recovery. It is possible to incorporate non-invasive wearable sensors and motion tracking sensors into an online tool for monitoring and recording patient's performance during therapy. To facilitate post-stroke therapy remotely, this paper reports a framework to develop a state-of-the-art telerehabilitation tool which not only guides patients for post-stroke therapy but also assesses their performances to estimate their recovery rates and patterns. It integrates three platforms together (standardised exercises, live audio–video interface with the rehabilitation expert and motion tracking sensor) to guide stroke patients through the rehabilitation training at patient's home. The tool will also include interactive game-based therapy, e.g. audio-visual (AV) guidance during exercises, group-based exercises, performance scores, etc., to increase motivation and engagement for patients to participate in the rehabilitation programme.

2 Design Framework

The framework (Fig. 1) represents a secure online platform for patients, doctors, healthcare workers and technical support providers to be connected supporting telerehabilitation. A novel tele-neurorehabilitation tool will be developed where specific exercises will be shown to patients without involving rehabilitation experts, instead post-stroke therapy will be guided by an AI-assisted software. The list of specific exercises required for stages of rehabilitation, guidelines, and instruction for delivering the exercises will be prepared by the rehabilitation experts at the East Kent Hospitals University NHS Foundation Trust, UK. All types of exercises will be programmed into this online tool using simulated avatar's movement. In case patients need any help, they can still contact the experts using a live AV feed through a secure channel.
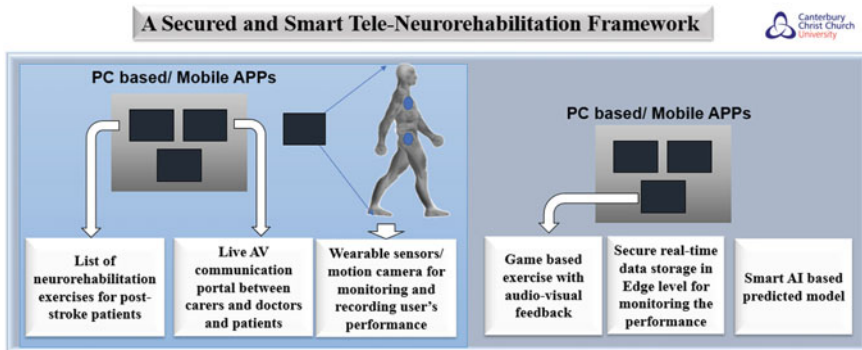
Fig. 1 Tele-neurorehabilitation tool

Non-invasive wearable sensors and motion capture cameras will be connected to the rehabilitation tool for acquiring and recording patient's performance during the therapy. Recorded data can be further compared with optimum parameters, and a predictive model will be developed using machine learning algorithm to estimate the recovery rate for an individual patient. Thus, in the process of therapy, it is possible to consistently assess recovery by comparing performances between present and past health conditions.

Due to the capture of patient's sensitive data by the tele-neurorehabilitation tool, appropriate security design must be incorporated in the framework. Figure 2 shows three layers of the system: device, edge and cloud, and the framework includes security components in all of these three layers. Device layer refers to the hardware level of the Internet of Medical Things (IoMT) solution, where hardware architecture-level security will be implemented by incorporating a secure crypto processor and secure booting technique to ensure system integrity to stop unauthorised modifications of data and the system environment [10]. Physical protection barrier will be also implemented by using physical shielding covering internal circuitry.

Due to sensitive nature of the data, while data are processed in transit (e.g. over the physical and network layer before reaching to cloud), unsecure communication can be susceptible to intrusions such as the man-in-the-middle attack; so, it is important that the framework should include strong secure encryption techniques and an automated intrusion prevention system to detect unwanted intrusions and prevent malicious activities. A distributed system will be used where patient's data will be stored in an edge node, and healthcare providers will request for data with a secure transactional ID in real-time [11] through a cloud-based web portal. As patient's data are pulled on request, the profile information will be created dynamically on a cloud-based dashboard. The proposed distributed architecture for data storage and processing in the edge layer will have advantage over a centralised cloud-based solution, as the latter is prone to denial-of-service (DoS) attacks, where attackers can easily flood the system and attempt to shut down the server. The proposed secure distributed architecture will prevent DoS attack ensuring better response time of the systems.
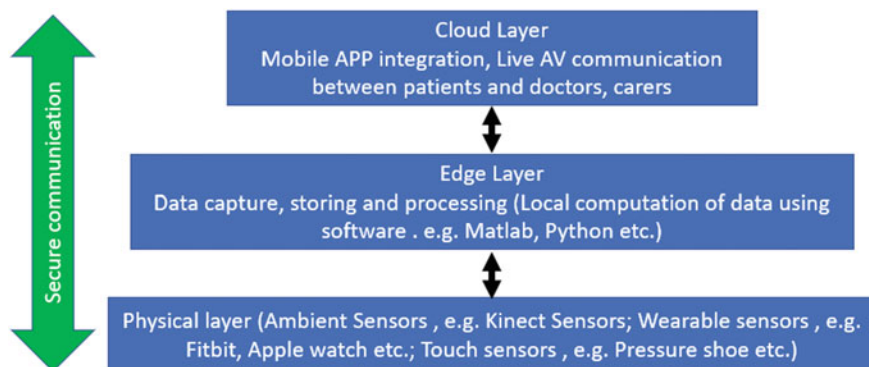
Fig. 2 Three layers of framework

2.1 Physical Layer

Physical layer (or ground layer) may consist of several physical sensors (Fig. 3), such as Kinect sensor [12], Intel depth camera [13], pressure sensor [14] and inertial measurement unit (IMU) sensors [15]. This array of sensors will be connected to an embedded controller for acquiring and recording patient's performance during the therapy. An insole pressure shoe consisting of force sensors and IMU will be developed for measuring gait analysis of users, such as profiling of strike and swing phases [14]. To demonstrate the measurement of the gait data during strike phase, we have developed a force plate (Fig. 4) consisting of four force sensitive registers (FSRs) connected at four major points under the feet.

Figure 4 shows the points under the feet where four sensors were connected: heel (FH), first and fifth metatarsal bones ($F1$, $F5$) and toe (FT). These locations are the most critical points for estimating gait cycle such as (1) heel strike, (2) foot flat, (3) heel-off and (4) toe-off [14]. These sensors will be used for measuring the distributed force under feet due to body weight while walking. As shown in Fig. 4, all FSRs are connected to analog pins of Arduino board using potentiometers. The voltage drop across the variable terminal of potentiometer has been measured and calibrated against the known force. Use of Arduino is feasible for developing the prototype system as it usually takes 0.1 ms (millisecond) to read the signal from force sensors. The pressure range of the force sensors is around 0–175 psi, and the force accuracy is $\pm 5 - \pm 25\%$ [16].

Kinect sensor will track human body joints and reflects joint vectors of a user. Currently, the new version of Kinect sensor $V2$ can track six people at a time and estimates 3D position of 25 joints of each user. The recorded data will be analysed
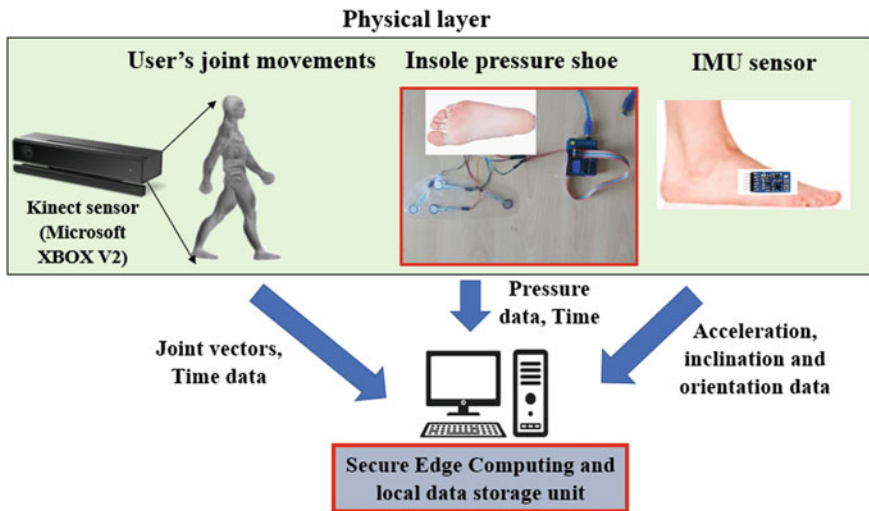
Fig. 3 Physical layer
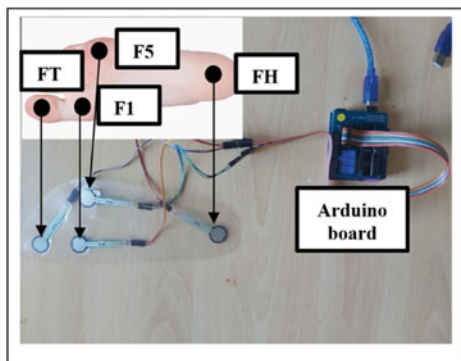
Sensor points	
FT	Force sensor at Toe
F1	Force sensor at first metatarsal bones
F5	Force sensor at fifth metatarsal bones
FH	Force sensor at Heel

Fig. 4 Force plate and its circuit diagram

to generate important joint parameters (angle, velocity, posture, stiffness, spasticity, jerk and torque) as shown in Table 1. Combining the sensor data will make it possible to measure a patient's health status continuously.

2.2 Edge Layer

Edge layer (Fig. 5) will convert raw user's data into clinically useful information. This layer can be used for local computation along with filters and computing algorithms. The user's interaction model will provide a list of specific biomechanical exercises for stages of rehabilitation, and clinicians from the hospital will recommend the required therapy to influence joint spasticity and stiffness based on user's agreement and previous activities. User's performance data will be stored at the edge level. Historic patterns in the data will be analysed to train an artificial intelligence model to predict and guide the rate of recovery to the patients. The edge layer will also push notifications to doctor's critical conditions of patients, such as when joint parameters exceed a threshold limit. Due to distributed nature, several edge nodes can be connected and synchronised in this layer.

Preliminary work has already been done on how to create virtual reality-based rehabilitation game [12] and to analyse the recorded data for extracting important joint parameters [17]. Figure 6 demonstrates an example graphical user interface (GUI), which has been developed in a MATLAB platform. There are two sections in the GUI: user exercise module (UEM) and data monitor (DM). The UEM section is used for showing specific post-stroke exercise to patients and camera feed for recording user's activities, whereas the DM section is used for displaying and recording user's performance through wearable sensors and Kinect sensor. Patients will be able to view the exercises as integrated animations or videos to show the standard way to perform them. The platform also includes interesting features to enhance

Table 1 Measurable joint parameters

Joint parameters	Computation method	Sensor involved
Angle	Computed from the recorded 3D vectors of user's joints	Kinect sensor
Velocity	Computed by differentiating the joint angle with reference to time	Kinect sensor
Acceleration	Computed by differentiating the joint velocity with reference to time	Kinect sensor
Posture	Estimated by connecting adjunct joint vectors	Kinect sensor
Workspace	Computed by collecting the reachable Cartesian coordinates in 3D space	Kinect sensor
Torque	Calculated from rigid body dynamics of human body where the information of segment mass of user, distance of the centre of gravity are measured from user's anthropometric data, and joint parameters are measured from Kinect sensor	Kinect sensor
Jerk	Computed from the sudden change of joint torque over time	Kinect sensor
Stiffness	Calculated from joint torque and rotation angle	Kinect sensor
Spasticity	Computed from muscle contraction which depends on the stiffness or tightness of muscles	Kinect sensor
Gait (strike phase)	Accessed from pressure data using force sensors fitted under foot in an insole during strike phase	Foot pressure sensor
Gait (swing phase)	Calculated from joint velocity, acceleration, orientation and inclination measured by IMU sensor	IMU sensor
Walking pattern	Accessed from the combination of pressure data, acceleration and orientation	Foot pressure and IMU sensor
Footsteps	Computed from heel strike with respect to time frame	Foot pressure and IMU sensor
Foot orientation	Measured from the acceleration and digital compass attached to IMU sensor	IMU sensor

patient engagement in exercises, such as game-based activities. Audio-visual feedback will be incorporated into the game window, where users will be prompted with feedback when physiological parameters from sensors (Kinect + FSR + IMU) and user's voice are inputted.

The bottom left graphs inside the GUI (Fig. 6) shows the real-time pressure sensor data from four force sensors placed at the heel (FH), first and fifth metatarsal bones ($F1$, $F5$) and the toe (FT) as detailed in Fig. 4. The response time of these sensors is
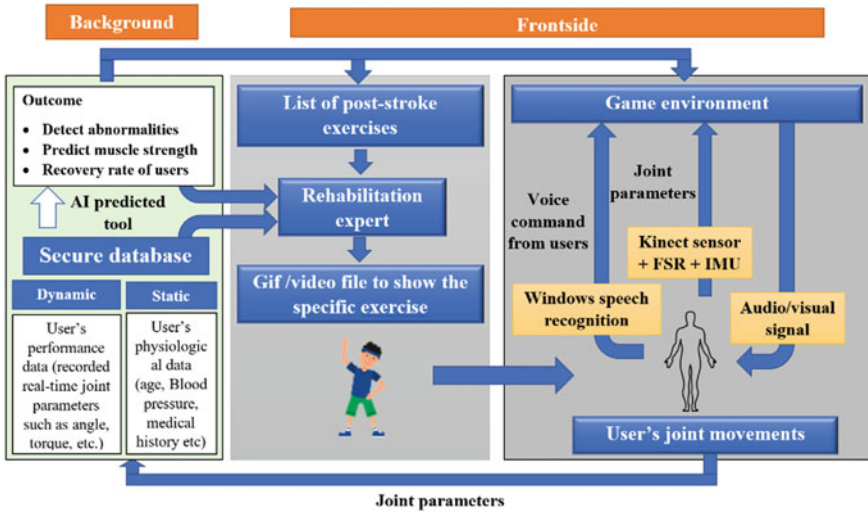
Fig. 5 Edge layer
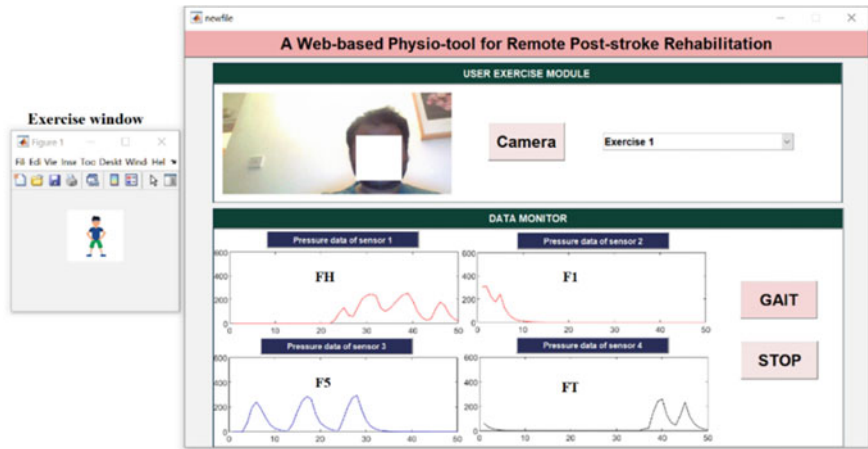
Fig. 6 Demonstration of graphical user interface (GUI)

near about 1–2 ms. The plots in the GUI demonstrate how the sensors work; however, it does not represent any gait information as we have not conducted any experiments with human subjects yet.

2.3   Cloud Layer

Healthcare professionals will use the cloud-based interface (e.g. web portal) to initiate secure connections and transaction with the edge node to pull patient data securely so that patient's profile will be created dynamically in the web portal. The cloud layer will also include necessary mobile APPs integration and live AV communication between patients and doctors. Through online remote connectivity, clinical instructors and rehabilitation therapists can guide patients on how to operate the system and/or initialise any initial parameters of the system. Cloud interface will also provide remote access for technical support and ensures security, system updates and maintenance. Through the web portal clinicians are able to view patients' health data and assess their progress. The system will allow doctors to select specific data and convert it into a portable format for secure electronic transfer of files to the hospital.

3   Conclusion

Currently, we are working in collaboration with the clinicians to develop a prototype system to evaluate the efficacy, usability and feasibility of the rehabilitation tool. After thorough evaluation of the system, the tele-neurorehab tool will be rolled out to the clinical trial phase once appropriate ethical approvals are being sought. Ethics play an important role in the application of tele-technologies to neurological conditions because several issues are associated with it, such as user privacy, accessibility, equity, social isolation, stress and mental and physical health [18]. Patient's empowerment should not be compromised while considering cost cutting through online tool. Relationships between clinicians, patients and family and/or carers can influence the rehabilitation process significantly. Therefore, ethical approval will be considered before starting any trials with human subjects, and informed consent will be taken from patients before the commence of clinical trial.

The proposed tele-neurorehabilitation tool can guide stroke patients assisting with the required exercises without the need for face-to-face interactions with the clinicians, especially during a pandemic. But the solution can be sustainable even after the pandemic is over as it cuts down cost for care considerably. The success of this tool depends on the assurance of privacy and security. The proposed framework ensures that the security measures are in place across all levels of the system (device, edge and cloud). Since the user's performance data will be stored in its secured internal memory and with all the secure protocol stacks installed, the framework will not be vulnerable to cyberattacks or network intrusions. The user interaction model will also integrate features such as online game-based therapy and group exercises to enhance patient engagement. By using the patients' performance data, a predictive model will be developed to guide the dose and duration of exercises, as well as estimate the recovery rate of patients. Implementation of the framework will significantly reduce the costs associated with post-stroke rehabilitation by allowing more patients to be

supported by fewer staff with the help from AI-enabled software. In addition, using the tool clinicians can reach out to patients globally, especially to those living in low- and middle-income countries. And finally, use of the tool will reduce carbon foot-prints significantly by offering a full-service rehab to post-stroke patients entirely online.

References

1. Roser, M., Ritchie, H., Ortiz-Ospina, E., Hasell, E.: Coronavirus pandemic (COVID-19). https://ourworldindata.org/coronavirus. Last accessed 2021/06/14
2. Rowe, F., Hepworth, L., Howard, C., Lane, S.: Orthoptic services in the UK and Ireland during the COVID-19 pandemic. Br. Irish Orthoptic J. **16**(1) (2020)
3. Gorelick, P.B.: The global burden of stroke: persistent and disabling. Lancet Neurol. **18**(5), 417–418 (2019)
4. Chidambaram, S., Erridge, S., Kinross, J., Purkayastha, S.: Observational study of UK mobile health apps for COVID-19. Lancet Digital Health (2020)
5. Jnr, B.A.: Use of telemedicine and virtual care for remote treatment in response to COVID-19 pandemic. J. Med. Syst. **44**(7), 1–9 (2020)
6. Iyengar, K., Upadhyaya, G.K., Vaishya, R., Jain, V.: COVID-19 and applications of smartphone technology in the current pandemic. Diabetes Metab. Syndr.: Clin. Res. Rev. (2020)
7. Tan, C.O.: Is remote rehabilitation after stroke as effective as conventional therapy? Neurology **95**(17), 2462–2464 (2020)
8. Sarsak, H.I.: Telerehabilitation services: a successful paradigm for occupational therapy clinical services? Int. Phys. Med. Rehabil. J. **5**(2), 93–98 (2020)
9. Anton, D., Berges, I., Bermúdez, J., Goñi, A., Illarramendi, A.: A telerehabilitation system for the selection, evaluation and remote management of therapies. Sensors **18**(5), 1459 (2019)
10. Lu, D., et al.: xTSeH: a trusted platform module sharing scheme towards smart IoT-ehealth devices. IEEE J. Sel. Areas Commun. **39**(2), 370–383 (2021)
11. Bilal, M.A., Hameed, S.: Comparative analysis of encryption techniques for sharing data in IoMT devices. Am. J. Comput. Sci. Inf. Technol. **8**(46) (2020)
12. Dubey, V.N., Manna, S.K.: Design of a game-based rehabilitation system using Kinect sensor. In: Frontiers in Biomedical Devices (2019)
13. Siena, F.L., Byrom, B., Watts, P., Breedon, P.: Utilising the intel realsense camera for measuring health outcomes in clinical research. J. Med. Syst. **42**(3), 1–10 (2018)
14. Ngueleu, A.M., Blanchette, A.K., Bouyer, L., Maltais, D., McFadyen, B.J., Moffet, H., Batcho, C.S.: Design and accuracy of an instrumented insole using pressure sensors for step count. Sensors **19**(5), 984 (2019)
15. Anwary, A.R., Yu, H., Vassallo, M.: An automatic gait feature extraction method for identifying gait asymmetry using wearable sensors. Sensors **18**(2), 676 (2018)
16. Adafruit: https://learn.adafruit.com/force-sensitive-resistor-fsr/overview. Last accessed 2021/06/14
17. Manna, S.K., Dubey, V.N.: Assessment of joint parameters in a Kinect sensor based rehabili-tation game. In: International Design Engineering Technical Conferences and Computers and Information in Engineering Conference, vol. 59179, ASME, USA (2019)
18. Mackenzie, R., Sakel, M.: Teleneurology: ethics of devolving responsibilities from clinicians to families and/or carers. Br. J. Neurosci. Nurs. **7**(2), 490–493 (2011)

Machine Learning Based Prediction of COVID-19 Infection in India

Soumit Das, Tuhin Das, Jaydip Nandi, and Arijit Ghosh

Abstract The novel coronavirus (COVID-19) infection had spread throughout the globe since the beginning of 2020 giving rise to a pandemic situation. In this paper, attempts have been made to model the COVID-19 infection in India using exponential, logistic and Gompertz-based mathematical machine learning regression models. These predictive methods show an excellent fit with the daily count of confirmed cases for the period between January 30, 2020, and February 3, 2021. The mean squared logarithmic error (MSLE) of the Gompertz model being lowest among the three machine learning regression methods considered in this paper making it ideal at least as a case study for future predictions in Indian scenario. Nevertheless, the epidemiologists, healthcare personnel, or other Government authorities may use this study as a reference for future planning in prevention of such pandemic situation in similar developing nations.

Keywords COVID-19 · SARS-CoV-2 · Pandemic · Machine learning regression · Logistic model · Exponential model · Gompertz model

1 Introduction

The recent outbreak of coronavirus disease (COVID-19) [1] has become a severe health threat to human civilization post-2003 severe acute respiratory syndrome (SARS) pandemic and 2012 Middle East respiratory syndrome (MERS) pandemic. The first case of COVID-19 was posted on December 29, 2019. Gradually, it spread all over the world, and the World Health Organization (WHO) finally proclaimed the disease as an epidemic on March 11, 2020.

S. Das · T. Das · J. Nandi · A. Ghosh (✉)
Department of Applied Electronics and Instrumentation Engineering, RCC Institute of Information Technology, Canal South Road, Kolkata 700015, India

India had posted its first COVID-19 case on January 30, 2020, in the state of Kerala. As of 3rd February, 2021, India has reported 10,791,056 number of confirmed cases, out of which 10,479,346 has recovered and 154,151 died due to the pandemic [2]. The symptoms for this disease range from fever, dry cough, body pain, breathlessness for pneumonia and failure of kidney and can take up to 2–14 days to appear [3]. Some patients have not shown any symptoms as they are asymptomatic, and this type of cases is very dangerous for spreading the virus and very difficult to trace out. One of the important tools to analyze real-time data of the virus is statistical models. In this paper, exponential, logistic and Gompertz regression models have been used to analyze the epidemic status in India. The modeling, analysis and prediction presented here are based on the data, which is taken from the Ministry of Health and Family Welfare (MoHFW), Government of India (GoI), from January 30, 2020, to February 3, 2021 [4].

2   Related Literatures

Many models like deterministic mass action model, Bayesian network, regression models, SEIR model, prediction rules, ARIMA forecasting model, etc., are used in many research papers. [5]. The current evaluation includes classic SIR and SEIR models for predicting the transmission of a pandemic [6]. Interpretation of Ebola epidemic happened in 1995 [7] and 2014 [8], and recently, occurred SARS epidemic of 2003 [9] was done by these models. The SEIR model to analyze the control measures established soon with some moderation [10]. It seems to be unnecessary that SIR and SEIR models are controlled by the constraint of susceptible population as in case of COVID-19 [11].

Another work shows a control model for COVID-19 by using fuzzy dynamical system, which is analyzed based on granular differentiability [12]. Population infected by COVID-19 can be identified by fuzzy model using linguistic information of a COVID-19 susceptible person [13]. The future behavior tendency for a short term has been done by evaluating the curve pattern during the last days [14]. For brief forecasting of the COVID-19 pandemic, dynamic mathematical growth models have been compared in [15]. Gompertz function [16] is another similar growth model where the saturation of the growth factor is linear to the Verhulst equation. These functions being similar are used many times in the representation of epidemics and particularly for observing various epidemic situations [17].

3   Methodology Used

The three mathematical functions, i.e., exponential, logistic and Gompertz methods, have been employed in this study to model the epidemic spread in India.

3.1 Exponential Model

Thomas Robert Malthus (1766–1834) was the first to observe that any species can increase potentially in a number according to a geometric series [18]. The generalized exponential model for an infection outbreak can be expressed as

$$N(t) = N(t_0)e^{g(t-t_0)} \tag{1}$$

where

- $N(t)$ represents the count of contamination at time t;
- $N(t_0)$ represents the count of contamination at time t_0;
- g represents growth rate;
- t refers time (in days);
- e represents Euler's Number (e = 2.71828 …).

Growth rate of the infection will not be exponential forever; the slope shall decrease and eventually become logistically shaped curve after some time.

3.2 Logistic Model

Belgian mathematician Pierre Verhulst proposed logistic growth to model the population growth [19] in 1838. The model can be expressed as

$$y(x) = \frac{c}{1 + e^{-(x-b)/a}} \tag{2}$$

3.3 Gompertz Model

Another special case of generalized logistic function used to describe human mortality was proposed in 1825 by Benjamin Gompertz [16]. The analytical expression of this model is

$$y(x) = ce^{-be^{-x/a}} \tag{3}$$

where (for Eq. 2 and 3):

- a represents speed of the infection;
- b represents the day when the highest infections took place (i.e., halfway point);

- c represents the total count of noted infections at the end;
- e represents Euler's Number (e = 2.71828 …).

Rate of infection growth, $r = \frac{1}{a}$

3.4 R^2 Score

If the forecast value of ith sample is $\hat{y}$, and the corresponding true value is y_i for total n samples, the calculated R^2 score is described as

$$R^2(y, \hat{y}) = 1 - \frac{\sum_{i=1}^{n}(y_i - \hat{y}_i)^2}{\sum_{i=1}^{n}(y_i - \overline{y})^2} \tag{4}$$

where

$$\overline{y} = \frac{1}{n}\sum_{i=1}^{n} y_i$$

3.5 MSLE

If the forecast value of ith sample is $\hat{y}$, and the corresponding true value is y_i, then the MSLE calculated over n_{samples} is described as

$$\text{MSLE}(y, \hat{y}) = \frac{1}{n_{\text{samples}}} \sum_{i=0}^{n_{\text{samples}}-1} \left(\log_e(1 + y_i) - \log_e(1 + \hat{y}_i)\right)^2 \tag{5}$$

4 Data Analysis

The daily time series data of COVID-19 confirmed cases has been taken from the MoHFW, GoI [4], out of which data from 30th January, 2020 to 3rd February, 2021 were used for modeling, whereas, data from 4th February, 2021 to 15th February, 2021 were used for testing the prediction to achieve decent accuracy calculation. On January 30, 2020, India posted its first COVID-19 case, which was considered as day $(n) = 1$ in this study. The daily cumulative data of confirmed COVID-19 cases across India for the period of this study is shown in Fig. 1.

Fig. 1 COVID-19
confirmed cases (cumulative)
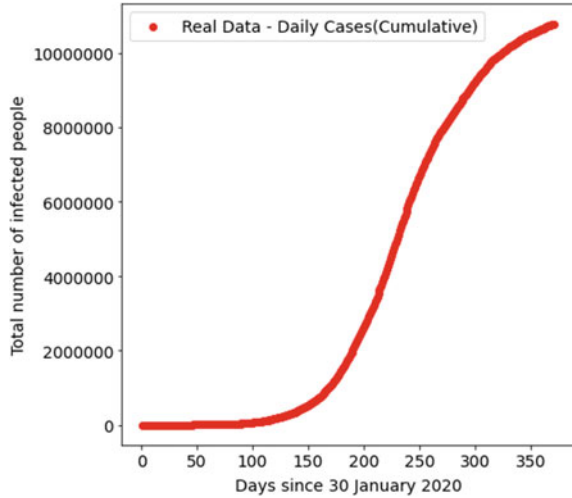
Table 1 COVID-19 daily dataset

Date	Day (n)	Total confirmed cases	Daily growth (%)	Growth factor
30th Jan, 2021	367	10,747,024	0.12	1.001
31st Jan, 2021	368	10,758,551	0.11	0.882
1st Feb, 2021	369	10,767,130	0.08	0.744
2nd Feb, 2021	370	10,778,131	0.1	1.282
3rd Feb, 2021	371	10,791,056	0.12	1.175
		Average	0.11	1.017

The average growth factor (i.e., 1.017) is greater than 1, which indicates that the growth is still in the exponential phase, but at the same time, average daily growth is very low (i. e., 0.11%) (Table 1) which means that the curve is flattening. As the growth factor is somewhat stable and will gradually saturate, the curve looks like a "sigmoid function".

5   Results and Predictions

The training dataset is applied on the exponential model (Eq. 1) to obtain the resulted infection rate (g) to be around 0.0016.

Figure 2 shows the curve fitting of the training dataset on the model with R^2 score of -0.897, which indicates a decent fit. This model exhibits that the COVID-19 infection in India has left the exponential phase and moved toward the logistic phase. The calculated MSLE as per Eq. 5 for this model is 21.476.

Fig. 2 Exponential model
curve fitting (R^2 0.897)
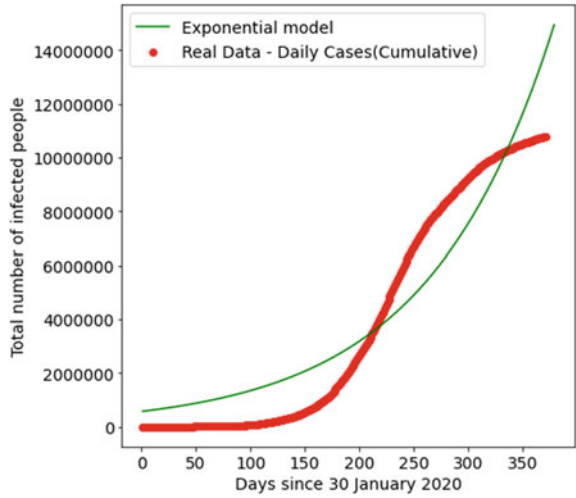
Since a pandemic cannot continue exponentially forever, the logistic model is used to predict the flattening of the curve and obtainment of the infection rate (r) to be around 0.032.

Figure 3 shows curve fitting of the logistic model with an R^2 score of 0.999, which indicates a good fit. The calculated MSLE as per Eq. 5 for this model is 8.051.

Gompertz model is a special logistic model, which shows slower growth at the starting and ending phase. Infection rate (r) is found to be around 0.018 after application of the dataset on the model.

Fig. 3 Logistic model curve
fitting (R^2 0.999)
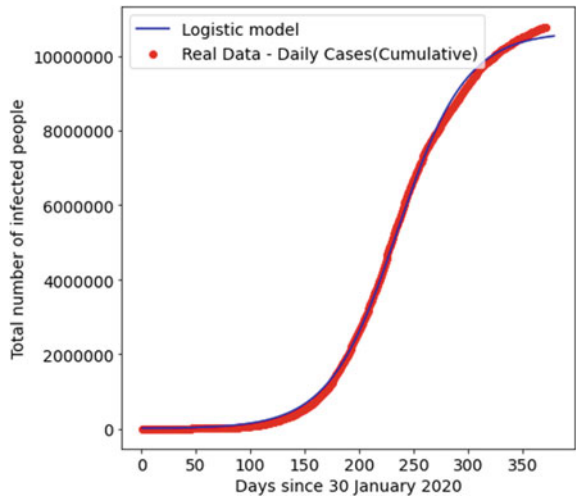
Fig. 4 Gompertz model
curve fitting (R^2 0.999)
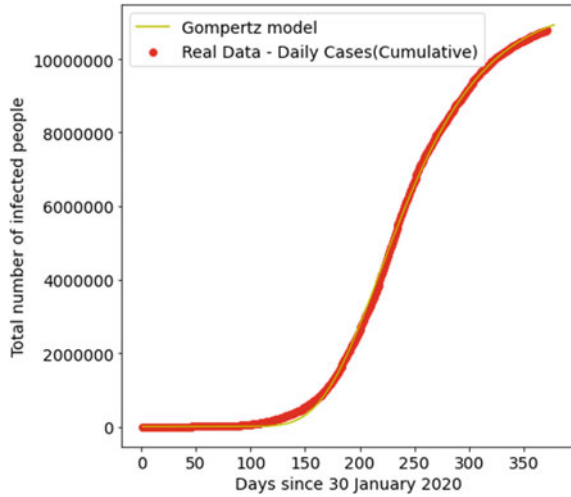
Figure 4 shows curve fitting of the Gompertz model with R^2 score of 0.999, which indicates the best fit. This model is able to follow the curve with most accuracy. Calculated MSLE as per Eq. 5 for the Gompertz model is 7.074.

Table 2 shows the R^2 score of 0.897, 0.999 and 0.999 for exponential, logistic and Gompertz model, respectively, which indicates a good fit for the provided dataset. MSLE of the Gompertz model is 7.074, which is lowest among all considered models. Hence, the Gompertz model gives the best results in this study in comparison with others.

The models are then used to forecast the number of cases for the period from February 4, 2021, to February 15, 2021, and are validated with the test dataset to determine its accuracy. As the curve fitting of the exponential model is not decent enough, it has not been used for predictions. The results of logistic and Gompertz are presented in Table 3, respectively.

The accuracy for future case prediction of the Gompertz model is highest followed by the logistic model as observed here.

Table 2 Model parameters

Model	R^2	MSLE	Infection rate (r)
Exponential	0.897	21.476	0.0016
Logistic	0.999	8.051	0.032
Gompertz	0.999	7.074	0.018

Table 3 Prediction dataset

Date	Actual confirmed cases	Logistic model		Gompertz model	
		Predicted confirmed cases	Error in prediction (%)	Predicted confirmed cases	Error in prediction (%)
February 4, 2021	10,803,457	10,519,098	−2.63	10,870,413	0.62
February 5, 2021	10,815,168	10,523,345	−2.7	10,882,140	0.62
February 6, 2021	10,827,237	10,527,462	−2.77	10,893,664	0.61
February 7, 2021	10,839,023	10,531,454	−2.84	10,904,988	0.61
February 8, 2021	10,847,738	10,535,324	−2.88	10,916,115	0.63
February 9, 2021	10,858,469	10,539,076	−2.94	10,927,048	0.63
February 10, 2021	10,871,008	10,542,712	−3.02	10,937,791	0.61
February 11, 2021	10,880,361	10,546,238	−3.07	10,948,347	0.62
February 12, 2021	10,892,498	10,549,655	−3.15	10,958,719	0.61
February 13, 2021	10,904,696	10,552,968	−3.23	10,968,909	0.59
February 14, 2021	10,916,402	10,556,179	−3.3	10,978,921	0.57
February 15, 2021	10,925,488	10,559,292	−3.35	10,988,758	0.58

6 Conclusion

In this study, three mathematical regression models are implemented to model the COVID-19 cases in India. The outcome of these models indicates a proper fit between the calculated data and actual data, as the R^2 scores are 0.897, 0.999 and 0.999 for exponential, logistic and Gompertz models, respectively. Despite of having decent accuracy of the Gompertz model in predicting the future cases, the predictions for longer term will be unreliable due to change in disease transmission pattern for different regions, increase in number of testing, mutation of coronavirus, etc. The spread of different COVID-19 [1] strains and recent spike of new cases in India, referred as the second wave, have not been considered while doing the predictions and can be part of our future investigations.

References

1. Coronavirus disease (COVID-19) pandemic WHO Homepage. https://www.who.int/emerge ncies/diseases/novel-coronavirus-2019. Last accessed 07-April-2021
2. Chauhan, P., Kumar, A., Jamdagni, P.: Regression analysis of COVID-19 spread in India and its different states. Cold Spring Harbor Laboratory (2020)
3. Gupta, R., Pandey, G., Chaudhary, P., Pal, S.K.: SEIR and regression model based COVID-19 outbreak predictions in India. Cold Spring Harbor Laboratory (2020)
4. Shukla, A.: Covid19 India: a crowdsourced initiative (2020). https://api.covid19india.org/csv/ latest/case_time_series.csv. Last accessed 07-April-2021.
5. Doms, C., Kramer, S.C., Shaman, J.: Assessing the use of influenza forecasts and epidemiological modeling in public health decision making in the united states. Sci. Rep. **8**(1), 1–7 (2018)
6. Anderson, R.M., May, R.M.: Infectious diseases of humans: dynamics and control. Oxford University Press (1992)
7. Lekone, P.E., Finkenstädt, B.F.: Statistical inference in a stochastic epidemic SEIR model with control intervention: Ebola as a case study. Biometrics **62**(4), 1170–1177 (2006)
8. Althaus, C.L.: Estimating the reproduction number of Ebola virus (EBOV) during the 2014 outbreak in West Africa. PLoS Curr. (2014)
9. Ng, T.W., Turinici, G., Danchin, A.: A double epidemic model for the SARS propagation. BMC Infect. Dis. **3**(19) (2003)
10. Riley, S., et al.: Transmission dynamics of the etiological agent of SARS in Hong Kong: impact of public health interventions. Science **300**(5627), 1961–1966 (2003)
11. Catala, M., et al.: Robust estimation of diagnostic rate and real incidence of COVID-19 for European policymakers. Cold Spring Harbor Laboratory (2020)
12. Khatua, D., De, A., Kar, S., Samanta, E., Seikh, A.A., Guha, D.: A fuzzy dynamic optimal model for COVID-19 epidemic in India based on granular differentiability (2020). Available at SSRN: https://ssrn.com/abstract=3621640
13. Majumder, S., Kar, S., Samanta, E.: A fuzzy rough hybrid decision making technique for identifying the infected population of COVID-19. Soft Comput. (2020). https://doi.org/10. 1007/s00500-020-05451-0
14. Anastassopoulou, C., Russo, L., Tsakris, A., Siettos, C.: Data-based analysis, modelling and forecasting of the COVID-19 outbreak. PLOS ONE **15**(3), e0230405 (2020)
15. Roosa, K., et al.: Short-term forecasts of the COVID-19 epidemic in Guangdong and Zhejiang, China. J. Clin. Med. **9**(2), 596 (2020)
16. Gompertz, B.: On the nature of the function expressive of the law of human mortality, and on a new mode of determining the value of life contingencies. Philos. Trans. R. Soc. Lond. **115**, 513–583 (1825)
17. Bürger, R., Chowell, G., Lara-Díıaz, L.Y.: Comparative analysis of phenomenological growth models applied to epidemic outbreaks. Math. Biosci. Eng. **16**(5), 4250–4273 (2019)
18. Malthus, T.R.: An essay on the principle of population: library of economics. J. Johnson (London) (1798)
19. Verhulst, P.F.: Notice sur la loi que la population poursuit dans son accroissement. Corresp. Math. Phys. **10**, 113–121 (1838)

Investigations on Characteristic Features of Cyclonic Storm 'MORA 2017' Through Radio Signal, Satellite and Radar Over the Bay of Bengal

Hirak Sarkar and Sudarshan Chakraborty

Abstract The coastal districts of West Bengal and Bangladesh observed tropical cyclones with the devastating consequences on socio-economic conditions of the affected region and the daily life of human beings. This study provides an understanding of localization, tracking, threat identification and characterization of cyclone and lightning associated with the cyclonic storm Mora 2017 over the Bay of Bengal. Three types of observations as derived from radio signal data recorded at Kolkata, satellite data of INSAT-3D enhanced imageries and the cyclone detection Doppler radar data have been considered for investigating the characteristic feature of the said cyclone. The radio receiver in the ELF and VLF bands recorded the EM wave radiated from the core of cyclone due to lightning discharges. Analyzing the observed data, we have been reported some interesting features noted during the cyclone Mora.

Keywords Radio signal · Satellite · Radar · Cyclonic storm · EM wave

1 Introduction

The cyclone Mora was the name suggested by Thailand, came from a Thai word, meaning 'star of the sea.' In this work, we have examined characteristic changes of tropical cyclone Mora experienced during the pre-monsoon month May 2017, and identified some interesting features using a combination of observations from radio signal in ELF/VLF (Extremely low frequency/Very low frequency) band, satellite imagery and data of cyclone detection Doppler Weather Radar. The investigation has been executed by dividing the life cycle of the TC (Tropical Cyclone) into various stages of intensification and weakening.

H. Sarkar (✉) · S. Chakraborty
Techno India University, Kolkata, West Bengal 700091, India

1.1 Previous Work Related to Tropical Cyclone

In the satellite period 1981–2020, Tropical Cyclone (TC) data have shown the intensity of the strongest Tropical Cyclones had increased tremendously over the northern Indian Ocean [1–3]. In fact, TCs in the Bay of Bengal and the Arabian Sea were grouped together. A subsequent observation reported that the Bay of Bengal Cyclones, in the post monsoon season, increased the intensity over the past 40 years which creates large-scale changes in ocean-atmospheric conditions [4, 5]. But, a large number of early studies of Bay of Bengal Tropical Cyclones pointed up on the post monsoon season. Most of the climatic phenomena which impact global climate at inter annual timescales, e.g., the El Niño–Southern Oscillation (ENSO) and Indian Ocean Dipole, tend to visible more strongly during winter. A significantly large-scale ocean-atmosphere state was observed for Tropical Cyclone development in the post monsoon Bay of Bengal during La Niña and the negative phase of the Indian Ocean [6, 7]. However, the impact on the surroundings, pre-monsoon TCs at inter annual timescales is not clearly noted. But, after the study of correlation between Niño 3.4 SST anomalies and the accumulated cyclone energy for the months of March–May in the pre-monsoon Bay of Bengal, ENSO is not having a proper impact on pre-monsoon Bay of Bengal Tropical Cyclones activity [8–11]. Scientist Emanuel collected data for a long period of time to calculate the Tropical Cyclone power dissipation index (PDI) and the intensification tendencies [10]. The power dissipation index for a season and for a particular tropical cyclone strength category, i.e., tropical storm, tropical cyclone, major tropical cyclone, is estimated as the sum of the cubes of the maximum wind speed at every 6 h. Tropical Cyclone location during the months of October–November is the maximum wind speed of the storm is within the range defined for the particular category [12–14]. During 1981–1995, it was observed that total of eight storms obtained Tropical Cyclone strength which was higher than total strength of 27 storms. Alternatively, between 1996 and 2010, 10 cyclones out of 24 tropical cyclones gained total strength or higher, causing a higher conversion rate of about 42%. A thrilling characteristic features of the Bay of Bengal Tropical Cyclone formation is the zonally asymmetry in nature. All seven sub-tropical cyclones take place in the Bay of Bengal in 90°E longitude. This geographical weakness of Tropical Cyclones can be credited to the longer time spent over the warm ocean for cyclonic storms which forms in the 90° E [2]. Moreover, it was executed that the frequency of storms during the two consecutive 15-year periods, 1981–1995 and 1996–2010, was statistically same. Moreover, further investigations exposed that the total occurring storm days were nearly the same for the above two consecutive periods. Again, the mean duration, of each Mid Troposphere Cyclone in Mid Troposphere Cyclone-phase during the 15-year period 1996–2010, was statistically identical from that during the 15-year period 1981–1995. Also, it was observed that the mean maximum intensity carries due to the storms during Mid Tropospheric Cyclonic phase increased with time. On an average, the maximum wind speed of storms during the first period 1981–1995 was nearly 54 ms^{-1}, category 3 and the mean maximum wind speed for storms during the second period 1996–2010 was about 62 ms^{-1}, category 4. Just

observing this authentication, it can be noted that the intensity of post monsoon Bay of Bengal cyclonic storms is increasing [15, 16].

2 Equipment Used for Measurements Related to Cyclone MORA

Three major equipment provided data for the present investigation. The first one is a Radio signal receiver; operating in our Laboratory at Techno India University, in the ELF and VLF bands which recorded EM wave radiated signal originating from the core of cyclone as radiation owing to lightning discharges. The second one is the satellite INSAT-3D enhanced imageries and the third is the real-time data as derived from the cyclone detection Doppler radar. We have used RAS-make (Radio Astronomical Supplies, USA) radio signal receiver for recording signal in the ELF/VLF frequency band. This radio signal receiver recording data round-the-clock. The RAS-make receiver is unique in type and can be used suitably for filtering, decoding, receiving and demodulating signals with the soundcard or other audio input devices [17, 23].

3 Investigations Related to MORA Storm Path

Under favorable atmospheric conditions, convective area developed over the Bay of Bengal (BoB). It causes advancement of a circulation and low-pressure area (LPA) over southeast and adjoining central BoB on May 27, 2017 [18–20]. It is then concentrated into a depression over the central Bay of Bengal at 0000 UTC on May 28, 2017 and rapidly reinforced into a deep depression on the same day. During the early hours of May 29, the storm attained the intensity of the cyclonic storm and named as MORA which followed an NNE track parallel to Burma coast, reaching its maximum strength as a severe cyclonic storm with the wind speed of 110 km/h and lowest mid pressure of 978 hpa during 0300 UTC on May 30. We have shown the Mora tracker in Fig. 1 showing the storm path when entered into Bangladesh, touching Dhaka and Chittagong. The tropical cyclone MORA made landfall in Bangladesh in the morning of May 30, 2017 accompanied by heavy rains and winds estimated at 117 km/h (73 mph).

After the land interaction, the cyclone weakened gradually to be lost into a distinct LPA over Nagaland and its surroundings at 0000 UTC on May 31, 2017 [21]. The low-lying areas of the coastal districts and their offshore islands and chars of Bangladesh and Myanmar are inundated by the storm surge of the cyclone. The well-marked LPA centered at 0000 UTC on May 28 over SE and adjoining areas of central Bay of Bengal, which then concentrated into a depression and moved along NE and lay centered at 1200 UTC on May 28, over EC BoB near (15.7° N, 90.7° E). Continuing

Fig. 1 MORA tracker
showing the storm path when
entered into Bangladesh.
Courtesy IMD

its movement, the system slowly weakened into a DD and lay centered at 1200 UTC
on May 30 over Tripura and surrounding areas (24.2° N, 92.2° E) and into a well-
marked LPA over Nagaland and neighborhood at 0000 UTC on May 31. According to
the report of India Meteorological Department, on May 30, 2017 between local time
7:30 AM and 9:30 AM the cyclone MORA made landfall along the SE coastal area of
Bangladesh in the vicinity of Kutubdia Island between Cox's Bazar and Chittagong
[22].

Some prominent INSAT-3D imageries in association with CS MORA have shown
in Fig. 2. The convection experienced during May 28, 2017 exhibits curved band
pattern with well-marked wrapping into the center from eastern sector. Broken low
to medium clouds accompanied by intense to very intense convection covered over
BoB between latitude 11.0–19.0° N and longitude 84.0–91.0° E.

As pointed out before, the cyclone Mora made landfall in the morning of May 30,
2017 as a Category 1 cyclone between Chittagong and Cox's Bazar. The powerful
cyclone damaged largely with packing winds of up to 117 km per hour and moved
toward India's Northeast. Satellite image of the cyclone Mora is shown in Fig. 3.

As a result of this severe cyclone, heavy rainfall occurred to lash the states of
Mizoram, Tripura, Arunachal Pradesh, Meghalaya, Assam and Nagaland on May 30
and 31.

In Fig. 4, Typical Kalpana-1 imageries of cloud top temperature obtained by using
VHR (very high resolution) sensor at 0445 UTC on May 30, 2017 in association with
CS MORA. The cyclonic storm was detected by the above satellite and the related
imageries are send to the observatory through radio communication.

Doppler Weather Radar (DWR) imageries of some typical selected Max (Z) as
recorded by IMD, Kolkata center using cyclone detection radar during May 29 and
May 31, 2017 associated with cyclone Mora are presented in Fig. 5.

(a)

(b)

(c)
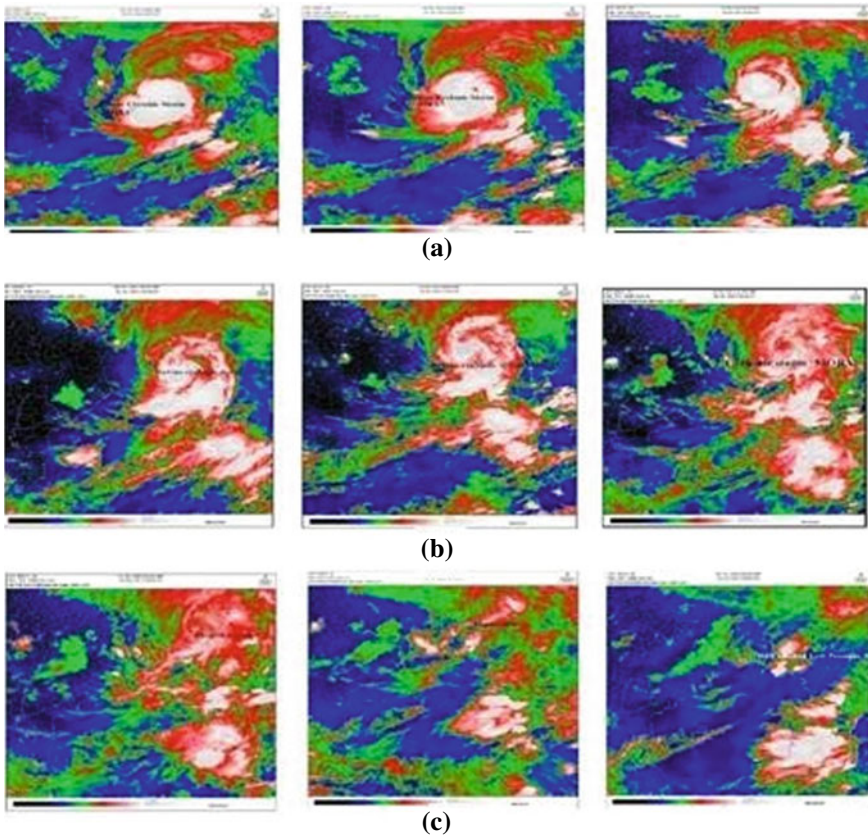
Fig. 2 INSAT-3D enhanced colored imageries associated with CS MORA during May 29 and May 31, 2017. *source* IMD

4 Analysis and Results

The ELF/VLF data recorded with an embedded instrument in our observatory [23]. The recordings of the data shown in Fig. 6. Figure 6a shows a typical sample of the data on an undisturbed day, May 23, 2017, while Fig. 6b exhibits the spectral pattern of the signal which was received and recorded on May 30, 2017 when the cyclone was severe in nature. It appears from the figure that on an undisturbed day the noise level of the spectra in the ELF/VLF range was low as compared to that on the disturbed day. The level was enhanced rapidly with the atmospheric perturbations due to cyclone MORA and maintained throughout the period of its existence. When it disappeared, the level further came down as before which is not shown in the figure. It is further clear from the record of Fig. 6b that the noise level in the ELF range is slightly higher in comparison with that in the VLF range. When compared both the

Fig. 3 Satellite image of cyclone Mora. *Credit* IMD
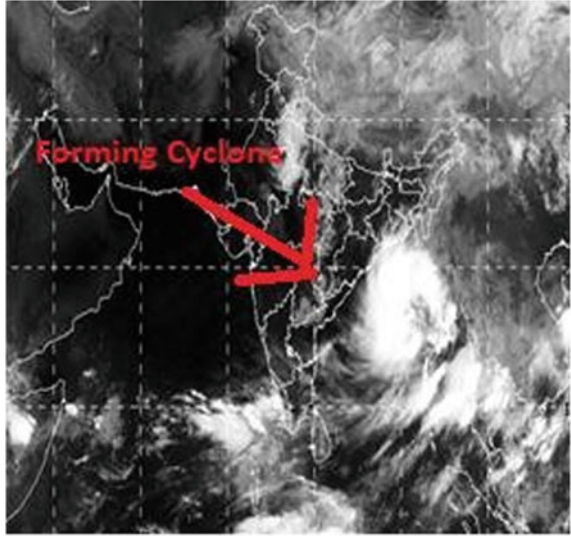
Fig. 4 Kalpana–1 satellite imageries of cloud top temperature using VHR sensor with 8000 m resolution at 0445 UTC on May 30, 2017 in association with cyclonic storm MORA. *source* IMD
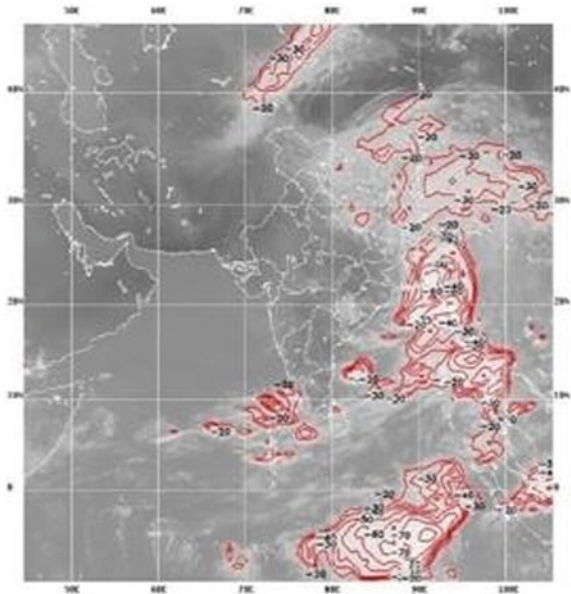
records of Fig. 6a, b, we find that the peak-to-peak excursion of the noise level is smaller on a clear day as compared to that on a disturbed day.

Comparison with existing methods as desired, is beyond the scope of this paper as it dealt with the observations in disturbed day as the cyclonic storm MORA was passing through the area.

(a)

(b)

(c)
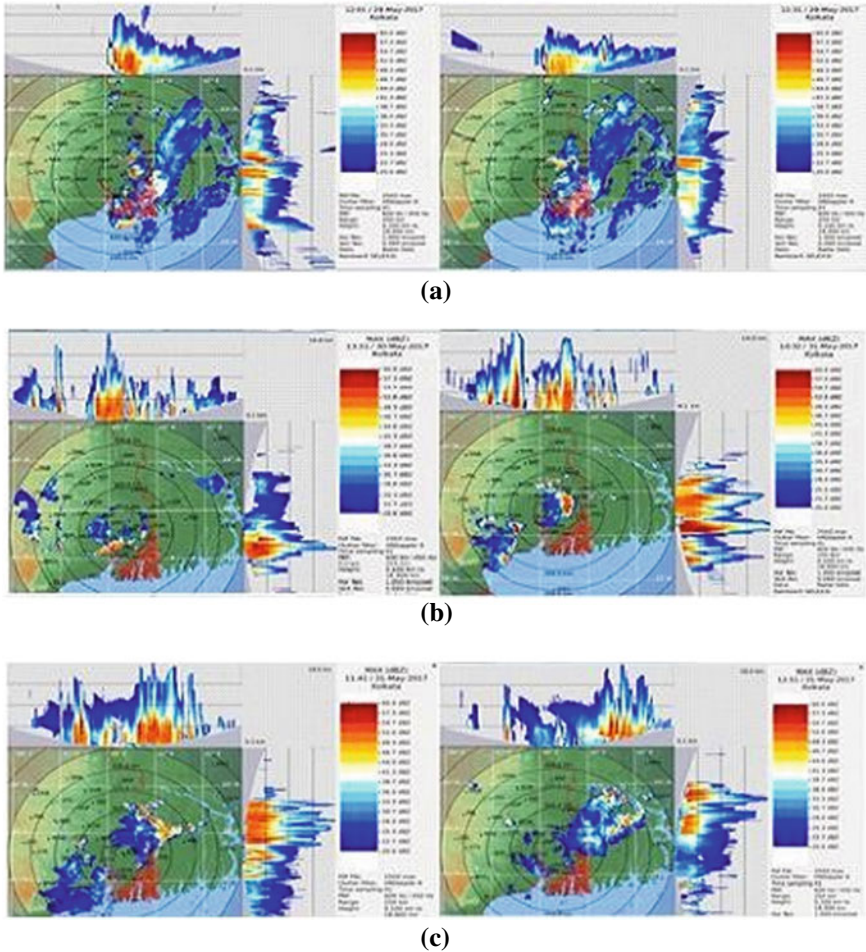
Fig. 5 (**a**) (**b**) (**c**) Doppler weather radar (DWR) imageries of some typical selected max (Z) as recorded by IMD, Kolkata center using cyclone detection radar during May 29 and May 31, 2017. *source* IMD, Kolkata

5 Observations

Tropical cyclones and associated lightning are the most destructive and recurrent natural hazards in the tropical and sub-tropical areas of the globe with widespread impacts. A significant number of the deadliest cyclones, like the cyclone Mora reported here, have occurred in the Bay of Bengal affecting widely the state of West Bengal and Bangladesh. A combination of factors like a flat coastal terrain and high population density of the related areas of West Bengal to Bangladesh always has devastating consequences upon landfall for the cyclones over Bay of Bengal.
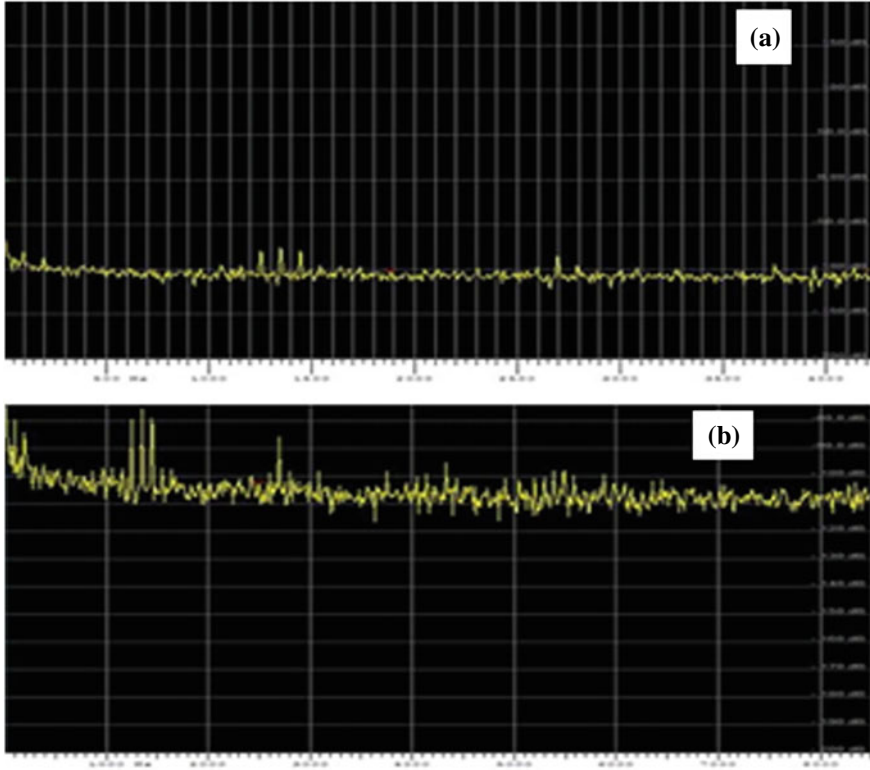
Fig. 6 a Typical sample of ELF/VLF data on an undisturbed day, May 23, 2017, **b** the spectral pattern of the signal on May 30, 2017 when the cyclone was severe in nature

The annual cycle of tropical cyclones (TCs) in the northern Indian Ocean exhibits a clear bimodal structure. The season starts from April when the sea surface temperatures increase and continues to intensify through May. By the second week of June, the monsoon sets in and the accompanied strong vertical wind shear and unfavorable atmospheric vortices largely limit the formation of TCs during the monsoon from June to September. In October, the TC activity increases further, getting a second peak during the month of November. While more TCs form during the post monsoon months, the most intense storms are found to form during the pre-monsoon period. Large ocean heat content and strong variability of northward propagating intra seasonal oscillations during April–May are mainly responsible for the formation of intense TCs during pre-monsoon months.

6   Conclusions

The work is associated with disaster study which is a combination of consequences of hazardous natural or social phenomenon and environmental condition at the place of occurrence. As a consequence of a devastating Tropical Cyclone, both fishing and tourism are seriously affected. The outcome of the study strongly supports the socio-economic activity of the government. This interdisciplinary program may promote an understanding of key environmental issues with localization, tracking, threat identification and characterization of cyclone and associated lightning and precipitation which can serve largely to the society and environmental management related to studies of severe cyclones in West Bengal. Similar study will impart knowledge on environmental issues at local and regional levels.

Further, percentage frequency distribution, radial profile as well as quadrant-wise mean rain rates can be determined for each Tropical Cyclone.

References

1. Behringer, D., Xue, Y.: Evaluation of the global ocean data assimilation system at NCEP: the Pacific Ocean. In: Proceedings Eighth Symposium on Integrated Observing and Assimilation Systems for Atmosphere, Oceans, and Land Surface, AMS 84th Annual Meeting, Washington State Convention and Trade Center, Seattle, Wash (2004)
2. Girishkumar, M., Ravichandran, M., Han, W.: Observed intraseasonal thermocline variability in the Bay of Bengal. J. Geophys. Res. Oceans **118**, 3336–3349 (2013). https://doi.org/10.1002/jgrc.20245
3. Bhat, G., Srinivasan, J., Gadgil, S.: Tropical deep convection, convective available potential energy and sea surface temperature. J. Meteorol. Soc. Jpn. **74**(2), 155–166 (1996)
4. Chang, Y.-S., Zhang, S., Rosati, A., Delworth, T.L., Stern, W.F.: An assessment of oceanic variability for 1960–2010 from the GFDL ensemble coupled data assimilation. Clim. Dyn. **40**(3–4), 775–803 (2013)
5. Dee, D., et al.: The ERA-INTERIM reanalysis: configuration and performance of the data assimilation system. Q. J. R. Meteorol. Soc. **137**(656), 553–597 (2011)
6. Elsner, J.B., Kossin, J.P., Jagger, T.H.: The increasing intensity of the strongest tropical cyclones. Nature **455**(7209), 92–95 (2008)
7. Emanuel, K.: Increasing destructiveness of tropical cyclones over the past 30 years. Nature **436**(7051), 686–688 (2005)
8. Girishkumar, M.S., Ravichandran, M.: The influences of ENSO on tropical cyclone activity in the Bay of Bengal during October–December. J. Geophys. Res. **117**, C02033 (2012). https://doi.org/10.1029/2011JC007417
9. Kanamitsu, M., Ebisuzaki, W., Woollen, J., Yang, S.-K., Hnilo, J., Fiorino, M., Potter, G.: NCEP-DOE AMIP-II reanalysis (R–2). Bull. Am. Meteorol. Soc. **83**(11), 1631–1643 (2002)
10. Kikuchi, K., Wang, B.: Formation of tropical cyclones in the northern indian ocean associated with two types of tropical intraseasonal oscillation modes. J. Meteorol. Soc. Jpn. **88**(3), 475–496 (2010)

11. Klotzbach, P.J.: Trends in global tropical cyclone activity over the past twenty years (1986–2005). Geophys. Res. Lett. **33**, L10805 (2006). https://doi.org/10.1029/2006GL025881
12. Webster, P.J.: Myanmar's deadly daffodil. Nat. Geosci. **1**(8), 488–490 (2008)
13. Yu, L.: Variability of the depth of the 20 °C isotherm along 6° N in the Bay of Bengal: its response to remote and local forcing and its relation to satellite SSH variability. Deep Sea Res. Part II **50**(12), 2285–2304 (2003)
14. Webster, P.J., Holland, G.J., Curry, J.A., Chang, H.-R.: Changes in tropical cyclone number, duration, and intensity in a warming environment. Science **309**(5742), 1844–1846 (2005)
15. https://agupubs.onlinelibrary.wiley.com
16. Balaguru, K., Ruby Leung, L., Lu, J., Foltz, G.R.: A meridional dipole in pre-monsoon Bay of Bengal tropical cyclone activity induced by ENSO: tropical cyclones, monsoon and enso. J. Geophys. Res. Atmos. (2016)
17. Sengupta, D., Goddalehundi, B.R., Anitha, D.: Cyclone-induced mixing does not cool SST in the post-monsoon north Bay of Bengal. Atmos. Sci. Lett. **9**(1), 1–6 (2008)
18. Hazer, R.D., Warjri, et al.: Physical and electrical properties of a tropical cyclone as derived from satellite imageries and cyclone detection doppler weatheradar: a case study **1**(1), 77–90 (2019)
19. Singh, O., Khan, T.M.A., Rahman, M.S.: Has the frequency of intense tropical cyclones increased in the north Indian Ocean? Curr. Sci. **80**(4), 575–580 (2017)
20. RSMC bulletin (IMD)—MORA (2017). http://www.rsmcnewdelhi.imd.gov.in
21. Erdman, J. (2017). https://weather.com/storms/hurricane/news/deadliest-cyclone-history-bangladesh-20130605#/2
22. PTI. (2017). http://www.dnaindia.com/world/report-cyclone-mora-hits-bangladesh-hundreds-of-thousands-evacuated-2455330
23. Sarkar, H., Banerjee, A., Mitra, S.P., et al.: A comparative study of ELF and VLF noise characteristics of nor'wester at a low latitude tropical station. SN Appl. Sci. **1**, 154 (2019). https://doi.org/10.1007/s42452-018-0158-9

Modified Multiloop Finite Dimensional Robust Repetitive Controller for Supply Air Pressure Loop of a Heating, Ventilation, and Air Conditioning System

Sagarika Sarkar, Amrita Mukherjee, Ujjwal Mondal, and Anindita Sengupta

Abstract The objective of this paper is to apply the conventional Proportional Integral Derivative (PID) controller and Repetitive Controller based PID controller (RCPID) for the supply air pressure loop of a Heating, Ventilation, and Air Conditioning (HVAC) system in terms of tracking the given step reference signal and also rejecting periodic disturbances having known periods. The Internal Model Principle (IMP) based Repetitive Controller (RC) gives infinite number of pairs of poles on the imaginary axis in the *s*-plane leading the system to instability. Thus, Finite Dimensional Repetitive Control System (FDRCS) is introduced. Multiple loops Robust Repetitive Controller (RRC) has been used to cope up with the small period uncertainties. Finally, this paper shows the comparison of the conventional PID controller and different models derived Finite Dimensional Robust Repetitive Controller (FDRRC) based PID controllers for the supply air pressure loop of the HVAC system so that the step reference signal is tracked and periodic disturbances get rejected producing minimum error.

Keywords PID controller · HVAC system · Supply air pressure loop · IMP · RC · FDRC · FDRRC · FDRRC based PID controllers

1 Introduction

In practice, reference signals that are given to any process may be periodic in nature. Even the process may be affected by periodic disturbances. In that case, repetitive controller gives a far better performance in tracking repetitive reference signal and also in rejection of periodic disturbances in comparison with the normal PID controller.

S. Sarkar (✉) · A. Mukherjee · U. Mondal
Department of Applied Physics, University College of Science and Technology, Kolkata, India

A. Sengupta
Department of Electrical Engineering, Indian Institute of Engineering Science and Technology, Shibpur, Howrah, India

Repetitive controller was first introduced to control proton synchrotron magnetic power supply. It is also applied to several research areas like tubular heat exchanger, computer hard disk, power supply (UPS), CD player, pulse-width modulated (PWM) inverters, robot control, thickness control in cold rolling, continuous steel casting, noise cancelation and many other industrial applications.

Repetitive Control System (RCS) shows its simplicity on the basis of Internal Model Principle (IMP). This IMP includes a fixed period time delay (L) in the positive feedback loop and this time delay is actually the period of the reference signal. Due to the periodic signal generator in the control loop, RCS can track periodic reference signal and reject periodic disturbances properly.

Heating, Ventilation, and Air Conditioning (HVAC) systems have become one of the most essential parts for industrial purposes. Both purposes of heating and cooling are served by this system depending on the requirement.

This paper deals with the comparison of the applications of normal PID controller, Repetitive Controller (RC) and Modified Repetitive Controller in Supply Air Pressure Loop of HVAC system.

2   Description of the System

2.1   Basic Functions of HVAC System

HVAC is the technology to provide the indoor and vehicular environmental comfort. An HVAC system provides thermal comfort along with the acceptable air quality. The basic functions of an HVAC system are heating, cooling, humidifying, dehumidifying, ventilating, cleaning and controlling the air movement. This system acts as the air conditioning system in summer and as the heater in winter. The obtained temperature is expected to be constant which is maintained by the supply air pressure loop present in the HVAC system.

2.2   Importance of Supply Air Pressure Loop of HVAC System

Here, Fig. 1 represents a typical HVAC system which includes the supply air pressure loop. Here, the outside air is mixed with the return air of either building or vehicle. A supply fan helps the cooling coil to suck the mixed supply air. The obtained cooled air is delivered to multiple zones. A valve CHWS regulates the off coil air temperature by controlling the supply of chilled water. The supply air pressure should be maintained at a fixed value by regulating the speed of the supply air fan [1] in order to make each zone work properly. Each zone temperature is finely tuned by damper of the Variable Air Volume box in each zone.
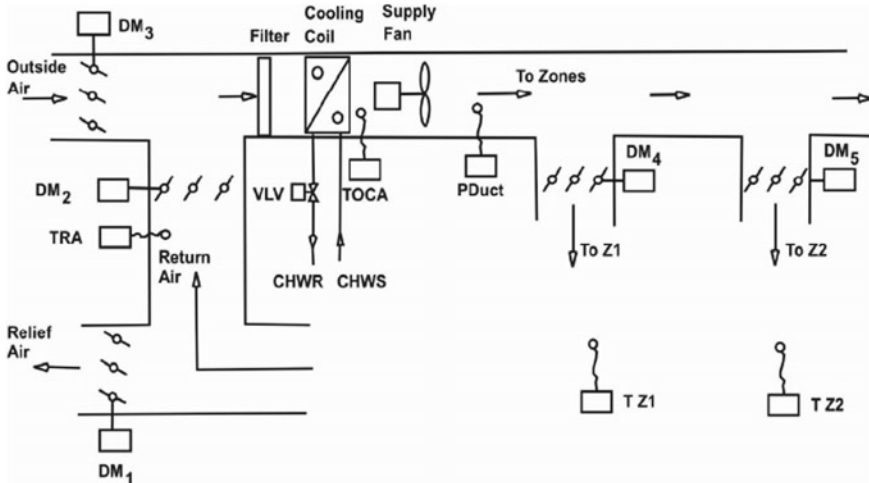
Fig. 1 A typical HVAC system

One of the most important components needed for a functional HVAC system by avoiding either overload or underload condition is the right amount of air flow. This right amount of air flow can be ensured if speed of air flow be regulated and disturbance can be eliminated. The regulation in air flow and disturbance elimination can be assured using Repetitive Controller (RC). The supply air pressure is directly proportional to the speed of the supply air fan.

The transfer function of the supply air pressure loop, having time delay of 0.5 s, is given as

$$G(s) = \frac{0.81}{(0.97s + 1)(0.1s + 1)} e^{-0.5s} \tag{1}$$

3 Control Strategy

The aim of this paper is to use different control strategies on the process and compare them to have the appropriate one. It is desired to obtain the perfect tracking of step reference signal and rejection of periodic disturbances along with minimum error.

The different controllers used in this paper are discussed below:

3.1 Conventional PID Controller

Generally, PID (Proportional-Integral-Derivative) controllers are used in HVAC systems because of the simple structure, hassle free tuning and easy implementation. They are acceptable in many industrial applications but they show inefficiency to meet desired specifications. It is a tough call to obtain a proper tuning of PID controller for supply air pressure loop of an HVAC system in a building [2].

3.2 IMP with Periodic Signal Generator and RC Based PID Controller

According to the Internal Model Principle (IMP), proposed by Wonham and Francis, "Perfect tracking of a reference signal can be assured if the generator of the reference signal is included in the stable closed loop system." [3] The inclusion of the generator of reference signal within the closed loop system results in addition of pole(s).

The following example is given for an open loop transfer function $G(s) = 1/(s + 2)$ with a unit step reference signal ($1/s$) in Fig. 2b. The obtained steady-state error (E_{ss}) is 66.67% without using IMP, whereas introducing the generator of the reference signal in the stable closed loop system based on IMP gives E_{ss} as 0%.

Repetitive Control System (RCS) designed by Hara et al. [4] in 1985 is based on a simple learning control method mainly to track a periodic reference signal and reject a periodic disturbance signal properly by including periodic signal generator in its control loop. Here, Fig. 3a, b and c shows the basic repetitive control loop, infinite number of open loop pole pairs on the imaginary axis in the s-plane [5] and frequency response of the system with Repetitive Controller based PID (RCPID) Controller.
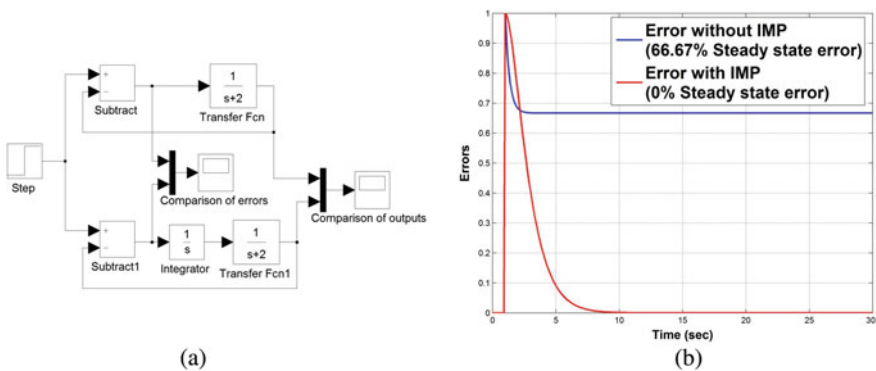
Fig. 2 Tracking of reference step signal without and with IMP; **a** Simulink model, **b** errors without and with IMP
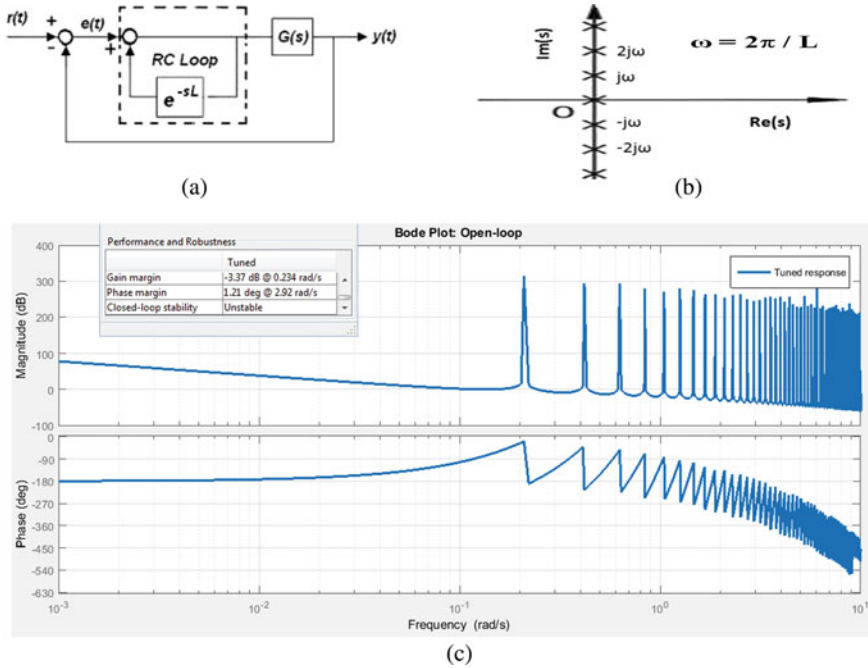
Fig. 3 Basic RC loop and unstable frequency response of the process; **a** Basic repetitive control loop, **b** infinite number of open loop pole pairs on the imaginary axis, **c** bode plot of the system with RCPID

The factor $\left(\frac{1}{1-e^{-Ls}}\right)$, included within RCS, produces poles at $jp\left(\frac{2\pi}{L}\right)$ where $p = 0, \pm 1, \pm 2, \pm 3, …. \pm \infty$, corresponding to the harmonic and sub harmonics of the period (L) of the reference signal. Thus, the controller is led to track any periodic signal as well as reject any periodic disturbance of period L [4]. In the case of tracking and/or rejecting periodic signal, RCPID controller is used instead of conventional PID controller [6]. RC is sometimes known as Infinite Dimensional Repetitive Controller (IDRC) [7] as use of this controller produces infinite number of poles located on the imaginary axis in the s-plane which cause instability of the system.

3.3 Finite Dimensional Repetitive Controller (FDRC) Based PID Controller

IDRC becomes FDRC by cascading an LPF with the time delay element in the positive feedback loop [8]. This increases the stability of the closed loop system by filtering away the high-frequency modes by this LPF. Here, Fig. 4a, b shows the
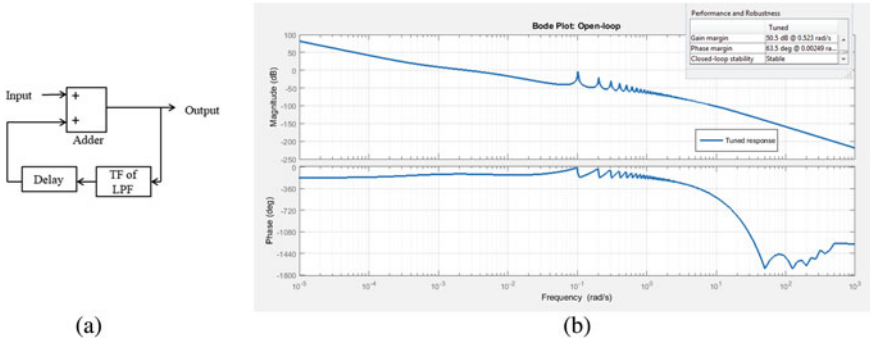
Fig. 4 FDRC loop and stable frequency response of the process; **a** Basic FDRC loop, **b** bode plot of the system

FDRC loop and system's stable frequency response obtained using FDRC based PID controller.

3.4 Multiple Loop RC Based PID Controller

Single loop FDRC gives better performance than RC. But the problem of instability due to the inappropriate estimation of the period of the reference signal and the mismatch of it with the delay of RC loop can be resolved with the help of multiple loop Repetitive Controller [9]. Conventional RC can't handle the uncertainties of the reference signal.

More than one memory loops are used to modify the frequency dynamics of RC and increase its robustness to small period changes. The multiple memory loops act as storing elements of errors for more than one previous trial to implement more robustness and thus RRC is designed [10]. This paper follows the models of Repetitive Controllers given by Singh, Owens, and Ujjwal Mondal.

FDRRC derived from Singh's Model According to Singh's model [11], the time delay serves as a feed forward delay element and the delay is added cumulatively for each successive stage in the design of the controller [10]. The representation of FDRRC loop derived from Singh's model and the obtained frequency response are shown in Fig. 5a, b.

FDRRC derived from Owens' Model According to Owens [12], a multi-periodic repetitive controller loop is designed as shown in Fig. 6a, b shows the stable frequency response of the system obtained by this approach.

It is a linear combination of single-periodic repetitive control elements with a stable filter, in each loop, introduced to filter out noise. Here, each internal loop is provided with a gain which represents relative weight.
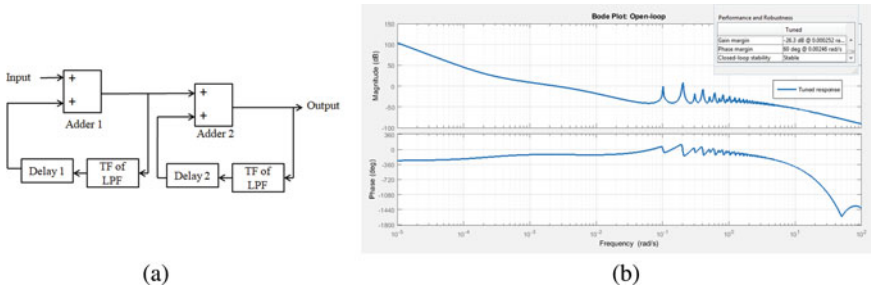
Fig. 5 FDRRC loop derived from Singh's model and stable frequency response of the process; **a** Simulink model, **b** bode plot of the system
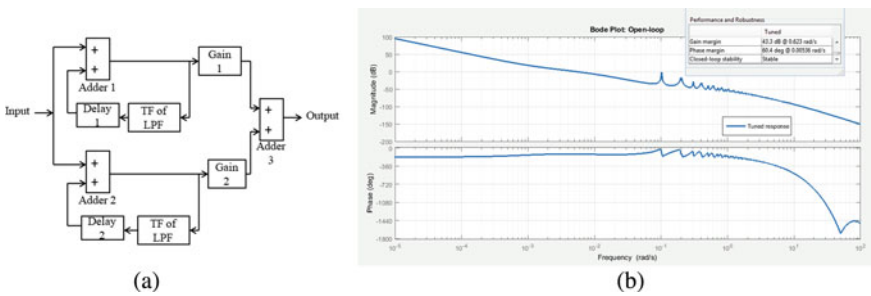
Fig. 6 FDRRC loop derived from Owens' model and stable frequency response of the process; **a** Simulink model, **b** bode plot of the system

FDRRC derived from Mondal's Model The FDRRC loop derived from the model of multiloop RC given by Dr. Ujjwal Mondal and the system's frequency response by applying this controller are shown in Fig. 7a, b, respectively.
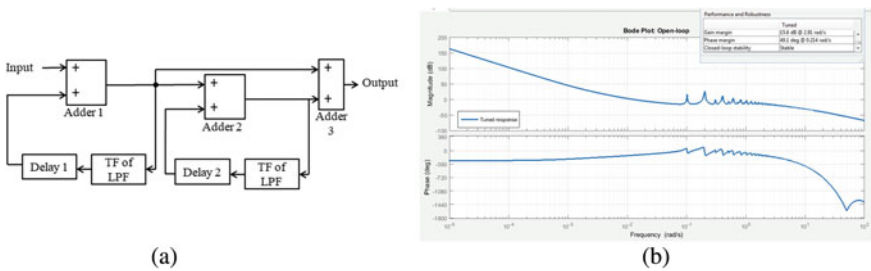
Fig. 7 FDRRC loop derived from Mondal's model and stable frequency response of the process; **a** Simulink model, **b** bode plot of the system

4 Reference and Disturbance

This paper has dealt with effectiveness of FDRRC based PID controllers for step reference and periodic disturbances over conventional PID controller. The step reference signal is given as

$$r(t) = 2.5u(t) \tag{2}$$

The periodic disturbance is given as the sum of two periodic disturbances having different periods. The disturbance is given as

$$d(t) = d_1(t) + d_2(t) \tag{3}$$

where,

$$d_1(t) = 0.5 \sin\left(\frac{2\pi}{30}\right)t \text{ and } d_2(t) = 0.5 \sin\left[\left(\frac{2\pi}{60}\right)t + \frac{\pi}{2}\right] \tag{4}$$

5 Results

Here, the RC based PID controller has been applied to the system to have the comparison with the application of conventional PID controller. But RC leads the system to instability. The response of the system using RCPID controller is given in Fig. 8 along with the reference.
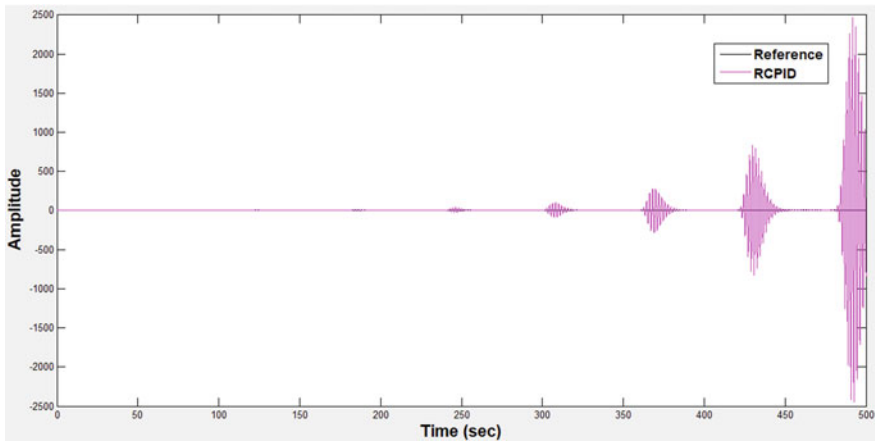
Fig. 8 System's response using RCPID controller with reference

A comparison among the responses of the Supply Air Pressure Loop of an HVAC System obtained by using conventional PID controller, FDRC based PID controller and different models derived FDRRC based PID controllers with the reference is shown in Fig. 9.

Also, a comparison among the tracking errors of the system obtained by using conventional PID controller and different models derived FDRRC based PID controllers is given in Fig. 10.

To have numerical representation of errors obtained in this paper, comparison of the values of Integral Absolute Error (IAE), Integral Time weighted Absolute Error
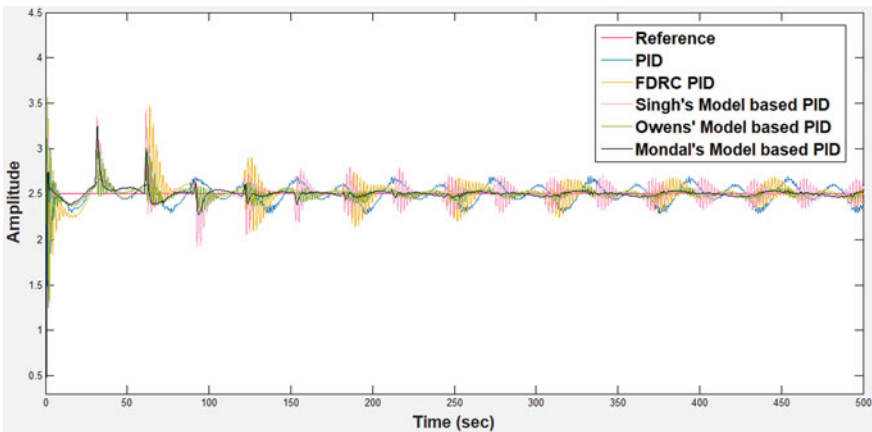
Fig. 9 Comparison of system's responses using PID controller, FDRC based PID controller and different models derived FDRRC based PID controllers with reference
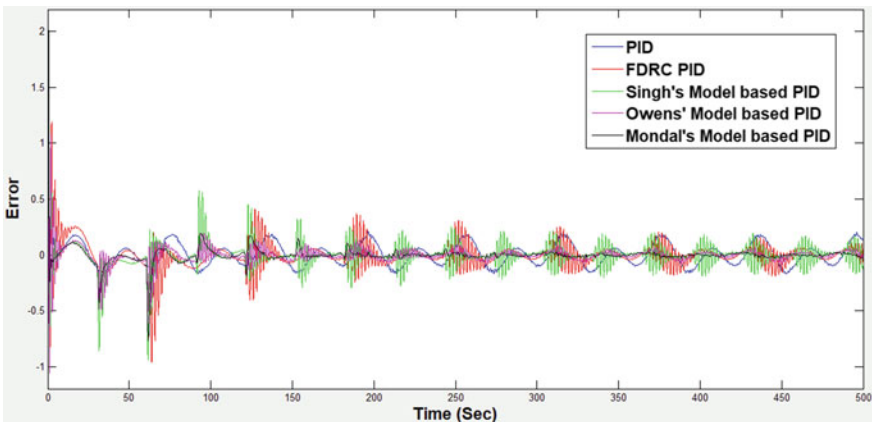
Fig. 10 Comparison of tracking errors of the system using PID controller, FDRC based PID controller and different models derived FDRRC based PID controllers

Table 1 Comparison of IAE, ITAE, ISE and ITSE of the system obtained using conventional PID controller, RC based PID controller, single loop FDRC based PID controller and Modified FDRRC based PID controllers

Control strategies	Comparison of errors (numerical representation)			
	IAE	ITAE	ISE	ITSE
Conventional PID controller	41.17	9815	7.038	1080
RC based PID controller	3.752×10^4	1.738×10^7	6.01×10^7	2.925×10^{10}
Single Loop FDRC based PID controller	37.55	6761	10.23	819.2
Singh's model derived FDRRC based PID controller	31.73	6409	7.991	784
Owens' model derived FDRRC based PID controller	20.56	3227	5.253	167
Mondal's model derived FDRRC based PID controller	15.94	2424	4.293	116.5

(ITAE), Integral Squared Error (ISE) and Integral Time weighted Squared Error (ITSE) [13] is given in Table 1.

6 Conclusion

To maintain the healthy and hygienic conditions in terms of temperature, humidity and proper air circulation, HVAC system is used in residential places as well as places like hospitals, office buildings and in vehicles also.

In this paper, basic functions of an HVAC system and importance of its supply air pressure loop have been described in brief. RCS, implemented using IMP, shows infinite dimensional nature and makes the system unstable. Thus, a properly designed Low Pass Filter has been incorporated so that the effect of the positive feedback in the RC loop gets minimized. The stability of the system obtained by suitable design of FDRRCs entails trade(s)-off between stability and tracking performances.

The various models derived FDRRCS have been used with the said system. Comparison among the conventional PID controller and the FDRRC based PID controllers, derived from different models, has been performed in terms of rejecting periodic disturbance and stability. Mondal's model derived FDRRC gives better result with respect to other approaches used in this paper.

References

1. Qiang, B., Cai, W.J., Wang, Q.G. et al: Advanced controller auto-tuning and its application in HVAC systems. Control Eng. Practice 633–644 (2000)

2. Wang, Y.G., Shi, Z.G., Cai, W.J.: PID autotuner and its application in HVAC systems. In: Proceedings of the American Control Conference, Arlington, VA (2001)
3. Francis, B., Wonham, W.: Internal model principle in control theory. Automatica **12**, 457–465 (1976)
4. Hara, S., Yamamoto, Y., Omata, T., Nakano, M.: Repetitive control-system—a new type servo system for periodic exogenous signals. IEEE Trans. Autom. Control **33**(7), 659–668 (1988)
5. Mondal, U., Sengupta, A.: Robust servo performance of repetitive controller for periodic reference signals. In: 2014 6th IEEE Power India International Conference (PIICON) (2014)
6. Mondal, U., Pathak, R.R., Sengupta, A., Sutradhar, A.: Repetitive controller in liquid level system: a discrete wavelet based approach. In: IEEE Calcon, pp. 52–55 (2011)
7. Mahato, J., Das, S.K., Mondal, U., Sengupta, A.: System identification of an AVR and it's control using finite dimensional repetitive controller. In: 2018 IEEE Applied Signal Processing Conference (ASPCON), pp. 59–63 (2018)
8. Mondal, U., Sengupta, A. et al.: Finite dimensional repetitive controller for identified model of a DC servo system. IEEE, ICPEN (2012)
9. Camacho, N.A., Mermoud, M.A.D.: Fractional adaptive control for an automatic voltage regulator. ISA Trans. **52**(6), 807–815 (2013)
10. Mondal, U., Basu, A., Bose, S., Sengupta, A., Saha, U.: Finite dimensional robust repetitive controller for tracking periodic reference input. In: 2015 IEEE International Conference on Electrical, Computer and Communication Technologies (ICECCT) (2015)
11. Singh, T., Vadali, S.R.: Robust time-delay control. J. Dyn. Syst. Meas. Control Trans. ASME **115**, 303–306 (1993)
12. Owens, D.H., Liand, L.M., Banks, S.P.: Multi-periodic repetitive control system: a Lyapunov stability analysis for MIMO systems. Int. J. Control 505–506 (2007)
13. Duarte-Mermoud, M.A., Prieto, R.A.: Performance index for quality response of dynamical systems. ISA Trans. 133–151 (2004)

Modified Multiloop Finite Dimensional Robust Repetitive Control for 7 Degrees-of-Freedom Robot Arm

Amrita Mukherjee, Sagarika Sarkar, Ujjwal Mondal, and Anindita Sengupta

Abstract The objective of this paper is to apply and compare the results of the Internal Model Principle (IMP) derived multiple loops Repetitive Controller (RC) based PD controller in the 7 Degrees-of-Freedom (DoF) robot arm for tracking the triangular reference signal with different frequencies during different time intervals along with that attenuation of periodic disturbances with known period will also be done. The Repetitive Controller (RC) sometimes leads the system to instability as it provides infinite number of pole pairs on the imaginary axis in the *s*-plane. Thus, Finite Dimensional Repetitive Control System (FDRCS) is introduced. For dealing the small period uncertainties, multiple loops Robust Repetitive Controller (RRC) has been designed and implemented in this paper. Finally, this paper shows the comparison of the conventional RC based PD controller and different model derived Finite Dimensional Robust Repetitive Controller (FDRRC) based PD controllers in terms of tracking triangular reference and rejecting periodic disturbances, while producing minimum error.

Keywords PD controller · 7-DoF · Robot arm · IMP · RC · FDRC · FDRRC · RC based PD controller · FDRRC based PD controllers

1 Introduction

In practice, reference signals that are given to any process may be periodic in nature. Even the process may be affected by periodic disturbances. In that case, repetitive controller offers a much better performance in tracking repetitive reference signal and additionally in rejection of periodic disturbances in comparison with the conventional PD controller.

A. Mukherjee (✉) · S. Sarkar · U. Mondal
Department of Applied Physics, University College of Science and Technology, Kolkata, India

A. Sengupta
Department of Electrical Engineering, Indian Institute of Engineering Science and Technology, Shibpur, Howrah, India

53

In 1981, Inoue et al. first introduced the repetitive controller for controlling the proton synchrotron magnetic power supply. It is also applied to several research areas like tubular heat exchanger, computer hard disk, power supply (UPS), CD player, pulse-width modulated (PWM) inverters, robot control, thickness control in cold rolling, continuous steel casting, noise cancelation and lots of different industrial applications.

Repetitive Control System (RCS) shows its simplicity based on Internal Model Principle (IMP). This IMP works by including a time delay (L) having fixed period. The period of the reference signal present in the positive feedback loop is to be identical to the period of the time delay. The presence of periodic signal generator in control loop enable RCS to attenuate periodic disturbances and track periodic reference signal properly.

A robotic arm is taken into account as a sort of mechanical arm. It is usually programmable and can perform similar functions to a person's arm. The arm may be a part of a lot of advanced automation or is also the assemblage of the mechanism. Robotic arms are generally used for multiple industrial applications from spot and arc welding, material handling to laser cutting etc. In a variety of environments, the robotic technology offers human-like dexterity. Therefore, the high level control is needed for these applications.

This paper deals with the comparison of the applications of conventional RC based PD controller and Modified Repetitive Controller in 7-DoF robot arm.

2   Literature Survey

Repetitive Control theory has been evolved over the last three decades and its popularity has been growing due to its highly accurate tracking property or periodic error reduction capability. In 1981, Inoue et al. first introduced the repetitive controller for controlling the proton synchrotron magnetic power supply. In the year 2011, an attempt was made by Doh and Ryoo to design a Robust Repetitive Controller on the Track-Following Control System in Optical Disk Drives [1]. Out of the focused applications of RC in disk drives or periodic disturbance attenuation, its application in actuators and robotic manipulators was also worthwhile over the long period from 1989 to 2013. In 2007, H. Tinone and N. Aoshima have experimented the parameter identification of robot arm with repetitive control. In 2011, L. Wang et al. developed a two inputs and two outputs system that can be configured as a robot arm [2], the closed loop performance of the predictive-repetitive control system is demonstrated by this robot arm in terms of tracking of reference trajectory, disturbance rejection as well as measurement of noise attenuation. Designs of predictive multi-input and multi-output repetitive control systems have been implemented and experimented on a 2-joint robot by Wang et al. in 2013 and 2016. Repetitive control has been also experimented for Multi-Joint Arm Movements based on Virtual Trajectories in 2020 by Uno et al. and recently, a repetitive control scheme has been applied on a

2-DoF robotic manipulator based on the improved cubic B-spline curve in 2021 by Xingyu Wang et al.

3 Description of the System

To specify the location of all the links present in a robot in space, independent joint variables are required, the number of these variables can be considered as Degree of Freedom (DoF) of a robotic arm. The minimum number of actuated joints required for controlling the system is equal to the DoF [3]. To work like a human arm, the shoulder motion of a robotic arm can be considered as pitch (up and down) or yaw (left and right). Elbow can move in upward and downward directions, so its motion is considered as pitch. Motion of wrist will occur as yaw or pitch. For wrist and shoulder, rotation (roll) may also be possible. Such a robotic arm has 5–7 degrees of freedom. If a robot consists of two arms then its total number of degrees of freedom becomes double. In this paper, 7 degrees-of-freedom (DoF) Robotics Research Corporation robotic arm has been used where 7 degrees-of-freedom is assumed of as Shoulder Pitch, Arm Yaw, Shoulder roll, Elbow Pitch, Wrist Pitch, Wrist Yaw, and Wrist Roll.

This 7-DoF geometry displays the highest level of dexterity (skill in performing tasks, especially with the hands) accessible nowadays. An end effector can be positioned and oriented by this type of arm throughout a complete sphere, with an infinite range of arm poses. Additionally, this arm is also allowed to fold compactly, a valuable feature in operations requiring manipulation through risers or tiny portholes, as well as minimizing the stowage requirements when safe. Here Fig. 1 represents the labeled diagram of 7 Degrees-of-Freedom robotic arm.

The robotic arm model shown in Fig. 1 with 7 Degrees-of-Freedom (DoF) is nonlinear system but it is simplified by assuming linearity and neglecting the interactions between the joints.

The transfer function of this 7-DoF robotic arm [4] is given as

$$G(s) = \frac{12{,}047.2}{s^3 + 45.8s^2 + 1694.6s + 12{,}047.2} \tag{1}$$

4 Reference and Disturbance

The periodic reference signal of the 7-DoF robotic arm is chosen as a triangular waveform with amplitude $\pm$ 0.7 having different frequencies during different time intervals. The frequencies are 0.8 Hz for (0–30) s, 0.833 Hz for (30–60) s, again 0.8 Hz for (60–90) s and 0.67 Hz for (90–120) s. Here Fig. 2 shows the reference triangular signal waveform.
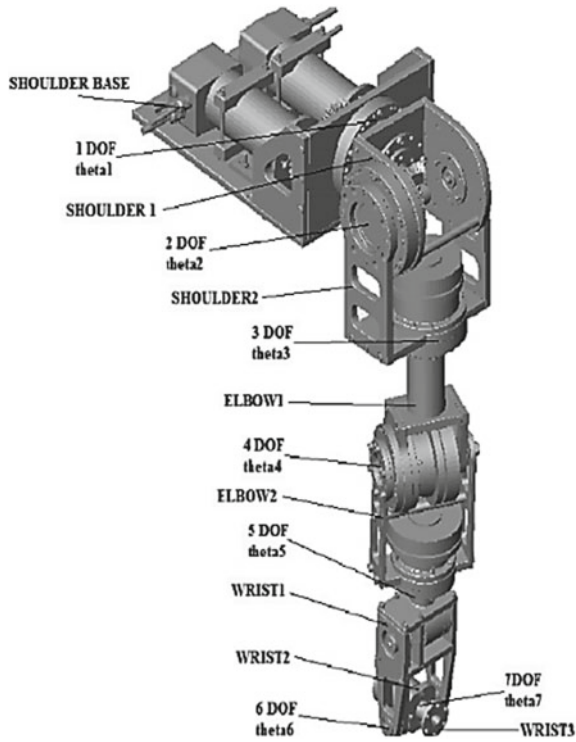
Fig. 1 7-degrees-of-freedom robotic arm
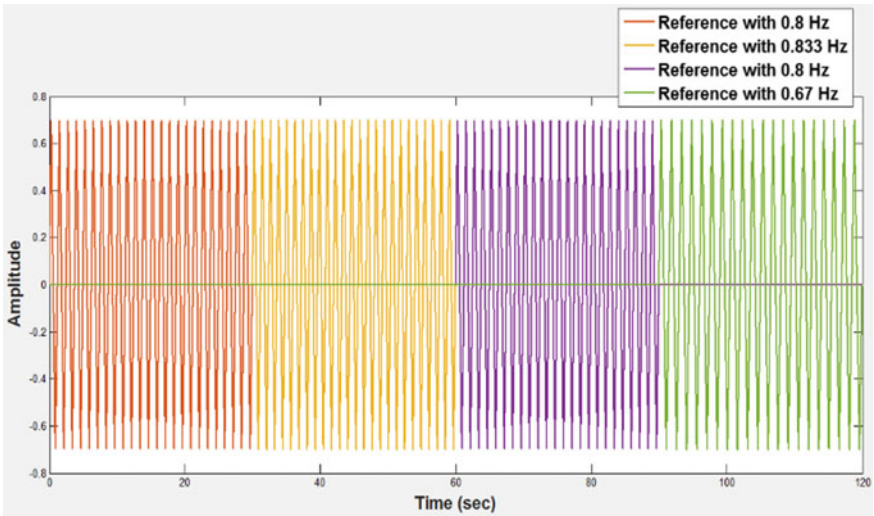
Fig. 2 Reference triangular signal waveform
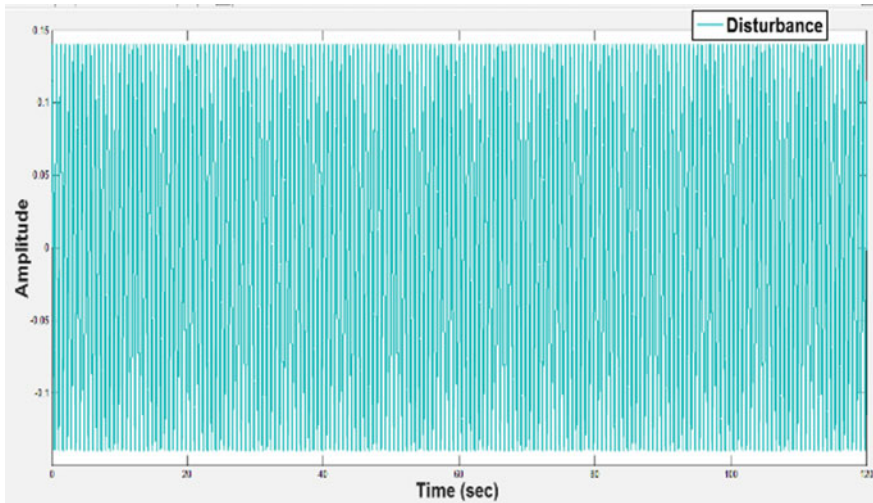
Fig. 3 Waveform of periodic disturbance signal

The disturbance signal $D(t)$ has been given as a sinusoidal signal as given below:

$$D(t) = 0.14 \sin(3.2\pi)t \qquad (2)$$

Here Fig. 3 shows the sinusoidal disturbance signal.

5　Control Strategy

The aim of this paper is to use different control strategies on the process and compare them to have the appropriate one. It is desired to obtain the perfect tracking of triangular reference signal with different frequencies during different time intervals and rejection of periodic disturbances along with minimum error.

The different controllers used in this paper are discussed below.

5.1　IMP with Periodic Signal Generator and RC Based PD Controller

According to the Internal Model Principle (IMP), proposed by Wonham and Francis, "Perfect tracking of a reference signal can be assured if the generator of the reference signal is included in the stable closed loop system." [5]. As the generator of reference
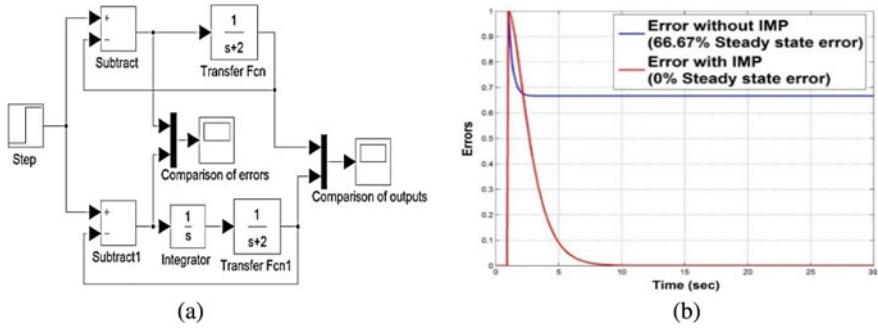
Fig. 4 Tracking of reference step signal without and with IMP; (**a**) Simulink model without and with IMP, (**b**) Errors without and with IMP

signal is included in the closed loop system, additional pole(s) occur. Design of Repetitive Control System (RCS) is based on IMP.

In the following example, the open loop transfer function of a stable unity feedback system is given as: $G(s) = 1/(s + 2)$. For a unit-step reference ($1/s$), its steady-state error (E_{ss}) becomes 66.67%. Here Fig. 4(a) shows the Simulink model for IMP. It can be seen that the steady-state error (E_{ss}) becomes zero when the generator of the reference signal (i.e., $1/s$) is introduced in the stable closed loop system as shown in Fig. 4(b).

Repetitive Control System (RCS) designed by Hara et al. [6] in 1985 is based on a simple learning control method mainly to track a periodic reference signal and reject a periodic disturbance signal properly by including periodic signal generator in its control loop. Here Fig. 5(a–c) shows the fundamental repetitive control loop, infinite number of open loop pole pairs lie on the imaginary axis and frequency response of the system with RCPD.

The factor ($\frac{1}{1-e^{-Ls}}$), included within RCS, has poles at $jk(\frac{2\pi}{L})$ where $k = 0, \pm 1, \pm 2, \ldots \pm \infty$. They correspond to the harmonic and sub harmonics of the period (L) of the reference signal, so the controller become enabled for tracking and/or attenuating any periodic signal of period L [6]. For dealing with a periodic reference signal PD controller is replaced by RCPD. Due to the addition of infinite number of poles on the imaginary axis in the s-plane RC is sometimes called Infinite Dimensional Repetitive Controller (IDRC), which causes instability of the system.

5.2 Finite Dimensional Repetitive Controller (FDRC) Based PD Controller

In the positive feedback loop, by cascading an LPF with the time-delay element IDRC becomes FDRC. This increases the stability of the closed loop system by filtering

(a)

(b)

(c)
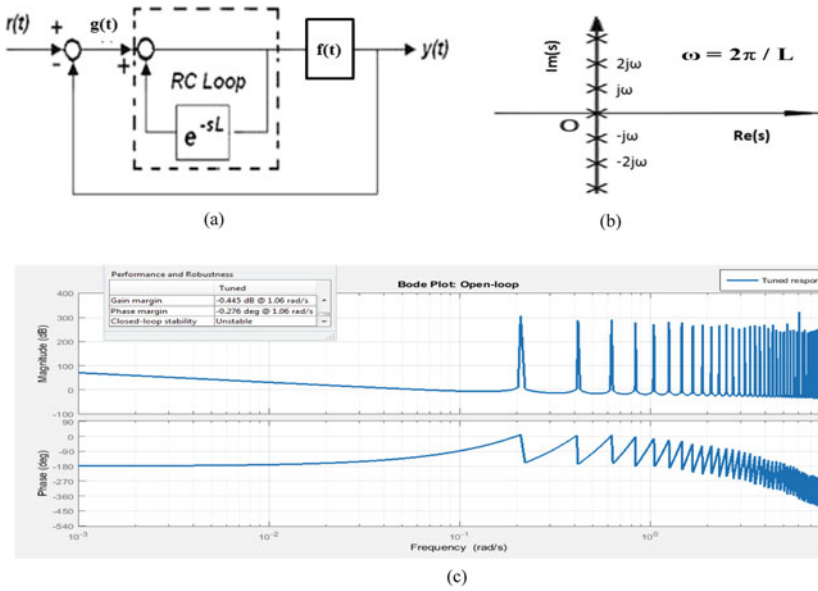
Fig. 5 Basic RC loop and unstable frequency response of the process; (**a**) Fundamental repetitive control loop, (**b**) Infinite number of open loop pole pairs lie on the imaginary axis, (**c**) Bode plot of the system with RCPD

(a)

(b)
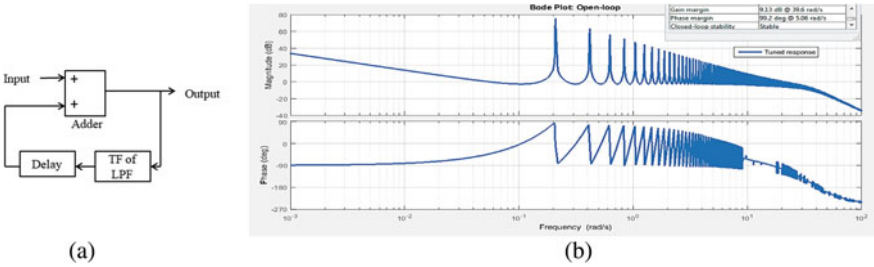
Fig. 6 FDRC loop and stable frequency response of the process; (**a**) Basic FDRC loop, (**b**) Bode plot of the system

away the high-frequency modes by this LPF. Figure 6(a, b) shows the FDRC loop and stable frequency response of the system controlled by FDRC based PD controller.

5.3 Multiple Loop RC Based PD Controller

Single loop FDRC gives better performance than RC. But the problem of instability due to the inappropriate estimation of the period of the reference signal and the

mismatch of it with the delay of RC loop can be resolved with the help of multiple loop Repetitive Controller [7]. Uncertainties present in the reference signal can't be handled by conventional RC. In order to modify the frequency dynamics of RC and for increasing its robustness to the uncertainties in the estimation of time period, more than one memory loop are used. The incorporation of multiple memory loops enable RC to make more robust decisions as they store errors for more than one previous trial and thus form Robust Repetitive Controller (RRC). The models of Repetitive Controller suggested by Dr. T. Singh [8], Dr. Ujjwal Mondal [9], and David H. Owens [10] have been considered in this paper.

FDRRC derived from Singh's Model. According to Dr. T. Singh's model, a feed forward delay element is represented by the transport delay, and the delay was added cumulatively for each successive stage of the controller. Here Fig. 7(a, b) represent the FDRRC derived from Singh's model and the obtained frequency response respectively.

FDRRC derived from Mondal's Model. The FDRRC loop derived from the model of multiloop RC given by Dr. Ujjwal Mondal and the system's frequency response by applying this controller are represented in Fig. 8(a, b) respectively.
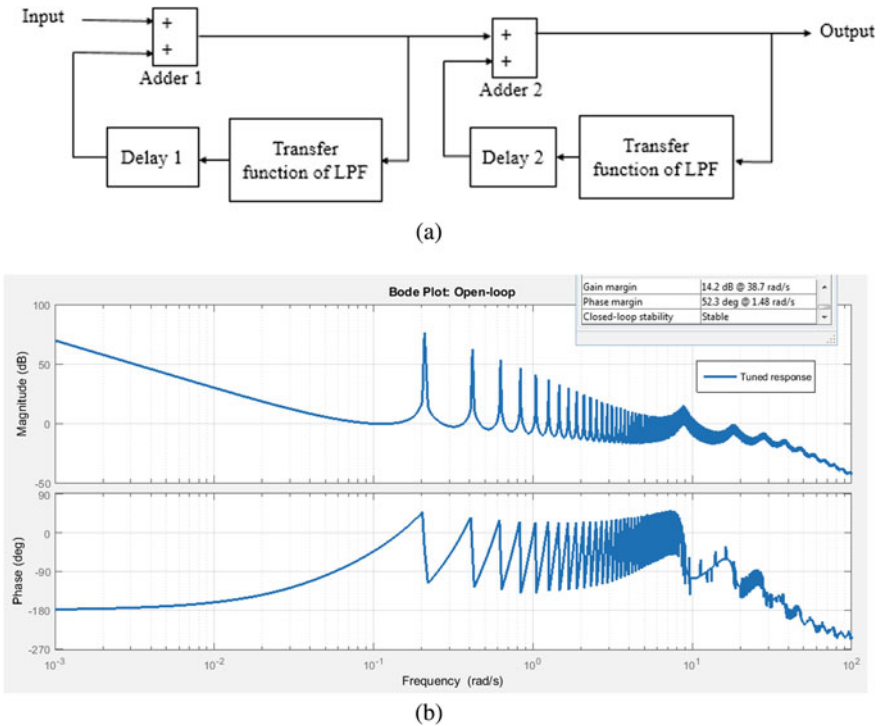
Fig. 7 FDRRC loop derived from Singh's model and stable frequency response of the process; (**a**) Simulink model, (**b**) Bode plot of the system

(a)

(b)
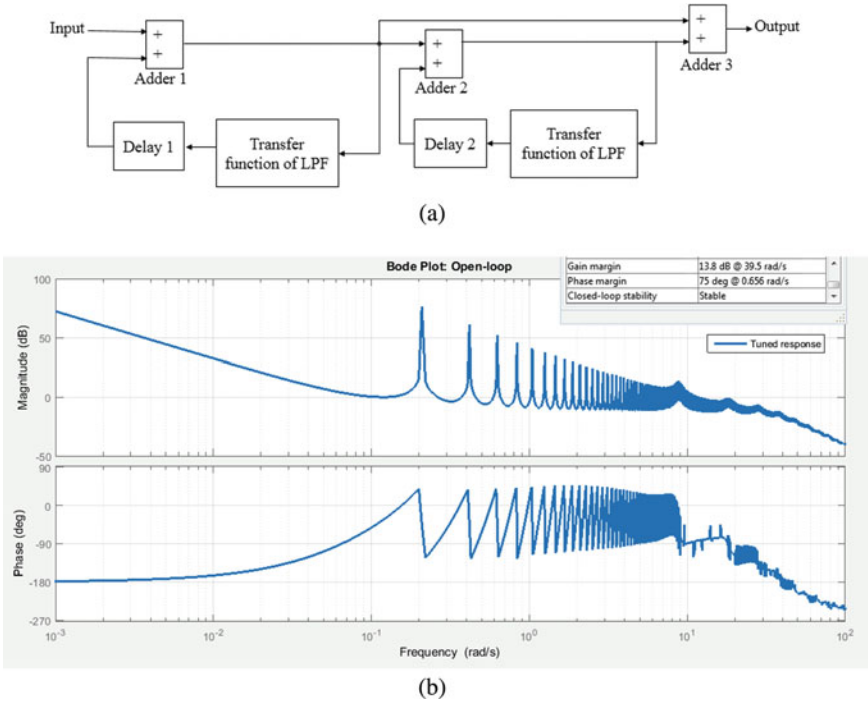
Fig. 8 FDRRC loop derived from Mondal's model and stable frequency response of the process; (**a**) Simulink model, (**b**) bode plot of the system

FDRRC derived from Owens' Model. According to D. H. Owens, a multi-periodic repetitive controller loop is designed as shown in Fig. 9(a). Figure 9(b) shows the stable frequency response of the system obtained by this approach.

It is a linear combination of single-periodic repetitive control elements with a stable filter, in each loop, introduced to filter out the noise. The relative weights given to each internal model are represented by the gains.

6   Results

This paper has dealt with effectiveness of FDRRC based PD controllers for periodic reference and periodic disturbances over RCPD controller. Then, an attempt is taken to show the effects of modified FDRC including multiple loops on the taken 7 degrees-of-freedom (DoF) robot arm.

Figure 10(a, b) represent the comparison among the tracking errors obtained by using RCPD and FDRC based PD controller and also among different FDRRC based PD controllers derived from different models given by Dr. Singh, Dr. Mondal, and D. H. Owens, respectively.

(a)

(b)
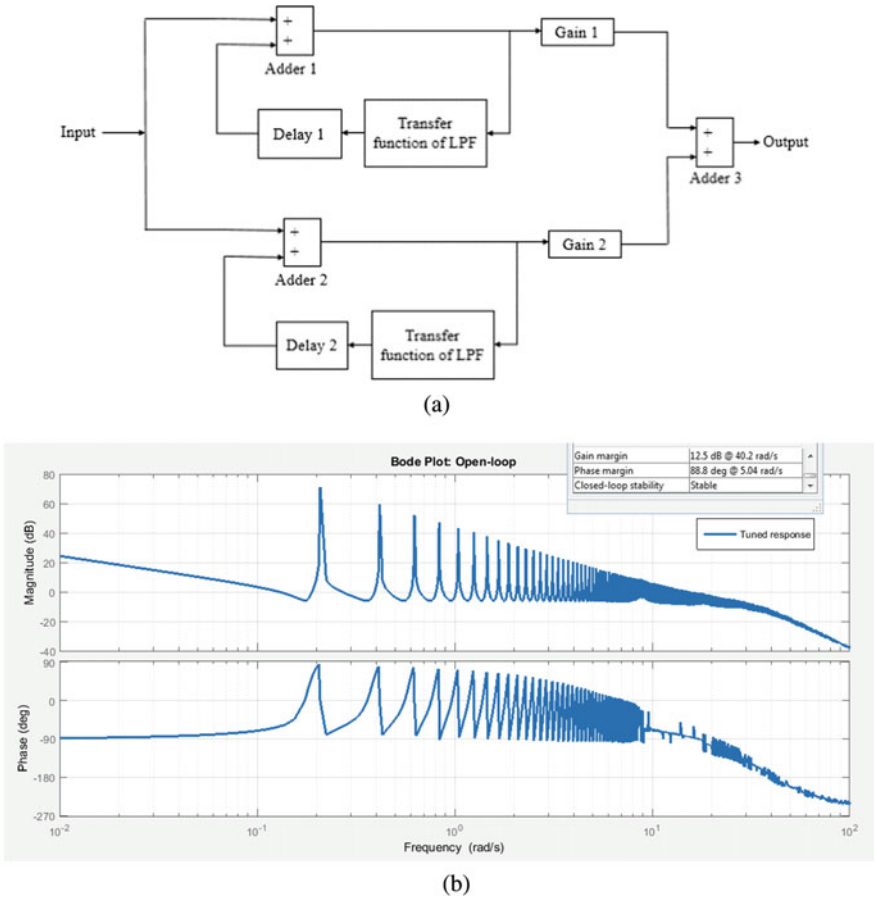
Fig. 9 FDRRC loop derived from Owens' model and stable frequency response of the process;
(**a**) Simulink model, (**b**) Bode plot of the system

The time integral performance criteria commonly used to measure errors like Integral Absolute Error (IAE), Integral Time weighted Absolute Error (ITAE), Integral Squared Error (ISE), and Integral Time weighted Squared Error (ITSE) [11]. For determining time integral performance criteria, a fixed experiment is needed to be performed on the system (i.e., a fixed set point or disturbance change) and over a fixed time period the integrals are evaluated. Theoretically, this time period should be infinite but practically it is the time needed for a system's responses to be settled. To have numerical representation of errors obtained in this paper, comparison of the values of Integral Absolute Error (IAE), Integral Time weighted Absolute Error (ITAE), Integral Squared Error (ISE), and Integral Time weighted Squared Error (ITSE) [12] is given in Table 1.
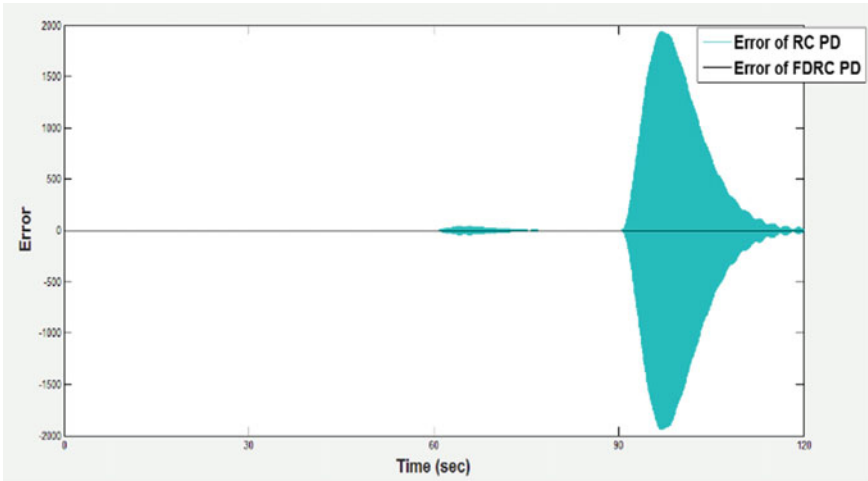
(a)
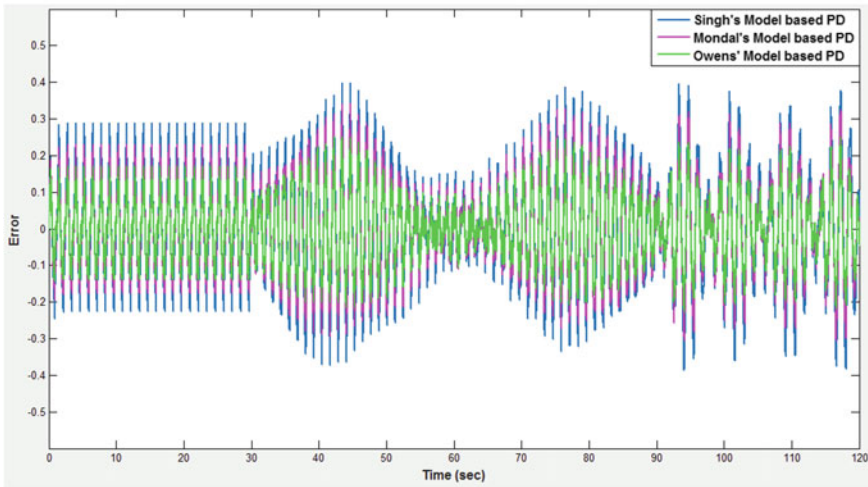
(b)

Fig. 10 Comparison of tracking errors of the process; (**a**) using RCPD and FDRC based PD controller, (**b**) using different models derived FDRRC based PD controllers

7 Conclusion

In this paper, basic description of a 7 degrees-of-freedom (DoF) robotic arm has been given in brief. RCS, implemented using IMP, shows infinite dimensional nature and makes the system unstable. In order to minimize the effect of the positive feedback in the RC loop, a suitably designed LPF is included. A trade(s)-off between stability and tracking performances is involved with the stability of the developed control

Table 1 Comparison of IAE, ITAE, ISE, and ITSE of the system obtained using RC based PD controller, single loop FDRC based PD controller and modified FDRRC based PD controllers

Control strategies	Comparison of errors (numerical representation)			
	IAE	ITAE	ISE	ITSE
RC based PD controller	1.369×10^4	1.358×10^6	1.432×10^7	1.41×10^9
Single loop FDRC based PD controller	17.30	1068	3.583	226.9
Singh's model derived FDRRC based PD controller	15.54	955.6	2.862	183.9
Mondal's model derived FDRRC based PD controller	12.41	768.6	1.88	120.1
Owens' model derived FDRRC based PD controller	9.297	575.8	1.062	67.47

system using FDRRCS. The various model derived FDRRCS have been used with the said system. Comparison among the RC based PD controller and the FDRRC based PD controllers derived from different models has been performed in terms of tracking errors, while following periodic reference signal as well as attenuating periodic disturbance signal. Owens' model derived FDRRC gives better result with respect to other approaches used in this paper.

References

1. Doh, T.Y., Ryoo, J.R.: Robust repetitive controller design and its application on the track-following control system in optical disk drives. In: 50th IEEE Conference on Decision and Control and European Control Conference, pp. 1644–1649 (2011)
2. Wang, L., Freeman, C.T., Chai, S., Rogers, E.: Multivariable Repetitive-Predictive Control of a Robot Arm with Experimental Results. International Federation of Automatic Control Milano, Italy (2011)
3. Briot, S., Khalil, W.: Dynamics of Parallel Robots. In: Springer, Mechanisms and Machine Science, vol. 35 (2015). https://doi.org/10.1007/978-3-319-19788-3
4. Kurniawan, E.: Robust Repetitive Control and Applications. Swinburne University of Technology, Melbourne (2013)
5. Francis, B., Wonham, W.: Internal model principle in control theory. Automatica **12**, 457–465 (1976)
6. Hara, S., Yamamoto, Y., Omata, T., Nakano, M.: Repetitive control-system—a new type servo system for periodic exogenous signals. IEEE Trans. Autom. Control **33**(7), 659–668 (1988)
7. Camacho, N.A., Mermoud, M.A.D.: Fractional adaptive control for an automatic voltage regulator. ISA Trans. **52**(6), 807–815 (2013)
8. Singh, T., Vadali, S.R.: Robust time-delay control. J. Dyn. Syst. Meas. Control Trans. ASME **115**, 303–306 (1993)
9. Mondal, U., Sengupta, A., et al.: Finite dimensional repetitive controller for identified model of a DC servo system. In: IEEE, ICPEN, pp. 1–4 (2012)
10. Owens, D.H., Liand, L.M., Banks, S.P.: Multi-periodic repetitive control system: a Lyapunov stability analysis for MIMO systems. Int. J. Control 505–506 (2007)

11. Fang, H., Chen, L., Shen, Z.: Comparison of different integral performance criteria for optimal hydro generator governor tuning with a particle swarm optimization algorithm. In: International Conference on Computational Science, pp. 1186–1189 (2007)
12. Duarte-Mermoud, M.A., Prieto, R.A.: Performance index for quality response of dynamical systems. ISA Trans. 133–151 (2004)

Median Filter Based Noise Reduction and QRS Detection in ECG Signal

Avishek Paul , **Saikat Panja, Nantu Das, and Madhuchhanda Mitra**

Abstract   In the present study, a nonlinear filtering technique using median filter is proposed for noise reduction and delineation of standard ECG signal. The advantage of using nonlinear median filter lies in the fact that no mathematical transformation is used. Hence, time and space complexity are also reduced. As the mathematical transformation introduces distortion in the acquired ECG signal, nonlinear median filter is a great choice to denoise the ECG signal. A single-median filtering technique is capable of removing all possible artifacts present in recorded ECG signals. QRS complex is identified from the filtered signal using the same median filtering technique. Result shows the effectiveness of the proposed method of artifact removal from recorded ECG signals. This method is computationally very simple and can be applied in real-time operations without any appreciable time delay due to signal processing stage.

Keywords Baseline wandering artifact · ECG · Median filter · Power line interference artifact · QRS detection

1 Introduction

Electrocardiogram (ECG) is one of the most familiar bio-signals which are able to identify several cardiac disorders. These recordings of ECG signals are normally superimposed with many artifacts or noises arising due to some muscular activity, power line interference (50 Hz), baseline wandering noise (0–1 Hz) or any other motor

A. Paul (✉)
Department of AEIE, RCC Institute of Information Technology, Kolkata, West Bengal 700009, India
e-mail: avishek.paul@rcciit.org

S. Panja · M. Mitra
Instrumentation Engineering, Department of Applied Physics, University of Calcutta, Kolkata, West Bengal 700009, India

N. Das
Department of AEIE, Techno International New Town, Kolkata, West Bengal 700156, India

movement. It is therefore essential to remove these noises before further processing in order to predict any probable disorders. Literature shows the application of adaptive filtering for bio-signals for filtering purpose [1] and has been used extensively in ECG processing [2]. In order to cancel out the power line interference signal, separate leads were also used to record the power line frequency component and then subtracted from the original recorded signal [3]. Multiple surface leads are used in order to increase SNR and noise removal procedure by discriminating P waves [4]. Method of cancelation of cardiogenic interference from impedance plethysmographic signal is also recorded in the literature [5]. Detection of P waves is also reported using similar technique [6]. Researchers have also used signal averaging method for suppressing random noise occurring during the recording session [7]. However, this technique does not provide satisfactory result for periodic noises like power line and base line artifacts [8]. Method of post recording interference elimination methods uses recursive notch filters for removing line interferences. Alternate method of subtraction of a shifted scaled version of a simultaneously recorded common mode line interference signal from the ECG is also reported [9]. Task Force Committee of the European Society of Cardiology, the American Heart Association, and the American College of Cardiology, discouraged the use of notch filters since optimizing the stop band of these filters result in an unwanted transient response which is most prominent in the late-potential region following the large QRS complex [10].

Van Alste and Schilder introduced a technique using finite impulse response (FIR) filter of reduced number of taps [11]. The authors claimed that the baseline and power line noises were satisfactorily removed to a certain extent. Use of linear phase filters having lower cut-off frequency of 0.8 Hz showed that the baseline wandering drift is canceled and the main specifications and clinical information contained in the slower ECG (case of the Bradycardia of 48 bpm) are preserved [12]. An integer coefficient band pass filter to eliminate the baseline wandering effect and both 50 and 100 Hz power line interference was also reported in literature [13]. Some other variants of digital filter, which are similar to the problem, were reported in [14–18], using, respectively, time varying digital filtering, nonlinear high pass filtering, fast adaptive notch filter, and a modified morphological filter. A new technique using the wavelet packet decomposition that computes energy calculation for each scale in order to evaluate a correct baseline signal was reported [19]. In another alternative technique, the DCT was effectively used by Shin et al. [20], for suppressing baseline and power line noises in recorded ECG signals. Zivanovic and González-Izal [21] proposed a combined model in order to remove baseline wandering and power line interference signal components from ECG and EMG recordings. Methods based on empirical wavelet transform (EWT) were used for power line and baseline noise cancelation from ECG signals [22].

Noise suppression can be effectively carried out using linear filters due to their inherent property of invariance and superposition principle. Normal noises which remain superimposed with the original signal are easily separated using linear filters without any distortion. However, there are certain instances where the noises are having sharp edges and high frequency components of the signal. Application of linear filters will smear out the edges and distort the sharp boundaries. Some noises

which are impulsive in nature cannot be removed using linear filtering because of its wide spectrum distribution which certainly overlaps with the signal component.

In view of the above mentioned problems, the authors present a simple and novel technique using median filter for removal of low and high-frequency noises such as baseline wandering and power line interfering noises. A median filter is capable enough to eliminate the above mentioned noises without any appreciable distortion in the original signal. Moreover, the same filter is used to identify the QRS complex from the ECG waveform which is the most critical part of the entire signal. The following topics mainly focus on:

a. Removal of baseline wandering noise
b. Removal of power line interference noise
c. Detection of QRS complex.

2 Methodology

The proposed algorithm of filtering technique using median filter comprises of the successive stages of filtering out the noise components from the acquired ECG signal as mentioned above. The flow diagram representation of the entire algorithm is depicted in Fig. 1.

2.1 ECG Signal Database

The database which was used for validation of noise reduction and delineation of proposed algorithm is MIT/BIH arrhythmia which is a standard database. The dataset contains forty eight records, where every record contains two-channel ECG signals for thirty minute duration of 47 individuals. Every record contains two leads; the limb lead 2 and one of the chest leads V1, V2, V4 or V5. ECG signals are filtered using band pass filter at 0.1–100 Hz and then sampled at 360 Hz per channel with 11-bit resolution over a 10 mV range. The data is obtained from MIT/BIH arrhythmia database in .mat format. The size of available data is 648,000 samples. For the present work, the samples of data from 3000 to 10,000 are used. So, the time duration is shown from 8.33 to 27.77 s.
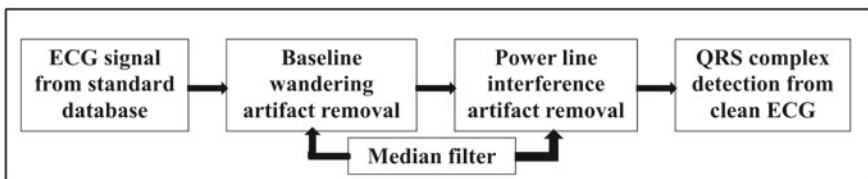
Fig. 1 Flow diagram of artifact elimination technique from ECG signal using median filter

2.2 Median Filter

The median filter operates on the signal sample by sample, replacing each sample with the median of adjacent samples. The size or width of the neighboring samples is called the "window," which slides sample by sample, for the entire signal array.

In mathematical form, filtering technique at time n for a filter of size N may be expressed as

$$Y[n] = \text{Median of } (X[n - N], \ldots, X[n], \ldots, X[n + N]) \tag{1}$$

where $X[n]$ signifies discrete input data sample and $Y[n]$ represents the filter output, at time n.

2.3 Baseline Wandering Artifact Removal

Baseline wandering artifact is normally present in almost all the recordings of ECG signal. These are basically low-frequency signal component which arises due to slight movement of the subject during recording. The frequency band of the baseline wandering noise is 0.8–1.25 Hz. The median filter is used as a low pass filter. Since the sampling frequency (f_s) of the recorded signal is 360 Hz, the value of sampling time period (Ts) = 2.77 ms = 0.00277 s. Taking the highest frequency of baseline wandering noise f_{BW} = 1.25 Hz, the time period of the baseline wandering noise comes out to be T_{BW} = 0.80 s.

If N be the number of point for median filtering, then

$$0.00277 * N = 0.8 \tag{2}$$

Thus, the value of N comes out to be 288. In order to remove the baseline wandering noise component, 288 point median filter was used. If, Y represent original sampled ECG signal, $Y1$ represent the output of the median filter which contain low frequency component of the sampled ECG signal, then $Y2 = (Y - Y1)$ is the sampled ECG signal which is devoid of baseline wandering artifact.

2.4 Power Line Artifact Removal

The power line interference noise component often contaminates the sampled ECG signal at 50 Hz frequency. This frequency component is normally superimposed with original ECG signal and often corrupts the record. Thus, this signal component is essential to be removed before further analysis.

Taking the sampling frequency (f_s) to be 360 Hz and power line noise frequency component (f) to be 50 Hz, the time period of power line frequency (T) comes out to be 0.02 s. If $N1$ be the number of point for median filtering,

$$0.00277 * N1 = 0.02 \tag{3}$$

The value of $N1$ comes out to be 7. After applying seven point median filter, the clean ECG signal is obtained which is free from power line interference noise.

2.5 QRS Complex Detection

The most important part of the ECG signal is the QRS complex and thus needs to be identified. QRS complex contain vital signs of various diseases which can be predicted if these segments are properly identified.

In ECG signal, P and T wave contain frequency band of (8 - 12.5) Hz. Since the maximum signal frequency component in P and T wave is = 12.5 Hz, the minimum time period contain in P and T wave is = 0.08 s. If N2 be the number of point for median filtering,

$$0.00277 * N2 = 0.08 \tag{4}$$

Thus, the value of $N2$ is 29. Taking a median filter of twenty nine points, the P and T component waves of the ECG signal are detected. Once, P and T wave components are identified, these components are subtracted from clean ECG signal in order to get the QRS complex contained in the original signal. If $Y3$ represents ECG signal which is free from baseline and power line interference noises, $Y4$ is the output of the Median Filter which contain P and T wave component of sampled ECG signal, $Y5 = (Y3 - Y4)$ contain the detected QRS complex in the ECG signal. One such representative method of QRS complex detection by eliminating the noises and the other segments of ECG signal is shown in Fig. 2.

3 Result

As mentioned in the methodology section, baseline wandering noise was removed at the first stage of the noise filtering procedure. One such comparison plot of original ECG record with baseline artifact and the baseline noise filtered signal is shown in Fig. 3.

Once the baseline noise was eliminated successfully, power line interference noise was eliminated from the original signal array for testing the algorithm using the process already stated above. Result of power line removed signal of one record is shown in Fig. 4 as a comparison plot with the signal containing power line artifact.
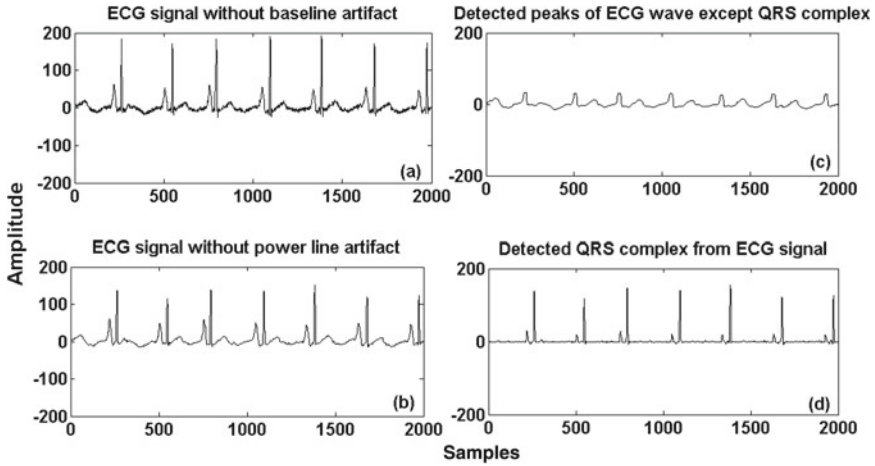
Fig. 2 Representative plot of **a** baseline artifact eliminated ECG wave, **b** power line artifact eliminated ECG wave, **c** detected segments of ECG other than QRS complex and **d** detected QRS complex from the ECG wave
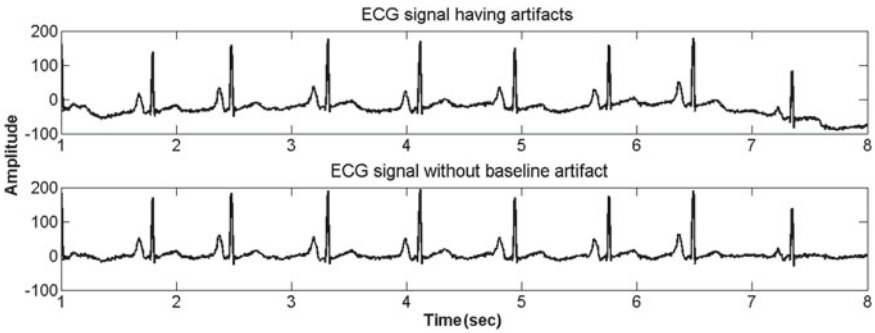
Fig. 3 Comparison plot of ECG signal before and after baseline noise removal
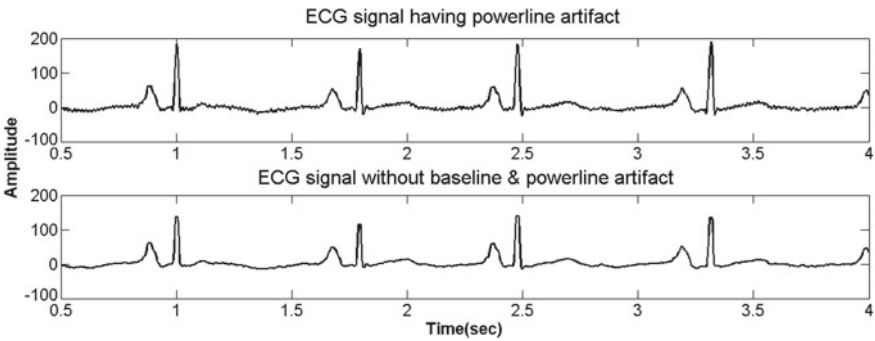
Fig. 4 Comparison plot of ECG signal before and after power line noise removal

The process of detection of QRS complex from the filtered ECG signal succeeded which is shown in Fig. 5 for a particular record. This was one of the major target for the present study and was tested separately.

Upon successful testing of all the above stages of the filtering process, the entire algorithm was applied on the raw ECG signal and final output is plotted to verify the validity of the method. These figures clearly indicate all the sub stages of the filtering process and necessary performance of the algorithm already proposed. The result shows the effectiveness of the proposed algorithm and justifies its novelty in the field of filtering mechanism.

In order to justify the validity of the proposed method, one representative plot of the acquired ECG signal is shown in Fig. 6 along with its filtered counterpart and the detected QRS complexes from the clean signal. It is very much conclusive that the filtered signal holds all the clinical attributes of the original signal and only
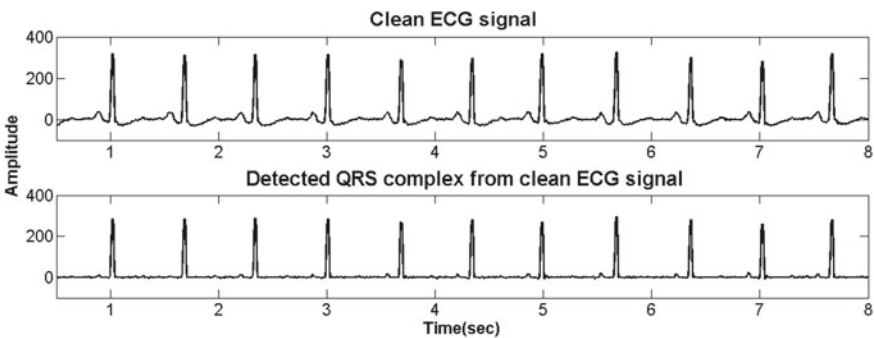
Fig. 5 Comparison plot of ECG signal before and after detection of QRS complex
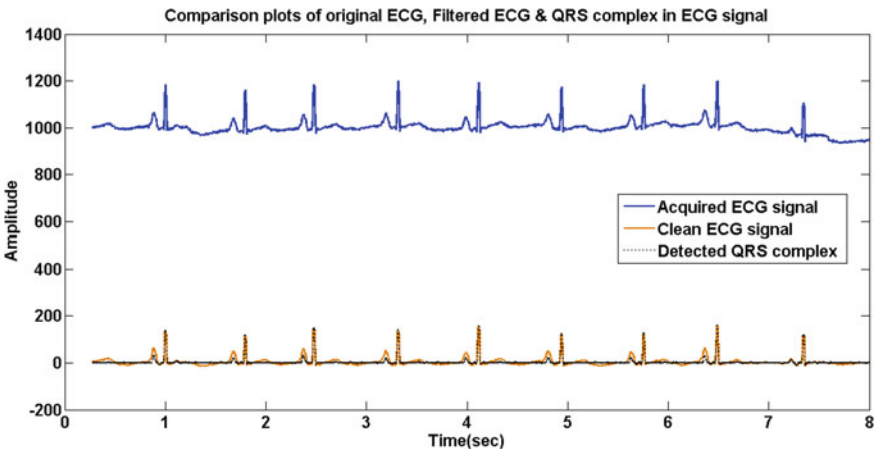
Fig. 6 Comparison plot of original ECG signal, clean ECG signal and QRS complex detected signal

the desired noise components have been eliminated. Thus, this method proves its importance in this field of ECG denoising and can be coined as a powerful tool in this context.

4   Discussion

The present study focuses on the extraction of QRS complex from the ECG signal since it is considered to be the most vital part of the entire waveform. The detection of QRS complex in a proper manner can lead to a successful diagnosis of several heart related diseases and thus could help the medical practitioners in order to predict some possible disorders. Apart from this QRS complex, the rest part of the ECG waveform is also of clinical importance as each of the segments such as P-Q, S-T, etc., carries vital information about the cardiac response of an individual. The proposed technique can be extended to clearly identify and filter out the necessary ECG segments in terms of their duration and amplitude. There are several cardiac related disorders which can be directly estimated from the values of these segments. This gives the flexibility and novelty of the proposed algorithm which can have widespread application in ECG denoising and disease prediction. The algorithm has been tested on all the available records in the database and the results show that there was no distortion or discontinuity in the clean ECG signal. However, the algorithm needs to be tested on ECG signal of different sampling frequencies and containing some additional noise components. From Fig. 6, it is clear that the proposed technique is a potential filtering method of ECG denoising and the detected QRS complex signal is matching with the clean ECG signal thus proving the validation of the median filter application.

5   Conclusion

The ECG signal used for the present study is taken from a standard database. The same procedure can also be used to eliminate the artifacts for real world ECG signal recorded with standard electrode system. Development of portable healthcare system in medical fraternity is growing rapidly. So, design of a standalone system is necessary for removal of noise and delineation of ECG signal is of primary importance. In standalone system, available memory space is small. So, complex transform based technique for noise reduction and delineation of biomedical signal is difficult in standalone system. The novelty of the proposed method is simplicity and low complexity. The method can be directly applied on acquired data samples and require very small processing time and memory. Although the above algorithm is tested for offline analysis, it is capable enough to use in an online application. In the present work, the proposed method was tested on ECG signal. The algorithm for artifact elimination from ECG signal using median filter based technique was implemented using MATLAB software. The proposed algorithm takes less than two seconds on

an average for its computation and thus does not introduce any time delay in the real time system. This method of artifact elimination can also be extended for other biomedical signals which often get corrupted by these types of noises. The proposed method is very simple and does not add any time lag due to the processing stage. The comparison plot shows the effectiveness of the algorithm for artifact elimination present in recorded ECG datasets. The authors feel that the challenge stated in the introduction part can be overcome using the proposed method.

References

1. Yelderman, M., Widrow, B., Cioffi, J.M., Hesler, E., Leddy, J.A.: ECG enhancement by adaptive cancellation of electrosurgical interference. IEEE Trans. Biomed. Eng. **BME-30**, 392–398 (1983)
2. Ferrera, E.R., Widrow, B.: Fetal electrocardiogram enhancement by time-sequenced adaptive filtering. IEEE Trans. Biomed. Eng. **BME-29**, 458–460 (1982)
3. Widrow, B., Glover, J.R., McCool, J.M., et al.: Adaptive noise cancelling principles and applications. Proc. IEEE **63**, 1692–1716 (1975)
4. Dufault, R.A., Wilcox, A.C.: Dual channel P-wave detection in the surface ECG via the LMS algorithm. In: Proceedings of the IEEE/8th Annual Conference of the Engineering in Medicine and Biology Society, pp. 325–328 (1986)
5. Sahakian, A., Kuo, K.H.: Cancelling cardiogenic artifact in impedance pneumography. In: Proc. 9th Annual Conference of the Engineering in Medicine and Biology Society, pp. 855–859 (1985)
6. Zhu, Y., Thakor, N.V.: P-wave detection by adaptive cancellation of QRS-T complex. In: Proceedings of the IEEE/8th Annual Conference of the Engineering in Medicine and Biology Society, pp. 329–331 (1986)
7. Berbari, E.J., Lander, P.: Principles of noise reduction. In: El-Sherif, N., Turitto, G. (eds) High Resolution Electrocardiography, pp. 51–66. Futura, New York (1992)
8. Evanich, M.J., Newberry, A.O., Partridge, L.D.: Some limitations on the removal of periodic noise by averaging. J. Appl. Physiol. **33**, 536–541 (1972)
9. Ider, Y.Z., Koymen, H.: A new technique for line interference monitoring and reduction in biopotential amplifiers. IEEE Trans. Biomed. Eng. **37**, 624–631 (1990)
10. Breithardt, G., Cain, M.E., El-Sherif, N., Flowers, N.C., Hombach, V., Janse, M., Simson, M.B., Steinbeck, G.: Standards for analysis of ventricular late potentials using high-resolution or signal-averaged electrocardiography: a statement by a Task Force Committee of the European Society of Cardiology, the American Heart Association and the American College of Cardiology. JACC **17**, 999–1006 (1991)
11. Van Alste, J.A., Schilder, T.S.: Removal of base-line wander and power-line interference from the ECG by an efficient FIR filter with a reduced number of taps. IEEE Trans. Biomed. Eng. **12**, 1052–1060 (1985)
12. Van Alste, J.A., Van Eck, W., Herrmann, O.E.: ECG baseline wander reduction using linear phase filters. Comput. Biomed. Res. **19**(5), 417–427 (1986)
13. Warlar, R., Eswaran, C.: Integer coefficient bandpass filter for the simultaneous removal of baseline wander, 50 and 100 Hz interference from the ECG. Med. Biol. Eng. Comput. **29**(3), 333–336 (1991)
14. Sörnmo, L.: Time-varying digital filtering of ECG baseline wander. Med. Biol. Eng. Comput. **31**(5), 503–508 (1993)
15. Keselbrener, L., Keselbrener, M., Akselrod, S.: Nonlinear high pass filter for R-wave detection in ECG signal. Med. Eng. Phys. **19**(5), 481–484 (1997)

16. Ma, W.K., Zhang, Y.T., Yang, F.S.: A fast recursive-least-squares adaptive notch filter and its applications to biomedical signals. Med. Biol. Eng. Comput. **37**(1), 99–103 (1999)
17. Taouli, S.A., Bereksi-Reguig, F.: Noise and baseline wandering suppression of ECG signals by morphological filter. J. Med. Eng. Technol. **34**(2), 87–96 (2010)
18. Hu, X., Xiao, Z., Zhang, N.: Removal of baseline wander from ECG signal based on a statistical weighted moving average filter. J. Zhejiang Univ. Sci. C **12**(5), 397–403 (2011)
19. German-Sallo, Z.: ECG signal baseline wander removal using wavelet analysis. In: International Conference on Advancements of Medicine and Health Care Through Technology, pp. 190–193. Springer, Berlin Heidelberg (2011)
20. Shin, H.S., Lee, C., Lee, M.: Ideal filtering approach on DCT domain for biomedical signals: index blocked DCT filtering method (IB-DCTFM). J. Med. Syst. **34**(4), 741–753 (2010)
21. Zivanovic, M., González-Izal, M.: Simultaneous powerline interference and baseline wander removal from ECG and EMG signals by sinusoidal modeling. Med. Eng. Phys. **35**(10), 1431–1514 (2013)
22. Singh, O., Sunkaria, R.K.: ECG signal denoising via empirical wavelet transform. Australas. Phys. Eng. Sci. Med. (2017). https://doi.org/10.1007/s13246-016-0510-6

Classification of Illuminance Images Using Eigenface Technique

Arijit Ghosh, Palash Kumar Kundu, and Gautam Sarkar

Abstract The present work proposes an experimental technique to classify the illuminance images after acquisition from a lux sensor interfaced with Wi-Fi-enabled microcontroller and placed over the roof of a remote operated car in a client–server wireless network configuration. The illuminance images thus generated experimentally are analyzed using image processing technique for evaluation of its illumination level in comparison with standard lux images. In the preprocessing stage, the captured illuminance images are converted into gray-scale form having spatial pixel intensity. Then, they are normalized and the Eigenface is detected for both training as well as testing image. The feature value of the Eigenface is used to find the composite distance. PCA based Eigenface method projects the large-dimensional image space into lesser dimensional image space by finding their principal components. Eigenface can calculate the proximity of neighboring pixels between training and testing images. The difference in composite distance is found out to check the similarity between the known Eigenface and test Eigenface obtained from the image formed by the captured illuminance data.

Keywords Illuminance · Principal component analysis · Eigenface · Euclidean distance · Similarity

1 Introduction

Image processing is a technique considered under the domain of signal processing. There are two major types of image processing methods namely, analog image processing which deals with time-varying two-dimensional signal processing and digital image processing which analyzes and manipulates mainly the quality and intensity distribution of a digital signal. Now, the processing of a digital image is

A. Ghosh (✉)
Department of AEIE, RCC Institute of Information Technology, Kolkata 700015, India

P. K. Kundu · G. Sarkar
Department of EE, Jadavpur University, Kolkata 700032, India

performed by the help of some algorithms applied through a digital device, e.g., a computer to modify the image of interest or extract meaningful insights from it [1]. Principal Component Analysis (PCA) is a popular pattern recognition method to substitute larger sized correlated vectors with the lower sized uncorrelated vectors to form a basis for the dataset to be used. The advantages of PCA are high efficacy; lesser sensitivity to noise as well as reduced memory requirements to handle computational burdens, and it is the basis of the Eigenface technique [2, 3], widely used in face recognition applications. The idea of using Eigenface for face recognition was conceived by Sirovich and Kirby. They showed that PCA could be used on a set of basis pictures called eigen-pictures to linearly combine and reconstruct images from the training dataset [4]. However, Turk and Pentland have applied the Eigenface method for successful recognition of face. They extracted the Eigenvectors of a covariant matrix for eigen-decomposition of a large number of higher dimensional facial image pixel numbers [5]. This technique was expanded with preprocessing to enhance the accuracy by multiple manifold approach to develop eigen vectors having various subjects and features, and thus, computerized face recognition is feasible nowadays [2]. For meteorological data analysis using PCA, Euclidean distance was used for finding out the similarity factor [6]. Wang et al. [7] used similar concept, for detecting the spatial relationship among image pixels. The comparative study of different age group dataset was performed by calculating the similarity factor of principal components [8]. Similarity checking of two images and also of multivariate time-series dataset can be done using Eigenface technique [9, 10]. The classification of thermal image to assess the heating quality was done in [11] using indirect measurement. In short, Eigenface technique using PCA has been applied for various classification techniques. However, our objective is to classify the illuminance distribution of an indoor space, which was not found in many literatures, while the survey was performed. Hence, this idea came into our mind to apply this technique and investigate if it can detect the illuminance level of the selected indoor space satisfactorily.

2   Adopted Methodology

2.1   Principal Component Analysis (PCA)

The datasets where multivariate analysis are applied are normally large in nature and otherwise not easily interpretable. In PCA, the dimensionality of larger datasets is reduced, particularly where the quantity of feature variables are way ahead of the sample size. PCA enhances the interpretability and reduces information loss; thus, create newer uncorrelated variables to increase the variance. The reason for using PCA is to decrease the multivariate data size yet sustain the orthogonality [12]. The target is to project the original vector-data, $X = [x_1 \ x_2 \ x_3 \ x_4 \ \ldots \ x_p]^{\mathrm{T}}$, comprising of certain characteristics to a new vector-data $Z = [z_1 \ z_2 \ z_3 \ z_4 \ \ldots \ z_m]^{\mathrm{T}}$, here m is

smaller than *p*. The original vector-data *X* is represented by the linear combination of an orthonormal vector-set v_i, where

$$X = \sum_{i=1}^{m} z_i v_i \tag{1}$$

Co-efficient z_i is formulated using the ensuing equation:

$$z_i = v_i^{\mathrm{T}} X \tag{2}$$

PCA can be formed by the decomposition method of eigenvalue. This is similar to the tuning of a coordinate system from actual dataset *X* into a new coordinate dataset denoted by *Z*. To reduce data dimensions, a subset (as $m < p$) of these v_i vectors are maintained that are termed as principal components—they remain same as the eigenvectors of covariance matrix dataset. The dimensionality trimming from *p* to *m* produces approximation error that can be decreased if eigenvectors are selected from the highest eigenvalues of covariance matrix such that it consists greater than ninety percent of actual knowledge.

2.2 Eigenface Method

PCA forms the basis of Eigenface technique. The steps to be followed for the Eigenface method comprises of extracting the exclusive image characteristics and represent it as a linear combination of Eigenfaces obtained by the component derivation procedure.

Principal components of the illuminance-training dataset are obtained. Then, the recognition process is followed by projection into a space developed by the Eigenface. A performance comparison depending upon the Euclidian distance of the eigenvectors are found out which means the Eigenface of training images and testing image is determined. If this distance is marginal to the heuristically chosen tolerance, then the test illuminance image is detected else, it remains to be uncategorized [2]. The entire procedure is described using Fig. 1. The Euclidean distance of test image weight vector (w_M) from training image database weight vectors (w_T) is perceived from Eq. (3):

$$d(w_{\mathrm{T}}, w_{\mathrm{M}}) = \left(\sum_{i=1}^{n} (w_{\mathrm{T}i} - w_{\mathrm{M}i})^2 \right)^{\frac{1}{2}} = w_{\mathrm{T}} - w_{\mathrm{M}} \tag{3}$$

Here, *n* is the chosen Eigenface number. For the test image, Euclidian distance is lesser than a prefixed set point and minimal in the illuminance Eigenface training database. The test image will remain unrecognized if the Euclidean distance is larger
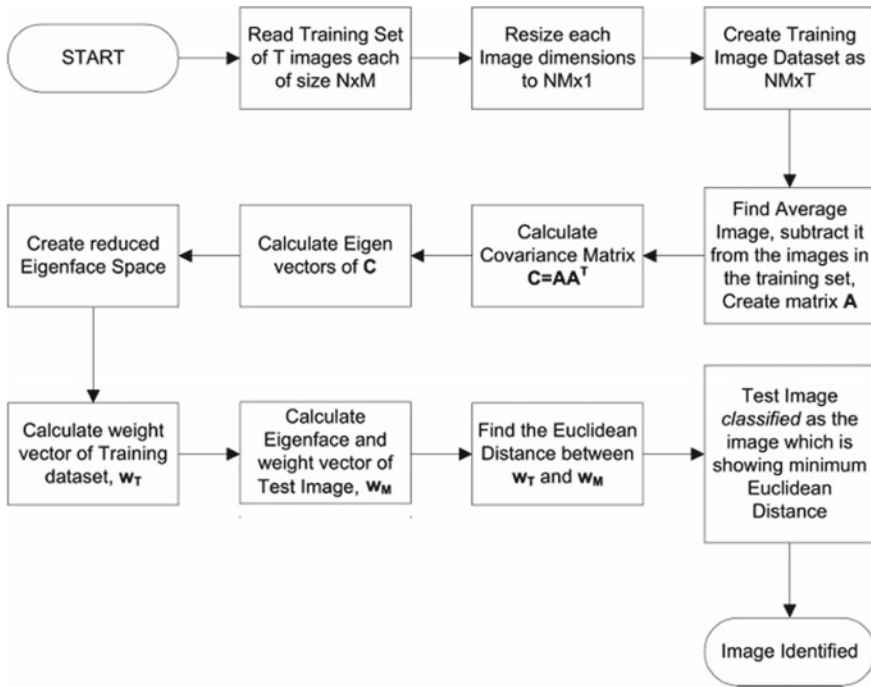
Fig. 1 Flowchart of Eigenface method for image recognition

than the set point. The Eigenface technique is very much easier to realize as there is no hardware necessities yet the accuracy is very high for image authentication. Although the computation time is quite high for image identity retrieval when the training dataset is large enough.

2.3 Steps Involved in Implementing Eigenface Calculation

The important steps involved for implementation of Eigenface calculation [9, 13] are as follow:

(a) Primarily, a dataset S comprising of all training images (Γ_1, Γ_2, …, Γ_n) is developed.
(b) Mean (Ψ) value is computed.
(c) Difference (Φ) between training image (Γ_i) and middle value (Ψ) is calculated
(d) Covariance matrix (C_M) value is found out.
(e) Eigenvalue (λ) and eigenvector (E_V) of covariance matrix (C_M) is computed.
(f) Eigenface for training images and testing images is found next.

Similarity is calculated depending on the minimal composite distance following the Euclidean distance method as shown in Eq. (4). Each individual sample is compared with the test matrix under study. The lowest feature value at the time of completion is considered to be the most similar sample.

$$D_{j,k} = \sqrt{\sum_{i=1}^{N}(E_{j,i} - E_{p,i})^2}, \quad \text{where } j = 1 \ldots n \text{ and } p = 1 \ldots k \qquad (4)$$

3 Experimentation Setup

An experimentation system was developed to acquire the illuminance values, then it is converted into illuminance image, and classification of unknown illuminance images were done using Eigenface technique. The performance comparison is done by determining the difference in composite distance for the unknown illuminance images and every training image from the database to classify the image category.

3.1 Client–Server System

The illuminance data are captured through a client–server configuration [14, 15] as described using Fig. 2.

a.   Client System: The client system comprises of BH-1750 module, which is an illuminance sensor capturing the lux information and IR transceiver block to capture the positional data. The sensing system is interfaced with NodeMCU ESP-8266 unit having integrated Tensilica microcontroller with ESP-8266 Wi-Fi module in I^2C (inter-integrated circuit) communication mode. The client system is driven by a rechargeable battery and is placed over the roof of a RF
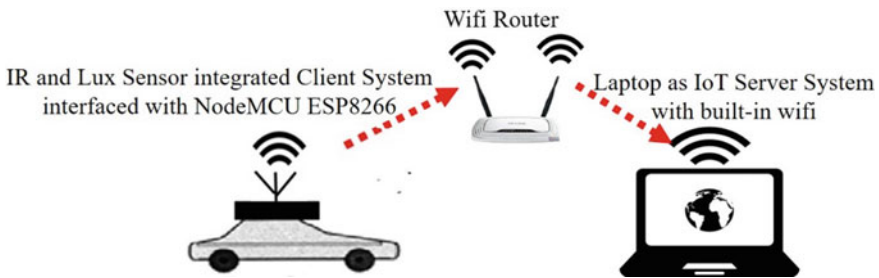
Fig. 2 Positional illuminance acquisition system

(radio-frequency) remote operated car. The client system moves through the selected indoor space locations, captures the illuminance values of user-defined positions, and transmits them to the server system.

b. Server System: The server system consists of a laptop with Intel Core I3-5th Generation x64-based processor, Windows 10 Operating System, 4 GB RAM, 802.11ac, 5-GHz wireless network adapter. It is connected to a wireless network through a proper network cable using Wi-Fi-router.

c. Wireless Router System: A dual-antenna wireless router is used, which supports IEEE 802.11X wireless standard, speed upto 20 Mbps, and WEP/WPA/WPA2 network security to establish the client–server wireless communication. It communicates to an Ethernet port through IP address. The locational illuminance data is stored in the server system in MS-Excel file for further processing.

3.2 Image Domain Transformation

The positional illuminance values along the selected indoor space (in X–Y domain) are transformed to an image in the server system. Suitable preprocessing techniques like filtering may be required to remove the presence of any noise in the captured data. Gaussian method of filtering was adopted in this study to remove linear noise and to filter nonlinear impulse noise and to obtain a supreme quality image, median filter was chosen [16]. Various illuminance environments were created and illuminance images were formed for each of them and are considered as training image. Three different illuminance classes were considered for generation of training data in this study.

4 Results and Discussion

The training dataset used in this study comprises of illuminance images belonging to three various class—Class-I: Non-uniform lux, Class-II: Uniform lux and Class-III: Highly non-uniform lux as indicated in Fig. 3a–c, respectively. Each image is having 3600 × 2400 pixel dimension. Primarily, the images are cropped into 1600 × 1500 pixel and then only they are converted to gray-scale image from RGB color domain. For minimizing the computational burden and speed up the process, the trained images were resized to 160 × 150 pixel dimension. Post normalization, following Eigenface method, the Eigenfaces possessing the highest eigenvalues were derived from the training dataset. A single-training image was considered to be a linear combination of the derived Eigenfaces. Each image could be reconstructed from the chosen Eigenfaces. Eigenfaces having the largest eigenvalues, represent major variations in the illuminance-training database. For testing purpose, unknown illuminance images as shown in Fig. 4a–c, respectively, are chosen to examine the
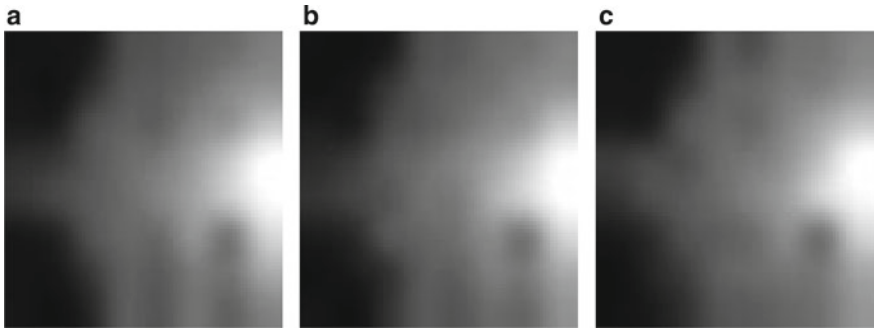
Fig. 3 **a** Training image class-I. **b** Training image class-II. **c** Training image class-III
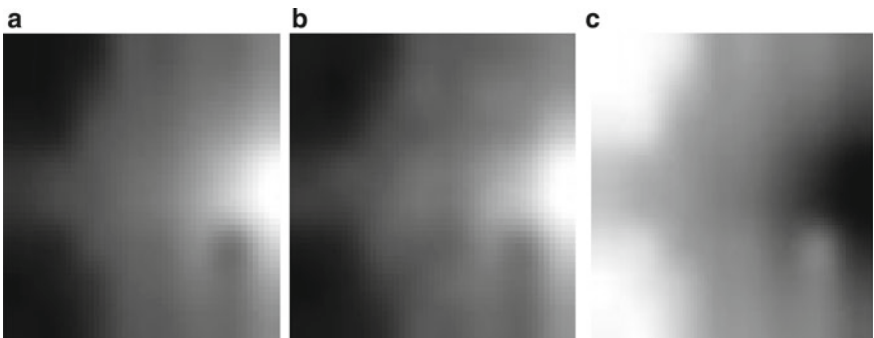
Fig. 4 **a** Test image-I. **b** Test image-II. **c** Test image-III

Table 1 Difference in composite distance between training and testing images	Test image No.	Class-I	Class-II	Class-III
	Test image-I	0.5623	0.4211	0.8478
	Test image-II	0.7045	0.6112	0.6483
	Test image-III	9.6867	9.7584	8.5598

illuminance class, which it actually represents. The difference in composite distance between the training and testing images is represented in Table 1.

5   Conclusion

An image comprises of information about a specific incident or it may be generated as an outcome of an experiment. If there is a similarity among the images, it may not be always separable by the human eye. Eigenface technique can be applied for image similarity measurement to find out if there is a meaningful difference between

the training images and a testing image. In this work, we have observed that within a known measured illuminance boundary, and the steady state illuminance distribution inside a contour can be estimated efficiently. The generated illuminance images from the acquired sensor data can be examined properly using Eigenface technique and difference in composite distance was determined for evaluation of the illuminance quality inside an indoor space. This type of information can be helpful in designing other corrective and preventive measures that may be required as a follow-up. In addition, this technique may be applied in similar studies [17] to find uniformity of any sensor data where direct measurement is difficult to obtain or in face recognition and thermal imaging related sensor applications.

References

1. Sharma, N., Mishra, M., Shrivastava, M.: Colour image segmentation techniques and issues: an approach. Int. J. Sci. Technol. Res. **1**(4), 9–12 (2012)
2. Çarıkçı, M., Özen, F.: A face recognition system based on Eigenfaces method. Procedia Technol. **1**, 118–123 (2012)
3. Slavković, M., Jevtić, D.: Face recognition using Eigenface approach. Serb. J. Electr. Eng. **9**(1), 121–130 (2012)
4. Sirovich, L., Kirby, M.: Low-dimensional procedure for the characterization of human faces. J. Opt. Soc. Am. A **4**, 519–524 (1987)
5. Turk, M., Pentland, A.: Eigenfaces for recognition. J. Cogn. Neurosci. **3**(1), 71–86 (1991)
6. Elmore, K.L., Richman, M.B.: Euclidean distance as a similarity metric for principal component analysis. Mon. Weather Rev. 540–549 (2001)
7. Wang, L., Zhang, Y., Feng, J.: On the Euclidean distance of images. IEEE Trans. Pattern Anal. Mach. Intell. **27**(8), 1334–1339 (2005)
8. Krzanowski, W.: Between-groups comparison of principal components. J. Am. Stat. Assoc. **74**, 703–707 (1979)
9. Putri, N.A., Siahaan, A.P.U., Wadly, F.: Image similarity test using Eigenface calculation. Int. J. Sci. Res. Sci. Technol. **3**(6), 510–514 (2017)
10. Yang, K., Shahabi, C.: A PCA-based similarity measure for multivariate time series. In: Proceedings of the Second ACM International Workshop on Multimedia Databases. ACM-MMDB 2004, Washington, DC, pp. 65–74 (2004)
11. Basak, C.K., Kundu, P.K., Sarkar, G.: Classification of thermal tomographic images using Eigenface method. In: Proceedings of Second IEEE International Conference on Control, Measurement and Instrumentation, CMI-2021, Kolkata (2021)
12. Kundu, M., Kundu, P.K., Damarla, S.K.: Chemometric Monitoring: Product Quality Assessment, Process Fault Detection and Applications. CRC Press (2018)
13. Tamimi, A.A., Al-Allaf, O.N.A., Alia, M.A.: Eigen faces and principle component analysis for face recognition systems: a comparative study. Int. J. Comput. Technol. **14**(4), 5650–5660 (2015)
14. Ghosh, A., Kundu, P.K., Sarkar, G.: Automated lux measurement for lighting design in indoor space using mobile sensor. In: Proceedings of IEEE International Conference on Applied Signal Processing, ASPCON-2018, Kolkata, pp. 106–109 (2018)
15. Ghosh, A., Kundu, P.K., Sarkar, G.: Design and real-time implementation of cloud based indoor illumination monitoring system. J. Inst. Eng. (India) Ser. B **101**(3), 223–227 (2020)

16. Ghosh, A., Kundu, P.K., Sarkar, G.: Computer vision based obstacle identification using real-time illumination sensor data. In: Proceedings of Second IEEE International Conference on Control, Measurement and Instrumentation, CMI-2021, Kolkata (2021)
17. Ghosh, A., Kundu, P.K., Sarkar, G.: Internet of human centric lighting: a brief overview on Indian aspects. Sci. Cult. J. 350–356 (2020)

Smart Agriculture Implementation—Blockchain IoT-Based Approach

Samira Bhattacharya and Naiwrita Dey

Abstract Over the years it has really been challenging working with Internet of Things (IoT) devices in terms of security as every IoT device offers a potential entry point. Blockchain is an emerging technology which is capable of minimizing the inherent risk of security and privacy issues of IoT. In this paper, blockchain IoT (BIoT)-based approach has been proposed to develop a smart agricultural system. It uses a distributed ledger which automatically stores the sensor data across different locations in a decentralized manner. Proposed method is beneficial compared to conventional IoT-based system as BIoT offers public access to the distributed ledger and time stamping of the sensor data. For the smart agriculture system, temperature and humidity of environment, moisture content and dielectric soil moisture content which are the fundamental parameters are measured here with three different sensors. NodeMCU has been used as IoT device. An Ethereum blockchain created via Ganache. Latency rate for the same is calculated.

Keywords Smart agriculture · Internet of Things · Blockchain · Ethereum · Smart contracts

1 Introduction

Internet of Things has paved its way in the technical world, thereby making work easier for everyone. It allows physical objects to communicate together, coordinate decisions and share information via certain protocols. IoT has challenged traditional devices to turn into intelligent ones, with the help of Internet Protocols, communication techniques, applications and sensor networks. The "things" in Internet of Things is a device which is an intelligently programmed computer sensor which can be driven around in the real world with sensors, driving output in the real world

S. Bhattacharya
Department of AEIE, RCCIIT, Kolkata, West Bengal, India

N. Dey (✉)
Department of ECE, RCCIIT, Kolkata, West Bengal, India

itself, all embedded into an everyday object which involves an Internet connection. The "thing" is present in the real world. Hence, it takes information from the real world and transforms those into data which is taken by the sensor and sends it over the Internet for collection, processing and manipulation. The presence of the "thing" which is also a device enables it to give output in the real world with the help of "actuators" or devices which are able to perform the task in the real world. Some of the outputs could be triggered by the information from the sensors which has been processed and collected over the Internet [1]. Blockchain has been executed in the Internet of Things (IoT) to ensure security and privacy of the data sent to the other party. Blockchain has been used as a transaction (data here is called transaction) ledger and stored in encrypted form to provide a transparent system. This is an effective way of avoiding data manipulation by making data available in the hands of a large population, thereby implementing data distribution to ensure monitoring and contribution of the public in their own agricultural products [2]. It describes the technology of storing data in cryptographically secured blocks and verifying them in a decentralized manner [3]. Blockchain uses a technology called peer-to-peer network which enables a group of computers to share information or files amongst themselves. The nodes at a given time have the information/file and a copy of the file with them. Hence, it acts as a system which is a transaction ledger which keeps track of all the files (data passed in the blocks), thereby making it transparent amongst users. Nodes support a lot of functions like mining, routing and storing the blockchain data and serving as a wallet [4]. Smart contract is used by blockchain technology which validates whether all terms are met by the party. Smart contracts are a set of instruction codes written in the blockchain to satisfy all the conditions which are ought to be met as a decentralized system; that is, all the blocks have to grant permission for the new block to be added in the chain of blocks. From Fig. 1, all nodes have access to the ledger; all nodes have to agree to a protocol (smart contract) to achieve consensus or the "true state" of the ledger. Blockchain is a data structure, where data can be stored in blocks. Smart contracts are used to eliminate third-party breaches. When each transaction (data) is signed (or granted) by the blockchain, the structure checks the validity of the information by comparing certain values, checking certain parameters and validates smart contracts. Each participant has the authority
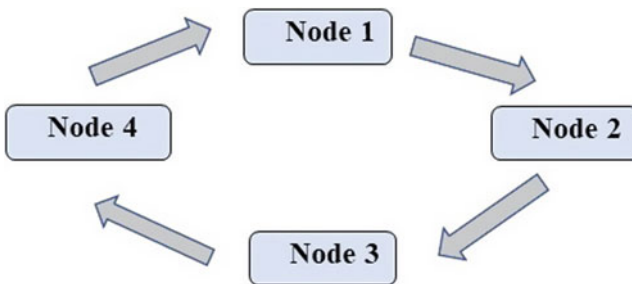
Fig. 1 Distributed ledger where all nodes have the same access to the ledger

to form block. However, only one block will be accepted. Every block checks the validity of the block being accepted or rejected to form a chain amongst the blocks. Hence, every block has to agree that a new block will be added to the queue in order to form chains with the help of cryptographic functions like SHA-256. Now, each block has a unique timestamp and hash value. Blockchains check this timestamp and hash value; the hash values are based on their previous and next block that is their position. On any manipulation of the existing blocks, it would produce incorrect hash values and thus would be noticed by all the participants [5]. On checking the validation of a block based on their hash value, all the other blocks permit its entry to the chain, thereby collecting blocks, and in the process, they form a chain. This is called blockchain theory. When a transaction is being requested, the validity of the request is checked with the help of blockchain technology which has certain protocols to grant permission to the transaction to take place. Smart contract falls under the protocol to validate a transaction [6]. As per the Food and Agricultural Organization (FAO), global food production needs to be risen by 70% to feed 2.5 billion people by the end of 2050. With this, efficient systems are required to run the market and administer in the form of IoT and automation. Data is to be brought clearly in front of the consumers to have a trustworthy and efficient system. Internet of Things (IoT) could be utilized across agricultural industries as suggested in agricultural pursuits [7]. It has discussed how Internet of Things can be used to influence climatic factors for more suitable growth of agricultural crop, ensuring a more sustainable future [8]. Endeavor also has been made to eradicate political and socioeconomic obligations in order to create a more efficient system with the help of emerging technologies [9]. In smart agriculture with IoT, different segments have been identified, such as soil, water, nutrients and livestock maintaining, services such as irrigation—automatic irrigation systems. Major IoT in smart agriculture is in livestock tracking and vehicle tracking. All of this could be achieved with the proper linkage of sensors and appropriate data storage and monitoring sections. Extreme weather conditions are responsible for the deteriorating conditions of the crops. In order to monitor that data without the help of an interim but with the help of peer-to-peer network, blockchain is used. Smart agriculture consists of all the steps involved starting from the production to the end result. The use of edge or fog computing with applications adapting to Internet of Things has been discussed [10]. A paradigm shift to wireless sensing systems in agricultural pursuits has been seen [11, 12]. However, by understanding blockchain technology and its work, it has been found out that it is a more reliable method in IoT data computing, security and maintenance which is the basic motivation of this work. This paper is intended for blockchain to be able to encapsulate sensor data into blockchain for secured transactions.

It is organized as follows. In Sect. 2, blockchain technology and its implementation are explained briefly. Section 3 depicts the overall methodology of the work. In Sect. 4, the real-time data acquisition and storing the same using blockchain discussed followed by conclusive statement of this work.
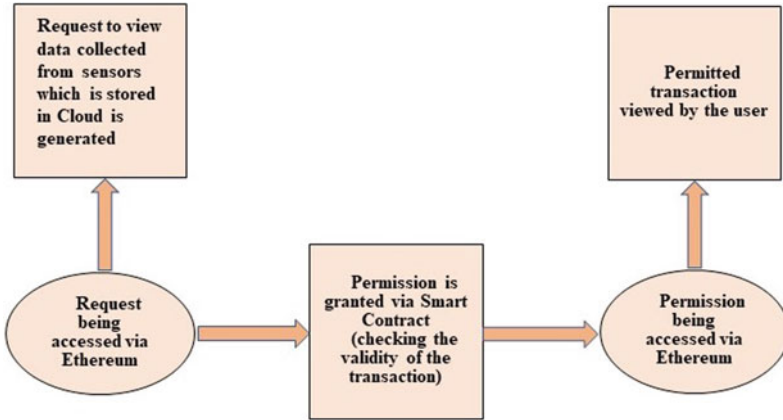
Fig. 2 Block diagram of the transaction process in Ethereum blockchain

2   Blockchain Technology

Blockchain acts as an archive to trace all the activities performed in the server when data is stored in the blocks. Central authority—that is a peer-to-peer network—is required for the trust to be placed with the help of cryptography. Transactions (request to access the data or to view data) can be traced between anonymous participants by issuing an Ethereum blockchain format; blockchain is used to archive the data, to prevent no third-party breach to provide better scope for the data to be viewed by viewers across a wide region [13].

Ethereum Blockchain

Ethereum is an open source, blockchain-based decentralized software platform which enables smart contracts which eliminate third-party breach. Smart contracts are essential for having a decentralized system as it makes sure that the pre-defined conditions set by the owner of the code are met by the client requesting transactions to view the data. Smart contracts lock the ether before it reaches the farmer for enabling the viewing of the data. Ether is a form of payment for network participants (suppose a consumer is requesting the data to be viewed from the time when the crops have been cultivated—the concept of *farm-to-fork*, to ensure transparency and knowledge of the ingredients consumed enabling a more aware society) to execute operations on the network [14] (Fig. 2).

3   Methodology

Food safety and agricultural pursuits have been endeavored to achieve by implementing blockchain in IoT. Sensors have been used to retrieve true data by setting
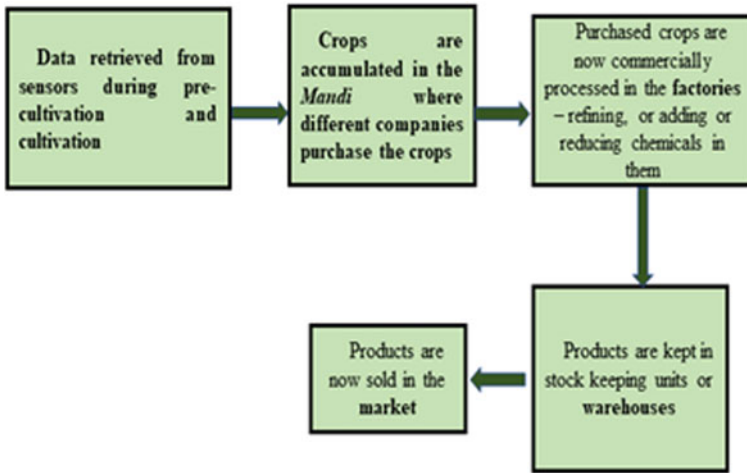
Fig. 3 Smart agriculture distribution

parameters and deploying the data with the help of a cloud platform. NodeMCU—
ESP8266 module—is used for data acquisition. Proposed smart agriculture distribu-
tion using BIoT can be given as in Fig. 3.

- At the basic level, where farmers are cultivating the crops, sensors are set to
  measure the pH level of the soil and the water intake or the temperature and
  humidity of the environment which are prevailing factors for the growth of the
  crops.
- Ethereum blockchain can also be set up in Google Cloud Console with features
  like smart contracts being available to the programmers.
- After being in the Mandi, at the next level, in the factories, data is read again by
  the sensors to provide an honest and healthy manner of food processing. Data
  here cannot be manipulated because the data is directly read from the sensors.
- Any attempt to manipulate or change the data will not be entertained by the
  blockchain technology due to its exclusive manner of encryption and decentralized
  system of operating (Fig. 4).

From Fig. 5, we see that data is being stored in the blocks. Now, for the next step,
transaction validity has to be checked. This is checked by converting the additional
data of the timestamp and other parameters into cryptographic form with the help of
SHA-256 from the previous and next block. For example (from Fig. 2), Blocks 1, 3
and 4 have to agree that Block 2 will be placed before Block 3 and after Block 1. In
other words, the logic of Block 2 coming after Block 1 and before Block 3 will be
determined by the timestamp and other parameters provided to the other Blocks in
the encrypted format. To note is that the logic is nothing but smart contracts which
is being implemented (Fig. 6).
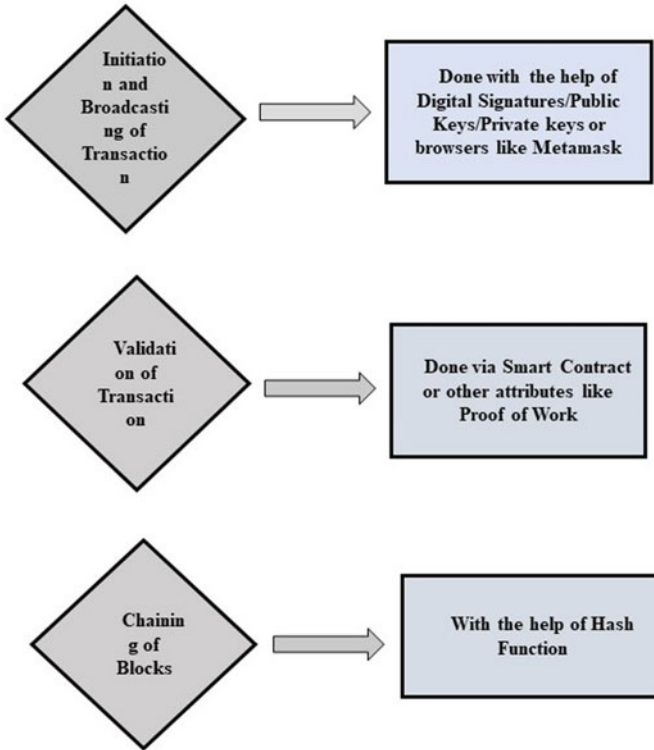
Fig. 4 Areas of usage of cryptography implemented in blockchain
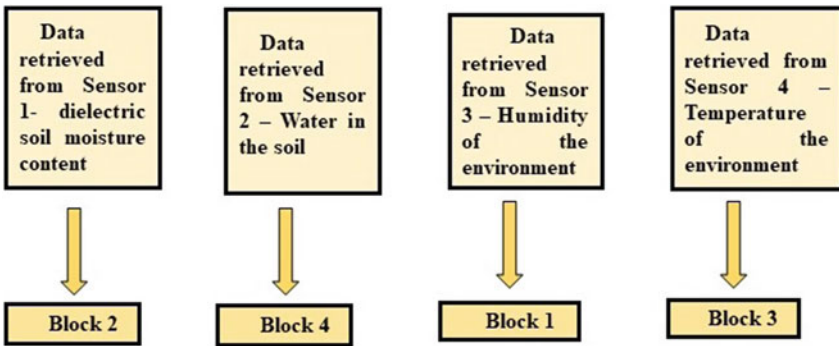
Fig. 5 Data being stored in the blocks in blockchain from different sensors
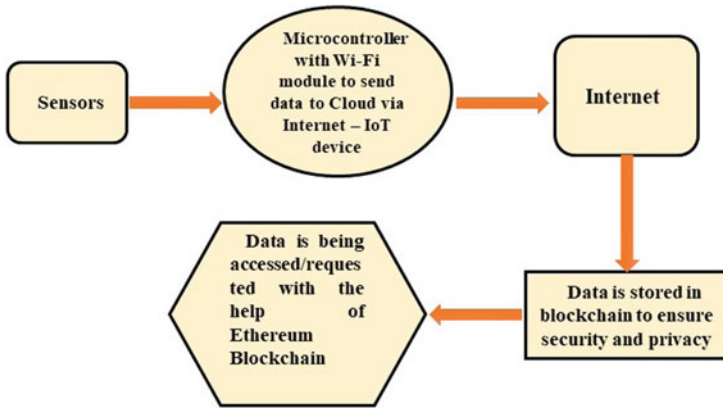
Fig. 6 Block diagram of the overall system

Information has been taken from the sensors from the agricultural field and transformed as data and sent over the Internet to the sender—where the data is accumulated and made ready to send to the receiver (externally owned account, to whom data is being sent). Now, this data has to be sent over the cloud using Internet. Cloud computing is implemented here to analyze and maintain the data. Ethereum can be implemented in Big Query of Google Cloud Console. Blockchain network is implemented further ensuring security along with it's timestamp availability feature.

4 Implementation and Result

The Ethereum blockchain has been implemented in a machine equipped with 8GM RAM 10th Gen Intel Core i5-10210U processor (1.6 GHz base frequency, up to 4.2 GHz with Intel Turbo Boost Technology, 6 MB cache and 4 cores). Operating System Windows 10th Generation has been opted (Fig. 7).

The data from the sensors is directly sent to the cloud for data maintenance and analytics with the help of Internet. Transactions are only executed here, when the consumer or the factories intend to be aware of the different data collected from different sensors during the cultivation of the crops. To avoid tampering of the data and no-person manipulation, data is only retrieved from the sensors (electronics). To create a transparent system with no scope of data manipulation by the sender or receiver, or no third-party breach, blockchain technology is implemented.

With the help of Ethereum blockchain, each block has a number and a specific time stamp of its creation, transaction number, a hash value and the amount of gas used for the transaction. A request for the shipment is sent from the consumer/retailer to farmer, requesting the details of the pH level of the soil, water level of the soil, temperature and humidity of the environment while cultivation of the crops. Then, the farmer sends the required data along with the transaction hash. Smart contract is

Fig. 7 Dacquisition via
NodeMCU
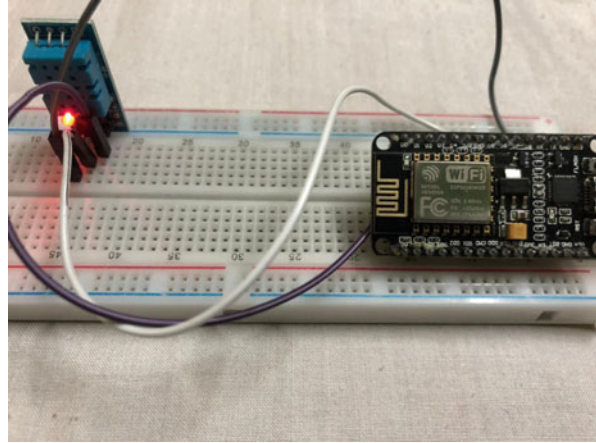
executed in Ethereum blockchain with the help of Ganache and Remix IDE. Fig. 8
shows the execution of a smart contract with the help of Ganache software.

In the Ethereum network (from Fig. 2), which is to be executed with the help of
smart contracts, a transaction is made. The transaction comprises the following:

Address (From)—This is the address transaction sender. We can consider the
user in the external world to be denoted with the help of address (size: 20-byte).

Address (To)—This is the recipient of the transaction (size: 20 bytes).

At the end, the user has to have a private key to derive the 20-byte address to obtain
the decrypted result. Note: The bytecode will not be accessible till it is deployed on
the Ethereum blockchain.

Value—For the private key to be passed to the ends for signing or sanctioning of
the transaction (because without that private key the transaction will not be signed),
it demands some services charges or transaction fee. The value is represented in the
form of ether.
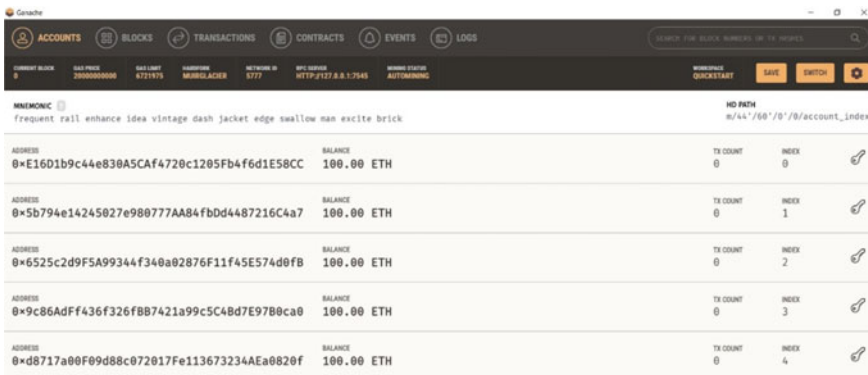
Fig. 8 Personal blockchain network is running with the help of Ganache

$$1 \text{ ether} = 10^{18} \text{ weis.}$$

Gas Price—This is the price paid per instruction.

Gas Limit—Number of Ethereum Virtual Machine (EVM) instructions executed.

From Fig. 8, lists of accounts with address, which can be seen here, are connected to the network with 100 ether each. With the RPC server, interaction with this personal Ethereum blockchain takes place.

A Web browser—here, MyEtherWallet is used to turn into a blockchain browser for security purposes. In cases, it is observed that only extensions are available. This is because entering the private key or accessing personal blockchain is considered to be in discretion and security. This browser is an online wallet and responsible for providing the interface for client interaction on a blockchain network (Fig. 9).

After writing the code for smart contract—that is the business logic in Remix IDE, from compilation details, copy the details. By entering necessary details on the page from Fig. 10, signing of transactions is done at that instant. Note: It has been done with the help of Deploy Contact here. One can opt both methods.

After the execution of the act of signing of transaction, the smart contract is executed (Fig. 11).

The logic and application of blockchain have been shown with the help of applications like Ganache, Remix IDE and MyEtherWallet. Note here that the mining status
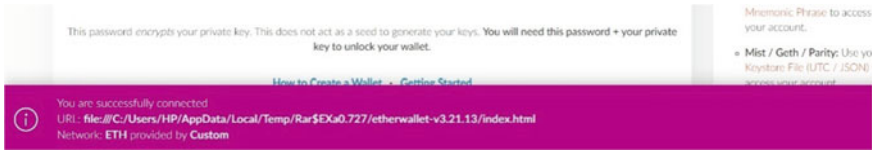
Fig. 9 Creating custom node

Fig. 10 Signing of transaction
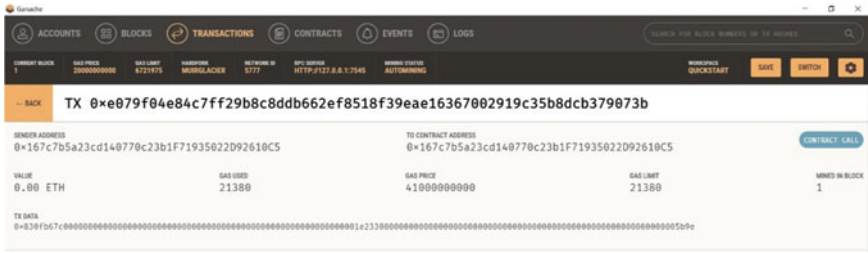
Fig. 11 Smart contract executed via Ganache

Table 1 Performance based on latency, network, traffic and CPU load

Network	Latency (s)	Network tx (bytes)	Network rx (bytes)	CPU load (%)
Ethereum	14.17	482′204	582′149	50.48

is auto mining, which means that data is being stored in the blocks of the blockchain automatically when the personal Ethereum blockchain is set up.

Gas Price = 41000000000

Recipient Address = 20 bytes—167c7b5a23cd140770c23b1F71935022D92610C5 = 20

Gas limit = 21380// same as the gas used

//Null Ether (0.00ETH)

Transaction fee is calculated in the following manner [9]:

gasPrice = 21,000 + (data_size_in_bytes) × (price_per_byte)

TX DATA (transmitter data) which is given is used in Table 1 is calculated for the system along with latency, receiver data and CPU usage. After running a number of tests, the following parameters are obtained.

5 Conclusion

The encapsulation of sensor data on a decentralized system has become extremely important in the society. Here, a smart agriculture system has been developed with BIoT approach data that can be continuously sent over the Internet to the cloud. The cloud can implement smart contract to validate a permission to view files and to download them over cloud itself by using a private and public key in the network. This decentralized data access is not in case of conventional IoT-based system. In other uses of smart agriculture system, data can be continuously sent over the Internet to the blockchain. Business to Consumer (B2C) referes the transaction between the business process and consumer. Using this socioeconomic ideology, consumers are aware of the ingredients consumed by them. The factories and farmers also come into a pressure of transparency without deceiving the people at the end of the chain.

Data is accessed without third-party breach, thereby eliminating the possibility of manipulation, thereby creating a smart, trustworthy, secure and transparent system where awareness is also created in the minds of the consumers. This work can be extended further by designing node-based architecture of IoT to ensuring smooth data transaction.

References

1. Xiong, H., Dalhause, T., Wang, P., Huang, J.: Blockchain technology for agriculture and rationale. Front. Blockchain (2020). https://doi.org/10.3389/fbloc.2020.00007
2. McEwen, A., Cassimally, H.: Designing internet of things, Chap. 1. In: The Internet of Things: An Overview (2014). ISBN 978-1-118-43063-7 (ebook)
3. Nakamoto, S.: Bitcoin: A Peer-to-Peer Electronic Cash System (2008). Website: www.bitcoin.org
4. Bagchi, R.: Using Blockchain Technology and Smart Contracts for Access Management in IoT Devices Research Thesis (2017). https://helda.helsinki.fi/bitstream/handle/10138/228832/blockchain_thesis_RupshaBagchi.pdf
5. Kullig, N., Lämmel, P., Tcholtchev, N.: Prototype implementation and evaluation of a blockchain (2020). https://doi.org/10.1016/j.procs.2020.07.054
6. Ayaz, M., Ammad-Uddin, M., Sharif, Z., Mansour, A., Aggoune, E.M.: Internet of things (IoT) based smart agriculture: toward making the fields talk. IEEE Access (2019). https://doi.org/10.1109/ACCESS.2019.2932609
7. Sisinni, E., Saifullah, A., Han, S., Jennehag, U., Gidlund, M.: Industrial internet of things: challenges, opportunities, and directions. IEEE Trans. Ind. Inf. (2018). https://doi.org/10.1109/TII.2018.2852491
8. An, X., Zhao, Q., Liu, H., Xia, L., Sun, X., Guo, Y.: State of-the-art internet of things in protected agriculture (2019). https://doi.org/10.3390/s19081833
9. Ayaz, M., Ammad-Uddin, M., Baig, I., Aggoune, M.: Wireless sensor's civil applications, prototypes, and future integration possibilities: a review. IEEE Sens. J. (2018). https://doi.org/10.1109/ACCESS.2019
10. Lin, J., Yu, W., Zhang, N., Yang, X., Zhang, H., Zhao, W.: A survey on internet of things: architecture, enabling technologies, security and privacy, and applications. IEEE Internet Things J. (2017). https://doi.org/10.1109/JIOT.2017.2683200
11. Elijah, O., Rahman, T.A., Orikumhi, I., Leow, C.Y., Hindia, M.N.: An overview of internet of things (IoT) and data analytics in agriculture: benefits and challenges. IEEE Internet Things J. (2018). https://doi.org/10.1109/JIOT.2018.2844296
12. Wang, N., Zhang, N., Wang, M.: Wireless sensors in agriculture and food industry—recent development and future perspective (2006). https://doi.org/10.1016/j.compag.2005.09.003
13. Wood, G.: Ethereum: a secure decentralized generalized transaction ledger. Ethereum Yellow Paper (2014)
14. https://cloud.google.com/blog/products/data-analytics/ethereum-bigquery-public-dataset-smart-contract-analytics

Prediction of Fiducial Parameter of PPG Signal—A Comparative Study Between Radial Basis and General Regression Neural Network Performance

Rashmi Rekha Sahoo and **Palash Kumar Kundu**

Abstract For assessing the human health, pulse wave monitoring has been used for years and years ago. Currently, the photoplethysmogram (PPG) is drawing attention because of its obvious advantages as non-invasive, simple structure, less volume, inexpensive, and convenient computer-based radial artery pulse diagnostic tool. PPG waveform contains significant information regarding cardiovascular systems about systolic, diastolic, and dicrotic index points, which helps to measure the physiological parameter like heart rate (beat), blood pressure, oxygen saturation (SpO2), and respiration in the blood. The PPG signal, which is an indicator of blood volume change, is captured with an IR light source and a photo detector, when arranged in reflective-type configuration. The fiducial parameters (time, amplitude of systolic, dicrotic and diastolic, and pulse wave time) are calculated by inflection points of the first and second-order derivatives of raw PPG waveforms. The present work focuses the applicability of artificial neural network as a predictor or estimator of these crucial fiducial parameters by using RBNN and GRNN, with modeling via Gaussian distribution function. Out of twenty subjects, training is done on ten subjects with RBNN and GRNN networks separately. The same has been tested with another ten subjects. The overall performance and accuracy of RBNN are found to be better than GRNN.

Keywords Photoplethysmogram · Fiducial parameters · Artificial neural network · GRNN · RBNN · Gaussian distribution function

1 Introduction

Because of tremendous development in nanotechnology advancement in miniature device, low energy consumption, high sensitivity, mobile, and tremendous computing power fostered an exponential increase growth of interest of wearable technology.

R. R. Sahoo (✉) · P. K. Kundu
Electrical Engineering Department, Jadavpur University, Kolkata, India

R. R. Sahoo
I&E Department, CET, Bhubaneswar, Odisha, India

99

Now, wearable bio-sensor-based[1] systems are the emerging trend, and its application covers from cardiovascular monitoring to military, battle, patient monitoring to many more. Photoplethysmography (PPG) is a non-invasive, vivo, and optical technique to detect disorders and diseases related to cardiovascular system to measure and monitor the physiological parameter such as blood pressure, oxygen saturation (SpO2), heart rate (beat), and respiration in the blood [2].

The proposal is to put the sensor, i.e., a IR transmitter (photodiode), which emits the light pulse periodically into the skin of fingertip, where some may be absorbed by tissue, some scattered, and some reflected (reflectance mode) to the photodetector (typically phototransistor). The absorption intensity utilizes Beer–Lambert's law [2], which illustrates when contraction of heart occurs blood comes out and enters into the blood vessel (artery) in accordance to the blood pressure. Hemoglobin (Hb) absorbs more light, so less light reflects and ultimately resistance of PD (photo resistor) increases. The PPG signal not only contains AC and DC components but also some noise components due to motion artifacts. AC component is caused by arterial blood in correspondence to every heartbeat. PPG waveform has three major fiducial components [3], namely systolic part, diastolic part, and dicrotic notch. These three parts are very much prominent in second derivative PPG (SDPPG) [4, 5].

There are some complex problem statements, where it is not so easy to establish an input and output relationship through mathematical modeling. For those situations, artificial neural network (ANN) plays a vital role. To have good prediction, precision in terms of RMS error and relative error [6] leads to statistical neural network (SNN). Depending upon the statistical method and probability theory, two major neural network, i.e., RBNN and GRNN are being used.

The present work thrusts the applicability of artificial neural network as an estimator of these crucial fiducial parameters of PPG by using *Radial Basis Neural Network* (RBNN) [6–8] and *General Regression Neural Network* (GRNN) [9, 10] with modeling done by a Gaussian function [11].

2   Methodology

The current work proposes the measurement of fiducial parameter like systolic (amplitude, time), diastolic (amplitude, time), dicrotic phases (amplitude, time), and pulse wave time (PWT) in photoplethysmography with experimental result [12]. The two maxima in PPG waveform show the systolic and diastolic peak, from which heart rate can be calculated. Dicrotic notch time and amplitude are calculated, when blood flows backward before the closer of aortic valve. Hence, each PPG cycle (waveform) having the fiducial parameter manifests the physiological performance of cardiovascular system of human body. The measurement process is illustrated in the subsequent paragraphs.

2.1 PPG Data Acquisition System

Module (HRM2511E Easy Pulse Plug in V1.1) is used as reflectance-type PPG sensor which is connected to analog channels of microcontroller ATMEGA328 board shown in Fig. 1a. The data acquisition program is implemented by ARDUINO embedded C language which runs on the ATMEGA328 embedded controller to capture PPG signal with sampling rate 250 Hz, as normal range of PPG signal is 0.5–4 Hz [13]. The microcontroller (ATMEGA328) transfers the data via USB and save (.txt) format containing the real-time signal sampled data of PPG waveform from subject.

Noise and Baseline Removal

After sampling at 250 Hz, PPG waveforms of four subjects are preprocessed by MATLAB 15b program through three steps. The steps are the following: (i) To remove high-frequency noise as a result of motion artifacts, filtered by a band pass type, having corner frequencies as 2 and 40 Hz, (ii) to have adequate level, automatic gain control (AGC) technique is used, and (iii) To remove wandering of baseline.

Beat Extraction

From the sampling data, local minima points are extracted with index number [13] and amplitude. One beat is formed between two consecutive index values. All the beats are stored in "ppg_beat_matrix.txt." Simply, saying ppg beat matrix will return all sample values over each respective cycle. Figure 3a shows the PPG of a particular person and its corresponding filtered signal. Beat 1–5 is correspondence to the information of each cycle.
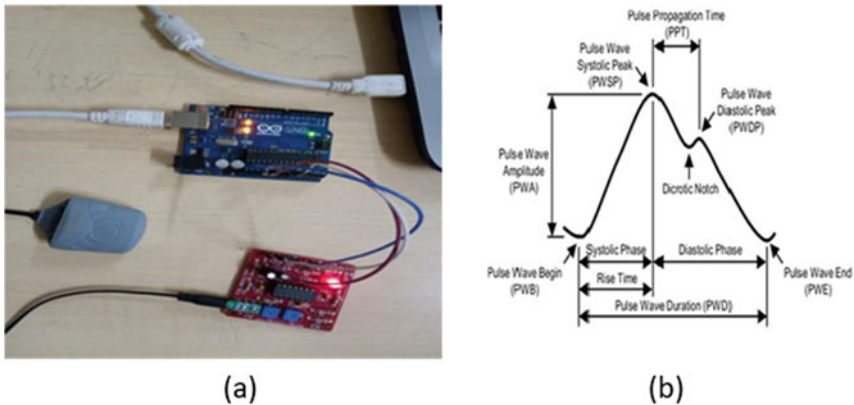
Fig. 1 **a** Data acquisition system for capturing PPG signal. **b** Fiducial parameter of PPG

3 Fiducial Parameter of PPG

A systolic peak amplitude, diastolic peak amplitude, dicrotic notch, systolic phase, diastolic phase, and pulse wave width are considered to major fiducial parameters for clinical analysis as shown in Fig. 2b.

3.1 *Gaussian Modeling*

Each PPG signal, after simulation-based signal processing, was modeled with a mixer set of two independent Gaussian functions as each cycle PPG has one systolic peak and one diastolic peak for better reconstruction and accuracy [13, 14]. The widely addressed probabilistic distribution function or Gaussian function or normal function at input x is characterized as:

$$f(x) = \frac{1}{\sigma_1\sqrt{2\Pi}}e^{\frac{-(x-\mu_1)^2}{2\sigma_1^2}} + \frac{1}{\sigma_2\sqrt{2\Pi}}e^{\frac{-(x-\mu_2)^2}{2\sigma_2^2}} \tag{1}$$

where mean $= \mu$, SD $= \sigma$, and variance $= \sigma^2$.

The philosophy behind this Gaussian distribution function is that it is highly used for initialization of random data and centered at around a value, i.e., the mean and usually set as zero. The modeling parameters (A, μ, and σ) were determined from sampled data as shown in Table 1a.

(a)

(b)
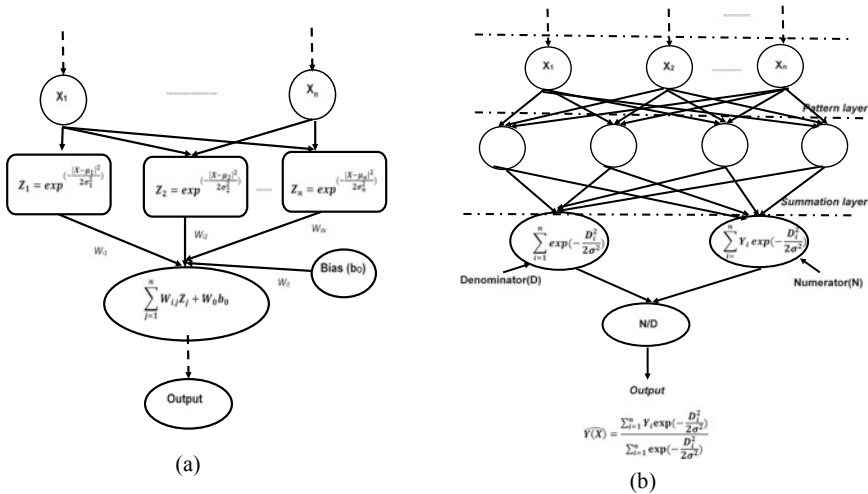
Fig. 2 a Radial basis neural network, **b** General regression neural network architecture
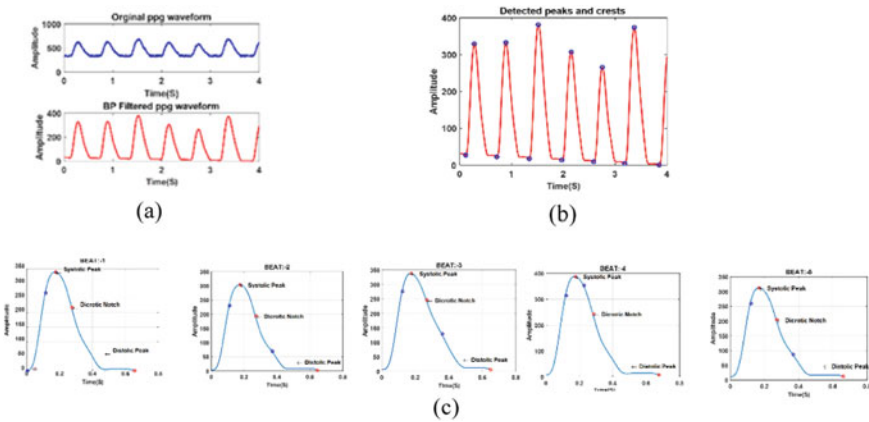
Fig. 3 **a** Noisy and filtered PPG signals, **b** detected peak and crests of PPG signal, **c** PPG waveforms of five beats for 50 years female subject.

Table 1a 2-Gauss model parameters and pulse wave time

Beat No.	2-Gauss model parameters						PTIME (s)
	A_1	μ_1	σ_1	A_2	μ_2	σ_2	
ID:50yr_high_bp_female_ppg(rest)							
1	0.6280	0.1490	0.0851	0.7010	0.1380	0.6980	0.4560
2	0.6630	0.3720	0.0849	0.6560	0.3230	0.9020	0.6640
3	0.4670	0.3880	0.0815	0.7840	0.6010	1.1000	0.7760
4	0.5280	0.2650	0.0805	0.7870	−0.1340	1.6500	0.5160
5	0.6430	0.4060	0.0864	0.6940	0.1820	0.9370	0.7160
ID:50yr_high_bp_male_ppg(rest)							
1	0.8820	0.1110	0.0680	0.9050	0.2250	0.2120	0.4560
2	0.9920	0.1170	0.0687	1.0100	0.3000	0.2110	0.4440
3	0.8000	0.1120	0.0656	0.8220	0.2110	0.3740	0.4480
4	0.8610	0.1140	0.0685	0.8740	0.2500	0.2760	0.4480
5	0.8140	0.1100	0.0630	0.8030	0.2460	0.3070	0.4520

Radial Basis Neural Network (RBNN)

Because of global approximation to input or output mapping, multilayer perceptron (MLP) network is not capable of fast learning. So, RBNN [11, 15] was proposed by Broomhead and Lowe in 1988 as shown in Fig. 2a. The network activity depends upon the activation function and weights. Generally, RBNN uses different activation functions [16] out of which radial basis function (RBF) is one.

Most widely used RBF using Gaussian function [16], having X as input pattern, "μ" as the center of function, and radius as σ^2, is shown in Fig. 2a with weight "w_j"

where output as $Y(x)$ (with bias b_0) and the Gaussian function ($z(x)$) are expressed as:

$$Y(x) = \sum_{j=1}^{n} w_j z_j(x) + w_0 b_0 \tag{2}$$

$$z(x) = \exp\left(\frac{-(x-\mu)^2}{2\sigma^2}\right) \tag{3}$$

Due to additive noise, when input data are corrupted RBNNs are preferably used for function approximation and pattern reorganization [17]. The architecture is shown in Fig. 2a. RBNNs are three-layered feedforward parallel network. Input layer is the first layer where individual neuron is fed with predictor variable. Next is a single hidden layer built with RBFs centered on a point. Location of input vector is calculated by Euclidean distance. The weight associated with the corresponding output from neuron of hidden layer is multiplied, and the sum gives the output of the NN is the last layer. In the RBNNs, first phase of the training is done in calculating RBF parameters (i.e., radius, coordinate of center), and in the second phase, the weights between hidden and output unit are estimated. The σ, μ, and the final weight are to be modeled.

General Regression Neural Network (GRNN)

GRNN which is coming under the category of probabilistic neural network (PNN) [15] is a feedforward supervised neural network. Because of feedforward architecture, the training becomes very fast. GRNN can be applied for interpolation, regression problem, prediction, and classification. GRNN can also be a good solution for online dynamical systems. GRNN is a regression estimator technique, where there is a Gaussian function to estimate the probability density function. Like BPNN, a GRNN [10] do not do repetitive training. The topology of GRNN has four layers. It is clearly visible in Fig. 2b that it has input layer, pattern layer, summation layer, and output layer. The measured X is fed to the first input layer neuron. Then, second layer (1st hidden layer) having N nodes for N sampled data, known as a pattern layer, is connected to first layer. The squaring of difference result (D) is taken between input vector, Xi, and the vector assigned to the node, and Xj for jth sample in training data is fed to exponential function with a smoothing factor (σ). This output patterns are given to the two sum units of summation layer (second hidden layer). First, summation neuron gives the sum of product of the second layer outputs and observed output y_i. Likewise, second summation neuron is the sum of the second layer activation. Output layer is the last one to divide the result of two sum node to predict the result, i.e., to estimate $Y(X)$ as:

The output is given by:

$$\widehat{Y(X)} = \frac{\sum_{i=1}^{n} Y_i \exp\left(-\frac{D_i^2}{2\sigma^2}\right)}{\sum_{i=1}^{n} \exp\left(-\frac{D_i^2}{2\sigma^2}\right)} \tag{4}$$

4   Result and Analysis

PPG waveforms are recorded from fingertips of ten subjects (five male and five female) with age group ranging from 22 to 57 years. The stored datasets are filtered with second-order band pass filter having corner frequency from 2 to 40 Hz. The filtered datasets are corrected with gain adjustment multiplying factor to main peak-to-peak value to its original PPG waveform as shown in Fig. 3a. The local minima of filtered dataset in PPG waveform are detected as shown in Fig. 3b. The sampled datasets within successive minima point are extracted and stored in an array PPG beat matrix. The first and second derivatives of sampled datasets within each beat are computed.

The filtered PPG waveform data samples for ten subjects are converted to beat matrix array, the column of which is used as one period of PPG waveform, called pulse time and stores the total data samples in it. Thus, dataset for five beats (i.e., five PPG waveform cycles) is stored into ppg beat matrix file. Each PPG beat is modeled with mixtures of two Gaussian functions as given by Eq. 1, which results six coefficients. The model coefficients are considered the features of PPG waveform. Thus, all beats are modeled by Gaussian method, and they are stored into data file, where each record in file consists of six model coefficients, and the PPG pulse time period in second.

The fiducial point of interest is computed with the help of index located at +ve and −ve zero crossing points first-order derivative and −ve peak of second-order derivative of PPG waveform for all the beats as shown in Fig. 3c. The fiducial points of five subjects as systolic peak and time, dichotic notch peak and time, and diastolic peak and time are shown in Table 1b. Systolic and diastolic phase durations, and pulse wave time.

The Gaussian model as features of input and fiducial parameters (time and amplitude) as target outputs is utilized for training radial basis and generalized regression neural networks. The trained RBNN and GRNN networks are tested by applying beat-wise feature input of 50 years female subject. The predicted values of fiducial parameters by RBNN and GRNN are shown in Tables 2a and 2b, respectively. The errors with respect to original value as computed for all the beats are shown in Tables 3a and 3b. It is clearly observed that performance by RBNN is better as the errors found in case RBNN are much less than that by GRNN.

Table 1b Time and amplitude of fiducial parameters and pulse wave time

Beat No.	Fiducial parameters						PTIME (s)
	Systolic		Dicrotic		Diastolic		
	Time (s)	Peak	Time (s)	Level	Time (s)	Level	
ID:50yr_high_bp_female_ppg(rest)							
1	0.152	1.320	0.224	1.020	0.456	0.573	0.456
2	0.372	1.310	0.444	1.000	0.664	0.573	0.664
3	0.388	1.210	0.464	1.000	0.776	0.584	0.776
4	0.264	1.260	0.336	0.996	0.516	0.671	0.516
5	0.404	1.290	0.480	0.975	0.716	0.518	0.716
ID:50yr_high_bp_male_ppg(rest)							
1	0.124	1.560	0.180	1.240	0.456	0.235	0.456
2	0.128	1.460	0.176	1.230	0.444	0.231	0.444
3	0.120	1.550	0.180	1.150	0.448	0.517	0.448
4	0.124	1.540	0.176	1.240	0.448	0.516	0.448
5	0.116	1.460	0.172	1.120	0.452	0.493	0.452

Table 2a Time and amplitude of fiducial parameters and pulse wave time predicted by RBNN

Beat No.	Fiducial parameters predicted by RBNN						PTIME (s)
	Systolic		Dicrotic		Diastolic		
	Time (s)	Peak	Time (s)	Level	Time (s)	Level	
ID:50yr_high_bp_female_ppg(rest)							
1	0.152	1.320	0.224	1.020	0.456	0.573	0.456
2	0.372	1.310	0.444	1.000	0.664	0.573	0.664
3	0.388	1.210	0.464	1.000	0.776	0.584	0.776
4	0.264	1.260	0.336	0.996	0.516	0.671	0.516
5	0.404	1.290	0.480	0.975	0.716	0.518	0.716
ID:50yr_high_bp_male_ppg(rest)							
1	0.124	1.560	0.180	1.240	0.456	0.235	0.456
2	0.128	1.460	0.176	1.230	0.444	0.231	0.444
3	0.120	1.550	0.180	1.150	0.448	0.517	0.448
4	0.124	1.540	0.176	1.240	0.448	0.516	0.448
5	0.116	1.460	0.172	1.120	0.452	0.493	0.452

5 Discussion

In present work, captured PPG signal from index finger and later waveform data has been cleaned from baseline and noise. When the heart muscle contracts, blood flows in peripheral tissues and changes the fiducial parameter of PPG (i.e., systolic, diastolic

Table 2b Time and amplitude of fiducial parameters and pulse wave time predicted by GRNN

Beat No.	Fiducial parameters predicted by GRNN						PTIME (s)
	Systolic		Dicrotic		Diastolic		
	Time (s)	Peak	Time (s)	Level	Time (s)	Level	
ID:50yr_high_bp_female_ppg(rest)							
1	0.203	1.420	0.269	1.100	0.521	0.493	0.521
2	0.317	1.320	0.389	1.020	0.634	0.539	0.634
3	0.370	1.260	0.445	1.000	0.717	0.567	0.717
4	0.274	1.260	0.346	0.996	0.533	0.658	0.533
5	0.325	1.320	0.398	1.020	0.640	0.542	0.640
ID:50yr_high_bp_male_ppg(rest)							
1	0.145	1.630	0.207	1.270	0.484	0.275	0.484
2	0.150	1.690	0.216	1.310	0.498	0.218	0.498
3	0.146	1.570	0.207	1.220	0.478	0.350	0.478
4	0.144	1.610	0.206	1.260	0.481	0.300	0.481
5	0.144	1.580	0.205	1.240	0.477	0.334	0.477

and dicrotic index, and pulse transit time) over every cycle or beat. Depending upon sex, age and movement condition or rest pulse transit time and HRV parameters varies. Hence, for diagnosis of cardiovascular diseases, PPG waveform dataset can be used to monitor HRV. Fiducial parameters (time and amplitudes of index points) of PPG signal were computed from first-and second-order derivative of PPG signal [5], which requires the large computation time for processing PPG waveform dataset extraction of sampled dataset into beat matrix format and thereafter locating the index points at systolic, diastolic, and dichroitic regions. The ANN method can reduce the computation time for determining the fiducial parameters. However, instead of using raw data relating sampled data of PPG waveform, features have been extracted after modeling it by the sum of two Gaussian functions, which yields the six coefficients (e.g., A_1, μ_1, σ_1 and A_2, μ_2, σ_2) and pulse transit time (PTIME). The features as input vectors with their corresponding fiducial parameter values of systolic, diastolic, dichroitic regions (e.g., time and amplitudes), and pulse transit time (PTIME) as target vectors are utilized to train general regression and radial basis neural networks separately. The radial basis (RBNN) and general regression (GRNN) network are a good alternative and advantageous to the multilayer perception back Propagation (MLP BP) network as these has only three-layer architecture, and it has a much faster training process compared to the MLP. The trained networks are tested by feature of one subject randomly for prediction about their fiducial parameter. The percentage error with respect to original values as determined analytically has been found. It is observed that the performance of RBNN is better as the error is very low compared to that by GRNN. The RBNN and GRNN methods can also be used for prediction of HRV parameters (e.g. PPG augmented index for arterial stiffness measurement, mean value of P-P interval time, standard deviation of successive P-P interval time,

Table 3a Error in fiducial parameters by RBNN

Beat No.	Error (%) in fiducial parameters by RBNN						PTIME (s)
	Systolic		Dicrotic		Diastolic		
	Time (s)	Peak	Time (s)	Level	Time (s)	Level	
ID:50yr_high_bp_female_ppg(rest)							
1	5.79E−12	1.13E−12	−1.85E−11	3.91E−11	−9.50E−13	1.46E−10	−1.31E−12
2	3.86E−12	2.74E−12	1.81E−11	−1.29E−11	1.99E−12	−7.25E−12	1.49E−12
3	9.59E−13	−1.69E−12	9.01E−12	−7.34E−12	3.15E−13	1.71E−11	6.87E−13
4	1.87E−12	−2.06E−12	1.19E−11	1.32E−11	2.58E−13	2.78E−11	5.59E−13
5	1.80E−12	1.95E−12	3.89E−12	1.52E−11	1.55E−13	9.72E−11	1.86E−13
ID:50yr_high_bp_male_ppg(rest)							
1	3.18E−12	4.49E−12	−2.87E−11	1.66E−11	−2.90E−12	5.55E−10	−1.70E−12
2	2.04E−12	3.25E−12	9.75E−12	2.85E−11	−7.50E−14	2.01E−10	−8.50E−13
3	4.39E−12	2.53E−12	6.82E−12	1.86E−11	−3.15E−12	7.78E−11	−2.33E−12
4	1.75E−12	3.90E−12	−6.40E−12	2.27E−11	−7.68E−13	1.59E−10	−3.47E−13
5	4.18E−12	5.75E−12	−3.71E−12	7.27E−12	−1.06E−12	1.03E−10	−1.82E−12

Table 3b Error in fiducial parameters by GRNN

Beat No.	Error (%) in fiducial parameters by GRNN						PTIME (s)
	Systolic		Dicrotic		Diastolic		
	Time (s)	Peak	Time (s)	Level	Time (s)	Level	
ID:50yr_high_bp_female_ppg(rest)							
1	33.6000	7.2900	20.0000	7.8600	14.2000	14.1000	−14.2000
2	14.8000	1.2800	12.5000	2.0800	4.4900	5.8700	4.4900
3	4.5500	3.8900	4.1300	−0.0472	7.6600	2.8400	7.6600
4	3.7400	−0.1770	3.0100	0.0463	3.2100	1.8200	−3.2100
5	19.5000	2.1800	17.2000	4.1800	10.6000	4.6900	10.6000
ID:50yr_high_bp_male_ppg(rest)							
1	−16.5000	4.6100	15.0000	3.1000	6.2200	17.1000	−0.0284
2	17.1000	15.6000	22.5000	6.4400	12.2000	5.4700	−0.0542
3	21.5000	1.3100	14.9000	6.0300	6.6700	32.3000	−0.0299
4	16.2000	4.8200	17.0000	1.3600	7.4000	41.9000	−0.0331
5	23.8000	8.0400	19.0000	10.0000	5.5700	32.3000	−0.0252

parentage of successive P-P interval time, which differs from more than that by 50 ms, standard deviation of instantaneous and long term P-P interval variability).

References

1. Rawal, V., Dhamija, A., Gupta, S.: Recent advances in wearable bio-sensors application. Int. J. Sci. Res. Comput. Sci. Eng. Inf. Technol. **1**(5), 154–159 (2012). ISSN: 2278-0882
2. Yang, Y., Zhu, J., Zhu, P.: SpO2 and heart rate measurement with wearable watch based on PPG. In: IEEE Conference 2015 IET International Conference on Biomedical Image and Signal Processing (2015)
3. Chan, G., Middleton, P., Celler, G.: Automatic detection of left ventricular ejection time from a finger photoplethysmographic pulse oximetry waveform, comparison with Doppler aortic measurement. Physiol. Meas. **28**, 1–14 (2007)
4. Toshiaki, O., Tomoyuki, K., Masao, K., Chikao, I.: Utility of second derivative of the finger photoplethysmogram for the estimation of the risk of coronary heart disease in the general population. Circ. J. **70**, 304–310 (2006)
5. Hashimoto, J., Chonan, K., Aoki, Y.: Pulse wave velocity and the second derivative of the finger photoplethysmogram in treated hypertensive patients: their relationship and associating factors. J. Hypertens. **20**(12), 2415–2422 (2002)
6. Celikoglu, H.B.: Application of radial basis function and generalized regression neural networks in non-linear utility function specification for travel mode choice modelling. Math. Comput. Model. **44**, 640–658 (2006)
7. Sun, N., Zhang, S., Peng, T., Zhou, J., Sun, X.: A composite uncertainty forecasting model for unstable time series: application of windspeed and streamflow forecasting. IEEE Open Access J. **8**, 209253–209266 (2020)

8. Ge, Y., Yang, L., Ma, X.: A novel terminal sliding mode control based on RBF neural network for the permanent magnet synchronous motor. In: 2018 International Symposium on Power Electronics Electrical Drives Automation and Motion (SPEEDAM), pp. 1227–1232 (2018)
9. Hannan, S., Manza, R., Ramteke, R.: Generalized regression neural network and radial basis function for heart disease diagnosis. Int. J. Comput. Appl. **7**(13) (2010)
10. Liu, F., Si, Y., Luo, T.: The ECG identification based on GRNN. In: IEEE International Conference on Communication Systems (ICCS) (2019). ISBN: 978-1-5386-7865-7
11. Korürek, M., Dogan, B. : ECG beat classification using particle swarm optimization and radial basis function neural network. Expert Syst. Appl. **37**, 7563–7569 (2010)
12. Qawqzeh, Y., Uldis, R., Alharbi, M.: Photoplethysmogram second derivative review: analysis and applications. Acad. J. Sci. Res. Essays **10**(21), 633–639 (2015)
13. Bhowmick, S., Kundu, P., Mandal, D.: IoT assisted real time PPG monitoring system for health care application. In: 2021 IEEE Second International Conference on Conference on Control Measurement and Instrumentation (CMI), pp. 122–127 (2021)
14. Kundu, P., Gupta, R.: Electrocardiogram synthesis using Gaussian and Fourier models. In: International Conference on Research in Computational Intelligence and Communication Networks (ICRCICN), pp. 312–317. IEEE Computer Society (2015)
15. Blanco, M., Miranda, V., Vargas, G.: Generalized regression neural networks with application in neutron spectrometry. In: Artificial Neural Networks—Models and Applications. InTech-Open Science|Open Mind, Chap. 3, pp. 49–83 (2016)
16. Spetch, D.F., Romsdhal, H.: Experience with adaptive probabilistic neural networks and adaptive general regression neural networks. IEEE Int. Conf. Neural Netw. **2**, 1203–1208 (1994)
17. Spetch, D.F., Shapiro, P.: Generalization accuracy of probabilistic neural networks compared with back propagation networks. In: IJCNN-91-Seattle International Joint Conference on Neural Networks, vol. 1, pp. 887–892 (1991)

IPMC as EMG Sensor to Diagnose Human Arm Activity

Suman Das, Somobrata Ghosh, Rohan Guin, Abhirup Das, Bijoy Das, Sampurna Saha, Srijan Bhattacharya, Bikash Bepari, and Subhasis Bhaumik

Abstract The Ionic Polymer-Metal Composite (IPMC) is a sandwiched polymer with metal electrode. It is used as sensors and actuators in different bio-engineering applications, for this property of Electro Active Polymer (EAP) researcher across the globe using IPMCs in robotics, sensors, actuators and biomedical application, in this article, a comparative study between standard Electromyography (EMG) electrode and IPMC electrode is revealed for extracting EMG signal from human forearm. The stretching/bending of IPMC which results an output response are observed, the difference in response yields, while grasping different object can be mapped for diagnose the activity of different posture of gripping. In this experimental report, it is also revealed that using IPMC sensors/electrodes are capable of identifying the activity of a human arm. Thus, it is reported in this article that IPMC can be used for sensing EMG signals, and it can be used for identification of human gripping activity.

Keywords Ionic polymer-metal composite (IPMC) · Electro active polymer (EAP) · Electromyography (EMG) · Human arm activity · Gesture control

S. Das (✉)
Department of Electrical Engineering, MCKV Institute of Engineering, Howrah, India

S. Ghosh · R. Guin · A. Das · B. Das · S. Saha · S. Bhattacharya
Department of Applied Electronics and Instrumentation Engineering, RCC Institute of Information Technology, Kolkata, India

B. Bepari
Department of Production Engineering, Haldia Institute of Technology, Haldia, India

S. Bhaumik
School of Mechatronics and Robotics, Indian Institute of Engineering Science and Technology, Shibpur, Howrah, India

1 Introduction

Human muscles are of three types—voluntary muscle, involuntary muscle, skeletal muscle. Whenever any muscle contracts or expands, it emits some voltage signal in the range of milli volts (~10 mV). Here, in this study initially, EMG signal is captured from the skeletal muscle of human forearm with the help of standard EMG electrodes. Then, the same process is repeated for capturing the signal of EMG used IPMC electrodes. This experimental study gives a poise to use IPMC sensors instead of standard EMG electrodes. This experiment is applied to both male and female samples, and the response is captured in Digital Storage Oscilloscope (DSO).

The prevalent advantage of using an IPMC as a sensor is its active output, and there is no requirement of external power source for operation. Also can be modeled as a simple mechanical structure and can be implemented onto a glove to mimic the hand gesture. The idea of implementing IPMC in data gloves originated in the research works of Shahinpoor and Kim [1] implies the results of ion-exchange Polymer Membrane implies the biomimetic sensing applications [2]. The other applications in the field of soft Robotics, biomimetic sensors, artificial fingers, etc., represents the basic feature of IPMC sensors as ion-exchange polymer composites. Electromechanical changes under the skin generates variation in voltage levels. This phenomena is detected by the EMG electrodes which results the equivalent EMG signals for the measurement and analysis point of view using sophisticated instrumentation and data extraction mechanism [3]. By EMG diagnosis, health conditions can be evaluated by monitoring muscles and nerve cell which controls the movement of muscles.

IPMC membrane has the property to detect the variation of pressure exerted on the strip which has the analogous effect with EMG electrodes [4]. Park et al. [5] highlighted the application of IPMC encapsulated with silicon membrane for signal extraction from elbow, and they modeled the system and reported the EMG signal captured by IPMC. In this report, no standard calibration or comparative result of EMG signal is highlighted. Jain et al. [6] actuated IPMC using EMG signal and applied in mechatronic application for micro gripping. IPMC sensor based data glove was introduced by Bhattacharya et al. [7]. In this application, the bending angle with voltage generation is mapped and applied for identification of different object, while grasping using data glove [8]. Chattaraj et al. [9] introduced the bending pattern identification techniques of a 20-link hyper-redundant serial IPMC manipulator. Different bending profile of IPMC strip immersed in different ionic solvents are studied. Alternative approach model of IPMC bending profile using Cantilever deflection theory is proposed by Chattaraj et al. [10]. Tractrix based hyper-redundant kinematic algorithm was applied to study the bending pattern of the membrane soaked in distilled water and LiCl solution. Two jaw and modified passive jaw gripping compliant mechanism were tested under the abovementioned ionic solution to study the dynamic bending response.

From the above literature review, it is observed that IPMCs are not used for EMG signal capturing and object identification at the same time, which motivated the authors to work on this area.
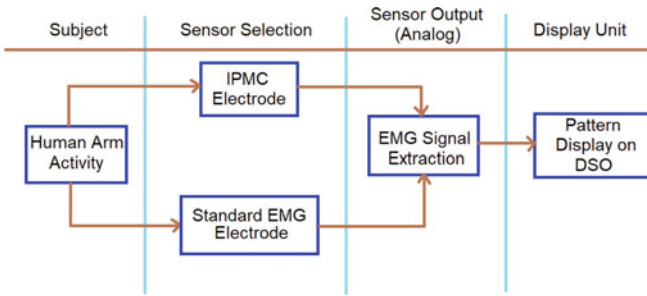
Fig. 1 Learning-based grasp generation scheme failure

2 Block Diagram of the Overall System

2.1 Selection of IPMC for Use as EMG Sensor

An IPMC of sample size: $279 \times 190 \times 0.2$ (mm) (length, width, thickness) is used for design an IPMC based EMG sensor. The sensor is used in human forearm to extract EMG signal. The dynamic electric field produced due to dynamic bending of the elector active polymers are captured and stored by DSO. Figure 1 summarized the present methodology adopted to carry-out the present findings. The four sections are subject, sensor selection, analog sensor output and display unit (DSO). Firstly, IPMC based EMG electrode and standard EMG electrode is placed in human fore arm, and the analog signal from the arm is captured with DSO.

2.2 Comparative Study of Standard EMG and IPMC Sensor Electrode

EMG Sensing technologies are categorized into two types, such as, surface EMG and Intramuscular EMG. Muscular activity under skin is accurately measured by surface EMG; conversely intramuscular EMG is an invasive technology to get EMG signals due to muscle movements. In surface EMG, the electrodes are placed on the opposite sides of the hand, one attached on the forearm, and the other is attached under the elbow which behaves as a reference electrode. The potential difference between the electrodes gives the measure of EMG signal in terms of Potential difference (Volts). IPMC membrane is placed on the surface of the forearm, when arm activity takes place producing muscle contraction or relaxation, the small force generates bending deformation of the membrane. The resulting small voltage which is generated by this process are measured by DSO.

The mode of interest for this experiment is to identify the potentiality of IPMC sensor electrode for using EMG signal extraction from human forearm. To do the

Fig. 2 Output signals from the IPMC sensor and standard EMG sensors

same, few steps are taken to identify the EMG signal extracted through IPMC. The IPMC sensor was thoroughly soaked in water, and surface of the IPMC strip was wiped carefully prior to each measurement, then the leads of IPMC analogous EMG sensors are connected by flexible wires for real-time online data recording and analog voltage signal capturing in DSO shown in Fig. 3. Green lines represents IPMC based EMG signal and Yellow lines represents EMG signal extracted by standard EMG signal. All the signals are taken in same environmental and same scaling condition, Voltage division 1 V and Time division 1 μs. The IPMC and standard EMG electrodes are fitted on the human's forearm. The forearm is kept lying flat on the table initially (Fig. 2).

The corresponding output from the IPMC and EMG electrode under such condition is observed. After flexion of forearm in different gesture, the signal is generated and captured in DSO. A sudden rise in the amplitude is recorded in different gesture produced from male and female forearm. The relaxing and flexion mode are clearly recorded from Fig. 3. It is vibrant that the IPMC sensor and standard EMG senses produces signal at the same instant of time.

3 EMG Signal for Human Arm Activity with Different Gesture

From the above discussion, it is observed that the IPMC is having the potential for EMG signal capturing, using the same features, the next step is taken to observe the potentiality of IPMC for different object identification and activity monitoring and capturing. Figure 4 shows some of the activity that is observed by using IPMC as EMG sensor.

(i)

(ii)

(iii)
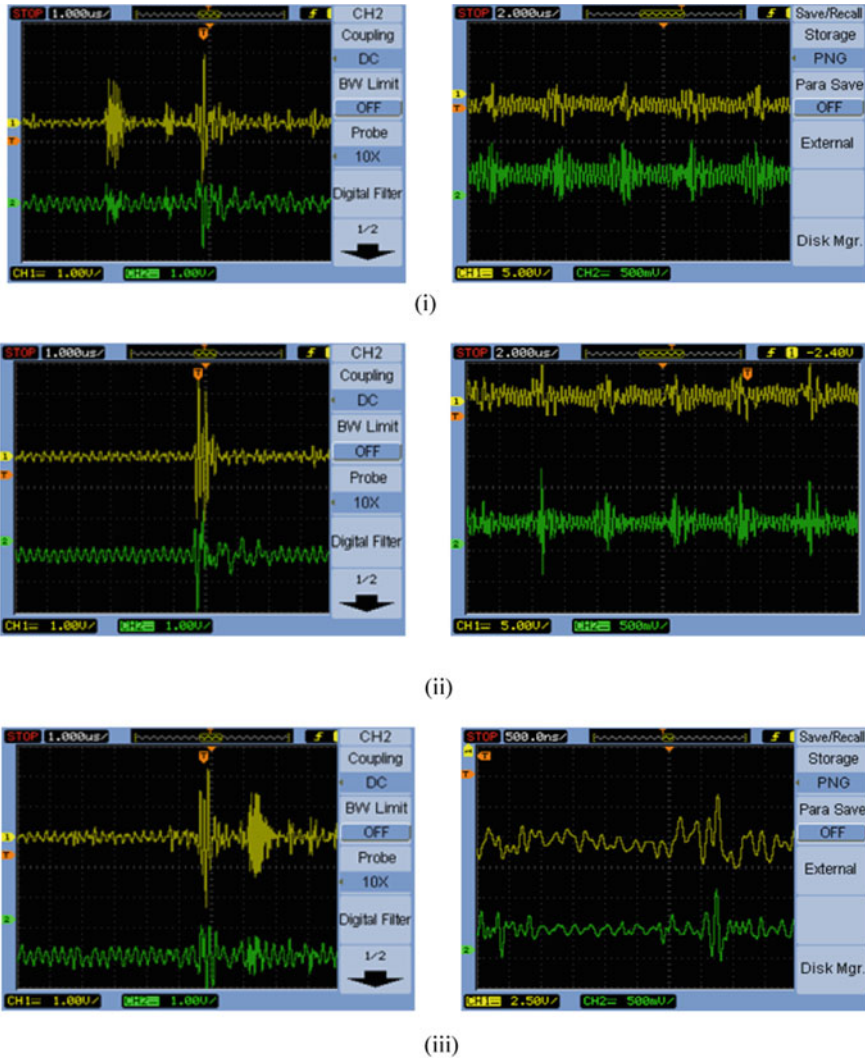
Fig. 3 Comparative study of standard EMG and IPMC sensor electrode applied in human forearm. Green lines represent IPMC based EMG signal, yellow lines represent EMG signal extracted by standard EMG signal. Left side and right side DSO screen capture of **i–iii** represents the arm activity of male and female forearm, respectively, for different gesture.

From the captured signals it is confirmed that for different activity different signal pattern is generated which can be distinctly identified after proper signal processing.
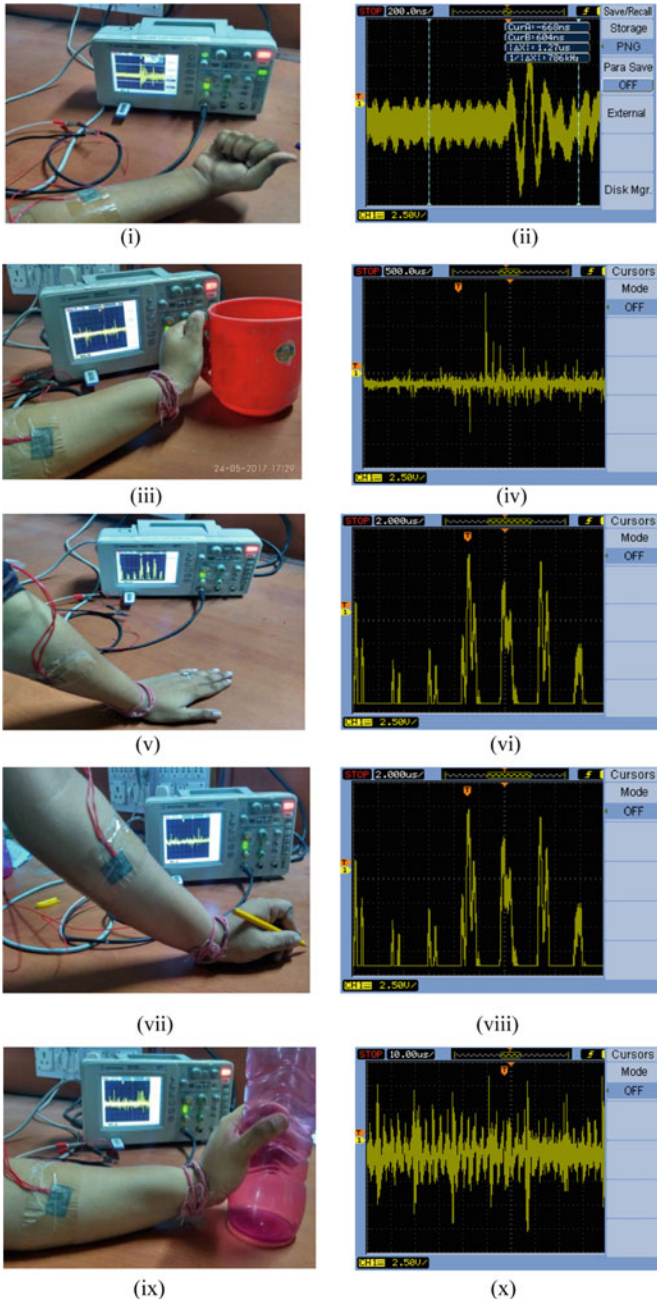
Fig. 4 **i–x** shows the gripping position and respective EMG waveform received from IPMC sensor. **i**, **ii** Pressure on palm, **iii**, **iv** holding a mug, **v**, **vi** perpendicular pressure on a surface, **vii**, **viii** holding and writing with a pen, **ix**, **x** holding a bottle

4 Conclusion

In this study, the performance of standard and IPMC (Pt electroded) electrode with comparative study is reported for application in biomedical, especially in rehabilitation. As IPMC is soft and biocompatible, it can be considered as an alternative EMG electrode which is capable of generating useable signal from human forearm. Using the signal generated for different gesture, object can be identified with proper training of the signals. The unique attributes and favorable responses demonstrated in the present work is useful for cardiac diagnosis using IPMC human body surface mounted IPMC membranes/electrodes.

References

1. Shahinpoor, M., Kim, K.J.: Ionic polymer–metal composites: III. Modeling and simulation as biomimetic sensors, actuators, transducers, and artificial muscles. Smart Mater. Struct. 1362–1388 (2004)
2. Bhattacharya, S., Bepari, B., Bhaumik, S.: IPMC-actuated compliant mechanism-based multifunctional multifinger microgripper. Mech. Des. Struct. Mach. **42**(3), 312–325. ISSN: 1539-7734 print/1539-7742 online. https://doi.org/10.1080/15397734.2014.899912
3. Paul, A., Dey, N., Bhattacharya, S.: Similarity analysis of IPMC and EMG signal with comparative study of statistical features. In: Advancements in Instrumentation and Control in Applied System Applications, vol. 1, pp 1–16. IGI Global (2020). https://doi.org/10.4018/978-1-7998-2584-5.ch001
4. Bhattacharya, S., Halder, S., Sadhu, A., Banerjee, S., Sinha, S., Banerjee, S., Kundu, S., Bepari, B., Bhaumik, S.: Characteristics of ionic polymer metal composite (IPMC) as EMG sensor. In: Advancements in Instrumentation and Control in Applied System Applications, pp. 98–107. IGI Global (2020). https://doi.org/10.4018/978-1-7998-2584-5.ch006
5. Park, I.K., Lee, B., Kim, H.M., Choi, K.S., Hwang, G., Byun, G.S., Lee, H.K.: IPMC based biosensor for the detection of biceps brachii muscle movements. Int. J. Electrochem. Sci. **8**, 4098–4109 (2013)
6. Jain, R.K., Datta, S., Majumder, S.: Design and control of an EMG driven IPMC based artificial muscle finger. In: Computational Intelligence in Electromyography Analysis—A Perspective on Current Applications and Future Challenges, 17 Oct 2012
7. Bhattacharya, S., Khan, S., Sil, T., Bepari, B., Bhaumik, S.: IPMC based data glove for finger motion capturing. In: 2nd International Conference of Robotics Society of India, BITS Goa, India, 2–4 July 2015
8. Bhattacharya, S., Das, R., Chakraborty, R., Dutta, T., Mondal, A., Sarkar, S., Bepari, B., Bhaumik, S.: IPMC based data glove for object identification. In: 6th ICIEV & 7th ISCMHT, University of Hoyogo, Himeji, Hoygo, 1–3 Sept 2017
9. Chattaraj, R., Khan, S., Bhattacharya, S., Bepari, B., Chatterjee, D., Bhaumik, S.: Shape estimation of IPMC actuators in ionic solutions using hyper redundant kinematic modeling. Mech. Mach. Theory **103**, 174–188 (2016). https://doi.org/10.1016/j.mechmachtheory.2016.05.002
10. Chattaraj, R., Khan, S., Bhattacharya, S., Bepari, B., Chatterjee, D., Bhaumik, S.: Development of two jaw compliant gripper based on hyper-redundant approximation of IPMC actuators. Sens. Actuators A Phys. **251**, 207–218 (2016). ISSN 0924-4247. https://doi.org/10.1016/j.sna.2016.10.017

Identification of Biologically Relevant Biclusters of Gene Expression Dataset of Parkinson's Disease Using Grey Wolf Optimizer

Joy Adhikary and Sriyankar Acharyya

Abstract This research has proposed an improved version of grey wolf optimizer, namely randomized move grey wolf optimizer (RM-GWO). The original version and proposed variant have been applied to identify biclusters from the Parkinson's disease dataset. This is the first attempt in applying biclustering approach to Parkinson's disease dataset. This dataset contains expressions of different genes at different conditions of a disease. Biclustering is a procedure to identify sub-matrices which have similarity in expression behaviors across some subsets of conditions. These subsets of genes and conditions together form sub-matrices, known as biclusters. This research identifies shifting and scaling pattern-based biclusters using an original and proposed variant of GWO (RM-GWO). The proposed method incorporates a strong exploration capability of search that helps to identify the better-quality biclusters compared to that obtained by other method. The efficacy of the proposed variant is tested through several benchmark functions and also verified with statistical testing.

Keywords Gene expression · Biclustering · Swarm intelligence · Meta-heuristics

1 Introduction

Microarray technology is used to investigate the activity level of genes under different conditions or samples. It provides a high-dimensional gene expression matrix [1, 2]. Gene expression is the process of protein formation where the instructions in our DNA are converted to a functional product that determines what functions a particular cell can perform.

In gene expression analysis, biclustering is a kind of searching approach that identifies local patterns of gene expressions in the whole dataset. These local patterns

J. Adhikary (✉)
Department of Computer Science, Bijoy Krishna Girls' College, Howrah, West Bengal, India

S. Acharyya
Computer Science and Engineering, Maulana Abul Kalam Azad University of Technology, BF-142, Sector-1, Salt Lake, Kolkata, West Bengal, India

are subsets of genes which have similarity in expression behavior across a subset of conditions. In gene expression analysis, these statistically significant local patterns contain subsets of co-expressed genes that are also biologically important [2, 3].

Mean squared residue (MSR) was used by Cheng and Church (CC) [4] to measure the coherence of genes and conditions of a biclusters having shifting pattern [4]. But, MSR metric is not able to identify shifting and scaling pattern biclusters separately. To overcome this difficulty, scaling mean squared residue (SMSR) metric was proposed by Mukhopadhyay et al. [5]. To achieve better efficiency, an evolutionary algorithm (EA) approach was proposed by Huang et al. [3], named condition-based evolutionary biclustering (CBEB). This strategy used MSR metric and a predefined threshold that together provides better efficacy. Pontes et al. [2] proposed evolutionary biclustering based on expression patterns (Evo-Bexpa) [2] where the cost function consists of four different objectives (quality, volume, overlapping amount, and gene variance). This cost function is found suitable for identifying simultaneous shifting and scaling pattern of biclusters.

It is observed that in Parkinson's disease [6], certain nerve cells in the brain gradually break down or die. Due to a loss of neurons, dopamine (chemical messenger) production rate reduces gradually causing abnormal brain activity that leads to impaired movement and other symptoms.

Biclustering is a well-known NP-hard problem [4]. In this work, swarm intelligence (SI)-based technique, namely grey wolf optimizer (GWO) [7] and its proposed variant randomized move grey wolf optimizer (RM-GWO) have been applied to identify shifting and scaling pattern-based biclusters. The proposed method has provided a randomized move (using student's t distributed random numbers) of grey wolf that helps achieve better exploration capability in the search process. Benchmark functions and statistical analysis have been used to validate the performance of the proposed variant (RM-GWO) [8]. The relevant biclusters from Parkinson's disease [6] dataset have not yet been searched in existing literature.

The rest of the paper is organized as follows. Section 2 briefly describes the problem. Section 3 describes the methods applied. Experimental results are given in Sect. 4. Section 5 concludes the paper and mentions some future scopes of work.

2 Problem Description

2.1 Biclustering

A bicluster (or a two-mode cluster) [1, 2] is defined as a set of genes whose expression behaviors are mutually similar within a subset of experimental conditions/samples. A sub-matrix is considered as a bicluster if the entries of rows follow a similarity in expression behavior across some of the conditions (columns). Let X be a bicluster consisting of a set of genes (g) and a set of conditions (c). Each element in X is represented by $x_{ij}(x_{ij} \in X)$, $i \in g$ and $j \in c$. Types of biclusters depend on gene

expression patterns. Here, shifting and scaling pattern-based biclusters [2] are considered. For example, suppose D is a 4×3 data matrix, where rows imply a set of genes $\langle g_1, g_2, g_3, g_4 \rangle$ and columns imply a set of conditions $\langle c_1, c_2, c_3 \rangle$. From data matrix ($D$), a shifting and scaling pattern-based bicluster (X) is selected, where the genes are $\langle g_1, g_3 \rangle$ and the conditions are $\langle c_2, c_3 \rangle$. The mathematical notation of x_{ij} in X is $x_{ij} = \Pi_j \times \alpha_i + \beta_i$ (α_i = scaling coefficient and β_i = shifting coefficient). In the pattern of X, $\langle \Pi_1, \Pi_2 \rangle = \langle 10, 15 \rangle$, $\langle \alpha_1, \alpha_2 \rangle = \langle 4, 6 \rangle$, and $\langle \beta_1, \beta_2 \rangle = \langle 3, 9 \rangle$.

Data matrix (D) is:

$$
\begin{array}{c}
g_1 \\ g_2 \\ g_3 \\ g_4
\end{array}
\left(
\begin{array}{ccc}
c_1 & c_2 & c_3 \\
321 & 43 & 63 \\
115 & 13 & 87 \\
110 & 69 & 99 \\
243 & 142 & 421
\end{array}
\right)
$$

Shifting and scaling pattern-based bicluster (X):

$$
\begin{array}{c}
g_1 \\ g_3
\end{array}
\left(
\begin{array}{cc}
c_2 & c_3 \\
43 & 63 \\
69 & 99
\end{array}
\right)
$$

Mathematical notation of X is:

$$
\begin{array}{c}
g_1 \\ g_3
\end{array}
\left(
\begin{array}{cc}
c_2 & c_3 \\
10 \times 4 + 3 & 15 \times 4 + 3 \\
10 \times 6 + 9 & 15 \times 6 + 9
\end{array}
\right)
$$

2.2 Initial Population

Each candidate solution in a population is a sub-matrix (bicluster). The sum of number of rows and number of columns of the sub-matrix represents the length of a candidate solution (Table 1). The Bits 0's and 1's are randomly selected for positions in rows and columns. In this case, Bits 1 and 0 indicate that the corresponding gene or condition is selected and not selected, respectively.

Table 1 Complete structure of a candidate solution

g_1	g_2	g_3	g_4	c_1	c_2	c_3
1	0	1	0	0	1	1

2.3   Cost Function

The cost function $(\mathrm{Cos}t(X))$ is made of four objectives: transposed virtual error, volume, overlapping amount, and gene variance [2]. The cost function contains weighted terms $(W_s, W_{ov}, \text{and } W_{var})$. The quality of shifting and scaling pattern-based bicluster [1, 2] depends on minimization of this cost function.

$$\mathrm{Cos}t(X) = \frac{\mathrm{VE}^t(X)}{\mathrm{VE}^t(D)} + W_s \times \mathrm{Volume}(X)$$
$$+ W_{ov} \times \mathrm{Overlap}(X) + W_{var} \times \frac{1}{1 + \mathrm{Var}(X)} \tag{1}$$

Transposed virtual error (VE^t) (Eq. 5) is used to identify the degree of relationship among genes [1, 2]. It is represented in the following equations:

$$\rho_i = \frac{1}{|J|} \sum_{j=1}^{|J|} x_{ij} \tag{2}$$

where ρ_i is the virtual condition of gene i, x_{ij} is the gene expression value, and $|J|$ is the number of conditions

$$\hat{\rho}_i = \frac{\rho_i - \mu_p}{\sigma_p} \tag{3}$$

where $\hat{\rho}_i$ is the standardized values of virtual condition, μ_p is the arithmetic mean, and σ_p is the standard deviation.

$$\hat{x}_{ij} = \frac{x_{ij} - \mu_{c_j}}{\sigma_{c_j}} \tag{4}$$

where $\hat{x}_{ij}$ is standardized bicluster and σ_{c_j} and μ_{c_j} represent the standard deviation and arithmetic mean of all expression values for condition j.

$$\mathrm{VE}^t(X) = \frac{1}{|I|.|J|} \sum_{i=1}^{|I|} \sum_{j=1}^{|J|} abs\left(\hat{x}_{ij} - \hat{\rho}_i\right) \tag{5}$$

Bicluster volume (volume) is defined in Eq. 6. The lesser the volume, the greater will be the chance to obtain a bicluster pattern [1, 2] with perfection.

$$\mathrm{Volume}(X) = \left(\frac{-\ln(|I|)}{\ln(|I|) + w_g}\right) + \left(\frac{-\ln(|J|)}{\ln(|J|) + w_c}\right) \tag{6}$$

where $|I|$ is the number of genes, $|J|$ is the number of conditions, and w_g and w_c are control parameters.

The overlapping term (Overlap(X)) is the number of occurrence of an element of a bicluster in other biclusters [2]. The larger the value of Overlap(X), the more will be the chance of getting erroneous pattern.

$$\text{Overlap}(X) = \frac{\sum_{i \in I, j \in J} W(x_{ij})}{|I|.|J|.(n_b - 1)} \tag{7}$$

where W is weight matrix and n_b is the number of biclusters.

Gene variance (Var(X)) (Eq. 8) is the mean of variances of all gene expressions in a bicluster [2]. The higher the gene variance, the lower will be its significance.

$$\text{Var}(X) = \frac{1}{|I|.|J|} \sum_{i=1}^{|I|} \sum_{j=1}^{|J|} (x_{ij} - \mu_{g_i})^2 \tag{8}$$

where $|I|$ and $|J|$ refer to the number of genes and conditions and μ_{g_i} is arithmetic mean of all expression values for gene i.

3 Method

This research has used a meta-heuristic method (GWO) and its proposed variant (RM-GWO) to identify shifting and scaling pattern-based biclusters.

3.1 Grey Wolf Optimizer (GWO)

GWO [7] is swarm intelligence (SI)-based meta-heuristic algorithm. Four kinds of grey wolves (α, β, δ, and ω) exist in this algorithm.

Social hierarchy: The alpha wolf (α) is considered as the leading wolf because they take decision about searching and hunting a prey. The beta wolf (β) assists the alpha in the searching and hunting process. The delta (δ) is considered at the third level of hierarchy. It surrenders to alpha and beta and at the same time dominates over omega. The omega (ω) is considered at the lowest level in this social hierarchy of grey wolves, and all searching and hunting strategies are observed by them [7].

Encircling prey: Before going to the hunting stage, wolves are encircling the prey. In this stage, positions of wolves are updated by Eq. (9). Equation (10) has been used to calculate the difference vector $\left(\overrightarrow{\text{Diff}} \right)$ [7].

$$\vec{Z}(t+1) = \vec{Z}_p(t) - A.\overrightarrow{\text{Diff}} \tag{9}$$

$$\overrightarrow{\text{Diff}} = \left| C.\vec{Z}_p(t) - \vec{Z}(t) \right| \tag{10}$$

where t indicates the current iteration no, $\vec{Z}_p$ is the position vector of prey, and $\vec{Z}$ is the position vector of a grey wolf. The coefficient parameters A and C are given by,

$$A = 2.a.r_1 - a \tag{11}$$

$$C = 2.r_2 \tag{12}$$

$$a = 2 - 2.(t/t_{\max}) \tag{13}$$

where t denotes iteration no. and $t_{\max}$ denotes the maximum number of iterations. r_1 and r_2 are the random variables, $r_1 \in [0, 1]$, $r_2 \in [0, 1]$.

Hunting: The best three solutions are already preserved as they have better knowledge about the position of the prey. In GWO, the positions of each search agent (wolf) are updated according to the position of the alpha, beta, and delta with the help of Eqs. (14), (15), and (16) [7].

$$\overrightarrow{\text{Diff}_\alpha} = \left| C_1.\vec{Z}_\alpha - \vec{Z} \right|, \overrightarrow{\text{Diff}_\beta} = \left| C_2.\vec{Z}_\beta - \vec{Z} \right|, \overrightarrow{\text{Diff}_\delta} = \left| C_3.\vec{Z}_\delta - \vec{Z} \right| \tag{14}$$

$$\vec{Z}_1 = \vec{Z}_\alpha - A_1.\left(\overrightarrow{\text{Diff}_\alpha} \right), \vec{Z}_2 = \vec{Z}_\beta - A_2.\left(\overrightarrow{\text{Diff}_\beta} \right), \vec{Z}_3 = \vec{Z}_\delta - A_3.\left(\overrightarrow{\text{Diff}_\delta} \right) \tag{15}$$

$$\vec{Z}(t+1) = \frac{\vec{Z}_1 + \vec{Z}_2 + \vec{Z}_3}{3} \tag{16}$$

3.2 Randomized Move Grey Wolf Optimizer (RM-GWO)

One of the problems of meta-heuristic optimization techniques is its premature convergence (confinement to local optimum), which occurs due to lack of exploration capacity of search. Proposed algorithm (RM-GWO) enhances exploration capacity by providing random moves to wolf using student's t distributed random numbers. The function trnd($v, 1, d$) generates $1 \times d$ student's t distributed random numbers with v degrees of freedom, where d implies the dimension.

$$U_i = Z_i(t+1) + \text{trnd}(v, 1, d) \tag{17}$$

```
Algorithm                    RM-GWO
Input the population of grey wolves;
Initialize  a, A and C;
Calculate the fitness value of each grey wolf (solution) and consider
the best three solutions Zα,Zβ,Zδ among them w.r.t. fitness;
for t = 1 to tmax do
    for each grey wolf do
            Update the position of each wolf by Z⃗i(t+1) = (Z⃗₁+Z⃗₂+Z⃗₃)/3  (Eq. 16)
    end for
    for each grey wolf do
        Update the position of each wolf by Ui = Zi(t+1) + trnd(v,1,d) (Eq. 17)
        if f(Ui) ≤ f(Zi(t+1)) then
            Zi(t+1)= Ui;
        end if
    Update A, C and a by equation (11),(18) and (13);
    Update the best wolf(Zα),second best wolf(Zβ) and third best wolf(Zδ)
end for
Return the best wolf (Zα);
```

Fig. 1 Algorithm of Randomized Move Grey Wolf Optimizer (RM-GWO)

In Eq. (17), U_i is the updated solution, and if the cost of U_i is better than that of $Z_i(t+1)$, then $Z_i(t+1) = U_i$; otherwise, old $Z_i(t+1)$ will be retained. To enhance the exploration further, Eq. (12) has been modified in the following way. The value of the multiplier of r_2 has been changed from 2 to 3. This is obtained from tuning experiments (Fig. 1).

$$C = 3.r_2 \tag{18}$$

4   Numerical Experiments

The methods have been implemented in a machine with Pentium Dual-Core CPU and a 4 GB memory; the software environment is Microsoft Windows 7, and the platform is MATLAB R2012b.

4.1   Results on Benchmark Functions

In this section, the performance of GWO [7] and the proposed variant (RM-GWO) has been validated through several benchmark functions. The size of the population is taken as 10, and the maximum number of iterations is 100. For each benchmark function, 50 independent runs have been taken and 8 benchmark functions (F1 to F8) have been used. Among them, 4 functions are unimodal (F1 to F4) and other 4 are multimodal (F5 to F8) [8]. Table 2 shows the experimental results, where the

Table 2 Comparative performance between GWO and RM-GWO for benchmark functions

		Mean	Std. dev	Median	Min	Max
Sphere (F1)	GWO	5.30E−07	7.27E−07	2.23E−07	2.35E−09	3.86E−06
	RM-GWO	**2.40E−08**	**3.89E−08**	**1.18E−08**	**4.15E−10**	**2.30E−07**
Zakharov (F2)	GWO	**2.795**	5.692	**0.4403**	**0.0089**	25.38
	RM-GWO	3.1397	**3.645**	1.6574	0.0479	**14.61**
Dixon price (F3)	GWO	0.7104	0.1110	0.6696	0.6671	1.030
	RM-GWO	**0.6749**	**0.0470**	**0.6679**	**0.6668**	**1.000**
Shifted sphere (F4)	GWO	961.02	1.41E+03	587.68	**2.923**	7.68E+07
	RM-GWO	**16.957**	**13.135**	**12.936**	4.501	**65.118**
Rastrigin (F5)	GWO	**4.929**	**2.397**	**4.418**	1.208	**12.76**
	RM-GWO	7.031	5.074	5.576	**0.0015**	21.49
Levy (F6)	GWO	0.4096	0.2194	**0.364**	0.0805	1.0286
	RM-GWO	**0.3624**	**0.1211**	0.365	**0.0018**	**0.5816**
Ackley (F7)	GWO	0.0056	0.0062	0.0041	0.0011	0.0348
	RM-GWO	**0.0011**	**9.89E−04**	**6.41E−04**	**4.05E−05**	**0.0048**
Shifted rastrigin's (F8)	GWO	37.673	11.72	37.212	16.67	62.294
	RM-GWO	**25.472**	**8.737**	**23.730**	**8.422**	**48.473**

Bold value indicates the better results

best value (minimized cost) has been bolded in each row. In Table 2, RM-GWO has outperformed GWO in all metrics for functions F1, F3, F7, and F8. Moreover, it performs better than GWO in of most of the metrics for F4 and F6. So, the overall performance of RM-GWO is better in benchmark functions.

4.2 Convergence Analysis

In this section, convergence characteristics of GWO and RM-GWO have been analyzed. Convergence graphs are given for benchmark function F1 in Fig. 2. The convergence graph shows that the cost decreases slowly but steadily for RM-GWO, and the search process reaches the most promising part in the search space in a steady and efficient manner compared to GWO.

4.3 Statistical Testing

The proposed variant (RM-GWO) is statistically validated by Wilcoxon's rank-sum test [8] on eight benchmark functions (F1 to F8). In this test, the final outcome (*p*-value) is less than 0.05 for functions (F1 to F4 and F7 to F8), which validates the better performance of RM-GWO (Table 3).
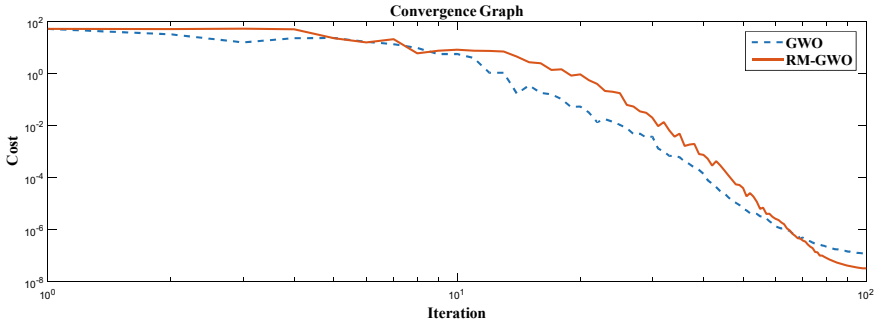
Fig. 2 Convergence graph for sphere (F1) benchmark function

Table 3 Results of statistical testing (GWO vs. RM-GWO)

Function	F1	F2	F3	F4	F5	F6	F7	F8
p-value	4.44E−15	2.48E−04	9.76E−06	1.53E−17	0.070	0.898	1.55E−12	1.03E−08

Table 4 Results on real dataset (Parkinson's)

Dataset	Algorithm	Number of biclusters	Mean of Cost(X)
Parkinson's [6]	GWO	100	5.73E+03
	RM-GWO	100	**1.98E+01**

Bold value indicates the better results

4.4 Results on Real-life Problem

This research has used Parkinson's disease [6] dataset for biclustering. It has 50,683 genes and 27 samples. Hundred biclusters are extracted from Parkinson's dataset by GWO and RM-GWO. The mean of cost (Cost(X)) of 100 biclusters is presented in Table 4. Mean of Cost(X) is minimum (bolded) in RM-GWO, so it has discovered better-quality biclusters compared to GWO.

5 Conclusion

Biclustering is a very well-known problem in bio-informatics. In this paper, the attempt has been made for the first time to analyze the Parkinson's dataset by finding subgroups of genes that show similar responses under a subset of conditions. It plays an important role in gene augmentation therapy. The proposed variant RM-GWO performs better than other variants on various benchmark functions, and its performance is also statistically verified. To identify the best-quality shifting and

scaling pattern-based biclusters, RM-GWO is applied to Parkinson's dataset. In this dataset, RM-GWO has performed better than other GWO variants in finding the best-quality biclusters.

References

1. Pontes, B., Giraldez, R., Aguilar-Ruiz, J.S.: Biclustering on expression data: a review. J. Biomed. Informa. **57**, 163–180 (2015)
2. Pontes, B., Giraldez, R., Aguilar-Ruiz, J.S.: Configurable pattern-based evolutionary biclustering of gene expression data. Algorithms Mol. Biol. **8**(1), 4 (2013)
3. Huang, Q., Tao, D., Li, X., Liew, A.: Parallelized evolutionary learning for detection of biclusters in gene expression data. IEEE/ACM Trans. Comput. Biol. Bioinf. **9**(2), 560–570 (2011)
4. Cheng, Y., Church, G.M.: Biclustering of expression data. Intell. Syst. Mol. Biol. **8**(2000), 93–103 (2000)
5. Mukhopadhyay, A., Maulik, U., Bandyopadhyay, S.: A novel coherence measure for discovering scaling biclusters from gene expression data. J. Bioinform. Comput. Biol. **7**(05), 853–868 (2009)
6. Lehnen, D., Barral, S., Cardoso, T., Grealish, S., Heuer, A., Smiyakin, A., Kirkeby, A., Kollet, J., Cremer, H., Parmar, M., Bosio, A.: IAP-based cell sorting results in homogeneous transplantable dopaminergic precursor cells derived from human pluripotent stem cells. Stem Cell Rep. **9**(4), 1207–1220 (2017)
7. Mirjalili, S., Mirjalili, S.M., Lewis, A.: Grey wolf optimizer. Adv. Eng. Softw. **69**, 46–61 (2014)
8. Jordehi, A.R.: Enhanced leader PSO (ELPSO): a new PSO variant for solving global optimisation problems. Appl. Soft Comput. **26**, 401–417 (2015)

Repairing TSVs for 3D ICs Using Redundant TSV

Sudeep Ghosh, Mandira Banik, Tridib Chakraborty, Chowdhury Md. Mizan, Trishita Ghosh, and Soumyadipta Basu

Abstract The manufacturing defects of through silicon via TSVs-based three-dimensional integrated circuit (3D IC) are one of the major problems in semiconductor industry. Shortcoming lenient 3D IC dependent on TSV is an arising space of semiconductor industry. As 3D IC is gaining significant importance because of shrinking size, increasing integration density and interconnection delay of modern devices, so it is necessary to repair TSVs faults occur during various manufacturing processes. An effect method would be the use of redundant TSV to repair the faulty functional TSV and also, we can enhance the reliability of a chips. Most of the existing solutions cannot guarantee to repair clustered defects when TSVs are dispersed non-consistently everywhere on the chip. Our fundamental point is to fix, however, much as could reasonably be expected sequential TSVs deficiencies. In this paper, we have proposed a method to make interconnection between functional TSVs and direct association between functional and redundant TSVs utilizing multiplexors (MUXs) in such way that necessary number of MUXs will least, reliance will be greatest, and furthermore can repair successive flaws.

Keywords Redundant TSV · Faulty TSV · MUX · Dependency first section

S. Ghosh (✉) · T. Chakraborty · C. Md. Mizan · T. Ghosh · S. Basu
Department of Information Technology, Guru Nanak Institute of Technology, Sodepur, Kolkata 700114, India
e-mail: sudeep.ghosh@gnit.ac.in

T. Chakraborty
e-mail: tridib.chakraborty@gnit.ac.in

C. Md. Mizan
e-mail: chowdhurymd.mizan@gnit.ac.in

T. Ghosh
e-mail: trishita.ghosh@gnit.ac.in

M. Banik
Department of Computer Science and Engineering, Guru Nanak Institute of Technology, Sodepur, Kolkata 700114, India
e-mail: mandira.banik@gnit.ac.in

1   Introduction

The shirking size increasing integration density and interconnection delay of modern devices have become the most important issue in semiconductor industry. Hence, 3D IC has been arisen as most significant field in semiconductor industry. 3D IC is made out of a few kicks, the bucket is stacked individually to shape various layers, and all layers are upward associated by TSVs. The upsides of 3D IC over 2D IC are cost viability, less power utilization, decreased interconnection delay, and improved performance [1, 2]. Because of different complex assembling measure, there may have different kinds of TSV shortcomings [3]. The dependability quality of TSVs-based 3D IC is the significant concern in light of the fact that a solitary broken TSV may annihilate the absolute chip. Subsequently, compelling recuperation technique is needed for dependability quality improvement.

An excess TSV is utilized to fix a broken useful TSV to reroute the sign from lower die to upper die. For ununiformly distributed TSVs, grouping of functional and redundant TSVs is an appealing answer for execute redundant TSV architecture design. Different strategies for gathering of utilitarian and excess TSVs for nonuniformly distributed TSVs are discussed in [4–8]. In [9, 10], authors proposed a redundant TSV architecture for uniformly distributed architecture. However, most of the time TSVs are circulated non-consistently all over the chip. In this paper, we have proposed a strategy to fix a broken TSV by redundant TSV to further develop dependable quality of chip. We have attempted to utilize least number of MUXs as utilization of number of MUXs is limited because of little space of chip. Additionally, we have planned this technique to keep in mind that it can fix clustered fault. Hence, we have focused to give grouped flaw fix capacity by utilizing least number of MUXs so that absolute region for MUXs will be least. In our proposed technique, signal shifting strategy is utilized between functional TSVs and direct association is made between excess TSVs and functional TSVs.

The remainder of this paper is organized as the following way. Section 2 demonstrates preliminaries and the previous works. In Sect. 3, we depict our inspiration and issue. In Sect. 4, we present proposed strategy and illustrative model. Section 6 shows exploratory outcomes and examination with others-related works, and lastly, segment 7 finishes up the paper.

2   Prior Work

In recent years, some works on TSVs testing and fault tolerant 3D IC have been done by various researchers. Functional TSVs have important roll-on chip functionality as a single faulty TSV is enough to destroy a chip. Various types of TSV faults are discussed in [3]. In [11, 12], authors have discussed various TSVs testing techniques to distinguish flawed TSVs and furthermore creators recommended a heuristic

method to diminish TSVs testing time. An excess TSV, design for 3D memory is supportive of presented in [13].

The idea of various reliance is proposed in [4, 7, 8]. Authors proposed various methods to shape gatherings of utilitarian and excess TSVs in a manner at least one gathering are covered. So covered utilitarian TSVs can be fixed by excess TSV present in another gathering. But authors have not considered clustered faults. These architectures cannot support clustered fault. Method suggested in [4] cannot support four consecutive faults in a group. It can support 96.66% three consecutive faults. Due to impact bonding [14, 15], defective TSVs will in general be clustered and in [16] author shows that grouping prompts area reliance of TSV imperfection probabilities.

In this paper, we have focused to repair clustered fault. We suggest a method to form groups between functional and redundant TSVs which can repair clustered fault with in a group so that dependability of chip is improved.

3   Inspiration and Problem Formulation

In the previous works, researchers focused to increase dependency as dependency plays a vital role for chip functionality but they did not consider realistic defect distribution like clustered fault. Dependency of a group is determined as number of functional TSVs supported by a redundant TSV and sum of the dependency of all groups is called absolute dependency. Also, it is needed to focus to use a smaller number of MUXs as use of number of MUXs is limited due to small size of chip. In [8], all group proportion of functional and redundant TSVs is same and huge number of MUXs is needed to carry out this design. In [4], authors tried to use a smaller number of MUXs but in this architecture, number of MUXs varies if the position of redundant and functional TSVs change for same number of TSVs. Also, this architecture cannot repair 100% clustered fault in a group.

To enhance reliability of a chip, we need an architecture which can repair clustered shortcoming by utilizing least number of MUXs. Spurred by above, we propose a method to fix clustered TSVs shortcomings by utilizing least number of MUXs.

The objective of this paper is to make legitimate group of functional and redundant TSVs so that it can fix clustered issue by utilizing least number of MUXs. In this way, the issue articulation can be characterized as follows.

Given, the quantity of functional TSVs (N) and the quantity of redundant TSVs (R) with their area, track down the proper group of functional and redundant TSVs so it can fix clustered faults. Required number of MUXs will be least and reliance will be greatest.

To tackle this issue, we propose a heuristic technique as characterized in next section.

4   Proposed Method

In this segment, a heuristic calculation is proposed to tackle the issue as depicted in Sect. 3. This technique has two stages. These are (i) making association between all functional TSVs and (ii) making association among functional and redundant TSVs.

4.1   Steps to Make Interconnection between All Functional TSVs

As we do not have the data about the size of chip and the situation of TSVs, so we arbitrarily create the arrange of each functional and redundant TSVs in standardized space (going from 0 to 1) with the goal that it tends to be planned to any realized chip size.

The following advances are followed to make entomb association among redundant TSVs:

1.   All nodes (all functional and redundant TSVs) are numbered by their separation from (0, 0) facilitates. Assume, we give number to functional TSVs as 1, 2, 3… and redundant TSVs as $R1$, $R2$, $R3$, and so on.
2.   Now, we connect all odds number of TSVs, i.e., 1, 3, 5, and so on.
3.   In these steps, we connect all even number of TSVs, i.e., 2, 4, 6, 8, and so on.

So as of now, we have all odd number functional TSVs interconnected and all even number functional TSVs interconnected.

4.2   Steps to Make Association between Functional TSVs and Redundant TSVs

Every one of the hubs (all practical and repetitive TSVs) are numbered by their separation from (0, 0) facilitates. Effectively, all odd number of functional TSVs and even number of functional TSVs are directly connected. Now, first redundant TSV is connected to first and second functional TSV. In the same way, last redundant TSV is connected to last and second last functional TSVs. After that, all excess TSVs are associated to its nearest and next to nearest functional TSV. Now, some groups have been formed. Group one has been created containing redundant TSV number one and redundant TSV number two along with all functional TSVs connected in between these two redundant TSVs. Similarly, group two is created containing second and third redundant TSVs along with all functional TSVs associated in between these two redundant TSVs. In this way, group number three is created containing third and fourth redundant TSVs together with all the functional TSVs connected in between third and fourth redundant TSVs. Now, we can observe that redundant TSV number

two in common to group number one and group number two and redundant TSV number three is common to group two and group three, i.e., group overlapped. If there is "*R*" number of redundant TSV, then total $(R − 1)$ number of groups will be formed. All functional TSVs except first and last functional TSVs can shift signal both ways, i.e., to next functional TSV and the previous TSVs. So, to increase the path diversity and to repair cluster fault for first and last functional TSVs, we make direct connection between second functional TSV and second redundant TSV. And also, we connect functional TSV number $(N − 1)$ and redundant TSV number $(R − 1)$. We chose that there is "*N*" number of functional TSVs, and "*R*" is the quantity of redundant TSVs.

4.3 Calculation of Required MUXs

In our architecture, we have connected all odd number functional TSVs and all even number functional TSVs. Let, we are given "*N*" number of functional TSVs and "*R*" number of redundant TSVs.

Case 1: If N is odd, then the number of odd number functional TSV would be $(N + 1)/2$ and total quantity of even number functional TSVs would be $(N − 1)/2$. To create interconnection between $(N + 1)/2$ number of functional TSVs, we need to interface each functional TSV to its past and next functional TSVs. So, we need one 3-to-1 MUX to make interconnection for each useful TSV. In any case, first functional TSV simply associated with second functional TSV and last functional TSV is associated with its past TSV. To carry out to this, we need one 2-to-1 MUXs.

Hence, actual number of required MUXs is $[\{(N + 1)/2\} − 2]$ 3-to-1 MUXs and two 2-to-1 MUXs. We can design one 3-to-1 MUXs by two 2-to-1 MUXs. So, actual number of 2-to-1 MUXs required to create interconnection all odd number TSVs is

$$2[\{(N + 1)/2\} − 2] + 2 = (N + 1) − 2 \tag{1}$$

Similarly, for even number of TSVs actual number of 2-to-1 MUXs required is

$$2[\{N − 1)/2\} − 2] + 2 = (N − 1) − 2 \tag{2}$$

Total number on MUXs needed to create interconnection all functional TSVs is

$$(1) + (2) = 2(N − 2) \tag{3}$$

Case 2: If N is even number, then the number of odd number functional TSV would be $N/2$ and number of even number functional TSVs would be $N/2$. Number of required MUXs would be

replacing $(N − 1)/2$ by $N/2$ in Eq. (1), we get

$$(N − 2) \tag{4}$$

Similarly, from Eq. (2), we get

$$(N-2) \tag{5}$$

So, altogether number of MUXs required is

$$(4) + (5) = 2(N-2) \tag{6}$$

From Eqs. (3) and (5), we can conclude that the number of required MUXs is same for even and odd number of functional TSVs.

Each redundant TSV is directly connected to two functional TSVs. But second and second last redundant TSV are connected second functional TSV and second last TSV.

So complete number of expected 2-to-1 MUXs for making association among functional and redundant TSV is

$$2R + 2 = 2(R + 1) \tag{7}$$

So MUXs need for total architecture is

$$2(N - 2) + 2(R + 1) = 2(N + R - 1) \tag{8}$$

4.4 Repairing Path

To fix a flawed functional TSV by supplanting redundant TSV, we will follow the accompanying advances:

1. First, we will examine whether clustered faults occurred or not and in which position fault occurred. For clustered faults, if we start counting from left to right, first faulty functional TSV will be replaced by first redundant TSV, second faulty functional TSV will be replaced second available redundant TSV and will repeat this step until all functional faulty TSVs replaced.
2. If there is no clustered fault, then faulty functional TSV will examine whether it is directly connected with redundant TVS or not; if directly connected, then it will be replaced. Otherwise, signal will be shifted through its next or the previous functional TSV.

5 Illustrative Example

Assume, we are given a chip with known number functional and redundant TSVs as shown in Fig. 1. Now, we need to generate coordinate of each functional and
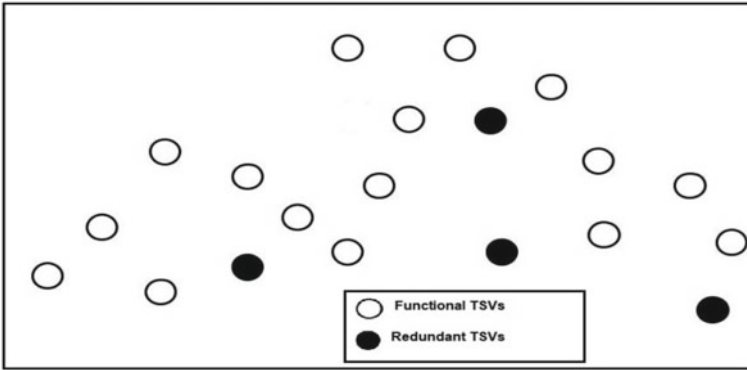
Fig. 1 Functional and redundant TSVs

redundant TSVs ranging from 0 to 1. And numbers are given according to the distance from (0, 0) coordinates. We denote functional TSVs as 1, 2, 3, and so on, and also we denote redundant TSVs as $R1$, $R2$, $R3$, and so on as showing in Fig. 2.

Now, we connect all odd number functional TSVs and all even number functional TSVs as shown in Fig. 3.

To create interconnection among functional and redundant TSVs, we will follow the step B. Figure 4 showing the connection among functional and redundant TSVs. Redundant TSV $R1$ will be connected to functional TSV number one and two. Redundant TSV $R4$ will connect with functional TSV number 15 and 16. Redundant TSV $R2$ will connect with functional TSV number seven and eight. Redundant TSV $R3$ will be connected to functional and TSV number ten and 11. Functional TSV number two and 15 are connected to redundant TSV $R2$ and $R3$, respectively.
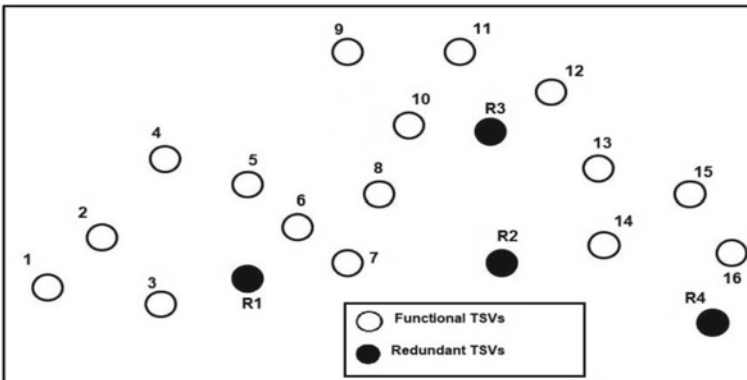
Fig. 2 Number given to functional and redundant TSVs
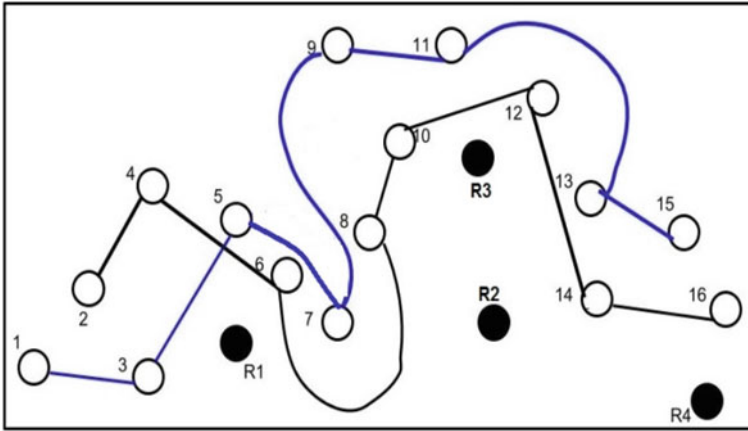
Fig. 3 Interconnection among functional and redundant TSVs
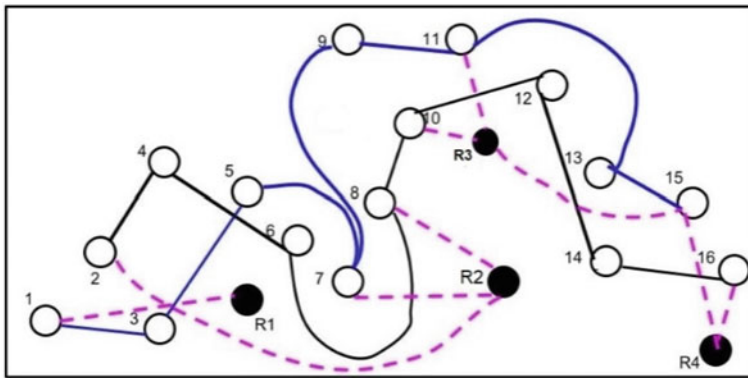
Fig. 4 Connection among functional and redundant TSVs
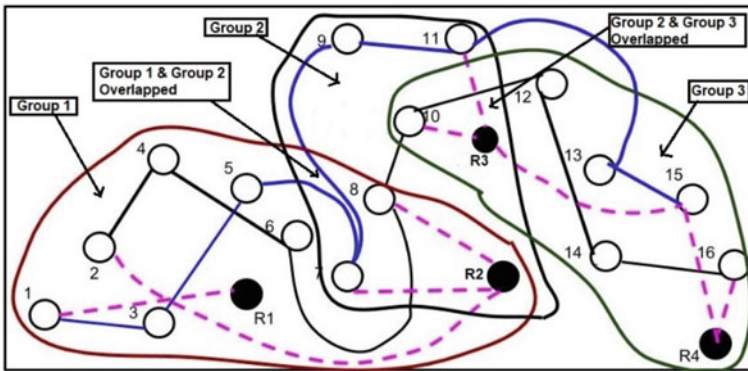
Fig. 5 Group formation of functional and redundant TSVs
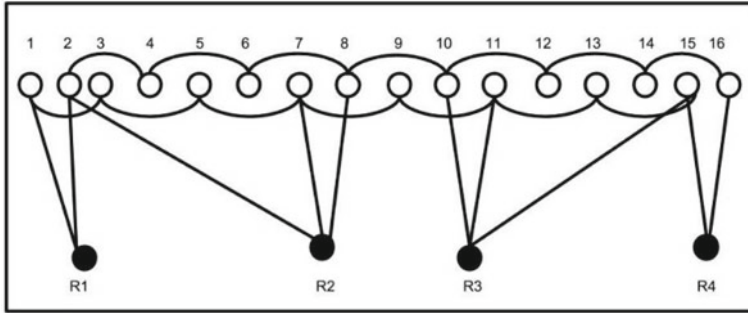
Fig. 6 Connections of functional and redundant TSVs

Figure 5 shows the various groups. Also, we can observe that all groups are overlapped. We can show Fig. 5 as Fig. 6 for better understanding of various connections between functional and redundant TSVs as described in Sect. 4.

In our suggested method, every group contains two redundant TSVs. But our proposed method can repair up to four consecutive faults in a group. Method described in [4] cannot repair four consecutive faults in group and also it can repair 99.66% of three consecutive faults. Figures 7, 8, and 9 show repairing path of clustered faults in various positions. In our architecture, we cannot repair more than four faults in a group. If faults are distributed all over the chip, we can repair "*R*" faults where *R* is number of TSVs.
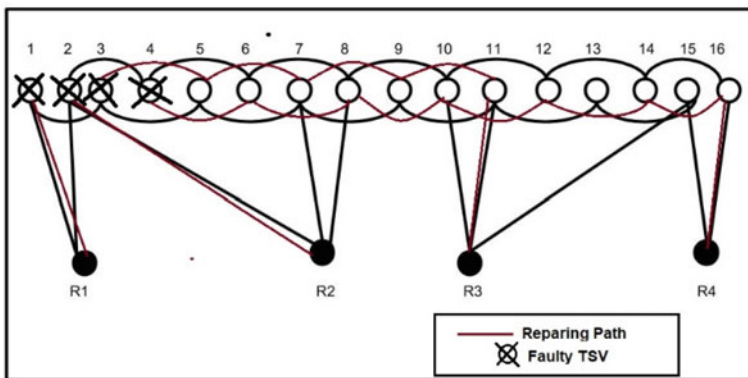
Fig. 7 Repairing path of clustered faults in group one
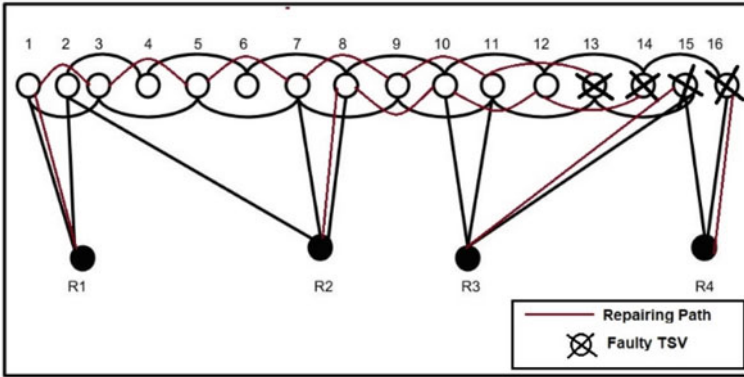
Fig. 8 Repairing path of clustered faults in group three
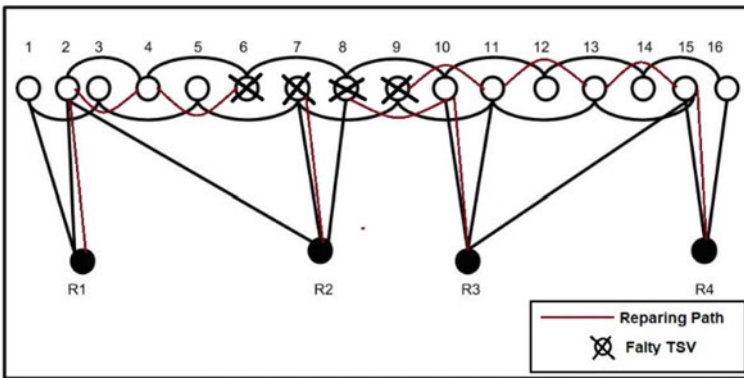
Fig. 9 Repairing path of clustered faults

6 Experimental Result

We evaluated effectiveness of our algorithm by considering 27 functional TSVs and four redundant TSVs. Table 1 shows the quantity of required MUXs and dependency of various groups. Group number one, two, and three are formed by taking the functional TSVs between two consecutives redundant TSVs. Other groups are formed by overlapping these groups. Table 2 shows the required MUXs is minimum in our architecture compare to [4, 8–10]. Though required MUXs of [4] are closed to our work, but in [4], they have taken minimum number of required numbers of MUXs. If the position changes, the number of required MUXs will increase for same number of functional and redundant TSVs. But in our work, required number of MUXs are same irrespective of the position of functional and redundant TSVs.

Table 3 shows dependency is same as work [4] but maximum compare to [8–10].

Table 1 Dependency and number of MUXs needed for various groups

# Group Number	# Number of functional TSVs	# Number redundant TSVs	# Number of required MUXs	# Dependency
1.	7	2	16	14
2.	10	2	22	20
3.	12	2	26	24
4.	16	3	36	48
5.	18	3	40	54
6.	27	4	60	108

Table 2 Correlation of required MUXs with past works

# Number of functional TSVs	# Number of redundant TSVs	Comparison of required MUXs				
		Work [4]	Work [8]	Work [10]	Work [9]	Our work
18	3	44	–	–	–	40
20	4	50	76	–	–	46
27	4	67	–	–	–	60
30	5	75	95	–	–	68
56	8	140	–	–	160	126
60	4	150	–	–	164	126
64	16	160	–	484	–	158

Table 3 Dependency comparisons with others works

# Number of functional TSVs	# Number. of redundant TSVs	Comparison of dependency				
		Work [4]	Work [8]	Work [10]	Work [9]	Our work
10	3	30	–	–	–	30
30	10	300	–	–	–	300
20	4	80	40	–	–	80
30	5	150	60	–	–	150
56	8	448	–	–	448	448
60	4	240	–	–	240	240
60	4	240	–	–	240	240

Table 4 depicts that in our work, a smaller quantity of functional TSVs is directly connected with the redundant TSVs compare to work [4]. So, wire length in our work is less compare to work [4] but dependency is same.

Table 4 Comparison of wire length with others works

# Number of functional TSVs	# Number of redundant TSVs	# Number of functional TSVs directly connect to redundant TSVs	
		Work [4]	Our work
10	3	8	8
30	10	23	22
20	4	12	10
30	5	17	12
64	16	40	34
60	4	32	10
56	8	34	18

7 Conclusion

We have suggested a method to repair consecutive functional TSVs fault by replacing redundant TSVs. Our proposed technique makes entomb association between functional TSVs and direct association between some functional and redundant TSVs to shape group. We can fix greatest number of flaws. Required MUXs in our technique are least, and dependency is most extreme contrast with past work. Additionally, required wire length for making connections among functional and redundant TSVs is least. Subsequently, equipment cost and space of chip will be less.

References

1. Burun, J., Mcllrath, L., Keast, C., lwes, C., Loomis, A., Warner, K., Wyatt, P.: Three dimensional integrated circuit for low power, high-bandwidth system-on-chips. In Proceedings of IEEE International Solid-State Circuit Conference (ISSCC), pp. 268–269 (2001)
2. Weerasekera, R., et al.: Extending systems-on chip to the third dimension: performance, cost and technological tradeoffs. In International Conference on Computer-Aided Design, pp. 212–219 (2007)
3. Chen, H., Shih, J.-Y., Li, S.-W., Lin, H.-C., Wang, M.-J., Peng, C.-N.: Electrical tests for three-dimensional ICs (3dics) with TSVs. In Proceedings of 3D Test Workshop Informal Digest (2010)
4. Ghosh, S., Roy, S.K., Rahaman, H., Giri, C.: TSV repairing for 3D ICs using redundant TSV. In Proceedings of 7th IEEE International Symposium on Electronics System Design (ISED-2017), pp. 1–5 (2017)
5. Zhao, Y., Khursheed, S., Al-Hashimi, B.M.: Cost-effective TSV grouping for yield improvement of 3D-ICs. In Proceedings of Asian Test Symposium, pp. 201–206 (2011)
6. Hsieh, A.-C., Hwang, T., Chang, M.-T., Tseng, C.-M., Li, H.-C.: TSV redundancy: architecture and design issues in 3D IC. In Proceedings of DATE, pp. 166–171 (2010)
7. Roy, S.K., Roy, K., Giri, C., Rahaman, H.: Recovery of faulty TSVs in 3D ICs. In Proceedings of 16th International Symposium on Quality Electronics Design, pp. 533–536 (2015)

8. Roy, S.K., Chatterjee, S., Giri, C., Rahaman, H.: Repairing of faulty TSVs using available number of multiplexers in 3D ICs. In Proceedings of Asian Symposium on Quality Electronics Design (ASQED 2013), pp. 155–160 (2013)
9. Lo, W.-H., Chi, K., Hwang, T.: Architecture of ring-based redundant TSV for clustered faults. In Design, Automation and Test in Europe Conference and Exhibition (DATE), pp. 549–553 (2015)
10. Jiang, L., Xu, Q., Eklow, B.: On effective TSV repair for 3D-stacked ICs. In Design, Automation and Test in Europe Conference and Exhibition (DATE) 2012, pp. 793–798 (2012)
11. Noia, B., Chakraborty, K.: Pre-bond probing of TSVs in 3D stacked ICs. In Proceedings of IEEE International Test Conference, pp. 1–10, 20–22 (2012)
12. Roy, S.K., Chatterjee, S., Giri, C.: Identifying faulty TSVs in 3D stacked IC during pre-bond testing. In Proceedings of IEEE International Symposium on Electronics System Design (ISED), pp. 162–166 (2012)
13. Kang, U., Chung, H.-J., Heo, S.: 8 Gb 3-D DDR3 DRAM using through-silicon-via technology. IEEE J. Solid State Circ. **45**(1), 111–119 (2010)
14. Singh, E.: Impact of radial defect clustering on 3D stacked IC yield from wafer to wafer stacking. In Proceedings of International Testing Conference, pp. 1–7 (2012)
15. Singh, E.: Analytical modeling of 3D stacked IC yield from wafer to wafer stacking with radial defect clustering. In Proceedings of IEEE VLSID, pp. 26–31 (2014)
16. Xie, J., Wang, Y., Xie, Y.: Yield-aware time-efficient testing and self-fixing design for TSV-based 3D ICs. In Proceedings of IEEE Asia South Pacific Design Automation Conference, pp. 738–743 (2012)

Design and Analysis of Robotic Microgripper Using ABS and PLA

Neeta Sahay and Subrata Chattopadhyay

Abstract In this study, the design and analysis of the compliance microgripper made up of acrylonitrile butadiene styrene) and polylactic acid (PLA) are presented. With the possibilities of making prototypes of the grippers, it is becoming necessary that the prototype should be lightweight and of low cost. The aim of this work is to design a robotic microgripper of compliant structure with materials using acrylonitrile buta-diene styrene (ABS) and polylactic acid (PLA). ABS and PLA are lightweight, low cost, very stiff and capable of handling jobs of weight higher than that of their own. The gripper is designed and analyzed by the Pro Release 5.0 software. By stress and displacement analysis, it is shown that with the application of the pressure load in the range of MPa (1 to 3 MPa) the displacement of the tip of the microgripper can be obtained in the mm (about 0.3 to 0.5 mm) range. The prototype will be developed using 3D printing technology.

Keywords ABS · Displacement analysis · PLA · Pro Release 5.0 software · Robotic microgripper · Stress analysis

1 Introduction

Robotics, the study of robot and robot dynamics, is based on the three fundamental laws, has been evolved as one of the important aspects of industrial automation, in medical applications as well as in the space science [1]. Consequently, the design of robotic arm and gripper is giving its influential aspects in the research area over a decades. This aspect leads to the development of micro-assembly in industrial applications described by Jain et al. [2] in the year of 2017.

N. Sahay (✉)
Institute of Engineering and Management, Kolkata, West Bengal, India

S. Chattopadhyay
National Institute of Technical Teachers' Training and Research, Kolkata, West Bengal, India

Fig. 1 Top view of
microgripper (mm)
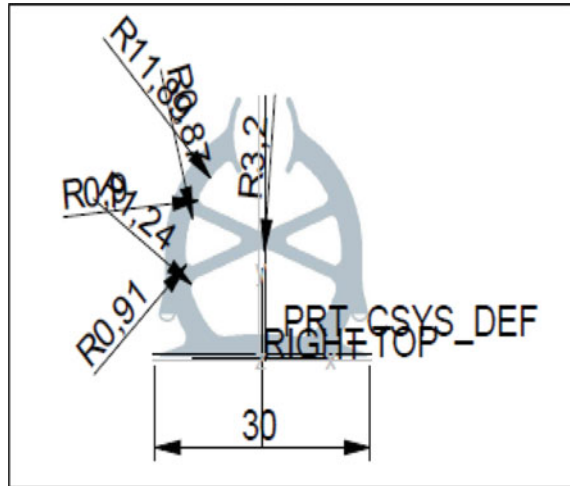
The different control solutions are required to obtain the path traced by a robotic
arm as well as for a gripper. So, it is very much needed to design an appropriate proto-
type. Among the other fundamental design parameters, another important parameter
to be considered is the ratio of the structural weight and the load carrying capacity [3].
Our objective is to expand the key parameter using ABS and PLA in the design and
structure of a robotic gripper of compliant structure [4–8] and appropriate actuation
such as piezoelectric actuation presented by Nah et al. [9] in 2007.

In the year of 2014, Bhargava et al. [10] have shown that SU-8 holds high aspect
quotient (large thickness related to thinnest in-plane feature) which makes it a mate-
rial for the microgrippers that need to have high out-of-plane strength. ABS and PLA
are comparatively light material among the most suitable used for making educational
robotic arms prototypes [11]. ABS and PLA both are thermoplastics; that is, they
are soft and moldable when heated and become a solid when cooled. These mate-
rials, most suitable for 3D printing, have strong features of resistance and hardness;
moreover, they are of considerably less expensive than aluminum or steel.

The present paper works on the design of a robotic microgripper of compliant
structure with the ABS and PLA materials which are lightweight, low cost, very stiff
and capable of handling jobs of weight higher than that of their own. The stress and
displacement analysis has been performed by the Pro Release 5.0 software where it
is shown that with the application of the pressure load at a specific area of interest,
the displacement of the tip of the microgripper can be obtained.

Fig. 2 3D view of microgripper
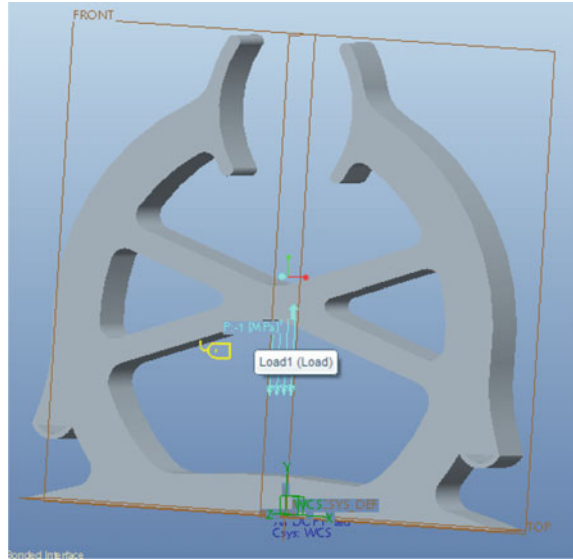
2 Design of the Microgripper

The design of the microgripper has been presented by Pro Release 5.0. In Fig. 1, the top viewed gripper with all major dimensions has been given, and in Fig. 2, the 3D view has been presented with a thickness of 5 mm. The area of application of pressure (1 MPa) is also shown.

3 Stress and Displacement Analysis with ABS and PLA Material

The analysis of the microgripper has been done with the help of Pro Release 5.0 software which has been shown in Figs. 3, 4, 5 and 6.

4 Design Analysis and Results

The two dominant plastics ABS and PLA are explored for 3D printing. Both ABS and PLA are most effective when they stored for long-term sealed off from the atmosphere before use to prevent the captivation of humidity from the air. The properties are shown in Table 1. The analysis results from simulation for ABS and PLA is shown in Tables 2 and 3, respectively. The characteristic curves representing the maximum
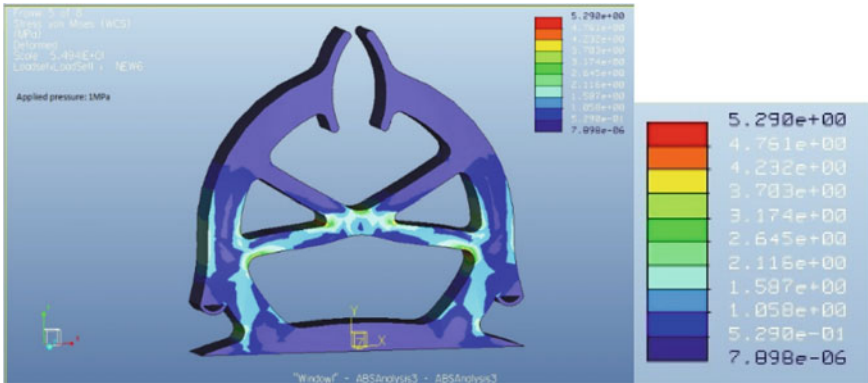
Fig. 3 Stress distribution in MPa for ABS (maximum stress: 5.29 MPa)
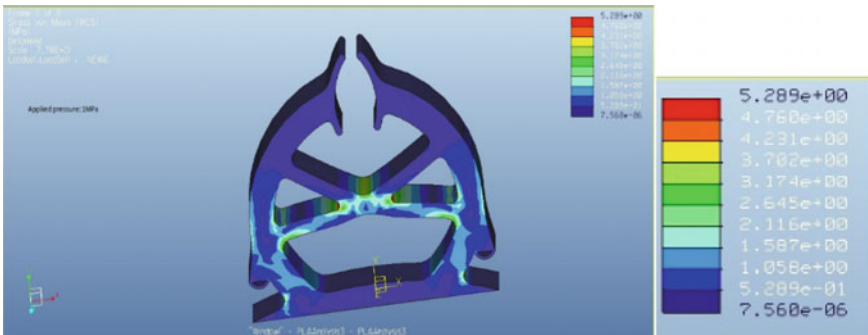
Fig. 4 Stress distribution in MPa for PLA (maximum stress: 5.289 MPa)
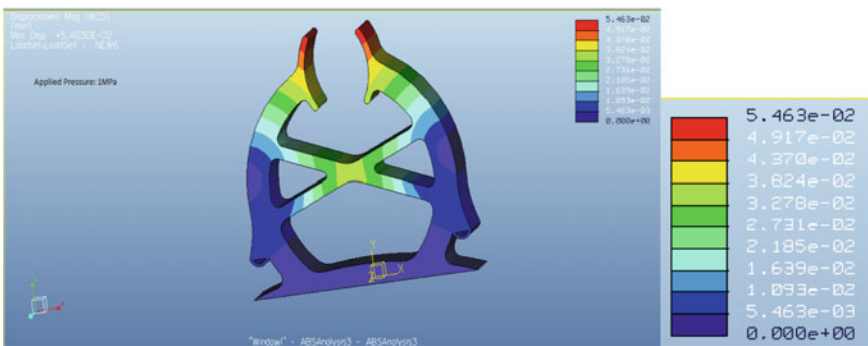
Fig. 5 Displacement analysis in mm for ABS (maximum displacement: 0.0546 mm)
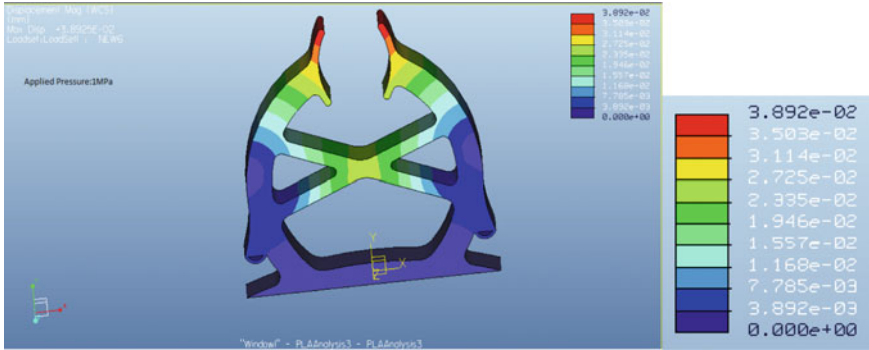
Fig. 6 Displacement analysis in mm for PLA (maximum displacement: 0.0389 mm)

Table 1 Material properties

	Young's modulus (GPa)	Poisson's ratio	Yield strength (MPa)
ABS	2.5	0.35	18.5–51
PLA	3.5	0.36	70

Table 2 ABS analysis results

	Derived value from simulation		Expected value for linearity		% Deviation from linearity	
Applied pressure (MPa)	Maximum stress (MPa)	Maximum displacement (mm)	Maximum stress (MPa)	Maximum displacement (mm)	Maximum stress	Maximum displacement
1	5.29	0.0546	5.2944	0.0546	0.0831	0.0000
3	15.87	0.1639	15.8598	0.1636	−0.0643	−0.1834
5	26.42	0.2728	26.4252	0.2726	0.0197	−0.0734
7	36.99	0.3819	36.9906	0.3816	0.0016	−0.0786
10	52.84	0.5456	52.8387	0.5451	−0.0025	−0.0917

Table 3 PLA analysis results

	Derived value from simulation		Expected value for linearity		% Deviation from linearity	
Applied pressure (MPa)	Maximum stress (MPa)	Maximum displacement (mm)	Maximum stress (MPa)	Maximum displacement (mm)	Maximum stress	Maximum displacement
1	5.289	0.0389	5.2944	0.0389	0.1020	0.0000
3	15.87	0.1169	15.8598	0.1169	−0.0643	0.0000
5	26.42	0.1945	26.4252	0.1949	0.0197	0.2052
7	36.99	0.2723	36.9906	0.2729	0.0016	0.2199
10	52.9	0.3896	52.8387	0.3899	−0.1160	0.0769
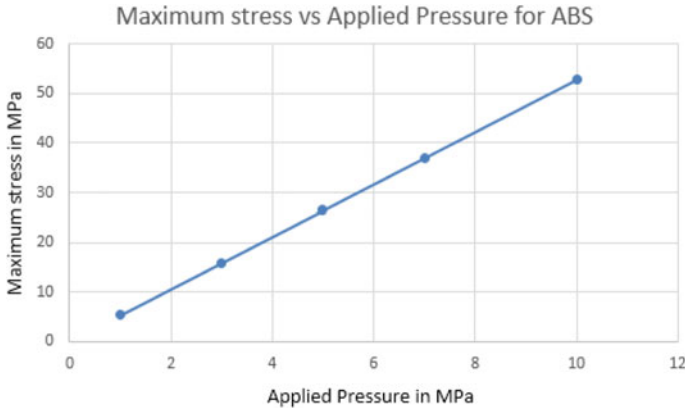
Fig. 7 Characteristic curve for ABS material (stress analysis)
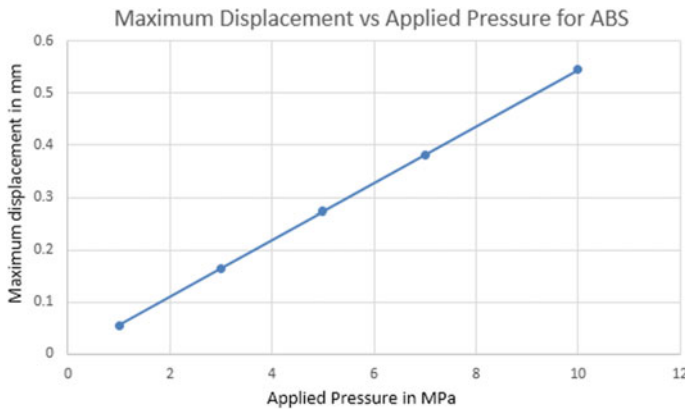
Fig. 8 Characteristic curve for ABS material (displacement analysis)

stress versus applied pressure and maximum displacement versus applied pressure for ABS and PLA are given, respectively, in Figs. 7, 8, 9 and 10.

5   Conclusion

As seen from the above analysis results, both the ABS and PLA material can be used to develop the compliant microgripper. They both are possessing the linear response curve in terms of stress and displacement within the range of interest. The error characteristics showing the percentage deviation from linearity of both the material have been plotted which are also within the range of tolerance (±0.3%) as shown in Figs. 11 and 12. From the material properties given in Table 1, as the Young's
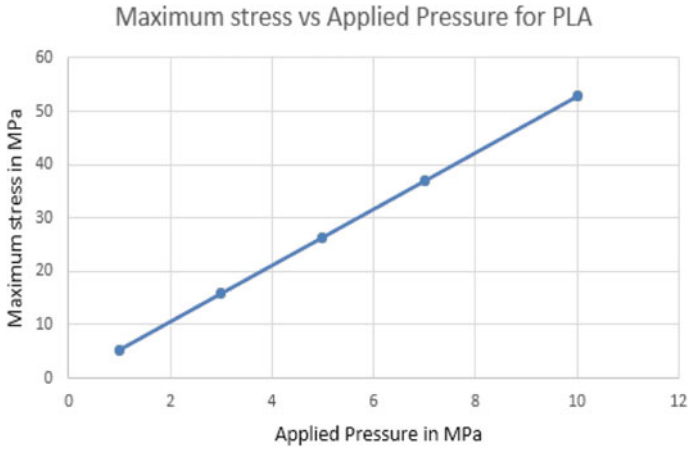
Fig. 9 Characteristic curve for PLA material (stress analysis)
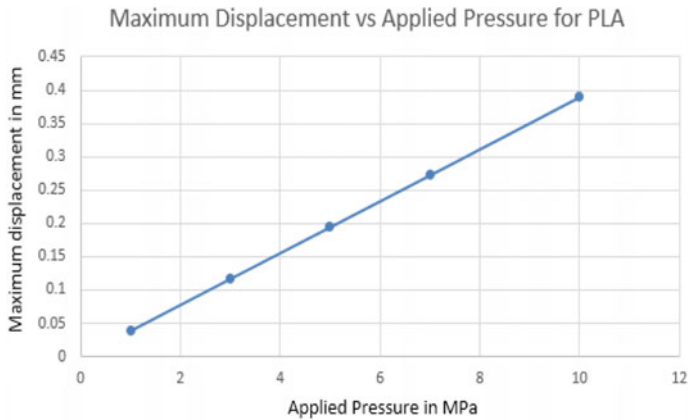
Fig. 10 Characteristic curve for PLA material (displacement analysis)
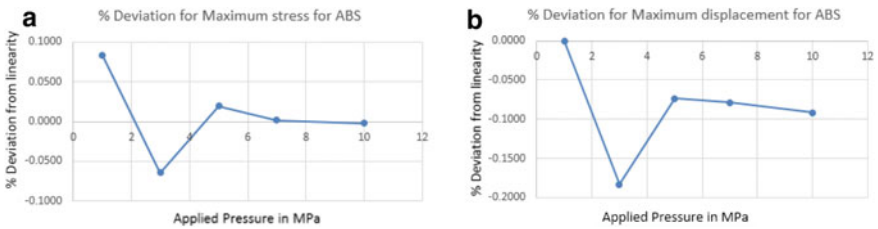
Fig. 11 % deviation from linearity for ABS material **a** for stress, **b** for displacement
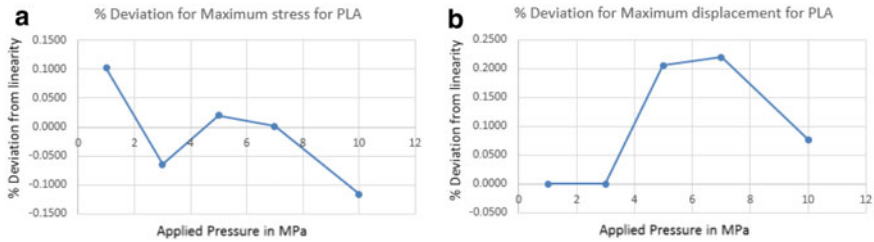
Fig. 12 % deviation from linearity for PLA material **a** for stress, **b** for displacement

modulus of ABS is less than that of PLA material, the maximum displacement obtained (Tables 2 and 3) at the tip of the gripper with ABS material is larger than that of the PLA gripper. Although due to less yield strength of ABS, the material is restricted to apply the pressure less than 10 MPa, whereas the PLA can be used for larger application of pressure (approx. 14 MPa).

References

1. Scheide, A.W.: History of the robotics industry committee. IEEE Trans. Ind. Appl. **IA-20**, 1052–1052 (1984)
2. Jain, R.K., Majumder, S., Ghosh, B., Saha, S.: Analysis of multiple robotic assemblies by cooperation of multimobile micromanipulation systems. Int. J. Adv. Manuf. Technol. **91**, 3033–3050 (2017)
3. Younkoo, J., Dongjoon, L., Kyunghwan, K., Jongoh, P.: A wearable robotic arm with high force-reflection capability. In 9th IEEE International Workshop on Robot and Human Interactive Communication, pp. 411–416 (2000)
4. Aia, W., Xu, Q.: Overview of flexure-based compliant microgrippers. Adv. Robot. Res. **1**(1), 001–019 (2014)
5. Sahay, N., Das, S.: Design analysis of a fish-shaped PVDF compliance microgripper. Int. J. Robot. Autom. (IJRA) **5**(2), 67–71 (2016). ISSN: 2089-4856
6. Jain, R.K., Saha, S., Majumder, S.: Development of piezoelectric actuator based compliant micro gripper for robotic peg-in-hole assembly. In IEEE International Conference on Robotics and Biomimetics (ROBIO) 2013. 978-1-4799-2744-9
7. Jain, R.K., Majumder, S., Ghosh, B., Saha, S.: Micro manipulation by a compliant piezoelectric micro gripper towards robotic micro assembly. Int. J. Mechatron. Manuf. Syst. **9**(1) (2016)
8. Joshi, R.S., Mitra, A.C., Kandharkar, S.R.: Design and analysis of compliant micro-gripper using pseudo rigid body model (PRBM). Mater. Today Proc. **4**(2, Part A), 1701–1707 (2017)
9. Nah, S.K., Zhong, Z.W.: A microgripper using piezoelectric actuation for micro-object manipulation. Sens. Actuators A **133**, 218–224 (2007)
10. Bhargava, S.D.B., Jorapura, N., Ananthasuresha, G.K.: Fabrication of compliant micro grippers using SU-8 with a single mask. Inst. Smart Struct. Syst. (ISSS) J. **3**(2), 7–13 (2014)
11. Rivas, D., Manjarres, F., Mena, J., Carrillo-Medina, J.L., Bautista, V., Erazo, M., Perez, M., Galarza, O., Huerta, M.: Inverse engineering design and construction of an ABS plastic, six DOF robotic arm structure. In Proceedings of the 6th International Conference on Automation, Robotics and Applications, 17–19 Feb 2015

Robot Kinematic of Three-Link Manipulator and Computation of Joint Torque by Phase Variable Method

Neeta Sahay, Subrata Chattopadhyay, and Tanmay Chowdhury

Abstract In this paper, the analytical solution of the dynamic model of the three-link robotic manipulator has been presented where the mathematical formulation of direct kinematics is presented using Newton–Euler approach. The robotic manipulator can be assumed as a three-link robotic arm where all the joints are revolute and planar. This study establishes the relationship between the angular position of each link member, angular velocity and angular acceleration using forward equation of motion, and the actuation torque at each joint is calculated by backward equations. The three simultaneous differential equations of second order corelating torque and angular position of each joint-link pair can be reformed into six ordinary differential equations of first order. The analytical solution represents the dynamic response of each link rotation with respect to time for a constant torque applied to each joint.

Keywords Direct kinematic · Three-link · MATLAB · Newton–Euler · Joint torque phase variable

1   Introduction

The study of robot and robot dynamics has been carried out over a decades using different types of approaches. One of the methods is to reduce the order of the multi-robot system with some of the properties of the model [1]. Deshpande et al. [2] compare computational complexities of various forms of the equations of motion for open chain systems for dynamics of robot manipulator. Yamane and Nakamura [3] describe a simulation model of human body for its motion analysis, and the algorithms

N. Sahay (✉)
Institute of Engineering and Management, Kolkata, West Bengal, India

S. Chattopadhyay
National Institute of Technical Teachers' Training and Research, Kolkata, West Bengal, India

T. Chowdhury
Mrinalini Datta Mahavidyapith, Kolkata, West Bengal, India

were developed in robotics which are combined with physiological models to solve the difficulties arise of handling real human structure.

Dynamic modeling and simulation of the industrial robot, Stiiubli TX40, are presented by Cheraghpour et al. where a precise simulation for experimental analysis of kinematics, dynamics, and control is described [4]. In this study, inertial and geometric parameters are accurately measured and recorded in the software database. Dynamic modeling of a nonholonomic wheeled manipulator is carried out which consists of elastic joints and a self-directed wheeled movable platform [5, 6]. Gibbs–Appell (G–A) recursive algorithm is adopted to avoid computation of Lagrange multipliers. The proposed algorithm recursively and methodically derives the dynamic equation, moreover all mathematical processes are done by 3×1 and 3×3 matrices to improve the computational complexity. Also, local coordinate system is assigned to all dynamic equations of a link by which the algorithm was generalized where the implementation and simulation of a greater degrees of freedom wheeled movable robotic manipulator become easier. However, the damping and friction were not considered to improve joint modeling and flexibility. Lagrange–Euler dynamics are presented in [7–9] where the aim is to derive simple and well-structured dynamic equations of motion. Again, the Newton–Euler model was used to form the dynamic equations and a comparative study is given experiencing major difficulties in using both methods. For development of a robotic system, complete modeling of a well-known robotic manipulator UR5 is presented [10] where the dynamic properties, inertia matrix, coriolis and centrifugal matrix, and gravity vector are derived based on the Lagrange method, and the derived mathematical model has been implemented in MATLAB. In many research article, forward kinematics of a manipulator are discussed [11, 12] with different joint structures such as triangular prism structured links where the varying positions of the end effector were calculated and plotted against joint angles in MATLAB.

In this paper, the dynamic equations of motion have been derived using Newton–Euler formulation. The direct kinematic solution is obtained analytically by expressing the three nonhomogeneous nonlinear second order differential equations into six differential equations of first order and rearranging them in phase variable form. The angular displacement and angular velocities of each link are presented graphically with respect to time for constant torques applied for a specific period of time using MATLAB. Then, the optimum torque ratio is obtained which gives the feasible angular positions of three-links for practical implementations.

2 Three-Link Manipulator

In this work, a robotic manipulator of three-links of lengths l_1, l_2, l_3 and three joints J_1, J_2, J_3 is shown in Fig. 1. The links are having mass m_1, m_2, m_3 and link parameters are $\alpha_1 = \alpha_2 = \alpha_3 = 0$. All the revolving rigid joints can rotate in a two-dimensional space about the z-axis. The link parameters to be considered as $\alpha_1 = \alpha_2 = \alpha_3 = 0$,

Fig. 1 Three-link manipulator with coordinate assignment
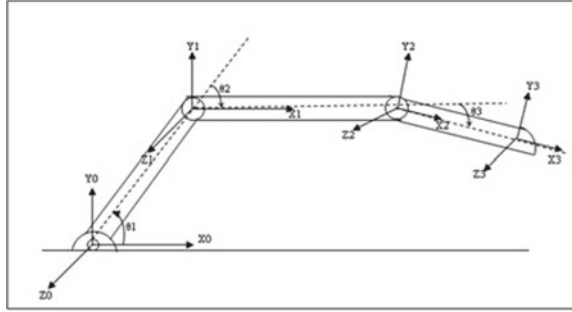
and θ_1, θ_2, and θ_3 are considered as angular displacement of each joint-link pair of the system.

The initial conditions can be considered as

$$\omega_0 = 0, \dot{\omega}_0 = 0, v_0 = 0$$

where ω_0 is the initial angular velocity, $\dot{\omega}_0$ is the initial angular acceleration, v_0 is the initial linear velocity, and $\dot{v}_0$ is the initial linear acceleration.

Therefore,

$$\dot{v}_0 = \begin{bmatrix} g_x \\ g_y \\ g_z \end{bmatrix}$$

$$\dot{v}_0 = \begin{bmatrix} 0 \\ g \\ 0 \end{bmatrix}$$

$$g = 9.8 \text{ m/s}^2$$

Joint variables: angular position, angular speed, and angular acceleration

$$q_i = \theta_i = [\theta_1, \theta_2, \theta_3];$$

$$\dot{q}_i = \dot{\theta}_i = [\dot{\theta}_1, \dot{\theta}_2, \dot{\theta}_3];$$

$$\ddot{q}_i = \ddot{\theta}_i = [\ddot{\theta}_1, \ddot{\theta}_2, \ddot{\theta}_3];$$

Link variable:

$$F_i, f_i, n_i, \tau_i$$

where

    F_i: Total external force exerted on link i at the center of mass

    f_i: Force exerted on link i by link $i-1$

    n_i: Moment exerted on link i by link $i-1$

    τ_i: Torque applied to joint i.

3 Computed Joint Torque by Newton–Euler Equations of Motion

The Newton–Euler approach has been adopted to compute the kinematic model relating joint torque and angular displacement as given in (1) to (3).

Joint torque computed to each joint actuator for link $i = 3, 2, 1$ [for link3, link2, link1 are τ_3, τ_2, τ_1, respectively]

$$
\begin{aligned}
\tau_3 = {} & \frac{1}{2}m_3l_1l_3\left[\cos(\theta_2+\theta_3)\ddot{\theta}_1 + \sin(\theta_2+\theta_3)\dot{\theta}_1^2\right] \\
& + \frac{1}{2}m_3l_2l_3\left[\sin\theta_3\left(\dot{\theta}_1+\dot{\theta}_2\right)^2 + \cos\theta_3\left(\ddot{\theta}_1+\ddot{\theta}_2\right)\right] \\
& + \frac{1}{3}m_3l_3^2\left(\ddot{\theta}_1+\ddot{\theta}_2+\ddot{\theta}_3\right) + \frac{1}{2}m_3l_3g\cos(\theta_1+\theta_2+\theta_3) \qquad (1)
\end{aligned}
$$

$$
\begin{aligned}
\tau_2 = {} & \frac{1}{2}m_3l_1l_3\left[\cos(\theta_2+\theta_3)\ddot{\theta}_1 + \sin(\theta_2+\theta_3)\dot{\theta}_1^2\right] \\
& + \frac{1}{2}m_3l_2l_3\left[\sin\theta_3\left(\dot{\theta}_1+\dot{\theta}_2\right)^2 + \cos\theta_3\left(\ddot{\theta}_1+\ddot{\theta}_2\right)\right] \\
& + \frac{1}{3}m_3l_3^2\left(\ddot{\theta}_1+\ddot{\theta}_2+\ddot{\theta}_3\right) + \frac{1}{2}m_3l_3g\cos(\theta_1+\theta_2+\theta_3) \\
& + \left(m_3 + \frac{1}{2}m_2\right)l_1l_2\left[\cos\theta_2\ddot{\theta}_1 + \sin\theta_2\dot{\theta}_1^2\right] \\
& + \left(m_3 + \frac{1}{3}m_2\right)l_2^2\left(\ddot{\theta}_1+\ddot{\theta}_2\right) \\
& + \frac{1}{2}m_3l_2l_3\left[\cos\theta_3\left(\ddot{\theta}_1+\ddot{\theta}_2+\ddot{\theta}_3\right) - \sin\theta_3\left(\dot{\theta}_1+\dot{\theta}_2+\dot{\theta}_3\right)^2\right] \\
& + \left(m_3 + \frac{1}{2}m_2\right)l_2g\cos(\theta_1+\theta_2) \qquad (2)
\end{aligned}
$$

$$
\begin{aligned}
\tau_1 = {} & \frac{1}{2}m_3l_1l_3\left[\cos(\theta_2+\theta_3)\ddot{\theta}_1 + \sin(\theta_2+\theta_3)\dot{\theta}_1^2\right] \\
& + \frac{1}{2}m_3l_2l_3\left[\sin\theta_3\left(\dot{\theta}_1+\dot{\theta}_2\right)^2 + \cos\theta_3\left(\ddot{\theta}_1+\ddot{\theta}_2\right)\right] \\
& + \frac{1}{3}m_3l_3^2\left(\ddot{\theta}_1+\ddot{\theta}_2+\ddot{\theta}_3\right) + \frac{1}{2}m_3l_3g\cos(\theta_1+\theta_2+\theta_3)
\end{aligned}
$$

$$+ \left(m_3 + \frac{1}{2}m_2 \right) l_1 l_2 [\cos\theta_2 \ddot{\theta}_1 + \sin\theta_2 \dot{\theta}_1^2]$$

$$+ \left(m_3 + \frac{1}{3}m_2 \right) l_2^2 (\ddot{\theta}_1 + \ddot{\theta}_2)$$

$$+ \frac{1}{2} m_3 l_2 l_3 \left[\cos\theta_3 (\ddot{\theta}_1 + \ddot{\theta}_2 + \ddot{\theta}_3) - \sin\theta_3 (\dot{\theta}_1 + \dot{\theta}_2 + \dot{\theta}_3)^2 \right]$$

$$+ \left(m_3 + \frac{1}{2}m_2 \right) l_2 g \cos(\theta_1 + \theta_2) + \left(m_3 + m_2 + \frac{1}{3}m_1 \right) l_1^2 \ddot{\theta}_1$$

$$+ \left(m_3 + \frac{1}{2}m_2 \right) l_1 l_2 \left[\cos\theta_2 (\ddot{\theta}_1 + \ddot{\theta}_2) - \sin\theta_2 (\dot{\theta}_1 + \dot{\theta}_2)^2 \right]$$

$$- \frac{1}{2} m_3 l_1 l_3 \left[\sin(\theta_2 + \theta_3)(\dot{\theta}_1 + \dot{\theta}_2 + \dot{\theta}_3)^2 - \cos(\theta_2 + \theta_3)(\ddot{\theta}_1 + \ddot{\theta}_2 + \ddot{\theta}_3) \right]$$

$$+ \left(m_3 + m_2 + \frac{1}{2}m_1 \right) l_1 g \cos\theta_1 \qquad (3)$$

4 Kinematic Solution of Mathematical Modeling of N–E Model of Three-Link Manipulator

As the dynamics relating joint torque and angular displacement of three coupled joint-link are highly nonlinear in nature, a phase variable form has been adopted. In order to derive a systematic procedure, the three nonlinear differential equation of order two is transformed into a phase variable form representing a system of six first order differential equations.

Assuming $x_1, x_2, x_3, x_4, x_5,$ and x_6 are six phase variables given by

$$x_1 = \dot{\theta}_1 \qquad (4)$$

$$x_2 = \dot{\theta}_2 \qquad (5)$$

$$x_3 = \dot{\theta}_3 \qquad (6)$$

$$x_4 = \theta_1 \qquad (7)$$

$$x_5 = \theta_2 \qquad (8)$$

$$x_6 = \theta_3 \qquad (9)$$

Therefore,

$$\dot{x}_1 = \ddot{\theta}_1 \tag{10}$$

$$\dot{x}_2 = \ddot{\theta}_2 \tag{11}$$

$$\dot{x}_3 = \ddot{\theta}_3 \tag{12}$$

$$\dot{x}_4 = \dot{\theta}_1 = x_1 \tag{13}$$

$$\dot{x}_5 = \dot{\theta}_2 = x_2 \tag{14}$$

$$\dot{x}_6 = \dot{\theta}_3 = x_3 \tag{15}$$

Nondimensionalizing (1), (2), and (3), we have

$$
\begin{aligned}
\tau_3 = {} & \frac{1}{2}\cos(\theta_2 + \theta_3)\ddot{\theta}_1 + \frac{1}{2}\sin(\theta_2 + \theta_3)\dot{\theta}_1^2 \\
& + \frac{1}{2}\sin\theta_3\left(\dot{\theta}_1 + \dot{\theta}_2\right)^2 + \frac{1}{2}\cos\theta_3\left(\ddot{\theta}_1 + \ddot{\theta}_2\right) \\
& + \frac{1}{3}\left(\ddot{\theta}_1 + \ddot{\theta}_2 + \ddot{\theta}_3\right) + \frac{1}{2}\cos(\theta_1 + \theta_2 + \theta_3)
\end{aligned}
\tag{16}
$$

$$
\begin{aligned}
\tau_2 = {} & \frac{1}{2}\cos(\theta_2 + \theta_3)\ddot{\theta}_1 + \frac{1}{2}\sin(\theta_2 + \theta_3)\dot{\theta}_1^2 \\
& + \frac{1}{2}\sin\theta_3\left(\dot{\theta}_1 + \dot{\theta}_2\right)^2 + \frac{1}{2}\cos\theta_3\left(\ddot{\theta}_1 + \ddot{\theta}_2\right) \\
& + \frac{1}{3}\left(\ddot{\theta}_1 + \ddot{\theta}_2 + \ddot{\theta}_3\right) + \frac{1}{2}\cos(\theta_1 + \theta_2 + \theta_3) \\
& + \frac{3}{2}\cos\theta_2\ddot{\theta}_1 + \frac{3}{2}\sin\theta_2\dot{\theta}_1^2 + \frac{4}{3}\left(\ddot{\theta}_1 + \ddot{\theta}_2\right) \\
& + \frac{1}{2}\cos\theta_3\left(\ddot{\theta}_1 + \ddot{\theta}_2 + \ddot{\theta}_3\right) - \frac{1}{2}\sin\theta_3\left(\dot{\theta}_1 + \dot{\theta}_2 + \dot{\theta}_3\right)^2 \\
& + \frac{3}{2}\cos(\theta_1 + \theta_2)
\end{aligned}
\tag{17}
$$

$$
\begin{aligned}
\tau_1 = {} & \frac{1}{2}\cos(\theta_2 + \theta_3)\ddot{\theta}_1 + \frac{1}{2}\sin(\theta_2 + \theta_3)\dot{\theta}_1^2 + \frac{1}{2}\sin\theta_3\left(\dot{\theta}_1 + \dot{\theta}_2\right)^2 \\
& + \frac{1}{2}\cos\theta_3\left(\ddot{\theta}_1 + \ddot{\theta}_2\right) + \frac{1}{3}\left(\ddot{\theta}_1 + \ddot{\theta}_2 + \ddot{\theta}_3\right) \\
& + \frac{1}{2}\cos(\theta_1 + \theta_2 + \theta_3) + \frac{3}{2}\cos\theta_2\ddot{\theta}_1 + \frac{3}{2}\sin\theta_2\dot{\theta}_1^2 \\
& + \frac{4}{3}\left(\ddot{\theta}_1 + \ddot{\theta}_2\right) + \frac{1}{2}\cos\theta_3\left(\ddot{\theta}_1 + \ddot{\theta}_2 + \ddot{\theta}_3\right)
\end{aligned}
$$

$$-\frac{1}{2}\sin\theta_3\big(\dot{\theta}_1 + \dot{\theta}_2 + \dot{\theta}_3\big)^2 + \frac{3}{2}\cos(\theta_1 + \theta_2) + \frac{7}{3}\ddot{\theta}_1$$
$$+\frac{3}{2}\cos\theta_2\big(\ddot{\theta}_1 + \ddot{\theta}_2\big) - \frac{3}{2}\sin\theta_2\big(\dot{\theta}_1 + \dot{\theta}_2\big)^2$$
$$-\frac{1}{2}\sin(\theta_2 + \theta_3)\big(\dot{\theta}_1 + \dot{\theta}_2 + \dot{\theta}_3\big)^2 + \frac{1}{2}\cos(\theta_2 + \theta_3)\big(\ddot{\theta}_1 + \ddot{\theta}_2 + \ddot{\theta}_3\big) + \frac{5}{2}\cos\theta_1$$

$$(18)$$

Using (16), (17), and (18), $\ddot{\theta}_1, \ddot{\theta}_2,$ and $\ddot{\theta}_3$ can be formed as algebraic sum of $\theta_1, \theta_2, \theta_3$ and their first derivatives which give all first order nonlinear equations. Therefore, (10) to (15) are expressed as six equations of first order which can be solved graphically using MATLAB.

4.1 Transient Behavior of Link and Joint Movement

Figures 2, 3, and 4 describe the dynamic behavior of ω and θ of each link corresponding to each joint actuation torque, τ_1, τ_2, and τ_3, for different torque ratio applied for a finite length of time (0.5 s). The angular position versus torque characteristics are shown in Figs. 5, 6, and 7 for different torque ratio.
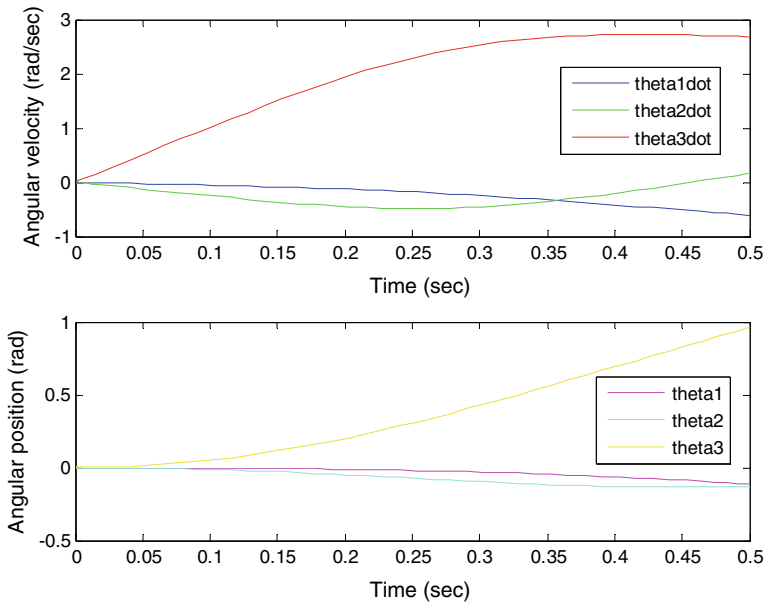
Fig. 2 Transient of angular velocity and angular position for τ_1, τ_2, τ_3:1, 1, 1 (in Nm), respectively
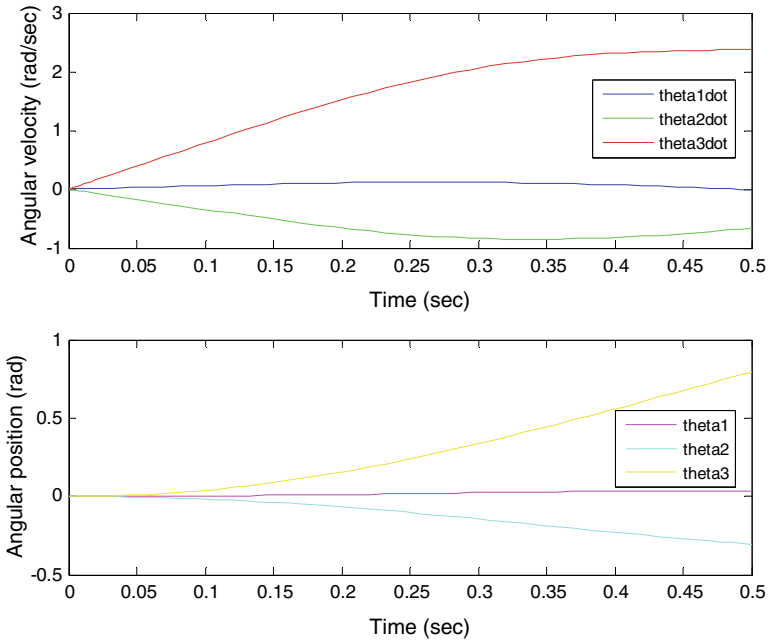
Fig. 3 Transient of angular velocity and angular position for τ_1, τ_2, τ_3:4, 2, 1 (in Nm), respectively
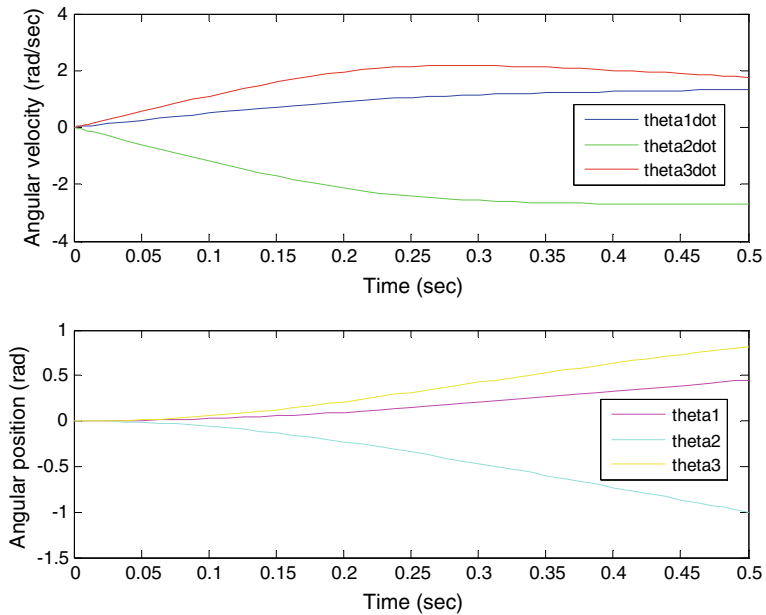
Fig. 4 Transient response of angular velocity and angular position for τ_1, τ_2, τ_3:9, 3, 1 (in Nm), respectively

Fig. 5 Angular position versus applied torque (τ_1:τ_2:τ_3::1:1:1 (in Nm); time: 0.5 s)
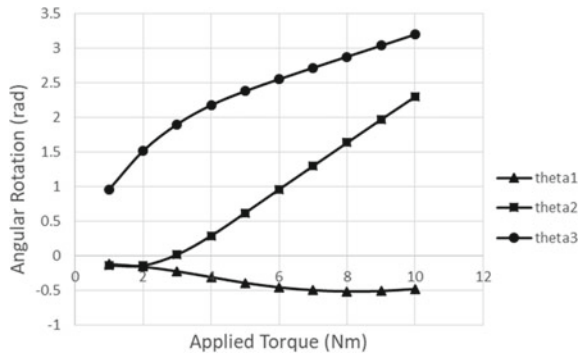
Fig. 6 Angular position versus applied torque (τ_1:τ_2:τ_3::4:2:1 (in Nm); time: 0.5 s)
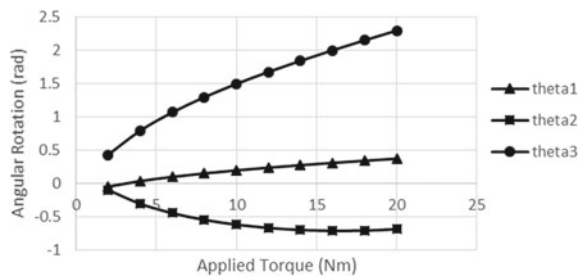
Fig. 7 Angular position versus applied torque (τ_1:τ_2:τ_3::9:3:1 (in Nm); time: 0.5 s)
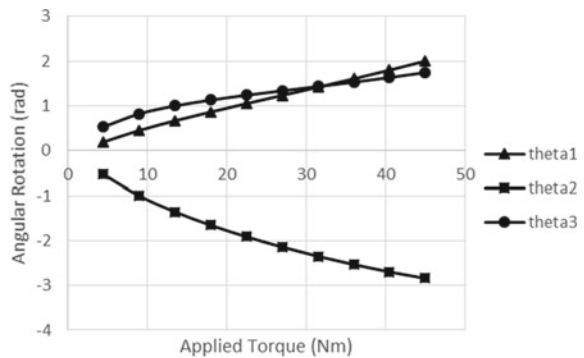
4.2 Characteristics of Link and Joint Movement with Applied Torque

See Figs. 5, 6, and 7.

Table 1 Angular position due to application of constant torques applied for 0.5 s

τ_1 (in Nm)	τ_2 (in Nm)	τ_3 (in Nm)	θ_1 (rad)	θ_2 (rad)	θ_3 (rad)
1	1	1	−0.1146	−0.1338	0.9641
4	2	1	0.0359	−0.3048	0.7929
9	3	1	0.4517	−1.0001	0.8221

5 Results and Discussion

Table 1 represents the results obtained from Figs. 2 to 4 which describe the angular position of each link after 0.5 s due to application of constant torques.

From Table 1, it is evident that in nondimentionalize condition of the manipulator, applying joint torques in equal proportion are not able to lift up the link1 and link2 as both θ_1 and θ_2 are negative. For practical realization, it can be assumed that $0 \leq \theta_1 \leq \frac{\pi}{2}$, $0 \leq \theta_2 \leq \frac{\pi}{2}$, and $0 \leq \theta_3 \leq \frac{\pi}{2}$. And if θ_2 is negative, it must follow the condition $|\theta_2| \leq \theta_1$. Therefore, to satisfy this condition the joint torques must be applied in the proportion of $\tau_1{:}\tau_2{:}\tau_3{::}9{:}3{:}1$ or higher (refer Table 1).

6 Conclusion

The dynamic equations, as stated in (1) to (3), describe the nonlinear nature of the system. Here, the open loop response of the system has been studied and result is as expected. Figures 5–7 show the angular rotation versus torque characteristics and the most linear characteristics and hence optimum torque can be obtained for the torque ratios of $\tau1{:}\tau2{:}\tau3{::}9{:}3{:}1$ as shown in Fig. 7 using MATLAB. Moreover, the system can be assumed to have a combination of three inverted pendulum will also be a chaotic system. As a very consequences, the system can be controlled with sliding mode controller as well as with proportional derivative controller which will give the system more stability.

References

1. Zribi, M., Karkoub, M., Huang, L.: Modelling and control of two robotic manipulators handling a constrained object. Appl. Math. Model. **24**, 881–898 (2000)
2. Deshpande, V.A., Verma, A.B.: Dynamics of robot manipulators: a review. Int. J. Eng. Res. Technol. **3**(3), 603–606 (2010). ISSN 0974-3154
3. Yamane, K., Nakamura, Y.: Robot Kinematics and Dynamics for Modeling the Human Body, Robotics Research, STAR 66, pp. 49–60. Springer (2010)
4. Cheraghpour, F., Vaezi, M., Jazeh, R.E.S., Ali, S., Moosavian, A.: Dynamic modeling and kinematic simulation of staubli TX40 robot using MATLAB/ADAMS co-simulation. In: Proceedings of the 2011 IEEE International Conference on Mechatronics 13–15 April 2011. https://doi.org/10.1109/ICMECH.2011.5971316

5. Korayem, M.H., Shafei, A.M., Shafei, H.R.: Dynamic modeling of nonholonomic wheeled mobile manipulators with elastic joints using recursive Gibbs-Appell formulation. Scientia Iranica B **19**(4), 1092–1104 (2012). https://doi.org/10.1016/j.scient.2012.05.001
6. Korayem, M.H., Rahimi, H.N., Nikoobin, A.: Mathematical modeling and trajectory planning of mobile manipulators with flexible links and joints. Appl. Math. Model. **36**, 3229–3244 (2012). https://doi.org/10.1016/j.apm.2011.10.002
7. Dhaouadi, R., Hatab, A.A.: Dynamic modelling of differential-drive mobile robots using Lagrange and Newton-Euler methodologies: a unified framework. Adv. Rob. Autom. (2013). https://doi.org/10.4172/2168-9695.1000107
8. Shah, J., Rattan, S.S., Nakra, B.C.: Dynamic analysis of two link robot manipulator for control design using computed torque control. Int. J. Res. Comput. Appl. Rob. **3**(1), 52–59 (2015). ISSN 2320-7345
9. Chenguang, Y., Hongbin, M., Mengyin, F.: Robot kinematics and dynamics modeling. Adv. Technol. Mod. Rob. Appl. (2016). https://doi.org/10.1007/978-981-10-0830-6_2
10. Kebria1, P.M., Al-wais, S., Abdi, H., Nahavandi, S.: Kinematic and dynamic modelling of UR5 manipulator. In 2016 IEEE International Conference on Systems, Man, and Cybernetics SMC 2016 9–12 October 2016. https://doi.org/10.1109/SMC.2016.7844896
11. Raut, N., Rathod, A., Ruiwale, V.: Forward kinematic analysis of a robotic manipulator with triangular prism structured links. Int. J. Mech. Eng. Technol. (IJMET) **8**(2), 08–15 (2017)
12. Himanth, M., Bharath, L.V.: Forward kinematics analysis of robot manipulator using different screw operators. Int. J. Rob. Autom. **3**(2), 21–28 (2017)

Improved Speech Activity Detection Using Cochleagram Spectral Basis by Nonnegative Matrix Factorization

Sujoy Mondal and Abhirup Das Barman

Abstract This paper presents a method to detect speech activity in a noisy environment. It is a supervised technique in which a set of speech spectral basis (SSB) vectors is derived from cochleagram features of clean speech using nonnegative matrix factorization. The selected SSB set is employed to find speech component from multiple input frames of noisy TIMIT speech dataset using cosine similarity method. The statistical measures obtained from the similarity measures on several consecutive training frames are used to train the logistic regression classifier model. Accuracy of speech detection performance is measured in terms of F1 score, and the result obtained by the proposed method outperforms the other state-of-the-art methods.

Keywords Cochleagram · Gammatone · Nonnegative matrix factorization · Speech activity detection

1 Introduction

Speech activity detection (SAD) is a task for identifying the presence of speech within audio signal. Among many applications of SAD include automatic speech recognition (ASR) [1], quality of speech in mobile telecommunication systems [2], voice command system [3], smart devices [4], audio forensic [5], etc. Continuous efforts are being made to improve detection techniques of SAD to overcome its challenges, so SAD becomes a popular research area in any speech processing applications since last few decades [6].

In general, the task of SAD consisting of mainly two stages: feature selection and speech/nonspeech discrimination. Among the important features used in SAD are zero crossing rate (ZCR) [7], spectral flux [8], single frequency filtering [9], speech

S. Mondal (✉)
Department of ECE, RCCIIT, Kolkata, India

A. Das Barman
Department of Radio Physics and Electronics, University of Calcutta, Kolkata, India

formant [10], mel-frequency cepstral coefficients (MFCC) [11], and mel scale energy [12]. However, the task of detection is more challenging under noisy condition. Recently, cochleagram-based features [13] are reported as robust features for SAD task. Cochleagram features are used in supervised [13] as well as in unsupervised [6] framework. Supervised methods [13, 14] require large amount of training with noisy dataset. Yet, supervised method is unable to detect speech at unseen noise category after successful training. On the other hand, the benefit of unsupervised method [6] is that it does not require any training data for the model but error in speech detection creeps in when noise in the signal is fast changing. To mitigate the issue, classification-based supervised SAD approach is always preferred specially in real-time application.

The objective of this work is to find an improved technique for training the classifier model with feature vectors such that redundancy in cochleagram spectral features do not affect classification process. So an alternative to direct training of the classifier by the cochleagram spectral pattern, we find selective speech spectral basis (SSB) sets from cochleagram features of clean speech. Redundancy in cochleagram features is discarded by nonnegative matrix factorization (NMF) method, and optimal SSB vectors are derived. The optimum selected SSB set is employed to find speech component of multiple input frames of noisy speech dataset using cosine similarity. Statistical measures are performed on these new set of speech feature vectors to train a logistic regression binary classifier model for speech/nonspeech detection. It may be mentioned here that in many recent audio applications [15, 16], NMF is used as basis selection mechanism.

Contribution: (i) The proposed method employs a new technique to train a logistic regression binary classifier model using a new set of feature vectors. These new feature sets are obtained from a set of SSB sets using nonnegative matrix factorization [17] of time-frequency cochleagram features of clean speech. (ii) An optimum SSB set is obtained in the proposed method to provide the best F1 score performance for speech/nonspeech detection. (iii) The use of clean speech database for SSB selection avoids hard annotation task which is required in the other classification-based approach. (iv) The proposed NMF-SAD technique shows a substantial improvement in detection performance compared to other baseline techniques for different noise category.

The rest of the paper is arranged as follows. In Sect. 2, system model is described in detail. In Sect. 3, experiment and result are shown. Finally, conclusion is drawn in Sect. 4.

2 System Modeling

System model consists of few steps: (i) cochleagram features are extracted from each frame of input clean speech data, and time-frequency (*TF*) pattern is computed using cochleagram features. Using *TF* cochleagram pattern, 64 dimensions (*d*) speech
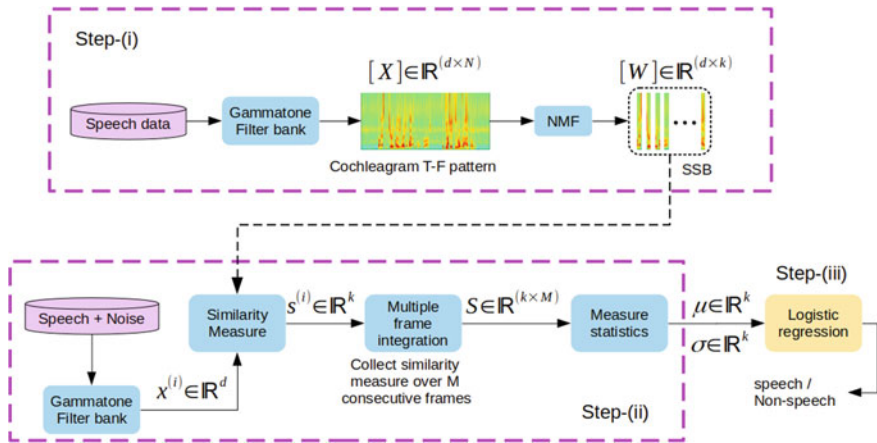
Fig. 1 Proposed SAD model. (i), (ii), and (iii) are different steps in the modeling

spectral basis vectors (k) are formed using nonnegative matrix factorization technique. Eight optimum SSB vectors or basis functions are chosen based on best performance of speech/nonspeech detection. (ii) First cochleagram features are extracted from the training dataset, then cosine similarity measures [18] are performed on these extracted features with the optimized eight SSB vectors obtained in previous step (i). Now, we have eight real numbers for each frame. The process is repeated for M consecutive frames of training dataset over which statistical measures are performed to obtain mean (μ) and standard deviation (σ). k number of mean and k number of standard deviations are computed over M frames, where k corresponds to number of SSB vectors as said earlier. Thus, M frames contain temporal information of *TF* patterns. In the final step (iii), mean and standard deviation vectors are used to train the logistic regression (LR) model for speech/nonspeech binary classification task. The whole process is depicted in Fig. 1, and details are given in the following subsections.

2.1 Extraction of Cochleagram Features from Gammatone Filter Bank

Motivated by the human auditory model, we choose 64 channel gammatone filter bank to process 16 kHz sampled speech/nonspeech signal. Short time energy over 20 ms time frame is computed at the output of each gammatone filter bank channel in every 10 ms hopping interval. Signal energies in a frame normalized by frame length are arranged in a two-dimensional (2D) time-frequency (*TF*) matrix, where frequency values are representing the center frequencies of the filter bank. Row values of the matrix are equal to the gammatone filter bank number or channel number (d).

Each column of the matrix represents the incoming successive 20 ms time frames and their energies are computed. This *TF* representation is referred to as 2D cochleagram [19]. So, each column of *TF* matrix is a 64 dimensional vector corresponds to energy values around different filter bank center frequencies. 64 dimension corresponds to 64 number of gammatone filters (d) in the filter bank. Detailed steps are given below to extract energy values using gammatone filter bank. Impulse response $g(t)$ of the gammatone filter [20] can be represented by

$$g(t) = t^{p-1}\mathrm{e}^{-2\pi tb(f_c)}\cos(2\pi f_c t); \quad t \geq 0 \tag{1}$$

p is the filter order of the filter which is typically set to a value less than or equal to 4 [20]. In this work, value of p is chosen as four and center frequencies (f_c) are chosen on equivalent rectangular bandwidth scale (ERBs) to simulate human auditory model [20]. The center frequencies are chosen in the range from 50 to 8000 Hz which is well beyond 3500 Hz of speech bandwidth in order to accommodate sufficient speech and nonspeech spectral patterns. So, Nyquist sampling rate is chosen as 16,000 Hz. ERB-scale [20] is defined by Eq. (2).

$$\mathrm{ERBs} = 21.4 \times \log_{10}(0.00437 \times \mathrm{hz} + 1) \tag{2}$$

In ERBs, d number of linearly spaced frequencies are chosen which can be converted into hz-scale by

$$\mathrm{hz} = \left[10^{\mathrm{ERBs}/21.4} - 1\right]/4.37 \times 10^{-3} \tag{3}$$

These hz-scale frequencies are the center frequencies (f_c) of gammatone filters. Human ear is more sensitive toward lower frequencies compared to higher frequencies [20]. Therefore, the bandwidth of each filter increases with the center frequencies of the filter and it is described by [20],

$$b(f_c) = 1.019 \times 24.7 \times (0.00437 \times f_c + 1) \tag{4}$$

Let us consider, N number of input frames and subsequent frames are made 50% overlapped. The time domain signal in each frame is processed through a FFT block [21], then the FFT spectrum is passed through d channel gammatone filter banks whose center frequencies and bandwidths are chosen according to Eqs. (3) and (4), respectively. Now, energy is computed in each gammatone filter bank output which is divided by the number of samples to get normalized filter bank output. Finally, the output energies are normalized in the range [0,1] by dividing with the maximum energy. The cochleagram output is represented by $X \in R^{d \times N}$ as shown in Fig. 1.

2.2 Extraction of Speech Spectral Basis (SSB)

Speech spectral basis (SSB) vectors are formed from cochleagram *TF* representation of clean speech using nonnegative matrix factorization as shown in Fig. 1. The elements of cochleagram output X are nonnegative as it originates from the energy values of a signal in a frame. NMF is used to compute the spectral basis matrix (W) using the following relationship

$$X \approx W \times H \tag{5}$$

where $W \in R_+^{d \times k}$ is the basis matrix consisting of k basis vectors and $H \in R_+^{k \times N}$ is the coefficient matrix. Usually, $k \leq \min(d, N)$ which has to be judicially selected by user. Each column vectors of the cochleagram matrix X are a linear combination of basis vectors from W. In this work, eight SSB vectors or basis functions are employed which we found to give best performance of speech/nonspeech detection. Results will be shown later. The linear combination coefficients are collected from the corresponding row of H matrix. To achieve the factorization in (5), we use Kullback–Leibler divergence [17] cost function (J_{KL}) which is defined by (6).

$$J_{KL}(X||WH) = \sum \left(X_{ij} \log \frac{X_{ij}}{[WH]_{ij}} - [X - WH]_{ij} \right) \tag{6}$$

The local optimum is obtained by updating the elements of W and H using multiplicative update rules [22] given by Eq. (7).

$$W \leftarrow W \otimes \frac{\frac{X}{WH} H^{\mathrm{T}}}{1 H^{\mathrm{T}}} \quad \text{and} \quad H \leftarrow H \otimes \frac{W^{\mathrm{T}} \frac{X}{WH}}{W^{\mathrm{T}} 1} \tag{7}$$

So, W in (5) is a matrix whose columns give the individual SSB vectors with 64 row values. During updating of W and H, all the matrix elements are updated. However, H matrix has no use in our case. Convergence of NMF guarantees that redundancy in cochleagram is discarded by NMF, and SSB vectors are formed.

2.3 Training of Logistic Regression Classifier Model

Logistic regression is a supervised learning classification model used here to predict the probability of a binary target variable, i.e., speech or nonspeech. Speech activity detection is a binary classification task where the trained model provides the speech presence score. In a classification task, the model needs to be trained to discriminate between speech and nonspeech signal from noisy dataset. Classification challenge to train LR model in the presence noise is undertaken by forming a new set of feature vectors using speech spectral basis vectors from cochleagram *TF* representation of

clean speech as explained below. A training database consisting of clean speech from TIMIT dataset [23] and noisy TIMIT dataset. Noisy dataset is prepared by adding noises from NOISEX92 database [24]. The schematic of training phase is shown in step (iii) in Fig. 1. Cochleagram column patterns are extracted from every frame of training noisy TIMIT dataset in the same way as described in Sect. 2.1. Now, cosine similarity measures are performed on cochleagram column pattern with the optimized eight SSB vectors frame wise to get speech component. The cosine similarity measures [18] are defined as follows

$$s^{(i)} = W^{\mathrm{T}} x^{(i)} \tag{8}$$

where $x^{(i)} \in R^d$ is the ith frame of training dataset cochleagram and $s^{(i)} \in R^k$ is the output similarity vector as shown in step (ii) of Fig. 1. The process is repeated for M consecutive training frames of noisy TIMIT dataset to incorporate the temporal information of training noisy speech. Generally, the choice of M is odd [6]. Typical value of M can be chosen as 21, as we have considered in our experiment. Thus, similarity matrix $S \in R^{(k \times M)}$ is formed. The mean $\left(\mu \in R^k\right)$ and standard deviation $\left(\sigma \in R^k\right)$ vectors are calculated from the similarity matrix S using the basis vectors as shown in the following to form the final feature vector to train the LR classifier model.

$$\mu_i = \mathrm{mean}(S(i, 1 : M)); \quad i = 1, \ldots k \tag{9}$$

$$\sigma_i = \mathrm{std}(S(i, 1 : M)); \quad i = 1, \ldots k \tag{10}$$

Therefore, the combined feature vectors $[\mu, \sigma] \in R^{2k}$ are used to train the classifier. Logistic regression is used as classifier with binary cross-entropy as the cost function [25]. The output of logistic regression gives a probability between [0,1] for an input frame to be a speech frame. We can set the threshold level at the output of logistic regression which calculates the probability in the range 0 to 1 and provides results for SAD. In this work, we use Python library function "*sklearn.linear_model.LogisticRegression*" to train the model. Once the model is trained, it is used to predict an input frame to be speech or not. Continuous speech consists of voiced, unvoiced, and silence portions. A smoothing technique [26] is used to further improve the SAD performance.

3   Experiment and Results

We evaluate the performance of our proposed nonnegative matrix factorization-based speech activity detection (NMF-SAD) and compare it with the performance of some baseline SAD techniques, namely Sohn [27], Sadjadi [8], rVAD [28], and GTFB-MWO [6]. For comparison purpose, the same database [6] is used. As only clean

Fig. 2 Average system F1 score (%) for different speech spectral basis (SSB) counts
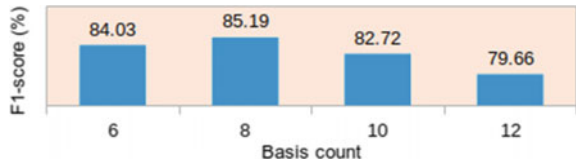
speech is used for finding the SSB, therefore, 80% of Corpus-I [6] is used for training the LR model and the rest of 20% is used for testing. Total duration of Corpus-I is about 600 min. Only the worst category noise-set data, namely babble, engine, and factory noises are considered. The evaluation matrices used are F1 score and half total error rate (HTER) [6]. The complete system is trained and tested in Python programming framework.

The most important parameter of the proposed model is the choice of number of basis sets through NMF task for improved SAD performance. To obtain the optimum basis set (SSB), we conduct an experiment with the no of basis sets starting from six up to 12 in step size of two and in each case F1 score is computed. Average F1 score is plotted, and comparison result is shown in Fig. 2. The best F1 score of 85.19% is obtained for $k = 8$. In the rest of the experiments, number of SSB set is kept at this value. Other important parameters are frame length $= 20$ ms, frame hopping interval $= 10$ ms, and number of consecutive frames for statistical parameter (mean and standard deviation) evaluation $M = 21$ as chosen in our previous GTFB-MWO model [6]. NMF-SAD is a supervised frame-based SAD technique. The results are obtained after smoothing the decision of logistic regression. At a lower threshold of logistic regression output, the system is more favorable toward speech. To make an unbiased estimation, we set the threshold value at 0.5 for our experiment. If the output of the classifier is more than 0.5, it is a speech frame otherwise classified as nonspeech.

We examine the performance of the proposed NMF-SAD method in terms of HTER (%) which is the average of total miss detection and total false alarm rate. The HTER (%) is evaluated for three noise categories (babble, engine, and factory) at -5, 0, 5, and 10 dB SNRs. The result is shown in Fig. 3. It is found that overall performance is better in case of engine noise compared to babble and factory noise.
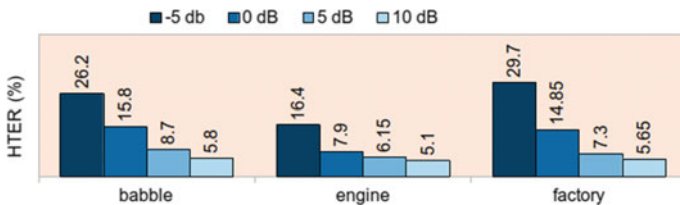
Fig. 3 System HTER (%) for four SNR levels (-5, 0, 5, and 10 dB) at babble, engine, and factory noise categories
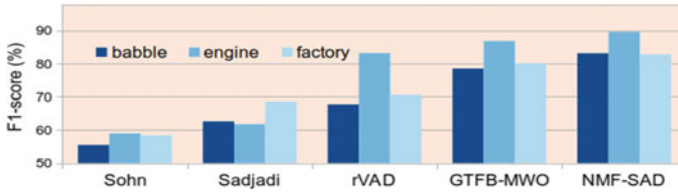
Fig. 4 NMF-SAD detection performances under babble, engine, and factory noises using F1 score (%) and its comparison with other baseline techniques

But at high SNR (~10 dB), the system performances are comparable under different noises.

Figure 4 shows speech activity detection performance of different systems in terms of F1 score (%). Comparison performance of our proposed system is made with the baseline techniques. It is found that the proposed system is consistently performing well under all conditions. Each F1 score value shown in Fig. 4 is averaged over four different SNRs. It is found that the proposed NMF-SAD model gives the best performance among all. The proposed method finds better performance compared to our previous cochleagram GTFB-MWO technique [6] due to the fact that the redundant spectral information is removed by the NMF process. This has led to the improvement of F1 scores by 4.62%, 2.75%, and 2.73%, respectively, for babble, engine, and factory. By taking average of the above three F1 scores, the overall improvement of average value of F1 score over the reported best state-of-the-art technique is about 3% across all noise categories (babble, engine, and factory). Results in Fig. 4 also show that except Sadjadi et al. [8], all other methods offer good result under engine noise compared to babble and factory. The training dataset volume is about 480 min, 80% of total duration of Corpus-I. However, with more training data, the accuracy of HTER and % F1 score performance will improve further.

4   Conclusion

A classification-based speech activity detection technique is proposed. NMF technique is used to select the speech spectral basis from the cochleagram features. The use of clean speech database for SSB selection avoids hard annotation task which is required in the other classification-based approach. Set of SSB vectors is used to maximize the speech components in a frame and thus separates speech from nonspeech frames. Statistical measures over multiple captured frames are used for speech/nonspeech classifications. It is found that speech spectral basis vector of dimension eight gives the best F1 score performance about 85.19% for speech/nonspeech detection. The % HTER performance for the proposed technique is evaluated at three different noise categories (babble, engine, and factory) and at different noise levels −5, 0, 5, and 10 dB SNRs. It is found that overall performance

of speech activity detection is better in case of engine noise compared to babble and factory noise. HTER is around 15% when SNR level of the input signal is at 0 dB but HTER is less than 5% when SNR is improved by 10 dB.

References

1. Vlaj, D., et al.: A computationally efficient mel-filter bank VAD algorithm for distributed speech recognition systems. EURASIP J. Adv. Sig. Process. **4**, 1–11 (2005)
2. Benyassine, A., et al.: A silence compression scheme for use with G. 729 optimized for V. 70 digital simultaneous voice and data applications (recommendation G. 729 Annex B). IEEE Commun. Mag. **35.9**, 64–73 (1997)
3. Principi, E., et al.: An integrated system for voice command recognition and emergency detection based on audio signals. Expert Syst. Appl. **42**(13), 5668–5683 (2015)
4. Lezzoum, N., Gagnon, G., Voix, J.: Voice activity detection system for smart earphones. IEEE Trans. Consum. Electron. **60**(4), 737–744 (2014)
5. Ali, Z., Talha, M.: Innovative method for unsupervised voice activity detection and classification of audio segments. IEEE Access **6**, 15494–15504 (2018)
6. Mondal, S., Barman, A.D.: Speech activity detection using time-frequency auditory spectral pattern. Appl. Acoust. **167**, 107403 (2020)
7. Zaw, T.H., War, N.: The combination of spectral entropy, zero crossing rate, short time energy and linear prediction error for voice activity detection. In: 2017 20th International Conference of Computer and Information Technology (ICCIT). IEEE (2017)
8. Sadjadi, S.O., Hansen, J.H.L.: Unsupervised speech activity detection using voicing measures and perceptual spectral flux. IEEE Sig. Process. Lett. **20**(3), 197–200 (2013)
9. Pannala, V., Yegnanarayana, B.: A neural network approach for speech activity detection for Apollo corpus. Comput. Speech Lang. **65**, 101137 (2021)
10. Yoo, I.-C., Lim, H., Yook, D.: Formant-based robust voice activity detection. IEEE/ACM Trans. Audio Speech Lang. Process. **23**(12), 2238–2245 (2015)
11. Kinnunen, T., et al.: Voice activity detection using MFCC features and support vector machine. In: International Conference on Speech and Computer (SPECOM07), vol. 2, Moscow, Russia (2007)
12. Jung, Y., et al.: Linear-scale filterbank for deep neural network-based voice activity detection. In: 2017 20th Conference of the Oriental Chapter of the International Coordinating Committee on Speech Databases and Speech I/O Systems and Assessment (O-COCOSDA). IEEE (2017)
13. Zhang, X.-L., Wang, D.: Boosting contextual information for deep neural network based voice activity detection. IEEE/ACM Trans. Audio Speech Lang. Process. **24**(2), 252–264 (2015)
14. Ong, W.Q., Tan, A.W.C.: Robust voice activity detection using gammatone filtering and entropy. In: 2016 International Conference on Robotics, Automation and Sciences (ICORAS). IEEE (2016)
15. Chan, T.K., Chin, C.S., Li, Y.: Semi-Supervised nmf-cnn for Sound Event Detection, pp. 1–5 (2020). arXiv preprint arXiv: 2007.00908
16. Zhou, Q., Feng, Z., Benetos, E.: Adaptive noise reduction for sound event detection using subband-weighted NMF. Sensors **19**(14), 3206 (2019)
17. Cichocki, A., et al.: Nonnegative Matrix and Tensor Factorizations: Applications to Exploratory Multi-Way Data Analysis and Blind Source Separation. Wiley (2009)
18. Li, B., Han, L.: Distance weighted cosine similarity measure for text classification. In International Conference on Intelligent Data Engineering and Automated Learning. Springer, Berlin, Heidelberg (2013)
19. Klingenberg, B., Curry, J., Dougherty, A.: Non-negative matrix factorization: Ill-posedness and a geometric algorithm. Pattern Recogn. **42**(5), 918–928 (2009)

20. Wang, D., Brown, G.J.: Computational Auditory Scene Analysis: Principles, Algorithms, and Applications. Wiley-IEEE Press (2006)
21. Proakis, J.G.: Digital Signal Processing: Principles Algorithms and Applications. Pearson Education India (2001)
22. Ludena-Choez, J., Quispe-Soncco, R., Gallardo-Antolin, A.: Bird sound spectrogram decomposition through non-negative matrix factorization for the acoustic classification of bird species. PloS ONE **12.6**, e0179403 (2017)
23. Garofolo, J.S., et al.: DARPA TIMIT acoustic-phonetic continuous speech corpus CD-ROM. NIST speech disc 1-1.1. NASA STI/Recon technical report n 93, 27403 (1993)
24. Varga, A., Steeneken, H.J.M.: Assessment for automatic speech recognition: II. NOISEX-92: a database and an experiment to study the effect of additive noise on speech recognition systems. Speech Commun. **12.3**, 247–251 (1993)
25. Kirasich, K., Smith, T., Sadler, B.: Random Forest vs logistic regression: binary classification for heterogeneous datasets. SMU Data Sci. Rev. **1**(3), 9 (2018)
26. Drugman, T., et al.: Voice activity detection: merging source and filter-based information. IEEE Sig. Process. Lett. **23**(2), 252–256 (2015)
27. Sohn, J., Kim, N.S., Sung, W.: A statistical model-based voice activity detection. IEEE Sig. Process. Lett. **6**(1), 1–3 (1999)
28. Tan, Z.-H., Dehak, N.: rVAD: an unsupervised segment-based robust voice activity detection method. Comput. Speech Lang. **59**, 1–21 (2020)

Fluorescence Spectroscopy as an Interface of Engineering and Basic Science: Its Evolution and Principle

Latibuddin Thander

Abstract The fluorescence spectroscopy is a very emerging research area. Its application is extended in the diverse arena of physical, chemical, analytical and medical sciences. Use of fluorescence for imaging is an important application in the field of biomedical sciences. It is multidisciplinary field of research area. Engineers can contribute a lot for its development. This review is aiming to cover its stages of development and underlying theories and principles that are very useful to interpret any experimental data in this field.

Keywords Fluorescence · Incandescent · Stokes' law · Fluorspar · Jablonski diagram

1 Introduction

The first known report of the phenomenon of the light emitting material without heating came in the literature in the long back in 1565 when Spanish botanist and physician Nicolus Monardes [1] talked about a slight blue colour of water originated when it had been kept in a special wood cup of a plant 'lignum nephriticum'. Afterwards, many greats (like Isaac Newton and Robert Boyle) of seventeenth and eighteenth centuries had interested in exploring this new arena. The cold light emitting materials (other types emit light in hot condition—known as incandescent material) had continued to be discovered during seventeenth and eighteenth centuries enriching the libraries of this new sort of materials. But the science behind this strange phenomenon had not been understood by them. Brewster [2] in 1833 again observed 'this light emission in cold' when he noticed a red light in an alcoholic solution of green leaves (chlorophyll) on exposing to white light. He also observed a blue light from a crystal of fluorspar and tried to explain the two phenomena on the basis of scattering of light. The research in this field then continued discovering many new facts centring basically in Europe.

L. Thander (✉)

Department of Basic Science and Humanities, Ramkrishna Mahato Government Engineering College, Purulia, West Bengal 723103, India

1.1 A New Scientific Look: Advent of Stokes

In nineteenth century, a huge advancement of this new field had occurred because of pioneering works of the investigators like J. Herschel, Stokes and many others. A very meaningful experiment was carried out by an English astronomer and mathematician John Herschel in 1845 [3]. He, with the help of a prism, used different part of a visible light to illuminate a solution of quinine sulphate and arrived at some important conclusions that—(i) only blue part of the light is responsible for the light emission from the 'surface' of the quinine solution and (ii) emitted light is made of a mixture of blue, green and yellow. But unfortunately, he could not understand that the emitted light had a higher wavelength than the absorbed light. Seven years later, an Anglo-Irish physicist and mathematician at the University of Cambridge, Stokes [4] at his young age of thirty-three published a monumental paper in *Philosophical Transaction* and coined the term 'fluorescence' in analogy with the mineral fluorspar (consisted of crystal of CaF_2 containing fluorescent impurities like Eu^{2+} and some other lanthanides). This mineral emits blue light. Stokes carried out some important investigations and reached to some significant decisions. He carefully observed that when sunlight had been split with a prism and various parts were exposed to the solution of quinine sulphate it was the invisible part of the spectrum beyond the ultraviolet region which causes the glow of the solution. He established that the glow was due to the *absorption of radiation* and not due to the *scattering*. Stokes next statement was emitted light which would always have the longer wavelength than the absorbed light. This is what that later becomes Stokes' law. Stokes had been continuing his research in this direction for many years and explained many important properties of 'fluorescence' such as its dependency on concentration and use as an analytical tool [5]. In the first half of twentieth century, a remarkable progress in this field had happened, many interesting aspects of the fluorescence disclosed, and people tried to apply it as a tool in diverse areas of physical, chemical and medical sciences. The design of *fluorescence microscopy* to study the living organism in the beginning of twentieth century by the companies like Carl Zeiss and Carl Reichert [6] put forward a thrust in research in the direction of fluorescence spectroscopy. Ellinger and Hirt also contributed a lot in the development of fluorescence microscopy where they treated living organism with fluorescent substances that can act as a source of light in that species. The discovery of green fluorescent protein (GFP) is another great finding which extends the use of fluorescence in the field of biomedical science. During the early second half of twentieth century, it was Davenport and Nicol who reported [7] the light emitting tissue in the eosinophils of a jelly fish called *Hydromedusae.* But the author had no idea about the origin of light. Seven years later Shimomura et al. [8] identified that the basic compound behind the origin of the light was a protein. This is what later popularly known as green fluorescent protein (GFP). The Nobel Prize in chemistry in 2008 went to Shimomura, Tsien and Chalfie for their outstanding contribution in the area of green fluorescent protein (Table 1).

Table 1 Chronological order in the evolution of fluorescence

Sl no.	Event	Scientist	Year
1	Bioluminescence of *lignum nephriticum*	N. Monardes	1665
2	Study of the green leaves solution in alcohol	D. Brewster	1833
3	Reporting of light emission by quinine sulphate solution	J. Herschel	1845
4	Publication of famous paper on 'refrangibility of light'	G. G. Stokes	1852
5	Theoretical distinction between fluorescence and phosphoresescence	F. Perrin	1929 [9]
6	An approach to the theoretical understanding of fluorescence	Aleksander Jablonski	1935
7	Reporting of luminescence in *hydromedusae*	D. Davenport and J. A. C Nicol	1955
8	Discovery of green fluorescent protein (GFP) in *hydromedusae*	Osamu Shimomura	1962
9	Using of green fluorescent protein as a marker for gene expression	Martin Chalfie	1994 [10]

2 Absorption of Light and Subsequent Phenomena

If a photon is absorbed by a molecule, the molecule will be raised to an excited state. Then, the excited molecule will try to return to the ground state, and the same can be achieved by many ways. One possibility is the occurrence of fluorescence (Fig. 1).

The various possibilities are summarized below:

It can return to the ground state without emission of photons, and the extra energy of the excited state is released via vibrational relaxation and collision with the surrounding medium. As a result, the energy of the photon is converted ultimately to the thermal energy. If during this whole process, the spin state of the excited and the ground state remains same, the process is called the internal conversion. Since no photon is emitted in this process, it becomes a radiation-less decay.

There may occur a transition from singlet to triplet state in the excited state. It is known as intersystem crossing, and it is generally followed by phosphorescence or delayed fluorescence.

The excited molecule may participate in chemical reaction which is the basis of photochemistry.

The excited molecule may transfer the extra energy to another system and reverts back to ground state. De-excitation may also be accompanied by proton transfer, electron transfer or conformation change of the molecule. Other fates of the excited molecule may be the formation of excited state complex, i.e., exciplex or the excited state dimer known as excimer. Lastly, one of the probabilities is the emission of the photons from the excited molecule leading to the phenomenon of fluorescence.

Fig. 1 Light absorption and
emission of fluorescence

Absorption of
light

Ground State

Excited State

Emission of
light

Fluorescence

Excited State

Ground State
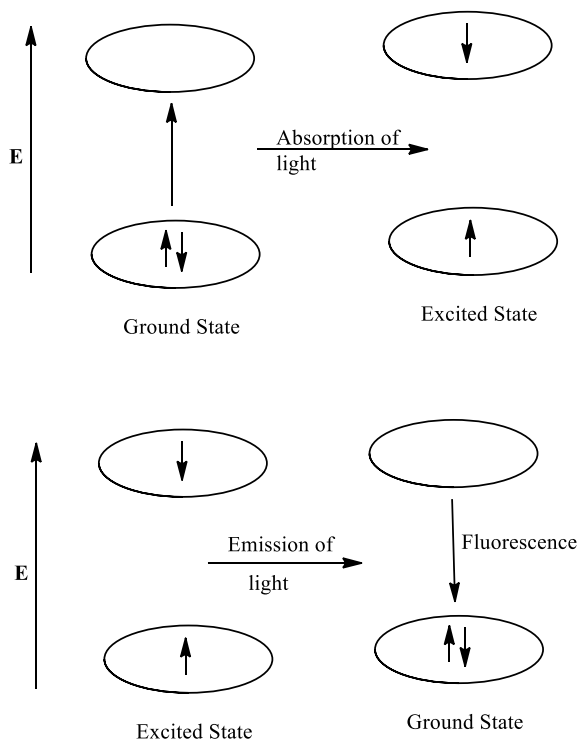
3   An Overview of Singlet and Triplet State

In a molecular singlet state, all electrons remain paired. Let us explain the concept
with Fig. 2.

hν

spin state
changed

E

(a)   (b)   (c)
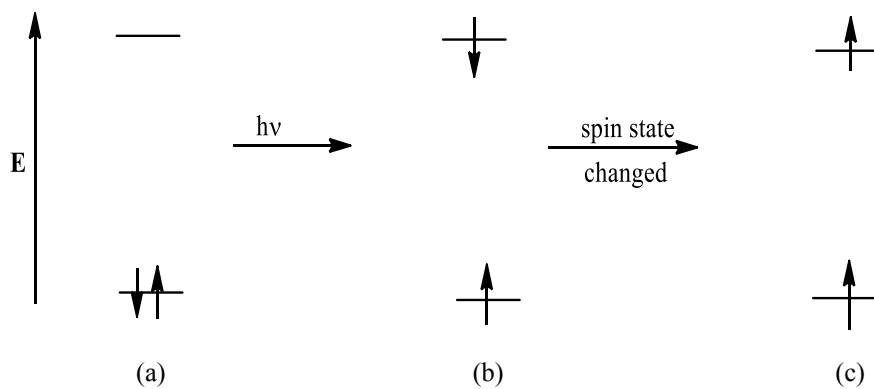
Fig. 2   Singlet and triplet state

In 'A', two electrons are remaining in the same orbital, and they are in spin-paired state. So, the total quantum number is zero $[(+1/2) + (-1/2) = 0]$. Therefore, the spin multiplicity will be $2S + 1 = 2 \times 0 + 1 = 1$. Thus, the state 'A' represents a singlet ground state which is symbolized as So.

In 'B', one electron has been promoted to a higher energy level by absorption of photon, but spin state of the electron in the higher orbital remains same. Hence, it is also a singlet state but in excited condition. It is symbolized as $S1$ (first excited singlet state). But in 'C', the case is different; here, both the electrons have the spin in the same direction. Hence, the spin multiplicity is 3, and this state is called the triplet state. Let us elaborate this idea in some more details by considering an example of a molecule, say, acetaldehyde.
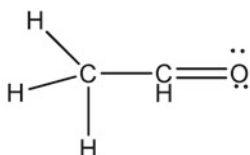
Here, there are three types of molecular orbitals: (i) σ—molecular orbital, (ii) Π—molecular orbital and (iii) n—(non-bonding) molecular orbital. We can draw a simple energy diagram as shown in Fig. 3.

Now, as shown in Fig. 3, many types of electronic transitions are possible upon absorption of light such as
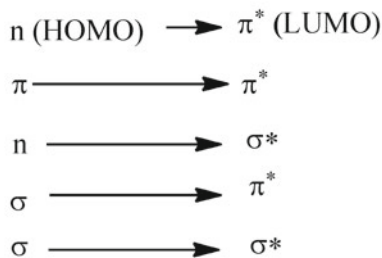
During the transition if the spin state of the promoted electron remains same, then the total spin quantum number $(S = \sum si)$ will also remain unchanged, for all paired up ground state, its value will be equal to zero, in this case, its spin multiplicity will be one, and accordingly, as discussed earlier, it should be termed as a singlet state. Since upon excitation, the spin state is also remaining same, and it is also said to be an excited state singlet. The ground state is designated as So, and the excited state involving lowest energy (n to π^*) is designated as $S1$. Similarly, (π to π^*) is $S2$ and so on. These types of transition are called singlet–singlet transition. It may happen that promoted electron has undergone a conversion process and the spin state has changed in such a way the two electrons now have parallel spin (Fig. 4).
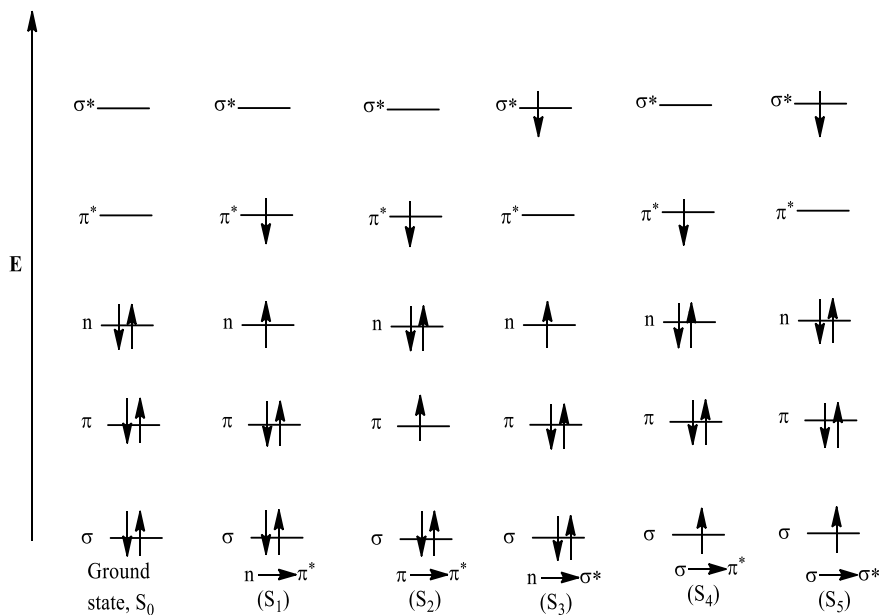
Not all n- and σ−electrons have been shown

Fig. 3 Various singlet states
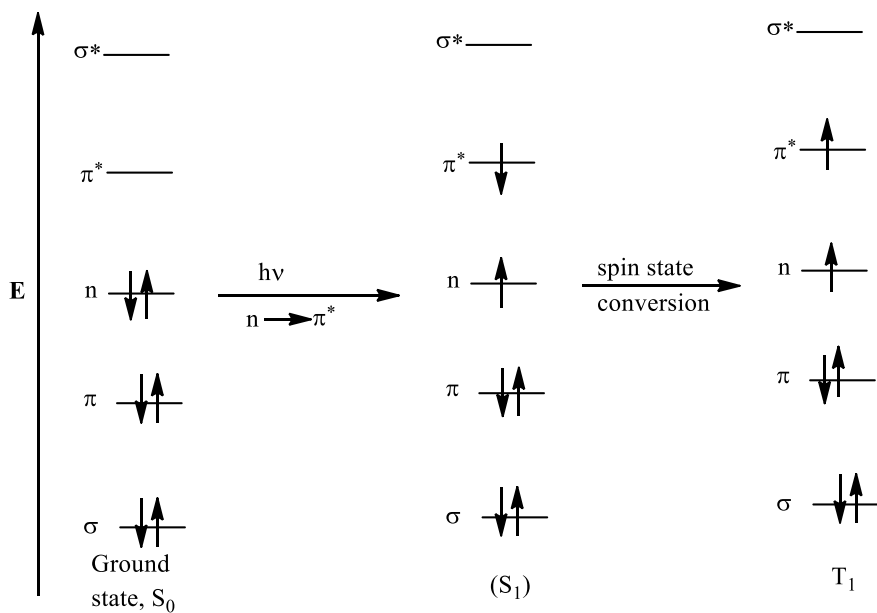
Fig. 4 Singlet–singlet transition and generation of triplet state

Since the spin multiplicity after the change of spin state is three, it is called a triplet state. Now, the triplet state associated with the $n \rightarrow \pi^*$ transition is designated as T1, $\pi \rightarrow \pi^*$ Is T_2 and so on. According to the Hund's rule, energy associated with the triplet state is lower than the singlet state having same electronic configuration, i.e., $T_1 < S_1$, $T_2 < S_2$, $T_3 < S_3$ and so on.

4 Jablonski Diagram: An Interpretation of Fluorescence

In a molecule, each electronic state is associated with a number of vibrational states. According to Boltzmann distribution, the majority of the molecules remains in the lowest vibrational state (zero vibrational level) of the ground state. After absorption of the light, many interesting phenomena may occur which can be beautifully shown by Jablonski diagram. Here, the lowest vibrational energy level of any electronic state is shown by a thick line, and other vibrational energy levels are shown by thin lines. Fluorescence phenomenon can easily be interpreted with the help of Jablonski diagram (Fig. 5) [11].
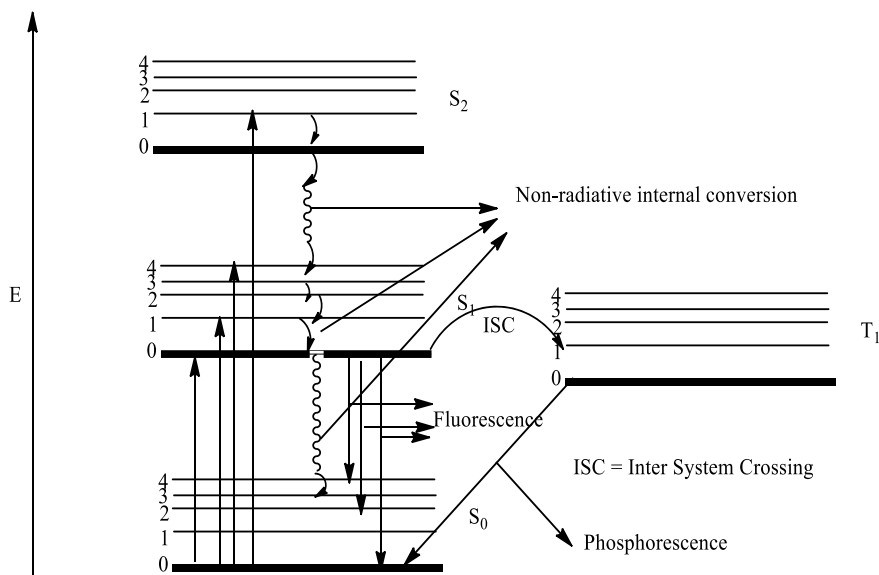
Fig. 5 Jablonski diagram

5   Conclusion

This mini-review on fluorescence spectroscopy may be helpful to (i) those who are the beginners in this field, (ii) those who belong to different discipline other than physics, chemistry but curious about the term 'fluorescence', (iii) those who are graduating and post-graduating in engineering and interested in biomedical imaging processes.

References

1. O'Haver, T.C.: Development of luminescence spectrometry as an analytical tool. J. Chem. Edu. **55**(7), 423–428 (1978)
2. Brewster, D.: Trans. Roy. Soc. Edinburgh. **12**, 538–545 (1834)
3. Herschel, J.F.W.: Formula No. I. On a case of superficial colour presented by a homogeneous liquid internally colourless. Phil. Trans. **135**, 143–145 (1845)
4. Stokes, G.G.: On the change of refrangibility of light. Phil. Trans. **142**, 463–562 (1852)
5. Valeur, B.: Molecular Fluorescence: Principles and Applications. First Edition. Wiley-VCH, New York (2001)
6. Renz, M.: Fluorescence Microscopy—A Historical and Technical Perspective. Cytometry Part A. **83A**, 767–779 (2013) and the references cited therein
7. Davenport, D., Nicol, J.A.C.: Luminescence in hydromedusae. Proc. R. Soc., London B. **144**, 399–411 (1955)
8. Shimomura, O., Johnson, F.H., Saiga, Y.: Extraction, purification and properties of Aequorin, a bioluminescent protein from the luminous hydromedusan. Aequorea. J. Cell. Comp. Physiol. **59**, 223–239 (1962)
9. Perrin, F.: Doctoral Thesis, Paris, Annales de Physique.**12**, 2252–2254 (1929)
10. Chalfie, M., Euskirchen, Y., Tu, G., Ward, W.W., Prasher, D.C.: Green fluorescent protein as a marker for gene expression. Science **263**, 802–805 (1994)
11. Jablonski, A.: Efficiency of anti-stokes fluorescence in dyes. Nature **131**, 839–840 (1933)

Smart and Integrated Garbage Management Application—A Step Towards IoT-Enabled Society

Kuntal Paul, Arpan Mukherjee, Debadrita Debnath, and Tiya Dey Malakar

Abstract The modern-day scientific technology is progressing very rapidly and so our society. The emergence of newer technologies and the growing affordability of integrated connectivity is reshaping our everyday life with the Internet of Things. And this inclination towards IoT is causing a paradigm shift in our day-to-day approach to modern society problems and their solutions. One of many burning problems of our society now is littering, even in the circumstances where sufficient garbage disposal measures are implemented. This is caused due to poorly maintained dustbin management system and irregular cleansing of the bins. This problem alone is resulting in lots of other issues, as well, which can sometimes cause harm to our social aesthetics. So, this paper is a proposal of an IoT-based smart and easy-to-implement-in-any-place solution, consisting of hardware, software, database and communication in between them, to optimize this problem with real-time analysis of data and responding to them accordingly. This smart garbage management system will fetch data from its hardware systems installed in the critical end-points and upload all the data received to the database which can be easily accessible to user (or customer) end. The data collected by each hardware will be checked against a threshold to send logical commands which dustbin is to be emptied and when—which will solve the unwanted littering problems caused due to unnoticed filling of bins.

Keywords Internet of things · Smart and integrated garbage monitoring application (SIGMA) · Wireless network · Sensor technology · Artificial intelligence

1 Introduction

The Internet of things (IoT) is composed of the interconnected network of physical "things" or objects, which are essentially embedded sensor-software system and other technologies purported to communicate with data between other similar systems over the Internet [1]. The rapid growth of IoT-based technology is fuelled by the growth

K. Paul · A. Mukherjee · D. Debnath · T. D. Malakar (✉)
Department of Electronics and Communication Engineering, RCC Institute of Information Technology, Kolkata, West Bengal, India

of VLSI [2] and embedded technologies, which caused the development of sensors, which are the essential receptors of an IoT network [3]. Besides this, the emergence of 5G connectivity and affordable 4G connectivity across the globe alongside the growing cloud and data storage services made this development possible [4]. But no technology is useful unless it solves the challenges of day-to-day needs. And IoT is the technology that can be used (and is being used as well) to solve many varieties of problems that the society today face. That is why it is the key player of today's smart cities program. And the smart waste management system is an essential part of this smart city and smart society schemes [5].

There have been many works in the field of smart waste management including technologies like ultrasonic sensing, temperature-humidity sensing, GPS tracking and GSM-based SMS query systems already, and many might be under development at the moment. Those works are enough efficient and primarily focus on monitored-and-recorded-based tracking of a total waste management that fits perfectly for large-scale cases like government municipal management. Also, these proposals are quite expensive systems and also demand large-scale cloud service because data collection is potentially of huge amount. And some cases, use of GSM module is an extra add-on, which can be easily eliminated by doing its job by the other way round [6–8].

Therefore, basically smart and integrated garbage management application, aka SIGMA, is a moderated, cost-effective and optimized version of all the works that had been done in the field of smart waste management that primarily focuses only on target problem of littering in any establishments having multiple footfalls each day. SIGMA is easily deployable and scalable system that makes an integrated smart garbage management within the institution.

But this proposed *Smart and Integrated Garbage Management Application (SIGMA)*, is a little different than the other Smart Waste Disposal systems. The SIGMA focuses particularly on the unwanted littering due to poor maintenance of garbage disposals that is often faced in institutions, schools, colleges, offices and in small apartment complexes/societies. In these circumstances, many of us noticed this problem that the dustbins get filled without getting noticed, and waste materials are found to be litter around the bins; sometimes, it is due to the poor maintenance management, sometimes due to irregular cleansing. This problem is essentially very evident where many people visit on everyday basis and garbage production is also huge, so it naturally becomes a tedious job for humans too. Even in case of an apartment society, multiple usage probability of different common space dustbins brings out the similar situation that is just mentioned in case of any institutional establishments [9].

In this paper, we have first discussed a few previous works in the same field, and then, the IoT architechture of SIGMA is described. In the next part, the hardware and software overview of the system are explained along with deployment and results. We have also discussed a little about the future aspects of the system.

2 Related Works

The paper by Belal Chowdhury and Morshed Chowdhury on "RFID-based Real-time Smart Waste Management System" proposes to incorporate RFID tags along with the dustbins for bringing down the cost [6].

The paper by Norfadzlia Mohd Yusof, Aiman Zakwan Jidin and Muhammad Izzat Rahim on "SMART GARBAGE MANAGEMENT SYSTEM" proposes a system containing ultrasonic sensors interfaced with NodeMCU development board. The data related to garbage levels are stored in a database, and it is analysed and displayed on two different dashboards that can be accessed by the admin and clients [10].

The paper by Shyamala S. C, Kunjan Sindhe, Vishwanth Muddy and Chitra C. N. on "Smart waste management system" is about implementing waste management using ultrasonic sensor, ATmega328 microcontroller. Here, they have used GSM/GPRS sim900A module for sending message to a centralized authority who would take action further for cleaning filled dustbins. Also, moisture sensor is used for measuring moisture level of waste in dustbin [11].

The paper by Ms. Akhila Joseph, Ms. Anjali, Ms. Suhaila B. M and Mr. Mahesh B. L. on "SMART GARBAGE MANAGEMENT SYSTEM" presented a garbage management system along with Android application. They used ultrasonic sensor not only for measuring garbage level, but also for making "smart bins" which will open automatically if someone comes near to dustbin to throw garbage (servomotor is also required). Here, ESP8266 is used as microcontroller [12].

Another paper by S. Vinoth Kumar, T. Senthil Kumaran, A. Krishna Kumar and Mahantesh Mathapati on "Smart Garbage Monitoring and Clearance System using Internet of Things." presents a garbage management system where they have also used a LCD display outside the dustbin to show relevant message, and also, a LED is used to indicate whether the dustbin is empty or not. Here, they have proposed to make an Android application where authorized member can login with corresponding username and password. After login, the user can browse through Google Map to see the position of dustbin [13].

The paper by Jetendra Joshi, Joshitha Reddy, Praneeth Reddy, Akshay Agarwal, Rahul Agarwal, Amrit Bagga and Abhinandan Bhargava on "Cloud Computing Based Smart Garbage Monitoring System" presents a solution about the SmartBin as a network of dustbins which implements the idea of IoT with wireless sensor networks. This concept is based on the stack-based front end approach of integrating wireless sensor network with the cloud computing. Here, they have applied decision forest regression (machine learning technique) to the sensor data leveraged by the system to gain useful insights so that the efficiency of the garbage monitoring can be improved [14].

3   Proposed Work

In this paper, we propose a smart waste management system with use of microcontroller (ESP8266), ultrasonic sensor and IFTTT logic platform API. In the system, we consider number of dustbins, each having US sensor and ESP8266 incorporated with them to form a IoT network, where the controllers interact with a database to store the data regarding waste level in the bins and a Website to show the status of multiple dustbins. The authorized workers can keep tracking the dustbin status there; in case they are filled up, a SMS will be sent to the authorized numbers as an alert (with the unique number of dustbin which is filled up). On the basis of that, further steps can be taken to clean the dustbin manually.

This system is cost-effective, flexible and user-friendly. Many papers have been published which propose the system of sending alert SMS to be done by GSM/GPRS module [8, 10, 11, 13, 15–17]. We have used IFTTT logic platform API to send SMS to worker instead of using GSM module to reduce cost and hardware complexity. Also, we have addressed the idea of waterproof casing for microcontroller module and ultrasonic sensor for protection from any type of fluid spillage.

Here, we have discussed waste management considering a school, college, office or small apartment, but our motive is to spread a general awareness towards the society on waste management, further making bigger steps to make a clean and healthy society.

3.1   IoT Architechture

The SIGMA has the following implementations as its part of architecture:

Sensor-Connected Nodes: This is installed in every dustbins of the institutional establishment. This includes necessary sensors and a microcontroller unit, where the data sensed by the sensors will be fetched and analysed and then will be sent to the IoT Gateway used with it.

IoT Gateway: The IoT Gateway is the most essential part as without it the system will not even be able to connect over the Internet. In this case, the institutional router is used as the gateway.

Cloud Server: The whole system is connected to a cloud-based relational database management system, where all the ambient data will be uploaded and stored. Also, an API is used for the trigger response system needed to inform concerned authority when to empty the bins.

Software Application: The system uses an Web-based monitoring application which will monitor all the condition of all the bins, also, there is a system provided to the Web application that can be used to trigger manually which dustbin is full and can send response, and this is done so as to tackle the situation if somehow the microcontroller

unit fails to trigger response. All the responses will be sent over SMS to the concerned person or authority who is in charge of cleansing.

3.2 Hardware

This proposed application SIGMA is composed of multiple sensors, microcontroller unit, an WiFi LAN connectivity and a central PC-based monitoring unit.

Microcontoller Unit: The smart and integrated garbage management application uses ESP 32 board which uses the ESP32-D0WDQ6 chip (Tensilica Xtensa LX6 microprocessor). The board is powered by 5 V supply, either at V_{in} pin or the USB input port, via on-board voltage regulator. Its CPU frequencies are up to 240 MHz. It includes 4 MB SPI flash memory and 520 KB of SRAM and varieties of interfacing options [18] (Fig. 1).

Ultrasonic Sensors: The ultrasonic sensor module used is the common HC-SR04. This sensor measures the volume level of the bins and reports the microcontroller unit with the data it received. It has an ultrasonic transmitter and receiver pair, a control unit based on op-amp and a maximum power supply of 5 V. A digitally high-level voltage pulse is applied with a pulse-width of 10 μs at the input pin which triggers 40 kHz ultrasonic signal that is transmitted, hit an object and returns. The time elapsed between transmission and detection of the reflected signal is used to calculate the level of the volume because the volume here is considered rather as the depth of the dustbin. The range of this module is 400 cm±3 mm with an angle of coverage of 15° [19]. For protection of the sensor from any kind of fluid spillage, waterproof casing is incorporated (Fig. 2).

Smoke Sensor: Here, MQ2 Grove Gas sensor is used, which can detect the presence of any combustible gas and smoke. The sensor uses Tin(IV) oxide which has lower conductivity in lean air. If targeted gas is present, then its conductivity increases. It has large measurement range of 300–10,000 ppm, high sensitivity and fast response time. The sensitivity can be varied with adjusting on-board potentiometer. This sensor is used to detect presence of combustible gas or smoke, and if the detection is positive,

Fig. 1 ESP32 dev board
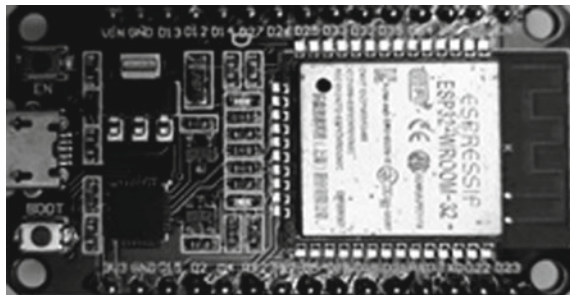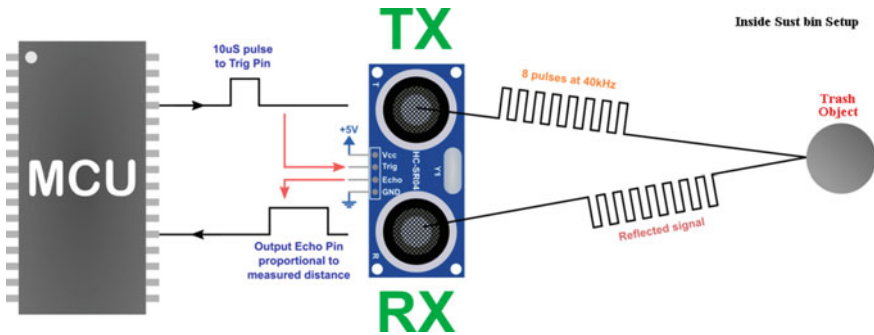
Fig. 2 HCSR04 working principle

then it immediately sends a software interrupt that will trigger SMS to immediately empty the corresponding bins, to avoid any potential dangers [20].

Cloud Server and API: For SIGMA, MySQL-based RDBMS server is used to store the data, and the Web application is purported to be hosted with the official domain of the institution's Web server. But for demonstration of the system, this is hosted at Webhostapp Platform. For SMS management, the IFTTT logic platform API is used which serves as a very simple IF-THIS-THEN-THAT logic [21].

3.3 Software Part

The ESP32 development board is programmed using the integrated development environment (Arduino IDE). The firmware flashed to the board has the main segments: (a) real-time measurement of the sensor data, (b) unconditional uploading of data on cloud, and (c) triggering the SMS API if trigger conditions are met. The algorithm of the whole system is described below as a flow chart (Fig. 3).

When the system is powered ON, all the sensors are initialized, and WLAN connection is established. The microcontroller keeps getting data from all the sensors, if at any moment, there is a positive detection from the gas sensor, it triggers SMS as an interrupt service routine, else the system keeps on tracking and uploading dustbin level to database. If the dustbin gets filled, an SMS fired to corresponding worker indicating which bin is to be cleaned.

4 Deployment and Results

The implementation of the system is shown with the following block diagram (Fig. 4):
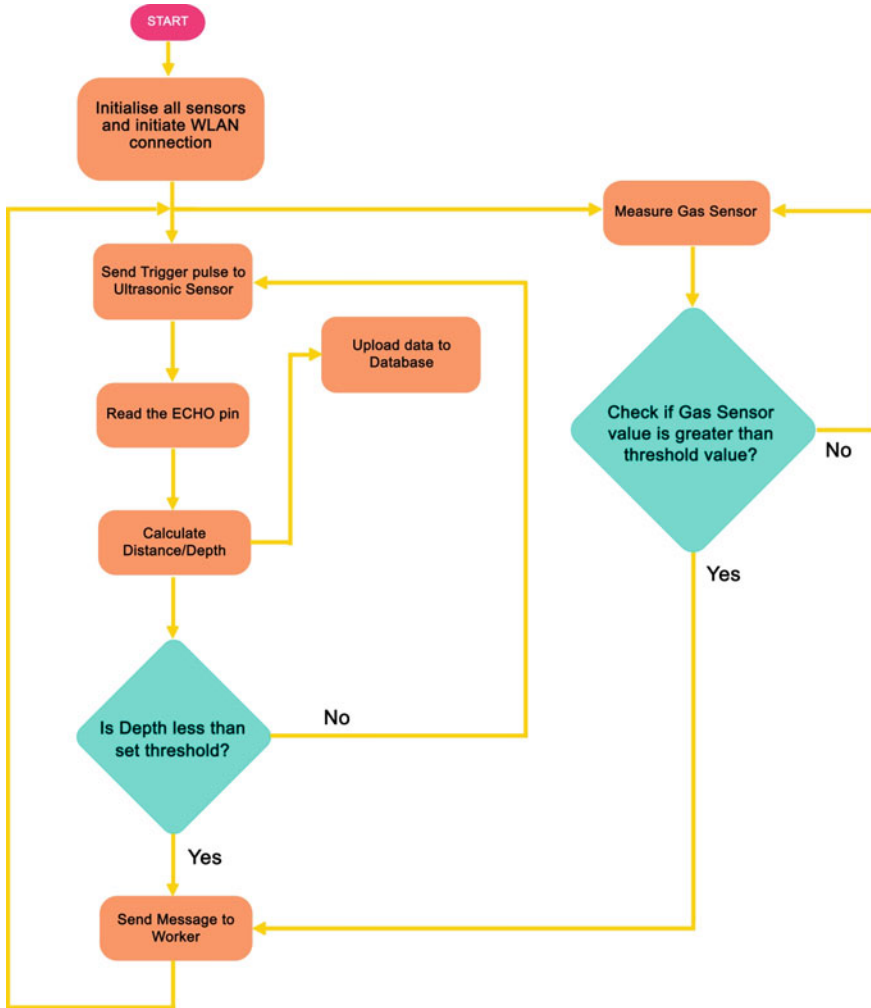
Fig. 3 Flow chart

So here, multiple dustbins will have tags assigned to them to identify them uniquely. The response SMS sent to the worker upon a trigger will contain that tag identity. In case of any emergency operation, with the help of the monitoring Web application, manually the SMS can be sent to the worker to empty particular dustbin(s).

In the following, there are some snaps showing the Web monitoring application and SMS responses received (Fig. 5).
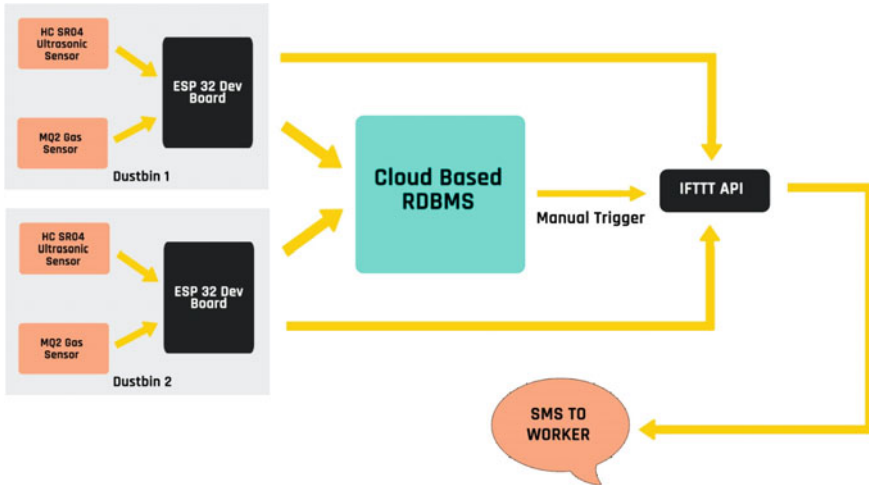
Fig. 4 Deployment model
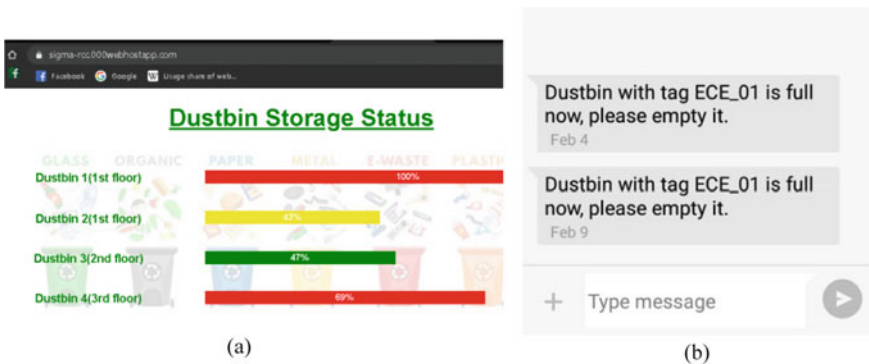
Fig. 5 Snapshots from **a** Web application, **b** SMS alert received

5 Future Aspects

The SIGMA proposes an optimum solution to its target problem. Also, it is the optimized form of all available similar approaches. But it has some potential future development, rather, upgradation possibilities. The main advantage of the system is that it collects huge amount of data unconditionally, and this means that the database contains all the information of dustbin fill-up percentage with corresponding time stamps. As the storage of data is unconditional, data will be stored even when the system has triggered to empty dustbins.

So with this, the data pattern can be found in two variants—when and how frequently a particular dustbin gets filled in a day and "usually" when the worker is

called to perform cleansing operation for a particular dustbin. These understanding of data can be analysed using proper machine learning regression models, and a part or branch of the SIGMA system can be trained against the dataset to predict which dustbin might get filled at a particular instant of time, more precisely at which instant of time—this machine learning approach will further optimize the system and make it smart and intelligent garbage management application [22].

6   Conclusion

The successful deployment of IoT-based smart and integrated garbage management application (SIGMA) is presented with this paper. With major steps taken towards the nationwide development of smart cities and Digital India, it is evident to start taking initiatives from the very basic level, and this work targets that field. Almost everyone has faced this situation either in schools, colleges or in some institutional establishments. The approach of SIGMA is efficient to tackle the littering problem caused by poor or irregular management of garbage and will help to maintain cleanliness and hygiene. Also, as this particular work is conceptualized on the basis of a particular area of problem, thus, it is well optimized and cost-effective and simplified to be used by everyone, because technology never discriminates. This system is very relevant for small state-funded schools and institutions and colleges where implementation of already available similar systems is expensive to be fit due to presence of multiple hardware elements. It is able to solve the problem effectively with minimal amount of hardware components, and the bandwidth requirement is very low. The system has been tested in real-time situation and proved to be successful. For power supply, the system can be connected to a plug point with a charger adapter, or it can be coupled with power banks or even solar power which will increase overall reliability and cost-effectiveness.

References

1. Tsiatsis, V., Karnouskos, S., Holler, J., Boyle, D., Mulligan, C.: Internet of Things, vol. **2**
2. Sepranos, D., Wolf, M.: Challenges and opportunities in VLSI IoT devices and systems. In: IEEE Design and Test, vol. 36, pp. 24–30 (2019)
3. Shenghe, S.: Development trend of modern sensor. J. Electron. Measur. Instrum. **1**, 1–10 (2009)
4. Ejaz, W., et al.: Internet of things (IoT) in 5G wireless communications. In: IEEE Access, vol. 4, pp. 10310–10314 (2016)
5. Kim, T.H., Ramos, C., Mohammed, S.: Smart city and IoT. In: Future Generation Computer Systems, vol 76, pp. 159–162 (2017)
6. Chowdhury, B., Chowdhury, M.: RFID-based real-time smart waste management system. In: IEEE, Australasian Telecommunication Networks and Applications Conference, Christchurch, New Zealand, pp. 175–180 (2007)

7. Folianto, F., Low, Y. S., Yeow, W. L.: Smartbin: smart waste management system. In: IEEE Tenth International Conference on Intelligent Sensors, Sensor Networks and Information Processing (ISSNIP), pp. 1–2 (2015)
8. Thakker, S., Narayanamoorthi, R.: Smart and wireless waste management. In: International Conference on Innovations in Information, Embedded and Communication Systems (ICIIECS), pp. 1–4 (2015)
9. Hing, C.K., Gunggut, H.: Maintaining urban cleanliness: a new model. In: Procedia-Social and Behavioral Sciences, vol 50, pp. 950–958 (2012)
10. Yusof, N., Jidin, A., Rahim, M.: Smart garbage monitoring system for waste management. In: MATEC Web of Conferences, vol 97 (2017)
11. Shyamala S., Sindhe, K., Muddy, V., Chitra C.: Smart waste management system. IJSDR **1**(9):223–230 (2016)
12. Joseph, A., Anjali, S.B.M., Mahesh, B.L.: Smart garbage management system. Int. Res. J. Eng. Technol. (IRJET) **07**(06):2017–2021 (2020)
13. Vinoth, S., Senthil, T., Krishna, A., Mathapati, M.: Smart garbage monitoring and clearance system using internet of things. In: 2017 IEEE International Conference on Smart Technologies and Management for Computing, Communication, Controls, Energy and Materials (ICSTM), pp. 184–189 (2017)
14. Joshi, J., Reddy, J., Reddy, P., Agarwal, A., Agarwal, R., Bagga, A., Bhargava, A.: Cloud computing based smart garbage monitoring system, In: IEEE, 2016 3rd International Conference on Electronic Design (ICED), pp. 70–75 (2016)
15. Nikam, R.: IOT based smart garbage system. In: JETIR January 2019, vol 6, Issue 1, pp. 227–230 (2019)
16. Bhor, V., Morajkar, P., Gurav, M., Pandya, D.: Smart garbage management system. Int. J. Eng. Res. Technol. (IJERT) **4**(03):1117–1120 (2015)
17. Sohag, M., Podder, A.: Smart garbage management system for a sustainable urban life: An IoT based application. In: Internet of Things, vol. 11 (2020)
18. ESP32-WROOM-32 Datasheet, v.3.1, Espressif Systems © 2021
19. HC-SR04 Ultrasonic sensor manual, May 2013
20. MQ2 smoke sensor manual, March 2015
21. If This Then That, IFTTT Services Platform
22. Acharya, M., Armaan, A., Antony, A.: A comparison of regression models for prediction of graduate admissions. In: IEEE, 2019 International Conference on Computational Intelligence in Data Science (ICCIDS), pp. 1–5 (2019)

Significance of Fractional Fuzzy Inference System in Intelligent Relaying Mechanism

Soumyadeep Samonto, **Debnarayan Khatua**, **Sagarika Pal**, **Samarjit Kar**, and **Arif Ahmed Sekh**

Abstract Application of typical Mamdani fuzzy inference system (MFIS) in power system protection has become a common artifact nowadays. The proposed articles on fuzzy logic-based protection initially designed the controller using typical MFIS. The related works mostly followed centroid defuzzification method. It is observed that the defuzzification method generally ensures multiple outputs. This output generally introduces lagging in detecting faults most of the time. It also delays the overall system by extending the coordination time as well. In this paper, a new FIS is discussed in terms of intelligent relaying benefits. Inverted pendulum model is considered to explain the novelty of granular differentiability. Initially, the proposed method is faster as due to its single solution-based features. This granular differentiability is considered as defuzzification method and incorporated into a new kind of fuzzy controller. The controller deals with a novel fuzzy inference system usually known as fractional fuzzy inference system. This fractional fuzzy inference system is found to respond 100% accurate and faster indeed as compared to Mamdani fuzzy inference system and reported.

Keywords Fault · Granular differentiability · Membership function · Protection · Restriking · TRIP

S. Samonto (✉) · D. Khatua
Global Institute of Science and Technology, Haldia, West Bengal, India

S. Kar
National Institute of Technology Durgapur, Durgapur, West Bengal, India

S. Pal
National Institute of Technical Teachers' Training and Research Kolkata, Kolkata, West Bengal, India

A. A. Sekh
UiT The Arctic University of Norway, Tromso, Norway

1   General Introduction

Manifestation of intelligent relaying in protection area nowadays has become the most discussed topics in power and energy sector. Various researches have been carried out on electrical protection by presenting artificial insights as discussed in [1–4]. Electrical fault is an unequal state that happens in any power system network. If impedance falls to exceptionally low value, then only fault appears within the system. The actual term to be associated with impedance is basically known as dynamic resistance. Hence, as impedance changes contrarily with the current, at the same time, current will increase to a most extreme surge or crest figure. In this regard, it is very much essential to find current error which implies the real value that overshoots the reference optimal current due to the colossal spikes obtained as due to impedance falls.

In this range of investigation, intelligent breaker is designed to control distributed load against over current fault as well as low voltage issues. Considering both input as well as output to the fuzzy inference system, an unique method is proposed by taking trapezoidal membership function but for only 230 V LT systems [5]. Monitoring of the fault location and operating time of a relay using intelligent algorithms like adaptive neural network and fuzzy logics was performed [6]. Reports on control methods of moving contact followed for fuzzy-based VCB were developed after thorough investigation. The method was incorporated by following adaptive fuzzy controlling algorithm [7]. Considering voltage and current as the inputs to the fuzzy engine, an algorithm was developed for quick intelligent relaying and presented prior [8]. Momesso et al. [9] have recognized a comparative study in terms of coordination time between both fuzzy and non-fuzzy-based time and current graded relaying mechanism. Other approaches also considered to create a unique kind of intelligent relaying [1, 2].

2   Literature Review and Origin of FFIS

Introducing fuzzy differential equations in any nonlinear system provokes the incorporation of nonlinear fuzzy dynamic systems (FDS) as a working model. The differential equations are considered FDE if ambiguity is present in the variable, parameters, or boundary conditions. Earlier, FDS was considered in diverse fields like [10], economics [11], fractional calculus [12], control theory [13], etc. After that, [11, 14] have discussed on production inventory system by introducing the fuzzy optimal control model. They have contributed the structure and explained how to control the model using a generalized Hukuhara differenciability in a FDS. A special kind of FDE solution strategy has been used as the name of the quasi-level-wise system based on the "e" and "g" operators [11]. Moreover, researchers [15] have proposed a new era of fuzzy derivatives known as granular derivatives based on granular differences using the functionality of horizontal MF.

Among the discussed articles, few of them have been displayed by considering current as well as voltage as two inputs to the FIS. Excluding fuzzy approach, digital signal processing (DSP) has been taken after to guarantee the dependable relay operation. Among discussed articles, one has approved the calculation utilizing Fourier investigation, but by improvising output membership function (MF) using Gaussian function and allotting it to the output segment of the FIS. Few papers included the MF as Gaussian for both input and output sections. Numerous discussed articles have displayed AI-based relaying along with the triangular MF as input. In the previous research work the major issue is with post defuzzification because of multiple solution-based output as defuzzification method followed is centroid and COG. All of the considered articles have proposed an approach to control load during fault location using typical Mamdani fuzzy inference system (MFIS). This actually creates problem while tripping with a multiple set of time frame for any specific range of fault intruded. No such algorithm is introduced to trip load instantly at any specific point connected to any feeder line.

In this paper, a novel fractional fuzzy inference system (FFIS) is discussed for intelligent relaying mechanism by introducing error and error rates of the current as input and Gaussian HMF as functional element to it. The objective of the FFIS-based intelligent relaying mechanism is to trip any load connected to a bus or feeder line more instantaneously and on a consistent basis. The yield planned here by taking both trapezoidal MF and triangular HMF. This whole plan is typified interior of an intelligent relay block and encouraged the same to a 440 V HT breaker for controlling a 440 V high tension (HT) system. A brief idea of fruitful yields of concerned intelligent approach is reported by taking an example of inverted pendulum with a brief justification. The actual novelty of this article is based on the importance of FFIS over MFIS in any intelligent relaying system for introducing fastest tripping mechanism in power system protection engineering.

This paper represents the following contributions: (1) Proposed an idea to think out of the box in implementing FFIS for intelligent relaying mechanism. (2) Presented the significance of FFIS over MFIS for intelligent relaying in brief. The entire paper organized the sections along with the fractional fuzzy inference system design, the significance of FFIS on intelligent relaying, and along with its proper application to develop one algorithm using the MATLAB environment as well. Finally, the main conclusion and discussions are discussed in Sect. 4.

3   Fractional Fuzzy Inference System Design

The process of concluding any un-encountered input is generally known as a fuzzy inference system (FIS) and plays a very significant role in designing a fuzzy system. The consequent parts of the rule base in any typical fuzzy inference system consist of fractional membership functions (MFs) is called fractional fuzzy inference system. The FFIS is considered as a kind of fuzzy if-then rule translation and known as

fractional translation rule. The FFIS has been proposed as a new era of fuzzy logic-based intelligent controller which can change the perception of outcome as compared to typical FIS in future [16].

The fractional fuzzy inference system (FFIS) is actually not yet included in any of the MATLAB version as GUI. A GUI tool is very reliable in implementing, which can be included directly in a simulation model like that of typical Mamdani or Sugeno fuzzy inference system. Rather here, it is possible to work with m files only. Though this m file has some certain attributes initially to be followed for simulating the FFIS based model, those are organized in Sects. 2.1, 2.2, 2.3 and 2.4.

4 Inputs to the Fractional Fuzzy Inference System

In this case, inputs to the FFIS are considered as separate files. Overall six separate m files are required to run one FLC based on FFIS during the fuzzification process. Two files are required for the inputs, one for the rules, one for aggregation, two for the horizontal membership functions including both α—cut and β—cut separately. The membership function $A \in E_1$ corresponding to a fractional horizontal MF whose fractional index is α^*_A is called the fractional MF and denoted by $\tilde{A}_{\alpha^*}$. The μ-level sets of the fractional MF $\tilde{A}_{\alpha^*}$ are discussed in [16] (Fig. 1).
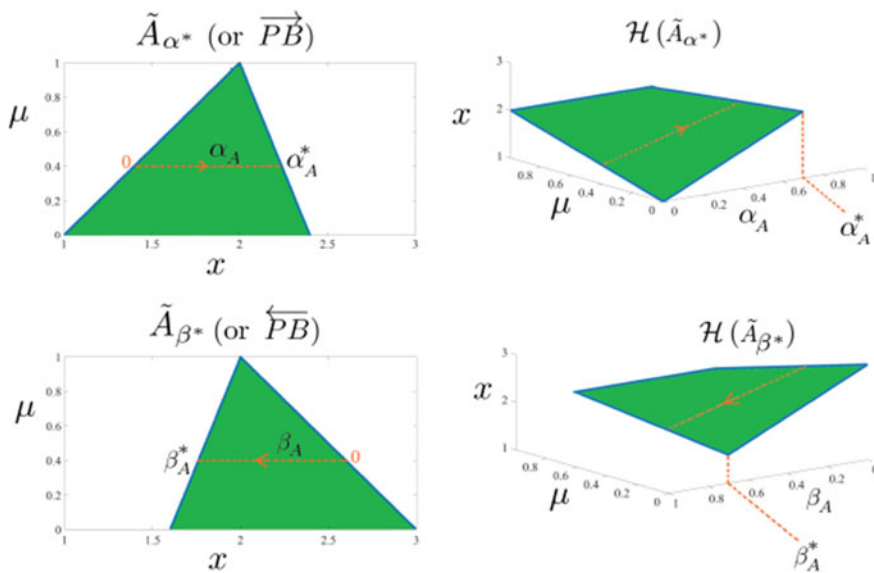
Fig. 1 Fractional concept incorporated on membership functions and horizontal membership functions [16]

Fig. 2 a Typical inference result of a fuzzy rule. **b** The fractional inference result of a fuzzy rule represented by a fractional horizontal MF [16]
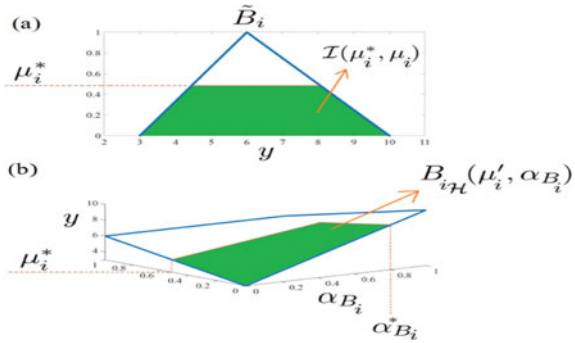
5 Development of Learning Rules for FFIS

Fractional fuzzy inference system is not much accustomed with the MATLAB environment, and thus, in-built tools are not easy to get. Thus, to introduce rules within the controller, it is necessary to develop rules using another separate m file. In this case also, rules are designed by implementing if-then concept.

6 Output of the Fractional Fuzzy Inference System

Output of the fuzzy engine is different as compared to the typical membership function followed in case of Mamdani FIS. In case of Mamdani, the concerned horizontal function usually ensures multiple ambiguous crisp outputs. Whereas, Fig. 2 explains the benefit of implementing horizontal membership function for FFIS over the multiple solution defuzzification-based MFIS.

In Fig. 2, the ith rule is clearly shown in two situations with respect to the antecedent and consequent parts, respectively. Figure 2a shows the ith rule inference result where the consequent part of the MF is cut by μ_i*. Again in Fig. 2b, it is shown that the consequent part of the horizontal MF is not only clipped by μ_i*, but also by the fractional index.

7 Defuzzification Process

The overall defuzzification process in case of a fractional fuzzy inference system depends on many definitions and proofs explained in [16]. In Fig. 1, it is very clear that since α^* fractional index cuts the MF from the bottom edges, defuzzification of fractional MF ensures an output that is directly proportional to the nature of the level of μ^* in all respect. This indicates that both are decreasing accordingly. It is also observed that since fractional membership function is cut by β^* from the top
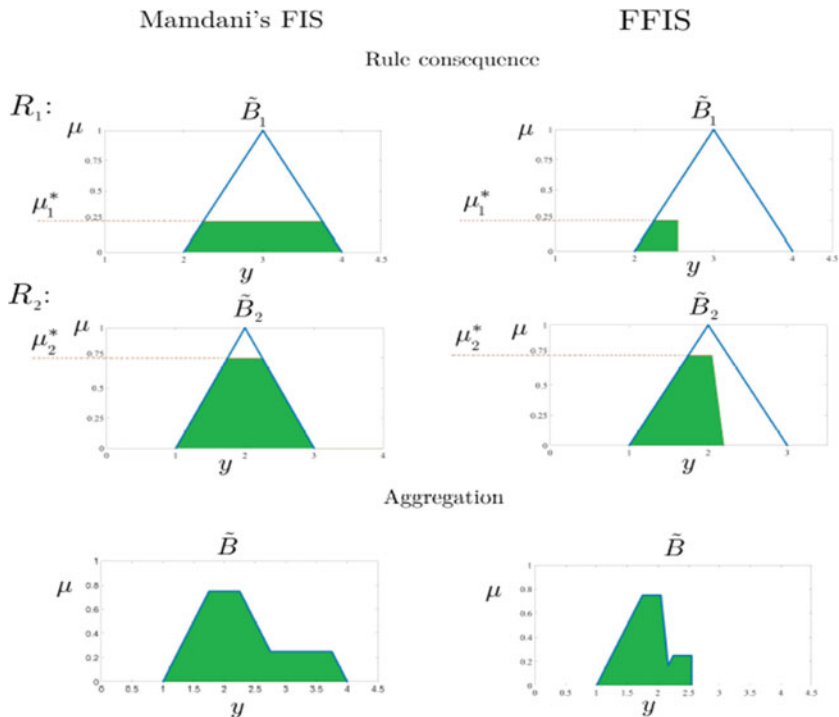
Fig. 3 Comparative analysis in terms of Mamdani FIS and fractional FIS defuzzification outcome is presented based on rule consequences and aggregation [16]

edges, the nature of the crisp output is inversely proportional to the level of μ^*, which means that output increases if the level of μ^* decreases. From Fig. 3, it is clear that the output MF of the FFIS is a fraction of the MFs belongs to Mamdani's FIS. The output of the FFIS coincides along with the output of Mamdani's FIS till the fractional indices consider the integer number as unity, i.e., $\alpha^*_{\tilde{B}_i} = 1$. So, here in this case due to these fractional indices, FFIS ensures a better defuzzified output as compared to MFIS with more improved ambiguous output as shown in Fig. 3, especially the aggregation portion.

8   Benefits of Implementing FFIS in Intelligent Relaying

In the case of the relaying mechanism, the most vital factor that ensures the best performance is the coordination time. Since this research is still an ongoing process and comparative case studies by considering typical Mamdani fuzzy inference system and fractional fuzzy inference system is not possible to present in this chapter. An
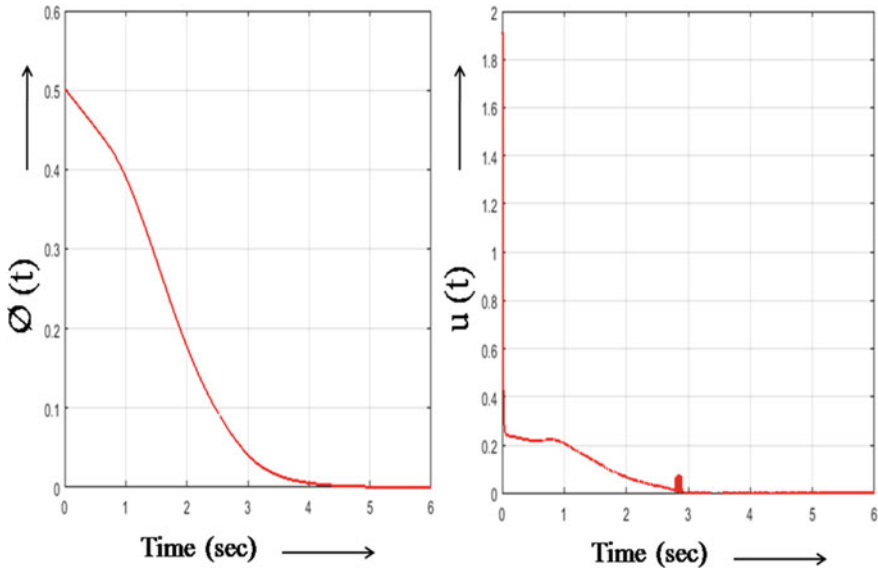
Fig. 4 Control signal generated by FFIS and angle trajectory of inverted pendulum

alternative study is considered for establishing the efficiency of the concerned technique and discussed here in this paper. This can be easily explained by taking an example of inverted pendulum model as discussed in [16]. In Fig. 4, if the plot between $u(t)$ versus time is considered, then it is very clear that a red-colored mark near to 3 s coordinate is obtained with an exact solution comprises single output. This ambiguous output from fuzzy engine ensures the plot between $\emptyset(t)$ versus time with a very stable controlled trajectory angle. The comparative study has been carried out in [16], using MFIS and Larsen FIS. This stable control ensures a better transient time and far improved indeed.

Now in case of any re-striking complex wave generates during any electrical fault, the novelty of fractional fuzzy inference system automatically improves the overall coordination time by reducing transient period and sub transient period as well. Hence, it will take lesser time to achieve a stable error and therefore assist the breaker to trip the overall system with a very fast operation based on highly improved coordination time.

The practical significance of this FFIS-based intelligent relaying system is to improvise delay in the fuzzy-based intelligent relaying. It will be a big finding to the way for having one solution to get rid of catastrophic fault actually in power system protection engineering. Sometimes, it is also very much necessary to save the aging factors of any equipment in case of multiple restriking voltages due to unstable supply system or might be something very big. Looking to the future science, it might be possible to think of incorporating protection devices against lighting strike after few decades from now onwards.

9 Conclusion and Discussion

In this paper, it is clearly observed and discussed regarding the benefits of FFIS over MFIS in the case of intelligent relaying mechanism. Nowadays, it is very true that in relaying mechanism due to incorporation of AI it is very difficult to control the coordination time due to some delay in the system. That is why implication of granular-based FFIS has been discussed and summarized as follows:

1. In this article, the application of novel concept proposed in [16] has been discussed in terms of its significance in intelligent relaying based on [17, 18].
2. The fractional fuzzy inference system helps in reducing the transient time of symmetrical waveforms and thus trip the system much faster as compared to other typical fuzzy engine.
3. In case of designing any intelligent relaying mechanism using FFIS, what are the steps to be followed to achieve the successful result has been discussed in this article.

References

1. Lee, S.J., Liu, C.C.: Intelligent approach to coordination identification in distance relaying. In: Proceedings of International Conference on Intelligent System Application to Power Systems, pp. 62–67. IEEE (1996)
2. Li, K., Lai, L., David, A.: Stand alone intelligent digital distance relay. IEEE Trans. Power Syst. **15**(1), 137–142 (2000)
3. Samonto, S., Pal, S., Banerjee, S.: FIS incorporated microcontroller based MCB. In: 2016 International Conference on Intelligent Control Power and Instrumentation (ICICPI), pp. 132–136. IEEE (2016)
4. Liu, Z., Duan, X., Liao, M., Zou, J., Ge, G., Lv, G.: Investigation on information monitoring technology for intelligent vacuum circuit breaker. In: 2016 27th International Symposium on Discharges and Electrical Insulation in Vacuum (ISDEIV), vol. 2, pp. 1–4. IEEE (2016)
5. Mandal, S.K., Pal, S., Samonto, S.: Distributed load control using flc based mcb. In: 2015 IEEE International Conference on Electrical, Computer and Communication Technologies (ICECCT), pp. 1–7. IEEE (2015)
6. Kezunovic, M.: Use of intelligent techniques for analysis of faults and protective relay operations. In: 2007 IEEE Power Engineering Society General Meeting, pp. 1–3. IEEE (2007)
7. Li, T.H., Fang, C.E., Li, W., Zhou, L.l.: Investigation on controlling techniques of moving contact behaviors for vacuum circuit breaker based on fuzzy control. In: 2010 Asia-Pacific Power and Energy Engineering Conference, pp. 1–4. IEEE (2010)
8. Panda, G., Mishra, R.: Fast intelligent relaying using fuzzy logic technique. In: Proceedings of IEEE International Conference on Industrial Technology 2000 (IEEE Cat. No. 00TH8482), vol. 2, pp. 159–163. IEEE (2000)

9. Momesso, A.E., Bernardes, W.M.S., Asada, E.N.: Fuzzy adaptive setting for time-current-voltage based over current relays in distribution systems. Int. J. Electr. Power Energy Syst. **108**, 135–144 (2019)
10. Najariyan, M., Farahi, M.H., Alavian, M.: Optimal control of HIV infection by using fuzzy dynamical systems. J. Math. Comput. Sci. **2**(4), 639–649 (2011)
11. Khatua, D., De, A., Maity, K., Kar, S.: Use of "e" and "g" operators to a fuzzy production inventory control model for substitute items. RAIRO-Oper. Res. **53**(2), 473–486 (2019)
12. Mazandarani, M., Najariyan, M.: Differentiability of type-2 fuzzy number-valued functions. Commun. Nonlinear Sci. Numer. Simul. **19**(3), 710–725 (2014)
13. Long, H.V., Son, N.T.K., Tam, H.T.T.: The solvability of fuzzy fractional partial differential equations under caputo gh-differentiability. Fuzzy Sets Syst. **309**, 35–63 (2017)
14. Najariyan, M., Farahi, M.H.: A new approach for solving a class of fuzzy optimal control systems under generalized hukuhara differentiability. J. Franklin Inst. **352**(5), 1836–1849 (2015)
15. Mazandarani, M., Pariz, N., Kamyad, A.V.: Granular differentiability of fuzzy-number-valued functions. IEEE Trans. Fuzzy Syst. **26**(1), 310–323 (2018)
16. Mehran, M., Xiu, L.: Fractional fuzzy inference system: the new generation of fuzzy inference system. IEEE Access. **8**, 126066–126082 (2020)
17. Landowski, M.: Method with horizontal fuzzy numbers for solving real fuzzy linear systems. Soft Comput. **23**(12), 3921–3933 (2019)
18. Samonto, S., Kar, S., Pal, S., Sekh, A.A., Castillo, O., Park, G.K.: Best fit membership function for designing fuzzy logic controller aided intelligent overcurrent fault protection scheme. Int. Trans. Electr. Energy Syst. **31**(5), p.e12875 (2021)
19. Mazandarani, M., Pariz, N., Kamyad, A.V.: Granular differentiability of fuzzy-number-valued functions. IEEE Trans. Fuzzy Syst. **26**(1), 310–323 (2018)

Sudden Cardiac Arrest Detection Based on Temporal Features of ECG Using Support Vector Machine Classifier

Prakash Banerjee, Saptak Bhattacherjee, and Kousik Dasgupta

Abstract Sudden cardiac arrest (SCA) is caused due to malfunctioning in heart rhythm, and the patient needs to be hospitalized as early as possible just after the onset of SCA; otherwise, it can lead to the death of the patient. Therefore, detection of SCA with a very high accuracy and within a very short time after the onset of symptoms is very crucial for patient survival. Several approaches for detection of SCA have been made using temporal and morphological variations in the electrocardiogram (ECG). However, the existing methods suffer from low accuracy or involve long-term monitoring of ECG. Therefore, in the present work, an intelligent algorithm to detect SCA based on the extraction of temporal features like RR interval and the QT interval from ECG and subsequently classifying them using support vector machine (SVM) has been proposed. Experimental evaluation of the proposed method on five SCA and five normal subjects demonstrates a high classification accuracy of 100% which proves the superiority of the proposed algorithm as an effective method for detection of SCA.

Keywords ECG · Sudden cardiac arrest · RR interval · QT interval

1   Introduction

Sudden cardiac arrest (SCA) causes unexpected death caused by abnormality of heart rhythm which occurs when the electrical system of heart starts malfunctioning and the heart beat suddenly becomes very irregular and as well as dangerously fast

P. Banerjee (✉)
Department of Electrical and Electronics Engineering, University of Engineering and Management, Kolkata, India

S. Bhattacherjee
School of Mechatronics and Robotics, Indian Institute of Engineering Science and Technology, Shibpur, Howrah, India

K. Dasgupta
Department of Computer Science and Engineering, Kalyani Government Engineering College, Kalyani, India

[1]. SCA is a serious health problem around the world, and in United States alone, there are more than 300,000 causalities per year due to this disease [2]. If SCA occurs outside of a hospital environment, patients have a mere 1–2% survival rate compared to patients in a hospital [3]. There are different signs and symptoms associated with SCA like chest discomfort, shortness of breath, weakness, palpitation, and rapid or irregular heartbeats. Severe arrhythmia correlate with SCA, but basically, ventricular tachyarrhythmia is the most common arrhythmia that leads to SCA [4]. Although a large number of researches have been carried out on the detection of SCA based on the ECG parameters, researchers are still facing problem to develop a method to detect SCA within a very short time and with a very high accuracy. In one research, Vijaya et al. demonstrated an approach to detect sudden cardiac arrest using the Pan–Tomkins algorithm [5]. In another research work, Murukesan et al. proposed a methodology for detection of SCA based on the variation in heart rate using machine learning approach, with a maximum accuracy of 96.34% [6]. In another research work, an approach for identification of SCA using modified wavelet transform has been studied [7]. In the present work, an algorithm to detect and classify the ECG of SCA patient from normal subject based on temporal features of ECG has been proposed. Here, first the ECGs of SCA patients and normal subjects were obtained from Physionet Sudden Cardiac Death Database (SDDB) and Fantasia Database, respectively. Next, the signals were preprocessed using a third-order Butterworth bandpass filter for removal of noise and artifacts present in the signals. After, that the ECG complexes were detected, and the statistical features like standard deviation of RR interval and standard deviation of QT interval were estimated from the SCA patient's and normal subject's ECG and were fed into a support vector machine classifier for classification. Experimental results demonstrated a high classification accuracy of 100% proving the efficiency of the proposed method over existing approaches. The block diagram of the proposed work has been shown in Fig. 1.

The paper is organized in the following manner: First the characteristics of ECG signal for SCA patients in comparison with normal subjects have been shown. Next, the signal preprocessing techniques have been discussed. After, the feature extraction technique is shown followed by the classification results. Finally, the conclusion of the proposed work has been drawn out along with the future scope.

1.1 Characteristics of ECG Signal for SCA Patient

Electrocardiogram (ECG) is the graphical recording of electrical activity of the heart, and it is also one of the most important physiological parameter that provides information regarding the functioning of the heart. Generally, modern ECG machines record ECG in the frequency range of 0.5–100 Hz and amplitude of 1–10 mV [8]. The ECG signal of a normal person over a single cardiac cycle contains a P wave, a QRS complex, and a T wave. However, it has been observed that the ECG signal of a SCA patient is often characterized by the absence of QRS complex over single or
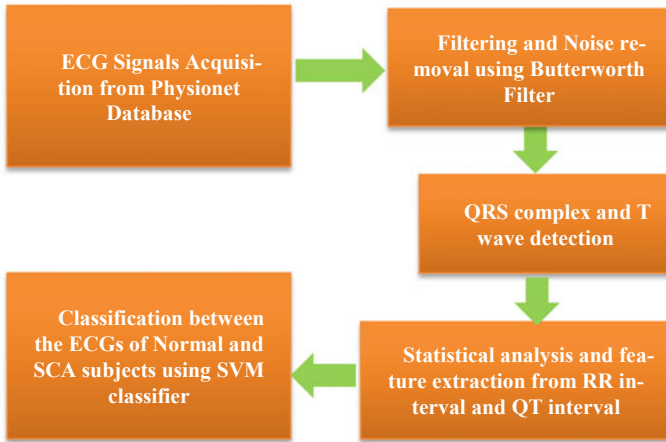
Fig. 1 Block diagram of the proposed work
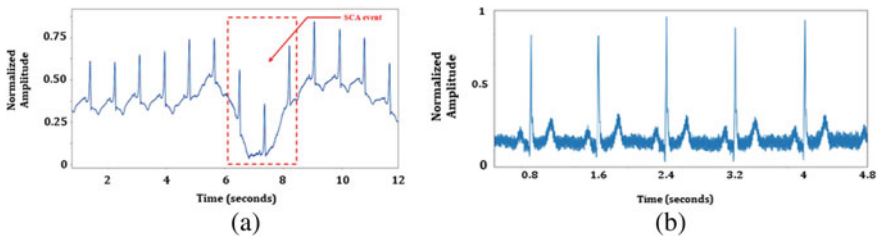
Fig. 2 Raw ECG signal of **a** SCA patient and **b** normal subject

multiple cardiac cycles, abrupt change in heart rate variability, and increased baseline wander [9]. A typical ECG signal of a SCA patient and a normal subject has been shown in Fig. 2 which highlights the occurrence of an SCA event.

2   Method

2.1   Preprocessing

The ECG signals of both SCA and normal subjects were obtained from MIT-BIH, Physionet database [10]. The ECG signals of five SCA patients and five normal subjects were selected from sudden cardiac death database (SDDB) and Fantasia database, respectively. In the present work, 5 min long ECG signals of SCA patients just after the occurrence of an SCA event have been considered for analysis and classification. Also, ECG signals of 5 min interval are extracted from Fantasia database
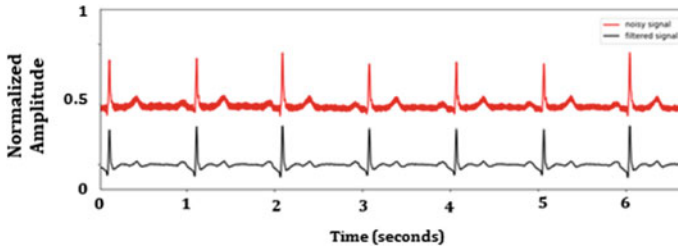
Fig. 3 ECG waveform before and after preprocessing

and considered for analysis. The ECG signals thus obtained for both normal and SCA subjects were then filtered using a third-order bandpass Butterworth filter with a pass band of 4–45 Hz for removal of base line wander and power line interference [11]. Next, the signals were appropriately scaled and normalized before feature extraction. The ECG signal before and after preprocessing has been shown in Fig. 3 which depicts the effect of using the bandpass filter by successfully removing the baseline wandering and high frequency noises present in the raw ECG waveform.

2.2 Feature Extraction

The QRS complex in the filtered waveform was then extracted using Pan–Tomkins algorithm [12] from which the RR interval and QT intervals were extracted. The implementation of Pan–Tomkins algorithm for detecting the peaks in the ECG waveform has been illustrated in Fig. 4 which shows the efficiency of the technique in detecting the ECG R peaks.

Statistical features like standard deviation of RR interval and standard deviation of QT interval were then estimated and fed into the support vector machine (SVM) classifier for further classification. Mathematically, standard deviation of RR interval
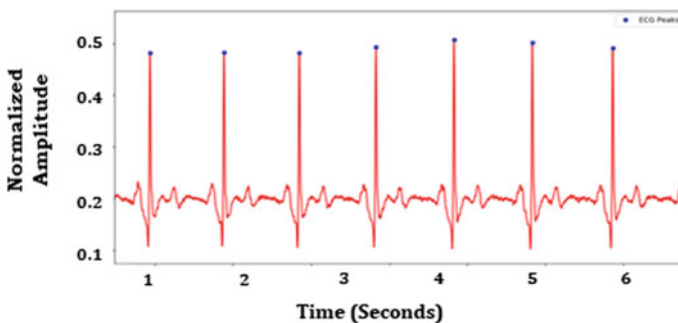
Fig. 4 Detected peaks in ECG waveform
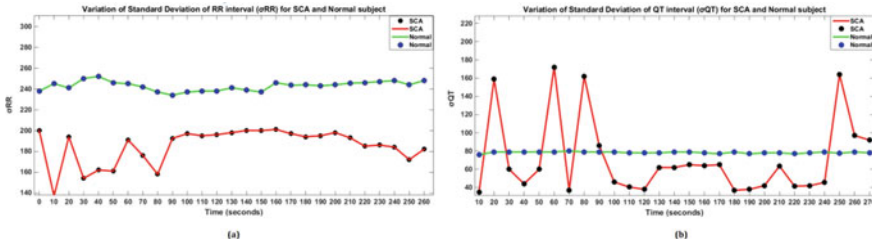
Fig. 5 Variation of standard deviation of **a** RR interval **b** QT interval for SCA and normal subject

and standard deviation of QT interval can be expressed as

$$\sigma_{R-R} = \sqrt{\frac{1}{n-1} \sum_{i}^{n} (x - \overline{x})^2} \tag{1}$$

$$\sigma_{Q-T} = \sqrt{\frac{1}{n-1} \sum_{i}^{n} (x - \overline{x})^2} \tag{2}$$

where x denotes the sample value, n denotes the number of samples, and $\overline{x}$ denotes the mean value of the samples.

The RR interval extracted from both the ECGs of SCA patient and normal subjects which have been shown in Fig. 5. From the figure, it can be noted the deviation in RR interval is much greater for an SCA patient than the normal subject. Hence, the standard deviation of RR interval (σ_{RR}) has been chosen as one of the distinguishing features for classification, and the standard deviation of QT interval (σ_{QT}) has been chosen as another feature. The variation of extracted features for SCA and normal subject has been shown in Fig. 5.

From Fig. 5, it is evident that the standard deviation of RR interval and standard deviation of QT interval for SCA subject significantly differs from the standard deviation of RR interval and standard deviation of QT interval of normal subject. Hence, these two features have been used for classifying the ECGs of SCA subject from the normal ones to obtain high classification accuracy.

2.3 Classification

In this proposed method, after extraction of standard deviation of RR interval and standard deviation QT interval from both SCA patient and normal subjects were fed into SVM classifier, in order to discriminate between the normal and SCA subject's ECG. For differentiating between SCA patients and normal subject, the
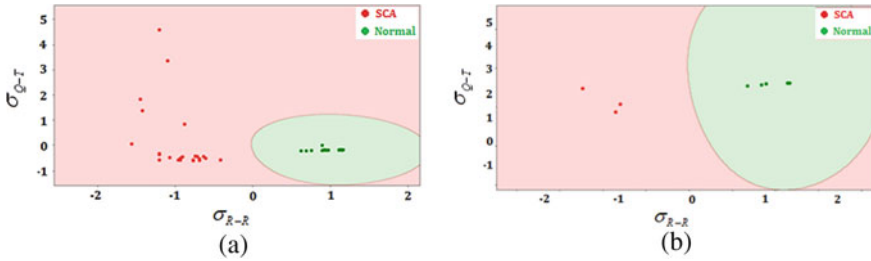
Fig. 6 SVM classification for **a** training set **b** testing set

optimum hyperplane [13] was estimated by training the classifier with a portion of the downloaded dataset.

During both training and testing, the dataset for normal and SCA subject was found to be nonlinearly separable. Hence, the SVM classifier with the larger margin has been used in the present study. Also, in this work, the RBF kernel is used for creating the hyperplane [14]. The output of the kernel is dependent on Euclidean distance of x_j from x_i, where x_j and x_i are support vectors and testing data points. The kernel equation in terms x_j and x_i can be expressed as

$$k(x_i, x_j) = \exp\left(\frac{\|x_i - x_j\|}{2\sigma^2}\right) \qquad (3)$$

To discriminate between the ECG of SCA patient and normal subject, the extracted features are fed into the support vector machine (SVM) classifier. The result of classification for training set and testing set has been shown in Fig. 6a, b.

The classification accuracy obtained for both training and testing was found to be 100%. This high classification accuracy is primarily due to the use of distinguishing features like standard deviation of RR interval and standard deviation of QT interval [15]. A comparative study of the present work with the existing studies has been shown in Table 1.

3 Conclusion

In this paper, an efficient algorithm for detection of SCA based on statistical features of ECG parameters has been proposed. The standard deviation of RR interval and the standard deviation of QT interval have been used as significant features for classification between the ECG of SCA patient and normal subject. Experimental result indicates that the proposed methodology can be used as an effective technique for SCA detection with high accuracy. In future, the proposed algorithm will be applied on a larger patient database. Moreover, the present algorithm will be modified

Table 1 Comparative study of the present work with the existing literatures

References	Method	Accuracy (%)
Murukesan et al. [6]	Using optimal heart rate variability features	96.4
Mirhoseini et al. [16]	Twenty-two features of HRV signal are applied with tree bagger classification algorithm on SVM classifier	83.2
Rohila and Sharma [17]	Using comparative analysis of heart rate variability (HRV) in between normal subjects and coronary artery disease and heart failure	91.7
Shi et al. [18]	Using empirical mode decomposition (EEMD)-based entropy features	96.1
Acharya et al. [19]	SCA is detected using nonlinear features	92.1
Present Work	Applying temporal features like as RR interval and QT interval	100

to predict an SCA event prior to its actual occurrence using deep learning techniques so that sufficient time can be obtained for patient hospitalization.

References

1. Caesarendra, W., Ismail, R., Kurniawan, D., Karwiky, G., Ahmad, C.: Sudden cardiac death predictor based on spatial QRS-T angle feature and support vector machine case study for cardiac disease detection in Indonesia. In: 2016 IEEE EMBS Conference on Biomedical Engineering and Sciences (IECBES), pp. 186–192. IEEE (2016)
2. Vanitha, L., Suresh, G., JenefarSheela, C.: Sudden cardiac death prediction system using hybrid classifier. In: 2014 International Conference on Electronics and Communication Systems (ICECS), pp. 1–5. IEEE (2014)
3. Devi, R., Tyagi, H.K., Kumar, D.: Early stage prediction of sudden cardiac death. In: 2017 International Conference on Wireless Communications, Signal Processing and Networking (WiSPNET). pp. 2005–2008. IEEE (2017)
4. Riasi, A., Mohebbi, M.: Prediction of ventricular tachycardia using morphological features of ECG signal. In: 2015 The International Symposium on Artificial Intelligence and Signal Processing (AISP), pp. 170–175. IEEE (2015)
5. Vijjaya, V., Rao, K.K., Sahrudai, P.: Identification of sudden cardiac arrest using the pan-tompkins algorithm. In: 2012 UKSim 14th International Conference on Computer Modeling and Simulation, pp. 97–100. IEEE (2012)
6. Murukesan, L., Murugappan, M., Iqbal, M., Saravanan, K.: Machine learning approach for sudden cardiac arrest prediction based on optimal heart rate variability features. J. Med. Imag. Health Inf. **4**(4), 521–532 (2014)
7. Ahmed, S.H., Razzaq, N., Zaidi, T.: Identification of sudden cardiac arrest (SCA) using modified wavelet transform. In: Proceedings of the 2nd International Conference on Biomedical Signal and Image Processing, pp. 7–12 (2017)
8. Tereshchenko, L.G., Josephson, M.E.: Frequency content and characteristics of ventricular conduction. J. Electro. Cardiol. **48**(6), 933–937 (2015)
9. Gacek, A.: An introduction to ECG signal processing and analysis. In: ECG Signal Processing, Classification and Interpretation, pp. 21–46. Springer (2012)
10. https://archive.physionet.org/cgi-bin/atm/ATM

11. Limaye, H., Deshmukh, V.: ECG noise sources and various noise removal techniques: a survey. Int. J. Appl. Innov. Eng. Manag. **5**(2), 86–92 (2016)
12. binti Ahmad, I.L., binti Mohamed, M., binti Ab Ghani, N.A.: Development of a concept demonstrator for QRS complex detection using combined algorithms. In: 2012 IEEE-EMBS Conference on Biomedical Engineering and Sciences, pp. 689–693. IEEE (2012)
13. Han, J., Kamber, M., Pei, J.: Data mining concepts and techniques third edition. Morgan Kaufmann Series Data Manag. Syst. **5**(4), 83–124 (2011)
14. He, R., Wang, K., Li, Q., Yuan, Y., Zhao, N., Liu, Y., Zhang, H.: A novel method for the detection of r-peaks in ECG based on k-nearest neighbors and particle swarm optimization. EURASIP J. Adv. Sign. Process. **2017**(1), 1–14 (2017)
15. Banerjee, P.: Machine learning-based rapid prediction of sudden cardiac death (SCD) using precise statistical features of heart rate variability for single lead ECG signal. Green Computing and Predictive Analytics for Healthcare, 1st edn., pp. 65–80. Chapman and Hall/CRC (2020)
16. Mirhoseini, S.R., JahedMotlagh, M.R., Pooyan, M.: Improve accuracy of early detection sudden cardiac deaths (SCD) using decision forest and SVM. In: IEEE Proceedings on International Conference on Robotics and Artificial Intelligence (ICRAI2016), Los Angeles, USA, pp. 1–5 (2016)
17. Rohila, A., Sharma, A.: Detection of sudden cardiac death by a comparative study of heart rate variability in normal and abnormal heart conditions. Biocybernetics Biomed. Eng. **40**(3), 1140–1154 (2020)
18. Shi, M., He, H., Geng, W., Wu, R., Zhan, C., Jin, Y., Zhu, F., Ren, S., Shen, B.: Early detection of sudden cardiac death by using ensemble empirical mode decomposition-based entropy and classical linear features from heart rate variability Signals. Front. Physiol. **11** (2020)
19. Acharya, U.R., Fujita, H., Sudarshan, V.K., Sree, V.S., Eugene, L.W.J., Ghista, D.N., San Tan, R.: An integrated index for detection of sudden cardiac death using Discrete wavelet transform and nonlinear features. Knowl. Based Syst. **83**, 149–158 (2015)

Depiction and Operation of Water Generator from Atmospheric Air

Sundeep Siddula, N. Sunder, S. K. Sadik, P. Tejasri, and K. Vinith

Abstract An atmospheric water generator (AWG) is a device which extracts water from the humidity of air. This method aimed to condense water vapor which is present in the atmospheric air by cooling with the help of thermoelectric cooler devices. These devices are operated by the principle of Peltier effect. In this device, it has two sides, when DC electric current passed through this device, it pumps the heat from one side to another side, by this, one side become hotter while other side become cooler. One heat sink is attached to the hot body of the device, so it remains at ambient temperature. At cool side temperature goes below room temperature, so water particles present in the atmospheric air will lies over the cold body of thermoelectric cooler devices. Then, the output of these devices produces the water slowly. This device is designed for the purpose of availability of pure drinking water. When it is constructed in huge size by using large TEC modules and installed at the see shores of our country, drinking water problem can be reduced up to some limit considerably.

Keywords TEC modules · Cooling fans · Heat sink · LM35 temperature sensor · PLC16F676 microcontroller · LCD display

1 Introduction

The concept of atmospheric water generator with the Peltier effect is done in this paper. This method develops water condensation system based on the thermoelectric cooler. This whole system consists TEC devices, heat sink, DC fans, temperature sensor, and LCD display. In this device, it generates the heat at very high temperature over it is hot side. To maintain the temperature between the hot and cold body sides, heat must be removed. This job will done by the heat sink which is connected with the hot surface of the TEC devices [1].

S. Siddula (✉) · N. Sunder · S. K. Sadik · P. Tejasri · K. Vinith
Vignana Bharathi Institute of Technology, Hyderabad, India

By using this TEC device, we can easily convert the atmospheric moisture into drinking water, the principle of this device is latent heat to convert molecules of water vapor into water droplets [2–7].

The technology of this TEC device can be used in refrigeration applications. In this method, two TEC devices are choose because of TEC devices are very small in size. When compared to the normal refrigerators, TEC devices are solid state devices. This is the one of the primary advantage. This TEC devices have long life, no moving parts, simple in design, and small in size [6].

This TEC devices consume the 3 A of current and 10 V DC supply. So somewhat huge rating power supply is required due this reaction, solar panels are not used. The meaning of Peltier cooler is an effect, where the heat is got when an electric current given to the junction between two materials. This power is known as Peltier effect.

Coming to the temperature sensor, it is LM35 temperature sensor and it will senses the temperature of the cold surface of the device and it is given to the microcontroller (16F676) and it is inbuilt with the ADC converter. It converts analog input to the digital output, it is given to the LCD (16 * 2) display, which is connected to the microcontroller. By this, we can measure the temperature of the cold side of the TEC device [8].

By this methodology, the pure drinking water as outlet. This process utilizes the humidity present in the air which is present in surrounding of the device. With the free of fuel cost, it can be generate the usable water depends upon requirement. If we want to increase the water generation, there should be a need of large size of TEC devices. That is totally depends upon the requirement of water [9].

2   Peltier Effect

When the two dissimilar conductors are joined together, then electricity is passes through them, at one junction will be losses heat and other will gains the heat, this phenomenon is known as Peltier effect. This is just like thermocouples at one junction is cooler, then, the other one is hotter. This is also known as thermoelectric effect. The thermoelectric cooler (TEC) works on this principle.

Thermoelectric effect is process of conversation of DC voltage to the temperature difference. This Peltier effect was discovered by the Jean Charles Peltier in 1834. Due to changes in the continuous current in junction, which leads to temperature difference between those junctions.

Two semiconductors, namely *n*-type and *p*-type, both, are used because it is need to have different electron densities. These semiconductors are thermally connected in parallel to each other but electrically in series and then joined through thermally conducting plate on both sides. Whenever the supply is given to the ends of the two semiconductors it will operate. There is an effect of temperature difference whenever DC current flows across the junction of the semiconductors.

On one side cooling plate absorbs heat, it is moved to other side where the heat sink is attached. These thermoelectric coolers are abbreviated as TECs are connected
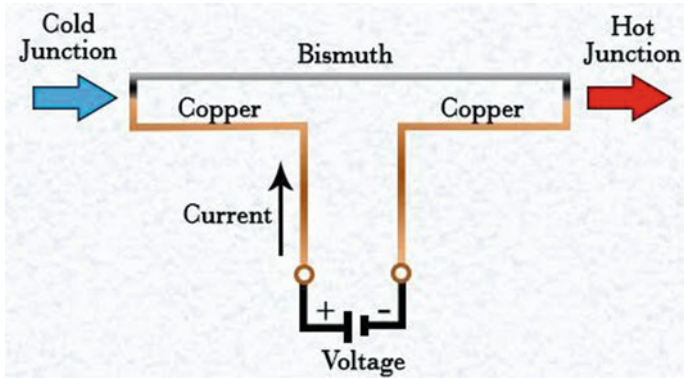
Fig. 1 Peltier effect

side by side like sandwiched type between the two ceramic plates. Then, the overall unit is proportional to the number of TECs in it Fig. 1 represents the Peltier effect.

3 Thermoelectric Cooler

In this paper, the major component is TEC modules. This thermoelectric cooler (TEC) module has two sides. Whenever the electric current passes through this module, due to the Peltier effect, one side will become hotter and other will be cooler. At cooler side, the water molecules are formed because of condensation (Fig. 2).
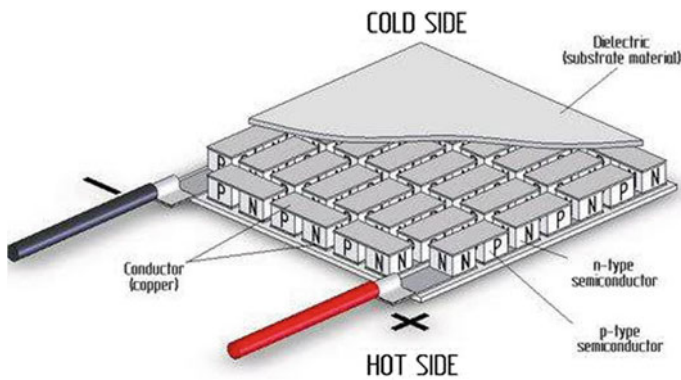
Fig. 2 Thermoelectric cooler module

4 Working Principle of an Atmospheric Water Generator

This paper works on the principle of Peltier effect. Whenever the current passes through Peltier cooler or thermoelectric cooler at one side of the TEC module gets cooler and other gets hotter, to dissipate this heat, a fan (heat sink) is attached to hotter side of TEC module. Coming to cooler side to measure the temperature of cooler body, a LM35 temperature sensor is connected, this sensor output was given to microprocessor (PIC16F676) which is inbuilt with ADC. This microprocessor output was given to LCD (16 × 2) unit, as the sensor senses the temperature and displayed in LCD with the help of microprocessor. At cooler side of TEC module, the water molecules are formed because of condensation, it was just like whenever a items from refrigerator were kept outside, we observe water molecules around that item, this phenomenon is called condensation. It mainly consists of two circuits.

4.1 TEC Module Circuit

This is main circuit, in this first, the input of 230 V AC supply was step down to 12 V by stepdown transformer, then this 12 V AC was converted in to 12 DC with the help of rectifier, this 12 DC consists of ripples so to eliminate the ripples, it passes through filter capacitors. Finally, this pure DC was given to TEC module then it will be cooed one side and other will hotter, at cooled side, water molecules are formed. As the number of TEC module, circuit is increase the output and water quantity was also increases. In this project, we are using two TEC modules, the circuit diagram was shown in Fig. 3.
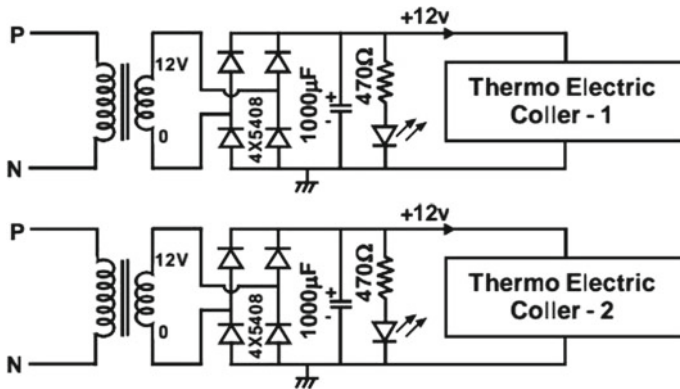
Fig. 3 Circuit diagram of TEC
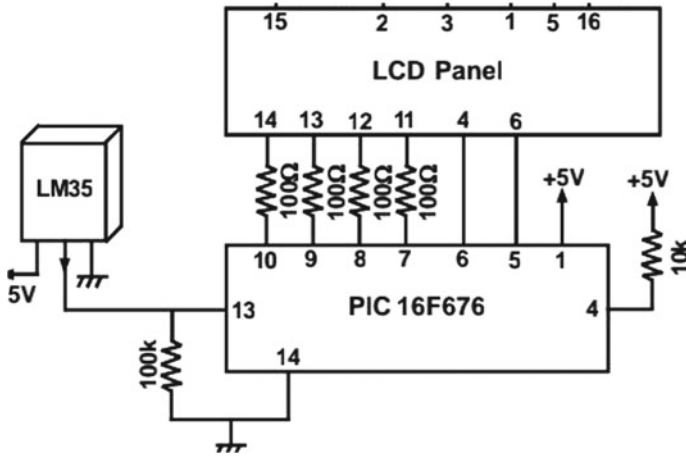
Fig. 4 Temperature monitoring circuit

4.2 Temperature Monitoring Circuit

In this circuit, the temperature of cooler side was monitor continuously by the LM35 temperature sensor. The input to this sensor was 5 V which is supplied by stepdown transformer (230/5V), this 5 V was rectified and given to sensor. This sensor senses the temperature and gives that information to the microprocessor, as this microprocessor (PIC 16F676) processes the data and displayed in the LCD display panel. This circuit helps to know at what temperature the water molecules are forming at cooler side of TEC module (Fig. 4).

Hardware model of atmospheric water generator shown in Fig. 5.

By the hardware implementation of this atmospheric water generator, water droplets are accumulated over the cold body of the device. That is shown in Fig. 6.

Hence, by this module, pure drinking water generated from air. Temperature of TEC module was displayed in the LCD.

The equipment which is used in this atmospheric water generator and is listed in Table 1.

5 Equipment of Atmospheric Water Generator

See Table 1.

6   Conclusion

This paper work is constructed by the model of atmospheric water generator and is
successfully designed and tested. Results are found. Since, it is prototype module and
experiment wise. This system is designed with two TEC modules, but for practical
time, many devices must be used depending upon requirement in fact, large size of
TEC modules are necessary to grab the water from air.

   A thermoelectric cooling system must be coupled with proper heat sink mecha-
nism, these are supposed to attach with hot body of TEC modules so the heat can
be generated by the device and absorbed effectively. If proper heat sink is not used,
then heat will pass through the cold body so that instant and continuous heat sucking
device must be used to maintain the continuous cooling effect. In this trail runs, water
droplets dropping from the cold body of the device.

Fig. 6 Formation of water drops

Table 1 Equipment details of atmospheric water generator

Equipment	Rating	Quantity
TEC modules	12 V, 3 A	2 No.
Transformers	230/12v 230/5v	2 No. 1 No.
PIC16F676 microprocessor	–	1 No.
LM35 temperature sensor	–	1 No.
16 × 2 LCD display	–	1 No.
Resistors	470 Ω 100 Ω 1 kΩ 100 kΩ 10 kΩ	3 No. 5 No. 2 No. 1 No. 1 No.
Capacitors	1000 μF	5 No.
DC fans	12 V	2 No.
Diodes	–	As per requirements
PCB board	–	1 No.

References

1. Tripathi, A., Tushar, S., Pal, S., Lodh, S., Tiwari, S., Desai, R.: Atmospheric water generator. Int. J. Enhanced Res. Sci. Technol. Eng. **5**(4), 69–72 (2019)
2. Yaseen, W.I.: Study of DC breakdown voltage in low pressure argon and nitrogen gases for several electrode gap. J. Al-Nahrain Univ. Sci. **20**(3), 87–90 (2017)
3. Lee, S., Hur, J.: Heterogeneous adsorption behavior of landfill leachate on granular activated carbon revealed by fluorescence excitation emission matrix (EEM)-parallel factor analysis (PARAFAC). Chemosphere **149**, 41–48 (2016)
4. Beaudoing, H., Rodell, M.: NASA/GSFC/HSL (2016), GLDAS Noah land surface model L4 monthly 1.0×1.0 degree V2.1, Greenbelt, Maryland, USA, Goddard Earth Sciences Data and Information Services Center (GES DISC), Accessed: August 3, 2017, https://doi.org/10.5067/LWTYSMP3VM5Z
5. Mei, J., Xia, X.: A reduced model for direct expansion air conditioning system and energy efficiency MPC control of indoor climate. In: 13th IEEE Int. Conf. Control Automat. Ohrid, Macedonia, pp. 624–629 (2017)
6. Tripathi, S., Tushar, S., Pal, S., Lodh, S., Tiwari, R.: Desai, "atmospheric water generator." Int. J. Enhanced Res. Sci. Technol. Eng. **5**(4), 69–72 (2016)
7. Ibrahim, M., BRIR, H., Khurasani, M.: Design and implementation of a smart multi-function air conditioner. In: International Conference on Computer, Control, Electrical, and Electronics Engineering (ICCCEEE), Khartoum, Sudan (2018)
8. Zeyad, M., Ghosh, S.: Designing of a low cost handy cooling system. In: 2018 4th International Conference on Electrical Engineering and Information & Communication Technology (iCEEiCT), pp. 557–560. IEEE (2018)
9. Matra, K.: Atmospheric non-thermal argon–oxygen plasma for sunflower seedling growth improvement. Japan. J. Appl. Phys. **57**(1S) (2017)

Statistical Approach to Develop a Suitable Algorithm for Prediction of Apnea Using Heart Rate Variability Rather Than Other Conventional Methods

Poulami Mandal, Pritam Saha, Kriti Kumari, Pallab Samanta, Olive Srimani, and Tarak Das

Abstract Apnea is cessation of breathing with no movement of inspiratory muscles. There is no suitable way to detect the sleep apnea; doctors take the help of expensive and complicated whole night polysomnography or electroencephalogram (EEG) to diagnose sleep apnea. Research work is going on to detect obstructive sleep apnea (OSA) using different approaches (Mendonca et al. in A review of obstructive sleep apnea detection approach 2–8, 2018) [1]. In present research work, researchers are using heart rate variability as the main tool to predict different kinds of biological disorder in human beings (Lado et al. in Detecting sleep apnea by heart rate variability analysis: assessing the validity of databases and algorithms 1–2, 2009) [2]. Our present research work has focused to detect OSA using heart rate variability analysis (HRV) as a diagnostic tool. HRV is the measure of variation in the time duration between consecutive heartbeats in milliseconds. The main objective of our work is to improve accuracy and help doctors for proper diagnosis of apnea disorder. There are many critical evaluation processes of apnea, but here we are dealing with the simplest apnea detection process by HRV analysis using KUBIOS. In the beginning, we have started to collect the normal and abnormal (i.e., person with OSA) electrocardiogram (ECG) data from different subjects (Court-Fortune et al. in Eur Respir J 22:937–942, 2003) [3]. Our work proposes a high accuracy method to predict OSA based on HRV analysis. A significant difference in changing is observed in various parameters associated with heart rate variability of normal and apnea patient's data, when different statistical parameters have been studied and compared. We have analyzed the heart rate variability using Kubios software (version 2.2). This work proposes few standard statistical parameters like root mean square of successive differences (RMSSD) or mean RR those will help to better prediction of OSA detection. Another parameters RR triangular index and TINN show a high difference in the range of results. Ultimately this work will instigate the research world that HRV can be used as a measuring tool for better prediction of OSA.

Keywords Apnea · Heart rate variability · Kubios · RMSSD · Mean RR · TINN

P. Mandal (✉) · P. Saha · K. Kumari · P. Samanta · O. Srimani · T. Das
Department of Biomedical Engineering, Netaji Subhash Engineering College, Kolkata, India

1 Introduction

Apnea is slowed or stopped breathing for a short span of time; basically, it is repeated or temporary pause of a breath. It has been observed that there is neither any change in lung volume, nor any movement of inspiratory muscles during apnea. Apnea may occur due to various reasons. It may be for drug-induced, mechanically induced or may be for neurological response like trauma. This repeated interruption in breathing makes it a potentially serious disorder. Obstructive sleep apnea is common, chronic, sleep-related breathing disorder [4] caused by intermittent airway obstruction which may have dangerous impact on daily living activities. Untreated OSA includes common symptoms like excessive daytime sleepiness, morning headache, nocturia, fatigue, lost productivity in workplace, and also motor vehicle accidents [5]. Different research work is going on to detect OSA using very simplest techniques not like EEG. In our work, we have focused on how OSA can be diagnosed using HRV analysis [6] as this may cause some changes in HRV.

Many diseases affect indirectly to the HRV [7], whereas pattern of effect is different in each case. It is already defined that HRV measures the variation in time interval between each heartbeat in milliseconds (ms). The pattern of variation is controlled by autonomic nervous system (ANS) [8] which is divided into two branches called sympathetic and parasympathetic. Parasympathetic nerve is considered as the non-invasive marker of ANS activity where sympathetic nervous system is responsible for the production of stress hormone which increases the heart's contraction rate and decreases the cardiac output (CO) and the heart rate variability. However, the parasympathetic branch increases HRV to restore stability. This natural exchange between the two systems allows the heart to a swift response in different circumstances. HRV is very sensitive indicator to predict any physical and psychological changes due to health hazards.

2 Methodology

2.1 Data Collection

In our present study, we have collected electrocardiogram (ECG) data from 50 healthy subjects (35 male, 15 female average age 22 ± 2) using three-lead ECG machines in lead II configuration and acquired the data in LabVIEW-2009 using NI DAQ 6008 with a fixed sampling rate. We have performed the preprocessing of raw data using MATLAB 8.3 R2014a. Our full work is on time domain analysis and is based on sampling rate of the signal. In the real situation as well as in this pandemic situation, it is quite difficult to collect apnea data ourselves using our own device. We have analyzed the signal which depends on sampling rate. There is no difference in any time domain analysis if we collect the apnea data even using different sources by keeping the perfect sampling rate. On the basis of that, we have collected apnea
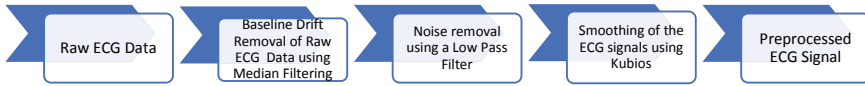
Fig. 1 Block diagram of preprocessing steps

patient's data from PhysioBank database [9] to increase the no of subject to get a reliable conclusion from the analysis. In this present analysis, as we have used two different sources of data, we have restricted our analysis only in time domain but not in frequency domain.

2.2 Preprocessing of ECG Data of Normal Patients

Figure 1 represents the basic steps to acquire ECG data using our own developed 3-lead ECG system.

We have used lead II configuration to acquire ECG data from our system as it lies close to the heart, and the data has been taken using NI DAQ USB-6008 in LabVIEW and then subtracted the baseline drift (low frequency omitted by using a median filtering). We made a low-pass filter to remove the unwanted signals from ECG. Then smoothing of the signal and peak detection is done by KUBIOS for HRV analysis, and different statistical time domain parameters are considered.

During this pandemic situation, as it is very difficult to collect real-time data from hospital, and in our work, we have taken data of 50 apnea patients from PhysioBank ATM and 50 real-time data from healthy person by using our own 3-lead ECG system. In the beginning of our B-tech project work and here we have considered the time domain statistical parameters only. The main statistical time domain parameters those we have been considered in our work are mean RR, STD RR or SDNN, STDRR, mean HR, SD HR, RMSSD, NN50, pNN50, RR triangular index, and TINN. The standard form of all considered parameters is given in (i)–(ix).

(i)   Mean RR

The average or mean interval between two heartbeats.

$$\text{Mean RR} = \frac{1}{N-1} \sum_{n=2}^{N} \text{RR}_n \tag{1}$$

Here RR_n stands for nth RR interval and N stands for the number of beats.

(ii)   STD RR or SDNN: Standard deviation of RR intervals or standard deviation of normal-to-normal RR intervals.

$$\text{STDRR} = \sqrt{\frac{1}{N-1} \sum_{n=2}^{N} (\text{RR}_n - \text{Mean RR})^2} \tag{2}$$

(iii)   Mean HR: We calculated heart rate from RR intervals. It is defined as no of RR intervals per minute. Mean HR stands for the mean heart rate.

$$\text{Mean HR} = \frac{60}{\text{Mean RR}} \qquad (3)$$

(iv)   SD HR: It is the standard deviation of the instantaneous heart rate values.
(v)   RMSSD: RMSSD stands for root mean square of successive differences between normal heartbeats.

$$\text{RMSSD} = \sqrt{\frac{1}{N-1} \sum_{n=2}^{N} (\text{RR}_{n+1} - \text{RR}_n)} \qquad (4)$$

(vi)   NN50: It is the number of successive intervals differing more than 50 ms or the corresponding relative amount.
(vii)   pNN50: It is the percentage of NN50 divided by the total number of RR intervals.

$$\text{pNN50} = \frac{\text{NN50}}{N-1} \times 100\% \qquad (5)$$

(viii) RR triangular index: It is the integral of density distribution divided by the maximum of the density distribution.

$$\text{RR triangular index} = \frac{\text{integral of RR interval histogram(area)}}{\text{height of the histogram}} \qquad (6)$$

(ix)   TINN: TINN stands for triangular interpolation of normal-to-normal intervals. It is the baseline width of the RR interval histogram.

3   Statistical Analysis

Kubios HRV analysis software [10] is used to calculate the time domain attributes [11] from the extracted time series data of the RR interval. We have extracted various heart rate variability parameters including mean RR interval (Mean RR), standard deviation of RR interval (STD RR), mean heart rate (Mean HR), standard deviation of the heart rate (SD HR), root mean square of successive difference between normal heartbeats (RMSSD), number of successive intervals differing more than 50 ms (NN50), percentage of NN50, RR triangular index, and triangular interpolation of normal-to-normal intervals (TINN).

   We extracted the data of both healthy and apnea patients individually to excel sheets from Kubios interface. To analyze the HRV parameters of both datasheets, we plotted them in time domain and different parameters have been presented by both

tabular and graphical form to distinguish between healthy and apnea patients and tried to establish a particular output to detect OSA disorder easily.

4 Results

Average measures	Mean RR (ms)	STD RR or SDNN (ms)	Mean HR (1/min)	SD HR (1/min)	RMSSD (ms)	NN50 (count)	pNN50 (%)	RR triangular index	TINN (ms)
Average of Apnea patients	953.402	156.81	72.25	15.19	182.41	15.44	27.93	5.82	64.7
Average of healthy subjects	707.35	55.06	86.46	6.29	45.70	68.56	19.69	16.95	283

Bar graph is used in our research work to compare things between different patients' data. We have plotted the average data of both apnea and healthy subjects using bar graph and done the comparisons among the discrete categories. The *X*-axis shows the specific parameters being compared, and the *Y*-axis represents the measured average value.

The plotted graphs are shown in Fig. 2.
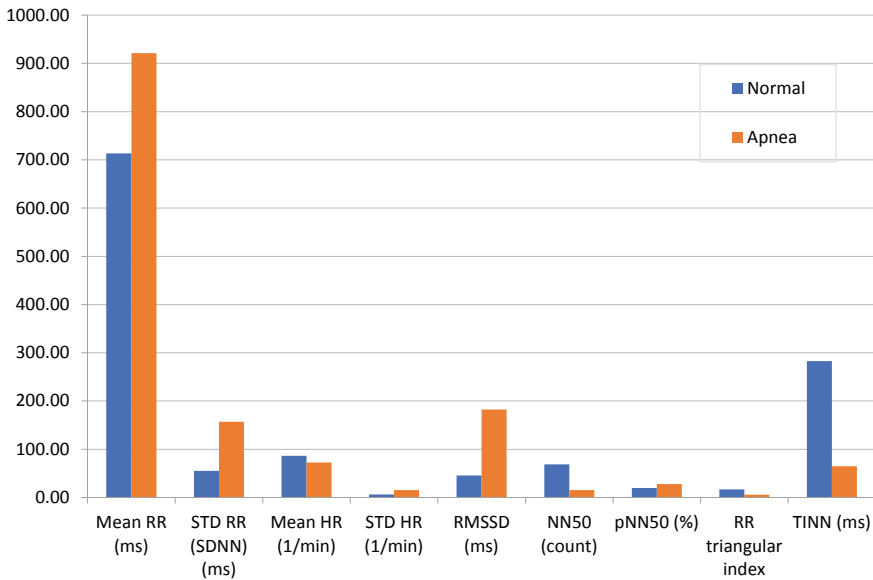
Fig. 2 Statistical analysis parameters

From the bar graph, it is clearly visible that average value of Mean RR, STDRR, RMSSD, pNN50, STD HR of apnea patients is greater than that of the healthy subjects. On the other side, mean HR, NN50, TINN values are smaller than healthy subjects' average. The parameters taking the standard deviation can be considered as more accurate parameters for apnea detection. Therefore, line graph of mean RR, RR triangular index, and TINN of the individual patients have been plotted and these show a high difference in the range of the result (Figs. 3, 4, and 5).
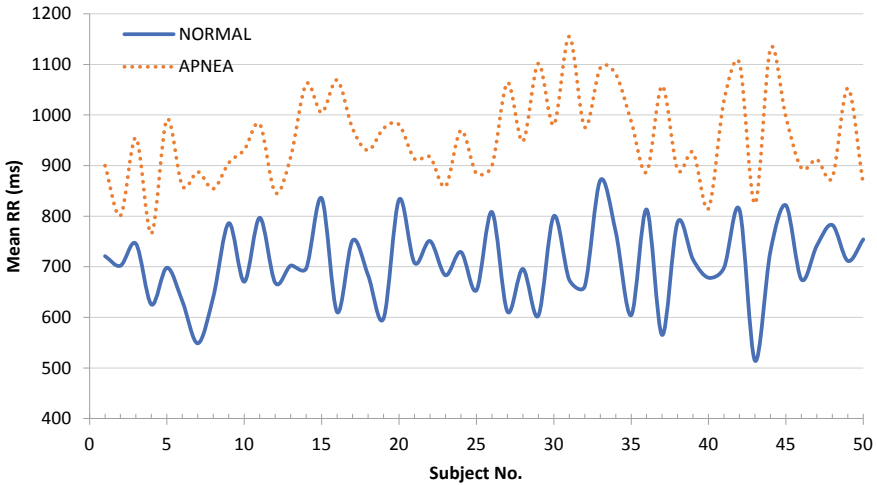
Fig. 3 Line graph representation of the mean RR
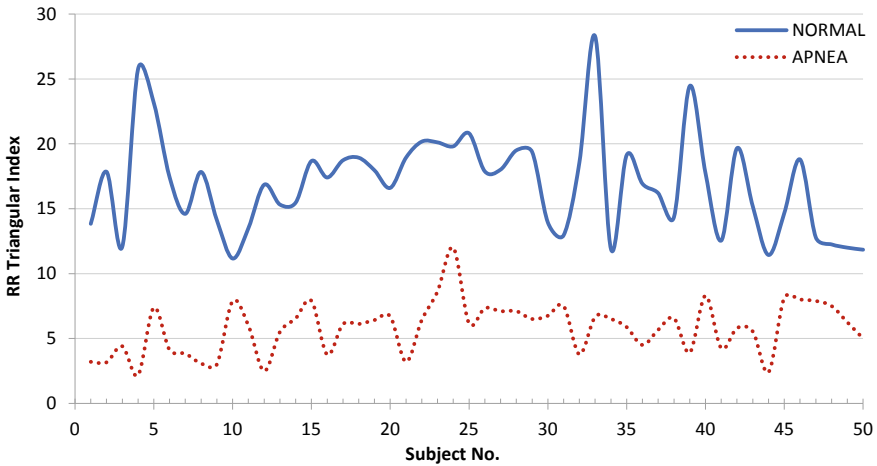
Fig. 4 Line graph representation of the RR triangular index
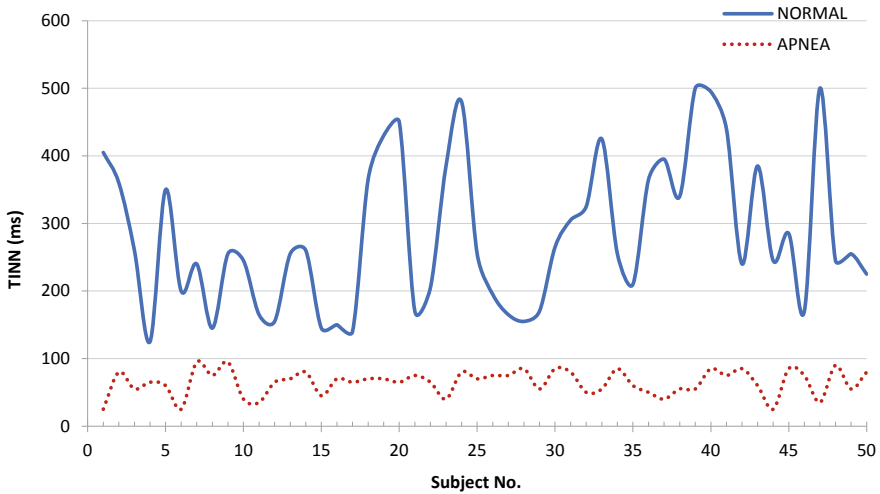
Fig. 5 Line graph representation of TINN

5 Conclusion

It has been observed that HRV analysis is a vital marker of apnea diagnosis. By analyzing the time domain attributes, we conclude that some HRV parameters (RMSSD, STD RR, STDHR, mean RR) of apnea patient's increase and some parameters (RR triangular index, TINN, NN50) are many times lesser than healthy subjects. From the above small-time domain analysis, we can conclude some HRV parameters are varying in apnea patients with respect to healthy subject predominantly which may take a leadership role in future research to detect apnea using HRV.

6 Future Scope

The scope of the work is enormous which will be carried out till the end of our work. Within this period of time, our work was limited only in time domain analysis, and in the future, it will be carried out with different frequency domain parameters so that we can reach our ultimate goal to use our innovation in real-time life of the world. As previously mentioned, due to two different sources of data this work is restricted only in time domain but our aim is to collect both the healthy and apnea patients' data ourselves using our own device and we will use also the frequency domain analysis in the future to establish more valuable conclusion in this research world, and in the future, HRV may be used as apnea detecting tool.

References

1. Mendonca, F., Mostafa, S.S., Ravelo-Garcia, A.G.: A review of obstructive sleep apnea detection approach 2–8 (2018)
2. Lado, M.J., Vila, X.A., Rodríguez-Liñares, L., Méndez, A.J., Olivieri, D.N., Félix, P.: Detecting sleep apnea by heart rate variability analysis: assessing the validity of databases and algorithms 1–2 (2009)
3. Court-Fortune, I., Costes, F., Sforza, E., Garet, M., Barthélémy, J.C., Roche, F., Pichot, V.: Predicting sleep apnea syndrome from heart period—a time-frequency wavelet analysis. Eur. Respir. J. **22**, 937–942 (2003)
4. Vat, S., Marques-Vidal, P., Heinzer R., et al.: Prevalence of sleep disordered breathing in the general population—the HypnoLaus study **3**(4), 310–318 (2015)
5. Ryan, C.F., Mulgrew, A.T., Fleetham J.A., et al.: The impact of obstructive sleep apnea and daytime sleepiness on work limitation. Sleep Med. 42–53 (2007)
6. Redline, S., Strohl, K.: Recognition of obstructive sleep apnea. Am. J. Respir. Crit. Care Med. **154**, 274–289 (1996)
7. Akselrod, S.: Components of heart rate variability-basic studies 147–163 (1995)
8. Giri, V.K., Gautam, D.D.: Analysis of HRV signal for disease diagnosis 1–2 (2016)
9. Matteucci, M., Mendez, M.O., Van Huffel, S., Penzel, T., Cerutti, S., Bianchi, A.M., Corthout, J.: Automatic screening of obstructive sleep apnea from the ECG based on empirical mode decomposition and wavelet analysis 1–2 (2010)
10. Ranta-aho, P.O., Niskanen, J.P., Lipponen, J.A., Tarvainen, M.P., Karjalainen, P.A.: Kubios HRV—heart rate variability analysis software. Comput. Methods Programs Biomed. **113**(1), 210–220 (2014)
11. Félix, P., Presedo, J., Fernández-Delgado, M., Vila, J., Palacios, F., Barro, S.: Time-frequency analysis of heart-rate variability. IEEE Eng. Med. Biol. Mag. **16**, 119–125 (1997)

Performance Investigation of Extended Kalman Filter During Power System Harmonics Estimation

Yuglina Pradhan and Aritro Dey

Abstract Noise pollution, harmonics and deviation of frequency may cause problems during operation of appliances in the power system. Extended Kalman filter (EKF) which is appropriate for nonlinear state estimation has been implemented for the estimation of harmonics encountered in power system. EKF works based on the concept of linearization of nonlinear functions about the current mean and covariance so as to follow Kalman filter (KF) for linear signal models. EKF has been preferred here for harmonics estimation to estimate frequency along with the harmonics parameters in the presence of noise in a power signal. Eventually, the performance of the EKF-based approach is demonstrated by Monte Carlo simulation. Monte Carlo simulation demonstrates the consistency and convergence of EKF during harmonics estimation when the power signal is influenced by noise. Suitability of this approach is also illustrated with the help of real data taken into account.

Keywords Kalman filter · Harmonics estimation · Extended Kalman filter · Monte Carlo simulation

1 Introduction

With the advanced application of the nonlinear loads, arc furnaces, industrial loads, motor drives and FACTS devices in power systems [1], the presence of harmonic contents in line voltage and current affect the operation of electric power system. Due to harmonic distortions power quality deteriorates, losses are increased in transmission system and grid, mal operation of protective devices like relays and circuit breakers, overheating of machines in the power system [2], etc.

Therefore, harmonic estimation is an essential part of a healthy power system. Along with harmonic, frequency estimation is also crucial for power system protection and control point of view. When the system integrity is at danger, the system frequency may face a huge and sudden change due to the fluctuation between energy

Y. Pradhan (✉) · A. Dey
Department of Electrical Engineering, National Institute of Technology Durgapur, Durgapur, West Bengal 713209, India

generation and consumption at load side. So it is necessary to estimate frequency at a fast and precise manner to track sudden changes [3]. For this reason, the frequency estimation algorithms must contribute a high precise and fast convergence so that small variation can be tracked. Different methods have been implemented for the estimation of harmonic components based on Fourier theory involving discrete Fourier transform (DFT) and fast Fourier transform (FFT) algorithm. DFT is generally used as the most powerful tool in digital signal processing such as in measurement analysis of spectrum, multi-carrier transceivers in wireless communications [2]. DFT is implemented by taking the help of FFT algorithm. Though in some real-time applications when there is needed to generate new DFT spectrum output for every sample, such sophisticated DFT algorithm is inefficient for real-time signal processing [4].

FFT algorithm is efficient one when the analysed waveforms are periodic. When FFT algorithm is applied to a non-periodic waveform, there is generation of harmonics with considerable magnitude due to the variation in frequency or in amplitude [5]. The drawbacks of FFT are aliasing, picket fence effect and leakage when it is applied to a non-periodic signal.

The conventional methods become inaccurate in time-varying conditions [6]. Thus, several adaptive filtering methods have been proposed to estimate the harmonic parameters like least mean square (LMS), recursive least square (RLS), forgetting factor RLS (FFRLS), extended LMS (ELMS). The LMS is an adaptive method based on the gradient approach of steepest descent. This filter is computationally efficient. But the convergence of LMS algorithm is less efficient as compared to RLS algorithm [3].

Kalman filter (KF) is an optimal, linear and robust algorithm for estimating the amplitudes and phases of harmonic parameters in undefined measurement noise. But this algorithm becomes inefficient when there are dynamic changes in signal. Recently, the artificial intelligence methods have been implemented for harmonic estimation. Practically, harmonic estimation is a nonlinear problem, so genetic algorithm (GA) technique is used as stochastic global searching algorithm for this estimation [7]. When KF is applied to a nonlinear system that time the filter estimation may diverge. So, in that case EKF is a suitable candidate. EKF works the same as KF but it linearizes nonlinear functions about the current estimate [8]. It is an alternative to KF during nonlinear state estimation wherein the nonlinear functions demonstrate lower degree of nonlinearities. By calculating Jacobian of state transition matrix and observation matrix around the current estimated state, the problem of nonlinearity is vanished by EKF. It is a recursive data processing algorithm. EKF is mainly used in state of charge (SOC) estimation of battery, simultaneous localization and mapping (SLAM) system. In the paper [9], a new proposed low computational ANN-EKF algorithm estimates harmonics or inter-harmonics at a low sampling frequency. Other nonlinear estimators are unscented Kalman filter (UKF), cubature Kalman filter (CKF), etc. [10].

In this paper, authors have illustrated the simulation results obtained during the harmonics estimation in power system using EKF which ensures the consistency of the estimation performance of estimator and also demonstrates acceptable estimation accuracy. The convergence of the filter is also secured by Monte Carlo simulation.

Additionally, the suitability of the estimation approach is also established during estimation of harmonics parameters and fundamental frequency with the help of real-time measurement data.

2 Harmonic Estimation Problem

Our objective is to estimate the harmonics parameters of a power signal. The nonlinear dynamic systems can be described by state-space equations [11] as below:

$$x_k = f(x_{k-1}, u_{k-1}) + \mu_k \tag{1}$$

$$z_k = h(x_k) + v_k \tag{2}$$

where z_k represents measurement vector, x_k defines the state vector, $f(.)$ and $h(.)$ are the nonlinear state and measurement function, respectively.

In general, a power signal having both the harmonics and noise components can be represented [10, 12, 13] below as:

$$y_k = \sum_{n=1}^{N} A_n \sin(n\omega kT_s + \varphi_n) + A_{dc}e^{-\alpha_{dc}kT_s} + \varepsilon_k \tag{3}$$

where N is the Nth harmonics, k represents time step, T_s indicates the sampling time, ω is the frequency in radian per second, φ_n specifies phase of nth harmonics, A_{dc} becomes the DC component amplitude, $e^{-\alpha_{dc}kT_s}$ is the exponential term representing DC component, and ε_k is the measurement noise parameter. For estimating the state, the above exponential term is expanded by applying Taylor series and neglecting the higher-order terms, the expression can be expressed as:

$$A_{dc}e^{-\alpha_{dc}kT_s} = A_{dc} - A_{dc}\alpha_{dc}kT_s \tag{4}$$

By replacing Eq. (4) in (3),

$$y_k = \sum_{n=1}^{N} A_n \sin(n\omega kT_s + \varphi_n) + A_{dc} - A_{dc}\alpha_{dc}kT_s + \varepsilon_k \tag{5}$$

By expanding terms of (5), we get (6)

$$y_k = \sum_{n=1}^{N} A_n \sin(n\omega kT_s) \cos(\varphi_n)$$

$$+ \sum_{n=1}^{N} A_n \cos(n\omega k T_s) \sin(\varphi_n) + A_{dc} - A_{dc}\alpha_{dc}k T_s + \varepsilon_k \tag{6}$$

Equation (6) can be written in terms of state-space equation as:

$$x_k = F_{k-1} * x_{k-1} + \mu_k \tag{7}$$

where k indicates the discrete time step, x_k specifies the state vector, F_k represents the state transition matrix, and μ_k is the Gaussian process vector, i.e., $(\mu_k \sim N(0, Q))$. The state transition matrix F can be written as:

$$F_k = \begin{bmatrix} 1 & 0 & 0 & 0 & 0 & \cdots & 0 \\ 0 & 1 & 0 & 0 & 0 & \cdots & 0 \\ 0 & 0 & 1 & \cdots & 0 & \cdots & 0 \\ \vdots & \vdots & \vdots & \ddots & \vdots & \cdots & 0 \\ 0 & 0 & 0 & 0 & 1 & \cdots & 0 \\ 0 & 0 & 0 & 0 & 0 & 1 & 0 \\ 0 & 0 & 0 & \cdots & 0 & 0 & 1 \end{bmatrix} \tag{8}$$

The state vector can be written as:

$$x_k = \begin{bmatrix} A_1 \cos \varphi_1 & A_1 \sin \varphi_1 & \dots & A_N \cos \varphi_N & A_N \sin \varphi_N & A_{dc} & A_{dc}\alpha_{dc} & w \end{bmatrix}^{\mathrm{T}} \tag{9}$$

Here from [11]

$$h(X_k) = X_k(1) \sin(X_k(2N + 3)kT) + X_k(2) \cos(X_k(2N + 3)kT)$$
$$+ \cdots + X_k(2N) \cos(N X_k(2N + 3)kT) + X_k(11) - X_k((11)kT).$$

So the amplitudes and phase angles of all the harmonics, DC component and fundamental frequency are obtained as:

$$A_n = \sqrt{x_k^2(2N) + x_k^2(2N - 1)} \tag{10}$$

$$\varphi_n = \tan^{-1}(x_k(2N)/x_k(2N - 1)) \tag{11}$$

$$A_{dc} = x_k(2N + 1) \tag{12}$$

$$\alpha_{dc} = x_k(2N + 2)/x_k(2N + 1) \tag{13}$$

$$w = x_k(2N + 3) \tag{14}$$

3 Algorithm

In EKF, the state transition matrix and observation matrix may not be linear, i.e. the presence of some nonlinearity in the system. Equations (1) and (2) represent the nonlinear state space equations. By calculating Jacobian of state transition matrix and observation matrix around the current estimated state, the problem of nonlinearity is avoided. These matrices are applied in KF algorithm for linearizing the nonlinear function around the current estimated mean and covariance [8]. There are two steps based on which EKF works, viz. prediction/a priori estimation/time update steps and correction/a posteriori estimation/measurement update. The algorithm is well known and therefore not presented here for the brevity of the paper. Readers are requested to refer [8] for the algorithm.

4 Problem Statement

A power signal consists of fundamental, 3rd-, 5th- upto 11th-order harmonics, and DC component is taken [13]. It is disturbed by a measurement noise μ having initial measurement noise covariance of $R = 0.0025$ and is represented by:

$$x(t) = 1.5 \sin(w_o t + 80) + 0.55 \sin(3w_o t + 70) + 0.2 \sin(5w_o t + 45)$$
$$+ 0.15 \sin(7w_o t + 36) + 0.1 \sin(11w_o t + 30) + 0.5\mathrm{e}^{-0.5t} + \mu$$

Here our objective is to determine the amplitudes and phase angles of all the harmonics, DC component and fundamental frequency of the above power signal. The process noise covariance is taken as $Q = 10^{-8} * I_{13 \times 13}$. The initial value of state vector of the filter is selected as $\hat{x}_0 = x_0 * 0.98$ and $\hat{P}_0 = I_{13 \times 13} * 100$.

5 Results and Discussions

In this section, the authors have represented the estimation results of the power signal which is described in problem statement part and Monte Carlo simulation has been carried out to check the estimation convergence and also real measurement data has been taken to validate the theoretical concept regarding EKF.

5.1 Simulation Results of EKF

The estimation results of all the harmonics and frequency are shown in Figs. 1, 2, 3, 4, 5, 6 and 7. It is obtained that the estimated values are almost getting converged with

Fig. 1 Fundamental amplitude versus run plot
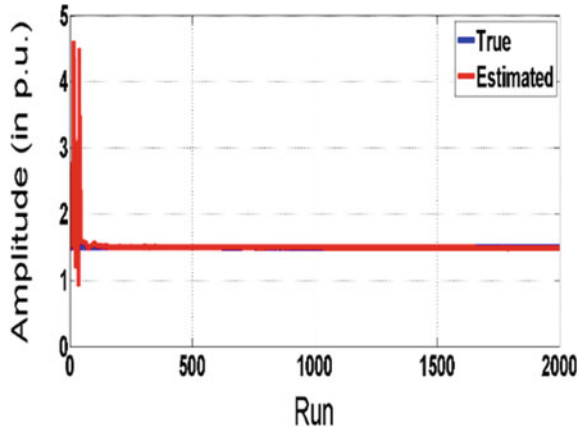
Fig. 2 11th harmonics amplitude versus run plot
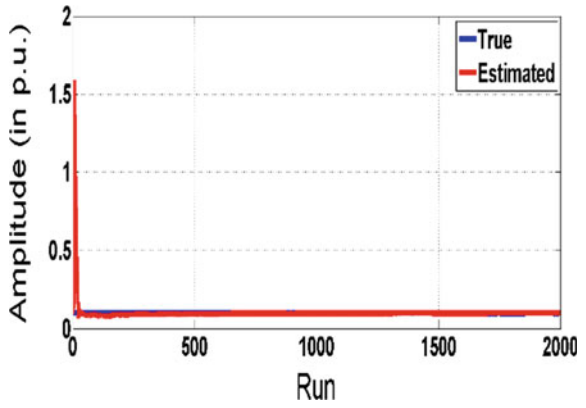
Fig. 3 DC amplitude versus run plot
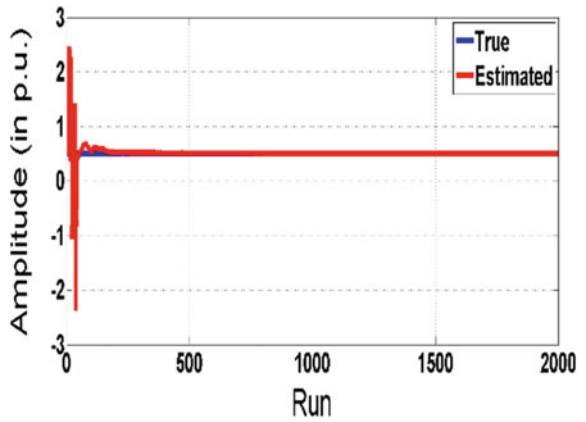
Fig. 4 DC component versus run plot
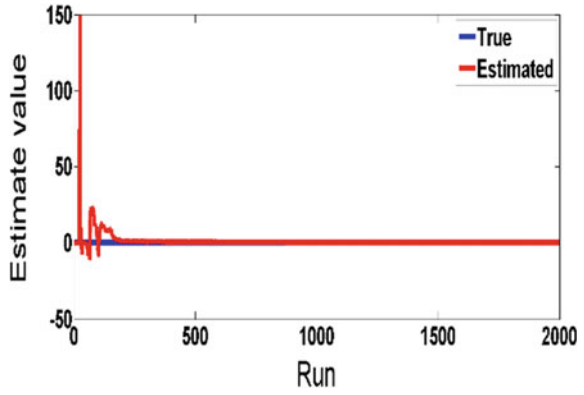
Fig. 5 Fundamental phase versus run plot
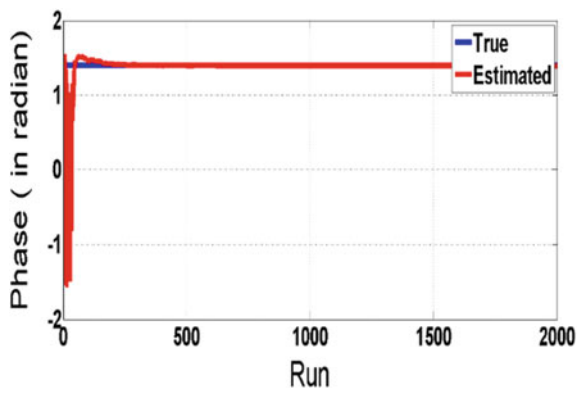
Fig. 6 Frequency estimate versus run plot
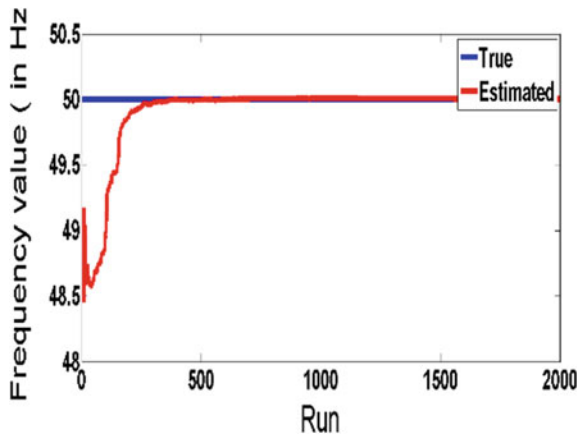
Fig. 7 11th harmonics phase versus run plot
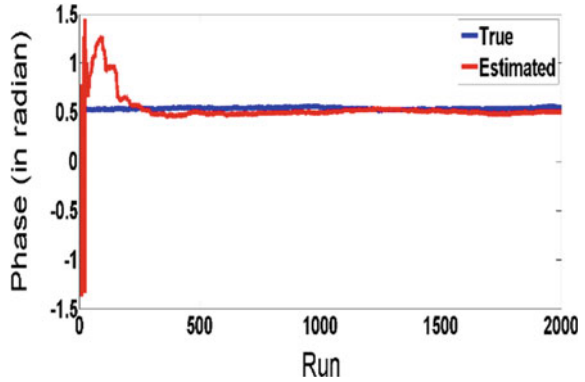
Fig. 8 Frequency MSE versus run plot
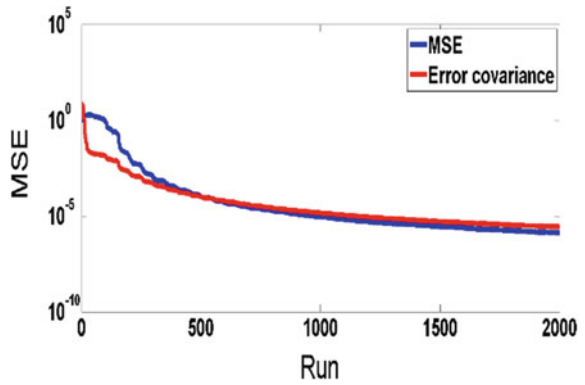
the true value as we approach to steady state. Due to inadequacy of space, the authors are not able to present the results of parameters of all harmonics. By applying Monte Carlo simulation, the consistency performance of this filter is studied. By studying MSE plots, it is observed that the MSE is closely following the error covariance. The MSE plots are shown in Figs. 8, 9 and 10.

5.2 Simulation Result with Real Data

By taking real measurement data of a system, following harmonics and fundamental frequency estimation results are obtained which are shown in Figs. 11, 12 and 13. It is observed that EKF estimates accurately when applied to the above nonlinear system.

Fig. 9 Fundamental amplitude MSE versus run plot
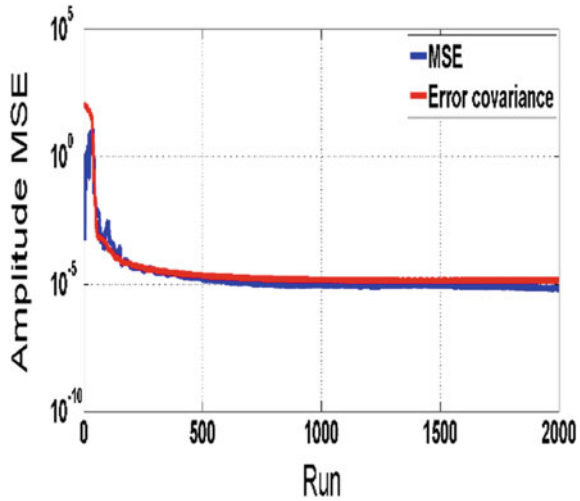
Fig. 10 11th harmonics amplitude MSE versus run plot
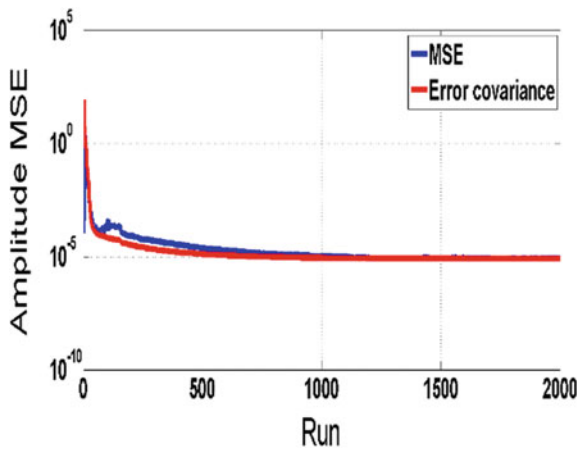
6 Conclusion

In this paper, EKF-based estimation approach is preferred during the estimation of harmonic parameters of a power signal along with the fundamental frequency. The estimation accuracy of EKF is found acceptable. Consistency and the convergence of the estimation strategy are secured by carrying out Monte Carlo simulation. Eventually, the suitability of this harmonics estimation strategy is exemplified with the help of real-time measurement data. Finally, based on the observation EKF is encouraged to use as a candidate suboptimal nonlinear filter for harmonics estimation in the presence of nonlinear measurement functions.

Fig. 11 Fundamental amplitude versus run
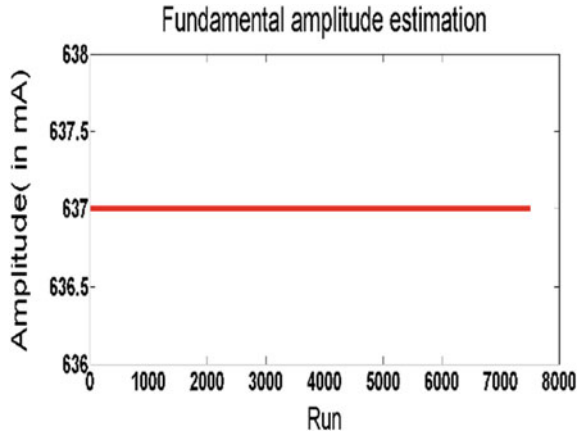
Fig. 12 Fundamental phase versus run
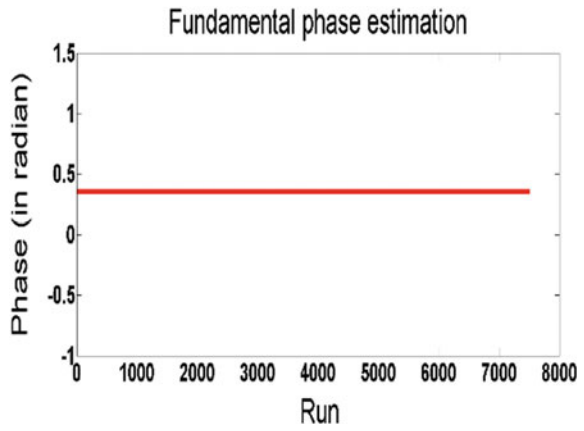
Fig. 13 Frequency estimation versus run
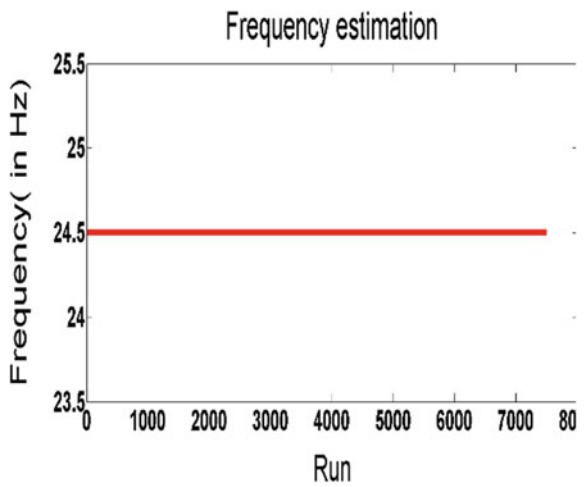
References

1. Sadinezhad, I., Agelidis, V.G.: Under sampled on-line ANN-EKF based estimation of harmonics. In: Interharmonics in Power Systems. IEEE (2010)
2. Varaprasad, O.V.S.R., Panda, R.K., Siva Sarma, D.V.S.S.: A novel synchronous sampling algorithm for power system harmonic analysis. IEEE (2013)
3. Katiraei, F., Iravani, M.R., Lehn, P.W.: Microgrid autonomous operation during and subsequent to islanding process 20, 248–257 (2005)
4. Wen, H., Teng, Z., Wang, Y., Yang, Y.: Optimized trapezoid convolution windows for harmonic analysis (2013)
5. Plates-Garza, M.A., de la O Serna, J.A.: Polynomial implementation of the Taylor-Fourier Transform for harmonic analysis. IEEE Trans. Instrum. Measur. 63(12) (2014)
6. Singh, S.K., Nath, A., Chakraborty, R., Kalita, J., Sinha, N., Goswami, A.K.: Variable constrained based LMS algorithm for power system harmonic estimation. In: International Conference on Communication and Signal Processing. IEEE, India (2014)
7. Subudhi, B., Ray, P.K.: Estimation of power system harmonics using hybrid RLS-Adaline and KF-Adaline algorithms. In: TENCON. IEEE (2009)
8. Simon, D.: Optimal State Estimation: Kalman, H Infinity and Nonlinear Approaches. Wiley, Hoboken (2006)
9. Sadinezhad, I., Agelidis, V.G.: Understand on-line ANN-EKF based estimation of harmonics. In: Interharmonics in Power Systems. IEEE (2010)
10. Pramanik, M., Ghosh, A., Routray, A., Mitra, P.: Harmonics estimation of a noisy power system signal using cubature Kalman filter. IEEE (2018)
11. Yadav, P., Dey, A.: Investigation of the suitability of adaptive extended Kalman filter for power system harmonics estimation. IEEE (2020)
12. Yadav, P., Dey, A.: Power system harmonics estimation using adaptive Kalman filter and its nonlinear variants. Indian Chemical Society (2020)
13. Singh, S.K., Sinha, N., Goswami, A.K., Sinha, N.: Several variants of Kalman filter algorithm for power system harmonic estimation. Int. J. Electr. Power Energy Syst. 78, 793–800 (2016)

An Artificial Intelligence Approach to the Prediction of Global Solar Irradiation in India

Sutapa Mukherjee

Abstract Due to a high demand in solar power generation, the predictions and integration of solar energy sources have become an important area of research work. Previous researches have shown that the artificial intelligent-based method for approximation of global solar radiation provides better accuracy and efficiency. The objective of the present work is to find the global solar radiation using multi-layer feedforward neural network (MLFF) for the year 2016 pertaining three cities Kolkata, Roorkee and Chennai based on five years (2011–2015) hourly radiation database collected from Photovoltaic Geographical Information System (PVGIS). Out of 1, 31,325 collected data, 70% were used for training, 15% were used for validation and the rest 15% were used for testing. This neural network model is developed by taking into consideration different parameters like month, day, time, latitude, longitude, elevation, slope, azimuth as inputs and global irradiance on the inclined plane as output. The obtained results indicate that the proposed technique predicts global solar irradiation with a high accuracy (98.74%) which proves the superiority of the applied method over the conventional one.

Keywords Global irradiance · Artificial neural network · Back-propagation

1 Introduction

One of the important challenges we are facing is energy crisis. Out of different renewable sources of energy, as a clean and cost-free, solar energy is very much popular everywhere. One should be conversant with the various components of solar energy for its effective use. There are various components which attribute to the solar energy to different extents like the duration of sunshine, maximum ambient temperature, any day and month, global radiation, latitude and longitude to name a few. The availability of solar energy is predominantly controlled by the global solar

S. Mukherjee (✉)
Electrical Engineering Department, B. P. Poddar Institute of Management & Technology, Kolkata 700052, India
e-mail: sutapa.mukherjee@bppimt.ac.in

237

radiation; however, the measurement of same is done only at a couple of locations due to the involvement of relatively expensive equipment and the subsequent maintenance charges. Researches to corelate the solar radiation with various climatic condition and geometrical factors have been done in the past and the major models were based on different inputs, equations and algorithms [1]. Models developed on the basis of the actual solar radiation reaching a given area outperformed the meteorological data model. Attempts were made to overcome the limitation of inaccessibility of insolation data in certain regions, and consequently, temperature-based models and other suitable modifications [2, 3] were proposed to overcome the shortcoming. ANN technique based on resilient propagation (RP) [4] with the physical features and atmospheric conditions as inputs resulted in a much better and consistent output compared to the classical modelling. Subsequently, soft computing technique was deployed to study the effectiveness in estimating the solar radiation and was found to be instrumental in dealing with practical problems where the nature is data is far more complex and dynamic because of the noise and the nonlinearity associated with it. AI-based approach which includes artificial neural network (ANN), fuzzy logic, adaptive neuro-fuzzy interface system (ANFIS) and data mining (DM) is some of the methods which have been effectively utilized to yield better results [5] than conventional modelling. Several models based on ANN and regression techniques [6] were compared and the former yielded in much better results.

Attempt has been made to devise an easier model for evaluating the total solar irradiation taking input parameters like month, day, time, latitude, longitude, elevation, slope, azimuth as inputs and global irradiance on the inclined plane (plane of the array) (W/m^2) as output for three places in India which are Kolkata, Roorkee and Chennai.

1.1 Dataset

It is already mentioned that this study was carried out using the PVGIS database for three Indian cities Kolkata, Roorkee and Chennai [7]. The parameters used in this study are: day, month, latitude, longitude, elevation, slope, azimuth and global solar irradiance which were collected for six consecutive years (2011–2016). From the total dataset, two separate datasets were created among which the first dataset (for 2011–2015) was used for training, testing and validation and the second dataset (for 2016) has been used for prediction. From the first dataset, out of 1, 31,325 collected data, 70% (91,927) were used for training, 15% (19,698) were used for validation and the rest 15% (19,698) were used for testing. From the second dataset, 8755 data points for each city were used for prediction to evaluate the proposed ANN model. Table1 shows the geographical locations of these three cities Kolkata, Roorkee and Chennai.

Table 1 Geographic information of three cities

City	Latitude	Longitude	Elevation (m)	Mounting type	
				Slope	Azimuth
Kolkata	22.57° N	88.37° E	11	45°	120°
Roorkee	29.86° N	77.89° E	274	45°	120°
Chennai	13.08° N	80.28° E	8	45°	120°

1.2 Artificial Neural Network

The ANN model is a mathematical simulation of the way in which the human brain works [8]. It is a highly interconnected network of neurons which is capable of processing the computational data in parallel. The input signal y_i, for $i = 0, 1, 2, \ldots,$ n is processed through the intermediate layers of neurons which assign a weightage w_{ij} to the inputs followed by an application of sigmoid function resulting in an output equivalent to the weighted mean which is given by Eq. 1.

$$u_j = \sum_{i=0}^{n} w_{ij} y_i \tag{1}$$

The multi-layer feedforward mechanism (MLF) along with the back-propagation is the most commonly used ANN method used for estimating the solar radiation [9–11]. This model can be used for problems which are not linearly separable. Apart from input (i) and one output layer (k), it usually contains one or two intermediate/hidden layer (j) which are interconnected by weights W_{ij} and W_{jk} and is shown in Fig. 1a, and the basic structure of a single artificial neuron is shown in Fig. 1b.

A bias is added to the input and a nonlinearity transforms the sum into an output. This is called the activation function of the node. Linear activations are usually present in the output nodes. The logistic sigmoid function given in Eq. 2 is used for hidden node while the linear equation given by Eq. 3 is used for output node [11].
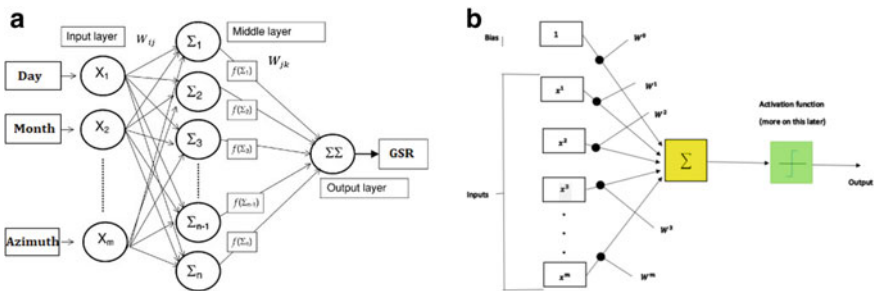
Fig. 1 **a** Typical structure of ANN **b** basic structure of a single artificial neuron

$$f(w) = 1/\left(1 + e^{-w}\right) \tag{2}$$

$$f(x) = x \tag{3}$$

The synaptic weight is updated on the basis of a procedure called back-propagation in which the error generated at the output after running a cycle is propagated backward through the intermediate layers finally to the input layer [12]. The training cycle is then repeated to minimize the error, and the network gradually moves towards stability. The estimated error used here is the mean squared error (MSE). In addition to the back-propagation technique, other methods like gradient descent, conjugate gradient algorithms, resilient back-propagation, gradient descent with momentum and quasi-Newton algorithms can be used. The number of neurons, the number of intermediate layers and the training algorithm vary from model to model.

1.3   ANN Model Architecture

A three-layer feedforward neural networks (FFNN) simulation has been used for the purpose of investigation. The input variables are fed into the first layer which is basically the input layer followed by the intermediate or the hidden layer which forms the second layer and the third layer is the output layer. Many real-world function problem modelling has been done following this topology [13, 14]. The selection of the neurons in the intermediate layer is very crucial as the complexity of system to be modelled is related to it. For this particular investigation, the selection of optimum number of neurons in the intermediate layer was done by trial-and-error method. Using a range of neurons between 2 and 80 the system was evaluated for minimum error between the predicted and the actual output. For the intermediate layer, the logistic sigmoid function was considered for the transfer function while the output layer was based on the linear transfer function. Back-propagation (BP) with the Levenberg–Marquardt was then applied to train the neural network as it is one of the fastest and more accurate algorithms. The stability of the steepest descent method [15] is combined with the speed of Newton algorithm. This combination is used to compute the Jacobian matrices bypassing the hessian matrix. This approach gives a faster convergence with minimalistic error.

1.4   Model Performance Evaluation [16]

Using two statistical indicators, mean squared error (MSE) and coefficient of determination (regression value (R)), the performance of the models was evaluated.

$$\text{MSE} = \frac{1}{n} \sum_{i=1}^{n} (H_p - H_a)^2 \tag{4}$$

where H_p is the predicted value and H_a is the actual value

$$R^2 = \frac{\left[\sum_{i=1}^{n} \left(H_p - H_{p,avg} \right) \left(H_a - H_{a,avg} \right) \right]^2}{\sum_{i=1}^{n} \left(H_p - H_{p,avg} \right)^2 \sum_{i=1}^{n} \left(H_a - H_{a,avg} \right)^2} \tag{5}$$

2 Results

In the first scenario, the artificial neural network was trained using 2011 to 2015 dataset consisting of the input parameters (day, month, time, latitude, longitude, slope and azimuth) and it was observed that the model achieved MSE value of 0.676 for training and 0.645 for testing which is shown in Table 2.

The regression plot [17] of training dataset has been shown in Fig. 2, from which it can be seen that the overall regression value was obtained of 0.94482 with the coefficients of regression line for slope and offset being 0.89 and 0.18, which indicates a good fit of the data. Also, the best validation performance of 0.665 was achieved after 148 iterations as shown in Fig. 4a. The regression plots of testing dataset are shown in Fig. 3 from which it is seen that the regression value was obtained of 0.93869 with the coefficients of regression line for slope and offset being 1.1 and 0.00013 for Kolkata.

The regression value was obtained of 0.95262 with the coefficients of regression line for slope and offset being 1 and 0.014 for Roorkee. The same was obtained of 0.9076 with the coefficients of regression line for slope and offset being 0.99 and 0.1 for Chennai.

The error histogram demonstrates that the maximum instance of error occurred at 0.2272 signifying the accuracy of the trained ANN model in predicting the GSR value for unknown inputs as shown in Fig. 4b. The error histogram chart during tested data for Kolkata, Roorkee and Chennai is shown in Figs. 5, 6 and 7, respectively.

The trained ANN model was used for the prediction of global solar radiation in three Indian cities (Kolkata, Roorkee and Chennai). The statistical performance measures (MSE and R2 value) for all the three cities are presented in Table 3 for both training and testing datasets.

Table 2 Performance evaluation of the proposed ANN model on the training datasets

Results	MSE	R
Training	0.676	0.944
Validation	0.665	0.945
Testing	0.645	0.948
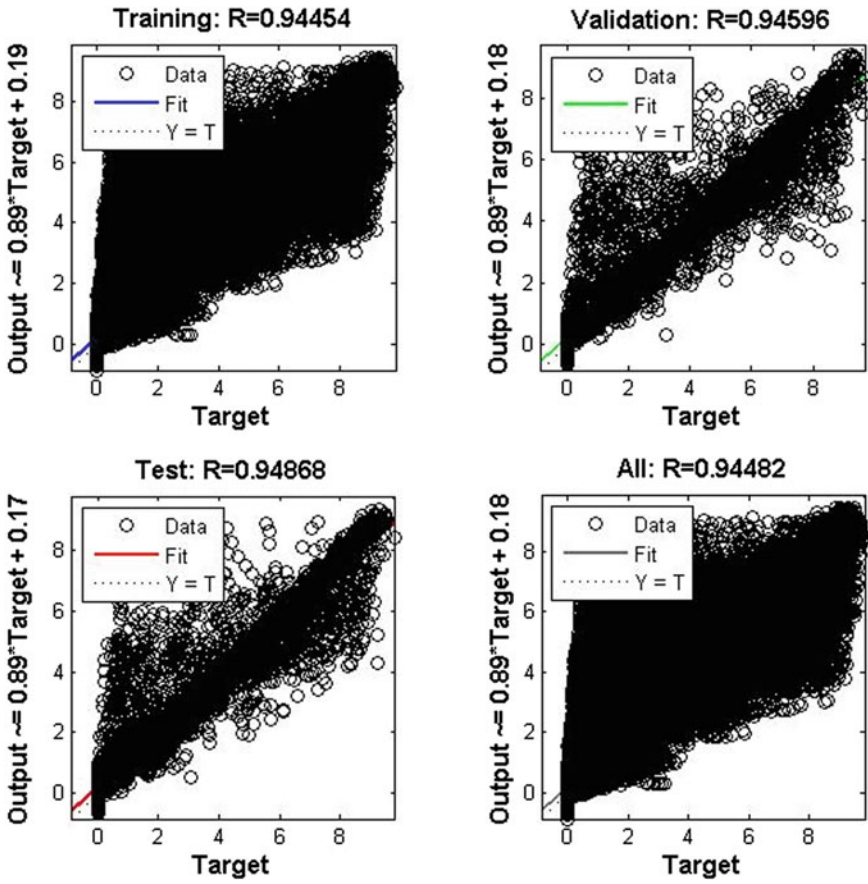
Fig. 2 Regression plot of training dataset
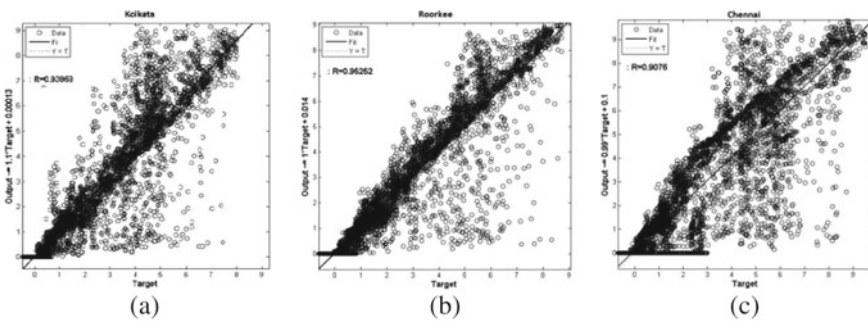
Fig. 3 Regression plot of testing dataset for **a** Kolkata **b** Roorkee and **c** Chennai
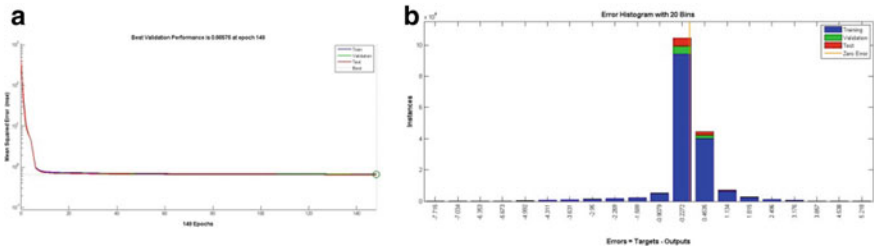
Fig. 4 **a** Best validation performance **b** error histogram of trained ANN
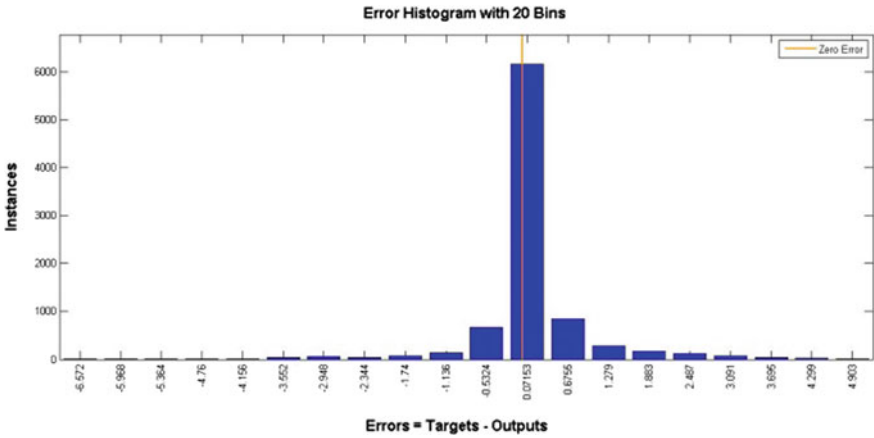
Fig. 5 Error histogram for tested data of Kolkata
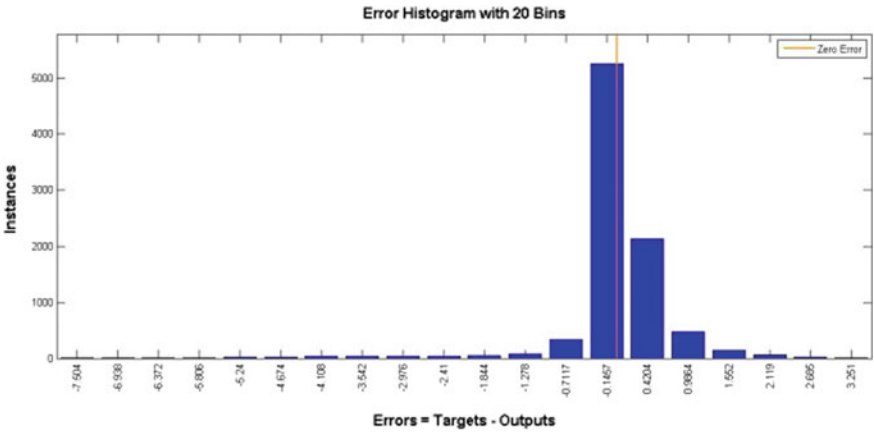
Fig. 6 Error histogram for tested data of Roorkee
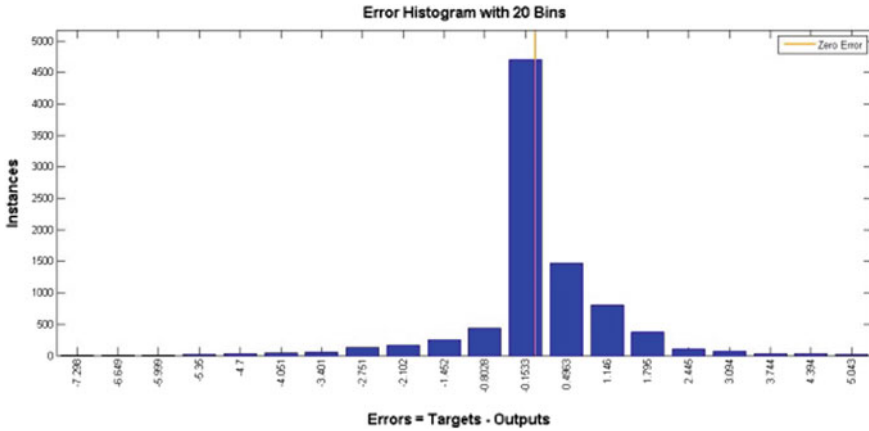
Fig. 7 Error histogram for tested data of Chennai

Table 3 Performance evaluation of the proposed ANN model on the prediction dataset

Cities	MSE	R^2
Kolkata	0.731	0.939
Roorkee	0.544	0.953
Chennai	0.129	0.908

From Table 3, it can be observed that the proposed ANN model can efficiently predict the GSR with low mean squared error and high R^2 value for all three cities.

3 Discussion and Conclusion

In this study, multilayer feedforward (MLFF) ANN technique [18] based on back-propagation algorithm is developed, trained and tested to predict hourly global solar radiation for 2016 for three cities Kolkata, Roorkee and Chennai. The model is developed and proposed by including input parameters like month, day, time, latitude, longitude, elevation, slope, azimuth and global solar irradiation as output. Using the prepared ANN model created with the PVGIS 5 years solar radiation dataset for three cities and testing this one for the prediction of 2016 data revealed that the predictions of solar radiation using our proposed model shows a better result with the obtained PVGIS dataset for 2016. This developed model is suitable for predicting solar radiation for any locations in India for which solar radiation is required for site-specific solar energy applications especially for solar power generation and production.

References

1. Besharat, F., Dehghan, A.A., Faghih, A.R.: Empirical models for estimating global solar radiation: a review and case study. Renew. Sustain. Energy Rev. **21**, 798–821 (2013)
2. Chen, J.-L., Liu, H.-B., Wu, W., Xie, D.-T.: Estimation of monthly solar radiation from measured temperatures using support vector machines—a case study. Renew. Energy **36**, 413–420 (2011)
3. Olatomiwa, L., Mekhilef, S., Shamshirband, S., Mohammadi, K., Petkovic, D., Sudheer, C.: A support vector machine–firefly algorithm-based model for global solar radiation prediction. Sol. Energy **115**, 632–644 (2015)
4. Senkal, O.: Solar radiation and precipitable water modeling for Turkey using artificial neural networks. Meteorol. Atmos. Phys. **127**, 481–488 (2015)
5. Gopalakrishnan, K., Khaitan, S.K. Kalogirou, S.: Soft Computing in Green and Renewable Energy Systems. Springer, Berlin (2011)
6. Paliwal, M., Kumar, U.A.: Neural networks and statistical techniques: a review of applications. Expert Syst. Appl. **36**, 2–17 (2009)
7. PVGISHomepage. https://ec.europa.eu/jrc/en/pvgis
8. Haykin, S., Lippmann, R.: Neural networks, a comprehensive foundation. Int. J. Neural Syst. **5**, 363–364 (1994)
9. Yadav, A.K., Chandel, S.S.: Solar radiation prediction using artificial neural network techniques: a review. Renew. Sustain. Energy Rev. **33**, 772–781 (2014)
10. Qazi, A., Fayaz, H., Wadi, A., Raj, R.G., Rahim, N.A., Khan, W.A.: The artificial neural network for solar radiation prediction and designing solar systems: a systemic literature review. J. Cleaner Prod. **114**, 1–12 (2015)
11. Rezrazi, A., Hanini, S., Laidi, M.: An optimisation methodology of artificial neural network models for predicting solar radiation: a case study. Theor. Appl. Climatol. **123**, 1–15 (2015)
12. Esmaeelzadeh, S.R., Adib, A., Alahdin, S.: Long-term stream flow forecasts by adaptive neuro-fuzzy inference system using satellite images and K-fold cross validation (case study: Dez, Iran). KSCE J. Civ. Eng. 1–9 (2014)
13. Ata, R.: Artificial neural networks applications in wind energy systems: a review. Renew. Sustain. Energy Rev. **49**, 534–562 (2015)
14. Antonopoulos, V.Z., Antonopoulos, A.V.: Daily reference evapotranspiration estimates by artificial neural networks technique and empirical equations using limited input climate variables. Comput. Electron. Agric. **132**, 86–96 (2017)
15. Wilamowski, B.M., Chen, Y., Malinowski, A.: Efficient algorithm for training neural networks with one hidden layer. In: IJCNN. Proceedings of the 1999 International Joint Conference, pp. 1725–1728. Citeseer (1999)
16. Quej, V.H., Almorox, J., Arnaldo, J.A., Saito, L.: ANFIS, SVM and ANN soft-computing techniques to estimate daily global solar radiation in a warm sub-humid environment. J. Atmos. Solar-Terr. Phys. **155**, 62–70 (2017)
17. Jain, R., Goel, B.: Prediction ofglobal solar radiation using artificial neural network. Int. J. Adv. Res. Electr. Electron. Instrum. Eng. **2**, 5170–5175 (2013)
18. Aghmadi, A., El Hani, S., Elbouchikhi, E., Naseri, N., Elharouri, K.: Prediction global solar radiation using ANN model based on meteorological data in Morocco. In: 8th International Conference on Power Science and Engineering, pp. 50–54 (2019)

MI EEG Signal Classification for Operation of a Lower Limb Exoskeleton Based on Cross-Correlation and Wavelet Features

Ganesh Roy and **Subhasis Bhaumik**

Abstract The study related to brain–computer interface (BCI) technology is a popular research topic in the present day. The primary objective of a BCI system is to identify the different activities from the recorded electroencephalography (EEG) signal. In the present paper, a four class motor imagery (MI) EEG signal is classified using two feature extraction methods, namely cross-correlation and wavelet energy. The extracted feature vector obtained from the two methods are fed to a linear discriminant analysis (LDA) classifier to obtain the performance accuracy. Binary as well as multiclass classification accuracies are tested through the algorithm. The best average binary class accuracy is obtained as 100%, and the best multiclass average accuracy is 99.86%. After a comparative analysis, it is evident that the wavelet energy method is one of the superior techniques of feature extraction from MI-based EEG data.

Keywords EEG signal · BCI · Wavelet · Cross-correlation · Classification algorithm

1 Introduction

In the field of brain–computer interfacing (BCI), the human brain is connected with a computer through a non-physiological connection. The most suitable form of the brain signal acquisition technique is EEG, where the signals are collected using non-invasive or invasive approach from a human brain. After accessing the raw EEG signal, it is required to process with suitable algorithm to establish a controlling action of an external electromechanical device with the desire of a user [1, 2]. Lower

G. Roy (✉) · S. Bhaumik
Department of Aerospace Engineering and Applied Mechanics, Indian Institute of Engineering Science and Technology, Shibpur, Howrah, India
e-mail: g.roy@cit.ac.in

G. Roy
Department of Instrumentation Engineering, Central Institute of Technology, Kokrajhar, Assam, India

247

limb exoskeleton is one of the best examples for an electromechanical device, which is greatly used in the medical rehabilitation area to provide as a supportive device for the patients who are unable to walk due to spinal cord injury, sports injury, etc. The motivation behind the present research work is to solve the problem of the lower limb-disabled people who are not able to walk although their motor imagery part of the brain is perfectly active to generate the required signal for their lower limb motion. The MI signals that generate from the motor cortex area of the human brain due to the imagination or real movement of the body parts are used to trigger the exoskeleton device. Review works based on BCI-controlled lower limb exoskeleton summarize the procedure exclusively [3, 4]. The primary important step of a BCI system is to obtain suitable sets of feature from the unprocessed EEG signals. After that, the feature vector has been fed to a classifier to identify the events that are associated with the raw signals. The research related to feature extraction and classification is very popular within the biomedical research community. As an example, four feature extraction methods-based comparative study has been proposed in a recent work by Roy et al. [5]. The four feature extraction methods are Haar wavelet energy, band power, cross-correlation, and spectral entropy-based cross-correlation. Similarly, cross-correlation is also used in the works mentioned in [6–9]. A method of energy entropy is used in [10]. Wavelet packet transformation technique is used to determine Renyi min-entropy feature for a multiclass EEG signals [11]. MI tasks are also classified using common spatial pattern (CSP) and long short-term memory (LSTM)-based network with optical predictor [12].

In this paper, four class MI database (left hand, right hand, foot, and tongue movement) has been utilized. Two different features extraction methods, viz. cross-correlation and wavelet energy have been used for obtaining the feature vector. Linear discriminant analysis (LDA) algorithm has been used to classify the feature vector to recognize the four MI events. The paper has been divided into five subsections. Section 2 describes the methods utilized in this paper. Results have been tabulated in Sect. 3. The discussion related to the obtained results is provided in Sect. 3. Finally, Sect. 4 discusses about the conclusion of the work.

2 Materials and Methods

The general procedure to classify the raw EEG signals is divided into four major steps as shown in Fig. 1. Each and every steps are elaborated in the following subsections.

2.1 Raw EEG Signals

The database is collected from BCI competition III (IIIa) [13]. The database contains four class MI-related EEG signals. A group of 60 channels was attached on the head of a subject during the data recording period. Neuroscan EEG amplifier of 64 channels
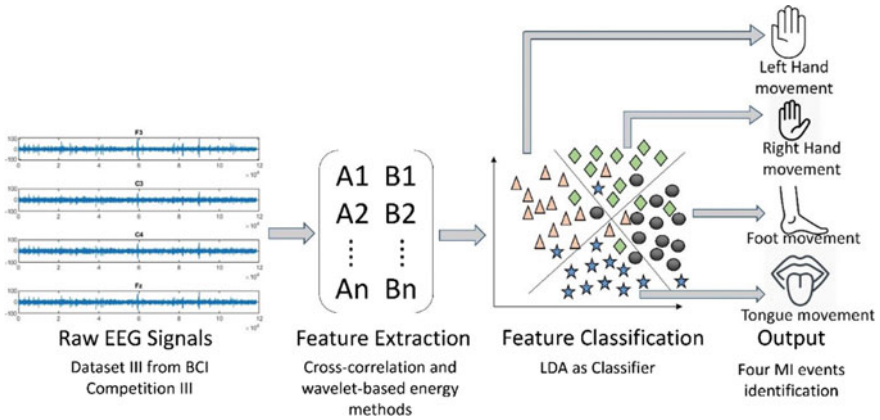
Fig. 1 General procedure for EEG signal processing

is used for necessary signal processing. The sample frequency of the signal is 250 Hz. The visual cue is considered for 7 s. Initially, there is a blank screen for 2 s. At 2 s a beep sound would be provided. A fixation cross would be in the screen associated with direction arrow for 3–7 s. Total 240 trials are made for the combination of four events (60 trials each). The thinking of the movement of the left hand (L), the right hand (R), the foot (F), and the tongue (T) is recorded by following the timing protocol.

2.2 Feature Extraction

Two groups of features have been extracted from the recorded EEG signal. The first group describes about the cross-correlation technique, whereas the second method deals with the wavelet transformation method.

Cross-Correlation. The specialty for this technique is that it can be useful for noise-free data and contains discriminative information. Initially, four class recorded data from the 60 channel/column have been separated and created a new dataset for 240 column. The Fp1 (channel name) electrode is selected as a reference signal for the cross-correlated equation. The mathematical equation based on the method is described as below.

$$R_{xy}(n) = \sum_{i=0}^{M-|n|-1} x(i)y(i-n) \qquad (1)$$

where $n = -(M-1), -(M-2), \ldots 0, 1, 2, \ldots (M-2), (M-1), M = $ number of sample, R_{xy} is the cross-correlated output between reference channel (x) and other channel (y).

Therefore, if the first column is selected as the reference signal, the cross-correlated operation produced results of a 239 column out of its 240 combinations. This new dataset becomes a dimension of $(118{,}570 \times 239)$. This is a large-dimensional data, which is also specious to classify. To reduce the dataset, the selected features are extracted from the database. The mean, median, mode, standard deviation, maximum values, and minimum values are the selected features for the present testing feature variables. The set of features obtained from this method is given in Fig. 2a as scatter plot. Actually, the target is not only to reduce the volume of the data but also to classify with the algorithm so that it can accurately separate out the signals from this small set of data. The box plot shows the four different classes with respect to each selected feature. From Fig. 2b, it is observable that mean and median features can differentiate the four classes from each other very efficiently. Mode is also a good measure to separate the individual class. But standard deviation, maximum value, and minimum value are not beneficial for separating the three classes like 2, 3, and 4. They have pointed out similar measurement for these three classes.

Wavelet Energy. A six-level wavelet energy has been determined using Haar method. One approximate coefficient and six detailed coefficients are obtained using this method. The total energy has been derived by adding the individual energy components. In this procedure also, six statistical features have been calculated for reduction of the feature vector dimension. The feature sets are drawn as a scatter plot in Fig. 3a. The box plot obtained from the method is shown in Fig. 3b.

It is clearly visible from the box plot of the two feature extraction methods that the wavelet energy can clearly separate the four events when compared with the cross-correlation technique.
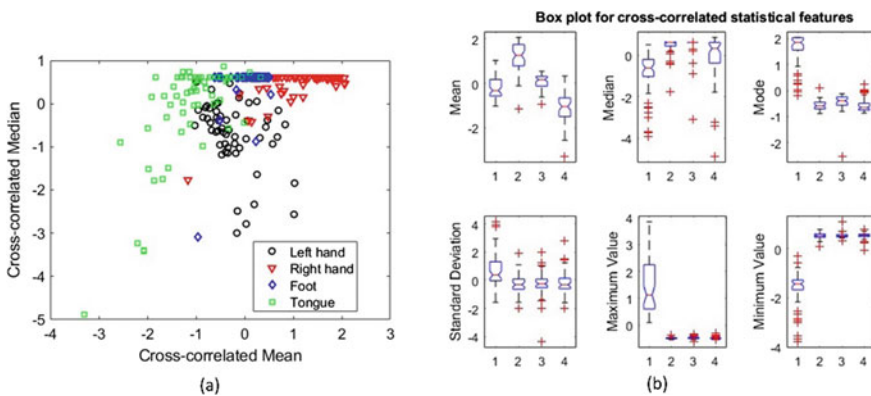
Fig. 2 **a** Four class scatter plot for cross-correlated feature set (subject k3b), **b** box plot for six cross-correlated feature sets (subject k3b), where 1, 2, 3, and 4 represent the left hand, the right hand, the foot, and the tongue-related MI EEG signals
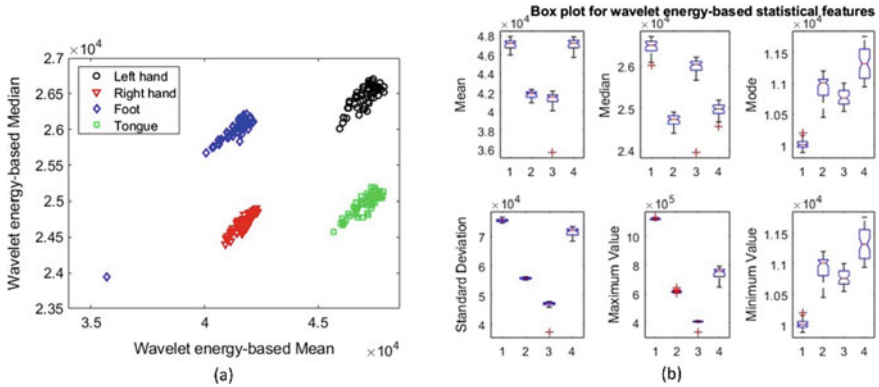
Fig. 3 **a** Four class scatter plot for wavelet energy feature set (subject k3b) and **b** box plot for six wavelet energy feature sets (subject k3b), where 1, 2, 3, and 4 represent the left hand, the right hand, the foot, and the tongue-related MI EEG signals

2.3 Feature Classification

The LDA classification machine learning algorithm is used for this current work. Initially, the process of LDA was first described by Duda et al. [14]. The classification boundaries for cross-correlated feature sets and wavelet energy-based feature sets are shown in Figs. 4 and 5, respectively.
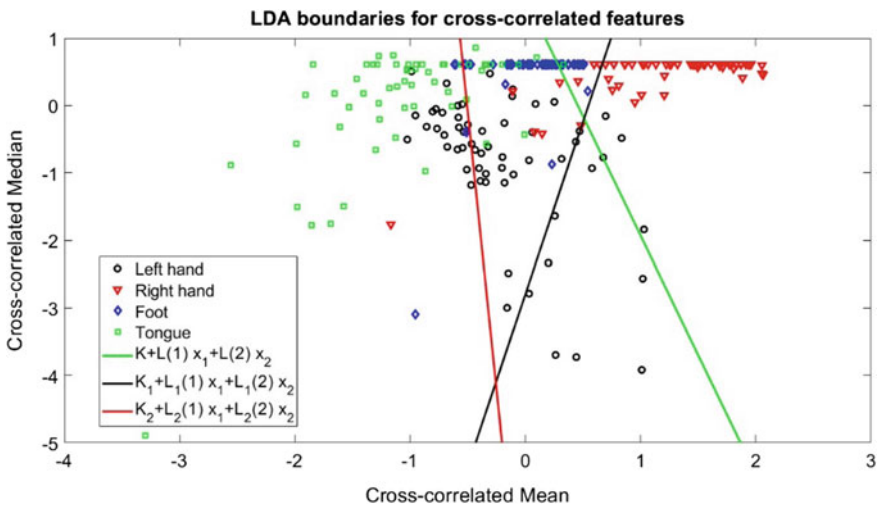
Fig. 4 LDA classification boundaries for cross-correlation features
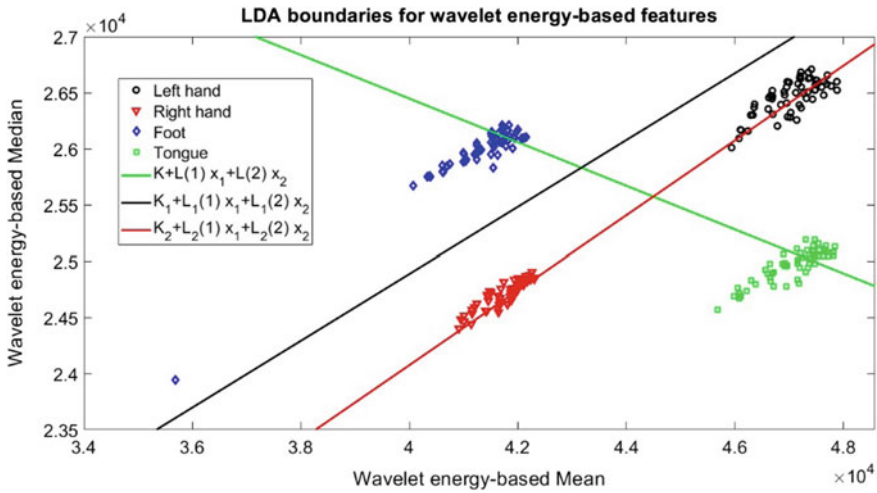
Fig. 5 LDA classification boundaries for wavelet energy features

3   Results and Discussions

The performance of the LDA classifier has been obtained by measuring the tenfold cross-validation accuracy. The feature sets generated by following cross-correlation and wavelet energy methods are used as input to the classifier. The results have been obtained using two ways, viz. binary class and multiclass. The binary class accuracy performance is provided in Tables 1, 2, and 3 for the subject named k3b, k6b, and l1b, respectively. Table 4 contains the results associated with multiclass (four class) classification.

A comparative analysis has been obtained by following three techniques (energy entropy, cross-correlation, and wavelet energy). The result is shown in Table 5, where the best performance accuracy is obtained using wavelet energy feature extraction method.

Table 1 Binary class tenfold cross-validation classification accuracy for LDA classifier (k3b)

Subjects	Class combinations	Cross-correlation-based classification accuracy (%)	Wavelet-based classification accuracy (%)
k3b	LR	94.12	100
	LF	88.24	100
	LT	83.19	100
	RF	88.33	100
	RT	96.33	100
	FT	85.00	100

Table 2 Binary class tenfold cross-validation classification accuracy for LDA classifier (k6b)

Subjects	Class combinations	Cross-correlation-based classification accuracy (%)	Wavelet-based classification accuracy (%)
k6b	LR	69.75	100
	LF	71.43	100
	LT	75.63	100
	RF	68.33	100
	RT	70.00	78.33
	FT	77.50	87.08

Table 3 Binary class tenfold cross-validation classification accuracy for LDA classifier (l1b)

Subjects	Class combinations	Cross-correlation-based classification accuracy (%)	Wavelet-based classification accuracy (%)
l1b	LR	94.96	99.17
	LF	92.44	99.17
	LT	94.12	100
	RF	72.50	100
	RT	64.17	100
	FT	65.83	100

Table 4 Multiclass tenfold cross-validation classification accuracy for LDA classifier

Subjects	Cross-correlated feature set accuracy (%)	Wavelet-based feature set accuracy (%)
k3b	89.96	100
k6b	73.22	100
l1b	65.27	99.58
Average	76.15	99.86

Table 5 Comparative study based on average classification accuracy

Sl. No.	Class combination	Accuracy based on energy entropy (%) (Dan Xiao et al.)	Accuracy based on cross-correlation (%) (proposed)	Accuracy based on wavelet energy (%) (proposed)
1	LR	84.4	86.27	99.72
2	LF	87.0	84.03	99.72
3	LT	82.4	84.31	100
4	RF	85.4	76.38	100
5	RT	82.8	76.83	92.77
6	FT	88.0	76.11	95.69

4 Conclusion

In this paper, a multiclass EEG signal is classified using two feature extraction methods, namely cross-correlation and wavelet energy. A popular classifier algorithm called LDA has been used to obtain the tenfold cross-validation accuracy. The best average accuracy obtained for multiclass and binary class is 99.86% and 100%, respectively. A 60-channel MI EEG database has been considered as a raw signal for the present work. After the comparative analysis with the published work, it is observed that the wavelet energy feature extraction method ranked top among the three techniques. Hence, using the proposed technique, a BCI design process can be improved further to identify the human MI-related activities more accurately.

References

1. Wang, C., Wu, X., Wang, Z., Ma, Y.: Implementation of a brain-computer interface on a lower-limb exoskeleton. IEEE Access **6**, 38524–38534 (2018)
2. Tariq, M., Trivailo, P.M., Simic, M.: EEG-based BCI control schemes for lower-limb assistive-robots. Front. Hum. Neurosci. **12**, 312 (2018)
3. Al-Quraishi, M.S., Elamvazuthi, I., Daud, S.A., Parasuraman, S., Borboni, A.: EEG-based control for upper and lower limb exoskeletons and prostheses: a systematic review. Sensors **18**(10), 3342 (2018)
4. Zhang, J., Wang, M.: A survey on robots controlled by motor imagery brain–computer interfaces. Cogn. Rob. (2021)
5. Roy, G., Bhoi, A.K., Bhaumik, S.: A comparative approach for MI-based EEG signals classification using energy, power and entropy. IRBM (2021). https://doi.org/10.1016/j.irbm.2021.02.008
6. Chandaka, S., Chatterjee, A., Munshi, S.: Cross-correlation aided support vector machine classifier for classification of EEG signals. Expert Syst. Appl. **36**(2), 1329–1336 (2009)
7. Siuly, S., Li, Y.: Improving the separability of motor imagery EEG signals using a cross correlation-based least square support vector machine for brain–computer interface. IEEE Trans. Neural Syst. Rehabil. Eng. **20**(4), 526–538 (2012)
8. Verma, N.K., Rao, L.V.S., Sharma, S.K.: Motor imagery EEG signal classification on DWT and cross correlated signal features. In: 2014 9th International Conference on Industrial and Information Systems (ICIIS), pp. 1–6. IEEE (2014)
9. Roy, G., Nirola, D., Bhaumik, S.: An approach towards development of brain controlled lower limb exoskeleton for mobility regeneration. In: 2019 IEEE Region 10 Symposium (TENSYMP), pp. 385–390. IEEE (2019)
10. Xiao, D., Mu, Z., Hu, J.: Classification of motor imagery EEG signals based on energy entropy. In: 2009 International Symposium on Intelligent Ubiquitous Computing and Education, pp. 61–64. IEEE (2009)
11. Rahman, M.A., Khanam, F., Ahmad, M., Uddin, M.S.: Multiclass EEG signal classification utilizing Rényi min-entropy-based feature selection from wavelet packet transformation. Brain Inform. **7**(1), 1–11 (2020)
12. Kumar, S., Sharma, A., Tsunoda, T.: Brain wave classification using long short-term memory network based OPTICAL predictor. Sci. Rep. **9**(1), 1–13 (2019)
13. BCI Competition III, Data sets IIIa. http://www.bbci.de/competition/iii/#data_set_iiia. Last accessed 20 Nov 2019
14. Duda, R.O., Hart, P.E., Stork, D.G.: Pattern Classification, 2nd edn. Wiley, New Delhi (2006)

Implementation of Offset Injection PWM Technique for Grid Integration

G. Renuka Devi , **S. Yuvaraja, and M. Syed Abdul Salam**

Abstract This paper addresses the offset injection-based PWM technique for grid integration. In the MATLAB/Simulink environment, the grid-tied inverter is developed. The sinusoidal pulse width grid-tied inverter is developed and studies the performance in terms of output current and THD. Compared to SPWM technique, the offset injection PWM technique provides low harmonic current, and power factor is improved, enhancing power management capability, improving storage capacity and to extract maximum power. The proposed offset injection is presented in steady-state and dynamic conditions. The existing and proposed technique performance is analyzed in different step change conditions and identifies the method suitable for grid integration.

Keywords Grid-tied inverter · Offset injection · Pulse width modulation · Total harmonic distortion

1 Introduction

The utilization of electrical energy in the world is growing drastically, and on the other side, depletion of fossil fuels is taking place. The world needs alternative sources which are abundant and ease of availability in nature such as PV, wind, tidal, in which solar PV energy is one of the favorable energy sources. With an increasing projected energy requirement and current power of coal electrification, India plays a vital role in universal carbon policies and the upcoming low-carbon revolution. In 2015, India emitted 1869 Mt CO_2 in the whole, of which 51% received from heat and power generation. At present, the Central Electricity Authority of India (CEA) projects total expected CO_2 emissions of 983 million tons for the year 2021–2022 and

G. Renuka Devi (✉)
Department of Robotics and Automation, Manakula Vinayagar Institute of Technology, Kalitheerthalkuppam, Puducherry, India

S. Yuvaraja · M. Syed Abdul Salam
Department of Electronics and Communication Engineering, M.A.M. College of Engineering & Technology, Trichy, Tamil Nadu, India

1165 million tons for the year 2026–2027. India submitted its Intended Nationally Determined Contribution (INDC) on October 1, 2015. On the nationwide stratum for India, it involves three main objectives to achieve this agreement: to reduce the emissions per gross domestic product (GDP) output by 33–35% by 2030 from the 2005 levels, to increase the growing electric power installed capacity from renewable energy resources up to 40% by 2030 and to produce an additional carbon which goes under of 2.5–3 billion tons of CO_2 equivalent through supplementary tree and forest covered by 2030.

The power quality is being an important concern while connecting any energy resource to the grid, and the power electronic interface plays a prominent role in the power quality control. Multilevel inverters play a major role for power quality control in terms of DC bus voltage utilization, fundamental voltage, THD and efficiency. But these inverters lead to increased circuit complexity, a greater number of switches and associated losses. DC link capacitor voltage unbalancing issues will occur. Thus, practically a two-level inverter is more generic and simpler in terms of circuit complexity. The three-phase two-level inverter has needed six IGBT switches. The lower order harmonics are obtained with the help of PWM technique with high frequency operating switches. The most commonly used PWM techniques are sinusoidal pulse width modulation technique (SPWM) and space vector pulse width modulation (SVPWM) technique. While doing control technique, parallel controller is needed; thus, it reads a DC sample very fast and reacts in algorithm in a nanosecond time period. So for cost-effective solution to stick on with two-level inverter, a new pulse width modulation (PWM) method by combining modified SVPWM and hysteresis current control can be proposed. It provides improved power factor, less harmonics and low ripple at neutral voltage which leads to more efficiency. And by using single FPGA controller, due to its parallel operation, we can interface all power electronic components in micro-grid setup. So micro-grid needs can be fulfilled such as THD, PF, power management, storage and measurement and MPPT, and SVPWM technique-based three-phase inverter is simulated and experimentally validated in dq-PLL algorithm. Using this method, grid synchronization is attained in [1–3]. Islanded and grid connected mode of operation for DC micro-grid is analyzed, and suggested AC voltage regulation and inner current loop for dual proportional integral controllers in D-Q frame are analyzed [4]. Importance of renewable energy sources, grid integration and grid impedance estimation is discussed in [5–7]. Different control strategy with stability enhancement for nonlinear load is elaborated in [8]. Power quality improvement using three-phase grid-tied inverter with linear and nonlinear load conditions with new control perception is analyzed in [9, 10]. Different PWM switching techniques and optimum technique for grid integration are discussed in [11–15].

The main objective of the paper is to improve the power quality of grid side inverter by using simple PWM techniques. To maintain the unity power factor and attain the less than 5% THD, offset injection technique places a major role in grid integration.

2 Solar PV-Based Grid-Tied System

Figure 1 shows the existing sinusoidal pulse width modulation-based solar PV grid-tied three-phase inverter. Figure 2 shows the proposed offset injection PWM-based solar PV grid-tied three-phase inverter. Initial input supply is given to the boost converter with the help of solar PV panels. The output of DC supply is fed to the three-phase inverter. The inverter switches are triggered with the help of offset injection PWM. The output of three-phase supply is controlled with the help of offset injection PWM technique. The current controller is used to monitor and control the current injected to the grid to obtain the nearly sinusoidal current and power factor making to
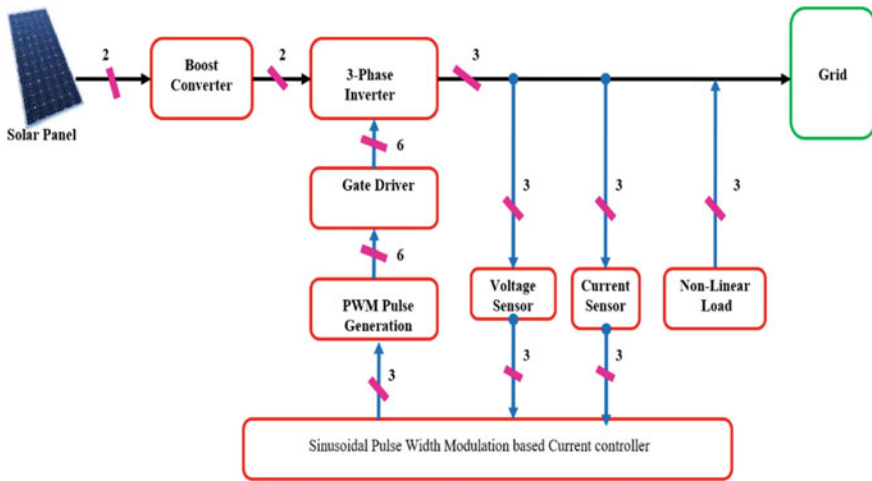
Fig. 1 SPWM-based solar PV grid-tied three-phase inverter
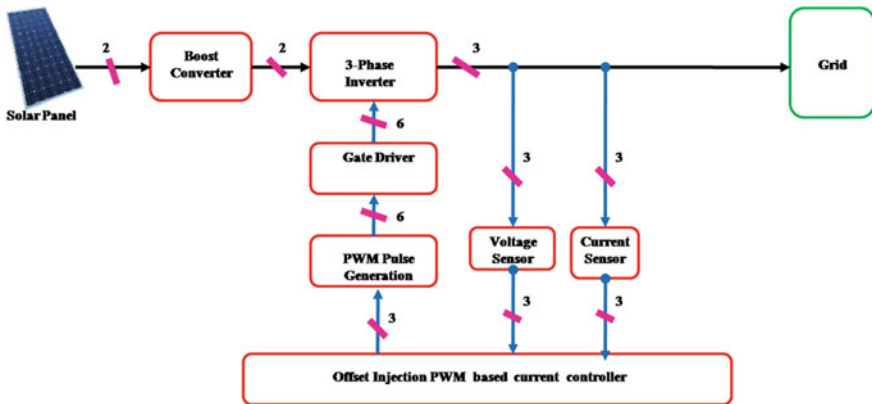
Fig. 2 Offset injection PWM-based solar PV grid-tied three-phase inverter

unity. Simulation is carried out for both the techniques and finds the optimum method used for grid integration. The SPWM and offset injection technique is discussed in the next section.

3 Sinusoidal Pulse Width Modulation Technique (SPWM)

Carrier-based SPWM is the most popular and widely used PWM technique because of its simple implementation in both analog and digital realization. The PWM signal is generated by comparing a sinusoidal signal with high-frequency carrier signal. In three-phase VSI, three reference signals (1) displaced by $2\pi/n°$ are compared with carrier waveform to generate pulses for inverter switches. The modulation index (MI) is the control parameter of the inverter which adjusts the output voltage according to the amplitude of the reference waveform. Modulation index is the ratio of peak magnitudes of the modulating waveform and the carrier waveform as given by Eq. (2).

$$
\begin{aligned}
v_a &= v \cos wt \\
v_b &= v \cos(wt - \alpha) \\
v_c &= v \cos(wt - 2\alpha)
\end{aligned}
\tag{1}
$$

where $\alpha = 2\pi/n$

$$
\text{MI} = \frac{V_{\text{ref}}}{V_{\text{car}}}
\tag{2}
$$

where MI is the modulation index. In the linear modulation range, MI is restricted to $0 \leq \text{MI} \leq 1$. When the peak magnitude of modulating signal exceeds the peak magnitude of carrier signal (resulting in MI > 1), the PWM inverter operates under over-modulation. Generally, over-modulation is not preferred because of the introduction of lower-frequency harmonics in the output waveform and subsequent distortion of the load current. When MI > 1, some other techniques are used to obtain the output voltage without moving into over-modulation range, and it is discussed in the following sections.

4 Offset Injection PWM Technique

In the proposed technique, a modified SVPWM approach [12] is developed by using the model of offset time for a three-phase VSI. It does not require a lookup table, sector identification, angle information and voltage space vector amplitude measurement. In the offset injection method, signal making only depends upon the sampled reference phase amplitude and the sampling period. The time duration for different voltages is

maintained completely related to the voltage modulation task according to the equal volt–second principle. Therefore, the modulation task can be greatly simplified by considering the relation between the time duration and the output voltage. For that purpose, introduce an imaginary time value. This value is directly related to the phase voltage and sampling time (T_s), as defined in (3)–(10).

$$V_{as}{}^* : V_{dc} = T_{as} : T_s \Rightarrow T_{as} = \frac{T_s}{V_{dc}} V_{as}{}^*$$

$$V_{bs}{}^* : V_{dc} = T_{bs} : T_s \Rightarrow T_{bs} = \frac{T_s}{V_{dc}} V_{bs}{}^*$$

$$V_{cs}{}^* : V_{dc} = T_{cs} : T_s \Rightarrow T_{cs} = \frac{T_s}{V_{dc}} V_{cs}{}^* \tag{3}$$

where V_{as}, V_{bs} and V_{cs}, are the (a, b, c) reference phase voltages, respectively. T_{as}, T_{bs} and T_{cs} are the imaginary switching times of respective phases. Now, the effective time or offset time (T_{offset}) can be defined as the time duration between the smallest and the largest of n-imaginary times, as given by

$$T_{offset} = T_{max} - T_{min} \tag{4}$$

$$T_{max} = \max\{T_{as}, T_{bs}, T_{cs}, T_{ds}, T_{es}, \ldots, T_{xs}\}$$
$$T_{min} = \min\{T_{as}, T_{bs}, T_{cs}, T_{ds}, T_{es}, \ldots, T_{xs}\} \tag{5}$$

The offset time T_{offset} should satisfy the following constraint.

$$0 \leqslant T_{min} + T_{offset},\ T_{max} + T_{offset} \leqslant T_s \tag{6}$$

Therefore, the range of T_{offset} can be computed as follows:

$$T_{min\ offset} \leqslant T_{offset} \leqslant T_{max\ offset} \tag{7}$$

where

$$T_{min\ offset} = -T_{min}$$
$$T_{max\ offset} = T_s - T_{max} \tag{8}$$

$$T_{offset} = 0.5(T_{max\ offset} + T_{min\ offset}) \tag{9}$$

$n =$ number of phases.

When the actual gating signals for power devices are generated in the PWM algorithm, there is one degree of freedom by which the effective time can be relocated anywhere within the sampling interval. Therefore, a time-shifting operation will be applied to the imaginary switching times to generate the actual gating times (T_{ga},

T_{gb}, T_{gc}), for each inverter pole.

$$T_{ga} = T_{as} + T_{\text{offset}}$$
$$T_{gb} = T_{bs} + T_{\text{offset}}$$
$$T_{gc} = T_{cs} + T_{\text{offset}} \qquad (10)$$

5   Simulation Results

A simulation is performed in order to prove the efficiency of grid-tied inverter-fed induction motor in terms of output voltage, output current and THD. The simulation model is developed in MATLAB/Simulink environment. Simulation results are obtained for SPWM and offset injection method. In the simulation, the output of solar PV is set to 450 V, and the modulation index M is set to 1. The switching frequency of the VSI is chosen as 1 kHz, and the reference fundamental frequency is kept equal to 50 Hz. The simulation model of grid-tied inverter is carried out with sinusoidal PWM technique and offset injection PWM technique. Figure 3 shows the SPWM-based grid-tied inverter results. From the observation in the existing method, current THD is 2.02%, but the output is nearly sinusoidal. Figure 4 shows the range of the available $T_{\text{max offset}}$ and $T_{\text{min offset}}$ and T_{offset}, respectively, when the modulation index is 0.9. Figure 5 represents the $T_{\text{min offset}}$ and $T_{\text{max offset}}$ with a variation of the modulation index from 0.2 to 1.0515. According to Fig. 5, $T_{\text{max offset}}$ and $T_{\text{min offset}}$ intersect with each other having the maximum modulation index point (1.0515) of offset injection method. Figure 6 shows the dynamic variation of offset injection-based grid voltage and current. Figure 7 represents the offset injection-based grid-tied inverter with current THD as 1.53%. Compared to the existing method in the proposed method, current THD is minimum, and output current is sinusoidal. Figure 8 shows the hardware results of grid voltage, current, frequency and THD.

6   Conclusion

An offset injection-based PWM technique for grid integration is presented in this paper. The simulation model is developed using simpower system block set of the MATLAB/Simulink software. The sinusoidal PWM and offset injection-based grid-tied inverter is analyzed in terms of output current and THD. From the results, it is found that the minimum THD (1.53%) is observed in the offset injection method. This offset injection method provides low harmonic current, maintains unity power factor and increases the inverter efficiency. So proposed PWM technique is optimum for grid integration.
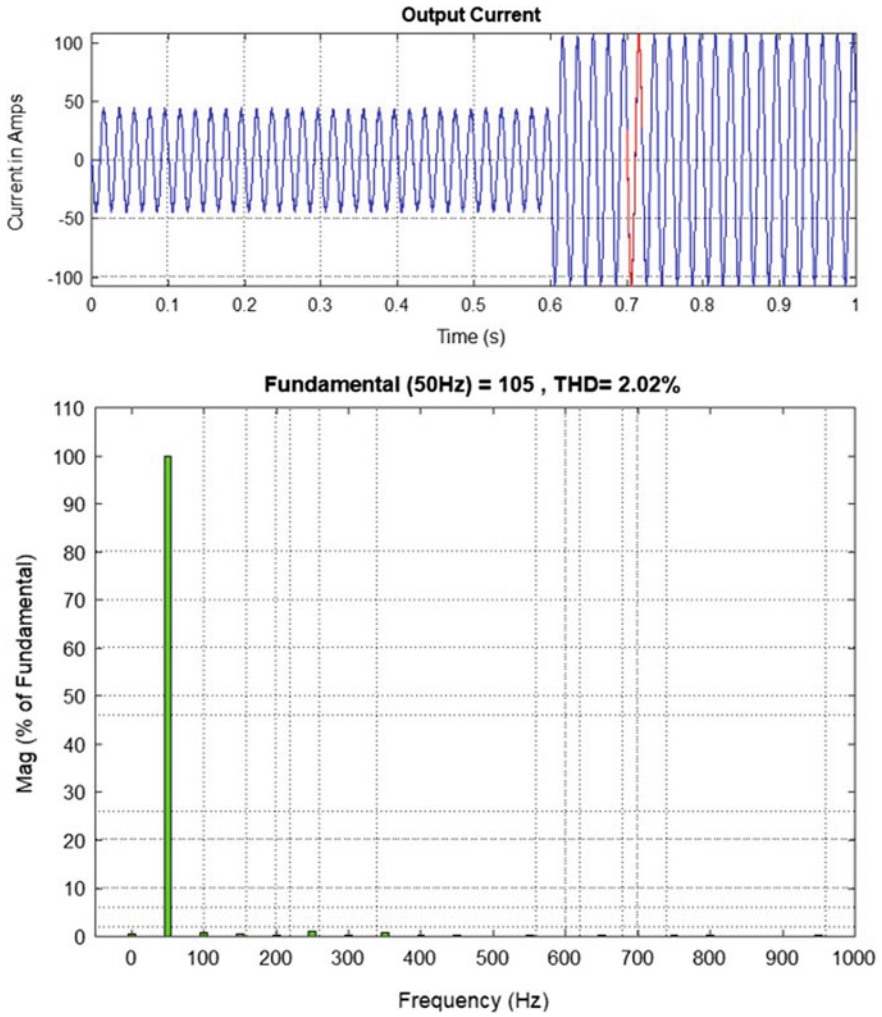
Fig. 3 Grid current and THD for the SPWM scheme
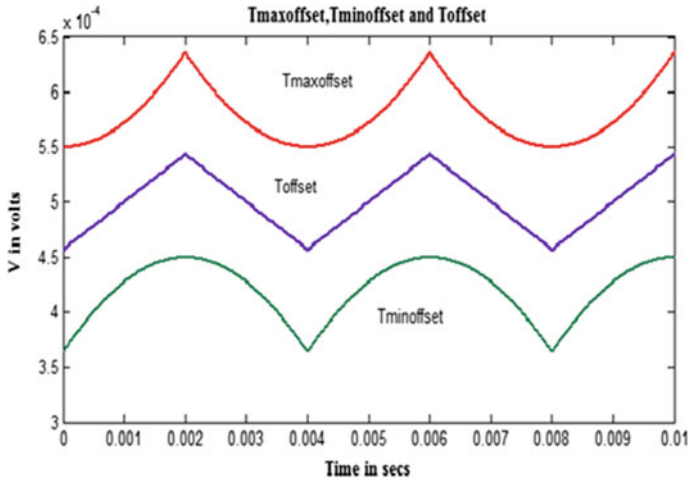
Fig. 4 $T_{\text{max offset}}$, $T_{\text{min offset}}$ and T_{offset} at MI-0.9
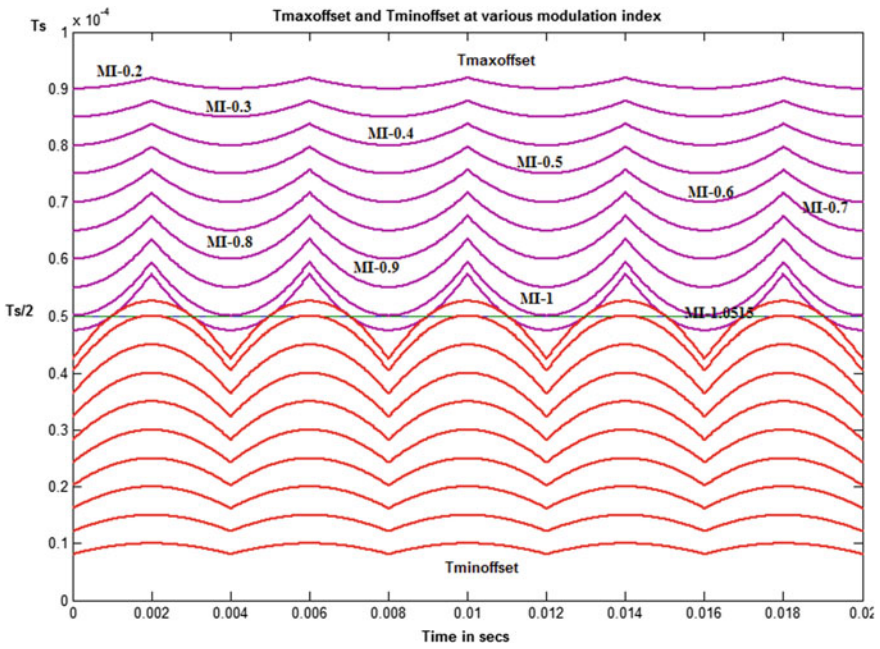
Fig. 5 $T_{\text{max offset}}$ and $T_{\text{min offset}}$ for varying modulation indices
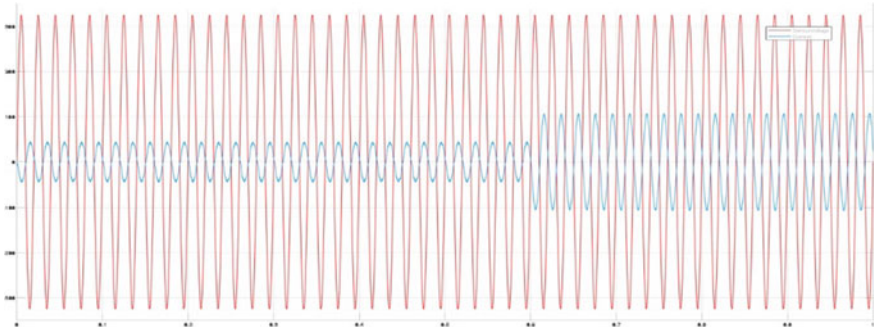
Fig. 6 Dynamic variation of offset injection-based grid voltage and current
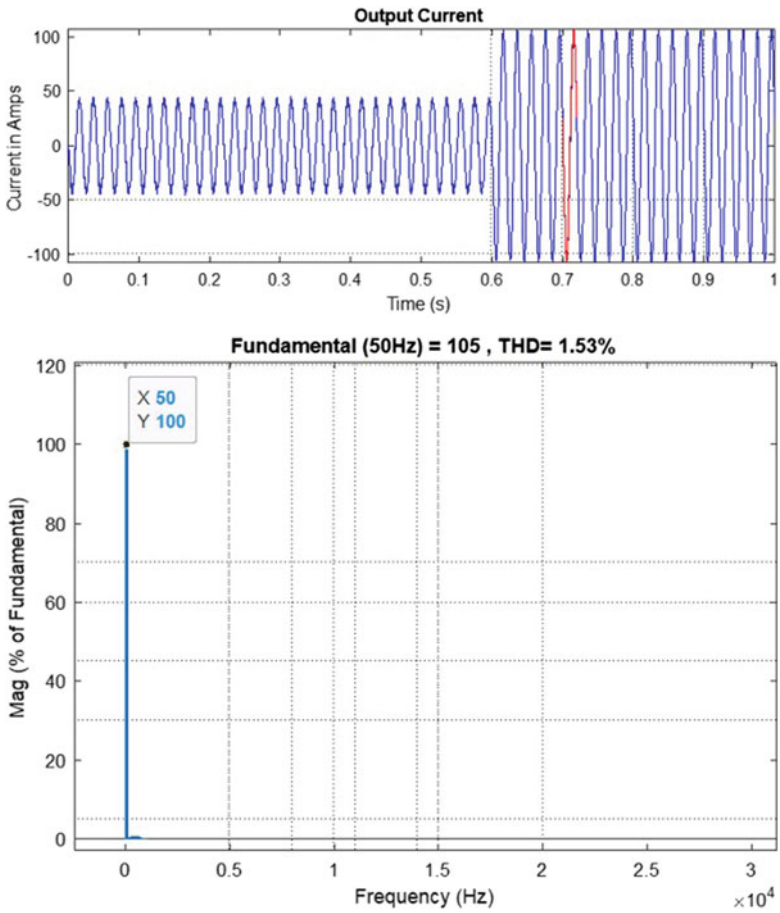
Fig. 7 Grid current and THD for the offset injection PWM scheme
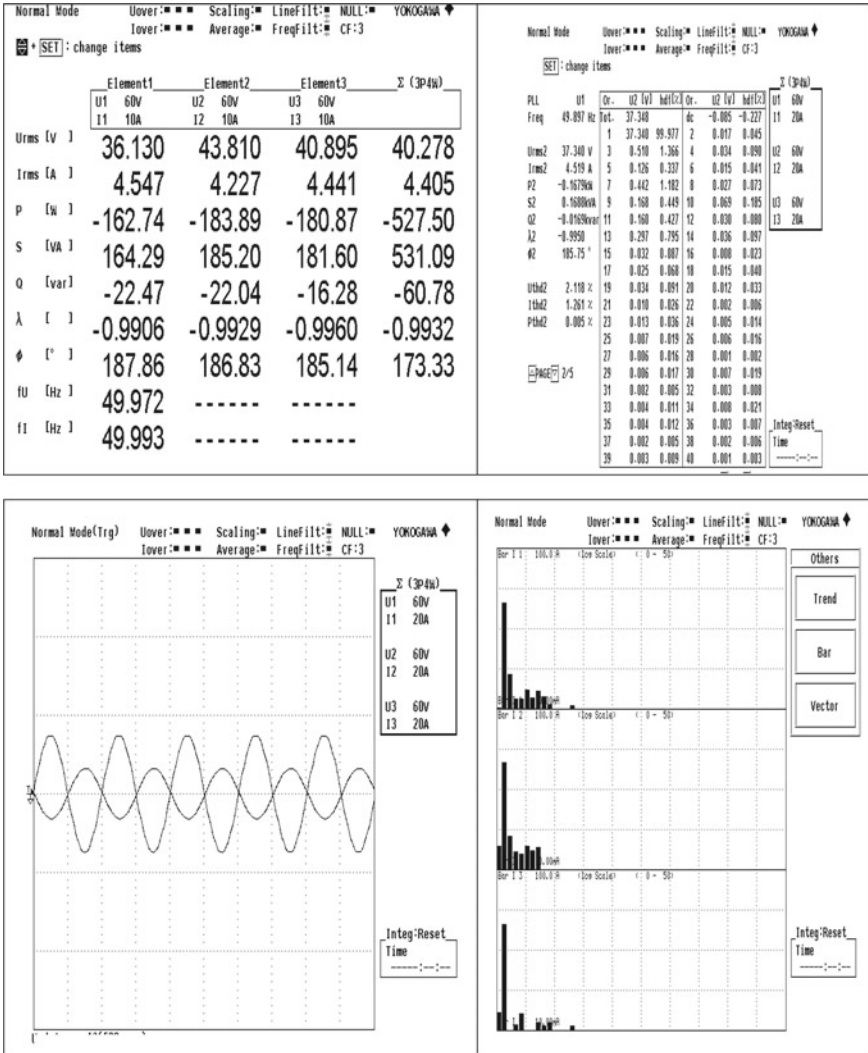
Fig. 8 Real-time implementation of grid voltage, current, frequency and THD

References

1. Sevilmiş, F., Karaca, H.: An experimental study of grid tied inverter for renewable energy systems. IEEE (2018)
2. Sevilmiş, F., Karaca, H.: Simulation of three-phase grid interactive inverter for wind energy systems. In: IEEE 15th International Conference on Environment and Electrical Engineering, Italy, pp. 1169–1174 (2015)
3. Sevilmiş, F.: Grid synchronization of wind energy systems. Ms. Thesis, The Graduate School of Natural and Applied Science of Selçuk University, Jan 2016, p. 1

 4. Kumar, M., Srivastava, S.C., Singh, S.N.: Control strategies of a DC microgrid for grid connected and islanded operations. IEEE Trans. Smart Grid **6**(4), 1588–1601 (2015)
 5. Liserre, M., Sauter, T., Hung, J.Y.: Future energy systems: integrating renewable energy sources into the smart power grid through industrial electronics. IEEE Ind. Electron. Mag. **4**, 18–37 (2010)
 6. Beres, R.N., Wang, X., Liserre, M., Blaabjerg, F., Bak, C.L.: A review of passive power filters for three-phase grid-connected voltage source converters. IEEE J. Emerg. Sel. Top. Power Electron. **4**, 54–69 (2016)
 7. Ciobotaru, M., Teodorescu, R., Rodriguez, P., Timbus, A., Blaabjerg, F.: Online grid impedance estimation for single-phase grid connected systems using PQ variations. In: Power Electronics Specialists Conference, 2007. PESC 2007, pp. 2306–2312. IEEE (2007)
 8. Ashabani, S.M., Mohamed, Y.A.-R.I.: A flexible control strategy for grid-connected and islanded microgrids with enhanced stability using nonlinear microgrid stabilizer. IEEE Trans. Smart Grid **3**(3), 1291–1301 (2012)
 9. Li, Y., Vilathgamuwa, D.M., Loh, P.C.: Microgrid power quality enhancement using a three-phase four-wire grid-interfacing compensator. IEEE Trans. Ind. Appl. **41**(6), 1707–1719 (2005)
10. Singh, M., Khadkikar, V., Chandra, A., Varma, R.K.: Grid interconnection of renewable energy sources at the distribution level with power quality improvement features. IEEE Trans. Power Delivery **26**(1), 307–315 (2011)
11. Iqbal, A., Lamine, A., Ashraf, I., Mohibullah: Matlab/Simulink model of space vector PWM for three-phase voltage source inverter. In: IEEE Proceedings of the 41st International Conference on Universities Power Engineering UPEC'06, UK, vol. 3, pp. 1096–1100 (2006)
12. Renuka Devi, G., Rajambal, K.: Performance investigation of multi-phase VSI with simple PWM switching techniques. Int. J. Eng. **26**(3), 289–296 (2013)
13. Renuka Devi, G., Rajambal, K.: Comparison of different PWM schemes for n-phase VSI. In: IEEE International Conference on Advances in Engineering, Science and Management (IEEE-ICAESM 2012), pp. 559–564, Nagapattinam, India, 30, 31 Mar 2012
14. Lee, J.-S., Lee, K.-B.: Time-offset injection method for neutral. IEEE Trans. Power Electron. **31**(3), 1931–1941 (2016)
15. Renuka Devi, G., Rajambal, K.: Comparative analysis of 5th harmonic injection and SVPWM technique for five-phase VSI. In: IEEE—International Conference on Research and Development Prospectus in Engineering and Technology—ICRDPET 2013, EGS Pillay Engineering College, Nagapattinam, vol. 2, pp. 92–97, 29, 30 Mar 2013

An End-to-End Topic-Based Sentiment Analysis Framework from Twitter Using Feature Set Cumulation

Subhashree Basu, Sourav Das, and Anup Kumar Kolya

Abstract Sentiment analysis from Web resources has been a well popular and cultivated area of research in recent years. However, relating a tweet's sentiment to its particular topic has not been widely explored yet. In this paper, we introduce a framework based on the selection of a new feature set based on information gain and topic extraction from gram selection from the live streamed tweets. We maintain subject topics in tweets from streaming to analyzing them, throughout the entire experimentation pipeline. This helps us to gain insight into the exact sentimental reflection of that particular topic as well as the tweet itself. We build a corpus based on such topic-motivated tweets and subsequently retrieve them to train the system. Followingly, we emphasize selecting distinct features set specifically determined from the nature of the corpus. Here, two feature sets are compared. The first set is bag of words with N-Gram identification. The second set of features is part-of-speech linguistic annotation. We explore comprehensively the choice-dependent decision tree algorithm to train and validate such features. Finally, we develop a Pyplot and Tkinter-based GUI dashboard to provide real-time tweets search and view on any given topic. It introduces two pivotal attributes, a live graph elaborating the popularity and polarity of the search topic with given time.

Keywords Twitter · Sentiment analysis · Topic · Feature selection

S. Basu
West Bengal State Council of Technical & Vocational Education and Skill Development, Kolkata 700013, India

S. Das
Department of Computer Science & Engineering, Future Institute of Technology, Kolkata, West Bengal 700154, India

A. K. Kolya (✉)
Department of Computer Science & Engineering, RCC Institute of Information Technology, Kolkata 700015, India

1 Introduction

In the last decade, natural language research has become inseparably associated with the microblogging Web sites such as Reddit and Twitter. The amount of raw data gathered from people's perspectives, opinions, and outlooks from these sites have become enormous both in size and information [1]. Twitter has become a vital tool for opinion mining and representing the polarity contrasts in election campaigns [2], economic reforms [3], pandemic sentiment analysis [4], and conversation modeling [5] to name only a few. Most of these works dealt with the large volume of data and the sheer complexity involved with it for sentiment extraction. Data collection from Twitter has mostly been focused on two key aspects, i.e., event and topic. A topic determines the popularity as well polarity of any tweets and the surge or declination of such tweets within a period [3].

In this work, we showcase a simple yet robust end-to-end framework for topic-based sentiment and analytical details of related tweets. For topic diversity, we stream live tweets consisting of random hashtags like #covid19, #movies, #entertainment, #president, #pm, #sports, and so on. We use multilabel parameter heads for the filtration of the tweets, to ensure no code-mixed, blank, or null tweets are being collected. At next, we select and deploy two distinct linguistic features as frequent word collection and relating to correspondent part-of-speech tagging for defragmentation of primary feature words, to further classify the tweets. These are good indicators of subjectivity and sentiment. Now for the training purpose for the already classified tweets, we deploy the decision tree algorithm as it provides the option for multistatement choice of branching for the classification of training and testing data. Here, we select the condition whether to associate a tweet with its corresponding topic (hashtag for streaming) and sentiment or not. We group seven categories of individual sentiments for successful train purposes of the tweets representing each category. Next, we develop a Pyplot and Tkinter-based functional user interface. Using this UI, any user can search, retrieve, and see the graphical analytics of tweets on particular topics. Pyplot preserves various states of topics and sentiments across function calls so that it keeps track of things like the figure and plotting area, and the plotting functions are directed to the axes of the parameters.

Our foremost contributions with this work are as follows:

- We showcase not only the sentiment analysis of live tweets but also the relevant topics associated in the form of keywords within the tweets,
- We propose a cumulation of two fundamental feature sets for better classification of tweet topics,
- We represent a system demonstration of an interactable robust user interface for better understandability of the entire framework for visualization of sentiment and topic extraction and also for figurative analytics.

The rest of the sections are organized as: We discuss some of the topic-based dynamic sentiment analysis research in Sect. 2. In Sect. 3, we show the methodology for tweet streaming and preprocessing. In Sect. 4, we show the feature selection and

cumulation, while in Sect. 5, we discuss the training activity using our proposed decision tree model. In Sect. 6, we demonstrate the end user UI of our work for real-time topic-based sentiment analysis of any tweet. Finally, in Sect. 7, we conclude our work with prospect and discussion.

2 Background Works

Topic-based dynamic sentiment analysis is a well broad area of research. In recent years, many works have been carried to address the linear combination of the topic with the sentiment and how it changes dynamically w.r.t time, subjectivity, or event. In a work from 2019 [6], researchers have addressed the issues of sentiment analysis on different events. They have also shown the techniques using natural language processing and how to bridge the gaps between textual content and graph-based of the network. In their work, they used support vector machine (SVM) and logistic regression (LR) machine learning techniques for their work.

Ravichandran et al. [7] have discussed opinion classification of sentence-level using an unsupervised algorithm rather than opinion classification of the topic of each message. They gave their system named bigram item response theory (BIRT). Here, authors have shown their work is different from traditional- and document-level classification. The entire contribution of work is divided into three segments (i) sentiment polarity of the tweet based on lexicon, (ii) Naïve Bayesian-based bigram co-occurrence relationship, and (iii) BIRT model on different topics where they have got a remarkable improvement of performances.

In [8], it is discussed analyzing sentiment needs a huge amount of information from various sources. This information contains a lot of topics on different events. Topics have fused that need to be retrieved with their sentiment. In this paper, the authors' main focus is subjectivity detection in sentiment analysis that means the exclusion of a lack of sentiment word 'neutral' or 'factual' comments from the text. Handcrafted rule performed well for strong sentiments and poor results for weak sentiment in the text. On the other hand, a deep learning-based automatic model with meta-level feature representation done well on new languages and domains whereas multimodal methods combine video and audio from social media data with text information from several kernels.

Ebrahimi et al. [9] developed a supervised multiclass classifier model for analyzing the sentiment about several parties' electoral candidates as giving opinions in the tweets. Here, multiclass means changes of opinion from positive to negative to neutral or vice versa. Finally, they trained their model for each party's representative individually. They used a support vector machine (SVM) with term frequency-inverse document (TF-IDF) for their system. The main goal for this isolation comes from their analysis that the same tweet on an event can be positive for one candidate but can be negative for another candidate.

3   Tweets Streaming

For ensuring the heterogeneity of the streamed tweets, we live streamed 50k mono-lingual (English) tweets of several diverse topics. The hashtag words within most of the tweets are a good indicator of their respective topics, and most of the keywords can be extracted from them. Focusing on whether the tweets are cohesive with their related topics, we take the approach as:

$$T = w_c \left(t_c \sum \kappa_{\text{topic}} \right) \tag{1}$$

Here t_c indicates the tweet body and κ_{topic} indicates the topic of the corresponding tweet. Both are corresponding and directly associated with each other. For, i.e., in a movie review tweet, almost no one uses the hashtag keywords as #economy or #foreignpolicy. Hence, these two parameters that keep the tweets cohesive and relevant to their topics.

Also, both the parameters are representative vector products, as they both have a weightage and capacity to influence (here retweet) the other users. Hence, the associativity is maintained by the vector production.

Now, monitoring the redundancy of the topics is also a pivotal point to measure. Reoccurrence of the topics in a congested space can lead to the streaming and clustering of tweets on similar topics only, even identical tweets too. To determine the topic comparability, we make a dictionary of topics, where:

$$\sum \kappa_{\text{topic}} = \{\kappa_0, \kappa_1, \kappa_2, \kappa_3, \kappa_4, \ldots, \kappa_n\} \tag{2}$$

where

$$\sum \kappa_{\text{topic}}\{\kappa_0 = \kappa_1, \kappa_2, \kappa_3, \kappa_4, \ldots, \kappa_n\}$$
$$\sum \kappa_{\text{topic}}\{\kappa_1 = \kappa_0, \kappa_2, \kappa_3, \kappa_4, \ldots, \kappa_n\}$$
$$.$$
$$.$$
$$.$$
$$\sum \kappa_{\text{topic}}\{\kappa_n = \kappa_0, \kappa_1, \kappa_2, \kappa_3, \ldots, \kappa_{n-1}\} \tag{3}$$

Here every topic word from the collected tweet is inter-compared with the other entries (topics) of the other tweets from the corpus.

3.1   Processing Tweets in JSON

The streaming process returns tweets with several parameters such as location, time, retweet count, deletion history, profile details, and followers in JSON format. Also,

by default, the tweets are known more generically as 'status update' on Twitter. JSON format helps to keep a track of such status updates (tweets) and further edit history. Data in this format is kept as records and can be fetched by any index key. Here, we performed preprocessing tasks such as the conversion of uppercase to lowercase letters tokenization, repetition of letters, removal of stop words, and emoticon replacements. Emoticon replacement is a fairly new approach, where we replace emoticons that are by their polarity by seeing the emoticon dictionary using textblob.

4 Feature Selection

For the feature set selection, we take the approach to relate the frequently appeared words with their part-of-speech tags to identify the actual form of such words. Our proposed features are (a) useful and frequent word election using *n*-gram categorization and (b) part-of-speech tag for manually annotating the defragmentation of the primary components of any sentences.

We select a list of useful and frequent words from the viewpoint of our targeted topics. Here, we extract such words from our preprocessed tweet corpus. We discard any code-mixed tweets and accept only monolingual (English) tweets for the time being. Following that, we relate the parts of speech with these words. This step establishes a transitive relation between the topic words and the part-of-speech tags. We particularly found that the adjectives, adverbs, nouns, and verbs are the overall better indicators of subjectivity and sentiments. Another thing worth mentioning is that negation is another important feature, but complex to interpret. The presence of negation usually changes the perspective of an apparently positive or even neutral statement.

4.1 Feature Set Cumulation

We represent a few feature words in relevance with corresponding tweets and topics in Fig. 1. We maintained the similarity attribute to increasing the training accuracy in a later phase. Also, the subjective expressions with the use of various punctuations and emoticons are representative of the overall sentiment of that tweet.

5 Training and Classification

Our objective is to classify the tweets based on their topics so that the prediction making on real-time UI validation takes place with better efficiency. It can be also termed as prediction making with the help of training data. Our training set comprises

@Sw1_ch: Robert Pattinson is the most underappreciated artist. Period. #TheLighhouse #GoodTime #Tenet #Movie	**Feature Words:** most, underappriciated, period **Topic:** Movie	**Sentiment:** Positive
@sportslync: Tell us your @NBA team without telling us who your NBA team is. #sports #whosyourteam	**Feature Words:** tell, team, us **Topic:** Sports	**Sentiment:** Neutral
@NewsfromScience: In ICU units, a common fungus has emerged as a threat to #COVID19 patients.	**Feature Words:** unit, common, emerged, threat **Topic:** Covid-19	**Sentiment:** Negative

Fig. 1 Feature words from distinct tweets representing relevant topics and sentiment categories

two sets of attributes, namely the tweets with relative sentiments and the feature words with topics for each corresponding tweet. By using this training set, we create the learning model, which tries to relate the information feature vectors into corresponding class labels. We use the textblob library with NLTK package for parsing and retrieving such information and load them into the decision tree model for training.

5.1 Decision Tree

The decision tree classifies choice-based instances by sorting them in a top-down tree manner starting from the root node. It provides generic classification, as well as diverse options for each instance.

For our approach, we develop a topic-based decision tree classifier, which with all intent prioritizes the tweet topic at the root. If the topic is relevant with the hashtag, and with our topic set, then only it further classifies that tweet for training purposes. In subsequent nodes, the feature words are checked w.r.t to the tweet body for sentiment classification. The set of choices is chained together using simple tautological syntaxes. Such a representative branch could be:

$$\text{tweet}_{ij} = (\text{polarity feature words} \wedge \text{relevant topic}) = \text{valid tweet} \qquad (4)$$

where tweet_i = valid tweet (p_1) = (tweet body $\vee$ preprocessing) and tweet_j = valid tweet (p_2) = (tweet body $\wedge$ expressing sentiment).

Here, the root node (tweet) tests an attribute first. If any of the immediate subsequent branches contain focus attributes such as positive feature words and/or relevant topics, then only the tweet is streamed. In the next level of the tree, again the parent node checks for two distinct properties, names as tweet (p_1) and tweet (p_2). The tweet
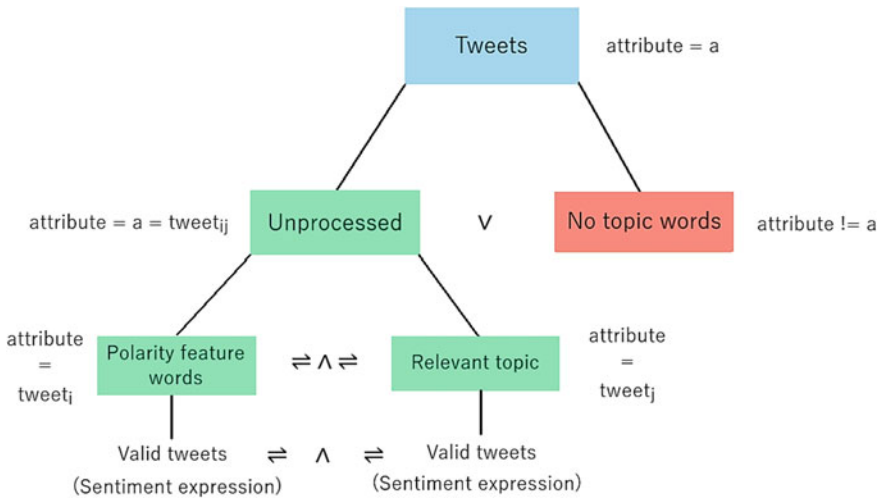
Fig. 2 Decision tree model for training only the tweets containing relevant topics and polarity feature words

bodies should be cleaned up and channeled in JSON format for indexing. Simultaneously, the tweet body should also contain sentiment expressions in the form of grams. If both the properties are satisfied, then only the tweet is considered for entering into a training epoch.

The block diagram representation of our proposed decision tree model w.r.t decision function can be visualized in Fig. 2.

We split our dataset in 90:10 ratio, keeping most of the corpus for training. With more time the model trains, the better it could perform in the UI system demonstration for tweet culture. We run our model for 500 epochs. We keep the string criteria at default as 'gini' for information gaining sustainability, splitter as scikit-learn 'best' with both min_feature_value, max_feature_value, and random splitter. We also keep the maximum depth node for tree traversal as 'none,' since we do not want to restrict the search levels. Here also, we select both the max_leaf_sample and min_leaf_sample for better search reach. We divide the min_sample_split as 2, as there are at most two children node at each level. We show our training performance in Table 1.

6   System Demonstration

Next, for validating the trained model in real time, we develop a system UI for the end users to visualize and understand the topic-based sentiment analysis of tweets. The UI is derived from the training classification output of the decision tree. We showcase the phases of the UI subsequently from Figs. 3, 4, and 5.

Table 1 Training metrics of topic and feature words-based decision tree model

Epoch	Training loss (%)	Training accuracy (%)	Runtime (≈) (min)	Error minimization (≅) (%)
100	31.18	70.11	36	8.64
200	29.10	77.91	34	8.90
300	25.14	82.36	29	10.21
400	22.78	87.15	31	12.35
500	20.08	**92.89**	30	15.52

In the 500th epoch, our model obtained the peak training accuracy in bold
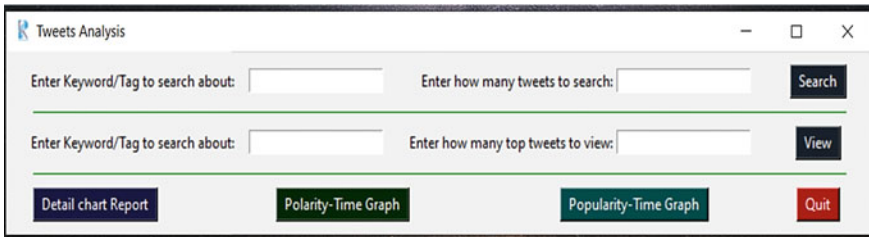
Fig. 3 Input collection window
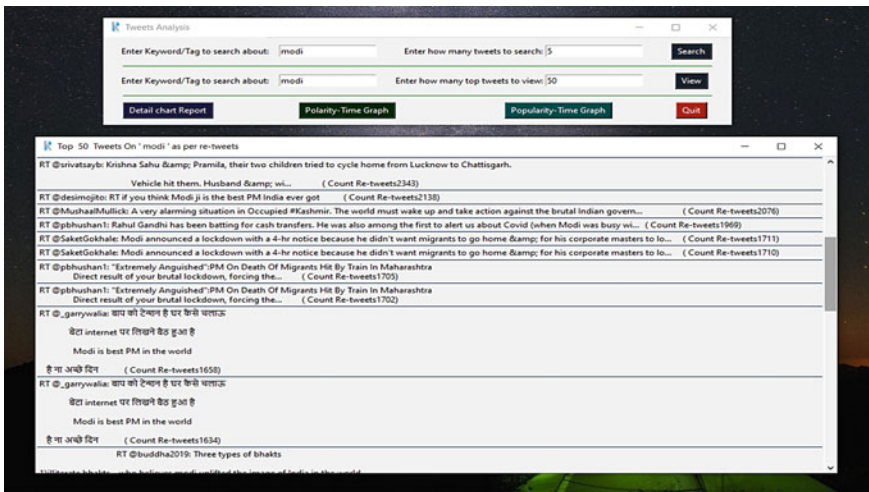
Fig. 4 Fetching *N* number of search topic-based tweets
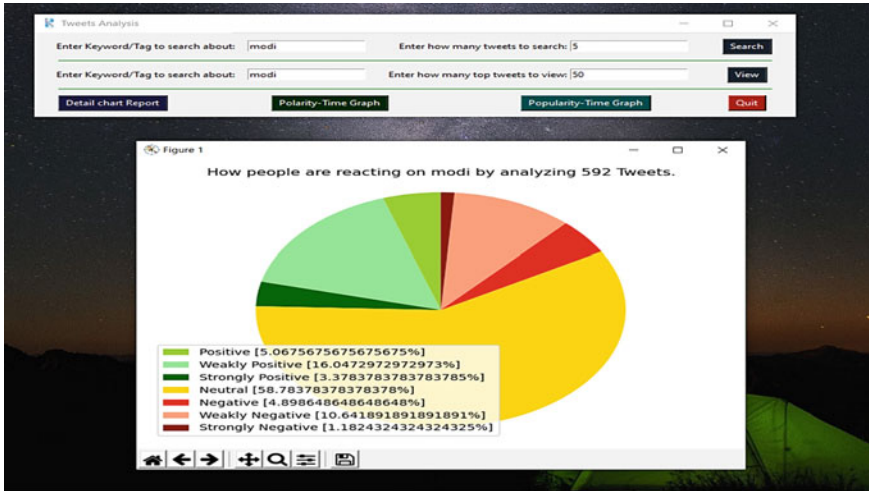
Fig. 5 Sentiment analysis in real-time from the fetched tweets

7 Conclusion

In this work, we represented a system for topic-based sentiment analysis with an end user interface. We collected live tweets on several topics, and after preprocessing, we selected two feature sets namely *n*-gram selection with the help of most frequent bag of words and the corresponding part-of-speech tagging for those n-grams relating to them to their original forms for better understandability of their sentiment and subjectivity. We further propose a decision tree algorithm to train our tweets. Our proposed algorithm works on the principle of valid branch node selection from the tweet features, using the tautological conception. After a successful training with 92.62% training accuracy, we connected the classifier with a UI developed using Pyplot and Tkinter. Here, the user can search any tweet based on an input topic, and the system shows the live sentiment of the tweets associated with that topic. For future extensions of this work, we want to address the sentiment shift of the users over time. We also want to distinguish between the tweets tweeted in different languages, even single multilingual tweets. With this approach, we hope to establish a work exhibiting the diverse tweet-topic relationship in the sentiment analysis research space.

References

1. Sang, E.T.K., van den Bosch, A.: Dealing with big data: the case of twitter. Comput. Linguist. Neth. J. **3**, 121–134 (2013)

2. Wang, H., Can, D., Kazemzadeh, A., Bar, F., Narayanan, S.: A system for real-time twitter sentiment analysis of 2012 US presidential election cycle. In: Proceedings of the ACL 2012 System Demonstrations, pp. 115–120 (2012)
3. Das, S., Das, D., Kolya, A.K.: Sentiment classification with GST tweet data on LSTM based on polarity-popularity model. Sādhanā **45**, 1–17 (2020)
4. Das, S., Kolya, A.K.: Predicting the pandemic: sentiment evaluation and predictive analysis from large-scale tweets on Covid-19 by deep convolutional neural network. Evol. Intel. 1–22 (2021)
5. Oraby, S., Gundecha, P., Mahmud, J., Bhuiyan, M., Akkiraju, R.: "How May I Help You?" modeling twitter customer service conversations using fine-grained dialogue acts. In: Proceedings of the 22nd International Conference on Intelligent User Interfaces, pp. 343–355 (2017)
6. Petrescu, A., Truică, C.-O., Apostol, E.-S.: Sentiment analysis of events in social media. In: 2019 IEEE 15th International Conference on Intelligent Computer Communication and Processing (ICCP), pp. 143–149. IEEE (2019)
7. Ravichandran, M., Kulanthaivel, G., Chellatamilan, T.: Intelligent topical sentiment analysis for the classification of e-learners and their topics of interest. Sci. World J. **2015** (2015)
8. Jiang, Y., Meng, W., Yu, C.: Topic sentiment change analysis. In: International Workshop on Machine Learning and Data Mining in Pattern Recognition, pp. 443–457. Springer, Berlin (2011)
9. Ebrahimi, M., Yazdavar, A.H., Sheth, A.: Challenges of sentiment analysis for dynamic events. IEEE Intell. Syst. **32**, 70–75 (2017)

Observer-Based Fuzzy Sliding Mode Control for Nonlinear Aeroelastic Models via Unsteady Aerodynamics

Zahra Ragoub, Mohand Lagha, and Smain Dilmi

Abstract In the present paper, a robust control algorithm is suggested to stabilize and enhance the behavior of flexible nonlinear airfoils of fixed-wing unmanned aerial vehicles (UAVs). The proposed controller combines sliding mode control (SMC) with high gain observer (HGO) and fuzzy logic control (FLC), applied to multiinput–multioutput aeroelastic model. The plunge and pitch motions are described by the dynamic model of a UAV's wing section equipped with trailing- and leading-edge control surfaces (TLECS). The two-degree-of-freedom model includes structural and aerodynamic nonlinearities interaction, which can lead to dynamic instabilities such as flutter and limit cycle oscillations (LCO). The lift and moment are expressed via Wagner's function for unsteady aerodynamics. The results show the system's responses behavior and demonstrate that the proposed controller leads effectively to have a well-stabilized and chattering-free system, with full suppression of LCO and accurate states' estimation.

Keywords Aeroservoelasticity · Unsteady aerodynamics · Limit cycle oscillations · Sliding mode control · Fuzzy logic control · High gain observer

1 Introduction

Nonlinear aeroelasticity studies the interactions between aerodynamic, structural, and inertial forces applied on aeroelastic systems in flow fields, considering aerodynamic and structural nonlinearities [1, 2]. Most of the time, these interactions lead

Z. Ragoub (✉) · M. Lagha · S. Dilmi
Aeronautical Sciences Laboratory, Institute of Aeronautics and Spatial Studies, Saad Dahlab Blida 1 University, B.P. 270, Road of Soumaa, C.P. 09015 Blida, Algeria
e-mail: ragoubzahra@univ-blida.dz

M. Lagha
e-mail: mlagha-aerospatiale@univ-blida.dz

S. Dilmi
e-mail: s.dilmi-aerospatiale@univ-blida.dz

to destructive aeroelastic instabilities such as flutter, limit cycle oscillations (LCO), or chaotic vibrations [3].

Aeroelastic structures' (such as wings, wing sections, and flexible aircraft) modeling and analysis are deeply investigated since a long time ago [4]. Xiang et al. [5] have given a detailed investigation about aeroelastic nonlinearities' analysis. The aeroelastic analyses visualize the aeroelasticity-resulting problems and their danger on the aeroelastic structures.

To overcome these aeroelastic instabilities, many techniques were adopted to analyze, predict, and eliminate these undesired phenomena. Firstly, the studies have focused on passive flutter suppression methods, which consist of increasing the stiffness of the structure [6]. But, because of the high cost and weight problems, most of the studies have been directed toward active flutter suppression (AFS) techniques. A variety of active controllers has been designed and applied on nonlinear aeroelastic structures with either trailing-edge control surface (TECS) [7] or with trailing- and leading-edge control surfaces (TLECS) [8], such as adaptive controllers [9], and robust controllers [10].

Most of the researches in active control domain have the aim of constructing robust control laws that can guarantee the performances' improvement and the stability of the systems asymptotically or in finite time. For this end, sliding mode control (SMC), which is one of the well-known controllers for variable-structure systems, is widely utilized thanks to its simplicity, robustness, and high precision [11]. However, the use of classical SMC can cause the apparition of chattering phenomenon [12]. To alleviate this inconvenience, conventional sliding mode control (CSMC) was combined with several controllers, such as second- or high-order SMC [13, 14], and fuzzy logic controller (FLC) [12, 15]. Liu and Wang [12] have explained in detail many SMC combinations, like fuzzy sliding mode control (FSMC) which is suggested to remove the chattering problem.

However, the consideration of unsteady aerodynamic charges and different nonlinearities existing in aeroelastic systems leads to having complicated models with increased number of systems' states from which some may be unmeasurable [16]. Then, researchers combined the states' estimation techniques with the applied controllers (such as observer-based SMC) to deal with these complexities [17]. The literature concerning observer-based SMC is relatively few [18]; however, this research subject is more and more investigated and used nowadays [19] thanks to its ability to ensure robust and stable models with only some known systems' states.

The contribution of this work is to design a new control law which is a combination of three controllers:

- SMC guarantees fast LCO elimination and system stabilization in a finite time, with high performances and increased flutter speed margins.
- FLC ensures the suppression of the chattering phenomenon.
- High gain observer (HGO) is used to estimate the system's states that are hard to measure.

This controller is applied on a nonlinear aeroelastic model that considers unsteady aerodynamic charges via Wagner's function, which is a recent direction in this

research field. And finally, the efficiency of the proposed controller is demonstrated by the obtained results.

This paper is organized as follows. Section 2 presents the nonlinear aeroelastic model and the design of the proposed fuzzy sliding mode with high gain observer controller (FSMHGOC). The results are discussed in Sect. 3, and a conclusion is given in Sect. 4.

2 Mathematical Modeling and Controller's Design

The studied nonlinear aeroelastic model for a wing section with TLECS is established based on Wagner's function $\varphi(t)$ for unsteady aerodynamics, with nonlinearity in the stiffness pitch coefficient $K(\alpha)$. All modeling equations and steps are detailed in the modeling section of [15]. This model describes pitch angle and plunge displacement behavior for the aeroelastic system with the following state representation:

$$[x_1 \ x_2 \ x_3 \ x_4 \ x_5 \ x_6 \ x_7 \ x_8]^{\mathrm{T}} = \begin{bmatrix} h & \dot{h} & \alpha & \dot{\alpha} & w_1 & w_2 & w_3 & w_4 \end{bmatrix}^{\mathrm{T}} \quad (1)$$

With:

$$
\begin{aligned}
\dot{x}_1 &= x_2 \\
\dot{x}_2 &= a_{31}x_1 + a_{32}x_3 + a_{33}x_2 + a_{34}x_4 + a_{35}x_5 \\
&\quad + a_{36}x_6 + a_{37}x_7 + a_{38}x_8 + b_{31}\beta + b_{32}\gamma \\
\dot{x}_3 &= x_4 \\
\dot{x}_4 &= a_{41}x_1 + a_{42}x_3 + a_{43}x_2 + a_{44}x_4 + a_{45}x_5 + a_{46}x_6 + a_{47}x_7 \\
&\quad + a_{48}x_8 + b_{41}\beta + b_{42}\gamma \\
\dot{x}_5 &= x_1 - \varepsilon_1 x_5 \\
\dot{x}_6 &= x_1 - \varepsilon_2 x_6 \\
\dot{x}_7 &= x_3 - \varepsilon_1 x_7 \\
\dot{x}_8 &= x_3 - \varepsilon_2 x_8
\end{aligned}
\quad (2)
$$

The coefficients of (2) are given in [15] also.

The following section explains in some detail the proposed control plant which combines CSMC with HGO and FLC, in order to have stabilized and chattering-free system without the need to know all of the system's states.

Referring to (2), the control vector $U(t)$ has the following expression.

$$U(t) = \begin{pmatrix} U_1 \\ U_2 \end{pmatrix} = \begin{pmatrix} b_{31} & b_{32} \\ b_{41} & b_{42} \end{pmatrix} \begin{pmatrix} \beta \\ \gamma \end{pmatrix} \quad (3)$$

The structure of the HGO used in this work for the first subsystem is the following.

$$\begin{cases} \dot{\hat{x}}_1 = \hat{x}_2 - \frac{q_2}{\varepsilon}(\hat{x}_1 - x_1) \\ \dot{\hat{x}}_2 = -\frac{q_1}{\varepsilon^2}(\hat{x}_1 - x_1) \end{cases} . \tag{4}$$

$\hat{x}_1$ and $\hat{x}_2$ are the estimated states, x_1 is the measured state, and ε is a sufficiently small constant. q_1 and q_2 are positive constants chosen such that the roots of the following equation for the second-order system are in the open left-half plane (in other words, with negative real parts).

$$s^2 + q_2 s + q_1 = 0 \tag{5}$$

The sliding surface S_1 and its time derivative $\dot{S}_1$ using the HGO have the following form.

$$S_1(\hat{x}) = \hat{S}_1 = k_1 E_1 + \dot{E}_1 = k_1 E_1 + E_2 \tag{6}$$

$$\dot{S}_1(\hat{x}) = \dot{\hat{S}}_1 = k_1 E_2 + \dot{E}_2 \tag{7}$$

where E_1, E_2 are, respectively, the error between the estimated state trajectories $\hat{x}_1$, $\hat{x}_2$ and the desired state trajectories x_1^d, x_2^d.

k_1 is a positive scalar.

The SMC with HGO (SMHGOC) is designed as follows.

$$U_1 = U_{1eq} + \Delta U_1. \tag{8}$$

U_{1eq} is the equivalent control, where:

$$U_{1eq} = \ddot{x}_1^d - k_1 E_2 = \ddot{x}_1^d - k_1(\dot{\hat{x}}_1 - \dot{x}_1^d) \tag{9}$$

ΔU_1 is the switching control, it has the following form:

$$\Delta U_1 = -l_1 \text{Sign}\left(\hat{S}_1\right) \tag{10}$$

l_1 is a positive scalar. Then:

$$U_1 = \ddot{x}_1^d - k_1\left(\dot{\hat{x}}_1 - \dot{x}_1^d\right) - l_1 \text{Sign}\left(\hat{S}_1\right) \tag{11}$$

In order to satisfy the Lyapunov stability criterion, the following Lyapunov function is considered:

$$V_1(x) = \frac{1}{2} S_1^2(x) \tag{12}$$

$$\dot{V}_1(x) = \dot{S}_1(x) S_1(x) \tag{13}$$

$$\dot{V}_1(x) = S_1\Big[k_1\big(\dot{x}_1 - \dot{\hat{x}}_1\big) + f_1(x) - l_1 \text{Sign}\big(\hat{S}_1\big) \Big] \tag{14}$$

$f_1(x) = a_{31}x_1 + a_{32}x_3 + a_{33}x_2 + a_{34}x_4 + a_{35}x_5 + a_{36}x_6 + a_{37}x_7 + a_{38}x_8$ is bounded, in other words: $|f_1(x)| \leq l_{f_1}$

$$\dot{V}_1(x) = \big(\hat{S}_1 + S_1 - \hat{S}_1\big)k_1\big(\dot{x}_1 - \dot{\hat{x}}_1\big) + \big(\hat{S}_1 + S_1 - \hat{S}_1\big)f_1(x)$$
$$- \big(\hat{S}_1 + S_1 - \hat{S}_1\big)l_1\text{Sign}\big(\hat{S}_1\big) \tag{15}$$

$$\dot{V}_1(x) \leq -\hat{S}_1 l_1 \text{Sign}\big(\hat{S}_1\big) + l_1\big|S_1 - \hat{S}_1\big| + \big(|f_1(x)| + k_1|x_2 - \hat{x}_2|\big)\big|\hat{S}_1\big|$$
$$+ \big|S_1 - \hat{S}_1\big|\big(|f_1(x)| + k_1|x_2 - \hat{x}_2|\big) \tag{16}$$

$$\dot{V}_1(x) \leq -l_1\big|\hat{S}_1\big| + l_1\big|S_1 - \hat{S}_1\big| + \big(|f_1(x)| + k_1|x_2 - \hat{x}_2|\big)\big|\hat{S}_1\big|$$
$$+ \big|S_1 - \hat{S}_1\big|\big(|f_1(x)| + k_1|x_2 - \hat{x}_2|\big) \tag{17}$$

$$\dot{V}_1(x) \leq -l_1\big|\hat{S}_1\big| + \big(l_{f1} + k_1|x_2 - \hat{x}_2|\big)\big|\hat{S}_1\big| + \Delta \tag{18}$$

$$\Delta = \big|S_1 - \hat{S}_1\big|\big(l_1 + l_{f1} + k_1|x_2 - \hat{x}_2|\big) \tag{19}$$

Because of the observer's convergence [12], $|x_2 - \hat{x}_2|$ and $\big|S_1 - \hat{S}_1\big|$ are bounded and sufficiently small. Therefore, Δ is sufficiently small to have $\dot{V}_1(x) < 0$.

In the aim of eliminating any eventual appearance of chattering, FLC is combined with the previously obtained SMHGOC. The input of the fuzzy controller is the sliding surface S, and its output is the variant membership μ. The controller's expression for the first subsystem becomes:

$$U_1 = U_{1eq} + \mu_1 \Delta U_1 \tag{20}$$

μ_1 is the variant membership of the first subsystem.

The fuzzy sets are chosen as follows [15]:

- FLC's input S_1: NB (Negative and Big); N (Negative); Z (Zero); P (Positive); PB (Positive and Big).
- FLC's output μ_1: NB; N; Z; P; PB.

The fuzzy rules are presented in Table 1 that gives the FLC's output μ_1 corresponding to every FLC's input S_1.

The criterion of the controller's stability stays satisfied since the introduced membership μ_1 that is multiplied by the positive switching coefficient l_1 in (10) is always positive.

Table 1 Fuzzy rules

Input S_1	Output μ_1
NB	PB
N	P
Z	Z
P	P
PB	PB

3   Results and Discussion

This section exposes simulation results of pitch and plunge motions (α and h, respectively). The parameters of the wing model used in this study are given in [8].

Figure 1 presents time responses of the plunge displacement and the pitch angle, with the initial conditions $\begin{bmatrix} h & \dot{h} & w_1 & w_2 & w_3 & w_4 \end{bmatrix}^T = [0.005\ 0\ 0.2\ 0\ 0\ 0]^T$ and a speed of 13 m/s. This figure shows that the system exhibits LCO caused by the nonlinearities in the model. Then, an active control process is needed to deal with this instability.

The proposed FSMHGOC is designed with the same initial conditions, and for a speed of 37 m/s, with the SMC parameters: $k_1 = k_2 = 15$, $l_1 = 32$, $l_2 = 18$, and the HGO parameters: $q_1 = q_3 = 3$, $q_2 = q_4 = 2$, and $\varepsilon = 0.001$ [12].

Figure 2 represents the closed-loop plunge displacement and pitch angle time responses, where Fig. 2b, d are zoomed parts of Fig. 2a, c successively. Figure 3 describes the observation error between the actual and the estimated plunge displacement (E_h) and pitch motion (E_α). One can see in Fig. 2 that the established controller has successfully stabilized the system, leading time responses to equilibrium position in a short time, even under unsteady gust loads and nonlinearities in the system, and for a high velocity. Also, it can be noticed from Fig. 2b, d and 3, that the estimated
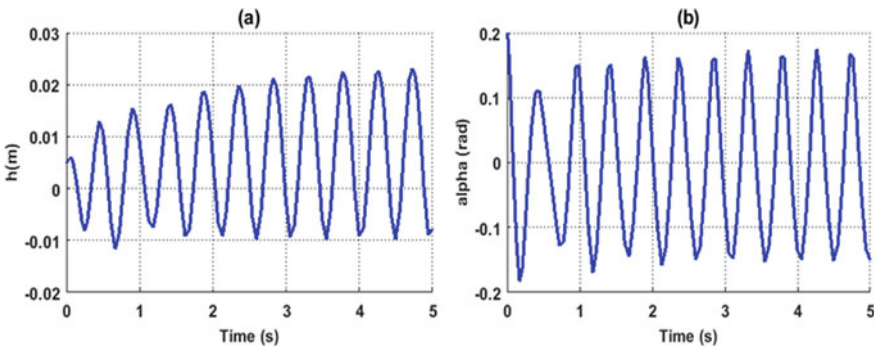
Fig. 1 System time responses without controller
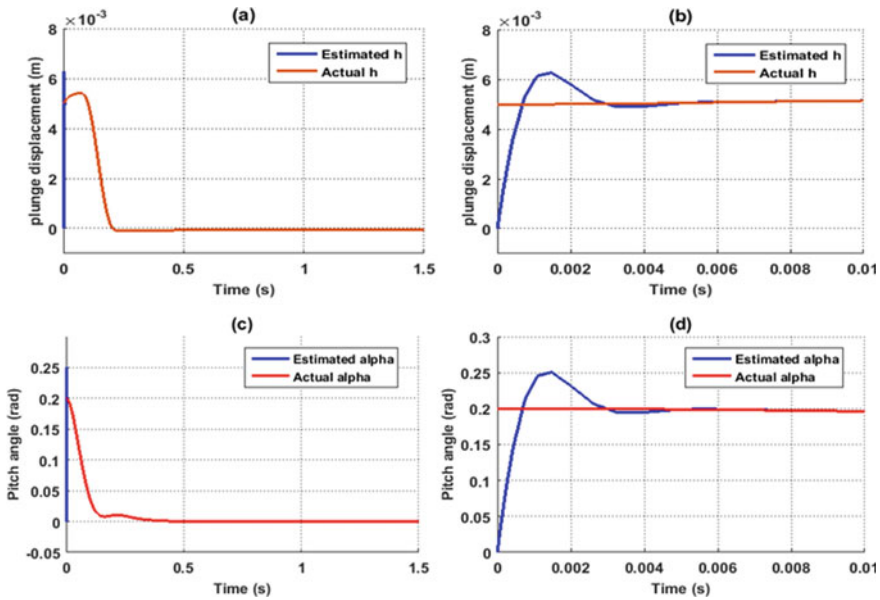
Fig. 2 System time responses using FSMHGOC
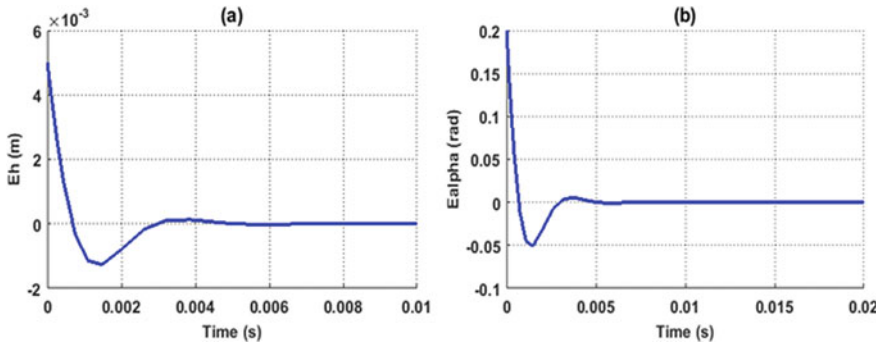
Fig. 3 Observation error between the actual and the estimated time responses

responses join rapidly the actual ones, and the errors converge toward zero in less than 0.01 s, which proves the observer's accurate estimation.

Figure 4 shows the variations of TLECS deflections that are constrained between ± 0.5 rad in order not to exceed the actuators' capabilities. These deflections present a smooth and fast convergence within the actuators' physical capacities, with no apparition of chattering. This is visualized in Fig. 5 that presents a comparison between the system's time responses using the proposed controller and with the SMHGOC designed with the same conditions and parameters. This figure proves
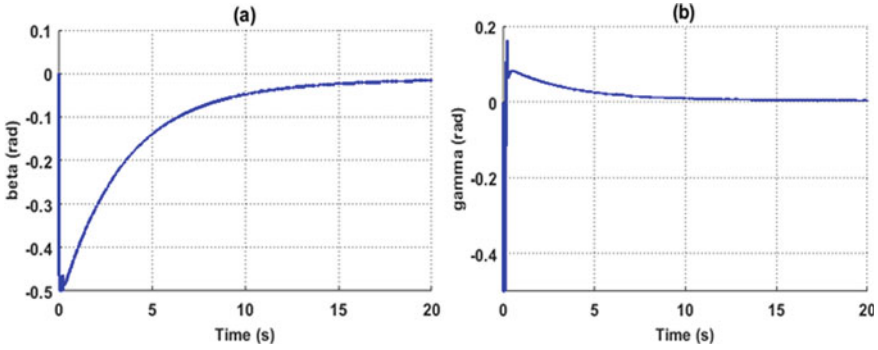
Fig. 4 TLECS deflections variations
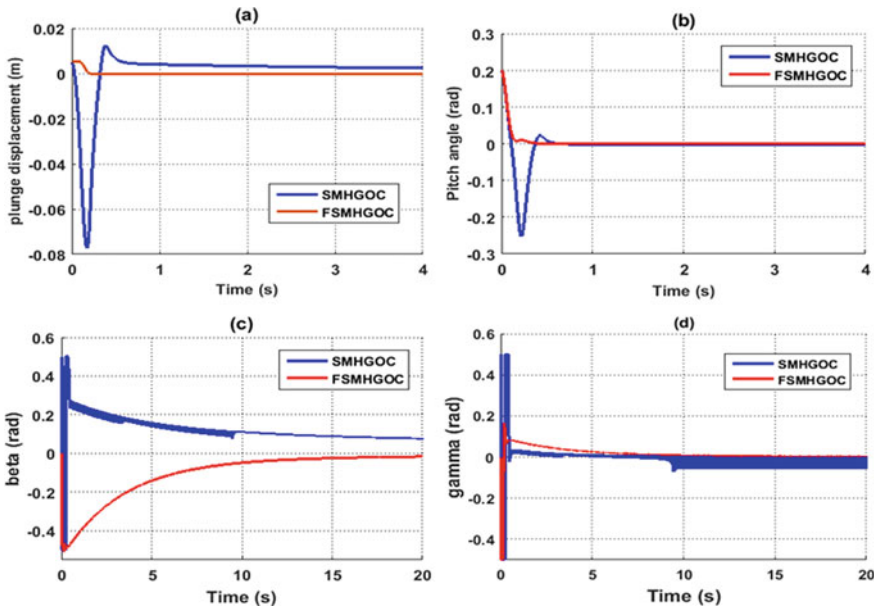
Fig. 5 Time responses comparison

that the use of FLC leads to eliminate the chattering phenomenon appearing in the SMHGOC case.

A summarizing comparison is given in Table 2. The latter shows that the proposed controller has effectively enhanced the system's performances in a short time and led to have increased flutter velocity margins. It has also removed any eventual appearance of the chattering phenomenon as has been noticed in the SMHGOC case.

Table 2 A summarizing comparison

	Open loop	SMHGOC	FSMHGOC
Performances	Degraded	Enhanced	Enhanced
Flutter speed	10.70 m/s	42.49 m/s	39.67 m/s
Chattering	Instability	Existing case	Removed

4 Conclusions and Future Directions

In this work, a fuzzy sliding observer is proposed to suppress aeroelastic instability on a nonlinear aeroelastic wing section and improve its performance. This model describes the plunge and pitch motions with leading- and trailing-edge control surfaces. The unsteady aerodynamic model via Wagner's function is considered. The high gain observer is used to estimate the states of the system that can be hard or expensive to measure. The sliding mode control algorithm is used to stabilize and enhance the system's performances, and the fuzzy system is introduced to suppress the chattering phenomenon. The obtained results have shown that without controller, the system's dynamics present destructive LCO over the flutter speed. The introduction of the proposed controller has led to stabilized and chattering-free system, with optimized performances, and important flutter speed margins, despite unsteady aerodynamic charges and the nonlinearities in the system. Also, the states of the system have been precisely estimated thanks to the HGO. This may confirm that the study can serve as a robust, effective, and accurate solution for stability problems in the active control domain for nonlinear aeroelastic systems, even under unsteady gust charges. Furthermore, it can be an economic tool to develop nonlinear aeroelastic airfoils in wind tunnels or fixed-wing drones.

This investigation stays open for some new directions in the AFS field from which observer-based neural SMC can be mentioned. Also, the system's modeling may be extended to 3D full wing models with unsteady aerodynamics.

References

1. Fung, Y.C.: An Introduction to the Theory of Aeroelasticity. Dover, USA (1993)
2. Hodges, D.H., Pierce, G.A.: Introduction to Structural Dynamics and Aeroelasticity, vol. 15. Cambridge University Press, Cambridge (2011)
3. Dowell, E., Edwards, J., Strganac, T.: Nonlinear aeroelasticity. J. Aircr. **40**(5), 857–874 (2003)
4. Mukhopadhyay, V.: Historical perspective on analysis and control of aeroelastic responses. J. Guid. Control Dyn. **26**(5), 673–684 (2003)
5. Xiang, J., Yan, Y., Li, D.: Recent advance in nonlinear aeroelastic analysis and control of the aircraft. Chin. J. Aeronaut. **27**(1), 12–22 (2014)
6. Bruce, R.R.J., Jinu, G.R.: A study on aeroelastic flutter suppression and its control measures—past and future. Int. J. Eng. Technol. **6**(2), 960–973 (2014)
7. Singh, S.N., Yim, W.: State feedback control of an aeroelastic system with structural nonlinearity. J. Aerosp. Sci. Technol. **7**(1), 23–31 (2003)

8. Platanitis, G., Strganac, T.W.: Control of a nonlinear wing section using leading- and trailing-edge surfaces. J. Guid. Control Dyn. **27**, 52–58 (2004)
9. Gujjula, S., Singh, S.N., Yim, W.: Adaptive and neural control of a wing section using leading- and trailing-edge surfaces. Aerosp. Sci. Technol. **9**(2), 161–171 (2005)
10. Fatehi, M., Moghaddam, M., Rahim, M.: Robust flutter analysis and control of a wing. Aircr. Eng. Aerosp. Technol. **84**(6), 423–438 (2012)
11. Vaidyanathan, S., Lien, C.H.: Applications of Sliding Mode Control in Science and Engineering, vol. 709. Springer, Switzerland (2017)
12. Liu, J., Wang, X.: Advanced Sliding Mode Control for Mechanical Systems: Design, Analysis and Matlab Simulation. Springer Heidelberg; Tsinghua University Press Beijing (2012)
13. Song, Z., Li, H.: Second-order sliding mode control with backstepping for aeroelastic systems based on finite-time technique. Int. J. Control Autom. Syst. **11**(2), 416–421 (2013)
14. Dilmi, S., Bouzouia, B.: Improving performance for nonlinear aeroelastic systems via sliding mode controller. Arab. J. Sci. Eng. **41**(9), 3739–3748 (2016)
15. Ragoub, Z., Lagha, M., Dilmi, S.: Classical and fuzzy sliding mode control for a nonlinear aeroelastic system with unsteady aerodynamic model. Int. J. Comput. Digit. Syst. **9**(6), 1099–1108 (2020)
16. Tian, W., Gu, Y., Liu, H., Wang, X., Yang, Z., Li, Y., Li, P.: Nonlinear aeroservoelastic analysis of a supersonic aircraft with control fin free-play by component mode synthesis technique. J. Sound Vibr. **493** (2021)
17. Zhang, F., Soffker, D.: Active flutter suppression of a nonlinear aeroelastic system using PI-observer. In: Motion and Vibration Control, pp. 367–376. Springer, Dordrecht (2009)
18. Qi, N., Zhang, C., Yuan, J.: Observer based sliding mode control for subsonic piezo-composite plate involving time varying measurement delay. Measur. Control 1–11 (2021)
19. Li, D., Yang, H., Qi, N., Yuan, J.: Observer-based sliding mode control for piezoelectric wing bending-torsion coupling flutter involving delayed output. J. Vibr. Control 1–18 (2020)

Face Detection in Unconstrained Environments Using Modified Multitask Cascade Convolutional Neural Network

Suchimita Bhattacharya, Manas Ghosh, and Aniruddha Dey

Abstract Due to occlusion and variation of poses, facial detection is a challenging task to accomplish. In facial detection, occlusion has always been a standing challenge. Facial occlusion like sunglasses, scarf, and mask and pose variation are crucial factors that affect the performance of face detection. Undesirably, in the real-world scenario, occlusions are a very common situation that arises in the face detection and recognition problem. To deal with this problem, we put forward the modified multitask cascade convolutional neural network (M-MTCNN) with a slight modification. MTCNN is a trainable unit which may be included in present CNN architectures. With end-to-end training supervised by only the private identity labels, Mask Net learns a correct way of adaptively generating different feature map masks for various occluded face images. This paper deals with an efficient method for the detection of numerous occluded and pose variation faces. In addition to the marking of the face with a square box, there are five landmarks drawn (the two eyes, one in the nose, and two identifying the lips). Also, using the landmark points of the eyes, we have tried to mark the eyes using the eye landmarks as the center point. Using the landmarks of the lips, we also have drawn a straight line marking the edge of the lips. The presented method has been tasted on WIDER database and obtained efficient detection of multiple occluded faces.

Keywords Convolutional network · Face detection · Partial occlusion · Pose variations · M-MTCNN

S. Bhattacharya · M. Ghosh
Department of Computer Application, RCCIIT, Kolkata, India
e-mail: manas.ghosh@rcciit.org

A. Dey (✉)
Department of Information Technology, MAKAUT, Kolkata, India

1 Introduction

Facial region detection [1–3] has gotten a lot of attention and has been widely used in various aspects of human life, such as video reconnaissance, face detection, human–machine interfaces, and picture recovery. Numerous variations in illumination, posture, impediment, and shot point present enormous challenges for face identification in real-world applications. Viola and Jones (VJ) [4] recently developed a course face location technique that was the major effort with an ongoing step and was prepared using Adaboost- and Haar-like elements. Many improved works based on VJ's suggested frameworks have been proposed in recent years [5, 6]. Li et al. [5] were the first to propose cascaded CNNs for face detection instead of Haar-like features and Adaboost of the framework.

In recent years, with the remarkable progress in convolutional neural networks (CNNs) [7], CNN has achieved path-breaking success in computer vision and multimedia, i.e., image classification objection detection [8, 9] and image retrieval [10, 11]. PyramidBox-based face detection methods based on CNN were developed [12] by Tang et al. However, the method is largely inefficient since the CNN structure is complicated. Huang et al. [13] proposed DenseBox to track face by using a single fully convolutional neural network (FCN) to predict the bounding box and the object class confidences directly. The accuracy of detection is further improved by performing localization of facial landmark. Yang et al. [14] have put forward a coarse-to-fine method, named Faceness-Net. In this method, the scores of facial parts are fused using several DCNN to obtain the face region followed by a refining network to achieve the goal face detection. Several works show that performing face detection and landmark localization concurrently improves the performance of face detection [5, 15].

Taking inspiration from cascade CNN and MTCNN, we have proposed a modified multitask cascade convolutional neural network (M-MTCNN) technique-based face detection which is presented in this paper. It is much more challenging to locate partial occluded and pose variation faces. The presented method is validated over on WIDER face database to validate severe occlusions.

In case of images of individuals in different orientations (images with half faces and other occlusions), only identifying the facial landmarks of the face is not enough, we have to clearly specify the distinct features of the face (i.e., eyes, ears, nose, and lips). So, here, in this paper, we have tried to achieve that part.

The rest of the paper is organized as follows: Section 2 defines proposed method using modified MTCNN. The experimental results on the face database are in Sect. 3. Finally, concluding remarks are summarized in Sect. 4.

2 Proposed Modified MTCNN Approach

It is suggested in traditional procedures due to the efficiency of the cascade structure. MTCNN is a face detection variation of the multitask neural network paradigm. MTCNN first uses a simple model to generate target region candidate boxes with a certain probability [12], in order to account for accuracy and performance, and then uses a more complex model for fine classification and higher precision region box regression, which is then made recursive to form a three-layer network, namely P-net, R-net, and O-net, to perform fast and efficient face detection. In the input layer, an image pyramid is utilized to change the scale of the original image. Then, using P-net, a large number of candidate target area frames is generated. The R-net is then employed for the initial selection and boundary regression of these target area frames, and the majority of the negative cases are filtered out. The remaining target area frames are then differentiated and regressed using the more composite and accurate network O-net. Here, we have proposed a modified MTCNN to find the modified landmarks of the eyes and lips areas of a face.

2.1 MTCNN Basic Network Structure

The original image is downsized after it has been processed using MTCNN to build a pyramid of images of various sizes. The different-sized images are then given to the three sub-networks for training to detect different human face sizes and detect multi-size targets. The entire process of P-net, which is the first sub-net in MTCNN, is depicted in Fig. 1. The basic structure is a completely connected convolution. The picture pyramid built in the previous stage of the method is utilized to bring out the prefatory features, scale the frame using an FCN, and produce an approximate estimate of the face candidate frame and frame regression vector. The candidate frames are then regressed by the frame, and the high-coincidence candidate frames are finally merged using the NMS algorithm. The bounding box regression adjustment window and NMS are used to filter the majority of the windows. The key difference between the FCN structure and the general convolution network is that the convolution kernel size is 11, which allows the network to take images of any size as training set samples. The deep learning training network model, in particular, requires a high number of training sets, and thus, the model training is more efficient since it eliminates the recurrent storage and convolution problems generated by the usage of pixel blocks. This feature of efficient model training can help you save time and improve your results. Its structure is more sophisticated than the above layer's P-net network structure. The constraint conditions are mostly added, and the added restriction scans the face prediction frame again.

The R-net network refines the higher layer's output window further, using the border regression process and the NMS algorithm to reject low-scoring face candidate
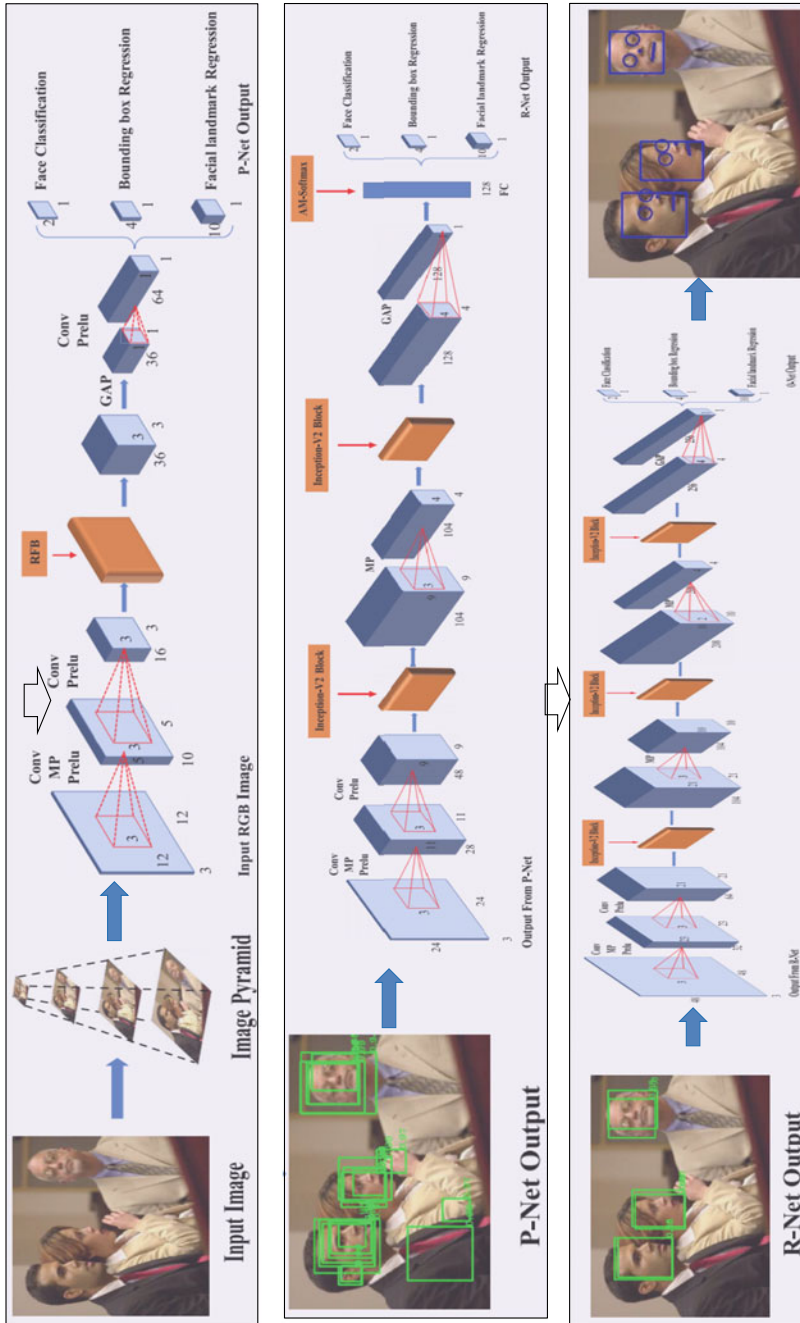
Fig. 1 Schematic diagram and the steps for the proposed method face detection method with M-MTCNN

frames and pick numerous sets of locally optimal face candidate frames. In comparison to the P-net network, R-net has an extra fully linked layer at the end, as seen in Fig. 1. The extra fully connected network's purpose is to provide a 128-dimensional vector that aids the R-net in filtering the prediction box's output.

O-net stands for output network in its entire form. The goal of the O-net network structure is to pick the best candidate frame again and produce the five feature important points that were discovered in the end. We have made changes to the landmarks, which will be addressed in the next part about the face detection procedure. O-network net's layer is deeper than the previous layer's, which explains why O-net's reaction to face identification is the best.

The size of filters is reduced from 5×5 to 3×3. The numbers of filters are also reduced. These reduction changes are done in order to lessen the computational strain. To boost the performance, the depth of the network is increased.

(a) **Proposal network (P-net)**: *classification of face*: To achieve learning, the problem is formulated as a two-class classification problem. For each sample x_i, we use the cross-entropy loss:

$$L_i^{Cl} = -\left(y_i^{Cl} \log(p_i) + \left(1 - y_i^{Cl}\right)(1 - \log(p_i))\right) \tag{1}$$

where p_i is the probability made by the neural network that states a face sample. The symbolization representation $y_i^{Cl} \in [0, 1]$ signifies the ground truth label.

(b) **Refine network (R-net)**: Using *R-net*, highly coincided detection windows in the facial image are marked; non-maximum suppression is used to scrap 90% of the coincided windows. The formula is given by:

$$L_i^{Rg} = \left\| \hat{y}_i^{Rg} - y_i^{Rg} \right\|_2^2 \tag{2}$$

(c) **Output network (O-net)**: Using O-net suggests more regulations to track the face region. Most significant of all, this stage points out five facial features. The Euclidean loss is defined below in Eq. (3); this is used to rectify the regression issue encountered during facial features detection.

$$L_i^{Lndmrk} = \left\| \hat{y}_i^{Lndmrk} - y_i^{Lndmrk} \right\|_2^2 \tag{3}$$

In Eq. (3), the coordinates of facial features that correlate to trained network and real condition for the ith input image are denoted by $\hat{y}_i^{Lndmrk}$ and y_i^{Lndmrk}. The five feature points are left eye, right eye, left mouth, right mouth, and nose. The facial features compose of these facial features.

(d) **Multi-source training**: Each CNN in the network has a different function; therefore, during the learning process, the MTCNN network is fed with different types of training images, like non-face and fragmentary aligned face. In this case, a number of the loss functions (i.e., Eqs. (1)–(3)) are not used. For instance, only the first two losses of the sample for background region are

computed, and other two losses are initialized to 0. This can be carried out directly with a sample-type indicator. Then, the overall learning target can be formulated as:

$$\min \sum_{i=1}^{N} \sum_{j \in (\text{Cl},\text{Rg},\text{Lndmrk})} \alpha_j \beta_i^j L_i^j \tag{4}$$

where N is the number of training samples. α_j states on the task significance. We use $(\alpha|\text{Cl} = 1, \alpha_{\text{Rg}} = 0.5, \alpha_{\text{Lndmrk}} = 0.5)$ in *P-net* and *R-net*, while $(\alpha|\text{Cl} = 1, \alpha_{\text{Rg}} = 0.5, \alpha_{\text{Lndmrk}} = 1)$ in *O-net* for more perfectly facial landmarks localization. $\beta_i^j \in \{0, 1\}$ denotes the sample-type indicator. In this process, it is very common to employ stochastic gradient descent to train the CNN.

2.2   Face Detection Process

In each of the three network, i.e., *P-net*, *R-net,* and *O-net*, both training and testing phases are carried out. At first, training the *P-net* in the dataset is randomly crop facial images and resized the cropped images to 12×12. Then, the cropped image was determined as positive or negative sample based on the *Intersection* over *Union* (IOU) ratio of the box to ground truth. Secondly, while training the *R-net*, images in the dataset are detected with a trained *P-net* model; each image generated a large number of candidate windows. For each candidate window, according to its IOU with ground truth, this candidate window was determined to be a positive and negative sample. After that, resizing these windows to 14×14 and train *R-net*. Finally, similar to the processing of training *R-net*, the trained *R-net* model was used to generate candidate windows, the candidate windows were determined to be positive and negative samples according to its IOU with ground truth. Finally, resized these windows to 48×48 and train *O-net*. The steps for training the proposed M-MTCNN are shown in Fig. 1. When conjecture was performed, first of all, image pyramid containing images of different sizes of images were generated. The candidate bounding boxes and scores were initially produced by *P-net*. And then, candidate bounding boxes with large overlap are found through NMS. Next, merge overlapped candidates of different scales. Secondly, image was detected with the *P-net* model, and the detected candidate window of the face was converted into the square boxes. Afterward, these square boxes in the original image were converted to new boxes starting at 0 coordinates and resize the new boxes to 24×24. Subsequently, the *R-net* model was used to detect these new boxes and get *R-net*'s candidate windows of the face and scores. After that, the overlapped candidate windows were merged with NMS. Finally, similar to *R-net*, the *O-net* model was used to detect these new boxes and output bounding boxes and scores. The steps for face detection with M-MTCNN are shown in Fig. 1. Apart from only drawing the square boxes around the faces, using the landmark points in the eyes, we have drawn circles around the eyes so that

it can be used to detect the whole portion of the eyes. We have also drawn a straight line along the lips area to identify the lips area more prominently.

3 Empirical Results

The performance of the proposed modified version of the MTCNN face detection method is validated on WIDER FACE [16] dataset. The WIDER dataset is a challenging dataset and is widely used to study the problem of unrestricted face detection. It contains 393,703 faces with a high degree of variability in scale, poses, and occlusion. We choose WIDER FACE as the training datasets for training the proposed M-MTCNN. Figures 2, 3 clearly demonstrates the results of faces detection from WIDER FACE [16] dataset achieved by our algorithm. The results also contain the modified landmarks as discussed. The efficiency of the proposed method is confirmed by WIDER FACE databases which can also handle the situations like size disparities of face, occlusions, and out of plane rotation. The periodical face detection is done to ensure recovery from errors. Detection of multiple faces with pose variant can easily be handled by using M-MTCNN.

The inclusion of landmarks (circles around the eye region, and straight line specifying the lip region) in the face detection process helps in more accurate face detection process of occluded images (occlusion such as images of individuals wearing hats, mask, glasses, and sunglasses.).
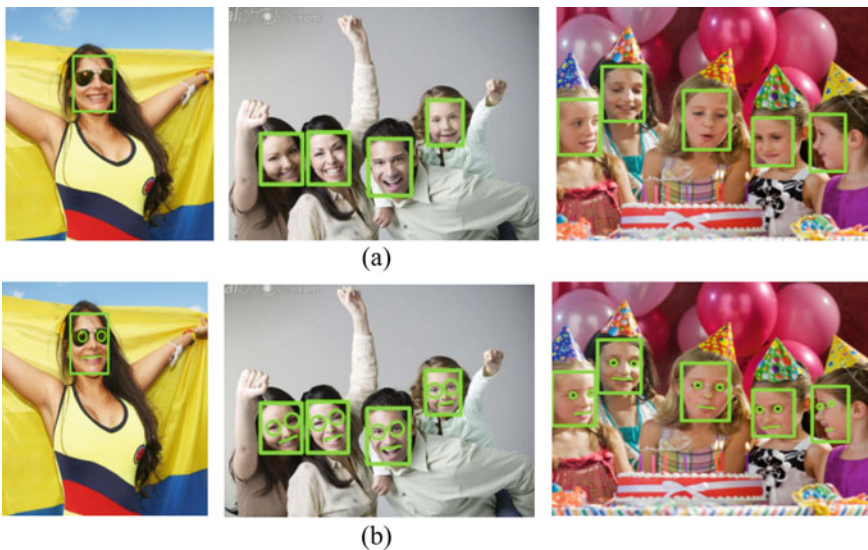
Fig. 2 Comparison with **a** MTCNN and **b** proposed MTCNN algorithm, pose, and face orientation variant locations detected by the green line rectangles using our proposed methods
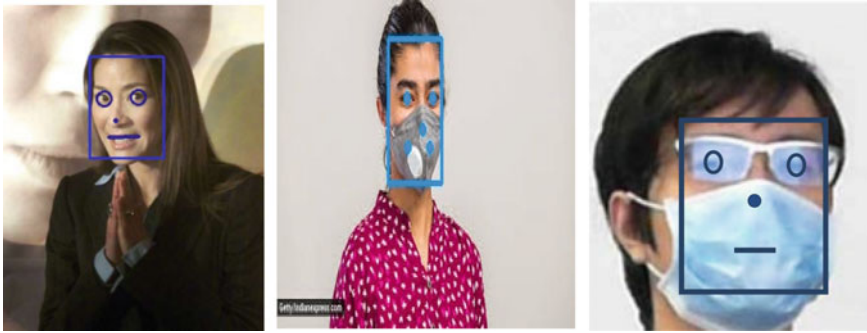
Fig. 3 Example image for face detection which contains human and picture of same human and occluded face image. The rectangles with blue line are the results using our methods

However, the detection results are strongly affected when the object environment is complex or with heavy occlusion. In order to further verify and analyze the performance of the model, we divided the test images into three categories with respect to the complexity of the environment. These three levels were easy, medium, and hard, and we carried out further experiments on these three levels. Figures 2, 3 show the results of the experiments at easy, medium, and hard levels, respectively.

4 Conclusion

We have presented an efficient modified MTCNN method to address the problems incurred during the detection of faces involving occlusion (glasses and mask scarf) and pose variance. Firstly, we have fed the modified MTCNN with input images, and then, the MTCNN can quickly generate the candidate windows. Secondly, modified MTCNN can truly detected aces that partially occluded and with different pose variations. With the modified landmarks in the detected faces. The proposed M-MTCNN model was trained with a sufficient large number of face training examples that include most partial occlusions and non-partial occlusions faces, to detect multi-view partially occluded and non-partially occluded faces efficiently. We have evaluated our proposed method on WIDER face datasets. The experimental results clearly show how accurately our model detects faces and the modified facial landmarks.

References

1. Dey, A., Chakraborty, S., Kundu, D., Ghosh, M.: Elastic window for multiple face detection and tracking from video. In: Proceeding of the CIPR 2019, pp. 487–496 (2019)
2. Dey, A.: A contour based procedure for face detection and tracking from video. In: Proceeding of the RAIT 2016, pp. 252–256 (2016)

3. Chowdhury, S., Dey, A., Sing, J.K., Basu, D.K., Nasipuri, M.: A novel elastic window for face detection and recognition from video. In: Proceeding of the ICCICN 2014, pp. 252–256 (2014)
4. Viola, P., Jones, M.: Rapid object detection using a boosted cascade of simple features. In: Proceedings of the CVPR 2001, pp. 511–518 (2001)
5. Li, H., Lin, Z., Shen, X., Brandt, J., Hua, G.: A convolutional neural network cascade for face detection computer vision and pattern recognition. In: Proceedings of the CVPR 2015, pp. 5325–5333 (2015)
6. Yang, S., Luo, P., Loy, C.C., Tang, X.: From facial parts responses to face detection: a deep learning approach. In: Proceeding of the ICCV, pp. 3676–3684 (2015)
7. Li, X., Yang, Z., Wu, H.: Face detection based on receptive field enhanced multi-task cascaded convolutional neural networks. IEEE Access **8**, 174922–174930 (2020)
8. Girshick, R., Donahue, J., Darrell, T., Malik, J.: Rich feature hierarchies for accurate object detection and semantic segmentation. In: Proceedings of the CVPR 2014, pp. 580–587 (2014)
9. Ren, S., He, K., Girshick, R., Sun, J.: Faster R-CNN: towards real-time object detection with region proposal networks. IEEE Trans. Pattern Anal. Mach. Intell. **39**(6), 1137–1149 (2017)
10. Nie, L., Wang, X., Zhang, J., He, X., Zhang, H., Hong, R., Tian, Q.: Enhancing micro-video understanding by harnessing external sounds. In: Proceedings of the ACMM 2017, pp. 1192–1200 (2017)
11. Song, X., Feng, F., Han, X., Yang, X., Liu, W., Nie, L.: Neural compatibility modeling with attentive knowledge distillation. In: Proceeding of the SIGIR'2018, pp. 5–14 (2018)
12. Tang, X., Du, D.K., He, Z., Liu, J.: PyramidBox: a context-assisted single shot face detector. In: Proceedings of the ECCV 2018, pp. 812–828 (2018)
13. Huang, L., Yang, Y., Deng, Y., Yu, Y.: DenseBox: unifying landmark localization with end to end object detection. arXiv:1509.04874
14. Yang, S., Luo, P., Loy, C.C., Tang, X.: Faceness-Net: face detection through deep facial part response. IEEE Trans. Pattern Anal. Mach. Intell. **40**(8), 1845–1859 (2018)
15. Zhan, K., Zhang, Z., Li, Z., Qiao, Y.: Joint face detection and alignment using multi-task cascade convolutional networks. IEEE Sig. Proc. Lett. **23**(10), 1499–1503 (2016)
16. Yang, S., Luo, P., Loy, C.C., Tang, X.: WIDER FACE: a face detection benchmark. In: Proceeding of the CVPR 2016, pp. 5525–5533 (2016)

Epilepsy Detection from Brain EEG Using Convolutional Neural Network

Dipankar Khorat and Soham Sarkar

Abstract Epilepsy is a chronic neurological disorder. Due to the random occurrence of seizures and time-consuming as well as costly diagnosis process, millions of epileptic patient cannot be treated appropriately. There is a requirement of integrated neural system for faster diagnosis and treatment. In this proposed model, a 5-layer convolutional neural network (CNN)-based algorithm is presented on the features, i.e., local maxima, lower threshold, sharply defined component, and disturbed background of electroencephalogram (EEG). Energy and power features are used to establish the sharply defined component, and channel clustering features have been utilized in this proposed model. Output of this proposed model is compared with recent techniques and found its uniqueness in detecting the epileptic seizure in human brain. This proposed framework is able to detect the seizure during experimental testing on patients with high accuracy (92.67%) and precision (97.09%).

Keywords Epilepsy · Seizure · Electroencephalogram · Convolutional neural network

1 Introduction

Epilepsy is possibly the most widely recognized and prevailing neurological issues of human beings [1]. An epileptic seizure is an abrupt synchronous and repeated discharge of neurons in brain [2]. New onset seizure among people is reported in recent surveys [3] who had no prior history of seizures. Restrictions on neurophysiological processes also increase the risk to the epilepsy patients [4]. While seizures cannot be avoided entirely, an accurate prediction of their occurrence would help to alleviate the impotence of the patients affected [5]. EEG is a proven diagnosis process for epilepsy detection, and it is well accepted in medical field in recent times. The EEG signals of the brain functions of epilepsy patients may be classified into different states, i.e., ictal, pre-ictal, and inter-ictal states. The EEG signals exhibit

D. Khorat (✉) · S. Sarkar
RCC Institute of Information Technology, Beliaghata, Kolkata 700015, India

peculiar patterns when a seizure occurs. In addition, both the pre-ictal and inter-ictal state EEGs also exhibit distinctive patterns.

In recent years, various automatic EEG signal recognition and seizure detection systems have emerged using different approaches. Among these studies, [6] introduced a high-tech framework for detecting a variety of seizures. Qu and Gotman [7] presented nearest neighbor EEG classifier to detect of epileptic seizures on features derived in both time and frequency domain. Adeli et al. [8], Güler et al. [9], and Übeyli [10] explored nonlinear time series analysis in the detection of seizures. Das et al. [11] presented an algorithm for epilepsy detection and [12] developed a model using wavelet transform to predict seizure from the pre-ictal EEG with accuracy about 92.66%. Several researchers have suggested CNN and artificial neural network-based detection systems for the treatment of epilepsy patients [10, 13, 14]. Various hybrid denoisings are recently applied in medical image processing [15, 16]. In terms of classification precision, with large data sets, deep learning performs admirably in conventional feature extraction, and pattern and image recognition [17]. Hu et al. [17] integrated CNN and SVM to extract and classify features and got an accuracy of 86.25%. Rajendra Acharya et al. [18] used EEG in a 13-layer CNN to detect epileptic seizures and attained 88.7% accuracy. Truong et al. [19] developed CNN to learn features from EEG signals' time–frequency energy map and performed 89.8% sensitivity classification. Khan et al. [20] have used a six-layer CNN architecture extracting EEG features to detect seizures, resulting accuracy of 87.8%. We have found special features in epileptic EEG data, i.e., local maxima, lower threshold, sharply defined component, and disturbed background. Using energy and power features, the sharply defined component characteristics can be established and channel clustering determines the region.

The paper is consisting of introduction in Sect. 1 and brief description of CNN in Sect. 2. In Sect. 3, proposed algorithm is described. In Sect. 4, we have presented the results and discussion, and Sect. 5 concludes the paper.

2   Convolutional Neural Network

Convolutional neural network (CNN) is one of the most prevalent neural networks. The novelty of CNN lies in architecture which considers the local and global characteristics of the input data. CNN is originally designed for image analysis. Recently, it is revealed that the CNN has also applied in neuroimaging to examine brain disorders. Under different constrictions of a specific predictive modeling, CNN proves revolution in learning numerous filters automatically in parallel explicit to a training data set. In CNN, using several filters, different features (feature map) are extracted from the data set by convolution, which summarizes the presence of detected features in the available data. To minimize the feature map dimension, subsampling is used. The output is exceptionally specific features which can be recognized in the signal. In Fig. 1, CNN of the proposed framework with input, hidden, and output layers is shown.
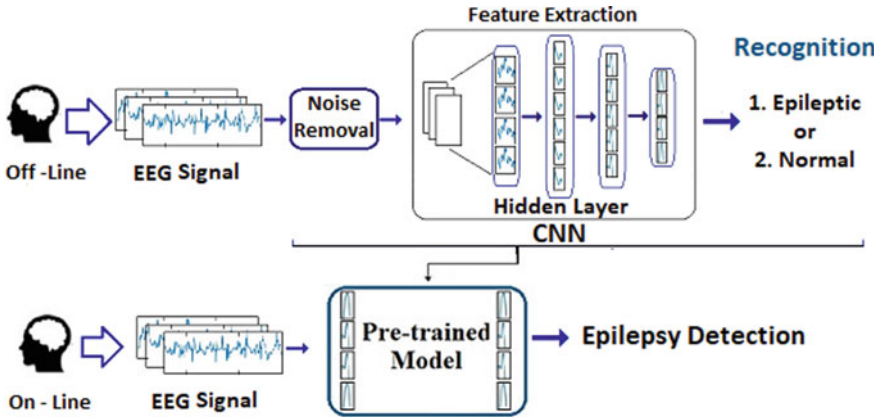
Fig. 1 Signal flow diagram of proposed model

3   Proposed Algorithm

In this section, we have discussed a comprehensive description of the proposed model to detect epileptic seizure. The proposed framework is represented using a signal flow diagram, as shown in Fig. 1. The EEG recording of patient is collected and passed through noise removal function, and then that data is transferred to input layer of CNN network. Using the algorithm, statistical features are being extracted to help the model in learning those features accordingly. In the output layer preceding the hidden layers, the seizures are detected. After classification of seizures, this model predicts whether the patient is seizurian or normal.

3.1   Feature Extraction

In this work, to predict seizure, various features are selected depending upon the constraints. The details of the features are discussed below.

A.   **Local Maxima**: Local maxima is the relative real-valued maxima within some neighborhood. For better clarification of this characteristic, we have induced mathematical terminology to find the local maxima. So, local maxima is

$$L_{\max} = \big(\text{Max}(\text{EEG}(i, j)) < \text{Lp}_{\max}\big) \tag{1}$$

where the number of channels (i) varies from 1 to N, j lies between 1 and CL (number of samples in each channel), and $\text{Lp}_{\max}$ is large positive value initially.

B.   **Least Threshold**: A calculated value which signifies the suspected spike will be considered for further processing or not. Least threshold ($\partial_{\text{threshold}}$) is expressed as

$$\partial_{\text{thresold}}\left(\text{EEG}_{\text{Lp}_{\text{max}}}(\text{index})\right) = \frac{\sum_{j=\text{Lp}_{\text{max}}(\text{index})}^{1\leq i\leq N} \text{EEG}(i,j)}{N} \qquad (2)$$

where the number of samples in a single channel is represented by N.

C. **Sharply Defined Component**: To establish the characteristics of seizure spike, sharply defined components are selected in terms of energy and power, which is performed in the hidden layer, shown in Fig. 1. In our EEG signal database, the recorded EEG data is discrete in nature. So, energy of EEG at ith instant is

$$E_{\text{eeg}}(i) = \sum_{j=0}^{N-1}|\text{EEG}(i,j)|^2 \qquad (3)$$

Similarly, power of EEG at ith instant is

$$P_{\text{eeg}}(i) = \lim_{N\to\alpha}\frac{1}{N}\sum_{j=0}^{N-1}|\text{EEG}(i,j)|^2 \qquad (4)$$

where $i = 0, 1, 2, 3, \ldots, n$ and $j = 0, 1, 2, \ldots, N-1$. Here, n is no. of channels and N is no. of samples in one channel or channel length.

D. **Selection of Window**: To establish disturbed background of a spike, a window is selected on both sides of the sharp component. In hidden layer 4 in Fig. 1, this is done.

$$\text{Window}(i) = \sum_{\delta=0}^{\frac{w}{2}} w(t\pm\delta) \qquad (5)$$

where w is window size and $w(t)$ is the spike which is found to be sharply defined.

E. **Channel Clustering**: To detect the affected channels among the different channels (Ch_i), clustering is performed and classified as epileptic channel (E_{Ch}) and non-epileptic channel (NE_{Ch}).

$$\text{Ch}_i \in E_{\text{ch}}; \quad \text{if } E_{\text{eeg}}(i) \geq \partial_{\text{thresold}}\left(\text{EEG}_{\text{Lp}_{\text{max}}}(\text{index})\right) \qquad (6)$$

$$\text{Ch}_i \in \text{NE}_{\text{ch}}; \quad \text{otherwise.} \qquad (7)$$

4   Result and Discussion

We have taken total 150 subjects including both male and female adults in this research. The EEG plotter which was used to record the EEG has the following

characteristics; i.e., the number of channels is 16, and sampling frequency is 256 Hz, with high frequency filter of 70 Hz, and low frequency filtration of 0.1 Hz, 4097 data samples per window.

4.1 Performance Evaluation

Performance of the proposed model is measured using confusion matrix in terms of sensitivity, specificity, precision, and accuracy, with the actual and predicted values, i.e., true positive (TP), true negative (TN), false positive (FP), and false negative (FN). Sensitivity is the measure of positive cases, classified as positive. Sensitivity can be considered as a detection rate.

$$\text{Sensitivity} = \frac{\text{TP}}{(\text{TP} + \text{FN})} \tag{8}$$

Specificity is the measure of negative cases, classified as negative correctly.

$$\text{Spicificity} = \frac{\text{TN}}{(\text{TN} + \text{FP})} \tag{9}$$

Precision or positive predict value (PPV) is the rate of positive prediction.

$$\text{Precision(PPV)} = \frac{\text{TP}}{(\text{TP} + \text{FP})} \tag{10}$$

Accuracy is determined by the total number of samples detected accurately.

$$\text{Accuracy} = \frac{\text{TP} + \text{TN}}{(\text{P} + \text{N})} \tag{11}$$

4.2 Result

As shown in Fig. 2, these are the basic representation of raw EEG data of five patients. In each EEG window of Fig. 2, the horizontal axis represents the time (0.0039 s per interval) and vertical axis represents the amplitude in microvolts (μV). Figure 3 shows the first layer output of this learning algorithm network, where one channel data is cross-related to the EEG pulse of same channel and to the other channel of the pre-trained model as well.

In Fig. 4, patient P-2 is having a sharp spike [21] in F3-A1 and patient P-4 is having sharp wave [21] in P3-A1 and F8-A2. Figure 5 represents the output of
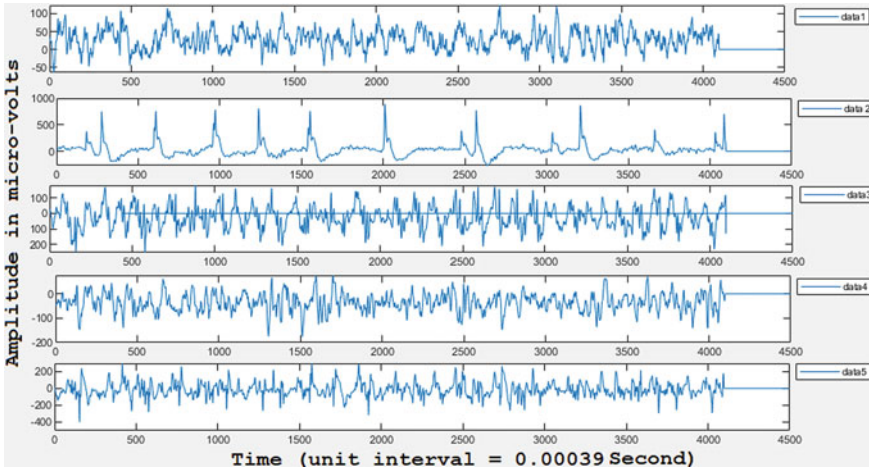
Fig. 2 Representation of sample EEG data of 5 patients
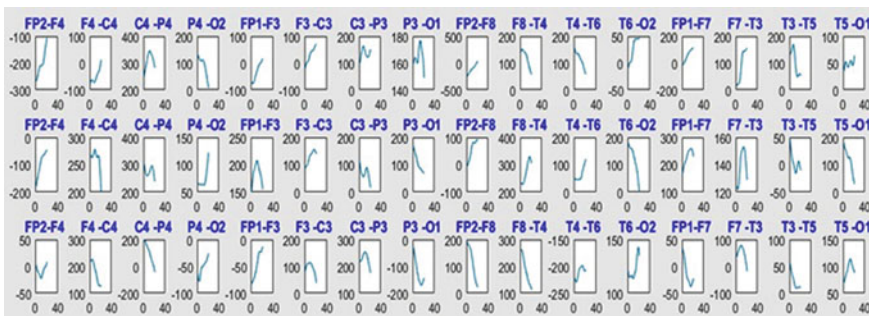
Fig. 3 Layer 1 output of three patients

channel clustering, classified into class-A (E_{Ch}) and class-B (NE_{Ch}) and the outcomes of the model are shown in Fig. 6 using confusion matrix.

A comparative analysis of the proposed framework with other papers from the same field has been shown in Table 1. Our proposed model provides more noteworthy sensitivity of 92.59% than [22] and better specificity of 92.86% than [18] and slightly less than [22, 23]. In terms of precision, it shows a far better response than [23] and [18]. The proposed model with 150 patients has attained a higher accuracy of 92.67% than many other recent works (e.g., [18, 23], and [22] with 05, 12, and 13 patients, respectively) in epilepsy detection.
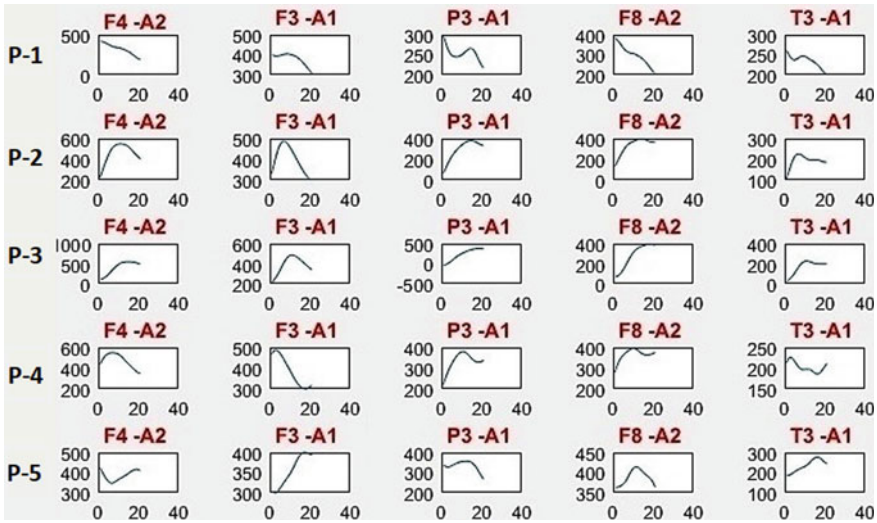
Fig. 4 Detected seizure output of 5 patients in 4th layer after online mode testing
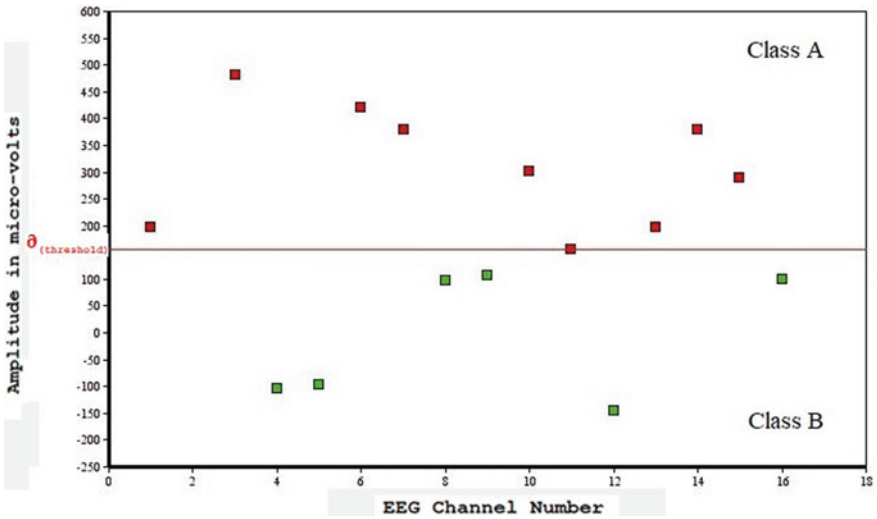
Fig. 5 Channel clustering based on least threshold for epileptic patient

5 Conclusion

In recent times, with the growing number of channels of EEG recording machines, it is getting to be very troublesome for neurologists to screen the EEG ceaselessly for a long time to distinguish the seizure. A CNN-based framework has been proposed to

Fig. 6 Performance evaluation using confusion matrix
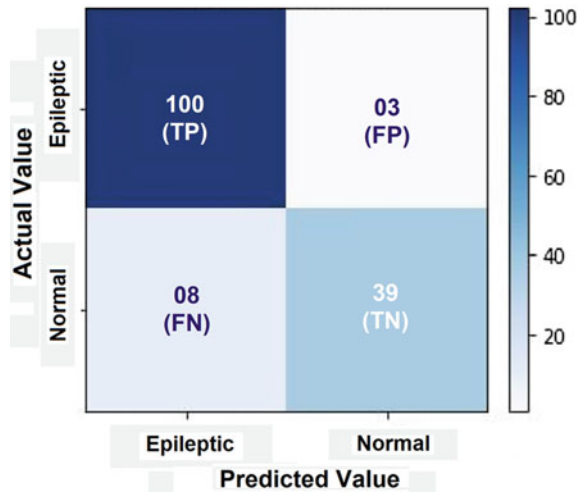
Table 1 Comparative analysis of overall performance

Measures	Birjandtalab et al. [23]	Rajendra Acharya et al. [18]	Wei et al. [22]	Our proposed model
Sensitivity	–	95%	88.90%	92.59%
Specificity	98.30%	90%	93.70%	92.86%
Precision	94.50%	95%	–	**97.09%**
Accuracy	90.60%	88.60%	90%	**92.67%**

predict the suspected epileptic patients which would be helpful for the neurologists to decide for further process of treatment. From the performance analysis matrices, a significant outcome has been achieved in terms of precision (97.09%), accuracy (92.67%), and other criterion. Going through all the imperatives, it is noticeable that the proposed model will contribute to major advancements in the field of epilepsy detection. In the future, we will concentrate on physiological field detection with larger data set.

References

1. Bernard, S.C., Daniel, H.L.: Epilepsy. New Engl. J. Med. **349**, 1257–1266 (2003). https://doi.org/10.1056/NEJMra022308
2. McGrogan, N., Supervisor Prof., Tarassenko, L.: Neural network detection of epileptic seizures in the electroencephalogram (1999). 10.1.1.8.9375
3. Albert, D.V.F., et al.: The impact of COVID-19 on epilepsy care: a survey of the American epilepsy society membership. Epilepsy Currents **20**(5), 316–324 (2020). https://doi.org/10.1177/1535759720956994

4. García-Ballestas, E., et al.: Risk of seizures after endovascular management of ruptured intracranial aneurysms: a systematic review and meta-analysis. J. Epilepsy Res. **10**(2), 55–61 (2020). https://doi.org/10.14581/jer.20009

5. de Tisi, J., Bell, G.S., Peacock, J.L., et al.: The long-term outcome of adult epilepsy surgery, patterns of seizure remission, and relapse: a cohort study. Lancet **378**(9800), 1388–1395 (2011). https://doi.org/10.1016/S0140-6736(11)60890-8

6. Gotman, J.: Automatic recognition of epileptic seizures in the EEG. Electroencephalogr. Clin. Neurophysiol. **54**, 530 (1982). https://doi.org/10.1016/0013-4694(82)90038-4

7. Qu, H., Gotman, J.: A patient-specific algorithm for the detection of seizure onset in long-term EEG monitoring: possible use as a warning device. IEEE Trans. Biomed. Eng. **44**(2), 115–122 (1997). https://doi.org/10.1109/10.552241

8. Adeli, H., Ghosh-Dastidar, S., Dadmehr, N.: A wavelet-chaos methodology for analysis of EEGs and EEG subbands to detect seizure and epilepsy. IEEE Trans. Biomed. Eng. **54**(2), 205–211 (2007). https://doi.org/10.1109/TBME.2006.886855

9. Güler, İ., Güler, N.F., Übeyli, E.D.: Recurrent neural networks employing Lyapunov exponents for EEG signals classification. Expert Syst. Appl. **29**(3), 506–514 (2005). https://doi.org/10.1016/j.eswa.2005.04.011. ISSN 0957-4174

10. Übeyli, E.D.: Analysis of EEG signals using Lyapunov exponents. Neural Network World **16**, 259–273 (2006)

11. Das, K., Prasad Saha, S., Kumar Singh, K.: Detection of epileptiform seizure from pre-ictal part of epileptic EEG recording. In: Advances in Systems Analysis, Software Engineering, and High Performance Computing, pp. 36–49. IGI Global (2020). https://doi.org/10.4018/978-1-7998-2584-5.ch003

12. Das, K., et al.: Epileptic seizure prediction by the detection of seizure waveform from the pre-ictal phase of EEG signal. Biomed. Sig. Process. Control **57**, 101720 (2020). https://doi.org/10.1016/j.bspc.2019.101720. ISSN 1746-8094

13. Tzallas, A.T., Tsipouras, M.G., Fotiadis, D.I.: Automatic seizure detection based on time-frequency analysis and artificial neural networks. Comput. Intell. Neurosci. **2007** (2007). https://doi.org/10.1155/2007/80510

14. Ghosh-Dastidar, S., et al.: Principal component analysis-enhanced cosine radial basis function neural network for robust epilepsy and seizure detection. IEEE Trans. Biomed. Eng. **55**(2), 512–518 (2008). https://doi.org/10.1109/TBME.2007.905490.0

15. Das, K., Maitra, M., Banerjee, M., Sharma, P.: Embedded implementation of early started hybrid denoising technique for medical images with optimized loop (2020). https://doi.org/10.1007/978-981-13-7403-6_28

16. Das, K., et al.: An embedded system for gray matter segmentation of PET-image. In: Advances in Intelligent Systems and Computing. Springer, Singapore (2020). https://doi.org/10.1007/978-981-15-2188-1_12

17. Hu, W., Cao, J., Lai, X., et al.: Mean amplitude spectrum based epileptic state classification for seizure prediction using convolutional neural networks. J. Ambient Intell. Human Comput. (2019). https://doi.org/10.1007/s12652-019-01220-6

18. Rajendra Acharya, U., et al.: Deep convolutional neural network for the automated detection and diagnosis of seizure using EEG signals. Comput. Biol. Med. **100**, 270–278 (2018). https://doi.org/10.1016/j.compbiomed.2017.09.017. ISSN 0010-4825

19. Truong, N.D., et al.: Convolutional neural networks for seizure prediction using intracranial and scalp electroencephalogram. Neural Networks **105**, 104–111 (2018). https://doi.org/10.1016/j.neunet.2018.04.018. ISSN 0893-6080

20. Khan, H., Marcuse, L., Fields, M., Swann, K., Yener, B.: Focal onset seizure prediction using convolutional networks. IEEE Trans. Biomed. Eng. **65**(9), 2109–2118 (2018). https://doi.org/10.1109/TBME.2017.2785401

21. Jaseja, H., Jaseja, B.: EEG spike versus EEG sharp wave: differential clinical significance in epilepsy. Epilepsy Behav.: E&B **25**(1), 137 (2012). https://doi.org/10.1016/j.yebeh.2012.05.023

22. Wei, X., et al.: Automatic seizure detection using three-dimensional CNN based on multi-channel EEG. BMC Med. Inf. Decis. Making **18** (2018). https://doi.org/10.1186/s12911-018-0693-8
23. Birjandtalab, J., et al.: Unsupervised EEG analysis for automated epileptic seizure detection. In: SPIE, vol. 10011, pp. 124–128 (2016). https://doi.org/10.1117/12.2243622

Design of a Smart Footwear Disinfecting Station for Crowded Premises

Ishani Mondal, Jahir Anwar Molla, Suman Karmakar, and Habib Masum

Abstract Since the first virus was identified in the early last century, many kinds of different viruses have been discovered until now that can harm a human being. One of these is severe acute respiratory syndrome coronavirus 2 (SARS-CoV-2) or well known as coronavirus, which has pushed the entire world into a deadly pandemic. The pandemic has been affecting public health, employment, lifestyle, and the entire food system. To protect our house, workplace, and heavily populated areas such as markets and hospitals from being infected by the virus, it needs to be stopped in every possible way to be spread. Footwear is one of the potential sources of contamination and possible carrier of the virus, especially if it touches an infected place or someone who has already infected sneezes or coughs nearby. Since most footwear is made of leather, rubber, and plastic, the virus can live on these for many days at room temperature. Even footwear can be a breeding ground for bacteria and viruses as it comes in contact with dirt and germs more than anything else. In this paper, a smart device for disinfecting footwear has been proposed for crowded premises. The sensing device will automatically sense the visitor's presence at the entrance and will disinfect his footwear by spraying disinfecting agent underneath the footwear or foot. This disinfecting station will allow visitors to disinfect their footwear without stopping and will ensure effecting sanitization of the entire sole even if the sole has deep flex grooves or high heels.

Keywords Crowded premises · Disinfecting station · Footwear sole

I. Mondal · J. A. Molla · H. Masum (✉)
Ghani Khan Choudhury Institute of Engineering and Technology (GKCIET), Narayanpur, Malda, West Bengal, India

S. Karmakar
eStore, Malda, West Bengal, India

1   Introduction

A virus, the submicroscopic agent, may replicate inside the residing cells and infect the living organisms [1]. The size of the virus is so small that cannot be visible to the bare eyes, but its effect is sometimes life-threatening [2]. Although the records of the virus are no longer truly acknowledged and people also do not recognize when the primary virus became seemed within the world, the first virus, named 'tobacco virus,' became observed in 1982 by the scientist from epidemic leaves [2, 3]. A scientific estimation indicates that there are at least 320,000 viruses awaiting discovery that can infect mammals. [4]. Human civilization has already witnessed the effects of the most dangerous viruses in the ongoing century, e.g., Ebola virus, Marburg virus, Dengue virus, etc. [5, 6]. According to the fatality rate, Ebola virus disease (EVD) has a fatality rate of around 90%, spreading through direct contact with infected animal like fruit bats. The Marburg virus, Dengue virus (DENV), and other viruses have different fatality rates and incubation duration. They have different carriers like animals, insects, i.e., mosquitoes, and so on, and they cause convulsions, bleeding of mucous membranes, pores and skin, and organs, also additionally spread human to human. In modern times, an acute respiratory illness in human beings resulting from a murderous virus named the 'Coronavirus', capable of generating severe symptoms and in a few instances even death, especially in older people and those with underlying health situations [7]. It became initially identified in China in 2019 and drives the entire world into a deadly pandemic in 2020. The COVID-19 pandemic has been already affecting public fitness, employment, lifestyle, and the whole food system [8]. As a preventative measure of spreading the virus, the lockdown has proven sometimes been effective. But it has many demerits like recession within the markets from lack of customers, transportation problems, restrictions in import and export of necessary commodities, medicine, etc. The tourism enterprise, aviation, and railways are suffering massive losses because of the lockdown [9].

Despite the consensus that severe acute respiratory syndrome coronavirus 2 (SARS-CoV-2) spreads by a bat, animals, and many others, it is also seen that the viruses can be carried by cloth, shoes, and other objects [8]. As a way to protect our residence, work region, and closely populated areas including markets and hospitals from being infected through the virus, it needs to be stopped in every possible manner. There are numerous approaches through which this could manifest, like droplets or aerosols. While an infected person coughs, sneezes, or talks, the droplets or tiny particles which pushed the virus into the air from their nostril or mouth are called aerosols.

Although people are adopting different methods to stop the communication of the virus from person to person like, wearing masks, gloves, face shields, hand sanitizers, and even some crowded places get disinfected using the household disinfectant. But footwear can also be a potential source of infection and feasible career of the virus [10, 11]. Researchers claim that even our footwear can be a breeding ground for bacteria and viruses.

So, the possibilities of having germs within the shoes are much higher and when the people are getting into their house or some other places, they carry the germs with them and unknowingly do a lot of harm to the people around them [9]. From the houses to the heavily crowded places just like the shopping malls, schools, colleges, workplaces, temples, mosques, etc., the virus can be tracked all around the floor by means of carrying the virus through footwear. Keeping disinfecting devices at the doorway of the houses or at the closely populated areas, with a purpose to sanitize or disinfect the footwear or shoes, there is a possibility to stop the transmission of the virus [12].

There are many solutions available in the market for disinfecting the footwear sole starting from disinfecting ground mat to automatic disinfecting device [13–16]. These are for different application areas and unique working principles. Some are for small with limited capacity, and some others are comparatively large areas like offices, cinema halls, shopping malls, etc., with different retention times (i.e., time to hold the footwear on the device for proper disinfection) to visitors. This either produces a large waiting time for the visitors to maintain the process of disinfecting their footwear at the crowded entrance or sometimes leads the visitors for bypassing the process which is not desirable at all. Even, some footwear disinfecting measures do not ensure effective disinfection of footwear having deep flex grooves or excessive heels. This has motivated authors to make an attempt for designing an automatic footwear disinfecting station that will be smart and allow visitors to enter without interruption (potentially zero retention time). This device is designed mainly for crowded premises like hospital entrances, schools/colleges, offices, cinema halls, shopping malls, bus terminals, railway stations, airports, etc., to ensure proper sanitization of footwear keeping all safety measures. In this work, the concept of the device, its working principle, selection of electrical components, design of the mechanical system, and its control algorithm are presented.

2 Development in This Field

The conventional method of shoe cleaning is swabbing the bottom face of footwear by rubbing it against a mat or rug as shown in Fig. 1a. Sometimes, the cleaning beneath the shoe can be done by putting it against rotating or moving brushes and the associated vacuum suction system removes and scoops up fine dust particles. One of such machines, namely the footwear sole cleaning machine, as shown in Fig. 1b, starts automatically with a sensor and cuts after a certain period of 10–12 s. This cleaning process is being done by an electric motor-driven cylindrical rotating grill [14]. This is an automatic footwear sole cleaning device that works mechanically without disinfecting facility.

Apart from the above, when the requirement of footwear cleaning comes with the objective of disinfection, it is essential to add a measure of killing viruses. Many solutions are already available for this purpose. Gradually, the necessity of various techniques to prevent the spread of the virus is increasing since the fatality rate of the
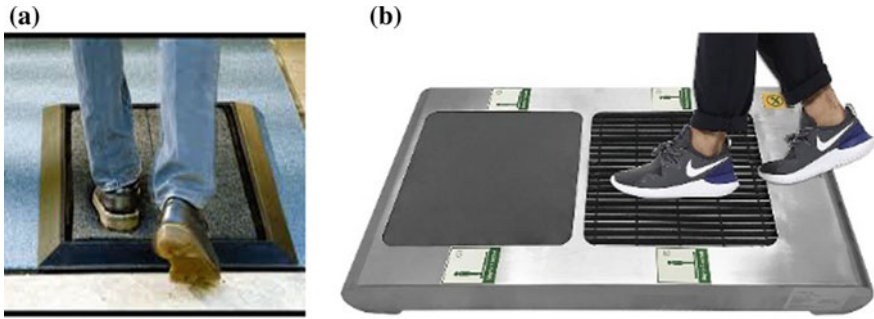
Fig. 1 **a** Doormat and **b** footwear sole cleaning machine [14]
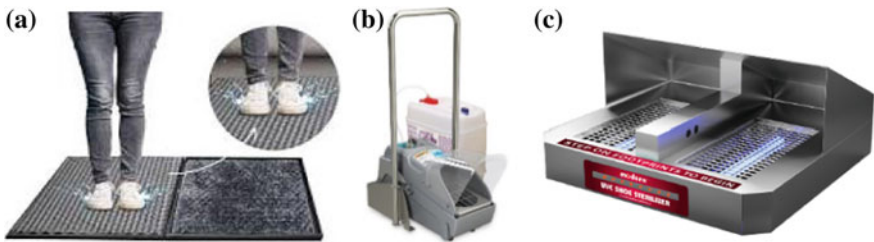
Fig. 2 **a** Sanitizing mats, **b** SmartStep [15], **c** UVC shoe sanitizer [16]

COVID-19 has been changed constantly during the early period of the outbreak. The very basic consent of disinfection is to use a sanitizing mat or disinfecting ground mat for footwear [13] as shown in Fig. 2a.

This disinfecting mat retains the sanitizing liquid agent within a flexible coil. The flexible coil also helps to remove dirt from the bottom surface of the sole. The mat's edges are molded to contain the liquid agent. It is very easy to use, maintain, and clean, but unable to completely disinfect the footwear having deep flex grooves or excessive heels. Also, it can be used only for homes or places with less frequent visitors.

Some other footwear sanitizing machine is also available in the marketplace that has the ability to add an extra layer for pathogenic safety and additionally enables to lessen the pass contamination from the shoes. SmartStep, as shown in Fig. 2b, is also a recently developed smart footwear sanitizing unit which utilizes the compressed air for spraying liquid sanitizing agent underneath the footwear [15]. The device is capable of spraying 5.91 ml of sanitizer per spray. It is designed with a collection basin for swap out for cleaning and a spray guard to prevent overspray.

The UVC shoe sanitizer, as shown in Fig. 2b, is another commercially available footwear disinfecting device that is developed to prevent the growth of bacteria and other conditions of fungal infection by exposing the foot sole above the UV ray. It takes around 10–30 s to sterilize a single foot sole using an ultraviolet-C (UVC) lamp [16]. Many research articles have been published on the effect of UVC radiation on

viruses [17–19]. This radiation destroys the protein-made outer coating of the virus and makes it inactive. Though the UVC is a very useful tool for disinfecting from viruses, it is effective only when the virus is directly exposed to the radiation and with a certain time duration. Besides the same, direct human exposure to UV rays can be a health hazard to the skin and eyes [20].

3   Methodology

Characterization of smart footwear disinfecting stations in this present pandemic situation is one of the challenging and useful works. From the review of previous works and various guidelines for combating the pandemic situation, the following salient features have been targeted:

(i) The system shall be safe for human, (ii) shall have very low retention time, preferably zero, (iii) shall be capable to ensure complete disinfection of different types of footwear, (iv) shall have minimal human intervention, (v) shall be designed for crowded premises like large offices/institutes, cinema hall, shopping malls, bus terminal, railway station, etc., (vi) shall eliminate the chance of wastage, and (vii) shall be a cost-effective solution.

To address the above features and to overcome the impediments of existing solutions, a smart device for disinfecting footwear with effective sanitization has been proposed. The sensory input-based footwear disinfecting station has been presented here for effective sanitization of shoes in this pandemic situation to prevent the contamination of the virus from one of the potential sources of contagion. The sensing elements of the device will automatically sense the presence of a visitor (person) passing on it and will activate the spray system on the predefined sequence. When he will progress further on his way and will reach the spray area, in the meantime first spray will start spraying. Accordingly, the next sprayers will follow the spraying patterns with the progression of the person. The details of the timing of the spray nozzle have been discussed later.

4   Working Principle

A schematic diagram of the smart footwear disinfecting station is presented in Fig. 3.

As shown in Fig. 3, when a visitor will reach to the starting point of an entry (it can be referred to as Level 0 of disinfecting station), the ultrasonic sensors will inform the system (microcontroller) about the entry of the persons. Accordingly, a signal will go to the relay module to open Solenoid Valve 1 (SV-1). When the person will reach to Level 1 (Spray Zone 1), in due course of time, the Spray Nozzle 1 will be activated through SV-1. Let us consider it as the first step of leg 1 under exposure of disinfecting liquid spray. Then, the next step (first step of leg 2) will reach Level 2 (Spray Zone 2 or Level 2) and within that time interval the Spray Nozzle 2 will be
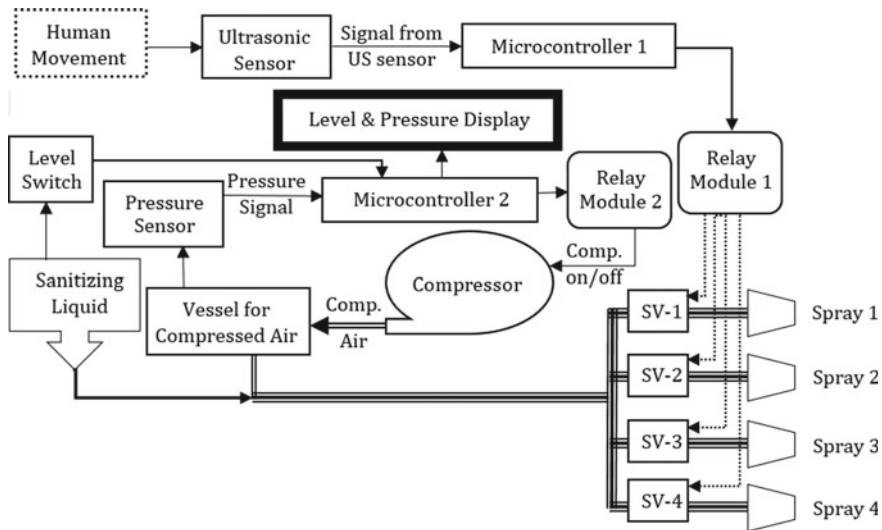
Fig. 3 Schematic diagram of the system

activated through SV-2. As soon as leg 1 will be lifted from Spray Zone 1 and go for Spray Zone 3 (Level 3), the mean time Spray Nozzle 1 will be stopped spraying, and Spray Nozzle 3 will start through SV-3. Similarly, while leg 2 will be lifted from Spray Zone 2 and go for Spray Zone 4 (Level 4), in the meantime Spray Nozzle 2 will be stopped and Spray Nozzle 4 will start through SV-4. Therefore, when the person will cross Level 4, both the footwear will be sanitized twice to ensure complete disinfection. All the sequence of starting and stopping spray nozzles will be decided by the microcontroller with predefined calculations considering a variety of walking speeds of different types of visitors. The activation of all four sprayers with a different timing and duration will eliminate the waste of disinfecting liquid.

The motive behind using two additional sprayers (i.e., 3rd and 4th) is to ensure complete disinfection of the sole of footwear, as some areas beneath the sole can be left shaded by the grill of the walking platform at Level 1 and Level 2 in one spray. It is expected that those shaded areas will be sanitized in the next successive spray at Level 3 and Level 4.

5   System Design

Ultrasonic sensor-based obstacle detection system has been considered here due to its reliability. ATmega 2560-based Arduino Mega 2560 microcontroller board has been considered as the main controller where sensors will be connected. A 4-channel 5 V solid-state relay (SSR) module has been considered here for operating solenoid valves. Another microcontroller board has also been considered for the

compressed air system and liquid sanitizing dispensing system. Compressed air is used here because it will mix with the sanitizing liquid to form a spray for proper delivery of sanitizing agents through the sprayer. The control of the spray system has been kept separate from the control of the compression system for fast, robust, and independent operation of the entire system. Stainless steel pressure transducer sensor has been envisaged for monitoring the compressed air pressure inside the air tank. The pressure data from the pressure transducer will be fed continuously to the second microcontroller board for monitoring and operating the compressor to maintain an optimal level of pressure in the compressed airline. The compressor will be operated through Relay Module 2 which will be connected to the second board. The level of sanitizing liquid within the dispensing tank will be monitored by a level switch, and related information will be relayed to a display unit through the second controller board for the alert purpose. Multistage air compressor shall be used with large air tank capacity which will allow less frequent on–off of the compressor. The sanitizing liquid shall be stored in the dispensing tank, and it will be fed to the spray network due to gravity.

The design of the mechanical system shall broadly depend upon the type of crowd and the type of visitors. The physical dimension of the disinfecting unit shall directly be linked with the age range of visitors and their walking patterns. The comfortable walking speed of different age groups is different [21] as shown in Table 1.

From Table 1, it is seen that if the visitors are all adult (in the case of office premises), the variation of walking speed is comparatively low and the system shall be designed considering less variation of walking speed. But for the other premises where persons of any age visit, the nozzle activation times and dimension of spray zones shall be designed considering a wide range. However, the design should be done considering the comfortable gait speed of humans with a reasonable margin. Figure 4a represents a different activation time for the spray nozzles from the detection time of visitor's entry for the premises with adults only (20–69 years) with the following consideration:

Max. walking speed on the disinfecting station is 150 cm/s, and min. is 135 cm/s.
Average stride length = 120 cm and average gait cycle time = 1.00 s.
Distance of sensing point from first spray zone = 2 m.

Then, the activation time of any nozzle from the obstacle sensing time shall be defined as follows:

$$\text{Nozzle start time (s)} = \frac{\text{Distance of the nozzle from detection point, i.e., Level 0 (cm)}}{\text{Walking Speed}_{\text{Max}} \text{ (cm/s)}}$$

$$\text{Nozzle stop time (s)} = \frac{\text{Distance of the nozzle from detection point, i.e., Level 0 (cm)}}{\text{Walking Speed}_{\text{Min.}} \text{ (cm/s)}} + \big[0.6 * \text{Gait Cycle Time (s)}\big]$$

Accordingly, Fig. 4b represents the activation times of spray nozzles for the premises with persons of any age. The platform of spray zones shall be made of

Table 1 Comfortable gait speed for different age groups

Age group (years)		Below 9	10–19	20–29	30–39	40–49	50–59	60–69	70–79
Average comfortable gait speed (cm/s)	Male	65.4	120.4	139.3	145.8	146.2	139.3	135.9	133.1
	Female	65.1	116.0	140.7	141.5	139.1	139.5	1296	127.2

(a)

For the premises with adults only

(b)

For the premises with Persons of any age
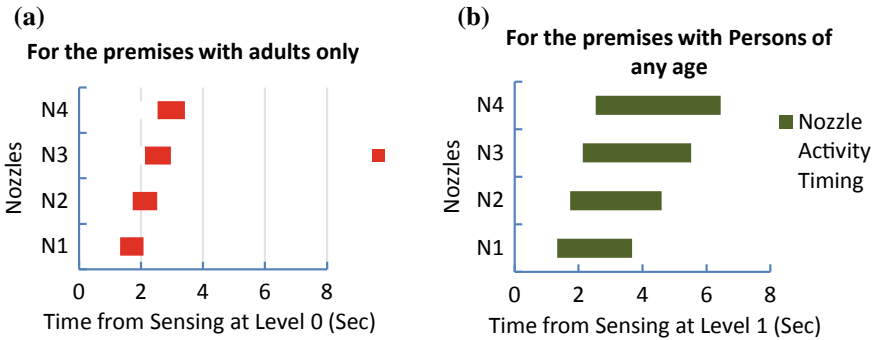
Fig. 4 Different spray activation timings from the sensing of visitors, **a** for the premises with adults only (20–69 years) and **b** for the premises with persons of any age

the grill structure to facilitate spray from the bottom. The spray nozzles should be kept inclined to restrict sprinkling of liquid disinfectant above the shoe.

6 Proposed Algorithm

Two algorithms have been suggested to control the entire system, one for compressor and the second one for controlling spray system. These are as follows:

Algorithm 1 (for air compression system)

(a) Read the pressure level of the compressed air tank.
(b) If it is below the set value P1, the power terminal of the compressor motor shall be connected.
(c) If the value is above the set value P1 but below P2, let the status of the compressor on or off be continued.
(d) If the value is above the set value P2, the power terminal of the compressor motor shall be disconnected.

Algorithm 2 (spray system)

i. Read the presence of visitors at Level 0.
ii. Start spray 1 at the time T1 through SV-1 for s1 second.
iii. Start spray 2 at the time T2 through SV-2 for s2 second.
iv. Start spray 3 at the time T3 through SV-3 for s3 second.
v. Start spray 4 at the time T4 through SV-4 for s4 second.
vi. Repeat steps (ii) to (v) upon detecting the next visitor.

The above two algorithms have been depicted by the process flow diagrams as shown in Fig. 5.
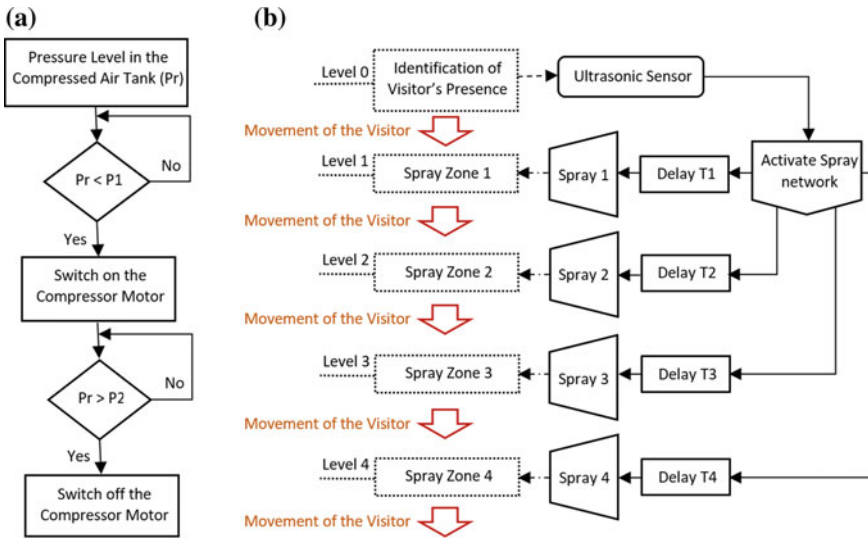
Fig. 5 Flowcharts, **a** air compression system and **b** disinfecting liquid spray system

7 Discussion

The disinfecting station has been designed with the objective to overcome the drawback of existing systems. The very first thing was to eliminate the retention time of the user which in most cases is a major factor for discouraging its uses. Sometimes, it is not feasible to use a disinfecting system having even a very small retention time when it is for crowded premises like schools/colleges, offices, airports, etc. The proposed system is capable to eliminate any retention time. The next challenge was to ensure proper sanitization of the entire sole of footwear, i.e., to overcome shaded area. This has been achieved by considering exposure of each step twice on the sprayer. This also makes sure effective disinfection of all kinds of shoes having either deep flex grooves or high heels. Additionally, it is safe from any kind of harmful radiation. This device will be very useful for a wide variety of premises, particularly with the large gathering. The station is designed to functions automatically with very little human monitoring effort and intervention. Various important statuses/parameters like compressed air pressure inside the tank, sanitizing level in the dispensing container, compressor on/off, etc., shall be displayed for central monitoring of the system.

8 Conclusion

The sensor-based automatic footwear disinfecting station has been presented here for effective sanitization of shoes in this pandemic situation to prevent the contamination

of the virus from one of the potential sources of contagion. This work focuses on improving the standard to decrease the human-to-human spreading capability of the virus posing enormous health, economic, environmental, and social challenges to the entire human population. This device is designed to safely remove harmful germs or microorganisms from the sole of the footwear or feet. Using this automatic sanitizing station, the periodic and regular hectic efforts of disinfecting can be eliminated. With the usefulness of this smart device, one can protect not only yourself but also the people surrounding them. This disinfecting mechanism offers safe and effective sanitization with zero retention time to the visitors. The device has been effective for premises with large gatherings like hospitals, clinics, malls, offices, institutes, bus terminals, railway stations, airports, etc. Finally, the low-cost and user-friendly proposed system is in progress.

References

1. Koonin, E.V., Dolja, V.V.: Virus world as an evolutionary network of viruses and capsidless selfish elements. Microbiol. Mol. Biol. Rev. **78**(2), 278–303 (2014)
2. Lodish, H., et al.: Molecular Cell Biology, 4th edn. W. H. Freeman, New York (2000)
3. Lu, Z.S., et al.: Proteomic and phosphoproteomic analysis in tobacco mosaic virus-infected tobacco (*Nicotiana tabacum*). Biomolecules 23; **9**(2), 39 (2019)
4. Simon, J.A., et al.: A strategy to estimate unknown viral diversity in mammals. mBio **4**(5) (2013)
5. Jadav, S.S., Kumar, A., Ahsan, M.J., Jayaprakash, V.: Ebola virus: current and future perspectives. Infect. Disord. Drug Targets **15**(1), 20–31 (2015)
6. Uno, N., Ross, T.M.: Dengue virus and the host innate immune response. Emergy Microbes Infect. **7**(1), 167 (2018)
7. Al-Osail, A.M., Al-Wazzah, M.J.: The history and epidemiology of Middle East respiratory syndrome corona virus. Multidiscip. Respir. Med. **12**, 20 (2017)
8. World Health Organization Homepage: https://www.who.int/emergencies/diseases/novel-coronavirus-2019/situation-reports. Accessed 25 Mar 2021
9. Chakraborty, I., Maity, P.: COVID-19 outbreak: migration, effects on society, global environment, and prevention. Sci. Total Environ. **728**, 138882 (2020)
10. Rashid, T., VonVille, H.M., Hasan, I., Garey, K.W.: Shoe soles as a potential vector for pathogen transmission: a systematic review. J. Appl. Microbiol. **121**(5), 1223–1231 (2016)
11. Guo, Z., Wang, Z., Zhang, S., et al.: Aerosol and surface distribution of severe acute respiratory syndrome coronavirus 2 in hospital wards, Wuhan, China, 2020. Emerg. Infect. Dis. **26**(7), 1583–1591 (2020)
12. Koganti, S., et al.: Evaluation of hospital floors as a potential source of pathogen dissemination using a nonpathogenic virus as a surrogate marker. Infect. Control Hosp. Epidemiol. **37**(11), 1374–1377 (2016)
13. Onlymat Homepage: https://onlymat.com/collections/sanitize-mats. Accessed 25 Mar 2021
14. Dolphy Homepage: https://dolphy.in/sole-cleaning-machine?gclid=Cj0KCQjw38-DBhDpA RIsADJ3kjkyMioa2B27_11mSzxqeBdL5KBOupieAO8mFrjD4Ds36GaVOGmt_S4aAuA NEALw_wcB. Accessed 25 Mar 2021
15. Bestsanitizers Homepage: http://www.bestsanitizers.com/products/footwear-sanitizers/haccp-smartstep-footwear-sanitizing-system. Accessed 25 Mar 2021
16. Moderncomforts Homepage: https://www.moderncomforts.in/product-page/shoe-sole-ste rlizer?gclid=Cj0KCQjw38-DBhDpARIsADJ3kjkHWn6ZtEBCTllC73Uc9rZen1Ldn0vdm-KQNJtXcFvNGGqyGCuGQZcaAjp6EALw_wcB. Accessed 25 Mar 2021

17. Budowsky, E.I., et al.: Principles of selective inactivation of viral genome. I. UV-induced inactivation of influenza virus. Arch. Virol. **68**(3–4), 239–247 (1981)
18. Kowalski, W.J.: Ultraviolet Germicidal Irradiation Handbook: UVGI for Air and Surface Disinfection. Springer, New York (2009)
19. Buonanno, M., Welch, D., Shuryak, I., et al.: Far-UVC light (222 nm) efficiently and safely inactivates airborne human coronaviruses. Sci. Rep. **10**, 10285 (2020)
20. Trevisan, A., et al.: Unusual high exposure to ultraviolet-C radiation. Photochem. Photobiol. **82**(4), 1077–1079 (2006)
21. Bohannon, R.W.: Comfortable and maximum walking speed of adults aged 20–79 years: reference values and determinants. Age Ageing **26**(1), 15–19 (1997)

An Intelligent Temperature Sensor with Non-linearity Compensation Using Convolutional Neural Network

Nancy Kumari and S. Sathiya

Abstract Thermocouple has immense application in industrial measurement, testing, and research laboratories. However, its non-linearity affects the measurement adversely at larger range (0–1800 °C) of temperature. Non-linearity makes the measurement less accurate, less precise, and less robust. This paper proposes two neural network approaches, namely back propagation neural network and convolutional neural network for linearization of the characteristics of the thermocouple to study the advantages of software linearization method over real-time linearizing circuits whose performance degrades over time. By using these methods, the weights are adjusted to train the neural network for the desired output. The error between train and tested outputs is 0.0428% by back propagation network, and it is 0.0397% with convolutional neural network. It is observed that convolutional neural network shows 7.24% of better accuracy by training when compared with back propagation neural network. Non-linearity gets reduced by 61.37% compared to the original characteristics of the thermocouple by using convolutional neural network.

Keywords Artificial neural network · Back propagation · Convolution · Linearization · Temperature measurement · Thermocouple

1 Introduction

Industrial processes are to be closely monitored for optimized production, safety, and less wastage. The temperature is one such parameter that is to be controlled in various critical process and manufacturing areas in industries. There are various types of sensors used to measure the temperature, and the most popular type of sensor is

N. Kumari (✉) · S. Sathiya
Department of Instrumentation and Control Engineering, Dr. B. R Ambedkar National Institute of Technology, Jalandhar, India
e-mail: nancyk.ic.19@nitj.ac.in

S. Sathiya
e-mail: sathiya@nitj.ac.in

thermocouple due to its interchangeability and relatively low cost [1]. The thermocouple sensor could be characterized as cheap, more accurate, repeatable, rugged, and stable, which is used for various industrial processes including measurement of temperature of kilns, gas temperature measurement in monitoring and control of furnace, calibration, radiation detection, manufacturing of steel, and also it adapts to different environment conditions [2, 3]. Though it fulfills the ideal standard of accuracy, there is a problem of non-linearity which is a crucial parameter, and it is to be reduced. The literature describes the hardware methods for reducing the non-linearity with minimal cost signal conditioning circuit for type J thermocouple using negative temperature coefficient with a voltage-to-frequency converter for reference junction compensation (RJC), and for calculating the temperature, fraction algorithm is being used [4]. However, the circuit design becomes complicated and delicate to environmental condition. The new digital technique is developed to reduce the non-linearity of low-level output by adjusting the traditional dual-slope analog-to-digital converter (ADC). The different segments use different gains by adjusting the charging period. Thus, this method removes the shortcoming in linearization technique in which precision amplifier and demultiplexer are used to achieve variable gain. This method ensures better reduction of non-linearity by changing digitally different gains required for increasing the number of segments. Besides this, stability also gets improved, and cost gets reduced [5]. However, the hardware compensation circuit is sensitive to offset error, gain, and temperature drift [6]. Because of limitations mentioned above, few software techniques were developed.

Linearization technique unit (LTU) gives an understanding between input yield esteems for nonlinear model. In this method, measured variable corresponding to output signal is stored in memory. Following ADC and measurement, the outcome is gazed upward in the table and closest accurate estimation is calculated. LTU is fast for linearization, but it needs more memory space. For improvement in accuracy, it requires resolution of the ADC module and more memory space [7]. Some intelligent techniques are also reported in the literature, and the multilayered artificial neural network (ANN) is used and trained by the Levenberg–Marquardt algorithm. For initializing the weight and biases, back propagation algorithm is employed to reduce the deviation between target and true output. As the training data increases, the error decreases to greater extent. The mean square errors as well as gross error for all type of thermocouple are calculated, and the non-linearity is reduced to greater extent by using ANN [4]. In this paper, the performance comparison of two neural network approaches for the non-linearity compensation of thermocouple has been compared. The accuracy between trained and tested outputs of both the approaches is determined, and non-linearity compensation of both the techniques is also analyzed.

2 Proposed Work

Figure 1 illustrates the block diagram of the proposed methodology for the linearization of thermocouple. In the first stage, a thermocouple sensor is used to generate the
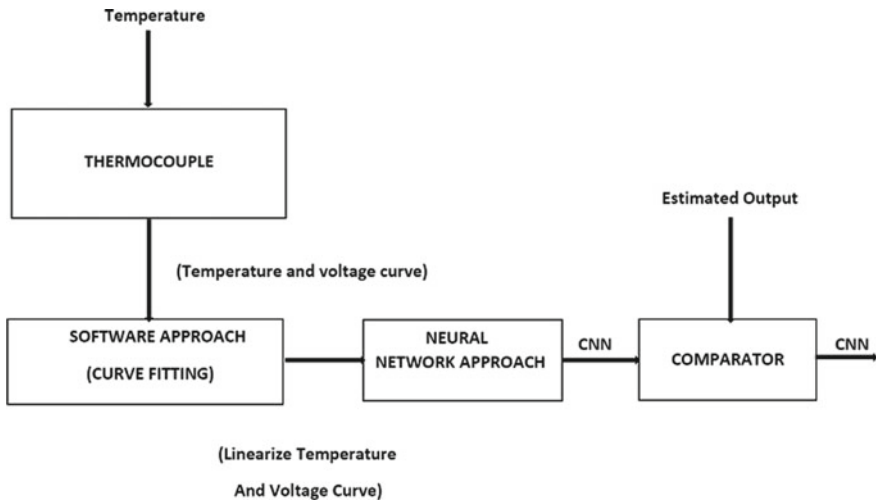
Fig. 1 Block diagram of proposed technique for linearization of thermocouple

voltage proportional to the measured temperature, which is then fed to the software approach for curve fitting. The linearized curve-fitted temperature–voltage characteristics of thermocouple are then fed to neural network for its training. To train the neural network for the given input data accurately, the weights are continuously adjusted until the errors are reduced to minimum possible value.

The general form of emf equation for thermocouple:

$$E = a_0 + a_1 t + a_2 t^2 + a_3 t^3 + a_4 t^4 + a_5 t^5 + a_6 t^6 \tag{1}$$

where E is output voltage in millivolt, t is temperature in degree Celsius, and a_0, a_1, a_n … are coefficients of thermocouple, which varies depending upon type of thermocouples. In this paper, type B thermocouple is used for performance analysis in the non-linearity compensation. The coefficient values used are $a_0 = 0.0000$, $a_1 = -0.2465 * 10^{-3}$, $a_2 = 0.5904 * 10^{-5}$, $a_3 = -0.1325 * 10^{-8}$, $a_4 = 0.1566 * 10^{-11}$. According to the emf equation, the voltage–temperature characteristic of thermocouple is nonlinear. The temperature value of cold junction is to be maintained at 0 °C using an ice bath and considering it as reference junction. The hot junction serves as the junction where the process temperature is measured. The difference of estimated temperature between hot junction and the reference junction produces the thermocouple yield voltage or thermo-voltage. The thermo-voltage measured using Eq. (1) is not linearly related to the estimated temperature. For the values of temperature and voltage, a polynomial curve fitting is done to construct a curve that has best fit for the data points which are then fed to the two types of a neural network approaches such as back propagation neural network and CNN for its performance comparison.

2.1 Back Propagation Neural Network

Back propagation (BP) is a popular machine learning approach for training feed forward neural networks. The chain rule is used to compute the gradient of the loss function for each weight of one layer at a time and iterates backward from the last layer in the chain rule to avoid redundant measurement results of the intermediate terms in the chain rule. To train the neural network, the temperature–voltage characteristics of type B thermocouple are obtained from the ITS-90 data table. The input to the neural network is difference between hot and cold junction temperatures (°C), and target output is the corresponding voltage in mV. The back propagation algorithm is a supervised learning process with three layers: input, hidden, and output. The sum operation is performed after multiplying each input with its weight and then fed into the hidden layers. Activation function is applied to the hidden layer and output layer. Learning rate is considered as 0.5. The output obtained from the hidden layer is then fed into the output layer. The output obtained through the neural network is compared from desired output, for the calculation of the error which is used to adjust the weight. The entire process is repeated until the error reaches its least possible value (Fig. 2).
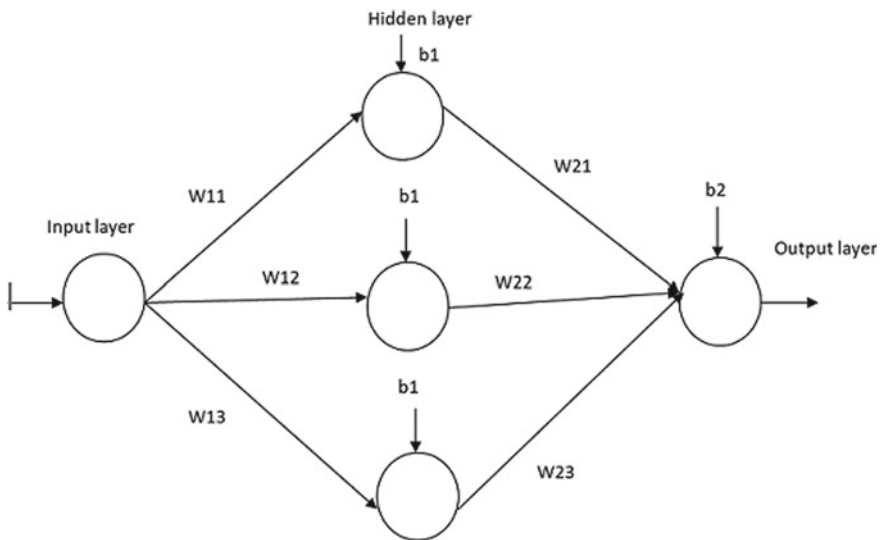
Fig. 2 Structure of back propagation neural network
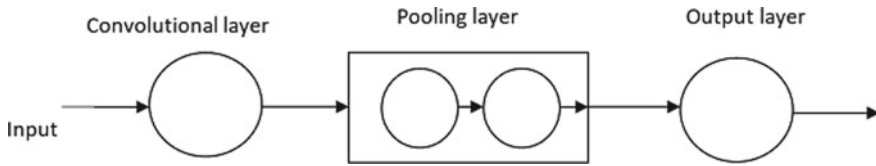
Fig. 3 Basic structure of convolutional neural network

2.2 *Convolutional Neural Network*

The convolutional layer of convolutional neural network (CNN) is fed with an input which is the CNN's primary building block of the network. Convolutional layer is followed by the pooling layer, and the last layer is output layer. The input data fed to the convolutional layer is then passed to the pooling layer where the weights are multiplied with convolutional layer output. Then, the output of the convolutional layer is passed into the output layer where the final output is compared with desired output for weight adjustment according to the cascaded feed forward back propagation algorithm (Fig. 3).

The convolutional neural network process is repeated till the trained output exactly matches with the desired output.

3   Results and Discussion

The type B thermocouple (platinum Rhodium 30%/platinum Rhodium 6%) is taken into consideration for linearization analysis. For the performance comparison of two neural network approaches in non-linearity compensation, the measured temperature ranges from 0 to 630 °C and has been taken as input, and the output voltage with respect to input temperature is obtained using the generic mathematical model of thermocouple. The obtained characteristic is illustrated in Fig. 4, where it is clearly seen that the temperature–voltage characteristics of thermocouple are nonlinear.

The obtained nonlinear characteristic of thermocouple is given to software curve fitting approach where it is used for the curve linearization of temperature–voltage characteristics of type B thermocouple as illustrated in Fig. 5. The data points obtained from the best fit curve by this software approach are further fed to the neural network approach.

The curve-fitted temperature–voltage data is first fed to train back propagation neural network. The weights are updated in every epoch until the error reaches its least possible value between the trained and the desired outputs. The input temperature ranges from 0 to 630 °C and is taken for consideration, and corresponding output voltage trained by the neural network on the desired output is illustrated in Fig. 6. From Fig. 6, the maximum error between trained and the desired outputs is calculated
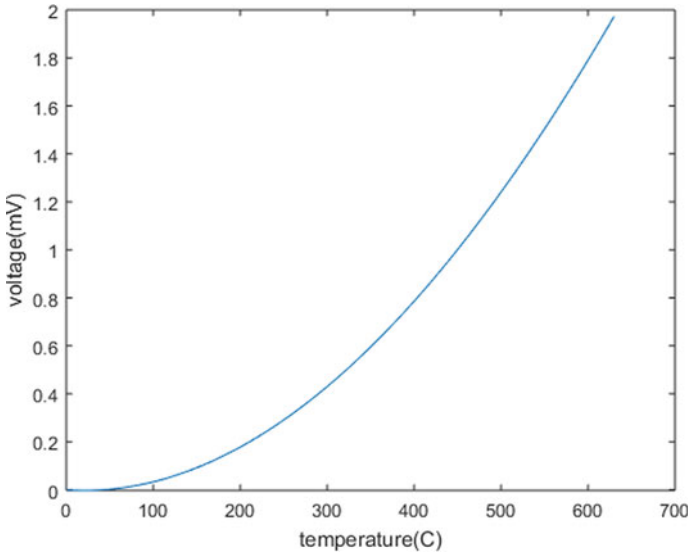
Fig. 4 Temperature–voltage characteristics of type B thermocouple
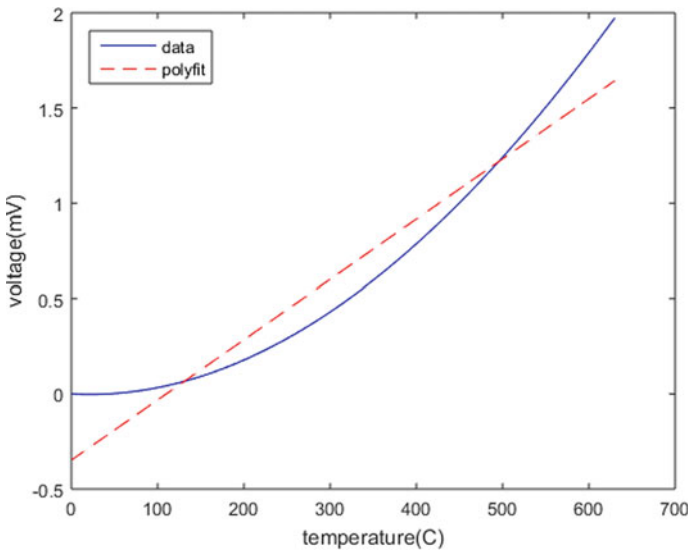
Fig. 5 Curve fitting characteristics of type B thermocouple
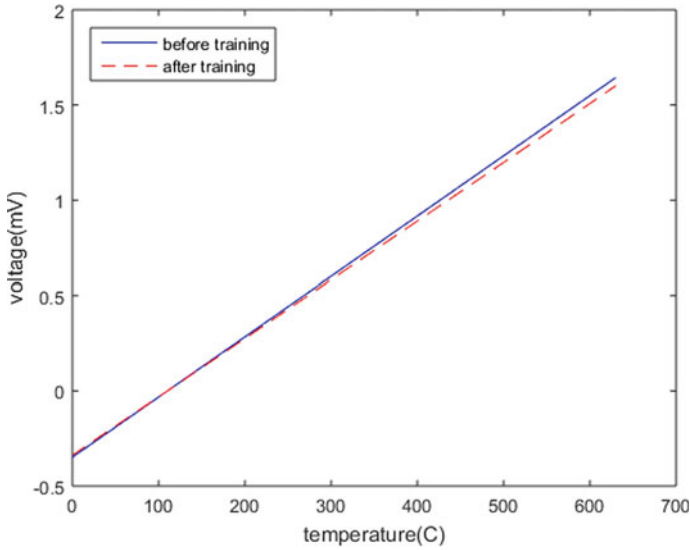
Fig. 6 Comparison of trained and desired temperature–voltage characteristics using BP neural network

as 0.042%. The parameters considered for back propagation neural network approach are listed in Table 1.

Similarly, the input–output data from the curve-fitted temperature–voltage characteristics of type B thermocouple is fed to convolutional neural network and the parameters considered are listed in Table 2. The maximum error between trained and desired output voltages with convolutional neural network is found as 0.0397% as illustrated in Fig. 7. When comparing with the performance of BPNN, the better accuracy of 7.24% is obtained with convolutional neural network in the training of temperature–voltage characteristics of thermocouple. Furthermore, it is also found that the better linearity compensation is obtained by using CNN, which is 61.37% improvement in the linearity compared to the original nonlinear characteristics of thermocouple. The CNN can be used as a best linearization software approach along

Table 1 Parameter considered in back propagation neural network	Back propagation neural network parameter	Thermocouple values
	Neural network	Back propagation type
	Number of neurons	Input layer, hidden layer 3, output layer 1
	Hidden layer	Three
	Weights	0.6969, 0.9420, 0.7112
	Activation function	tanh

Table 2 Parameter considered in convolutional neural network

CNN parameters	Thermocouple value
Neural network	CNN type
Number of neurons	Input neuron 1, hidden neuron 1, output neuron 1
Activation function	Sigmoid for input layer, tanh for hidden layer, and sigmoid l for output
Weights	4.3926, 4.8975, 0.1270
Training algorithm	Cascaded feed forward back propagation algorithm
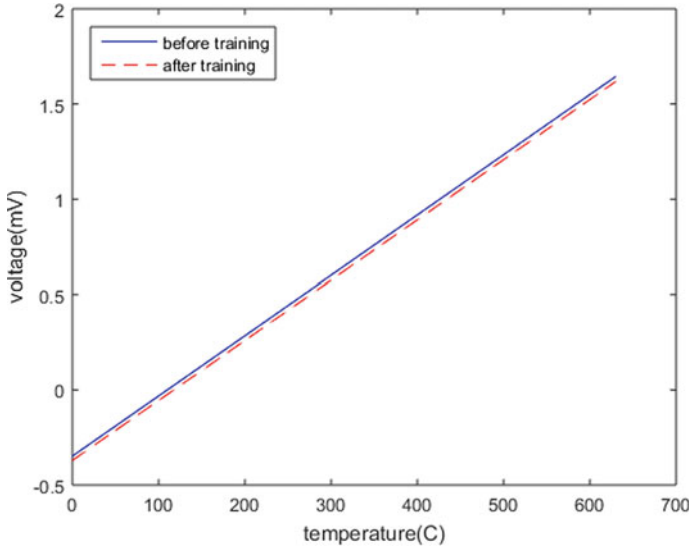
Fig. 7 Non-linearity correction using convolutional neural network

with the conventional thermocouple sensor with better accuracy and fast response time.

4   Conclusion

In this study, the two neural network approaches such as back propagation network and convolutional neural network are discussed for the linearization of temperature–voltage characteristics of type B thermocouple. Both the approaches are having different weight updating methods to reduce the error between the trained output and the desired output, to the least possible value. With the comparison of two approaches, the CNN shows better accurate result with the improved accuracy by 7.24%. It is also found that the convolutional neural network along with software

curve fitting approach improves the linearity of temperature–voltage characteristics of type B thermocouple. The non-linearity gets reduced by 61.37% compared to the original characteristics of the thermocouple with convolutional neural network. Thus, the combination of conventional thermocouple sensor along with CNN is well suited for temperature measuring applications with high accuracy and better linearity.

References

1. Agee, J.T., Masupe, S., Setlhaolo, D.: Feedforward neural-network conditioning of type-B thermocouple with variable reference-junction temperature. In: 2009 2nd International Conference on Adaptive Science & Technology (ICAST), pp. 296–300 (2009). https://doi.org/10.1109/ICASTECH.2009.5409710
2. Wei, G., Wang, X., Sun, J.: Signal processing method with cold junction compensation for thermocouple. In: 2009 IEEE Instrumentation and Measurement Technology Conference, pp. 1458–1462 (2009). https://doi.org/10.1109/IMTC.2009.5168685
3. Zeeshan, M., Javed, K., Sharma, B.B.: Signal conditioning of thermocouple using intelligent technique. Mater. Today Proc. **4**(9), 10627–10631 (2017). https://doi.org/10.1016/j.matpr.2017.06.432
4. Murmu, A., Bhattacharyya, B., Munshi, S.: A synergy of voltage-to-frequency converter and continued-fraction algorithm for processing thermocouple signals. Measurement **116**, 514–522 (2018). https://doi.org/10.1016/j.measurement.2017.11.047
5. Shamshi, M.A., Gupta, V.K.: New digital linearization technique for thermocouples. IETE J. Res. **34**(6), 466–470 (1988). https://doi.org/10.1080/03772063.1988.11436772
6. Danisman, K., Dalkiran, I., Celebi, F.V.: Design of a high precision temperature measurement system based on artificial neural network for different thermocouple types. Measurement **39**(8), 695–700 (2006). https://doi.org/10.1016/j.measurement.2006.03.015
7. Erdem, H.: Implementation of software-based sensor linearization algorithms on low-cost microcontrollers. ISA Trans. **49**(4), 552–558 (2010). https://doi.org/10.1016/j.isatra.2010.04.004

Cuk Converter-Assisted PV-Fed DC Water Pumping System with Modified Sliding Mode Controller for Enhanced Power Conversion

Khushboo Shah, Deepak Patel, and Tarun Sachdeva

Abstract Photovoltaic (PV) energy conversion systems have become increasingly important in many applications of stand-alone power generation as a result of rapid advancements in semiconductor and power electronic technology. This paper describes a Cuk converter-assisted PV-fed DC water pumping system for agricultural irrigation and industrial use in this environment. The suggested DC water pumping system eliminates the inverter and its complex control circuit for extra DC to AC conversion, lowering system losses. The DC motor-driven pump's operating characteristics, starting torque, and efficiency outperform the competition in water pumping applications. Furthermore, by extending the operating region of the PV array, the Cuk converter topology is investigated in order to improve energy harvesting and better utilize the source. In addition, the Cuk converter incorporates a nonlinear, resilient, modified PWM-based sliding mode control (SMC) technique for extracting maximum power under extremely variable environmental, load, and system conditions. To compare and validate the performance of the modified SMC algorithm, the traditional perturb and observe algorithm is used. For verification of the developed model, the entire system is built and tested under various conditions on the MATLAB/Simulink platform.

1 Introduction

To fulfil rising electricity demand, India has been largely dependent on conventional energy sources. The supply of conventional fuels, such as fossil fuel resources, is limited. As a result, the sole dependence on fossil fuels for electricity generation has resulted in a faster pace of natural resource depletion. The widespread usage of fossil fuels has resulted in massive carbon emissions into the atmosphere.

K. Shah (✉) · D. Patel · T. Sachdeva
MBM Engineering College, Jodhpur 342011, India

Furthermore, rapidly dwindling fossil resources are insufficient to supply global electrical demand, potentially resulting in a severe energy crisis. As a result, there will inevitably be a need to investigate other sources of power generation that are more sustainable, environmentally friendly, and low cost to operate. Wind and solar energy are renewable resources that are abundantly available [1].

Solar energy, when compared to other renewable energy sources, is free and readily available, and produces pollution-free electricity; hence, PV installation is rapidly growing. PV systems are simple to install and need little maintenance. PV offers a wide range of uses, including agricultural water pumping, electric cars, home and commercial water heating and lighting, and so on. The population of India is reliant on agriculture and conventional water pumping technologies. Pumping with traditional methods is inefficient and requires constant maintenance. Diesel/petrol generators have high operating expenses, emit a lot of noise and smoke as they burn fuels, and thereby pollute the environment [2]. Electricity-based modern water pumping is more efficient than the traditional water pumping technology. The current pumping method, however, is not practicable in rural locations due to the lack of grid access [3]. Furthermore, the cost of running the water pumps adds to the farmers' agricultural expenses. As a result, integrating renewable resources to power water pumps is an innovative way to bring the benefits of modern water pumping to rural India. PV-fed water pumping systems are among the renewable resources that are appropriate for rural locations due to their maintenance-free operation and modular design [4].

For irrigation and industrial purposes, India has around 7 million diesel generators and 18 million grid-connected water pumps. Furthermore, these pumps account for roughly 20% of electricity output, requiring nearly 90 million tonnes of coal per year. Annually, 4 billion litres of fuel is consumed by irrigation pumps powered by diesel generators. It is critical to research and promote alternative energy sources in order to assist agriculture while simultaneously lowering its reliance on conventional energy sources such as grid power and fossil fuels. The Indian government's Ministry of New and Renewable Energy (MNRE) has launched a "Solar pumping programme for irrigation and drinking water" to promote solar PV-based irrigation pumps [5].

In the agricultural sector, MNRE is giving a 30% capital subsidy for the installation of PV-based water pumping equipment. State governments are also providing subsidies ranging from 40 to 60% of the cost of installing a PV pump for agricultural use. DC water pumps are gaining traction, according to 6 W research, notably in the low HP market, due to their high efficiency and technical superiority over AC pumps [6]. Various AC and DC electric drives for PV-fed water pumping irrigation systems have also been proposed in the literature. Induction motors are rugged in construction and do not require frequent maintenance. The difficulty with the induction motor-driven water pumping system is addressed by Singh et al. It is unable to operate at light load settings due to excitation loss [7]. BLDC motors are highly efficient, have a high power density, and operate at unity power factor. The main disadvantage is that extensive and expensive control circuitry is required [8]. The DC system, on the other hand, does away with the inverter and associated control circuitry, lowering the system's overall cost significantly. In addition, reducing one conversion stage,

namely DC to AC, resulted in lower losses in DC water pumps. Furthermore, the proposed DC water pumping approach eliminates the requirement for batteries by treating water pumping as a time variable load [4]. For the most efficient use of PV panels and resources, maximum power extraction is required. In terms of irradiation, ambient temperature, and load, the maximum power output is calculated. As a result, a maximum power point tracking (MPPT) algorithm that tracks the operating point of PV corresponding to peak power must be built. The MPPT algorithm is based on the maximum power transfer theorem, which states that when the output impedance matches the input impedance, the maximum power transfer occurs. The duty ratio is changed according to the MPPT algorithm in a DC–DC converter control strategy; i.e. the output impedance related to input terminals of the converter as a function of the duty ratio is matched with the source impedance. In the literature, the boost converter arrangement has been widely used to track the MPP of PV panels. Using a boost converter, Belkaid et al. suggested a high-performance MPP approach [9]. A boost converter has been used as a power conditioning device between PV panels and loads because it avoids the need for an input filter and has low switching stress [10]. The boost converter, on the other hand, does not have a large operating range for MPP. Under low irradiance and temperature conditions, it fails to track [11]. The buck–boost converter family, which includes buck–boost and Cuk converters, is used to provide extensive operating areas for MPPT among all DC–DC converter topologies. The buck–boost converter, on the other hand, has a poor transient response, a discontinuous input current, and large peak currents, making it less efficient. The Cuk converter, on the other hand, has a constant input and load side current as well as lower switching losses, making it more efficient [12, 13].

To track the peak power from PV panels, many MPPT approaches have been presented in the literature. The perturb and observe (P&O) approach is simple to use and generally available; however, it causes MPP oscillations. The disadvantages of the P&O method are addressed by Subudhi and Pradhan. Deviation from MPP occurs in the event of rapid atmospheric changes. Furthermore, the precision of P&O is dependent on the right step size selection [14]. A modified P&O algorithm has been proposed in the paper [15] to solve this problem. In addition, incremental conductance has been created to eliminate oscillations, but it necessitates a complex circuit, a high implementation cost, and instability issues [16]. Intelligent control strategies based on fuzzy logic, neural networks, and other techniques have recently been implemented for MPPT. The precision of the fuzzy logic-based MPPT technique, on the other hand, is dependent on the designer's competence and experience in setting up the rule base table. It is challenging to train neural networks in a neural-based technique since the features of PV change over time [17]. The presence of a switched-mode converter and PV modules makes a PV-powered water pumping system nonlinear. As a result, a nonlinear sliding mode controller that is robust to system disturbances and uncertainties is the best choice for tracking maximum power point.

Unlike robust control strategies [16], Utkin's sliding mode control (SMC) methodology, which he invented in [18], when applied in control action, ensures stability regardless of system dynamic fluctuations [19, 20]. Various control approaches for designing control functions in order to obtain MPPT from PV systems have been

published in the literature. To track quick variations in irradiation levels, a two-loop SMC-based MPPT control approach has been developed [21, 22]. The complexity of implementing the two-loop-based SMC control approach grows as the number of sensors and loops grows. The issues of implementing multi-loop control are addressed by Fan et al. This work presents an SMC based on the single-loop control approach, although it lacks stability analysis and experimental confirmation [23]. Tan et al. [24] solved the problem of variable switching frequency associated with traditional SMC for MPPT algorithm in PV system. As a result, this work proposes a unique pulse width modulation (PWM)-based SMC that operates well under large load or parameter variations.

A solar-powered DC water pumping system is proposed in this paper. The Cuk converter is designed to combine the MPPT technique while working in both boost and buck modes, providing a wide operating range for MPPT. Furthermore, a unique PWM-based SMC-assisted MPPT method for precise MPP tracking has been proposed and developed. Due to the reduced number of components, the suggested MPPT technique is based on a single-loop control approach, making it less complex. Further, to highlight the superiority of the proposed technique, a comparative study has been carried out with a P&O algorithm.

The following is a breakdown of the article's structure. A description of the PV-fed DC water pumping system is offered in Sect. 2. Section 3 presents the sliding mode control-assisted MPPT algorithm with stability analysis. The suggested Cuk converter-assisted DC water pumping system's findings are discussed in Sect. 4.

2 Description of Proposed PV-Fed DC Water Pumping System

Figure 1 shows a schematic diagram of the Cuk converter-assisted PV-supplied DC water pumping system. It is made up of a 215 W PV array, a Cuk converter, and a DC motor with pump set. When photons from the sun strike a PV array, the solar irradiation is converted into DC current through the photovoltaic effect. PV produces a variable DC output that is dependent on irradiance and temperature. For each temperature and irradiation level, it is observed that the extracted power is greatest at a specific voltage. The Cuk converter is used to construct a PWM-based sliding mode MPPT controller due to the nonlinear behaviour in the extraction of maximum power. Cuk converters can function in both step-up and step-down modes, allowing them to track maximum points across the whole range by adjusting their duty ratio. By combining PWM and sliding mode, the problem of chattering and fluctuating switching frequency that plagued traditional SMC is alleviated. The proposed system uses a DC motor and a centrifugal pump to produce higher starting torque than an AC water pumping system.

PV module, Cuk converter, and DC motor pump set make up the entire configuration. A single-diode model is used to mathematically model the PV cell. PV current
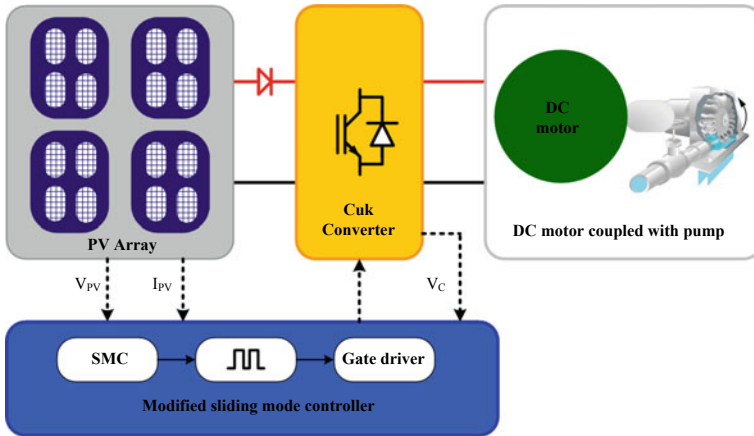
Fig. 1 Schematic diagram of proposed Cuk converter-assisted PV water pumping system with modified SM

(I PV) and PV voltage (V PV) have a nonlinear and exponential relationship that can be stated as:

$$I_{PV} = N_P[I_g - I_0]\left(e^{\frac{q V_{PV}}{N_S T \aleph K_b}} - 1\right) \tag{1}$$

where N_P = no. of PV modules connected in parallel, N_S = no. of PV modules connected in series, I_g = light generated current, I_0 = reverse saturated current, q = charge on electron, T = ambient temperature, $\aleph$ = ideality factor $\in$ [1, 5], and K_b = Boltzmann constant.

Circuit schematic of Cuk converter fed with PV is shown in Fig. 2. The duty ratio (D) of Cuk converter is given by Eq. (2) [25].

$$V_0 = -\frac{D}{(1 - D)} V_{in} \tag{2}$$
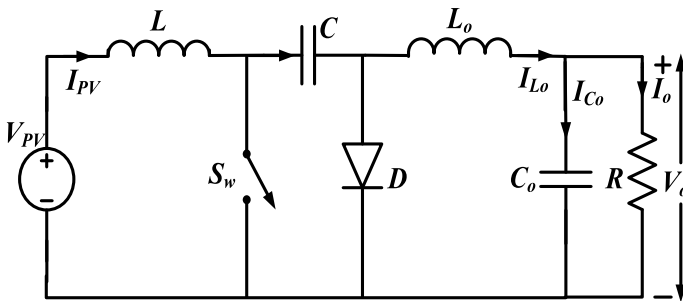
Fig. 2 Circuit diagram of Cuk converter

Table 1 Parameters of Cuk converter

Parameters	Value
Switching frequency (f)	10 kHz
Input inductor (L)	2 mH
Output inductor (L_0)	2 mH
Input capacitor (C)	300 μF
Output capacitor (C_0)	125 μF

The state-space equations of Cuk converter fed by PV panel are described in Eqs. (3)–(6) [16].

$$\dot{I}_{PV} = \frac{V_{PV}}{L} - \frac{(1-D)}{L} V_C \tag{3}$$

$$\dot{I}_{Lo} = \frac{DV_C}{L_o} - \frac{V_{C0}}{L_o} \tag{4}$$

$$\dot{V}_C = \frac{(1-D)}{C} I_{PV} - \frac{D}{C} I_{Lo} \tag{5}$$

$$\dot{V}_{Co} = \frac{I_{Lo}}{C_o} \frac{V_{C0}}{R_L C_o} \tag{6}$$

The parameters of Cuk converter incorporated between PV source and the load are listed in Table 1.

3 MPPT Algorithms

The main disadvantages of PV power generation are efficiency and the fact that power output is affected by irradiance, temperature, dust, shade, and other factors. The load cannot be altered continually for MPPT operation in practice. Because PV is not a steady power source, MPPT algorithms are required to extract maximum power for each load connected to the system [14, 16, 17]. P&O is the foundational tracking technology, which is easy to install and less expensive. P&O algorithm [15] shows oscillations around MPP and an inability to detect quick changes in temperature and irradiance.

3.1 PWM-Based SMC-Assisted MPPT Algorithm

Because of the non-linearity in the PV-fed water pumping system, nonlinear controllers are chosen for precisely tracking the maximum power point. Sliding

mode is a nonlinear controller that is resistant to parameter changes and Lyapunov stable. Furthermore, because the DC–DC converters utilized to implement MPPT are variable structured, SMC is acceptable [24].

The paper's proposed modified SMC system uses single-loop control to reduce the number of states needed to build the sliding surface. In comparison with two-loop SMC, the suggested PWM-based single-loop SMC implementation requires fewer sensors, resulting in lower MPPT controller costs. The Lyapunov stability theorem is used to provide robust stability. The proposed approach decreases the chattering amplitude by introducing a new-state dependent control variable $\mathbb{N}$ that is dependent on the sliding surface [26].

According to sliding mode control, sliding surface is decided using Eq. (1) [27].

$$\frac{\partial P_{PV}}{\partial I_{PV}} = \frac{\partial R_{PV} I_{PV}^2}{\partial I_{PV}} = I_{PV}\left[2R_{PV} + I_{PV}\frac{\partial R_{PV}}{\partial I_{PV}}\right] = 0 \tag{7}$$

where $R_{PV} = \frac{V_{PV}}{I_{PV}}$. When PV power becomes maximum, the state variables converge to the sliding surface and remains on it. Thus, sliding surface is given in (8):

$$\dot{s} = \left[2R_{PV} + I_{PV}\frac{\partial R_{PV}}{\partial I_{PV}}\right] \tag{8}$$

The discrete control signal d_{eq} is substituted by a smooth function using the invariance condition by setting $\dot{s} = 0$.

$$\dot{s} = \left[\frac{\partial s}{\partial I_{PV}}\right]\dot{I}_{PV} = 0 \rightarrow \dot{s} = \left(3\frac{\partial R_{PV}}{\partial I_{PV}} + I_{PV}\frac{\partial^2 R_{PV}}{\partial I_{PV}^2}\right)\cdot\left(\frac{V_{PV} - (1-d_{eq})V_C}{L}\right) = 0$$

$$d_{eq} = 1 - \frac{V_{PV}}{V_C} \tag{9}$$

The control signal can be written as:

$$d = d_{eq} + d_n \tag{10}$$

where

$$d_n = \mathbb{N}\text{sgn}(s) + k \cdot s, \quad \mathbb{N} = \mathbb{N}_o(|s| + \xi) \tag{11}$$

$\mathbb{N}_o, k, \xi$ are design constants which are always positive. The magnitude of chattering is reduced by selecting the parameters such that $\mathbb{N}_o \gg \xi$. Further, the control signal is equated with the carrier wave to produce the pulses to drive the converter.

Stability analysis: According to Lyapunov stability theorem, a system is stable when Lyapunov function (V) is positive symmetric and its time derivative is negative. Assume $V = (½)s^2$ and $\dot{V}$ can be written as follows:

$$\dot{V} = s\dot{s} = \frac{\dot{\partial s}}{\partial I_{\mathrm{PV}}} I_{\mathrm{PV}} \tag{12}$$

$\frac{\partial s}{\partial I_{\mathrm{PV}}}$ can be calculated using Eq. (3)

$$\frac{\partial s}{\partial I_{\mathrm{PV}}} = 3\frac{\partial R_{\mathrm{PV}}}{\partial I_{\mathrm{PV}}} + I_{\mathrm{PV}}\frac{\partial^2 R_{\mathrm{PV}}}{\partial I_{\mathrm{PV}}^2} \tag{13}$$

Taking $R_{\mathrm{PV}} = \frac{V_{\mathrm{PV}}}{I_{\mathrm{PV}}}$, the following equations can be obtained,

$$\frac{\partial R_{PV}}{\partial I_{PV}} = \frac{\partial}{\partial I_{PV}}\left(\frac{V_{PV}}{I_{PV}}\right) = \frac{1}{I_{PV}}\frac{\partial V_{PV}}{\partial I_{PV}} - \frac{V_{PV}}{I_{PV}^2} \tag{14}$$

From Eq. (1), V_{PV} can be written as

$$V_{\mathrm{PV}} = \frac{N_{\mathrm{S}}T\aleph K_{\mathrm{b}}}{q} \ln\left(\frac{N_{\mathrm{P}}I_{\mathrm{g}} + N_{\mathrm{P}}I_{\mathrm{o}} - I_{\mathrm{PV}}}{N_{\mathrm{P}}I_{\mathrm{o}}}\right) \tag{15}$$

Derivatives of PV voltage with respect to PV current are as follows:

$$\frac{\partial V_{\mathrm{PV}}}{\partial I_{\mathrm{PV}}} = -\frac{N_{\mathrm{S}}T\aleph K_{\mathrm{b}}}{q} \frac{N_{\mathrm{P}}I_{\mathrm{o}}}{N_{\mathrm{P}}I_{\mathrm{g}} + N_{\mathrm{P}}I_{\mathrm{o}} - I_{\mathrm{PV}}} < 0 \tag{16}$$

$$\frac{\partial^2 V_{\mathrm{PV}}}{\partial I_{\mathrm{PV}}^2} = -\frac{N_{\mathrm{S}}T\aleph K_{\mathrm{b}}}{q} \frac{N_{\mathrm{P}}I_{\mathrm{o}}}{\left(N_{\mathrm{P}}I_{\mathrm{g}} + N_{\mathrm{P}}I_{\mathrm{o}} - I_{\mathrm{PV}}\right)^2} < 0 \tag{17}$$

Using Eqs. (14)–(17), it can be noticed that derivative of sliding surface with respect to PV current is negative, i.e.

$$\frac{\partial s}{\partial I_{\mathrm{PV}}} < 0 \tag{18}$$

From Eqs. (3)–(10):

$$\dot{I_{\mathrm{PV}}} = \frac{V_{\mathrm{C}}}{L}d_{\mathrm{n}} > 0 \tag{19}$$

Using Eqs. (12)–(19), $\dot{V}$ can be written by

$$\dot{V} = s\frac{\partial s}{\partial I_{\mathrm{PV}}}\left[\frac{V_{\mathrm{C}}}{L}(\mathbb{N}_{\mathrm{o}}(|s| + \xi) \cdot \mathrm{sgn}(s) + k \cdot s)\right]$$

$$\dot{V} = \frac{\partial s}{\partial I_{\mathrm{PV}}}\left[\frac{V_{\mathrm{C}}}{L}\left(\mathbb{N}_{\mathrm{o}}s^2 + ks^2\right) + \frac{V_{\mathrm{C}}}{L}\mathbb{N}_{\mathrm{o}}\xi|s|\right] < 0 \tag{20}$$

From Eq. (20), $\dot{V}$ is negative which is satisfying Lyapunov stability criteria. Thus, it can be concluded that stability condition is fulfilled. The mathematical modelling of the proposed SMC is constructed under MATLAB/Simulink environment, and results are discussed in Sect. 4.

4 Results and Discussion

For cost-effective and environmentally friendly operation, a PV-fed Cuk converter-aided DC water pumping system is proposed to replace existing diesel generator-based water pumps. The PV array Soltech 1STH-P was chosen to power a PV-fed DC water pumping system. The SMC-assisted MPPT technique is created and implemented in MATLAB using a single-loop PWM.

4.1 Comparative Study of Proposed PWM-Based SMC-Assisted MPPT and P&O MPPT for PV-Fed DC Water Pumping System

To examine the performance of the proposed MPPT approach, two different scenarios are considered for simulation: (a) step variation in irradiation at constant temperature and load ($T = 25$ °C and motor speed = 1000 rpm), and (b) step variation in temperature at constant irradiation and load (1000 W/m^2 and motor speed = 1000 rpm).

Performance analysis of MPPT algorithm for step variation in irradiation: Fig. 3 shows the performance of P&O and the suggested PWM-based SMC-assisted MPPT algorithm for maximum power tracking. The waveforms of various operating point, i.e. PV voltage, PV current, and voltage at load terminals, are obtained.

The irradiation is increased from 600 to 1000 W/m^2 at $t_1 = 1$ s and dropped to 800 W/m^2 at $t_2 = 2$ s while maintaining a temperature of 25 °C and a load torque of 100 N m. PV arrays of 600 W/m^2 have a maximum power of 129.5 W, 1000 W/m^2 has a maximum power of 213.1 W, and 800 W/m^2 has a maximum power of 171.8 W. When the P&O algorithm is used for PV-fed DC water pumping, the highest power available is 126.55 W, 210.5 W, and 168 W, respectively, at 600 W/m^2, 1000 W/m^2, and 800 W/m^2. The results also show that the P&O method tracks MPPT in 36 ms. During 600 W/m^2 irradiation, the operating point oscillates between 27.1 and 31.1 V, and 27.1 and 30.2 V during 1000 W/m^2. Thus, power at PV terminals varies between 122.6 and 130.5 W when exposed to 600 W/m^2 irradiation, 206.8–214.2 W when exposed to 1000 W/m^2 irradiation, and 163–173 W when exposed to 800 W/m^2 irradiation.

At $t_1 = 1$ s and $t_2 = 2$ s, the proposed PWM-based SMC-assisted MPPT algorithm is used to track MPPT with step variation in irradiation. At 600 W/m^2 irradiation, the
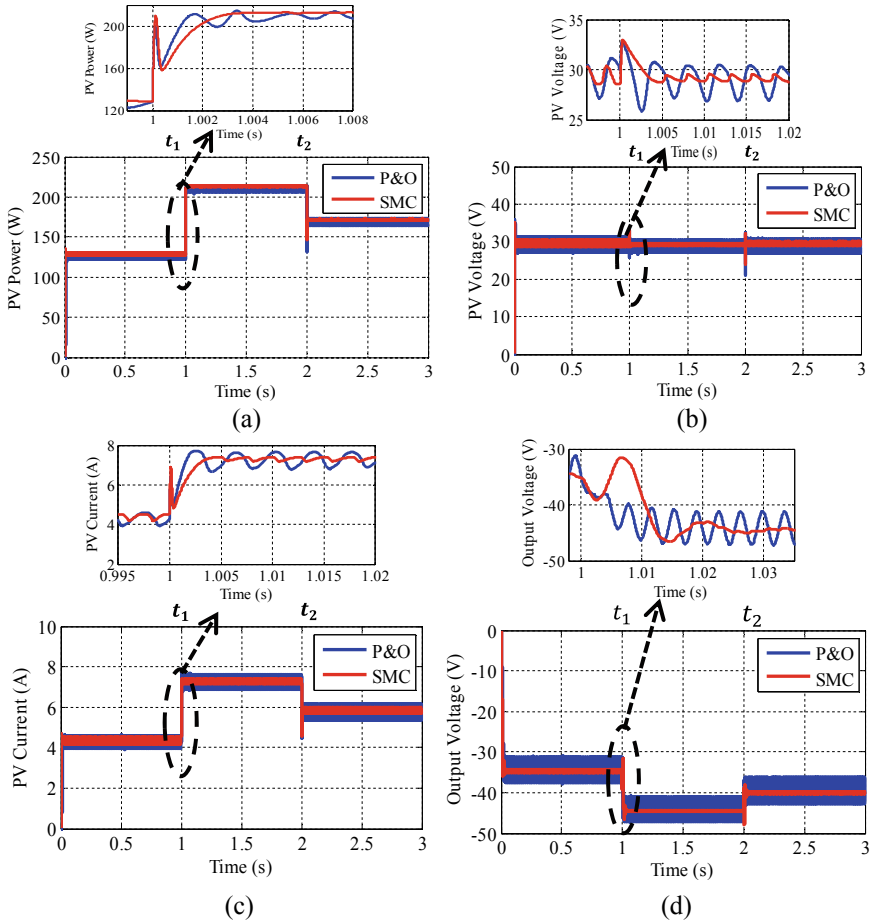
Fig. 3 Response of P&O and proposed PWM-based SMC-assisted MPPT algorithm when irradiance is step-up from 600 to 1000 W/m² at $t_1 = 1$ s and from 1000 to 800 W/m² at $t_2 = 2$ s: **a** PV power, **b** PV voltage, **c** PV current, **d** output voltage of Cuk converter

maximum power tracked by the proposed algorithm is 129.4, 213 W at 1000 W/m² irradiation, and 171.6 W at 800 W/m² irradiation, respectively. In 27 ms, the proposed SMC-assisted MPPT algorithm monitors MPPT. During 600 W/m², 1000 W/m², and 800 W/m², the operating point varies between 1.9 V, 0.7 V, and 1 V, respectively, and PV power varies between 128.4 W and 130.4 W, 212.4–213.6 W, and 170.6–172.6 W during 600 W/m², 1000 W/m², and 800 W/m², respectively.

Performance analysis of MPPT algorithm for step variation in temperature: The performance of P&O and proposed PWM-based SMC-assisted MPPT technique for maximum power tracking is presented in Fig. 4. The waveforms of various operating
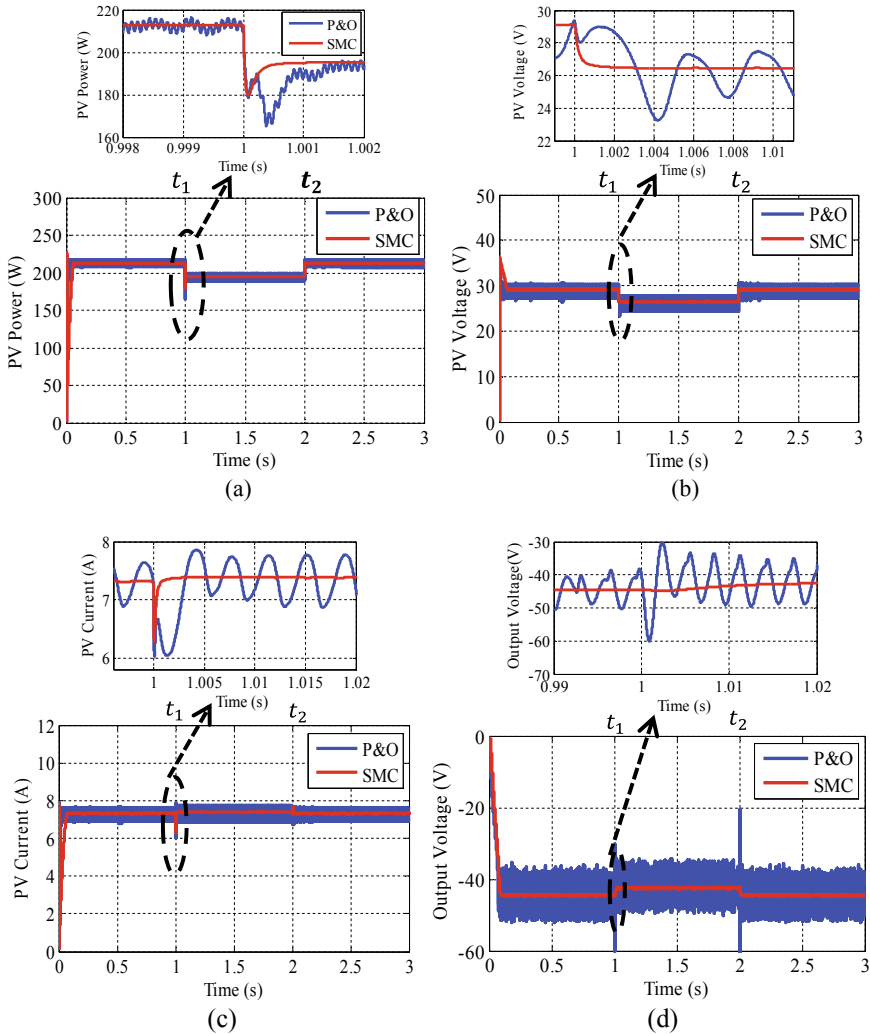
Fig. 4 Response of P&O and proposed PWM-based SMC-assisted MPPT algorithm when temperature is step changed from 25 to 45 °C at $t_1 = 1$ s and from 45 to 25 °C at $t_2 = 2$ s: **a** PV power, **b** PV voltage, **c** PV current, **d** output voltage at load terminal

points, i.e. PV voltage, PV current, and voltage at load terminals, are obtained and presented.

By keeping irradiation $= 1000$ W/m^2 and motor speed $= 1000$ rpm, the temperature is increased from 25 to 45 °C at $t_1 = 1$ s and lowered to 25 °C at $t_2 = 2$ s. At 25 °C, the maximum power of the PV array is 213.1 W, while at 45 °C, it is 195.4 W. When the P&O MPPT technology is used in the Cuk converter for PV-fed DC water pumping, the highest power available is 212.1 W and 194.3 W, respectively, at 25 °C

and 45 °C. In 15 ms, the P&O algorithm tracks MPPT. During 25 °C, the operating point oscillates between 27.1 and 30.2 V, and during 45 °C, it oscillates between 24.4 and 27.6 V. Thus, power at PV terminals varies between 207.8 and 216.4 W at 25 °C and 189.2 and 199.4 W at 45 °C.

The proposed PWM-based SMC-assisted MPPT algorithm is now used to track MPPT with temperature step variations at $t_1 = 1$ s and $t_1 = 2$ s. At 25 °C, the maximum power tracked by the proposed algorithm is 212.7 W, while at 45 °C, it is 195.1 W. In 8 ms, the proposed MPPT algorithm tracks MPPT. The operating point varies between 29 and 29.3 V at 25 °C and 26.1–26.4 V at 45 °C, with PV power varying between 212.4 and 213 W at 25 °C and 195–195.3 W at 45 °C.

5 Conclusions

The research presents and analyses a Cuk power converter topology for a PV-fed DC water pumping system. A modified PWM-based sliding mode controlled aided MPPT algorithm is developed and incorporated to improve energy conversion from PV systems. In the MATLAB/Simulink platform, detailed modelling and simulation studies on a Cuk converter-supplied DC water pumping system are carried out. The suggested SMC-assisted MPPT's responses are validated and compared to the P&O method. The results show that the suggested SMC-based MPPT has a better transient and steady-state performance than its counterpart in the face of uncertainty. By incorporating the state-dependent control variable, the Lyapunov theorem ensures resilience, stability, and reduced chattering amplitude. The study and results revealed that the proposed system had enhanced energy conversion efficiency and performance, as well as better source usage and energy harvesting. Overall, the suggested Cuk converter-assisted DC water pumping system combined with SMC-based MPPT approach appears to be a promising solution for accomplishing the MNRE goal of "Solar pumping programme for agriculture and drinking water". The proposed work could be done on a hardware platform in future.

References

1. Elrefai, M., Hamdy, R.A., ElZawawi, A., Hamad, M.S.: Design and performance evaluation of a solar water pumping system: a case study. In: IEEE Power Systems Conference (MEPCON), pp. 914–920 (2016)
2. Caracas, J., Farias, G., Teixeira, L., Ribeiro, L.: Implementation of a high-efficiency, high lifetime, and low-cost converter for an autonomous photovoltaic water pumping system. IEEE Trans. Ind. Appl. **50**(1), 631–641 (2014)
3. Malla, S.G., Bhende, C.N., Mishra, S.: Photovoltaic based water pumping system. In: IEEE Conference on Energy, Automation, and Signal (ICEAS), pp. 1–4 (2011)
4. Girma, Z.: Techno-economic analysis of photovoltaic pumping system for rural water supply in Ethiopia. Int. J. Sustain. Energy **36**(3), 277–295 (2014)
5. Final-Report-on-Implementation-Framework-for-Solar-Agriculture-Pump_FINAL.pdf

6. Feasibility-analysis-for-solar-High-Res-1.pdf
7. Singh, B., Mishra, A.K., Kumar, R.: Solar powered water pumping system employing switched reluctance motor drive. IEEE Trans. Ind. Appl. **52**(5), 3949–3957 (2016)
8. Kumar, R., Singh, B.: Solar PV powered BLDC motor drive for water pumping using Cuk converter. IET Electr. Power Appl. **11**(2), 222–232 (2017)
9. Belkaid, A., Gaubert, J.-P., Gherbi, A.: Design and implementation of a high performance technique for tracking PV peak power. IET Renew. Power Gener. **11**(1), 92–99 (2017)
10. Kish, G.J., Lee, J.J., Lehn, P.W.: Modelling and control of photovoltaic panels utilising the incremental conductance method for maximum power point tracking. IET Renew. Power Gener. **6**(4), 259–266 (2012)
11. Taghvaee, M.H., Radzi, M.A.M., Moosavain, S.M., Hizam, H., Marhaban, M.H.: A current and future study on non-isolated DC-DC converters for photovoltaic applications. Renew. Energy **17**, 216–227 (2013)
12. Safari, A., Mekhilef, S.: Simulation and hardware implementation of incremental conductance MPPT with direct control method using cuk converter. IEEE Trans. Ind. Electron. **58**(4), 1154–1161 (2011)
13. Farahat, M.A., Metwally, H.M.B., Mohamed, A.A.E.: Optimal choice and design of different topologies of DC-DC converter used in PV systems at different climatic conditions in Egypt. Renew. Energy **43**, 393–402 (2012)
14. Subudhi, B., Pradhan, R.: A comparative study on maximum power point tracking techniques for photovoltaic power systems. IEEE Trans. Sustain. Energy **4**(1), 89–98 (2013)
15. Ahmed, J., Salam, Z.: A modified P&O maximum power point tracking method with reduced steady-state oscillation and improved tracking efficiency. IEEE Trans. Sustain. Energy **7**(4), 1506–1515 (2016)
16. Loukriz, A., Haddadi, M., Messalti, S.: Simulation and experimental design of a new advanced variable step size incremental conductance MPPT algorithm for PV systems. ISA Trans. 1–9 (2015)
17. Dahmane, M., Bosche, J., El-Hajjaji, A., Pierre, X.: MPPT for photovoltaic conversion systems using genetic algorithm and robust control. In: American Control Conference, pp. 6595–6600 (2013)
18. Utkin, V.I.: Variable structure systems—present and future. Autom. Remote Control **44**(9), 1105–1120 (1984)
19. Edwards, C., Spurgeon, S.: Sliding Mode Control: Theory and Applications. CRC Press (1998)
20. Janardhanan, S., Satyanarayana, N.: Sliding mode control of uncertain systems using multirate output feedback functional observer. In: 12th International Workshop on Variable Structure Systems, pp. 314–318 (2012)
21. Bianconi, E., Calvente, J., Giral, R., Mamarelis, E., Petrone, G., Ramos-Paja, C.A., Spagnuolo, G., Vitelli, M.: A fast current-based MPPT technique employing sliding mode control. IEEE Trans. Ind. Electron. **60**(3), 1168–1178 (2013)
22. Montoya, D.G., Ramos-Paja, C., Giral, R.: Improved design of sliding-mode controllers based on the requirements of MPPT techniques. IEEE Trans. Power Electron. **31**(1), 235–247 (2016)
23. Zhang, F., Maddy, J., Premier, G., Guwy, A.: Novel current sensing photovoltaic maximum power point tracking based on sliding mode control strategy. Sol. Energy **118**, 80–86 (2015)
24. Tan, S.-C., Lai, Y.M., Tse, C.K.: General design issues of sliding-mode controllers in DC-DC converters. IEEE Trans. Ind. Electron. **55**(3), 1160–1174 (2008)
25. Selwan, E., Park, G., Gajic, Z.: Optimal control of the Cuk converter used in solar cells via a jump parameter technique. IET Control Theory Appl. **9**(6), 893–899 (2015)
26. Levant, A.: Chattering analysis. IEEE Trans. Autom. Control **55**(6), 1380–1389 (2010)
27. Mojallizadeh, M.R., Badamchizadeh, M., Khanmohammadi, S., Sabahi, M.: Designing a new robust sliding mode controller for maximum power point tracking of photovoltaic cells. Sol. Energy **132**, 538–546 (2016)

Study on Enhancement of Optical Output of In$_x$Ga$_{1-x}$N/GaN Parabolic Quantum Well LEDs, Varying Indium Compositions, and Well Widths

Dipan Bandyopadhyay, Apu Mistry, and JoyeetaBasu Pal

Abstract The variations of the transition energy (TE) as well as transition probability (TP) with current for various indium (In) concentrations and different QW widths have been investigated for In$_x$Ga$_{1-x}$N/GaN parabolic QW LEDs. A set of data for blue light emissions (2.75 eV) has been obtained for different indium mole fractions and well widths. Important observation is that for emission energy of 2.75 eV, parabolic QW LEDs provide maximum TP if the In mole fraction and well width are 0.23 and 28 Å, respectively. For further studies, these observations can be considered for In$_x$Ga$_{1-x}$N/GaN parabolic QW LEDs in order to achieve higher optical output for blue light emissions.

Keywords Parabolic QW · Transition energy · Transition probability

1 Introduction

Nowadays, owing to higher efficiency, nitride-based (III–V) quantum well (QW) light-emitting diodes (LEDs) have become popular in solid state light emissions [1–3]. White light emission is possible by LEDs using red, green, and blue lights. To emit green and red lights, higher indium (In) concentration is essential. This decreases the external quantum efficiencies of In$_x$Ga$_{1-x}$N/GaN QW LEDs. Optical performance of In$_x$Ga$_{1-x}$N/GaN QWLEDs degrades due to higher dislocation density, In content defects, and inbuilt strong polarization fields existing in InGaN materials [4–6]. Numerous solutions have been projected to minimize these undesirable effects and enhance the optical performance of parabolic QWs [7–18].

The piezoelectric polarization along with spontaneous polarization in the InGaN/GaN QW (c-plane wurtzite) leads to quantum confined stark effect (QCSE),

D. Bandyopadhyay · A. Mistry (✉) · J. Pal
RCC Institute of Information Technology, Kolkata 700015, India

A. Mistry
Institute of Radio Physics and Electronics, University of Calcutta, Kolkata 700009, India

this significantly decreases the square of the overlap of electron–hole wave functions (M_{eh}^2) [19, 20]. The carriers are separated spatially which reduces the radiative recombination process.

Significant improvement of transition probability (TP), i.e., M_{eh}^2 using parabolic QW (PQW) over rectangular QW structures has been addressed by McBride et al. [15]. In this paper, TE and TP variations with current for different In compositions and different QW widths have been investigated for In$_x$Ga$_{1-x}$N/GaN parabolic QW LEDs. A set of data for blue light emissions (2.75 eV) has been obtained for various In concentration and well widths and it is observed that for a specific value of In concentration and QW width, better optical output is achieved. Computations performed using self-consistent solutions of Schrödinger and Poisson's equations in MATLAB software [8, 21].

2 Theoretical Details

In this paper, parabolic QWs for different peak indium mole fractions have been considered as shown in Fig. 1. The chosen peak In concentrations are 0.23, 0.22, 0.21, 0.20, 0.19, and 0.18. For each QW, 3 nm well width is considered. The band gap of the In$_x$Ga$_{1-x}$N is calculated from the band gaps of GaN (3.43 eV) and InN (0.64 eV) using linear interpolation method [22], governed by Eq. 1

$$E_g(\text{In}_x\text{Ga}_{1-x}\text{N}) = x E_{g,\text{InN}} + (1-x) E_{g,\text{GaN}} - bx(1-x) \tag{1}$$

Fig. 1 Indium concentration profiles in the QW, varying peak In content
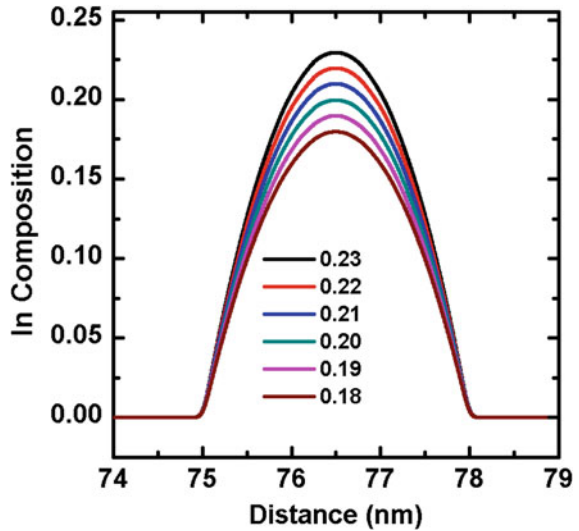
where $E_g(In_xGa_{1-x}N)$, $E_{g,GaN}$, and $E_{g,InN}$ are the band gap of In$_x$Ga$_{1-x}$N, GaN and InN, respectively, "*x*" is the indium mole fraction and the bowing parameter (*b*) is considered to be 1.4 eV [23]. The band-offset ratio is 68:32 [24]. The detailed theatrical and computational methods have been discussed in our previous papers [8, 21].

3   Results and Discussion

In Fig. 2, TE and the TP of the parabolic QWs and rectangular QWs are compared considering In composition and QW width of 0.23 and 3 nm, respectively. From Fig. 2a, it is observed that TE increases monotonically with current density though the dependency of TE is less for parabolic QW while the variation is more for the rectangular QW. The less dependency of TE on current density appears to be advantageous for LEDs. The TP is also increasing with current density which is depicted in Fig. 2b and it is noticed that for the same current density, the TP for a parabolic QW is above four times higher compared to that of rectangular QW. This notable observation will definitely motivate an optoelectronic designer in the path of device

Fig. 2 Variations of **a** TE, **b** TP of parabolic and rectangular QWs with change in current density are shown for In concentration of 0.23
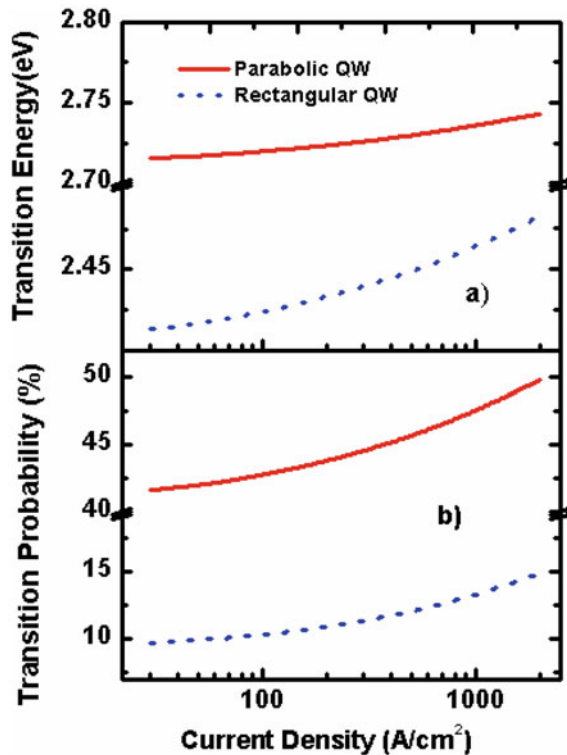
efficiency improvement. Abrupt In layer and lattice change in InGaN/GaN interface in rectangle QW lead to higher mismatch in polarization, resulting in increase in e–h wave functions separation. On the other hand, since there is no abrupt change in In profile at the InGaN/GaN interface, polarization mismatch is minimal at that interface of a PQW structure. Beside this, owing to parabolic band structure, the first potential energy levels are confined to the center of the QW thereby reduces the e–h wave functions separation and reduces the TE variations with the change in current.

Figure 3 shows the variation of TE with the change in well widths for various In concentrations at 60 A/cm^2 current density. It is observed that the TE decreases with the increase in well width and In mole fractions. To obtain the best optical output, a set of data for blue light emissions (2.75 eV) is collected from the figure and it is presented in Table 1. Moreover, it is important to note that for In mole fraction of 0.18, this emission cannot be achieved for the well width range considered here.

From Table 1, it is observed that for the same emission energy (2.75 eV), maximum TP is obtained for the mole fraction of 0.23, and well width of 28 Å. For further

Fig. 3 TE variation with the change in well width is presented here for various peaks In concentration for a PQW structure
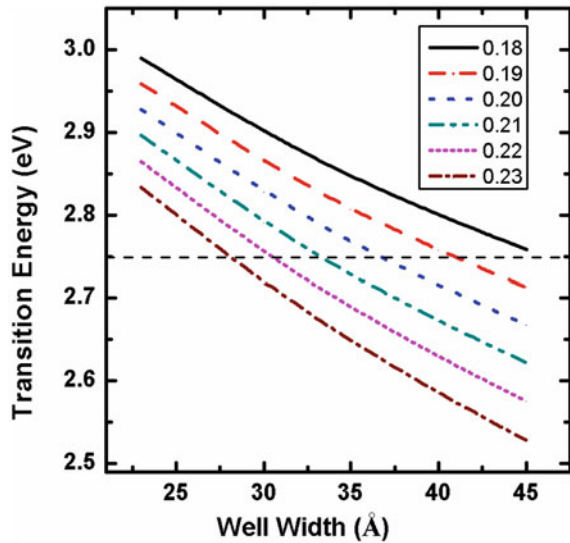
Table 1 Extracted In mole fractions and well widths and their corresponding TP, for the same blue emission of parabolic QW LEDs

Mole fraction	Well width (Å)	Transition energy (eV)	Transition probability (%)
0.23	28	**2.75**	48
0.22	30		44
0.21	33		38
0.20	37		32
0.19	41		26

Fig. 4 Variations of TP and TE with the change in current density for PQW structures are presented here
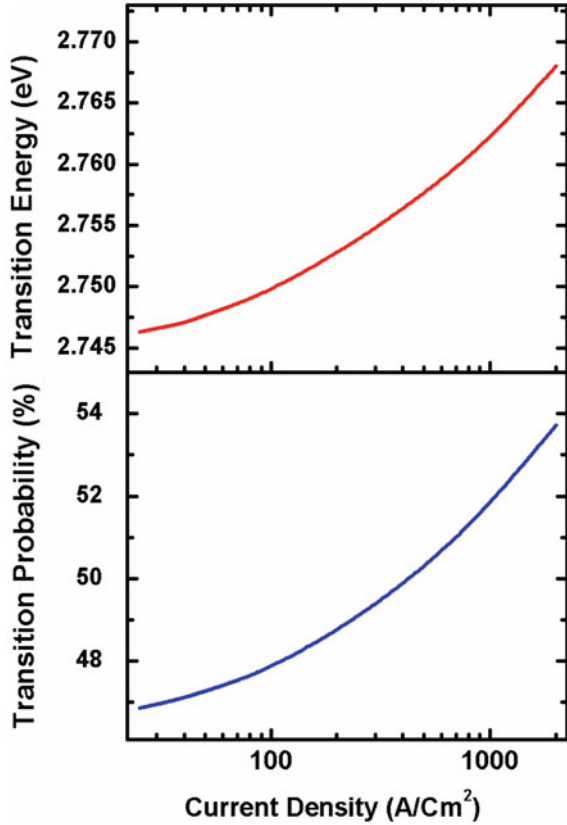
studies, the indium mole fraction of 0.23 and well width of 28 Å can be considered for parabolic QWs in order to achieve blue light emission.

The variations of TE and TP with the change in current density are shown in Fig. 4 for In mole fraction of 0.23 and well width of 28 Å. It is observed that, even though, the TE is increasing but the variation is negligible (~22 meV) for the large change in current density. Another notable observation is that the TP is increasing significantly with current density. These important observations will be helpful for optoelectronic device designer.

4   Conclusions

In this paper, In$_x$Ga$_{1-x}$ N/GaN parabolic QW and square QW LEDs for various In compositions and well widths have been studied. Best optical output is achieved, for an optimum In composition and QW width. This is the novelty of this work. It is observed that the TP for a parabolic QW is above four times higher compared to that

of rectangular QW. Moreover, to obtain the best optical output, a set of data for blue light emissions (2.75 eV) is extracted for various In compositions and well widths. Notable observation is that for the same emission energy (2.75 eV), maximum TP is obtained for the mole fraction of 0.23, and well width of 28 Å. For further studies, the In mole fraction of 0.23 and well width of 28 Å can be considered for $In_xGa_{1-x}N$/ GaN parabolic QWLEDs in order to achieve blue light emission. For In mole fraction of 0.23 and well width of 28 Å, it is observed that, even though, the TE is increasing but the variation is negligible (~22 meV) for the large change in current density while the TP is increasing significantly with current density. These observations may convey important information for optoelectronic device designer to achieve better device efficiency.

References

1. Nakamura, S., Fasol, G.: The Blue Laser Diode: GaN Based Light Emitters and Lasers. Springer Science & Business Media (2013)
2. Wierer, Jr., J.J., Tsao, J.Y.: Advantages of III-nitride laser diodes in solid-state lighting. Phys. Status Solidi A **212**(5), 980–985 (2015)
3. Wierer, Jr., J.J., Tsao, J.Y., Sizov, D.S.: Comparison between blue lasers and light-emitting diodes for future solid-state lighting. Laser Photonics Rev. **7**(6), 963–993 (2013)
4. Cho, H., et al.: Formation mechanism of V defects in the InGaN/GaN multiple quantum wells grown on GaN layers with low threading dislocation density. Appl. Phys. Lett. **79**(2), 215–217 (2001)
5. Shi, J.-J., Gan, Z.-Z.: Effects of piezoelectricity and spontaneous polarization on localized excitons in self-formed InGaN quantum dots. J. Appl. Phys. **94**(1), 407–415 (2003)
6. Yang, T.-J., et al.: The influence of random indium alloy fluctuations in indium gallium nitride quantum wells on the device behavior. J. Appl. Phys. **116**(11), 113104 (2014)
7. Zhao, H., Jiao, X., Tansu, N.: Analysis of interdiffused InGaN quantum wells for visible light-emitting diodes. J. Display Technol. **9**(4), 199–205 (2013)
8. Biswas, D., Mistry, A., Gorai, A.: Constructive and comprehensive studies on the advantages of using staggered $In_xGa_{1-x}N/In_yGa_{1-y}N$ QWs in LEDs. Opt. Mater. **66**, 367–373 (2017)
9. Kwon, S.-Y., et al.: Optical and microstructural studies of atomically flat ultrathin In-rich In Ga N/Ga N multiple quantum wells. J. Appl. Phys. **103**(6), 063509 (2008)
10. Gorai, A., et al.: Inclusion of indium, with doping in the barriers of $In_xGa_{1-x}N/In_yGa_{1-y}N$ quantum wells reveals striking modifications of the emission properties with current for better operation of LEDs. Photonics Nanostruct. Fundam. Appl. **28**, 70–74 (2018)
11. Park, S.-H., Park, J., Yoon, E.: Optical gain in In Ga N/Ga N quantum well structures with embedded AlGaN δ layer. Appl. Phys. Lett. **90**(2), 023508 (2007)
12. Park, S.-H., et al.: Dip-shaped InGaN/GaN quantum-well light-emitting diodes with high efficiency. Appl. Phys. Lett. **95**(6), 063507 (2009)
13. Zhao, H., et al.: Self-consistent analysis of strain-compensated InGaN–AlGaN quantum wells for lasers and light-emitting diodes. IEEE J. Quantum Electron. **45**(1), 66–78 (2008)
14. Park, S.-H., et al.: Comparison of light emission in InGaN/GaN light-emitting diodes with graded, triangular, and parabolic quantum-well structures. J. Korean Phys. Soc. **60**(3), 505–508 (2012)
15. McBride, P.M., Yan, Q., Van de Walle, C.G.: Effects of In profile on simulations of InGaN/GaN multi-quantum-well light-emitting diodes. Appl. Phys. Lett. **105**(8), 083507 (2014)
16. Mishra, P., et al.: Achieving uniform carrier distribution in MBE-grown compositionally graded InGaN multiple-quantum-well LEDs. IEEE Photonics J. **7**(3), 1–9 (2015)

17. Mistry, A., Gorai, A., Biswas, D.: The electron–hole overlap in the parabolic quantum well light emitting diode is much superior to the rectangular: even to that of a staggered quantum well. Opt. Quant. Electron. **51**(2), 42 (2019)
18. Yan, T., et al.: Optical properties of a novel parabolic quantum well structure in InGaN/GaN light emitters. Phys. Status Solidi A **212**(5), 925–929 (2015)
19. Arif, R.A., et al.: Spontaneous emission and characteristics of staggered InGaN quantum-well light-emitting diodes. IEEE J. Quantum Electron. **44**(6), 573–580 (2008)
20. Hangleiter, A., et al.: Optical properties of nitride quantum wells: how to separate fluctuations and polarization field effects. Phys. Status Solidi B **216**(1), 427–430 (1999)
21. Mistry, A.: Performance improvement of green QW LEDs, for the different doping in the barriers, using InAlN interlayer and strain compensated AlGaN interlayer at the InGaN/GaN interface. Opt. Materials **113**, 110863 (2021)
22. Wu, J.: When group-III nitrides go infrared: new properties and perspectives. J. Appl. Phys. **106**(1), 5 (2009)
23. Christmas, U.M., Andreev, A., Faux, D.: Calculation of electric field and optical transitions in in Ga N/Ga N quantum wells. J. Appl. Phys. **98**(7), 073522 (2005)
24. Das, T., Kabi, S., Biswas, D.: Calculations for the band lineup of strained In$_x$Ga$_{1-x}$N/GaN quantum wells: effects of strain on the band offsets. J. Appl. Phys. **105**(4), 046101 (2009)

Vehicle Detection and Tracking Based on Interest Points of Visual Appearance

Mallikarjun Anandhalli, A. Tanuja, Vishwanath P. Baligar, Pavana Baligar, and Santhosh S. Saraf

Abstract This paper presents a unique pattern of vehicle detection with the help of fundamental and successive algorithms. The characteristics of the vehicle are the important parameters to identify vehicles. A good number of corner points is compacted inside a vehicle region which is considered as the initial requirement for an algorithm. The densely packed corner points are grouped. This grouping gives a hint of points which are associated with each vehicle and they play a key in detection of vehicles. Once the grouping is performed, the non-vehicle region is segmented. The corner points are tracked with a Lucas-Kanade algorithm in order to maintain the stability of corner points. The detection rate with the proposed method is 93.95%.

Keywords Corner points · Tracking · Grouping

1   Introduction

With the drastic rise in the development of information technology, researchers have taken active participation in surveillance. Compared with ground-plane surveillance, aerial view surveillance has a major advantage in reducing occlusion problems. Intelligent traffic system (ITS) is one of the huge organizations actively working for better traffic management systems. The main challenges with traffic management systems are congestion, accidents, violation of traffic rules across the world. Addressing these issues is very much important for traffic management departments and researchers.

M. Anandhalli (✉) · A. Tanuja · S. S. Saraf
Department of Electronics and Communication Engineering, KLS Gogte Institute of Technology, Belagavi, India

V. P. Baligar
Department of Computer Science and Engineering, KLE Technological University, Hubbali, India

P. Baligar
Department of Computer Science Engineering, SKSVM. Agadi College of Engineering and Technology, Gadag, India

The traffic surveillance issues can be addressed by hardware components (i.e., loop detectors) and vision-based systems (i.e., software-based surveillance equipped with cameras). The vision-based system is cost-effective, portable, and can be accessed remotely. Vision-based algorithms are sensitive to resolutions, frames per second, road orientations, camera angles, etc. Considering all these sensitivities [5], many of the researchers have proposed vehicle detection algorithms [1–4]; but still, traffic surveillance is a challenging and nontrivial area.

The main *contribution* of this paper lies in extracting the corner points belonging to only vehicular regions by segmenting non-vehicular regions corner points (not regions of interest). The elimination of noninterest points is one of the best approaches with stationary cameras and it may not work as expected under certain criteria like complex background and camera shakes. This crisis must be understood to enhance the efficiency of the traffic supervision system. The efficiency is enhanced in the proposed algorithm by performing vehicle detection using stationary and moving cameras. The datasets with different climatic conditions and composite backgrounds are considered to check the efficiency and performance of the proposed algorithm. This approach of a paper is to detect the vehicle considering the corner points.

2   Literature Survey

Many of the researchers have proposed algorithms to address the detection of vehicles in traffic surveillance, and few of the works are discussed below.

Considering the features of the vehicle and constructing these features using the AND-OR graph for each vehicle, the authors Li et al. [5] detect the vehicle and also solve the occlusion problem. The features are extracted by taking only the front and rear views of the vehicle.

Tsai et al. [6] proposed an innovative technique of vehicle detection from stationary frames using the color and edge properties of the vehicles. The author generates new domains of color from the R, G, and B components. Later, vehicle and background color were categorized with the help of Bayesian classifiers.

The author Cheng et al. [7] proposed an algorithm for detection of a vehicle in aerial surveillance using pixel wise classification. In order to accomplish this, the authors extracted features by considering the color and edges of the vehicle. These extracted features are used to construct the Bayesian network that helps in classification.

Using the GMM and the blob detection approach, a method for detecting and tracking the vehicle is proposed by the authors Bhaskar et al. [8]. The GMM detects the vehicle in foreground, while the blob detection method accurately identifies the vehicle and places a rectangular box around the vehicle with 91% of accuracy.

3 Proposed System

The proposed system is represented using algorithm and same can be seen in the flowchart as shown in Fig. 1.

Algorithm

1. Localization of interest points on every 16th frame of video using Harris corner detection.
2. Elimination of corner points which are not associated with vehicles.
3. Grouping of selected regions of interest points.
4. Tracking region of interest points by applying Lucas-Kanade (LK) algorithm to firm up.

3.1 Interest Point Detection

Harris corner detector method is one of the corner methods to extract the corner points on the object, which are independent of illumination change, rotation, and scaling. Due to this unique feature, the corner approach is used to detect the vehicle which is given by Harris and Stephen [9].

Mathematically, change of intensity is given as

$$E_{q,r} = \sum_{x=0}^{y} W(x, y)[I(x + q, y + r) - I(x, y)] \tag{1}$$

where $I(x + q, y + r)$ gives shifted window intensity and $I(x, y)$ is intensity and window function is represented as $W(x, y)$. The interest points are extracted from the frame by using a detection algorithm. To minimize the time complexity, the algorithm runs on the 16th of every frame to extract the points instead of extracting the corner points on every frame.

Fig. 1 The proposed method flowchart
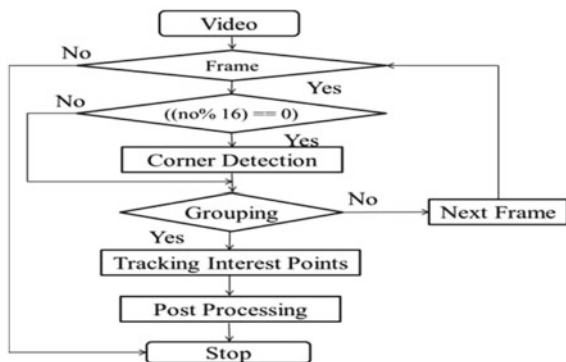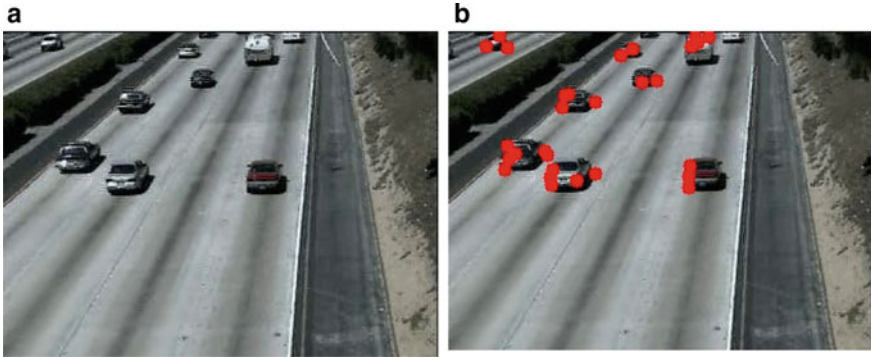
Fig. 2 **a** Video frame before corner detection and **b** frame after corner detection and eliminating noninteresting points

3.2 Eliminating Noninterested Points

Every corner point that is selected from a frame is not associated with the vehicle due to the environment, thus the points that do not associate with vehicles need to be eliminated. To eliminate the corner points, a background subtraction method is performed. Background points are eliminated from frame subtraction. The deviation between the frames at the pixel level is referred to as frame difference. Only the points that are associated with the vehicles are preserved as you can observe in Fig. 2b. Figure 2a shows one of the frames in a video without corner detection, and Fig. 2b shows the same frame retaining points only in the vehicular region.

3.3 Grouping Highly Dense Points

Once we get the foreground points, it is necessary to group the points in the vehicular region for detection. The grouping of points is made possible by using the Euclidean distance (ED). The threshold value (T) decides whether the corner points are able to form a cluster or not (Fig. 3). If the length between the points is beyond the T, then they are not clustered into a single group, else these points are grouped to form a single cluster. Assume $Q1(x1, y1)$ and $Q2(x2, y2)$ are two points, then ED among points is given by

$$ED = \sqrt{(x2 - x1)^2 + (y2 - y1)^2} \tag{2}$$
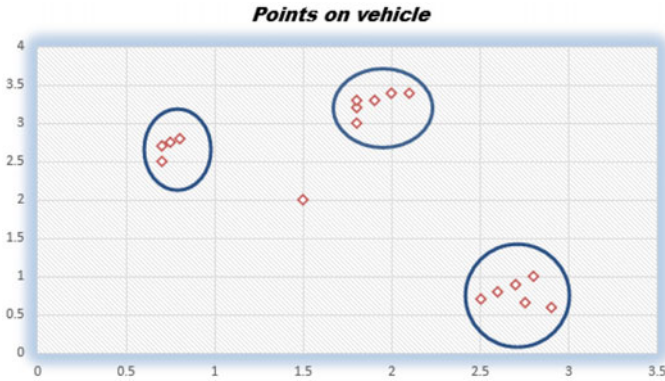
Fig. 3 Grouping of corner points

4 Tracking

Identification of points in successive frames is complex due to its instability, flickering nature, and it is also time-consuming. To stabilize the points, which in turn helps in tracking the points in each frame is possible using the LK algorithm [10]. The LK method helps in predicting the location of movement of pixels between consecutive frames and also trailing of selected corner points helps in reducing time complexity. As aforementioned above, the computational complexity is greatly reduced and extraction of points is only on every 16th frame of video.

5 Experiment Results

The proposed method is demonstrated on the different climatic datasets to check robustness and effectiveness of the algorithm.

5.1 Dataset

To check the stability of the algorithm, the proposed method is tested on different benchmark datasets like "Institut fur Algorithmen and Kognitive Systemes," KITTI, and highway.

Fig. 4 Result of rainy video

Fig. 5 Result of
low-resolution video

5.2 Identification of Vehicle in Wet Climate

The given algorithm is examined in diverse climate conditions. The algorithm is
examined on the rainy weather with wet ground and poor lightning, even with these
conditions, the performance is satisfactory as shown in Fig. 4. The frame rate for
video is 10 fps, and the detection rate is 15 fps. In the video, all vehicles were
identified and some consequence frames of a video are given in Fig. 5.

5.3 Identification in Bright Day with Less Perseverance

The video is examined on a bright day in various sites under a less perseverant
camera. In the least perseverance, corner points that are associated with vehicles are
not closely packed. Even in this condition, the algorithm performed effectively on

Fig. 6 Result of
high-resolution video

the video of a high identification rate with 30 fps. One of the frames of video with these constraints is given in Fig. 5.

5.4 Identification of Vehicle in Bright Day with More Perseverance

The next video is examined on a bright day with a more perseverance camera. The vehicle's corner points extracted were highly congested forming a group of points, and finding the vehicle was not complicated. All vehicles are identified in the video accurately with a frame rate of 30 fps, which can be seen in Fig. 6.

5.5 Identification of Vehicle in Snow

To detect the vehicle in the snow condition, it was a challenging task as the clarity of the objects will not be as good enough compared with other climatic conditions. But the algorithm gives a satisfactory result as shown in Fig. 7 with a frame rate of 30 fps. The detailed study is conducted on various datasets with low- and high-resolutions at different time duration and FPS. The study is shown in Table 1.

Fig. 7 Result of snow video
sequence

5.6 Experiment Results with Benchmark Dataset

To check the robustness of the proposed method, the experiments are being carried out on benchmark datasets like KITTI and highway. The KITTI [11] dataset videos are captured in a horizontal view which was not tested before and the algorithm performed effectively by detecting all the vehicles in each frame as shown in Figs. 8 and 9. Furthermore, testing is performed on the highway datasets containing shadow and occlusion problems. Even with this scenario, the proposed method showed satisfactory results which are as shown in Fig. 10.

5.7 Comparative Study with State of the Art

Table 2 gives the comparison of the proposed method with other detection and tracking methods. When compared to the other methods, the proposed method performance is appreciable.

6 Conclusion

The proposed algorithm detects a vehicle using only the corner points under different climatic conditions with an overall accuracy of 93.95%. The detection is invariant to the illumination, complex background, shadow, and weather. The false positive rate is greatly reduced due to the elimination of noninteresting points in an algorithm. The proposed method is tested on different datasets and standard datasets to check the robustness.

Table 1 Detail study on datasets

S No.	Frame size	Duration	FPS	Weather/condition	Number of vehicle detected	TP	FN	FP	Accuracy (%)
1	320 * 240	00:00:05	10	Rainy	7	7	0	0	100
2	320 * 240	00:00:20	29.75	Rainy	13	13	0	0	100
3	320 * 240	00:01:10	30	Snow	13	11	2	0	84.61
4	320 * 240	00:00:33	15	Sunny	38	38	0	0	100
5	320 * 240	00:00:30	25	Sunny	45	45	0	0	100
6	640 * 480	00:00:58	25	Sunny	37	36	1	0	97.29
7	320 * 240	00:00:32	30	Fog—video sequence 1	46	45	1	0	97.82
8	320 * 240	00:02:36	30	Fog—video sequence 2	117	116	1	2	97.47
9	320 * 240	00:02:36	30	Fog—video sequence 3	136	134	2	2	97.1
10	704 * 480	00:00:10	30	Moving camera—rear view	1	1	0	0	100
11	704 * 480	00:0010	30	Moving camera—rear view	4	3	1	0	75
12	720 * 640	00:00:33	25	Complex background	15	14	1	0	93.33
13	720 * 640	00:01:10	25	Complex background with camera shake	45	41	4	0	91.11
14	720 * 480	00:04:36	30	Complex background 1 at the intersection	78	70	8	0	89.74
15	720 * 480	00:04:32	30	Complex background 2 at the intersection	117	103	14	0	88.03
16	640 * 480	00:01:00	30	Intersection of roads	17	16	1	0	94.11
17	320 * 240	00:02:36	30	Fog with complex background	11	11	0	1	91.67

Fig. 8 Proposed method on KITTI dataset-1

Fig. 9 Proposed method on KITTI dataset-2

Fig. 10 Proposed method on highway dataset

Table 2 Comparative study with other methods

Authors	Features/method used	Remarks
Gu et al. [12]	Convolutional neural network—ImageNet dataset	Average precision—80.5%
Cepni et al. [13]	Yolo v3-spp with COCO dataset	Average IoU—84.88% and precision—72.02%
Proposed method	Corner-based detection and tracking	Accuracy—93.95%

References

1. Zhang, N., Fan, J.: A lightweight object detection algorithm based on YOLOv3 for vehicle and pedestrian detection. In: 2021 IEEE Asia-Pacific Conference on Image Processing, Electronics and Computers (IPEC), pp. 742–745 (2021)
2. Zhang, X., Story, B., Rajan, D.: Night time vehicle detection and tracking by fusing vehicle parts from multiple cameras. IEEE Trans. Intell. Transp. Syst. (2021). https://doi.org/10.1109/TITS.2021.3076406
3. Bin Zuraimi, M.A., Kamaru Zaman, F.H.: Vehicle detection and tracking using YOLO and DeepSORT. In: 2021 IEEE 11th IEEE Symposium on Computer Applications & Industrial Electronics (ISCAIE), pp. 23–29 (2021)
4. Guo, J., Gao, H., Yan, Z., Cao, J., Fu, Z.: Vehicle detection counting algorithm based on background subtraction algorithm and SORT. In: 2021 23rd International Conference on Advanced Communication Technology (ICACT), pp. 319–325 (2021)

5. Li, B., Li, Y., Tian, B., Yao, Q.: Vehicle detection based on the and– or graph for congested traffic conditions. IEEE Trans. Intell. Transp. Syst. **14**(2), 984–993 (2013)
6. Hsieh, J.-W., Tsai, L.-W., Fan, K.-C.: Vehicle detection using normalized color and edge map. IEEE Trans. Image Process. **16**(3), 850–864 (2007)
7. Weng, C., Cheng, H., Chen, Y.: Vehicle detection in aerial surveillance using dynamic Bayesian networks. IEEE Trans. Image Process. **21**(4), 2152–2159 (2012)
8. Yong, S., Bhaskar, P.K.: Image processing based vehicle detection and tracking method. In: 2014 International Conference on Computer and Information Sciences (ICCOINS), pp. 1–5 (2014)
9. Stephens, M., Harris, C.: A combined corner and edge detector. In: Alvey Vision Conference, vol. 15 (1988)
10. Kanade, T., Lucas, B.D.: An iterative image registration technique with an application to stereo vision. In: Proceedings of the 7th International Joint Conference on Artificial Intelligence— Volume 2. Morgan Kaufmann Publishers Inc., San Francisco, CA (1981)
11. Geiger, A., Lenz, P., Stiller, C., Urtasun, R.: Vision meets robotics: the KITTI dataset. Int. J. Robot. Res. (IJRR) (2013)
12. Chen, Z., Gu, X., Ma, T., Li, F., Yan, L.: Real-time vehicle detection and tracking using deep neural networks. In: 2016 13th International Computer Conference on Wavelet Active Media Technology and Information Processing (ICCWAMTIP), pp. 167–170 (2016)
13. Sumeyye, C., Atik, M.E., Duran, Z.: Vehicle detection using different deep learning algorithms from image sequence. Baltic J. Mod. Comput. **8**, 347–358 (2020). https://doi.org/10.22364/bjmc.2020.8.2.10

APT'sTTP: Deep Learning with Metaheuristics for Targeted Asset Prediction and Prioritization (TAPP) in Industrial Control System

Diana Arulkumar (ORCID) **and K. Kartheeban**

Abstract   In cyberdomain, advanced persistent threat's tactics techniques and procedures (APT'sTTPs) are related to gain threats information. APT'sTTPs describe the threats behavior and pattern of attack in the adversary. Effective identification of APT'sTTPs in timely manner leads to construction of effective strategy for diagnosis of cyber threats actors (CTAs) in the form of attack vector. Through effective process, appropriate prevalence and regularities are evolved for APT'sTTPs for CTAs. However, the existing techniques focused on classification of attacks influenced by attackers alone but fails to examine the hackers target assets. To highlight the goal of this paper, to prioritize and predict the target assets in industrial control system (ICS) using deep learning integrated with metaheuristics ABC optimization method. For identification of TTP utilized in the industrial application, a brain-inspired model of deep neural network (DNN) approach has been used. Those TTP is evaluated for the collection of cyber assets process adopted in people, technology, and infrastructure (PPTI). The Deep Neural Network (DNN) once trains the 15 TTP helps to map and prioritize the inventory asset. For prioritizing an asset in the forum, a bio-inspired intelligence of metaheuristics ant bee colony (ABC) optimization approach has been adopted as ABC for targeted asset prediction and prioritization (ABCTAPP). Analysis of results illustrated that input capture (IC) and Service Certifying Organization (SCO) exhibit higher utilization of 93%. Further, hackers target host address and IP protocol in industrial applications.

Keywords Tactics techniques and procedures (TTPs) · Deep neural network (DNN) · Ant bee colony for targeted asset prediction and prioritization (ABCTAPP)

D. Arulkumar (✉) · K. Kartheeban
Kalasalingam Academy of Research and Education, Krishnankoil, Tamil Nadu, India

K. Kartheeban
e-mail: K.Kartheeban@klu.ac.in

1 Introduction

In recent years, cyberattack has been emerging at drastic pace. As per [1], in the year of 2017, average cyberattack cost is recorded as 153 million USD. The increased number of malware and sophistic, an enhancement in security of the network particularly cyberthreats related to CTAs is required. At these circumstances, information related to cyberthreat plays major role in indication of attack and vulnerabilities employed in the CTA at particular campaign. The major limitation related to present Cyber Telephony Integration (CTI) is limited sharing of information with respect to static- and heuristics based signature approach those are not able to defend any dynamic and complex nature of threats. Generally, this CTI is classified into four categories such as technical, strategic, operational, and tactical threat intelligence [2]. The strategic-based CTI is related to identification and analysis of risks associated with collected information for making decision for gathered information. The CTI belonging to operational has minimal vulnerabilities and attacks at zero day, dark web, or collection of hackers in closed forums. The CTI with tactical is related to CTAs and APT'sTTPs which involves CTA operand and training with integral part. The representation of APT'sTTPs based on the characteristics of CTA interacts with affected network and operating system. CTA offers substantial effort in the development of operational module by means of customized software tools for attack campaigns. Based on this, it is difficult for CTA to cope with changes in the APT'sTTPs due to minimal attack or new attack emerged in specified time [3]. Hence, it is necessary for the identification of attack in APT'sTTPs with incident of attack for prevention of loss in the organization. The recent prevalent incident of cyberattack and behavior of CTAs are extracted for establishment of relation between APT'sTTPs attack pattern [4].

The CTI employs several technical resource factors such as intrusion detection system and firewalls. Those indicators are the signatures involved in attack such as IP address, file hashes, Command and Control (C&C) domains, and viral signatures. The indicators are ineffective in the identification of cyberthreats which are involved in CTA modification each time for bypass firewalls and intrusion detection system [5, 6]. The tactical and strategic threat intelligence are considered as an effective tool and provides long-life time when compared with technical and operational threat intelligence. To evaluate the TTP process, machine learning has exhibited significant performance; hence, for evaluation of TTP process in CTI, neural network offers significant performance characteristics.

Even, burgeoning market is involved in sale of those stolen data and malicious threats specifically in the Eastern Europe and Russia. Researches on enculturation of subculture of hacker are involved in recognition of status of particular hacking community. Due to the usage of the Internet in almost all countries, hacking has been increased drastically. Throughout the world, mainstream political factor and social movements are based on dependent broadcast ideologies in the world. To overcome such hacking, several tactics have been applied for perceived injustices for secure access to people. Other countries such as Zapatistas, in Chiapas, and Mexico focused

on post-information quality [7]. Cyberattacks have been engaged in drastic range by Chinese hackers where sensitive information is obtained through resources of USA by means of network infrastructure. In April 2006, hackers of Russian and Estonian specifically during war data have been hacked [8–12].

In the Internet, user application involves several assets specifically for industrial applications. The application of attacks is involved in identification of different assets in the network [13]. Hence, it is necessary to identify the assets those are targeted by hackers. In this research, a deep learning approach integrated with metaheuristics approach is developed for the identification of APT'sTTPs and assets. The data for analysis are collected from several hacking forums for training the deep neural network. The focused domain is CTI document which is based on structured threat information expression standard (STIX). Through testing and training, APT'sTTPs are identified in the hacking forums. Results demonstrated that file and discovery of TTP have been highly performed by hackers. For evaluation, this research considers 15 APT'sTTPs. In analysis of assets, hackers focused on technological aspects particularly for hacking data.

This paper provides the metaheuristics-based approach for developed for target asset. The proposed metaheuristics focused on 15 target assets to predict the hackers target for targeted assets. This paper is organized as follows: Sect. 1 presented general description about cyberassets. In Sect. 2, existing works related to target assets are presented. Section 3 presented about materials adopted for target asset along with TTP regulatory framework. In Sect. 4, results obtained for proposed metaheuristics approach are presented. In Sect. 5. the overall conclusion obtained for proposed metaheuristics approach is stated.

2 Illustrations

The analysis of CTI focused on defense mechanism in proactive and reactive approach for analytics. The CTAs are based on the consideration of behavior, capability, and persona. With consideration of cyberdefense factor profiling involved in collection of personal data [14]. In real-time scenario, based on attributes, threats are estimated. To evaluate the performance of hacking community, CTAs are involved in utilization of several software tools and assets for campaigns hacking [15].

In hacking communities, data related to generic topic is target asset for hackers. Those collected data from social media are labeled with inclusion of several emerging tools such as crypters, vulnerabilities in database, Web, and keyloggers. Those tools are subjected to minimal vulnerabilities and exploits certain factors. Even this provides effective guidance for administration security through proactive defense mechanism. In order to identify the attack patterns, [16] is necessary to streamline the workflow memory and performing the Indicator of compromises (IoC's) analysis of generated attack pattern in each and every phases of attack chain using the machine learning algorithm. Analysis of malware is involved in provision of automated solution to evaluate interrelationship instances of malware [17]. Through the review of

existing literature review, several domains are evaluated for measuring significance of tactics involved in CTI. Hence, this research focuses on several TTPs involved in regularities of attack in the system at right time. The analysis of existing literature stated that target assets are evaluated in terms of detecting attack. However, the existing techniques are focused on classification of attacks influenced by attackers alone but fails to examine the hackers target assets,

The APT'sTTPs for CTA's involved in formulation certain regularities. The framework comprises of feature selector, ARM miner modules, and feature extractor in which feature selector is used for encoding CTI document using STIX. The selected CTI document subjected to cyberthreat is considered in this research [18]. The collected CTI document contains unique attribute ID in elements of STIX. In elements of STIX, TTP is represented where similar to CTI, TTP also has unique IDs. Each and every TTP provides description about sub-elements of TTP features. For the selected CTI document using feature extractor module, TTP's information is gathered. This extraction is performed through CTI document unique reference and database information storage. The feature extracted is applied into module of feature selector for identification of most effective APT'sTTPs. To represent effective CTA terms, several approaches are implemented by means of deep learning approach for attack identification.

At present, deep neural network has been employed in due to evolution of artificial neural network. It facilitates training of network with tens and millions [19–21] or even billion parameters [22]. To withstand against cyberthreats, details from hacking forums are implemented by means of training and testing large amount of data for processing. In hacking community, minimal research has been conducted to drive hacker community. According to Honeynet projects, hacker community has six targets identified, namely money, entertainment, ego, cause, entrance to a social group, and status [23]. The above-mentioned factors are the major aim of hackers to steal particular data.

Even though deep neural network is similar to neural network, it is hard to train which requires appropriate number of data for processing. The major advantage of deep neural 'network is it provides information to the human for possible prediction of attack in the network. The common process of DNN model involved in data ingesting from the different data sources which offers artifacts sequence for probabilistic ML model using pre-trained performance. Every model perform training using application of various procedure to identify artifacts through pre-existing and labelled sequence data. The output derived from this model is using probabilities model with application of set of procedure fed by other trained ML models [24].

Through the collected data from the hacking forums, data are classified for testing and training. For collected TTP data, with assigned variables, training is adopted in deep network using cognitive agent. The network cognitive agent gains prior knowledge about previous observed attack models and assets inventory [25]. The cognitive agent determination of extent to which sequence of methods adopted by ML models with indication of attack compromised for provided asset. In case, attack within the cognitive agent is observed as ongoing, it will be able to identify human
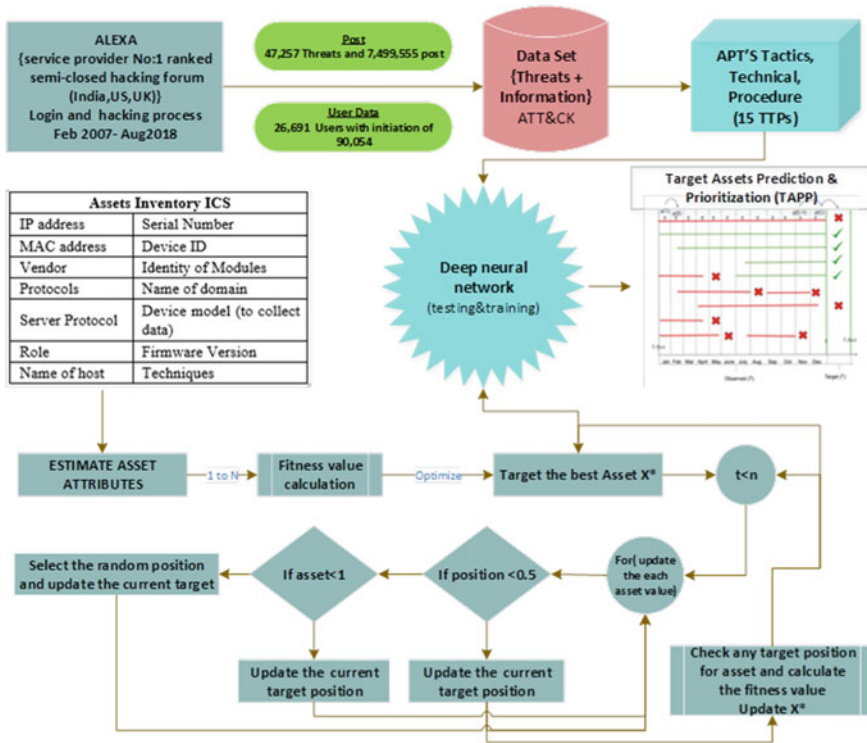
Fig. 1 Architecture of target asset prediction and prioritization (TAPP)

controller. Those are identified from the rank list involved in probable operation for prediction of objective [26].

3 Proposed System

3.1 Target Asset Prediction and Prioritization (TAPP) Architecture

Comparative analysis of the proposed scheme with existing technique observed that Samtani et al. [2] collected data from various online hacker forum such as OpenSc, Reverse 4you, and ExploitIN. It is observed that hacker details are sufficient trends related to reliable and credible for mislead defending community. Brynielsson et al. [1] examined the collected data related to cyberdefense exercises. The main purpose of this function is participants train with defend skill for the constructed network and organization of cyberwarfare. According to [1] the data from those sources

are credible and reliable are out of scope exercises are limited which cannot be full-fledged campaign for CTA. Another researcher, M. Lee and D. Lewis., [11] examined the data related to Symantec Anti-Virus (AV) and Intrusion Prevention System (IPS) corpus for tactical CTI in terms of authentic and reliable for attack processing. The comparative analysis of results expressed that proposed analysis technique offers proactive and reactive defense strategy for recent CTA tactics (Fig. 1).

Data collection

To evaluate the TTP assets in industrial application, deep learning with metaheuristic approach is applied. For analysis, data were collected from hacking forum. According to Alexa, the service provider is involved in management of Web traffic; hence, those forums are ranked as No. 1 which is considered as subcategory hacking forum. Based on analysis, Alexa is relied on Indian Web site forum those includes various hackers in India at the rate of 16.7%, USA 21%, and UK 9.1% for various countries. However, specific hacker forum is represented as hacker forum with inclusion of semi-closed forum which is used for login forum process. The setting of forum is similar to that of other forums where threats are discussed and organized. In those formats, user post-initiates threat is referred as header. With respect to post of header, comments of other user post with several threads are included in replies. On the other hand, post of header needs to be discussed as thread and provides vast range of replies. In this paper, to evaluate the target assets, online hacker forum is utilized for assessment, hackers are not provided with intention of users based on the information forum except same interest share mechanism. During data analysis, the users are selected based on the noticeable active performance in terms of posting in the forum.

The forum data for analysis are collected from February 2007 to August 2018. The downloaded forum data consist of wide range of posting related to hacking process. Specifically, the type of information was considered in the dataset [27–30].

Post-centric data: The data of each post consist of header or replies which includes post ID, post title, post category, post content, and post author. **User-centric data**: The data registered forum is utilized for user reputation, and this includes user ID, date, user level, and user name.

The final downloaded dataset consists of information related to 26,691 users with initiation of 90,054. Also, the downloaded threads consist of 47,257 threats and 749, 9555 posts. In Table 1, the details of collected forum are presented as follows:

APT'sTTP

For analysis, 15 TTP's are identified through hacking forums and presented about description. The selected APT'sTTPs are fed into deep learning technique through process of testing and training. The prediction of operation leads to inclusion of adversary techniques, and potential measures are utilized for prediction of objective and future technique. The human controller acts as information provided to offer information about cognitive agent through utilization of deep learning. For deep learning process, selected feature sets are larger and need to identify associations

Table 1 Forum details

Forum attributes	Registered time length for days	32
	Number contributes in unique factor for a month	1736
	Monthly user retention	781.7
	Post count for individual thread	8.33
	Unique number for each individual thread	5.46
Communication behaviors	Message generated for particular user	7.7
	Word count utilized for individual message	33.35
	Number of threats for individual contributor	1.91
	User replies for data	13.97
	Density of data discussed	22.62

Table 2 TTP and its description

TTP	Description
Credential dumping (CD)	Credential is extracted from the system
File deletion (FD)	Removal of pf malicious content with elimination of attack traces
Data compression (DC)	Before the process of exfiltration, collected system information are compressed
Scheduled task (ST)	For execution of malicious content, OS task is scheduled
Valid accounts (VA)	Within the system, credentials of valid users are compromised
Windows management instrumentation (WMI)	Access to the system is obtained either locally or remotely
Windows admin shares (WAS)	Access information of hidden network is shared with admin for accessing machine victims in the network
Obfuscated files (OF)	Detection of malicious content based on unintelligible mechanism for encoding or encryption
File and directory discovery (FDD)	Extraction of system credentials either from network share or from host
PsExec	Extraction of system credentials
Registry run keys (RRK)	Addition of malicious content from the entry to the registry, it executes user logs in
Remote file copy (RFC)	Files are copied to remote machine
Input capture (IC)	User inputs are captured
PoisonIvy	Remote access tool for DLL load with inclusion of keylogger
System user discovery (SUD)	Identification of principal user of the victim machine

Table 3 Asset inventory

Assets in industrial	Control system
IP address	Serial number
MAC address	Device ID
Vendor	Identity of modules
Protocols	Name of domain
Server protocol	Device model (to collect data)
Role	Firmware version
Name of host	Techniques

among them. In the following Table 2, describes about TTP's for APT which is used for prioritize the assets in our research.

Asset Inventory

Data related to industrial control system have been evaluated for schematic illustration of the assets. Hacking forums are involved in prediction of assets for prioritizing the assets. Through the optimization approach, assets are scheduled which helps in reducing the attack in the network [31]. This research considers 14 assets for evaluating the priority of the network. The assets considered are listed in Table 3

Metaheuristics of ABCTAPP

This paper utilized industrial data for target asset focused by the hackers; for analysis, data were collected from Alexa. The collected dataset from Alexa was processed as follows using ABC meta-heuristics algorithm. Initially, ABC optimization algorithm involved in construction of elements for randomly identify the position within the boundary range of asset values. The dataset elements with attribute 1 are selected from processing else it will be eliminated. The selection of elements is stated in Eq. (3).

$$x_m = l_i + \text{rand}(0, 1) * (u_i - l_i) \tag{1}$$

In the above equation, food source is stated as x_m, which means assets. The parameters u_i and l_i provide the upper- and lower-level solution space. rand$(0,1)$ represents random number value of range [0,1]. The targeted assets by the attacker are identified through consideration of target solution which is represented in Eq. (4):

$$v_{mi} = x_{mi} + \phi_{mi}(x_{mi} - x_{ki}) \tag{2}$$

The parameter I represents randomly selected index, randomly selected attributes are denoted as x_{ki}, and parameter φ_{mi} denotes randomly selected integer value of [−1, 1]. The parameter v_{mi} provides estimated asset value using fitness evaluation in Eq. (5) as follows:

$$fit_i = \begin{cases} \frac{1}{f_i+1} & f_i > 0 \\ 1 + |f_i| & f_i <= 0 \end{cases} \tag{3}$$

In the above Eq. (5), the asset objective equation is estimated using f_i which provides optimal value for targeted asset by the hacker. Through estimation of individual asset, values targeted by hackers are estimated using probability of asset selection using Eq. (6):

$$p_i = \frac{\text{fit}_i}{\sum_{n=1}^{N} \text{fit}_i} \tag{4}$$

The value N denotes total assets targeted by the hackers. fit_i provides the optimal value for identification of asset targeted by the hackers. The ABC algorithm for identification of target asset prediction and prioritization (TAPP) in hacking forum is presented below:

Algorithm 1: ABC for Target Asset Prediction and Prioritization (ABCTAPP)

Initialize the asset attributes estimation Xi (i = 1, 2, ..., n)
Calculate the fitness of each asset target
X*=the best asset target
while (t < maximum number of iterations)
 for each asset target
   Update a, A, C, l, and p
   if1 (p<0.5)
     if2 (|A| < 1)
      Update the position of the current asset target
     else if2 (|A|=>1)
      Select a random asset target (X_rand)
       Update the position of the current asset target
     end if2
   else if1 (p> 0.5)
       Update the position of the current asset target
   end if1
 end for
   Check if any asset target goes beyond the asset target   space and adjust it
   Calculate the fitness of each asset target
   Update X* if there is a better solution
 t=t+1
 end while
 return X*

Deep Learning—Deep Neural Network (DNN)

For Fig. 2, let us consider number of samples or assets as: $D = \{(X_i, Y_i)\}N$ where $N = 1$. The collected data from the Web sites are represented as X_i for the time period $[\Gamma - T + 1, \Gamma]$ with length of T. The prediction of assets for hackers is denoted as $Y_i \in Y = \{0, 1\}$; the targeted assets for window are shown as of length τ.
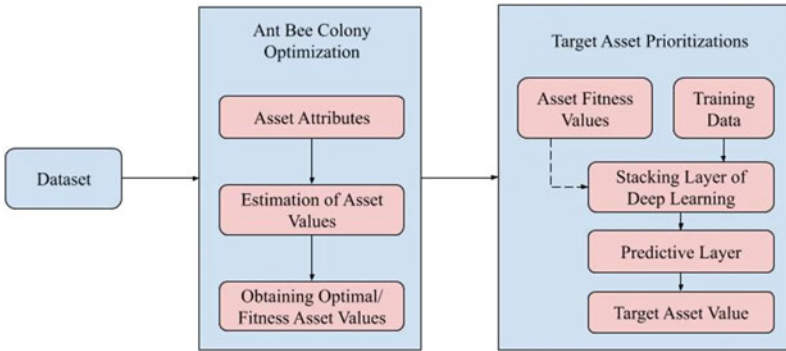
Fig. 2 ABCTAPP

$X_i[\Gamma - T + 1, \Gamma]$ For user data, X_i and $[\Gamma + 1, \Gamma + \tau]$ involves three heterogeneous primitive sub-components based on granularity of observed data as X_{ia}, dynamic user information X_{id}, and static user profiles X_{is}, namely, and it is given in Eq. (5) as follows (Fig. 3) [31]:

$$X_i = (X_{ia}, X_{id}, X_{is}) \in X \tag{5}$$

For evaluation of log components applied in target window is shown as time _x0010_span T right in which dynamic information is denoted in Eq. (6):

$$X_{id} = X(\Gamma - T + 1)_{id}, X(\Gamma - T + 2)_{id}, \ldots, X(\Gamma - 1)_{id}, X(\Gamma)_{id} \tag{6}$$
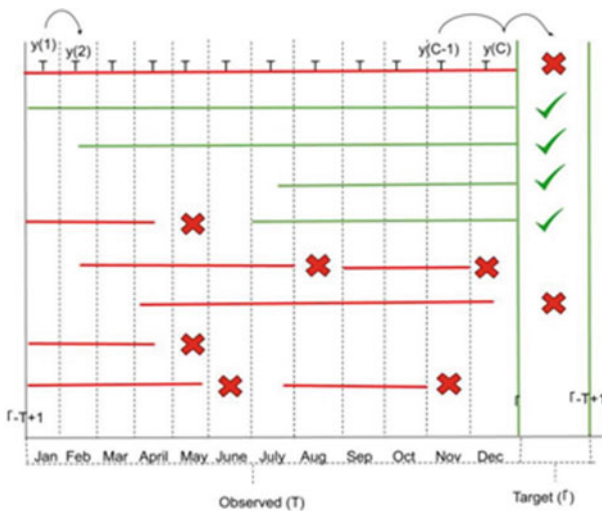
Fig. 3 Schematic overview of assets

The deep learning approach utilizes mapping rule for attribute for estimation of feature space attributes, which is represented as $R(\cdot): X \rightarrow Y$ and subsequently $R(\cdot)$ involved in estimation of future sample. The probability of sample i in attrition can be denoted as $p(y_i = 1|X)$.

4　Experimental Analysis and Results

The metrics considered for comparison are data sources, CTI type, data features, defense strategy, and outcome. The data sources metric is represented as data source collected for analysis. This data source metric is involved in authentication and credibility of analysis process. For future comparisons, ground truth is provided for data sources baseline. As stated earlier, this research utilizes ATT and CK dataset for processing [16]. The extracted ATP'sTTP list from ATT&CK is performed in each phases of intrusion Cyber Kill chain which connects CTA's and utilize appropriate software for processing. In Fig. 4, TTP in the industrial application is presented which is targeted by attackers. Through analysis of proactive and reactive defense strategy, it is observed that IC and SUD exhibit higher utilization in TTP asset by hackers at the rate of 93%. The DC offers TTP % values of 92%, failed directory deletion (FDD) provides TTP utilization rate of 90%, VA provides TTP value of 83%, WAS, WMI provides 73% and 70%, respectively. The parameter CD exhibits TTP of 78% and FD provides TTP of 85% (Tables 4 and 5).
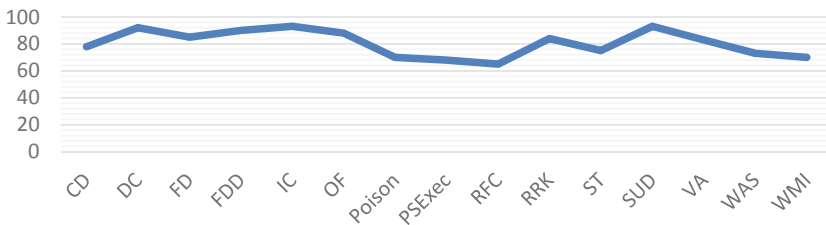
Fig. 4　APT'sTTP utilization in each phases of intrusion chain

Table 4　Data sources with hacker's forum

Data sources	Hacking forum, dataset, benchmark dataset
CTI type	Operational, tactical, technical, and strategic
Defense strategy	Proactive, reactive
Data features	Source code, attachments, tutorials, and emails
Outcome	Topic labels, language of implementation

Table 5 Applying the ABCTAPP with DNN to calculate target asset value

	CD	DC	FD	FDD	IC	OF	Poison	PSExec	RFC	RRK	ST	SUD	VA	WAS	WMI
IP address	1.00	1.00	1.00	1.00	1.00	1.00	1.00	1.00	1.00	1.00	1.00	1.00	1.00	1.00	1.00
MAC address	0.98	0.99	0.90	0.90	0.99	0.90	0.78	0.90	0.90	0.90	0.90	0.98	0.90	0.78	0.90
Vendor	0.78	0.97	0.98	0.77	0.95	0.70	0.50	0.70	0.75	0.70	0.70	0.98	0.70	0.70	0.70
Protocols	0.84	0.98	0.99	0.90	0.98	0.90	0.65	0.60	0.64	0.90	0.75	0.99	0.90	0.90	0.90
Server protocol	0.77	0.98	0.86	0.93	0.98	0.99	0.10	0.15	0.13	0.75	0.45	0.98	0.65	0.54	0.87
Role	0.71	0.87	0.83	0.98	0.95	0.90	0.88	0.90	0.83	0.95	0.89	0.99	0.89	0.90	0.85
Name of host	0.65	0.83	0.80	0.81	0.87	0.84	0.65	0.89	0.61	0.78	0.68	0.98	0.97	0.72	0.65
Serial number	0.56	0.95	0.96	0.98	0.97	0.88	0.69	0.73	0.69	0.96	0.42	0.99	0.65	0.60	0.62
Device ID	0.70	0.99	0.98	0.98	0.97	0.99	0.89	0.87	0.77	0.98	0.98	0.97	0.96	0.62	0.54
Identity of modules	0.42	0.80	0.68	0.79	0.77	0.70	0.74	0.80	0.78	0.63	0.77	0.65	0.75	0.30	0.40
Name of domain	0.35	0.95	0.94	0.99	0.98	0.96	0.99	0.98	0.98	0.97	0.97	0.98	0.95	0.98	0.58
Device model (to collect biometric data)	0.70	0.30	0.56	0.87	0.58	0.78	0.45	0.55	0.69	0.60	0.65	0.72	0.70	0.65	0.54
Firmware Version	0.28	0.88	0.76	0.85	0.88	0.87	0.79	0.74	0.73	0.79	0.75	0.90	0.87	0.74	0.54
Techniques	0.15	0.97	0.72	0.87	0.62	0.95	0.75	0.79	0.84	0.85	0.64	0.78	0.73	0.84	0.76

Fig. 5 Target asset prediction and prioritization
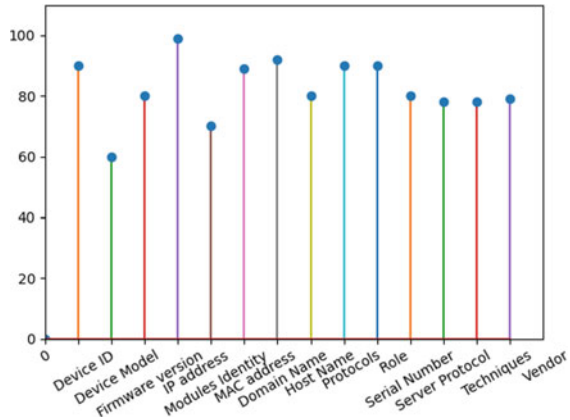
Table 4 portrays that the data can be collected from various sources such as cyber defense exercises [1], online hacker forum such as OpenSc, Reverse 4you and ExploitIN [2], Symantec Anti-Virus (AV) and Intrusion Prevention System (IPS) corpus [16]. The comparative analysis with existing technique is observed that Brynielsson et al., [1] said the function is to train participants with defend skill for the constructed network and organization of cyber warfare. Samtani et al., [2] that hacker details are sufficient trends related to reliable and credible for mislead defending community. Another researcher, M. Lee and D. Lewis., [16] examined for tactical CTI in terms of authentic and reliable for attack processing. The proposed analysis technique of combined model of deep neural networks and ABCTAPP. Table 5 offers proactive and reactive defense strategy for recent CTA tactics. Through analysis of proactive and reactive defense strategy, it is observed that IC and SUD exhibit higher utilization in TTP by hackers at the rate of 93%. The DC offers TTP % values of 92%, failed directory deletion (FDD) provides TTP utilization rate of 90%, VA provides TTP value of 83%, WAS, WMI provides 73% and 70%, respectively. The parameter CD exhibits TTP of 78%, and FD provides TTP of 85% .The asset prioritization is presented in Fig. 5; with asset prioritization, the collected dataset consists of 667 users with exhibition of similar pattern in casual hacker forum. From analysis, it is observed that behavioral pattern decreases with knowledge provision. The examination of assets stated that IP address, protocol, and role number are identified assets by the attackers. In secondary stage, serial number and name of host are targeted. From the graphical representation of calculated value of ABC TAPP wit9n front are targeted highly by the attackers (Fig. 6).

5   Conclusion

The TTPs represent the behavior of a CTA when interacting with the victims' resources such as operating system and network. This research adopted deep learning
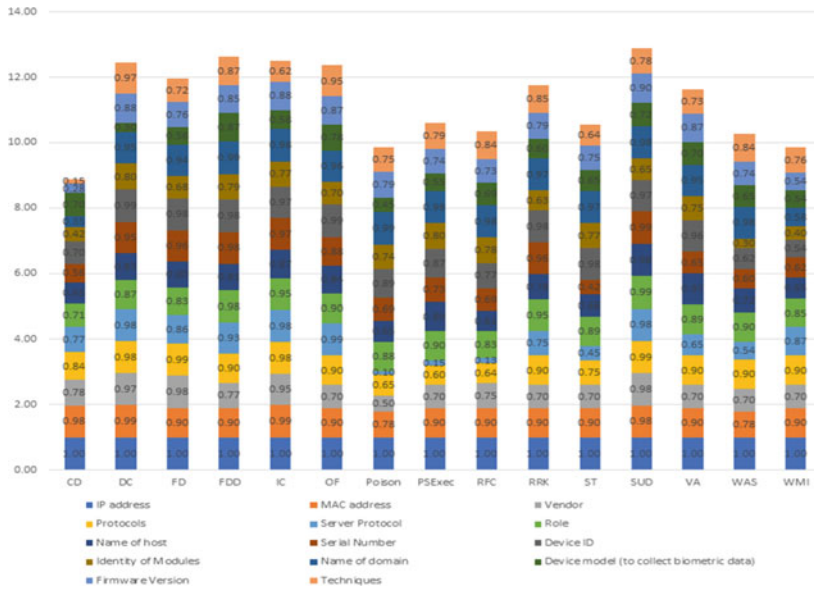
Fig. 6 ABCTAPP with DNN to calculate target asset value

method for identification of number of TTP used in hacking forum. Through the application of deep neural network, target asset and multiple target asset have been evaluated. The collected cyberassets are process adopted, people and technology, and infrastructure (PPTI). The assets are prioritized with the help of DNN by training 15 TTP and inventory asset processed with ABC algorithm. Simulation analysis stated that IC and SCO are highly utilized assets for hacking forum. Further, hackers use protocol, host address, and IP address as targeted assets in the network. In the future, this research can be implemented in other wireless communication system such as WSN and IoT for attack identification.

References

1. Brynielsson, J., Franke, U., Tariq, M.A., Varga, S.: Using cyber defense exercises to obtain additional data for attacker profiling. In: IEEE Conference on Intelligence and Security Informatics (ISI) (2016)
2. Samtani, S., Chinn, R., Chen, H., Nunamaker, J.F.: Exploring emerging hacker assets and key hackers for proactive cyber threat intelligence. J. Manage. Inf. Syst. **34**(4) (2017)
3. Agrafiotis, I., Nurse, J.R., Buckley, O., Legg, P., Creese, S., Goldsmith, M.: Identifying attack patterns for insider threat detection. Comput. Fraud Secur. **7** (2015)
4. Miles, C., Lakhotia, A., LeDoux, C., Newsom, A., Notani, V.: Virusbattle: state-of-the-art malware analysis for better cyber threat intelligence. In: 7th International Symposium on Resilient Control Systems (ISRCS) (2014)

5. Franklin, D., Ransomware, P.: Available https://exchange.xforce.ibmcloud.com/collection/Pet yaRansomware024ee880d86e353ef307155cfe936c5a. Accessed 28 Jan 2018
6. Han, J., Pei, J., Yin, Y.: Mining frequent patterns without candidate generation. ACM Sigmod Rec. (2000)
7. Simonite, T.: Chinese Hacking Team Caught Taking Over Decoy Water Plant (2013)
8. Daly, M.K.: The advanced persistent threat (or informationized force operations). In: 23rd Large Installation System Administration Conference (LISA) (2009)
9. Risk Based Security: A breakdown and analysis of the December 2014 Sony hack. Risk Based Secur. (2014)
10. O'Gorman, G., McDonald, G.: The Elderwood Project (2012)
11. Lee, M., Lewis, D.: Clustering disparate attacks: mapping the activities of the advanced persistent threat. In: Virus Bulletin Conference (2011)
12. Jiang, G., Caselden, D., Winters, R.: The EPS awakens. FireEye Threat Res. (2015)
13. Symantec Security Response: Hydraq—An Attack of Mythical Proportions. Symantec (2010)
14. Winters, R.: The EPS awakens—part 2. FireEye Threat Intell. (2015)
15. Selvaraj, K.: Hydraq (Aurora) Attackers Back? Symantec (2010)
16. Mandiant: APT1—Exposing One of China's Cyber Espionage Units (2013)
17. Hoglund, G.: Inside an APT Covert Communications Channel. Fast Horizon (2011)
18. Alperovitch, D.: Cyber Deterrence in Action? A Story of One Long HURRICANE PANDA Campaign. Crowdstrike (2015)
19. Kumar, B.S., Rukmani, K.: Implementation of web usage mining using apriori and fp growth algorithms. Int. J. Adv. Netw. Appl. **1**(6) (2010)
20. Győrödi, C., Győrödi, R., Holban, S.: A comparative study of association rules mining algorithms. In: Hungarian Joint Symposium on Applied Computational Intelligence (2004)
21. Bonchi, F., Goethals, B.: Fp-bonsai: the art of growing and pruning small fp-trees. In: Pacific-Asia Conference on Knowledge Discovery and Data Mining (2004)
22. Agrawal, R., Srikant, R.: Fast algorithms for mining association rules. In: 20th Proceedings of International Conference of Very Large Data bases (VLDB), pp. 487–4991(1994)
23. Krebs, B.: Anthem breach may have started in April 2014. Krebs Secur. (2015)
24. Yates, M., Scott, M., Levene, B., Miller-Osborn, J., Keigher, T.: Operation Ke3chang Resurfaces with New TidePool Malware. PaloAlto (2016)
25. Monnappa: 2nd Meetup—Reversing and Decrypting the Communications of APT malware. CYSINFO (2016)
26. Ducklin, P.: The Sandworm Malware—What You Need to Know. Sophos (2014)
27. Coogan, P.: Targeted Attacks Make WinHelp Files Not So Helpful. Symantec (2012)
28. Chang, Z., Lu, K., Luo, A., Pernet, C., Yaneza, J.: Operation Iron Tiger: Exploring Chinese CyberEspionage Attacks on United States Defense Contractors (2015)
29. Chen, X., Scott, M., Caselden, D.: New zero-day exploit targeting internet explorer versions 9 through 11 identified in targeted attacks. FireEye (2014)
30. Schworer, A., Liburdi, J.: Storm chasing: hunting hurricane panda. Crowdstrike (2015)
31. Kharouni, L., Hacquebord, F., Huq, N., Gogolinski, J., Mercês, F., Remorin, A., Otis, D.: Operation Pawn Storm Using Decoys to Evade Detection (2014)
32. Crowdstrike Global Intelligence Team: Use of Fancy BearAndroid Malware in Tracking of Ukrainian Field Artillery Unit (2016)
33. Raiu, C., Soumenkov, I., Baumgartner, K., Kamluk, V., G. R. A. A. Team: The MiniDuke Mystery: PDF 0-day Government Spy Assembler 0x29A Micro Backdoor (2013)

A Multicell Multiuser MIMO Uplink for a Finite-Dimensional Channel in OFDM System

Vaidehi Joshi, Vaishnavi Mundhada, Shivani Singh, Ruchita Narange, and Kanchan Dhote

Abstract For wireless transmission of high data rate, orthogonal frequency-division multiplexing (OFDM) is a well-known technology. For frequency-selective channels and on time-varying, OFDM can be paired with antenna arrays at the transmitter and receiver to improve system capacity and also gain, and as a result, we get multiple-input multiple-output (MIMO) arrangement. Modeling and measurements of physical channel, different approaches like error control coding, space–time for MIMO-OFDM, analog beam formation techniques employing adaptive antenna arrays, OFDM packet design and preamble, and signal processing are discussed in this work. Various algorithms are used to perform time and frequency synchronization, channel estimation, and channel tracking in MIMO-OFDM systems. At the end, MIMO-OFDM using a software radio implementation is considered in this paper. The latest wireless physical layer technologies, MIMO and OFDM, are used in 4G wireless cellular standards like high-speed WLAN standards, 3GPP long-term evolution, and for WiMAX (Microwave Access) worldwide interoperability through MIMO-OFDM, these standards of 4G cellular are expected to provide 100 Mbps data rates, validating high-rate wireless applications, such as HDTV on demand, broadcast/multicast video, Internet access of high speed, and interactive gaming, among others. As a result, researchers and wireless telecommunications designers are focusing their efforts on upgrading the resiliency of their systems. This paper focused on the analyzation of the performance of cooperative mobile stations in a frequency-selective channel. OFDM is familiar for the ability to withstand or overcome adverse conditions like multipath fading, and it is a type of modulation technique which is used to get out of the harmful results of inter-symbol interference (ISI).

Keyword MIMO · OFDM · Channel · ISI

V. Joshi · V. Mundhada · S. Singh · R. Narange · K. Dhote (✉)
Department of Electronics Engineering, Shri Ramdeobaba College of Engineering and Management, Nagpur, India
e-mail: dhotek@rknec.edu

V. Joshi
e-mail: Joshivm_1@rknec.edu

379

1 Introduction

The BER execution of disarray correspondence arrangement is enhanced by applying MIMO structure, considering the course that in irritation correspondence structure the message sign is broaden and has a lot of conferred pictures. MIMO strategy is used to pass on messages using unquestionable party contraptions by various ways [1, 2]. MIMO antenna encoding procedure is used considering the way that the necessity of data is relating to the proportion of radio wire, if distinctive social event mechanical get-togethers are connected with correspondence structure we propose jumble correspondence structure using 2X2 MIMO technique which utilizes relationship give up move keying BER and CDSK implementation is computed over obscuring channel Rayleigh MIMO. Alamouti STBC encoding of MIMO is used in this work to get better the BER implementation of the development. In addition, the zero-forcing assertion check is also included. While designing any MIMO antenna, the high energy and arrive at capacity of enormous different information diverse yield (MIMO) frameworks overwhelmingly build up the clarification that the base stations (BSs) get channel state data (CSI) with sensible quality, which is for the most part assessed by techniques for pilot movements [2, 3]. However, in the uplink huge MIMO structures, the pilot overhead referenced ought to look at the measure of clients and would be restrictively immense as the measure of clients increment. In the uplink multicell gigantic MIMO, this outcomes in pilot degradation as a tantamount pilot groupings ought to be reused by neighbor cells to serve limitless clients Moreover, the pilot defilement is a basic keeping part to framework execution [2–4]. Hence, the enormous MIMO genuinely needs skilled channel assessment conspire without making pilot contaminating and requiring a lot of pilot overhead. Considering the studied CSI, the signs got at base stations are routinely perceived through straight strategies with low intricacy, for example zero-persuading and created with channel. However, the presentations of direct finder are commonly far unacceptable appeared differently in relation to the ideal most important probability (ML) locater whose computational diverse nature definitely scales up with the sign social occasion of stars size and the measure of receiving wires.

2 Objectives

MIMO with OFDM is a basic response for the gathering of individuals on the way of distant correspondence structure to achieve the exceptional extension in the data rate. This is a result of its essential execution, high apparition profitability, resolute quality, and generosity against repeat explicit obscuring channels. Without a doubt [5, 6], OFDM disengages the entire repeat specific obscuring channel into many restricted-level equivalent sub-channels using covered balanced subcarriers which in like manner diminishes inter-symbol interference (ISI) and assembles the reach efficiency [4–6]. Moreover, the constancy is extended by abusing assortment of the

MIMO structure using space–time block code (STBC) without growing the sent power. However, MIMO-OFDM systems are the computation of the critical test glanced of the channel state information (CSI) at the recipient side to recover the conveyed data adequately and keep up the typical execution of the structure [7–9]. The assessor exactness clearly impacts the overall show of MIMO-OFDM structure. A couple of philosophies for channel appraisal have been proposed in the composition. Astonish channel assessor, taking into account the second demand estimations of the got signals, shows extraordinary presentations.

3 Block Diagram

When two or more multiple objects act separately then it is defined as orthogonal. In such case, any neighbor signal in OFDM can operate without interference or dependence with one another. Orthogonality is essential in OFDM for the reason that when one signal gain the highest peak, the other two signal ground at zero point. As a result, orthogonal signals are multiplexed in such a manner that the peak of one signal occurs at null of the other neighbor signal [7, 8, 10]. Based on this orthogonal feature, at the destination they will get separated by the de-multiplexer. If there will be comparison in FDM and OFDM, the existing bandwidth would be used better by OFDM which results in contributing higher data transmission rate. Thus, using orthogonality property, sub-channels can be overlapped without interference, and hence, the sub-channel can be placed as close as possible, therefore provides high spectral efficiency. Today, high-rate data transfer is very vital for high-speed communication. High bit rate data are transmitted over radio mobile channel which leads to the channel impulse response spread over various symbol periods as a result formation of inter-symbol interference (ISI) takes place in the condition. A narrow channel is used in order to eliminate the effect of delay spread. OFDM technique is very competent to get rid of ISI, and also, it is robust against frequency-selective fading or narrow band interference. It also provides high spectral efficiency. The use of FFT technique foe the modulation and demodulation help to maintain the orthogonality of the sub-carrier (Fig. 1).
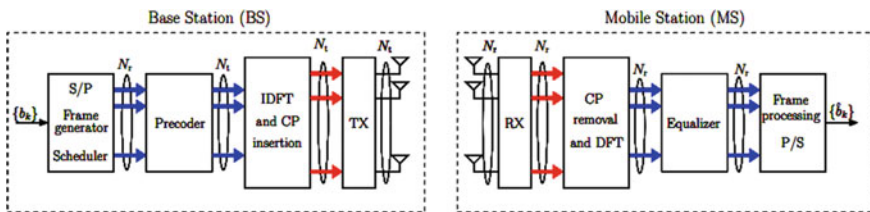

Fig. 1 MIMO-OFDM communication system

Multiple antennas are used in antenna technology for wireless communication at the transmitter (source) and the receiver (destination). At each end of the communication circuit, the antennas work together to optimize the data speed and minimize errors. To increase the network efficiency and to reduce fading effect, these multiple antennas play important role. It has the capability to increase the power of antenna contacts; hence, it is an important component of wireless communication.

4 Methodology

In this work, it is considered that the uplink of a multicell multiuser assorted information distinctive yield structure where the channel encounters both little and monstrous degree clouding. The information ID is finished by utilizing the quick zero-persuading methodology, and enduring the base station (BS) has shocking channel state data. We choose new, definite shut development articulations for the uplink rate, picture mess up rate, and blackout likelihood per client, and as a subordinate bound on the accessible rate. Here, the bound is mainly close and gets unequivocal in the huge number of social occasion mechanical gatherings limit. In addition, we assessed the asymptotic design execution inside the structures of high sign-to-disturbance degree (SNR), tremendous number of social occasion mechanical congregations, and huge quantity of clients per cell. It is shown that at high SNRs, the framework is impedance restricted in addition to consequently; we cannot pull through the construction execution by providing the force of every client. Considering everything, by developing the measure of BS receiving wires, the impacts of block and disturbance can be reduced along these lines improving the framework execution. We show that with gigantic get-together mechanical gathering packs at the BS, the confer force of every client can be made oppositely contrasting with the measure of BS radio wires while keeping an ideal nature of association. Mathematical outcomes are familiar with check our assessment. MIMO innovation can give an amazing expansion in information rate and unwavering quality contrasted with single-radio wire frameworks. As of late, multiuser MIMO (MU-MIMO), where the base stations (BSs) are outfitted with various reception apparatuses and speak with a few co-channel clients, has acquired a lot of consideration and is presently being presented in a few new-age remote principles; MU-MIMO frameworks have been determined from numerous points of view including correspondence, flagging, and data hypothesis in both downlink and uplink situations. For the uplink, the most extreme probability multiuser identifier can be utilized to get ideal execution [5]. In any case, this ideal collector instigates a critical intricacy trouble on the framework execution, particularly for enormous cluster designs. Along these lines, straight collectors, specifically zero-forcing (ZF) recipients, are specifically noteworthy as low-intricacy choices. Note that all the previously mentioned works have just examined a solitary cell situation, where the impacts of intercell obstruction have been dismissed. Be that as it may, co-channel impedance, showing up because of recurrence reuse, addresses a significant disability

in cell frameworks. Recently, there is an expanding research concern in the presentation of MU-MIMO in obstruction-restricted multi-cell conditions. Indeed, it has been revealed that the limit of the MU-MIMO downlink can be significantly diminished as a result of intercell obstruction. Several impedance dropping and moderation procedures have been anticipated for multicell MU-MIMO frameworks, for example, greatest probability multiuser location [11–13].

- Inter-symbol interference (ISI) is the major problem in wireless mobile communication.
- We have used the idea of orthogonal frequency division multiplexing in this research work in order to get better efficiency and to decrease the interference.
- As compared to conventional modulation techniques, OFDM provides much higher data rates. In case of OFDM, various sub-carriers are used that are orthogonal from each other. Every channel is divided into multiple sub-carriers.
- The modulation occurs at inverse fast Fourier transform (IFFT) of the transmitter.
- Two suboptimals are focused in this research work; first is in the form of bit error rate (BER), which is computationally feasible and second is for OFDM-based multiUser (MU) MIMO communications which is the channel estimation algorithms.
- The discussed algorithms are correlated to the LTE downlink frame structure, which comprised of a basic block of twelve subcarriers in a downlink slot, called as physical resource block (PRB). In the first algorithm, the channel is supposed to be constant which is referred to as resource block (RB).

5 Operation

In distinctive massive MIMO systems, along with the antenna, each cell has a BS with huge number of antennas, which allows the simultaneous consumption of resources (i.e., time slots or frequency band) by dissimilar users in the cell. In addition to that, the system model is introduced and elucidates the fundamental concepts of massive MIMO systems in the downlink and the uplink. A single-cell scenario with flat fading channels for ease has been considered. The extension to frequency-selective channels will be straightforward as a result of modulations like OFDM and SC-FDP is employed. A BS with M antennas and K single antenna users [5, 6, 10] without loss of generality is considered here (Fig. 2).

5.1 Orthogonality

OFDM would allow more data transmission than FDM. The point to discuss here is while multiple sub-channels overlap with each other in which manner the OFDM manage to prevent interference, let on one shared channel we have three different signals to send over simultaneously without interfering with each other [1, 2]. They
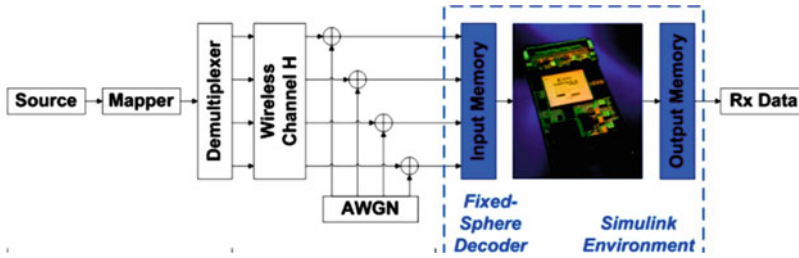
Fig. 2 MIMO-OFDM communication system transmitter and receiver for antenna

are orthogonal to each other as OFDM would combine them closely together. Any neighbor signal in OFDM operates without interference with one another or without dependence, in this case. Orthogonality is required in OFDM, this is because when one signal achieve the highest point peak, the other two signal will be at the lowest (zero) point. Hence, orthogonal signals are multiplexed in a certain extent that the peak of one signal overlapped at null of the other neighbor signal. Based on this orthogonal feature, at the destination end they are separated by the de-multiplexer. OFDM offering higher data transmission rate than FDM by better utilizing the available bandwidth [6, 10]. Thus, using orthogonality property sub-channels can be overlapped without interference, and hence, the sub-channel can be placed as close as possible, therefore provides high spectral efficiency [7–9].

5.2 Multiple-Input Multiple-Outputs (Mimo)

MIMO is explained as an antenna technology which is used in the wireless communication where multiple number of antennas are arranged at both the transmitter (source) and receiver (destination). At both transmitter and receiver of the communication circuit, the antennas are combined to optimize data speed as well as to minimize errors. Multiple antennas are used to reduce fading effect. It is also used to increase the performance in the form of throughput of a network. It has the skill to improve the capacity of antenna links, and this is the reason it is considered as a necessary component of wireless communication [9, 11, 14] (Fig. 3).

Fig. 3 MIMO system
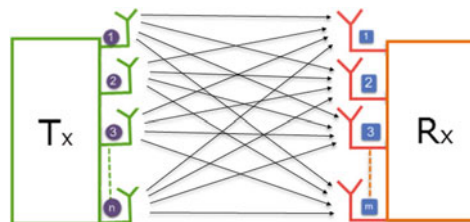
6 Result

The results were evaluated for BER presentation as a function of signal-to-noise ratio (Eb/No) in a MIMO-OFDM system with different equalizers employing QAM modulation techniques through multipath Rayleigh fading channel. On these terms, the MIMO-OFDM system with QAM and ML equalization to achieve BER of 10–5 in the case of QAM with MMSE equalizer system, 21 db of SNR is required, whereas in the case of QAM without MSME adjuster system, 21 db of SNR is required. At 1 dB SNR, the system only achieves a BER of about 10–4. This is a good example. QAM achieves high BER with low SNR requirements, resulting in high BER. MIMO-OFDM modulated with ML equalization system.

PLOT OF SNR V/S SER FOR AN OFDM SYSTEM WITH MMSE/LS ESTIMATOR BASED RECEIVERS
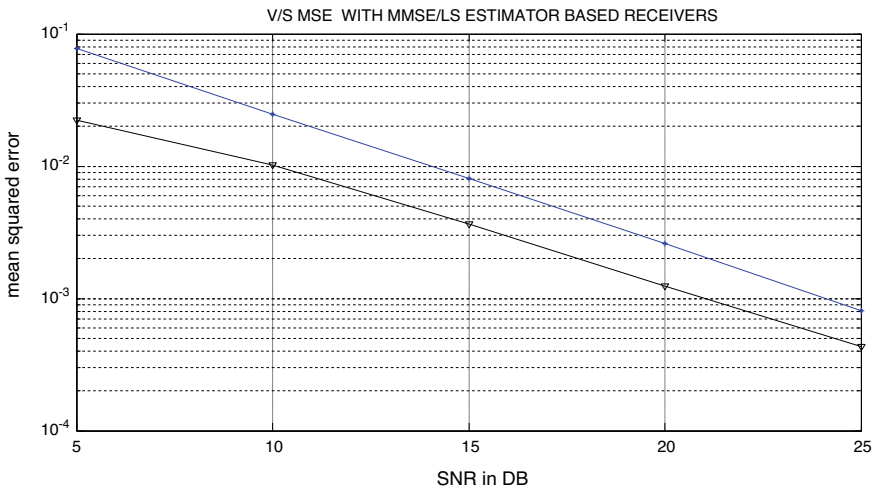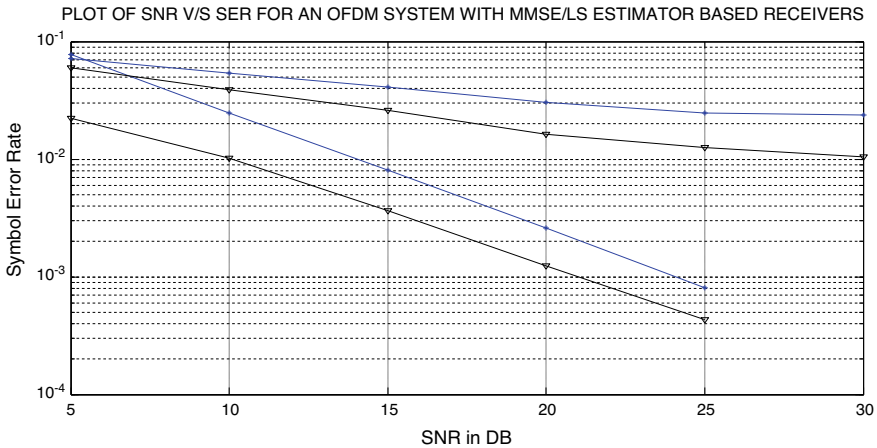
Parameters

- Required channel bandwidth in MHz (max 20 MHz) $= 20$
- choose cyclic prefix to overcome delays spreads, 1/4 for longest delay spread, 1/8 for long delay spreads, 1/16 for short delays spreads, 1/32 for very small delay spread channels $= 1/4$
- Enter the channel SNR in dB (it should be above 6.4 dB) $= 6.8$
- Modulation scheme of BPSK with coding rate 1/2 is chosen
- Enter 1 for including MIMO in the system and 0 otherwise $= 1$

7 Discussion

The groundbreaking future of cellular networking is defined by 5G. From 5G, massive MIMO is an innovative concept to revolutionize wireless communication systems, and it is intended to be implemented in the near future. This new conception is able to achieve growth in spectral efficiency and overall system's performance by deployment of a large-scale antenna arrays at the base stations. In this work, some difficulties are analyzed that arise with massive MIMO, more specifically, inter-cell interference caused by the reuse of training sequences in adjacent cells and also the increase in complication of channel estimation for the large channel matrices. As far as complexity concerns, in channel estimations techniques, the main problems are matrix inversions and factorizations. A channel estimation technique with Zadoff-Chu sequences was introduced in order to replace channel estimation based on matrix inversions, such as the MMSE estimator. In addition, pilot contamination was studied, and techniques of three channel estimation were proposed to achieve the best compromise between system performance, spectral efficiency, and complexity.

8 Conclusion

This paper focused on the assess of in detail the uplink execution of information transmission from K only antenna clients in a single cell to its N-receiving wire BS within the sight of impedance from different cells. The BS makes use of ZF to recognize communicated signals. We determined careful shut structure articulations for the main figures of legitimacy, to be specific the uplink rate, SER, and blackout likelihood, expecting a particular channel linking the clients, and the BS is influenced by Rayleigh blurring, shadowing, and way misfortune. Hypothetically, when N builds we acquire cluster and variety gains that influence equally the obstruction and ideal signals. Henceforth, considering this point of view exhibition is not significantly influenced. In any case, since when the quantity of BS radio wires be enormous, the channel vectors connecting the clients and the BS are pair wisely asymptotically symmetrical, the obstruction takes place counteracted with a straightforward direct ZF recipient. The result is that by the utilization of huge receiving wire cluster, the presentation of the multicell framework improves fundamentally. Moreover, we explored the attainable force effectiveness when utilizing enormous radio wire exhibits at the BSs. Huge radio wire exhibits empower us to lessen the sent force of every client relatively to $1/N$ with no presentation debasement, given that the BS has wonderful CSI. We further explained on the monstrous MIMO impact and the effect of recurrence reuse factors.

References

1. Andrews, J.G., et al.: What will 5G be? IEEE J. Sel. Areas Commun. **32**(6), 1065–1082 (2014)
2. Wong, K.-L., Tsai, C.-Y., Lu, J.-Y.: Two asymmetrically mirrored gap-coupled loop antennas as a compact building block for eight antenna MIMO array in the future smartphone. IEEE Trans. Antennas Propag. **65**, 1765–1778 (2017)
3. Xu, H., Zhou, H., Gao, S., Wang, H., Cheng, Y.: Multimode decoupling technique with independent tuning characteristic for mobile terminals. IEEE Trans. Antennas Propag. **65**, 6739–6751 (2017)
4. Zhao, A., Ren, Z.: Multiple-input multiple-output antenna system with self-isolated antenna element for fifth-generation mobile terminals. Microw. Opt. Tech. Lett. 61, 20–27 (2019)
5. Li, M.Y., Ban, Y.L., Xu, Z.Q., Wu, G., Sim, C., Kang, K., et al.: Eight-port orthogonally dual-polarized antenna array for 5G smartphone applications. IEEE Trans. Antennas Propag. **64**, 3820–3830 (2016)
6. Ban, Y.L., Li, C., Sim, C.Y.D., Wu, G., Wong, K.-L.: 4G/5G multiple antennas for future multi-mode smartphone applications. IEEE Access **4**, 2981–2988 (2016)
7. Yun, J.X., Vaughan, R.G.: Multiple element antenna efficiency and impact on diversity and capacity. IEEE Trans. Antennas Propag. **60**, 529–539 (2012)
8. Ai-Hadi, A.A., Iivonen, J., Valkonen, R., Viikari, V.: Eight-element antenna array for diversity and MIMO mobile terminal in LTE 3500MHz band. Microw. Opt. Technol. Lett. **56**, 1323–1327.
9. CST User Manual, 2018 [online]. Available http://www.cst.com. Google Scholar
10. MIMO antenna structure with UWB antenna element for handset devices, Sept 2018.Google Scholar 8. CST User Manual, 2018 [online]. Available http://www.cst.com

11. Rusek, F., Persson, D., Lau, B.K., Larsson, E.G., Marzetta, T.L., Tufvesson, F.: Scaling up MIMO: opportunities and challenges with very large arrays," IEEE Signal Process. Mag. **30**(1), 40–60 (2013)
12. Brandenburg, L.H., Wyner, A.D.: Capacity of the Gaussian channel with memory: the multivariate case. Bell Syst. Tech. J. **53**(5), 745–778 (1974)
13. Kaye, A.R., George, D.A.: Transmission of multiplexed PAM signals over multiple channel and diversity systems. IEEE Trans. Commun. Technol. **18**(5), 520–526 (1970)
14. Marzetta, T.L.: Noncooperative cellular wireless with unlimited numbers of base station antennas. IEEE Trans. Wirel. Commun. **9**(11), 3590–3600 (2010)

Water Evaporation Optimized PID Controller for Frequency Control of Isolated Renewable Microgrid

Pothula Jagadeesh, Bh Sudha Rani, and Ch. Durga Prasad

Abstract Frequency control of isolated microgrid with renewable energy sources is studied in this paper with biogas and biodiesel-based electrical power generating units in the presence of controllable energy storage. To change power production function as probabilistic signal, solar unit is integrated in the system. Two proportional-integral-derivative (PID) controllers are used in the system to control both bio plants and battery energy storage system. The study further extended to control of bio plants with various participation factors. In all the system scenarios, optimal parameter gains of controller are achieved by using water evaporation optimization (WEO) algorithm and comparisons are made with WEO-PI controller. Results are carried out in MATLAB-SIMULINK software platform.

Keywords Renewable microgrid · Water evaporation algorithm · PV · Biogas

1 Introduction

Green energy is an alternative to the conventional electric power generation sources to supply growing electrical demand of the countries. This migration is encouraged by stakeholders since green energy production is pollution free and economic [1, 2]. However, emergency power supply during sudden load disturbances is a challenging issue in this renewable power networks. Hence, several solutions are available in literature with photovoltaic (PV), wind, energy storage units and diesel generators [3–9]. With the help of emergency diesel generator, the power changes are compensated in isolated microgrid. Recently few solutions are provided fully with renewable sources in such power disturbances [10, 11].

P. Jagadeesh (✉) · B. S. Rani · Ch. D. Prasad
Department of Electrical and Electronics Engineering, SRKR Engineering College, Andhra Pradesh, Bhimavaram 534204, India
e-mail: jagadeesh.p@srkrec.ac.in

Ch. D. Prasad
e-mail: dpchinta@srkrec.edu.in

In literature, diesel-wind hybrid power system scenarios were suggested [3] extensively with different controller mechanisms. Frequency control is an issue in such scenarios during power demand variations mitigate by either PI or PID controllers tuned with genetic algorithm (GA). In [4], PV-diesel generator model and its control is presented. Further, intelligent power management is incorporated using fuzzy is used to balance the active power generation and demand. In grid connected mode, the frequency and voltage control aspects discussed in [5] for PV-diesel generator model. The influence of primary and secondary control loops for isolated microgrid with diesel generator is discussed in [6] with crow search based optimization tuned PI and PID controllers. Another alternative solution to balance power during disturbances is presented in [7]. Super magnetic energy storage (SMES) and batter energy storage system (BESS) are incorporated in the hybrid power system with wind and PV available in [7]. Such hybrid power system in coordination with thermal unit is presented in [8]. To control frequency, conventional PI and PID controllers are used with different tuning algorithms in [3–8]. Recently, other controllers are also applied for these isolated microgrid [9]. But these systems consist diesel generator produces pollution and is not economic. Therefore, renewable microgrid concepts are introduced to reduce the additional pollution [10].

In this paper, renewable isolated microgrid considered with controllable biodiesel and biogas units with PV. A PID controller is used in secondary loop of these plants reduces frequency oscillations caused by load and PV units. Water evaporation algorithm (WEO) algorithm [11, 12] is used to find the optimal parameter gains of the PID controller. Results show the advantages in various cases studies.

2   Test Simulated System

In this paper, microgrid system with fully green energy resources is opted to study the frequency control during load disturbances using water evaporation optimized PID controllers. Figure 1 shows the schematic block diagram of renewable microgrid system with PV generation, biogas and biodiesel plants. Along with these three renewable energy plants, storage units are necessary for continuous power supply. In the system, 2 PID controllers are utilized known as $C_1(s)$ and $C_2(s)$. Controller $C_1(s)$ is placed in the secondary loop of bio units to provide simultaneous control for both units. Controller $C_2(s)$ is used to control the power flow of battery energy storage system (BESS). The transfer functions of PV, BESS and load are presented in Fig. 1 and for BGTG and BDEG, the mathematical models are given by

$$G_{\text{bgtg}}(s) = \left(\frac{1 + sX_c}{(1 + sY_c)(1 + sb_B)} \right) \left(\frac{1 + sT_{\text{CR}}}{1 + sT_{\text{BG}}} \right) \left(\frac{1}{1 + sT_{\text{BT}}} \right) \tag{1}$$

$$G_{\text{bdeg}}(s) = \left(\frac{K_{\text{VA}}}{1 + sT_{\text{VA}}} \right) \left(\frac{K_{\text{BE}}}{1 + sT_{\text{BE}}} \right) \tag{2}$$
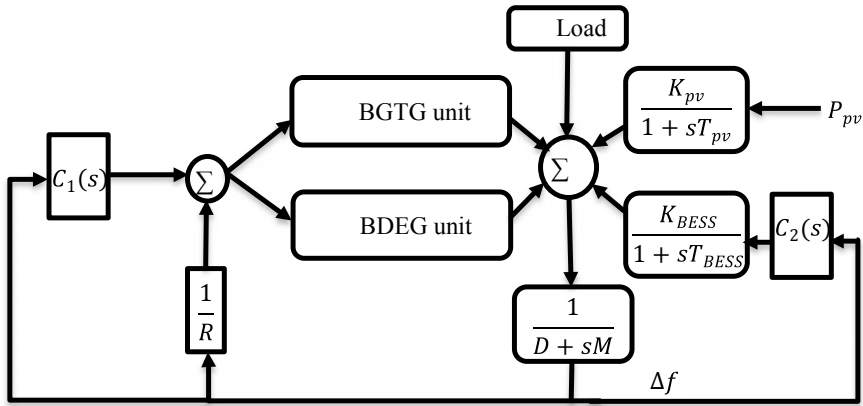
Fig. 1 Block diagram of isolated microgrid with biogas and biodiesel plants

The parameters and their numerical values are provided in [10] for all the isolated microgrid components.

3 Identification of Optimal PID Parameter Gains Using Water Evaporation Algorithm

Biogas, biodiesel and BESS are controlled by PID controller whose action is initiated whenever disturbances are created in the system due to occurrence of either generation or load variations. Therefore, Δf becomes input for both controllers and the output control signal produced from controller ii is given by

$$u_i(s) = \left(k_{pi} + \frac{k_{ii}}{s} + k_{di}s \right).\Delta f \tag{3}$$

In Eq. (3), $u_i(s)$ is the controller ii output signal with proportional gain (k_{pi}), integral gain (k_{ii}) and derivative gain (k_{di}) whose upper and lower limits are given by

$$k_{\min} \leq k_{pi}, k_{ii}, k_{di} \leq k_{\max} \tag{4}$$

The selection of optimal values of these controllers becomes an optimization problem with the help of a performance measure. As the objective of the paper is frequency control, errors in frequency signal with reference value are used as fitness function and is given by

$$\text{Fitness funtion} = \int_0^T \Delta f(t)^2 \mathrm{d}t \tag{5}$$

The best solution is obtained by using WEO algorithm. WEO implemented using the analogy of water particles evaporation from different wettability (WT) surfaces by A. Kaveh and T. Bakhshpoori in the year 2016 [11, 12]. Initial solutions are generated randomly based on the parameters of WEO and search space is denoted by surfaces with different WT. The solutions updated their positions using monolayer evaporation phase (MEP) and Droplet evaporation phase (DEP). In MEP, evaporation flux ($J(q)$) is calculated by using

$$J(q) = e^{-E_{\text{sub}}/K_B T}, q \geq 0.4e \tag{6}$$

where, E_{sub} represents the interaction energy, temperature T and K_B is the Boltzman constant. Variation of E_{sub} leads to objective function individuals (i) fitness (Fit) change for each iteration (t) given by

$$E_{\text{sub}}(i)^t = \frac{(E_{\max} - E_{\min}) * \left(\text{Fit}_i^t - \text{Fit}_{\min}\right)}{(\text{Fit}_{\max} - \text{Fit}_{\min})} + E_{\min} \tag{7}$$

Once $E_{\text{sub}}(i)^t$ evaluated for each water molecule, MEP matrix is generated as follows:

$$\text{MEP}_{ij}^t = \begin{array}{ll} 1 & \text{if } \text{rand}_{ij} < e^{E_{\text{sub}}(i)^t} \\ 0 & \text{if } \text{rand}_{ij} \geq e^{E_{\text{sub}}(i)^t} \end{array} \tag{8}$$

In case of DEP, Eq. (7) and (8) are replaced by Eqs. (9) and (10) to update water molecules given by

$$\theta(i)^t = \frac{(\theta_{\max} - \theta_{\min}) * \left(\text{Fit}_i^t - \text{Fit}_{\min}\right)}{(\text{Fit}_{\max} - \text{Fit}_{\min})} + \theta_{\min} \tag{9}$$

$$\text{DEP}_{ij}^t = \begin{array}{ll} 1 & \text{if } \text{rand}_{ij} < J\left(\theta_i^t\right) \\ 0 & \text{if } \text{rand}_{ij} \geq J\left(\theta_i^t\right) \end{array} \tag{10}$$

After MEP and DEP phases, the water molecules set updating for next iteration (WM^{t+1}) using the current molecules set (WM^t) and random permutation step size (S) given by

$$\text{WM}^{t+1} = \text{WM}^t + S * \left\{ \begin{array}{l} \text{MEP}^t t \leq t_{\max}/2 \\ \text{DEP}^t t > t_{\max}/2 \end{array} \right\} \tag{11}$$

Once WM attain new surfaces, iterative process continue until maximum iterations reached.

4 Simulation Results and Comparisons

Frequency control of isolated microgrid shown in Fig. 1 is investigated in this paper by simulating load and PV power disturbances at different participation factors (pf's) of biodiesel and biogas plants. When pf's of BGTG and BDEG are 0.75 and 0.25 (case-1), the frequency response of the system is presented in Fig. 2. Load change of 10% (increase) is happened at 80 s and PV changes of 10% (increase) and 5% (decrease) happened at 1 and 40 s as disturbances, and these changes are mitigate by all components of microgrid as shown in Fig. 3. When pf's changes to 0.5 each (case-2), the frequency and power sharing plots of the system are presented in Figs. 4 and 5. Here, the input PV power change is kept same as earlier case where as load change of–10% is initiated in the system at 40 s. Together, it is concluded that the power sharing of biodiesel and biogas components are based on their participation factors since the plants controlled by same PID controller. However, the BESS power changes based on the control output of controller 2.

In third case, the pf of BGTG is 0.25, whereas for BDEG, it is 0.75 (case-3). In this case, 10% load change is occurred in the demand side at 20 s, and PV changes are as it is similar to earlier cases. Results of change in frequency and change in power shared by individual components are presented in Figs. 6 and 7. From simulation cases 1 and 3, the power change occurred in bio units to compensate the change in power is proportional to the pf's. However, the proposed WEO based PID controller enhances

Fig. 2 Frequency deviation response for 10% load disturbance for case-1
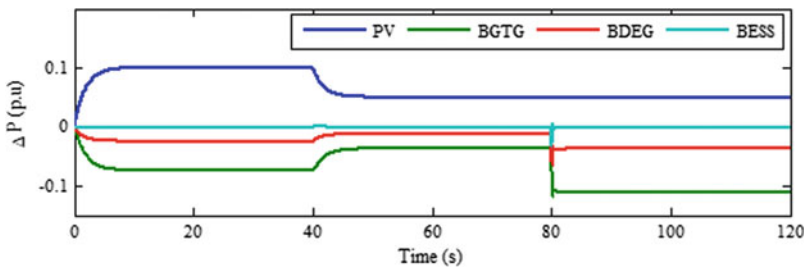
Fig. 3 Power changes of microgrid components for case-1

Fig. 4 Frequency deviation response for 10% load disturbance for case-2
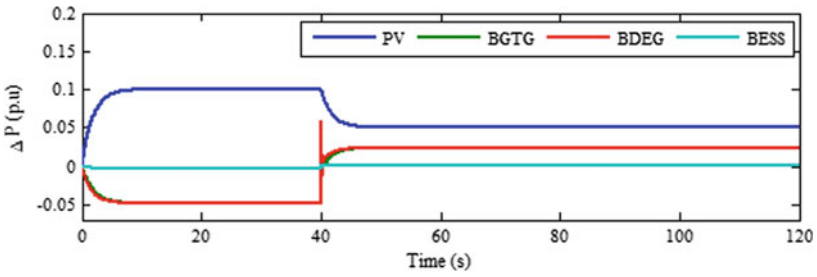
Fig. 5 Power changes of microgrid components for case-2

Fig. 6 Frequency deviation response for 10% load disturbance for case-3
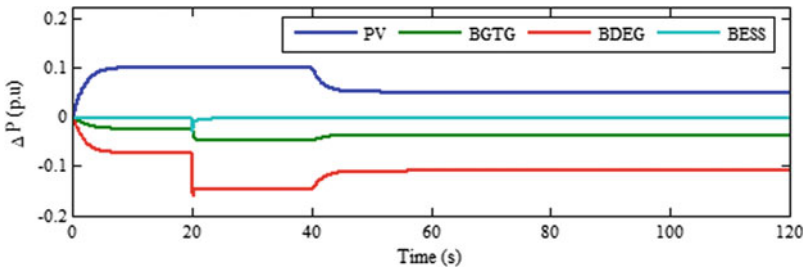
Fig. 7 Power changes of microgrid components for case-3

Table 1 Optimal parameter gains of the PID controller

parameter	Biogas and biodiesel plats contribution coefficients			
	0.75 and 0.25	0.5 and 0.5	0.25 and 0.75	Comparison
k_{p1}	− 9.4866	− 9.7911	− 3.8722	− 9.7168
k_{i1}	− 9.9081	− 9.6917	− 2.9974	− 4.7913
k_{d1}	− 8.1834	− 9.4734	− 5.3230	− 7.4088
k_{p2}	− 9.2853	− 7.8098	− 9.7183	− 4.9178
k_{i2}	− 2.9135	− 8.0742	− 1.8736	− 0.2676
k_{d2}	− 8.1325	− 0.9714	− 8.3964	− 1.8177

the transient parameters and stability of the isolated microgrid system during all types of disturbances. For all these cases, the optimal parameter gains achieved by using WEO are mentioned in Table 1.

Since PI controllers are extensively applied to control system frequency for an isolated microgrid as per literature, a comparison is presented in this paper in between PI and PID controllers (case-4). The PV input power variations are same as earlier cases where as load decrease of 10% is considered on user side. Figure 8 shows the change in frequency plot for both controllers. With PID controller, the response of system improved in greater extent, and therefore, good performance is guaranteed. Similar observations are identified in generating power changes whose information is available in Figs. 9 and 10. These results show the improvement in the system outputs when PID controller placed in secondary loop of biodiesel and biogas plants tuned by WEO algorithm irrespective of pf's and other disturbances. For PI controllers, the optimal parameter gains are − 0.9016, − 1.3191, − 9.7767 and − 8.4037 obtained by WEO algorithm.
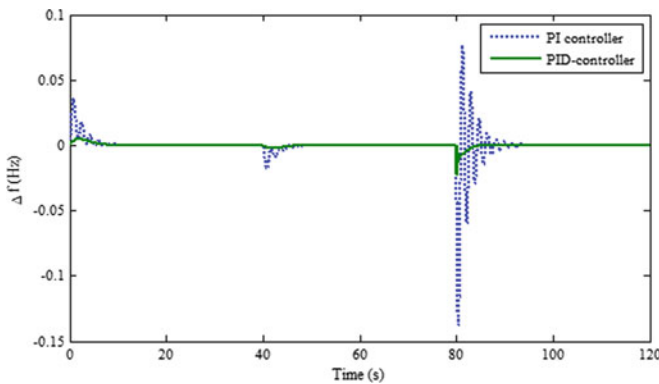
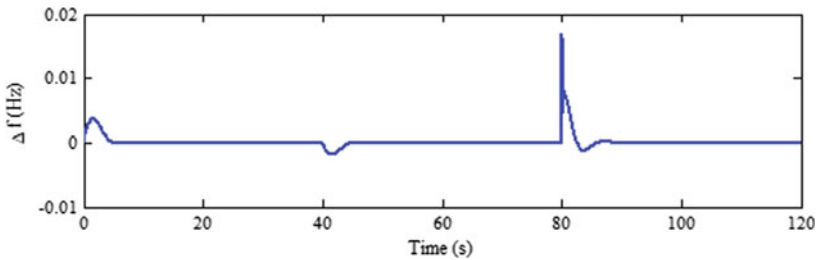**Fig. 8** Frequency deviation response for 10% load disturbance for case-4
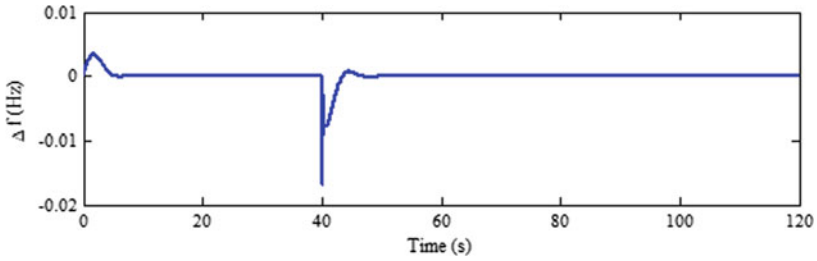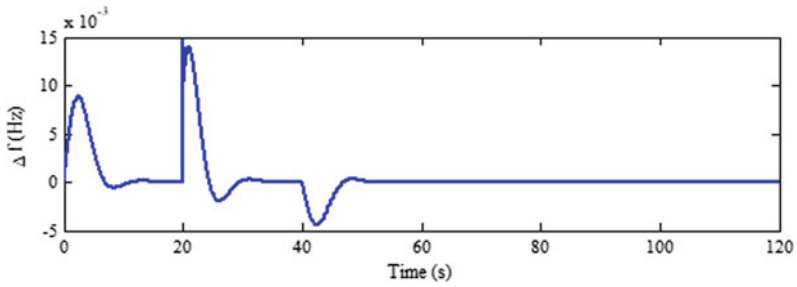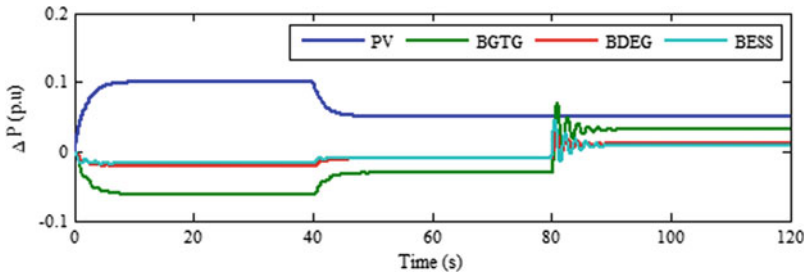
Fig. 9 Power changes of microgrid components for case-4 with PI controller
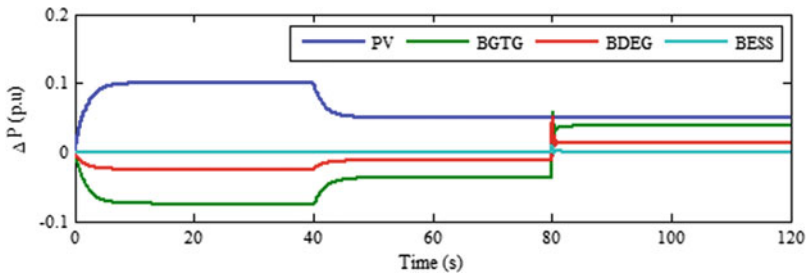
Fig. 10 Power changes of microgrid components for case-4 with PID controller

5 Conclusions

Frequency control of fully renewable isolated microgrid is studied in this paper during load perturbations and PV input power variations. Two PID controllers are used for reducing frequency deviations by controlling generations of biogas, biodiesel and BESS elements of microgrid. The WEO algorithm used to find optimal gains of controllers provides fast response and enhances the outputs of the system. For remote stations, this structure is more suitable and eco-friendly.

References

1. Karki, R., Billinton, R.: Reliability/cost implications of PV and wind energy utilization in small isolated power systems. IEEE Trans. Energy Convers. **16**(4), 368–373 (2001)
2. Begovic, M., Pregelj, A., Rohatgi, A., Novosel, D.: Impact of renewable distributed generation on power systems. In: Proceedings of the 34th Annual Hawaii International Conference on System Sciences, vol. 3, p. 2008. IEEE Computer Society, 1 Jan 2001
3. Bhatti, T.S., Al-Ademi, A.A., Bansal, N.K.: Load frequency control of isolated wind diesel hybrid power systems. Energy Convers. Manage. **38**(9), 829–837 (1997)
4. Datta, M., Senjyu, T., Yona, A., Funabashi, T., Kim, C.H.: A frequency-control approach by photovoltaic generator in a PV–diesel hybrid power system. IEEE Trans. Energy Convers. **26**(2), 559–571 (2010)

5. Mishra, S., Ramasubramanian, D., Sekhar, P.C.: A seamless control methodology for a grid connected and isolated PV-diesel microgrid. IEEE Trans. Power Syst. **28**(4), 4393–4404 (2013)
6. Patan, M.K., Raja, K., Azaharahmed, M., Prasad, C.D., Ganeshan, P.: Influence of primary regulation on frequency control of an isolated microgrid equipped with crow search algorithm tuned classical controllers. J. Electr. Eng. Technol. **2020**, 1–5 (2020)
7. Hussain, I., Ranjan, S., Das, D.C., Sinha, N.: Performance analysis of flower pollination algorithm optimized PID controller for wind-PV-SMES-BESS-diesel autonomous hybrid power system. Int. J. Renew. Energy Res. (IJRER). **7**(2), 643–651 (2017)
8. Ranjan, S., Das, D.C., Behera, S., Sinha, N.: Parabolic trough solar–thermal–wind–diesel isolated hybrid power system: active power/frequency control analysis. IET Renew. Power Gener. **12**(16), 1893–1903 (2018)
9. Mahto, T., Malik, H., Saad Bin Arif, M.: Load frequency control of a solar-diesel based isolated hybrid power system by fractional order control using partial swarm optimization. J. Intell. Fuzzy Syst. **35**(5), 5055–5061 (2018)
10. Barik, A.K., Das, D.C.: Expeditious frequency control of solar photovoltaic/biogas/biodiesel generator based isolated renewable microgrid using grasshopper optimization algorithm. IET Renew. Power Gener. **12**(14), 1659–1667 (2018)
11. Kaveh, A.: Water evaporation optimization algorithm. In: Advances in Metaheuristic Algorithms for Optimal Design of Structures 2017, pp. 489–509. Springer, Cham
12. Kaveh, A., Bakhshpoori, T.: A new metaheuristic for continuous structural optimization: water evaporation optimization. Struct. Multidiscip. Optim. **54**(1), 23–43 (2016)

FPGA Implementation of Asynchronous FIFO

Souradeep Das, Upasana Basu, Rohit Das, Shashwata Saha, and Abhishek Basu

Abstract In this paper, a FPGA (Field Programmable Gate Array) based architecture for an area efficient asynchronous FIFO (First-In-First-Out) has been presented. There are various technologies, and algorithms are used for data transfer from one domain to another. First-In-First-Out method is the simplest of all. FIFO requires multiple asynchronous clocks to access the data. Asynchronous FIFO is important for safe data transfer. Data moves from one clock domain to another clock domain where both the domain frequencies are different. The calculation of memory depth has been presented based on read and write clock frequency; so that the FIFO works perfectly for specified frequency without data loss. In this proposed model of asynchronous FIFO, an area efficient FIFO architecture has been demonstrated, and this paper also provides the results obtained through VHDL (Very high-speed integrated circuit Hardware Description Language) simulation and FPGA implementation to demonstrate the reliability of the proposed model.

Keywords FPGA · Asynchronous FIFO · Safe data transfer · Memory depth

1 Introduction

Asynchronous FIFO is very important for safe data transfer amid asynchronous domain. Data moves from one clock domain to another clock domain where both the clock domain frequencies are different [1]. So to avoid the data loss one memory structure is must for data transfer in asynchronous domain [2]. That memory structure is termed as buffer memory, and depth of that memory need to be calculated based of clock frequency of reading and writing side [3]. The write pointer is controlled by using write clock and write enable clock, and read pointer is controlled by read and read enable clock [4]. To compare the pointers are on zero, synchronizers have been used [5]. Synchronizers are used to make the data communicate between this right pointer and the read pointer [6]. Similarly, read pointer always points to the current

S. Das · U. Basu · R. Das · S. Saha · A. Basu (✉)
RCC Institute of Information Technology, Beliaghata, Kolkata, West Bengal, India

FIFO word to be read [7]. When reset, both pointers are reset to zero, FIFO is null, and the read pointer points to invalid data [8].

1.1 Literature Survey

This section reports the state of the art of Asynchronous FIFO cited in the literature survey. Cliff Cummings is president of Sunburst Design, worked on Simulation and Synthesis Technique for Asynchronous FIFO Design [1]. Xiao Yong, Zhou Runde worked on Low Latency High throughout Circular Asynchronous FIFO [2]. Hosuk Han, Kenneth S. Stevens work on Clocked and Asynchronous FIFO characterization and comparison [3]. Amit Kumar, Shankar, Neeraj Sharma, Verification of Asynchronous FIFO using System Verilog [4]. Hyoung-Kook Kim, Laung-Terng Wang, Yu-Liang, Wen-Ben Jone Testing of Synchronous and Asynchronous FIFO [5]. Uma Mahesh, Marty Long, Laura Simmons, Quad Asynchronous Communication Element [6]. S. Thenappan, ASYNCHRONOUS FIFO DESIGN USING VERILOG [7]. A. M. S. Abdelhadi, "Synthesizable Synchronization FIFOs Utilizing the Asynchronous Pulse-Based Handshake Protocol" [8]. S. Abdel-Hafeez and M. Q. Quwaider, "A One-Cycle Asynchronous FIFO Queue Buffer Circuit." [9] G. Liu, J. Garside, S. Furber, L. A. Plana and D. Koch, "Asynchronous Interface FIFO design on FPGA for high-throughput NRZ synchronization." [10]

2 Asynchronous FIFO Architecture

The proposed asynchronous FIFO has got 12 ports in total including all the input and output ports. There are 7 input ports and 5 output ports. The input ports contain the two clocks of writing and reading section, the two enables for the reading and the writing sections, the two reset sections of both the reading and the writing section. There are five output ports overall. The other output ports are full, empty almost full and almost empty. The entire architecture in the form of block diagram is shown Fig. 1.

   The proposed architecture has two different clocks, for reading section and writing section with different frequencies. Firstly, the writing section will be explained in the architecture, which is a very important and crucial part of the FIFO. The section contains five signals write pointer, pointer for write pointer to gray code conversion, pointer for read pointer to binary conversion, and two pointers for gray coded read pointer synchronization. Each and every pointer used inside the writing section of the FIFO is of width equal to width of the RAM address width. Figure 2 is the block representation of the writing section of the FIFO.

   In the reading section in Fig. 3, firstly it checks, whether the read reset block is high or not. If high then the read block resets all the signals for synchronization. Else it will check for whether read enable is high and at the same time empty signal is not
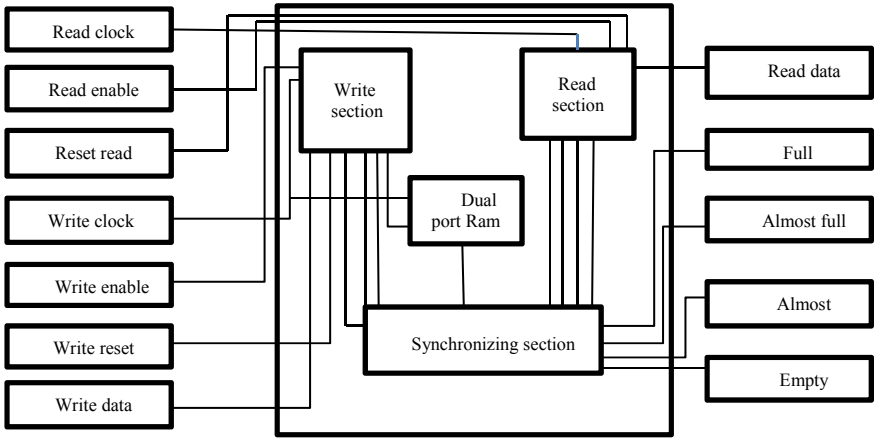
Fig. 1 Asynchronous FIFO architecture
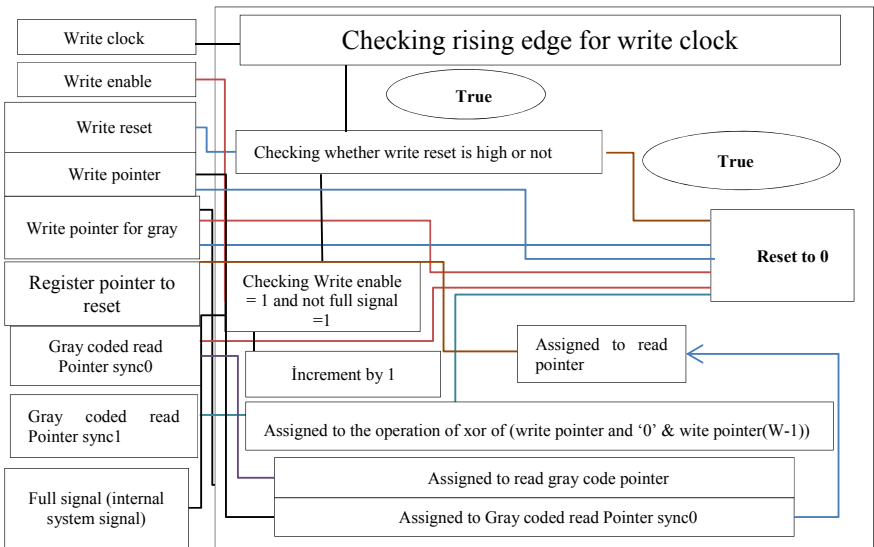
Fig. 2 Writing section

empty. Then, again it will check whether the toggle signal is high or not. If it is high the toggle will be assigned to low and the read pointer is incremented. Otherwise, if the toggle signal is found low then the toggle signal is set high. Now, read pointer to gray code conversion will take place. Then, gray code write pointer sync1 will be assigned to write gray pointer and write pointer sync0 will be assigned to write pointer sync0. This will provide the proper pointer result from read side. Figure 3 represents the reading section.
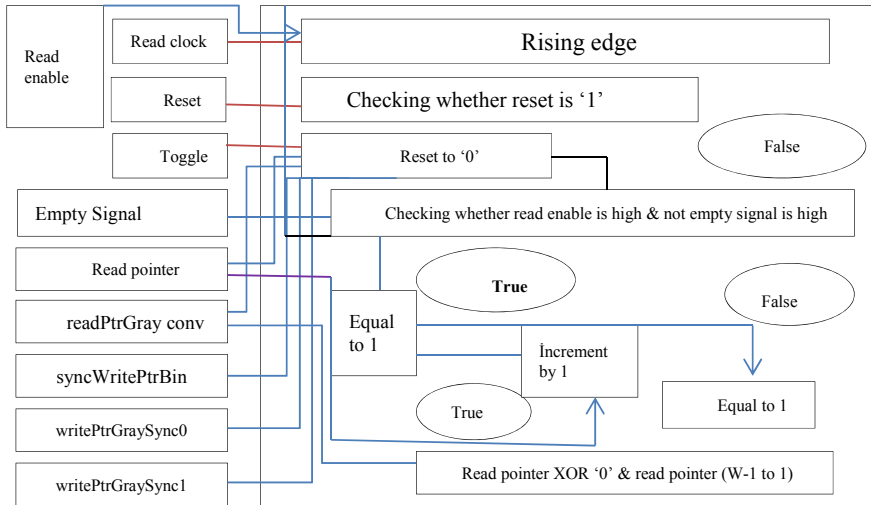
Fig. 3 Reading section

Now for both reading and writing sections the synchronization takes place. For the reading section, the write pointer to binary conversion takes place and for the writing section the read pointer to binary conversion takes place. Then, in the reading section the write pointer to binary is calculated by performing the xor operation between the write pointer binary conversion signal of the next bit with gray coded write pointer with synchronization of that particular position bit.

In dual port takes write clock into consideration then it checks whether write enable is high and full signal of the system is not full then only from the ram (write pointer) gets assigned to write data. The data which is read out from read data out port is read pointer signal from (B − 1 to B/2) when toggle signal is high else data read is from dual-port memory is ram read pointer ((B/2) − 1) to 0, where B denotes input bus width. Figure 4 illustrates synchronization section.

2.1 FIFO Depth Calculation

In this section, the minimum depth calculation of the FIFO model has been explained. To realize the architecture in FPGA, the writing clock frequency considered as 50 MHz and the reading clock frequency 20 MHz. For 100 bytes of data in the writing section.

Time taken to write 100 byte data $= \frac{1}{50\,\text{MHz}} \times 100 = 2000\,\text{ns}$.

For reading section:

The total data that can be read in 2000 ns $= \frac{1}{20\,\text{MHz}} \times 2000\,\text{ns} = 40$ bytes of data.
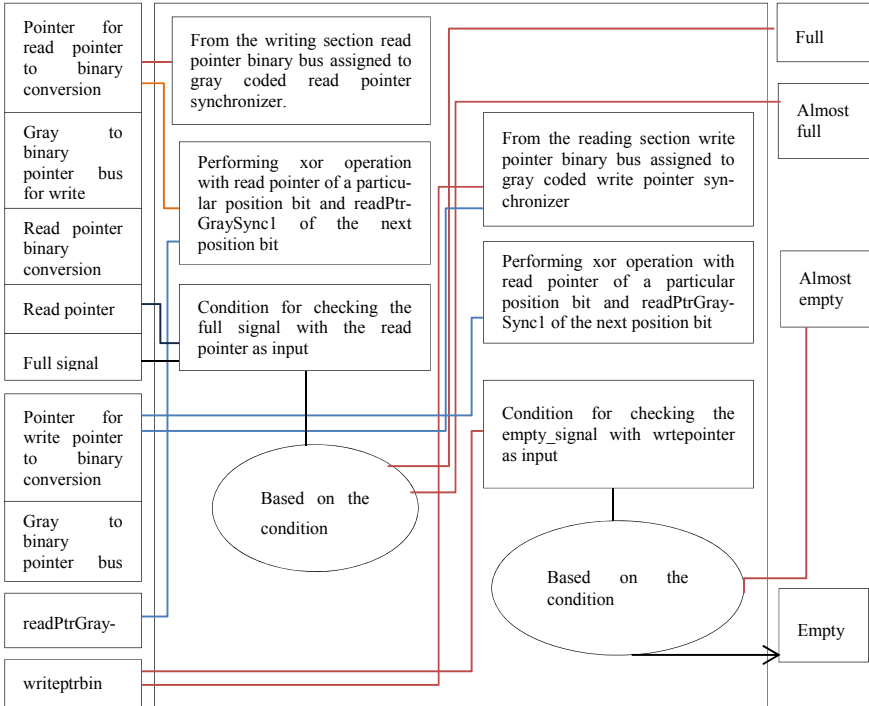
Fig. 4 Synchronization section

Thus, the minimum depth of this asynchronous FIFO for safe data transmission = $(100 - 40) = 60$.

While implementing in the simulation let us consider the RAM address width in bits be W. The RAM depth in lines is calculated as 2 W.

3 Result and Discussion

In order to validate the proposed FPGA, architecture described in the previous section. The architecture has been simulated in VHDL. The software used for this simulation is Xilinx Design Suite 14.5. The board used for realization is Artrix7. The internal architecture of the Asynchronous FIFO model in terms of RTL is shown in Fig. 5.

The output waveforms of VHDL simulation for verification of the design have been put together in figures below.

Initially the system gets reset, then we enable the write enable and the FIFO starts taking input data, after 100 ns the read enable is made high and the data become available at output. The other output ports like empty, almost empty, almost full and
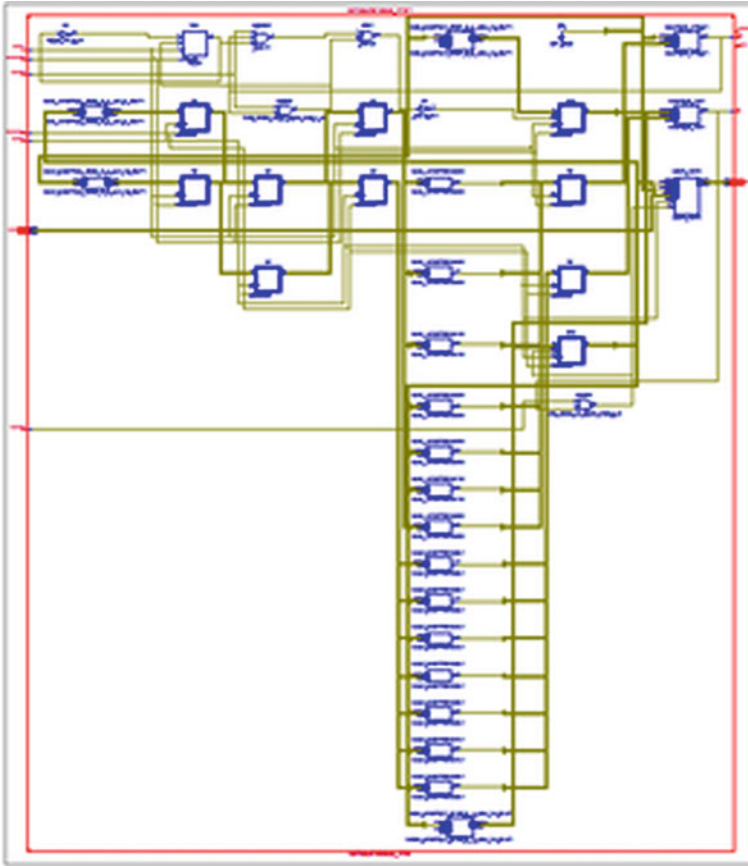
Fig. 5 Internal architecture of the asynchronous FIFO (RTL view)

full are controlled by the synchronizer of the asynchronous FIFO in every clock cycle. Figure 6 presents the normal writing and reading operation of FIFO (Figs. 7 and 8).

4 Conclusion

In this paper, authors have demonstrated an area efficient asynchronous FIFO architecture and its FPGA implementation for fixed writing and reading clock domain frequency. The VHDL simulation results exhibit the effectiveness of the architecture, and device utilization for FPGA implementation confirms low-logic utilization or area efficiency. In future, this architecture may be modified to work efficiently within a given range of reading and writing frequency (Table 1).
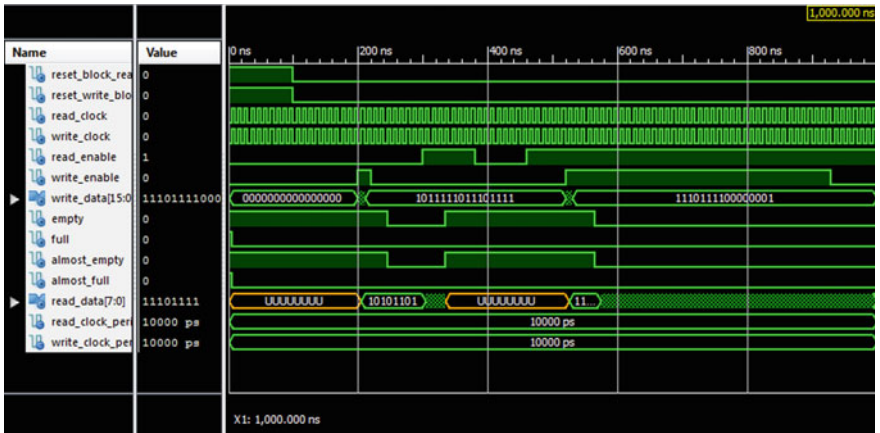
Fig. 6 Writing and reading operation
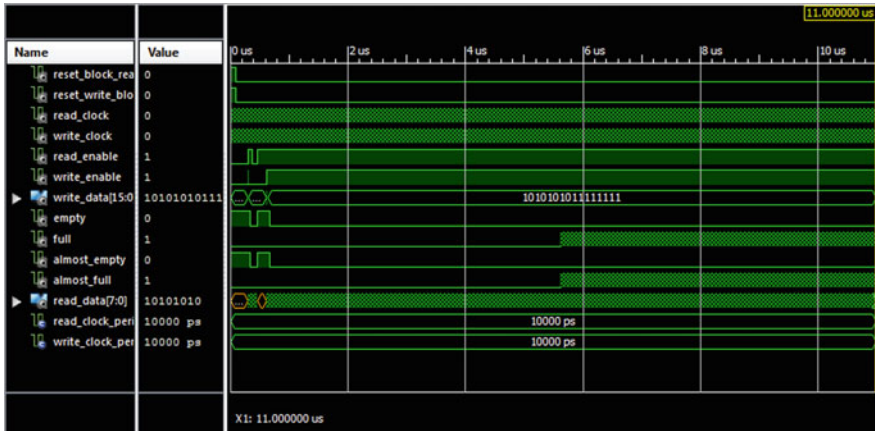
Fig. 7 System facing overrun
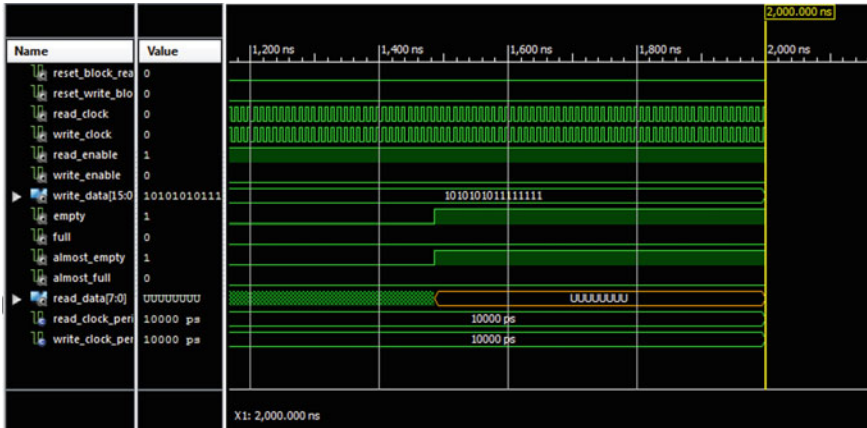
Fig. 8 System facing underrun

Table 1 Device utilization table

Logic utilization	Used	Available	Utilization (%)
Number of slice registers	87	126,800	0
Number of slice LUTs	174	63,400	0
Number of fully used LUT-FF pairs	60	201	29
Number of bonded IOBs	34	210	16
Number of BUFG/BUFGCTRL/BUFHCEs	2	128	1

References

1. Cummings, C., Sunburst Design, Inc.: Simulation and Synthesis Techniques for Asynchronous FIFO Design, SUNG (Synopsys Users Group Conference, San Jose, CA, 2002), A second FIFO paper by the same author was voted "Best Paper -1st Place"
2. Yong, X., Runde, Z.: Low latency high throughout circular asynchronous FIFO, pp. 812–816. IEEE Institute of Microelectronics, Tsinghua University, 2008
3. Han, H., Stevens, K.S., IEEE: Clocked and Asynchronous FIFO Characterization and Comparison, 2009
4. Kumar, A., Shankar, N.S.: Verification of asynchronous FIFO using system Verilog. Int. J. Comput. Appl. **86**(11), 06–20 (2014)
5. Kim, H.-K., Wang, L.-T., Liang, Y., Jone, W.-B.: Testing of synchronous and asynchronous FIFO. J. Electron. Test. **29**(1), 49–72 (2013)
6. Mahesh, U., Long, M., Simmons, L.: Quad Asynchronous Communication Element (ACE) with FIFO. IEEE, 1991
7. Thenappan, S.: Asynchronous FIFO design using Verilog. Int. Res. J. Eng. Technol. (2008)
8. Abdelhadi, A.M.S.: Synthesizable synchronization FIFOs utilizing the asynchronous pulse-based handshake protocol. In: 2020 IEEE Nordic Circuits and Systems Conference (NorCAS), Oslo, Norway, 2020, pp. 1–7.https://doi.org/10.1109/NorCAS51424.2020.9265139

9. Abdel-Hafeez, S., Quwaider, M.Q.: A one-cycle asynchronous FIFO queue buffer circuit. In: 2020 11th International Conference on Information and Communication Systems (ICICS), Irbid, Jordan, 2020, pp. 388–393. https://doi.org/10.1109/ICICS49469.2020.239548

10. Liu, G., Garside, J., Furber, S., Plana, L.A., Koch, D.: Asynchronous interface FIFO design on FPGA for high-throughput NRZ synchronisation. In: 2017 27th International Conference on Field Programmable Logic and Applications (FPL), Ghent, Belgium, 2017, pp. 1–8. https://doi.org/10.23919/FPL.2017.8056801.

Artificial Neural Networks for Waste-water Treatment Plant Control

Allaka Tarun and Ginuga Prabhaker Reddy

Abstract The operation of waste-water treatment plant is usually affected by numerous factors as biological, physical and chemical factors. The regulation of dissolved oxygen is a critical step for the plant's control and efficiency. The performance and design of a Neural Networks based Model Predictive Controller for DO (Dissolved Oxygen) control in a waste-water treatment plant are reported in this research. The novelty of present method is to address distributed system of five reactors in series as a single-lumped system with 65-ODE equations due to slow process dynamics. The present Neural Networks based MPC (Model Predictive Controller) happened to be faster response than conventional PID controller. The closed loop performance is evaluated through simulations using MATLAB and SIMULINK.

Keywords Waste-water treatment plant · Dissolved oxygen concentration · Neural networks based model predictive controller

1 Introduction

Waste-water treatment plants (WWTPs) are critical for protecting aquatic bodies from pollution. To get the desired profluent quality, these plants must perform efficiently. Nonetheless, the mind-boggling and non-direct aspects of the framework, as well as the consecutive and massive alterations in the influent, make their activity and management difficult. Alejandro et al. [1] looked at Neural NLMPC strategies for the control of the adopted muck measure. The reproduction convention BSM1 is used to apply the prescient regulator plans and investigate the shut circle measure conduct in distinct circumstances. This technique has the best execution when compared to NLMPC which has been decoupled plot, the exemplary BSM1 [2] developed PI framework or a concentrated NLMPC plot. Dunyamin et al. [3] have created three free ANN models prepared with back-proliferation calculation to anticipate emanating Suspended Solids (SS), Mixed Liquor Suspended Solids in air circulation

A. Tarun · G. P. Reddy (✉)
Department of Chemical Engineering, University College of Technology, Osmania University, Hyderabad, Telangana, India

tank (MLSS) and Chemical Oxygen Demand (COD), centralizations for the focal waste-water treatment plant in Ankara. Anuradha et al. [4] have given a plan of direct converse neural organizations regulator for an isothermal CSTR and brought about a quicker reaction in correlation with ordinary control framework. To work on the exhibition of direct backwards NN regulator for administrative issue, the IMC have organized two modes for the direct inverse framework, named as converse NN and forward models which are rememberable for them.

Holenda et al. [5] investigated the implementation of MPC (Model Predictive Control) of DO in a treatment plant of waste-water. The findings demonstrate that MPC may be used successfully in wastewater treatment plants for broken up oxygen control.

Mingzhi et al. [6] utilized multi target work for the plan and activity for the ANN control, initiated slop digester. The epic methodology thought about two functional destinations, controlling the quality of profluent and the fastest rate of biogas production, for example, and by the combination of factors from both phases, exploiting the distinction between the parts of the gas and fluid stages. Mohamed et al. [7] introduced the utilization of fake neural organizations for integrated waste-water treatment plant execution assessment. As a result, the obtained results show that NN (Neural Networks) are an all-rounder method for exhibiting complete operating plants for treatment of waste-water and give an elective philosophy for suggesting treatment facility presentation. Raduly et al. [8] used an ANN method to develop a quick WWTP execution assessment. The remaining influential time series (dynamic information for 20 years) developed using the influential upsetting impact generator is then reproduced using a fake neural organization (ANN) based on the accessible WWTP input-yield information. The ANN is proven to reduce reenactment time by a factor of thirty-six six in any case, when, even, accounting for the spent time preparing material and ANN training. Sergiu et al. [9] have given the plan of prescient regulator dependent on neural organizations as inside model of the interaction and modifies the weakening rate to satisfy the control objective. Xianjun et al. [10] have introduced a RRB neural organization (NN)-based versatile PID (RBFNNPID) computation and recreation for better DO control in an adopted slop measure-based waste-water treatment.

Presently, the PID, i.e., Proportional–Integral–Derivative and PI, i.e., proportional–integrators control technique is commonly used in waste-water treatment plant process control. It's worth noting that during the use of PID or PI control technique, the control impact can be influenced by hidden, unexpected aggravations and remarkable alterations in activity settings. Different arrangements, such as fluffy flexible PID, multivariable hearty control, and MPC (Model Predictive Control) system, are recommended to further develop the regulator's broken oxygen control execution in the waste-water treatment measure. Model Predictive Control (MPC) is a proven method for controlling DO levels, not just keeping up with the DO focus at a set worth, yet in addition finding the ongoing changes that happen in the process [5, 9]. This project's main aim is to build a NN-based MPC for a squander water treatment plant, also to evaluate the presentation of the NN-based MPC for a squander water

treatment plant using recreational considerations and to compare it to a conventional PID controller.

2 Mathematical Model of a Waste-Water Treatment Plant

The ASM (Activated Sludge Model) based main BSM1 Layout (Benchmark Simulation Model Layout) [2] is a simple design shown in Fig. 1. BSM1's first segment includes a natural/biochemical initiated reactor with 5 compartments in total, three are aeration tanks and two of which are anoxic tanks; the second segment of BSM1 also includes a settler.

Reactors 1 and 2 are open-loop reactors that are unaerated; reactors no. three, four and five are air-circulated reactors. In a case of open-loop, the coefficients of oxygen control (KL a) are fixed; for third and fourth reactors, KLa3 and KLa4 (coefficients) are set to be consistent at 240 d-1 (10 h − 1), implying that the air flow rate is constant; in case of reactor number five, KLa5 is chosen as controlled variable to DO fixation as controlled at a value of 2 g/m^3.

List of processes

Biological behavior of system is described through eight different processes.

$j = 1$: Heterotroph's Aerobic growth

$$\rho_1 = \mu_H \left(\frac{S_S}{K_S + S_S} \right) \left(\frac{S_O}{K_{O,H} + S_O} \right) X_{B,H} \tag{1}$$

$j = 2$: Heterotrophs Anoxic growth

$$\rho_2 = \mu_H \left(\frac{S_S}{K_S + S_S} \right) \left(\frac{K_{O,H}}{K_{O,H} + S_O} \right) \left(\frac{S_{NO}}{K_{NO} + S_{NO}} \right) \eta_g X_{B,H} \tag{2}$$

$j = 3$: Autotrophs Aerobic growth
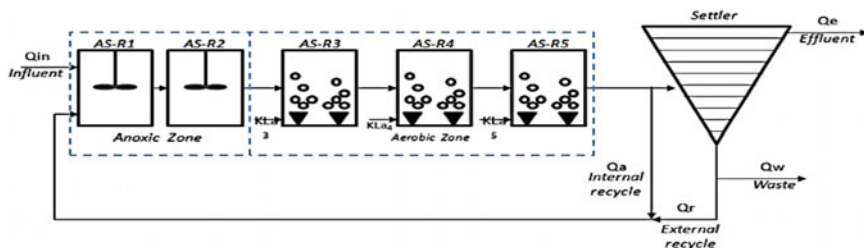
Fig. 1 Model No. 1 (BSM1) for benchmark simulation

$$\rho_3 = \mu_A \left(\frac{S_{\mathrm{NH}}}{K_{\mathrm{NH}} + S_{\mathrm{NH}}} \right) \left(\frac{S_O}{K_{O,A} + S_O} \right) X_{B,A} \tag{3}$$

$j = 4$: Heterotrophs decay

$$\rho_4 = b_H X_{B,H} \tag{4}$$

$j = 5$: Autotrophs decay

$$\rho_5 = b_A X_{B,A} \tag{5}$$

$j = 6$: Soluble organic nitrogen ammonification

$$\rho_6 = k_a S_{\mathrm{ND}} X_{B,H} \tag{6}$$

$j = 7$: Entrapped organics Hydrolysis

$$\rho_7 = k_h \frac{X_S / X_{B,H}}{K_X + (X_S / X_{B,H})}$$
$$\left[\left(\frac{S_O}{K_{O,H} + S_O} \right) + \eta_h \left(\frac{K_{O,H}}{K_{O,H} + S_O} \right) \left(\frac{S_{\mathrm{NO}}}{K_{\mathrm{NO}} + S_{\mathrm{NO}}} \right) \right] X_{B,H} \tag{7}$$

$j = 8$: Entrapped organic nitrogen Hydrolysis

$$\rho_8 = k_h \frac{X_S / X_{B,H}}{K_X + (X_S / X_{B,H})}$$
$$\left[\left(\frac{S_O}{K_{O,H} + S_O} \right) + \eta_h \left(\frac{K_{O,H}}{K_{O,H} + S_O} \right) \left(\frac{S_{NO}}{K_{NO} + S_{NO}} \right) \right]$$
$$X_{B,H} (X_{\mathrm{ND}} / X_S) \tag{8}$$

The conversion rates that has been observed

The conversion rates that has been observed (r_i) result from the basic processes combinations:

$$r_i = \sum_j \nu_{ij} \rho_j \tag{9}$$

$$r_1 = 0 \tag{10}$$

$$r_2 = -\frac{1}{Y_H} \rho_1 - \frac{1}{Y_H} \rho_2 + \rho_7 \tag{11}$$

$$r_3 = 0 \tag{12}$$

$$r_4 = (1 - f_P)\rho_4 + (1 - f_P)\rho_5 - \rho_7 \tag{13}$$

$$r_5 = \rho_1 + \rho_2 - \rho_4 \tag{14}$$

$$r_6 = \rho_3 - \rho_5 \tag{15}$$

$$r_7 = f_P\rho_4 + f_P\rho_5 \tag{16}$$

$$r_8 = -\frac{1 - Y_H}{Y_H}\rho_1 - \frac{4.57 - Y_A}{Y_A}\rho_3 \tag{17}$$

$$r_9 = -\frac{1 - Y_H}{2.86Y_H}\rho_2 + \frac{1}{Y_A}\rho_3 \tag{18}$$

$$r_{10} = -i_{XB}\rho_1 - i_{XB}\rho_2 - \left(i_{XB} + \frac{1}{Y_A}\right)\rho_3 + \rho_6 \tag{19}$$

$$r_{11} = -\rho_6 + \rho_8 \tag{20}$$

$$r_{12} = (i_{XB} - f_P i_{XP})\rho_4 + (i_{XB} - f_P i_{XP})\rho_5 - \rho_8 \tag{21}$$

$$r_{13} = -\frac{i_{XB}}{14}\rho_1 + \left(\frac{1 - Y_H}{14 * 2.86Y_H} - \frac{i_{XB}}{14}\right)\rho_2 - \left(\frac{i_{XB}}{14} + \frac{1}{7Y_A}\right)\rho_3 + \frac{1}{14}\rho_6 \tag{22}$$

In accordance with the system's mass balance, the biochemical reactions, in each Reactor can be explained as below.

Reactor 1

$$\frac{dZ_1}{dt} = \frac{1}{V_1}(Q_a Z_a + Q_r Z_r + Q_{in}Z_{in} + R_1 V_1 - Q_1 Z_1) \tag{23}$$

Reactor k, ($k = 2$) to ($k = 5$)

$$dZ_k/dt = 1/V_k(R_k V_k - Q_k Z_k + Z_{k-1}Q_{k-1}) \tag{24}$$

Special case when Oxygen Dissolved ($S_{O,k}$)

$$dS_{O,k}/dt = 1/V_k R_k + \left(S_O^* - S_{O,k}\right)K_L a + \left(S_{O,k-1}Q_{k-1} - S_{O,k}Q_{k-1}\right) \tag{25}$$

where flow rate (Q), concentration of mass of either bacterial or substrate mass (Z), reactor's volume (V), reaction rate (r), K_La = coefficient for the transfer of oxygen, S_O is the concentration of dissolved oxygen is oxygen's saturation concentration of oxygen is represented as S^*, and its value is given as ($S^* = 8$ g/m^3 at 15 °C).

$$Q_1 = Q_{in} + Q_r + Q_a; \ Q_k = Q_{k-1}. Z_a = Z_5, Z_f = Z_5.$$

$Z_w = Z_r. R$ stands for $r_i \ i = 1$ to 13. The Kinetic and Stoichiometric Parameters are considered for the present study are same as given in [2].

3 Design of a Waste-Water Treatment Neural Networks Based Predictive Controller Plant

System Identification

On the basis of inputs previously received and outputs of plants, this model of Neural Networks provide with the values of outputs of plants for future. Figure 2 shows the structural representation of the plant model of neural networks.

The above organization can be prepared disconnected in group mode, utilizing information gathered from the activity of the plant. The model prescient control strategy depends on the receeding horizon procedure. This neural organization model suggests the reaction of plant throughout a predefined period of time skyline. A mathematical improve programmed used to forecasts to predict the control signal that limits the accompanying show measure to a predefined horizon.

$$J = \lambda \sum_{j=1}^{N_u} (u^1(t + j - 1) - u^1(t + j - 2))^2 + \sum_{j=N_1}^{N_2} (y_r(t + j) - y_m(t + j))^2$$

(26)
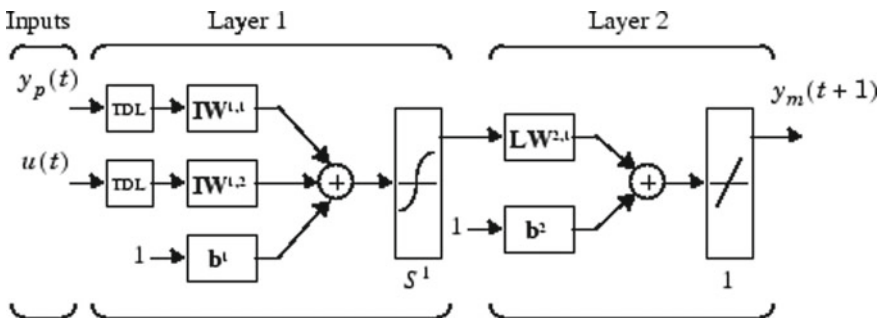
Fig. 2 MPC (model predictive controller) based on neural network structure
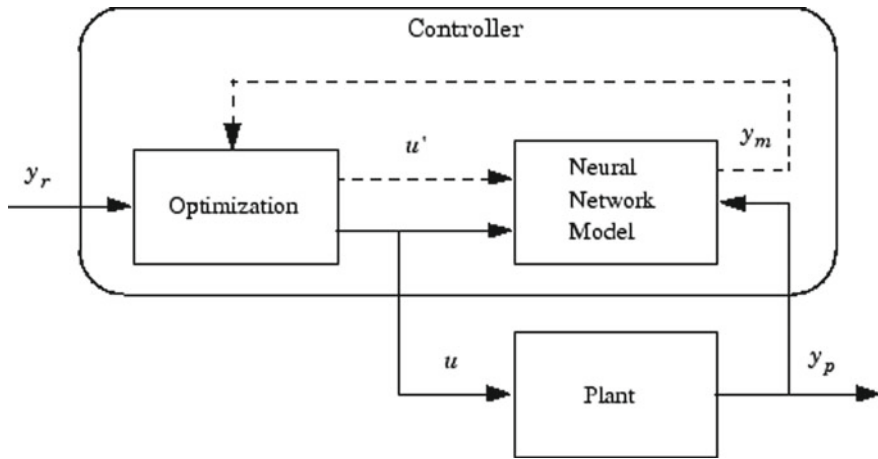
Fig. 3 MPC (model predictive controller) based on NN (neural networks) block diagram

In above equation, $N1$, $N2$ and Nu are the skylines that the control augmentations and following blunder are analyzed against. The preliminary control signal is u', the ideal reaction is y_r, and the organization model reaction is y_m. The esteem determines how much the number of squares in the control increases affects the presentation index. The block graph of the Neural Networks based model foresight control measure is shown in Fig. 3. The regulator is made up of the advancement block and the neural organization plant model. The benefits of u′ that constrain J are determined by the enhancement block, and the ideal u is the contribution of plant [7]. The present neural networks based Model Predictive regulator is planned with the accompanying boundaries dependent on experimentation arrangement, Size of Hidden layer $= 7$, Control Horizon $(N_u) = 7$, Cost Horizon $(N_2) = 6$ Control Weighing Factor $= 0.003$, Iterations per sample Time $= 5$ (Figs. 4 and 5).

As shown in Fig. 6, the identification or training of neural networks Model was successful, with a very low degree of error between NN output prediction and real plant output.

4 Results and Discussion

The present neural networks based Model Predictive Controller and PID Controller for the waste-water treatment facility are analyzed using MATLAB and SIMULINK. It is evaluated for different set points for DO concentrations of 1.5 and 2.5 g/m^3 from the initial value of 2.0 g/m^3.

The neural network-based model predictive controller has a shorter response time and less overshoot than the PID Controller, as shown in Figs. 7 and 8. Furthermore, both NN-MPC replies are obtained as smooth.
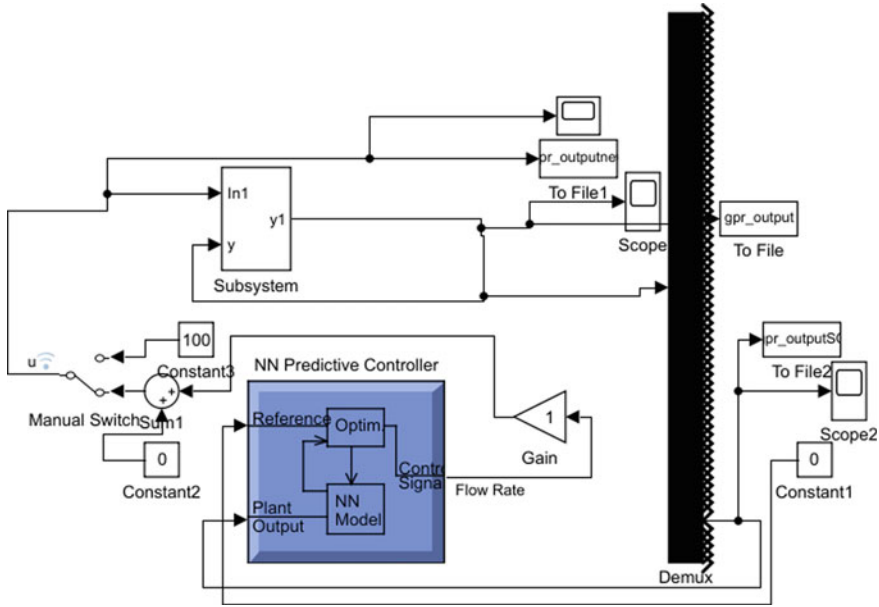
Fig. 4 Waste-water treatment plant model predictive control system based on neural networks
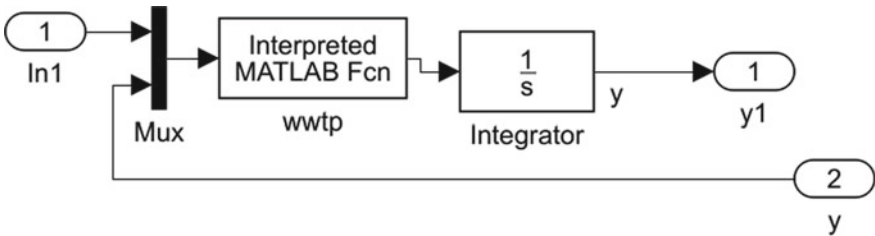
Fig. 5 Waste-water subsystem of BSM1

5 Conclusions

In the current study, a NN-based (Neural Network-based) MPC (Model Predictive Controller) for a waste-water treatment plant was designed using simulated random data of input and output. Four input neurons, seven hidden neurons, and one output neuron make up the optimum neural structure. For set point changes in DO control, the neural network Model Predictive Controller is found to be more effective than the PID Controller. The neural network based Model Predictive Controller's performace is found to be faster and has lesser overshoot, when compared to the PID Controller.
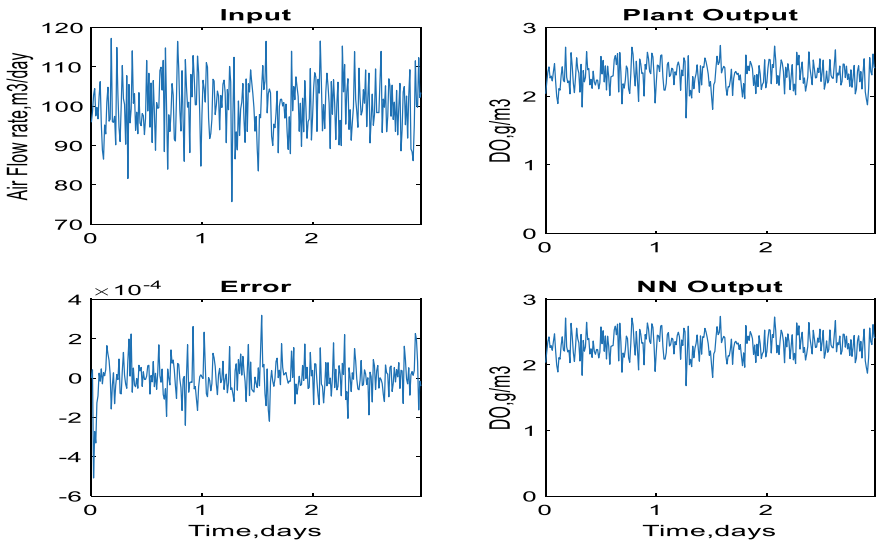
Fig. 6 Data for neural network model predictive controller training, process input is mass transfer coefficient (air flow rate), $K_L a$, and process output is DO Conc., g/m^3
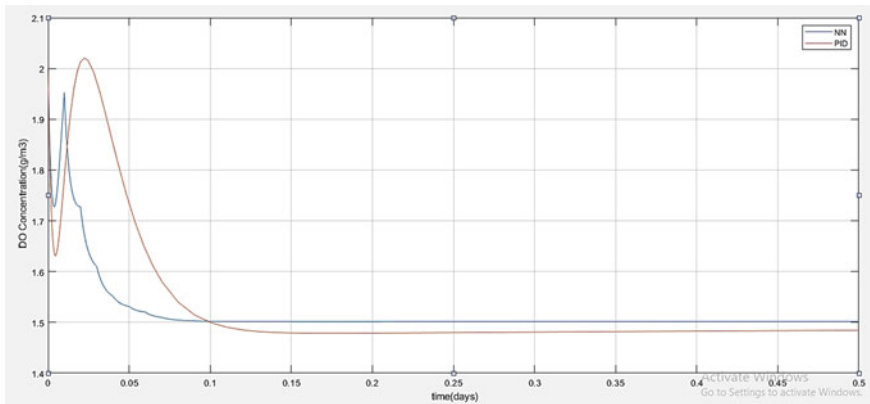
Fig. 7 DO responses of neural networks model predictive controller and conventional PID controller for a change in set point, i.e., from 2.0 to 1.5 g/m^3 (Blue-NNMPC and Yellow-PID)
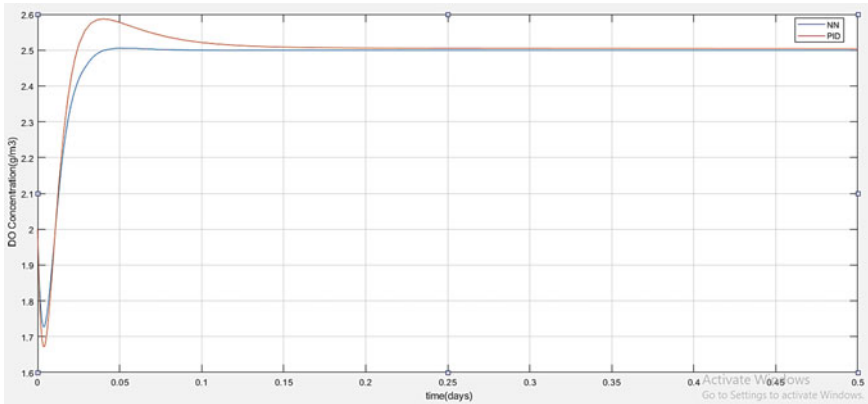
Fig. 8 DO responses of neural networks model predictive controller and conventional PID controller for a change in set point from 2.0 to 1.5 g/m^3 (Blue-NNMPC and Red-PID)

References

1. Goldar, A., Silvana, R.R., Lamanna, R., Vega P.: Neural NLMPC schemes for the control of the activated sludge process. In: 11th IFAC Symposium on Dynamics and Control of Process Systems (2016)
2. Alex, J., Benedetti, L., Copp, J., Gernaey, K.V., Jeppsson, U., Nopens, I., Pons, M.-N., Rieger, L., Rosen, C., Steyer, J.P., Vanrolleghem, P., Winkler, S.: Benchmark Simulation Model No. 1 (BSM1). Department of Industrial Electrical Engineering and Automation, Lund University CODEN: LUTEDX/(TEIE-7229)/1-62 (2008)
3. Guclu, D., Dursun, S.: Artificial neural network modelling of a large-scale wastewater treatment plant operation. Bioprocess Biosyst. Eng. **33**, 1051–1058 (2010). https://doi.org/10.1007/s00449-010-0430-x
4. Anuradha, D.B., Prabhaker Reddy, G., Murthy, J.S.N.: Direct inverse neural network control of a continuous stirred tank reactor (CSTR). In: Proceedings of IAENG International Conference on Control and Automation, ICCA2009, Hong Kong, 18–20 Mar 2009, ISBN: 978-988-17012-2-0)
5. Holenda, B., Domokos, E., Redey, A., Fazakas, J.: Dissolved oxygen control of the activated sludge wastewater treatment process using model predictive control. Comput. Chem. Eng. **32**, 1278–1286 (2008)
6. Huang, M., Han, W., Wan, J., Mac, Y., Chen, X.: Multi-objective optimisation for design and operation of anaerobic digestion using GA-ANN and NSGA-II (2014). https://doi.org/10.1002/jctb.4568
7. Mohamed, F., Hamoda, I., AI-Ghusain, A., Hassan, A.H.: Integrated wastewater treatment plant performance evaluation using artificial neural networks. Wat. Sci. Tech. **40**(7), 55–65 (1999)
8. Raduly, B., Gernaey, K.V., Capodaglio, A.G., Mikkelsen, P.S., Henze, M.: Artificial neural networks for rapid WWTP performance evaluation: methodology and case study. Environ. Modell. Softw. **22**, 1208–1216 (2007)

9. Caraman, S., Sbarciog, M., Barbu, M.: Predictive control of a wastewater treatment process. Int. J. Comput. Commun. Control **II**(2), 132–142 (2007)
10. Du, X., Wang, J., Jegatheesan, V., Shi, G.: Dissolved oxygen control in activated sludge process using a neural network-based adaptive PID algorithm. Appl. Sci **8**, 261 (2018). https://doi.org/10.3390/app8020261

Investigations of a Symmetrically Modulated Triangular Periodic Structures with Microstrip Lines and Its Application to Microwave Filter Design

Prashnatita Pal 📷 **, Bikash Chandra Sahana, Jayanta Poray, and Amiya Kumar Mallick**

Abstract The microwave filters having their inherent stopband and passband characteristics, supported by the necessary periodic structures. This is some alternative nature of signal propagation. The required position and width of microstrip lines are varying as per the structure of the passband and stop bands. The associated state-of-the-art model is well defined in different literature. The microstrip periodic structures, supported by symmetrically modulated triangular geometry are presented in this work. Several discrete N unit cells are derived as ABCD parameters for this proposed model. The entire framework is an analysis using a mathematical model and simulated by the MATLAB platform. The variation of input–output characteristics is noticeable similar to the stopband and passband filters. The overall simulation framework has been demonstrated in this paper. The associated metrics for the filter alone with the return loss**, i**nsertion loss, and the bandwidth varying by several pointers of periodicity (p), minimum width (a), maximum width (b). This novel signal filtering technique can be useful for several modern civilization applications. The signal transmission through the line and the presence of the passband and stopband has been verified with the simulation framework concerning the mathematical model.

Keywords Microstrip transmission lines · Periodic structures · Microwave filter

P. Pal (✉) · B. C. Sahana
Department of Electronics and Communication Engineering, National Institute of Technology, Patna, India

J. Poray
Department of Computer Science and Engineering, Techno India University, Kolkata, West Bengal, India

A. K. Mallick
Electrical Electronics and Communication Engineering, Indian Institute of Technology, Kharagpur, India

1 Introduction

The characterization of an ideal filter is well defined by the transmission line for a certain baseband range, whereas the attenuation is infinite in associated stopband bandwidth. This an ideal situation, very difficult to archive in reality. The object is to design the filter to approximate the standard inputs for a level of acceptability. There are three types of filters, namely: (1) low-pass filters that transmit all signals from zero frequency to a cut-off frequency ω_c and attenuate all signals with frequencies above the cut-off value; (2) high-pass filters that reject all frequencies below the cut-off value ω_c and pass all frequencies above ω_c; (3) bandpass filters that transmit signals with frequencies in the range between value ω_1 to value ω_2 and attenuate signals with frequencies outside this range; 4) The stopband filter is the complement to the passband filter, which rejects frequencies in the range from ω_1 to ω_2. The nature of filter elements at low frequency is inductors and capacitors. The design mechanism of the filter using inductors and capacitor are very much simple and the frequency characteristics are also very simple. So, a complete synthesis procedure can be developed using a general approach for the design of low-frequency filters. But filter design at microwave frequency range is very problematic because of the use of distribution parameter elements. The synthesis of the distributed parameter is very much complicated as well. If ideal inductance or capacitive reactance over a limited frequency range is present at many microwaves element, then it has a special frequency characteristic. For this case, a low-frequency range prototype filter is used as a model. Then, a suitable microwave circuit element can be realizing a microwave filter by replacing it with inductors and capacitors. Then, it has the same frequency characteristics over the range of microwave frequency.

The periodic structure with passband-stopband characteristics can be used as a filter. The advantages of using periodic structure filters over conventional ones are as follows:

(i)   Unlike conventional filter structures, periodically loaded lines exhibit alternating bands of propagation and attenuation, making it possible to realize a bandpass filter with an infinite number of passbands.

(ii)   The design procedure of filters is better controlled by the parameters of the periodic structure. For the capacitively loaded coaxial line susceptance B and periodicity d, adjust, respectively, with the width and the position of a passband.

(iii) Because of the smooth variation of the geometry of the structure, better compensation effects are automatically realized. The following conditions must be satisfied to design a periodic structure bandpass filter:

(a) The absolute value of the equation $\frac{A_u + D_u}{2}$ should be equal to unity at the desired corner frequencies of the passband. Where A_u, D_u represent as diagonal element of ABCD matrix.

(b) The characteristic impedance of the unit cell should be equal to 50 Ω at the center frequency.

The parameters of interest for a filter are the return loss and the insertion loss. For an ideal filter, the magnitude of these quantities should be zero and one, respectively, in the passband. The return loss and insertion loss can be found from the elements of the scattering matrix of the structure, and are

$$\text{Return Loss} = S_{11} = \frac{\textbf{Reflected voltage at port 1}}{\textbf{Incident voltage at port 1}}$$

$$\text{Insertion Loss} = S_{21} = \frac{\textbf{The incident voltage at port 2}}{\textbf{The incident voltage at port 1}}$$

S_{11} and S_{21}, in terms of the ABCD parameters of the structure, are obtained as follows:

$$S_{11} = \frac{A - B/Z_0 + CZ_0 - D}{A + B/Z_0 + CZ_0 + D} \tag{1}$$

$$S_{21} = \frac{2}{A + B/Z_0 + CZ_0 + D} \tag{2}$$

where Z_0 is the characteristic impedance of the input and output transmission lines.

The expressions for the complex propagation constant and characteristic impedance of the periodic structures were presented. The condition for propagation was also specified. It was noted that a periodically loaded transmission line exhibits alternating propagation and attenuation bands. The width and position of the passband are controlled by the multiple parameters for the associated model.

The organization of this paper is as follows:

After an introduction at the beginning, the literature survey has been considered. Then, the mathematical model of the Triangular Periodic Transmission Line has been incorporated to present the correlation, required for the realization of scattering attributes and transmission parameters alone with their mutual relationship. After that present the technique for evaluating, the ABCD parameter of the related connections for the transmission channel. The final simulation result is presented in the adjacent section, which is supported by the mathematical model. Finally, the paper resulted in the application of the proposed filter model. In the end, the extended model with future scope has been highlighted.

2   Literature Review

The periodic interval for the transmission lines having some reactive elements for the periodic structure. Such a loaded line may be an ordinary waveguide with periodically spaced identical obstacles inserted across it as shown in Fig. 1. It may
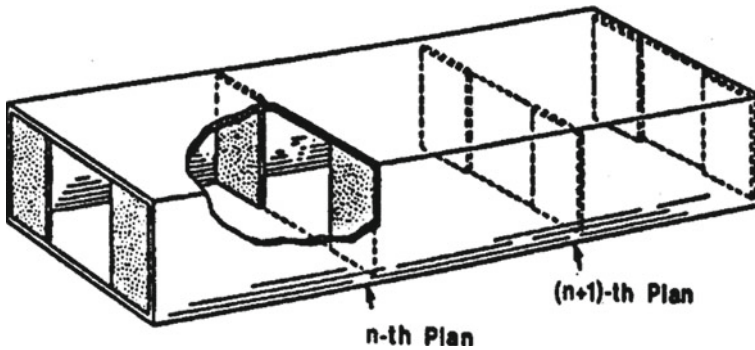
Fig. 1 Waveguide with periodically spaced irises

be a guide with periodically spaced tees, each similarly terminated, or it may be a more complicated structure such as a series of identical cavities each with two waveguide outputs, one on each side. The output of one cavity forming the input to the next. A coaxial transmission line can be made periodically loaded by introducing thin circular diaphragms at regular intervals. Also, there is a class of non-uniform microstrip lines where the non-uniformity is distributed periodically along the axial direction. The periodically loaded transmission lines have many interesting and useful properties. These properties have been studied by many investigators in the past. The analyzes of non-planar types of periodic structures are well documented in several pieces of works of literature [1–4]. Planar periodic structures are found to be of considerable importance because of their interesting and useful properties. These properties have been studied by many researchers in the past. The structures under consideration were (i) microstrip lines with sinusoidally varying width [1] and (ii) circular width modulated microstrip lines [5]. A simplified approach for analyzing a non-uniform line is modeling the structure as several small uniform transmission line sections of different widths, connected in a cascade [6–8]. From the solution of the wave equation, the electromagnetic fields inside the structure have been obtained. Defining the modal voltage and modal current, the admittance matrix of each of the radial lines has been determined. A compact microstrip dual-band bandpass filter is proposed utilizing a novel embedded scheme resonator [9] but it cannot use for 10–12 GHz operating frequency but our designed filter is applicable for this frequency band. The next paper [10] presents a new Narrow Bandstop Filter (NBSF) and Wide Bandpass Filter (WBPF) and integrating two different resonators for microstrip, supported by the Hilbert fractal geometry. This filter design is complex concerning our proposed filter model. A type of fragmented periodic transmission line with suppression features has been presented by Martel et al. [11]. The basic structure has been designed with the transmission line theory but the bandwidth is less than our proposed microstrip filter. The next paper represents the new type of dual-degenerate mode of bandpass filter for microstrip [12]. This filter uses Cantor square fractal geometry-based microstrip patch resonator having some associated

geometrical slots. But the operating frequency is varying upto 2 GHz. This is not working for at higher frequencies.

3 Mathematical Model of the Triangular Periodic Transmission Line

The width modulated periodic structure is mathematically described in the paper [13]. The periodicity of the structure is p, and the minimum and maximum widths are a and b, respectively. A unit cell of the structure is shown in Fig. 2. This cell can be modeled as a combination of two annular sectors joined face to face. Let the outer and the inner radii of the sectors be r and R, respectively. The angle of the sector denoted by notation θ can be defined as.

$$\frac{\frac{b}{2} - \frac{a}{2}}{\frac{p}{2}} = \frac{\tan \theta}{2} \tag{3}$$

$$\tan \frac{\theta}{2} = \frac{b - a}{p} \tag{4}$$

$$\theta = 2 \arctan \frac{b - a}{p} \tag{5}$$

$$2(R - r) = p \tag{6}$$

3.1 Equivalent Circuit Representation

Let the nodal voltage and current in an annular sector be defined as E_z and $-rH_\varphi$, respectively [14]. These definitions of the nodal voltage and the nodal current lead to asymmetrical Y-matrix of the structure, a necessary to be passive. The admittance matrix (Y-matrix) is defined as

Fig. 2 Triangular width modulated periodic structure: p = periodicity, a = minimum width, b = maximum width, θ = angle of the sector
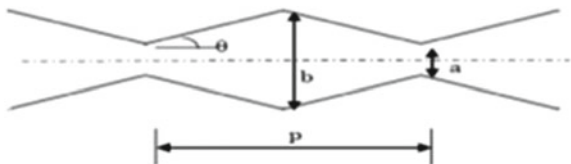
Fig. 3 An annular sector
with its equivalent π network
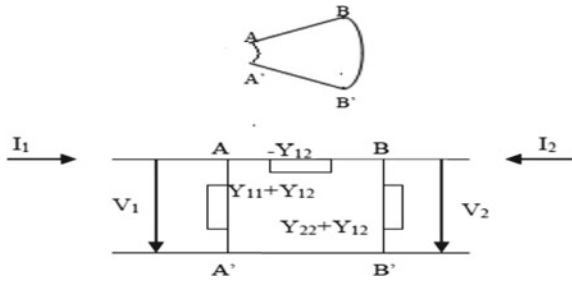
$$\begin{bmatrix} I_1 \\ I_2 \end{bmatrix} = \begin{bmatrix} Y_{11} & Y_{12} \\ Y_{21} & Y_{22} \end{bmatrix} \begin{bmatrix} V_1 \\ V_2 \end{bmatrix} \tag{7}$$

where I_1 and I_2 are the line currents and V_1 and V_2 are the line voltage at ports A and B, respectively (Fig. 3).

$$V_1 = E_z(r), \quad I_1 = -r\,H_\phi(r) \tag{8}$$

$$V_2 = E_z(R), \quad I_2 = -\mathrm{R}H_\phi(R) \tag{9}$$

The elements of the Y-matrix are determined from the relation,

$$Y_{11} = \frac{I_1}{V_1}(\mathrm{at}\,V_2 = 0) = -\frac{r\,H_\varphi(r)}{E_z(r)}(\mathrm{at}\,E_z(R) = 0) \tag{10}$$

Similarly, the expression for Y_{21} may be obtained. This shows that $Y_{21} = Y_{12}$. Thus, reciprocity holds justifying the definitions of the modal voltage and the modal current used. The Y-matrix of the other section can be obtained from the Y-matrix of the earlier one and its element values are given (Fig. 4).

$$Y_{11} = \frac{I_1}{V_1}(\mathrm{at}\ V_2 = 0) \tag{11}$$
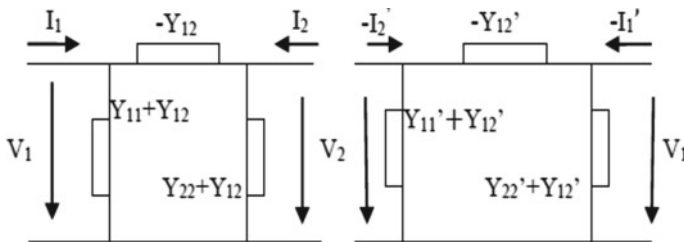
Fig. 4 Equivalent network when two annular sectors are cascaded

$$Y'_{11} = -\frac{I_2}{V_2}\,(\text{at } V_1 = 0) = -Y_{22} \tag{12}$$

$$Y_{22} = \frac{I_2}{V_2}\,(\text{at } V_1 = 0) \tag{13}$$

$$Y'_{22} = -\frac{I_1}{V_1}\,(\text{at } V_2 = 0) = -Y_{11} \tag{14}$$

$$Y_{12} = \frac{I_1}{V_2}\,(\text{at } V_1 = 0) \tag{15}$$

$$Y'_{12} = -\frac{I_2}{V_1}\,(\text{at } V_2 = 0) = -Y_{21} = -Y_{12} \tag{16}$$

$$Y_{21} = \frac{I_2}{V_1}\,(\text{at } V_2 = 0) \tag{17}$$

$$Y'_{21} = -\frac{I_1}{V_2}\,(\text{at } V_1 = 0) = -Y_{12} \tag{18}$$

Using the Y matrices of the two sections, the ABCD parameters of the unit cell are obtained.

For section (1),

$$\begin{bmatrix} A & B \\ C & D \end{bmatrix} = \begin{bmatrix} \frac{-Y_{22}}{Y_{21}} & \frac{1}{Y_{21}} \\ \frac{-(Y_{11}.Y_{22}-Y_{12}.Y_{21})}{Y_{21}} & \frac{Y_{11}}{Y_{21}} \end{bmatrix}$$

For section (2),

$$\begin{bmatrix} A' & B' \\ C' & D' \end{bmatrix} = \begin{bmatrix} \frac{-Y_{11}}{Y_{12}} & -\frac{1}{Y_{12}} \\ \frac{(Y_{11}.Y_{22}-Y_{12}.Y_{12})}{Y_{12}} & \frac{Y_{22}}{Y_{12}} \end{bmatrix}$$

The overall ABCD matrix is obtained by cascading two sections,

$$\begin{bmatrix} A & B \\ C & D \end{bmatrix} = \begin{bmatrix} 2\frac{Y_{22}Y_{11}}{Y_{12}^2} - 1 & 2\frac{Y_{22}}{Y_{12}^2} \\ 2\frac{Y_{11}}{Y_{12}}\left(\frac{Y_{11}Y_{22}}{Y_{12}} - Y_{12}\right) & 2\frac{Y_{22}Y_{11}}{Y_{12}^2} - 1 \end{bmatrix} \tag{19}$$

3.2 Propagation Constant

In a periodically loaded structure, an infinite number of special harmonics is inevitably and simultaneously present with varying propagation constants. The propagation constant [15] of the space harmonic β_0 is obtained as

$$\beta_0 = \frac{1}{p} \arccos A \qquad (20)$$

Since A is always real, and therefore β_0 is also really only when $|A| < 1$. substituting the expression for A, the condition for propagation becomes as given below

$$0 < \frac{Y_{11} Y_{22}}{Y_{12}^2} < 1$$

or,

$$0 < \left[\frac{\pi^2 k_1^2 Rr}{4} \Delta_1(R, r) \Delta_1(r, R) \right] < 1 \qquad (21)$$

The term inside the bracket in the previous equation is dependent on frequency. Thus, frequencies for which the previous equation is not satisfied lie in the stopband. Any imaginary value for β_0 can be considered as a stopband.

3.3 Characteristic Impedance

The characteristic impedance is another important parameter to be studied. The normalized characteristic impedance Z_0' [3] is obtained as

$$Z_0' = \frac{2A_{12} - A_{11} + A_{22} \pm \left[(A_{11} + A_{22})^2 - 4 \right]^{\frac{1}{2}}}{2A_{12} + A_{11} - A_{22} \mp \left[(A_{11} + A_{22})^2 - 4 \right]^{\frac{1}{2}}} \qquad (22)$$

Substituting the values of WAT matrix parameter in terms of ABCD parameters

$$Z_0' = \frac{\sqrt{(A^2 - 1)} - B/Z_0}{C Z_0 - \sqrt{(A^2 - 1)}} \qquad (23)$$

where in the above equation A, B, C, D are calculated before and $z_0 = \frac{120\pi}{r\sqrt{\epsilon_r}}$.

4 Simulation Result of Microstrip Triangular Periodic Structures

In modern engineering disciplines, MATLAB is used as a potential mathematical tool to performing various simulations and computations [16, 17]. Here, we have investigated the application of the circuit theory to designing and analyzing the microstrip filters using MATLAB. It has been verified that the performance of MATLAB results is satisfactory for HFSS (3D EM simulation tool) and CAD tool boxes Ansys/Ansoft circuit simulator [18]. The MATLAB tool has been set as the benchmark for RF/Microwave design. In this proposed model, the MATLAB algorithms are used for Triangular Periodic Structures microstrip filters supported by the circuit theory model. Here, the well-known ABCD parameters are used to generate the rousted filter performance with the stopband rejection rate, and associated input/output return losses and insertion loss. The equations obtained in the field analysis are simulated using MATLAB software are shown in Figs. 5 and 6. This will easier the calculation of design parameters and reduces the computation time reasonably. The entire simulation did the specific frequency range. The range is 8–12 GHz.
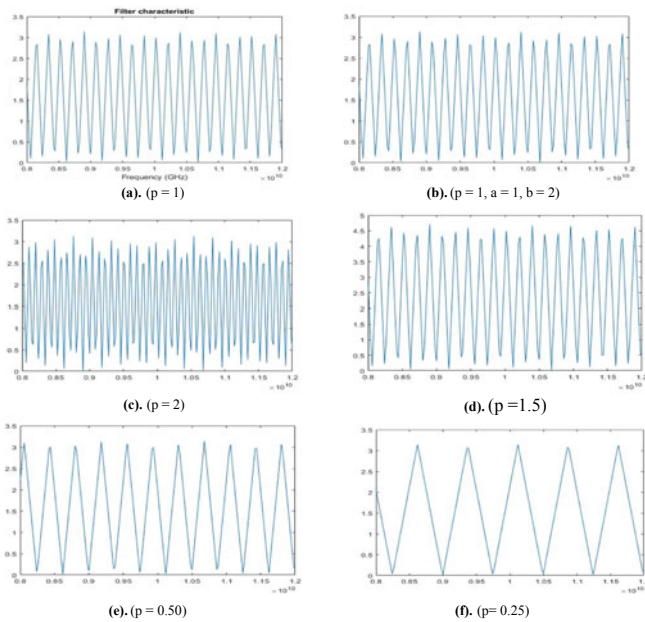
Fig. 5 a–f Propagation constant β_0 versus frequency plot
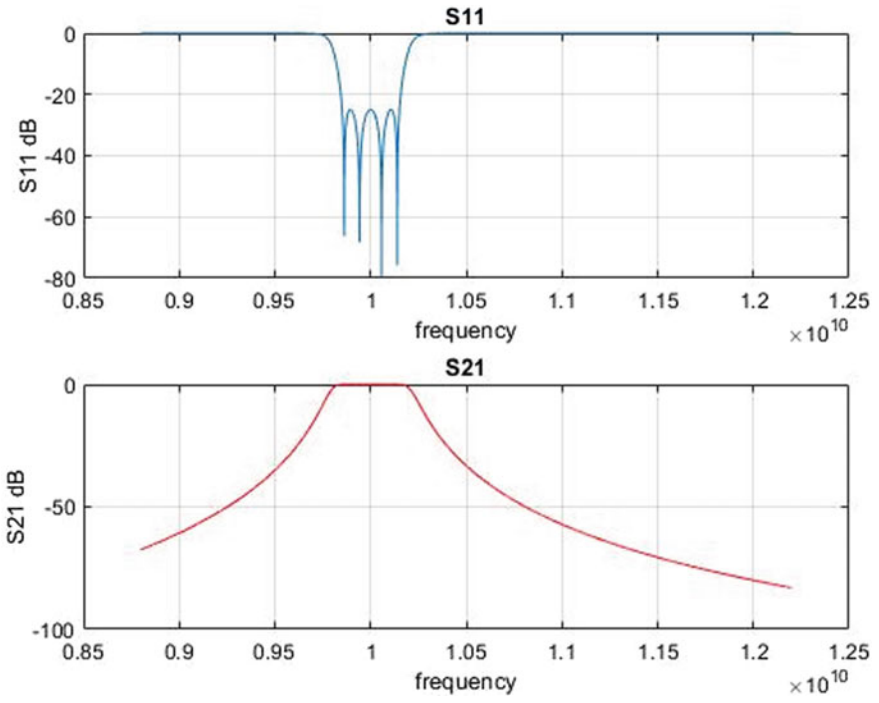
Fig. 6 Input/output return loss and insertion loss data obtained using MATLAB

Algorithm: input/output return loss and insertion loss of proposed filter

---

 Start
Step 1: Initialize two counters ii=count=1;
Step 2: Initialize start frequency(ff), end frequency(ff_end), increment;
Step 3: loop:
Step 4: Initialize center frequency as f0 and bandwidth as BW;
Step 5: Initialize the coupling matrix M
*Step 6: Compute lambda=(f0/BW) *(ff/f0-f0/ff)*
Step 7: Initialize R1 and R2
Step 8: Initialize R a 4x4 matrix which has x11= R1 and x44= R2 as its respective elements
Step 9: Initialize II as identity matrix
*Step 10: Compute a matrix AAA = lambda*II-R+M*
Step 11: Take the inverse of AAA
Step 12: Store inverse AAA_{11}, inverse AAA_{41}, inverseAAA_{44} to YY11, YY41 and YY44 respectively.
Step 13: Compute the following
               S11=1+2*i*R1*YY11;
               S21=-2*i*sqrt(R1*R2) *YY_{41};
               S22=S11;
               S12=S21;
Step 14: Create matrix SS= [S11 S12; S21 S22];
               and   str= [count ff S11 S12];
Step 15: Compute the following matrix for plotting
               ST (ii,1) = ff;
               ST (ii,2) =20*log10(S11);
               ST (ii,3) =20*log10(S12);
Step 16: Compute new start frequency ff=ff+increment;
               ii=ii+1;
               count=count+1;
Step 17: Check whether ff =ff_end
         if false
               go back Step 4;
Step 18: Plot the frequency vs Return Loss(S11) and Insertion Loss(S21)
 End

After simulating through MATLAB by changing all the design parameters, i.e., p = periodicity, a = minimum width, b = maximum width is shown all variations in Fig. 5a–f. After analyzing all the figures, it is concluded that if increase the periodicity (p), then the operating frequency also increases when all other parameters will remain constant. There is a nominal charge of operative frequency if change minimum width (a), maximum width (b) from the above analysis, another observation is the bandwidth of the passband and stopband. The bandwidth is gradually increased, if we decrease the value of periodicity. Next for Fig. 6, it has been established that the parameters for a proposed filter characteristic like the return loss (S_{11}) and insertion loss (S_{21}) are followed the approximate ideal filter for a particular predefined frequency band.

5   Application to Microwave Filter Design

In this section, we will describe a military application that involves radar technology. Radar is the real driver for microwave technology. Following this, we will

lock at satellite communication. This is followed by an examination of cellular communication.

5.1   Military Application

We know that Electronic Counter Measures (ECM) system and its associated Electronic Support Measures (ESM) are the critical parts of any military system [19]. The detection and classification of incoming radar signals by frequency, pules-width, and amplitude are detected by the ESM system. An analysis of the jamming process is possible with help of an ECM system. The bandpass filter can use to split the complete microwave frequency band into smaller subband. So, we can detect specific channels by individual frequency [20]. Typical specifications must be for a quarter duplexer and it is covering the range of the frequency 12–18, 8–12, 4–8 and 2–4 GHz with each channel. So, we can easily use our proposed microwave filter for this type of military application.

5.2   Satellite Communication

At the architecture of satellite communication [21], the uplink frequency ranges from 5.925 to 6.425 GHz. So, the uplink frequency band is 500 MHz at the base station of the satellite communication, after that it is amplified using a low-noise amplifier (LNA). Next, this signal frequency downgrades to make the downlink band from 3.7 to 4.2 GHz. Then, it is split into 12 channels with a 36 MHz frequency band using this bandpass filter. So, our proposed model can use this type of application for satellite communication.

5.3   Cellular Radio

The filter technology provides a significant role at cellular radio for both handsets and base- stations. The front-end configuration of this base—station is represented by the block diagram which is shown in Fig. 7 [22]. Here, the signal transmission and reception are performing simultaneously. The relative high-power signal is generating at the transmitter end and the reverse is happening at the receiver, i.e., the receiver needs to detect low-signal power. So, we can design our filter with appropriate configuration by changing different parameters, it acts as the transmitting (T_x) filter which must have a very high level of attenuation and low-passband insertion loss. Similarly, we can design the receiver (R_x) filter which consists of low insertion loss and high isolation in the transmitting band.
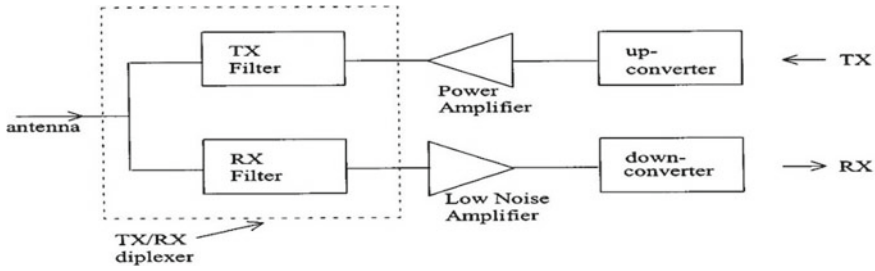
Fig. 7 Radio frequency front–end structure of a base-station at cellular radio

6 Conclusion

The analytical methods presented in this paper have been shown to provide accurate predictions of the simulation results. Also, it was demonstrated that the microstrip periodic structure can be used as a bandpass or bandstop filter. It has been verified that the position and width of a passband or a stopband can be controlled by adjusting the design parameters of the periodic structure such as b/a ratio and periodicity.

This type of microstrip line is used extensively because they provide a free and accessible surface on which solid-state devices can be placed. The open strip provides better interconnection features. They are used extensively to interconnect high-speed logic circuits in digital computers because they can provide the required uniform signal paths.

The fabrication of this filter, experimental framework and qualitative analysis are also under consideration along with the existing state-of-the-art module. And also, plain to include artificial intelligence (AI) and machine learning alone these filters.

References

1. Chowdhury, S.K., Bandyopadhyay, C.: Propagation of electromagnetic waves through a microstrip transmission line with sinusoidally varying width. AEU **35**, 135–137 (1981)
2. Mallick, A.K., Bhattacharyya, A.: Periodically reactive-loaded planar structure. AEU **43**, 370–373 (1989)
3. Collin, R.E.: Foundation for Microwave Engineering, Chap. 9. McGraw-Hill, New York (1966)
4. Slater, J.C.: Microwave Electronics. Van Nastrand Reinhold Company Mc Inc., Toronto (1951)
5. Itoh, T.: Applications of gratings in the dielectric waveguide for leaky-wave antenna and band-rejected filters. IEEE Trans. Microw. Theory Techniq. MTT **25**, 1134–1138 (1977)
6. Tsuji et al., M.: Guided wave experiments with dielectric waveguides having finite periodic corrugations. IEEE Trans. Microw. Theory Techniq. MIT **31**, 337–347 (1983)
7. Nair, N.V., Mallick, A.K.: An analysis of Width-modulated microstrip periodic structure. IEEE Trans. Microw. Theory Techniq. MTT **32**, 1984, 200–204 (1984)
8. Nagpal, M.: Studies on microstrip periodic structures with distributed loading, Ph.D. dissertation, IIT, Kharagpur (1983)

9. Zong, B.F., Wang, G.M., Zeng, H.Y., Wang, Y.W.: Compact and high-performance dual-band bandpass filter using resonator embedded scheme for WLANs. Radio Eng. Acad. J. **21**(4), 1050–1053 (2012)
10. Wu, Y., Guan, Y., Zhuang, Z., Wang, W., Liu, Y.: A novel tri-band T-junction impedance-transforming power divider with independent power division ratios. PLoS One (2017)
11. Martel, A.F.-P., Lujambio, A., Medina, F, Mesa, F., Boix, R.R.: A new differential line based on a periodic microstrip-CPW hybrid structure. In: IEEE MTT-S International Conference on Numerical Electromagnetic and Multiphysics Modeling and Optimization for RF, Microwave, and Terahertz Applications (NEMO), pp. 212–214 (2017)
12. Mezaal, Y.S., Eyyuboglu, H.T.: Investigation of new microstrip bandpass filter based on patch resonator with geometrical fractal slot. PLoS ONE **11**(4) (2016)
13. Pal, P., Sahana, B.C., Poray, J.: Filter characteristic of a triangular periodic transmission line in micro-strip structure. EasyChair Preprint 5321 (2021)
14. Liao, S.Y.: Microwave Devices and Circuits, 4th edn. Pearson Education Pvt. Ltd., New Delhi, pp. 380 (2003)
15. Liu, B.: Half Wavelength Open Circuit Stubs Filter Design. The University of Gavle (2013)
16. Atia, J.O.: Electronics and circuit analysis using MATLAB. CRC Press, Washington D.C. (1999)
17. http://mathworks.com/
18. Tomar, L., Gupta, S., Tomar, R., Bhartia, P.: Matlab-based computer-aided-design algorithm for designing stepped-impedance resonator low-pass filters in microstrip technology. Int. J. Wirel. Microw. Technol. **5**, 1–20 (2015)
19. Fano, R.M., Lawson, A.W.: Microwave transmission circuits. In: MIT Radiation Laboratory, vol. 9, no. 9, p. 10. McGraw-Hill, New York (1948)
20. Tsui, J.B.: Microwave Receivers with Electronic Warfare Applications. Wiley, New York (1992)
21. Kudsia, C., Cameron, R., Tang, W.: Innovations in microwave filters and multiplexing networks for communication satellite systems. IEEE Trans. Microwave Theory Tech. **40**, 1133–1149 (1992)
22. Yao, H.-W., Atia, A. E.: Temperature characteristics of combine resonators and filters. In: IEEE MTT-S International Microwave Symposium Digest, Phoenix, AZ, pp. 1475–1478 (2011)

Video-Based Heart Rate Measurement Using FastICA Algorithm

Sachin M. Karmuse, Arun L. Kakhandki, and Mallikarjun Anandhalli

Abstract Cardiovascular diseases are most important, and these diseases are causes of human death. Heart rate is one of the important parameters which define many important vital signs like blood pressure, respiration rate, oxygen saturation, and provides information of cardiovascular system in emergency situation. Nowadays, many contact and non-contact-based methods are available. This paper gives new idea about contactless heart rate measurement by FastICA. Recently, we have so many advancements in contactless physiological signal extraction and measurement. But proposed technology is more powerful to measure respiration and heart rate with the help of video. Effectiveness of proposed technique and overcoming previous technique will provide particular attention. We evaluate HR with the help of proposed technique in computer interaction session. For comparison purpose, HR was measured with finger probe sensor. Participant for our experiment was male gender from different age groups. To get better accuracy, we used machine learning approach.

Keywords Blood volume pulse (BVP) · Independent component analysis (ICA) · Joint approximate diagonalization of eigenmatrices (JADE) · Fast fixed-point independent component analysis algorithm (FastICA) · K-nearest neighbour (KNN)

1 Introduction

Heart rate is nothing but number of heart beats per minute. For healthy people, resting heart rate is in between 50 and 90 beats per minute. But it may vary as

S. M. Karmuse (✉)
D.K.T.E. Society's Textile and Engineering Institute, Ichalkaranji, India

A. L. Kakhandki
KLS Vishwanathrao Deshpande Institute of Technology, Haliyal, India

M. Anandhalli
KLS Gogte Institute of Technology, Belagavi, India

per the fitness of the person. Figure 1 shows heart rate for different age groups of male and female. Pumping of the heart enables the circulation of nutrient-rich blood and oxygen throughout the body. Heart rate defines the proper functioning of heart. Heart pumps blood throughout the body, so we can feel pulsating in blood vessels which are close to surface such as neck, forehead, wrist and upper arm. So, there are many diseases such as abnormal heart rhythms, congenital heart disease, heart valve disease, coronary artery disease (narrowing of the arteries), peripheral vascular disease, heart attack, heart failure, stroke, heart muscle disease (cardiomyopathy), rheumatic heart disease, pericardial disease and vascular disease that affect heart rate.

Figure 1 indicates the heart rate for different age groups of male and female [1]. People are more conscious about their personal health. Because of this, nowadays we have more number of mobile applications available in the market. All these applications have complex calculation and give vital information such as oxygen saturation, blood pressure, heart beat, respiratory rate and temperature. However, blood pressure and heart beat are most important and commonly measured parameters. Heart is consisting of muscles, and it conducts electrical signal. It consists of lower and upper chamber. Lower chamber is main pumping chamber. At right side of upper chamber, it has natural pacemaker. It is located near the superior arteries. Natural pacemaker is called sinoatrial (SA) node. Electrical impulse originates from natural pacemaker
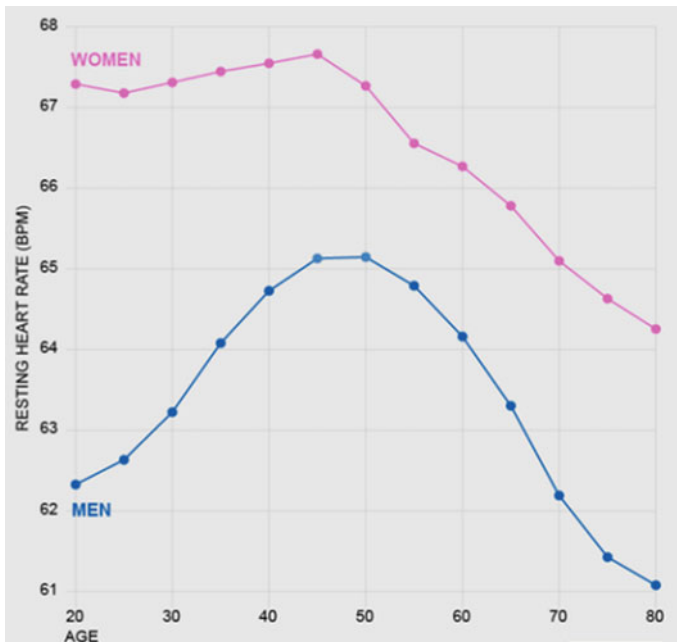
Fig. 1 Heart rate for male and female for different ages

and spreads out in upper chamber like a wave. This wave makes muscles alternately contracting and relaxing to pump blood through heart and define heart rate.

Standard method to measure heart rate is electrocardiogram (ECG) and pulse oximeter sensors [2]. These standard devices provide accurate heart rate, but the application of these devices can cause damage to elderly skin. Moreover, wearing these devices for long time duration can cause extreme discomfort to patients. Also, it cannot be used on neonates.

Electrocardiogram (ECG) and pulse oximeter sensors have complex hardware. Because of their complexity usage of these machines at home can become complicated and for that we require specialist's supervision. So, it is very important to measure heart rate without any contact between patients' skin with the device so that it can be measured without any discomfort.

From several years, researchers are focusing more on contactless systems for measurement of heart beat. Contactless system should be very easy to use with low cost. Still most of the contactless systems are available, but it required laboratory environments in offline situation and also it requires more modification before applied in real-time applications.

This paper presents contactless heart rate measurement using webcam. This method is simple and low cost to extract blood volume pulse (BVP) from facial video recording. For that, we can use independent component analysis for colour channel. We use Eulerian video magnification algorithm for better results. We use FastICA for analysis of colour channel because it has better performance than other ICA algorithm [3]. We use forehead as ROI because of uniform surface. Heart rate is quantified and compared with standard contact-based method. This method has more than 98% of accuracy. This method can be used to improve personal health care.

2 Literature Review

K. Kooij and M. Naber presented a paper entitled "An open-source remote heart rate imaging method with practical apparatus and algorithms" [4]. This proposed method is termed as remote photoplethysmography (rPPG). These studies have been focused on developing and publishing some of the basic open-source rPPG software, and the goal is to demonstrate the functionality of two experimental manipulations. First is the study of how exactly rPPG is able to detect a heart rate in the rest and compare this with the heart rate after exercise. And in second, rPPG is focused on the face, calves and ankles. Results are more accurate if rPPG is focused on face region. The accuracy of the rPPG has not been compared with previous studies using a similar combination of experiment.

Ming-Zher Poh, Daniel J. McDuff and Rosalind W. Picard presented a paper entitled "Advancements in Noncontact, Multiparameter Physiological Measurements Using a Webcam" [5]. This is one of the low-cost and simple methods for measuring different physiological parameters with the help of webcam. On video recording,

ICA is applied on the RGB colour channels and extracts the BVP from the facial ROI regions. In this, they used JADE for independent component analysis. Heart rate (HR) and respiratory rate were measured and approved by the competent authority.

Hamed Monkaresi, Rafael A. Calvo and Hong Yan proposed "A Machine Learning Approach to improve Contactless Heart Rate Monitoring Using a Webcam" [2]. This paper describes technique to measure HR in a specific controlled situation such as in exercise situation and in computer interaction session. During all these sessions, reading was also compared with HR which was measured at the same time using ECG device. The proposed work reduces root-mean-square error in the reading. With the help of machine learning techniques, build and train specific models for each participant. From the results, it is observed that KNN-based approach is better than other approach. KNN approach helps to select best independent component for HR measurement. By KNN technique, mean of absolute errors for HR measurement is reduced to 0.68 bpm. So KNN-based technique provides better result for HR estimation.

Daniel Lakens presented a paper entitled "Using a Smartphone to Measure Heart Rate Changes during Relived Happiness and Anger" [6]. This paper explains measurement of heart rate difference related to different emotions such as anger and happiness with the help of smartphone mobile application. This method measured HR outside the laboratory environment during different emotions such as anger and happiness. This is implemented by photoplethysmography. The result of this study shows smartphone usage to measure heart rate difference related to different emotions. Smartphone is a portable device. This device can be very easy to use, and for researchers, this device is a measurement tool for heart rate under different emotions. Because of smartphone, any inexperienced person can also collect physiological data. Camera was positioned at distance of 0.5–1.5 m from patient facial region to collect plethysmographic signals. This technique gives the relationship of heart rate under different emotions such as happiness and anger.

Hao-Yu Wu, Michael Rubinstein, Eugene Shih, John Guttag and William Freeman proposed "Eulerian Video Magnification for Revealing Subtle Changes in the World" [7]. We cannot see variations in videos with the open eye. This paper addresses video magnification technique, which we call "Eulerian video magnification". This method takes image frame from recorded video, and then, it was given to spatial decomposition, followed by temporal filtering. The output of temporal filtering was amplified to find hidden information. By this method, we can visualize hidden information. We can visualize blood flow which fills the face. This method also amplifies small motion which we cannot see through the naked eyes. This technique inputs the video and finds out small colour changes and imperceptible motions. With the help of spatio-temporal processing, we can magnify temporal colour change.

3 Methodology

3.1 Heart Rate Extraction Methodology

Volume of blood vessels which are present in facial region will change during every cardiovascular cycle. Because of this, there is a change in amount of reflected light. RGB colour sensors catch small changes which reflect on a plethysmographic signal. To measure heart rate from recorded videos, we developed a high-value acquisition algorithm using MATLAB 2017a. The main feature of this test is the three independent red, green and blue signals which are produced from the pixel present in forehead region.

3.1.1 Facial Recording

Video recording is the collection of image frame. A basic part of any video is image frame. This image frame shows the beginning and end of a video representing a quiet part of video. Figure 2 shows a block diagram of real-time HR monitoring system. In this, we can extract image frames at a specific time specified by the user [8]. It is important to note that the video adjustment must remain the same at each time. The image frame is released to get more stats. We use a video output algorithm that is used to maintain the same configuration, and it also reads image frames from video automatically.

3.1.2 Eulerian Video Magnification

The visual system of human has limitations. There are more number of signals which are informative, but still we cannot visualize. For example, because of blood circulation in human body the skin colour varies very slightly. But because of limitation of human visual system, this variation is not visible. With this invisible colour variation, we can extract BVP to find pulse rate. In a similar manner, motion with low amplitude in spatial domain is not possible for humans to see, so it is required to magnify video to understand invisible motion. This technique helps to reveal signal which is not visible signal in videos. Eulerian video magnification is a combination of temporal and spatial processing of videos which help to amplify small variations [7]. The basic approach of this video magnification is to consider the colour values at different time instants for different spatial locations. This method helps to amplify variations that are present in specified frequency band. The amplification is applied for facial region which gives the variation of red colour because of blood flows in facial region. Temporal filtering needs to raise input signal which should be above the noise form by quantization and camera sensor. This filtering by temporal approach helps to improve variation in colour. This also helps to improve motion of low amplitude. This method has a mathematical proof which describes how temporal filtering

Fig. 2 Heart rate extraction
methodology

Facial Recording

Eulerian Video Magnification

Face Tracking

Extract Forehead Region

Extract RGB Signal

Averaging & Detrending RGB Signal

Independent Component Analysis

Fast Fourier Transform

HR Prediction
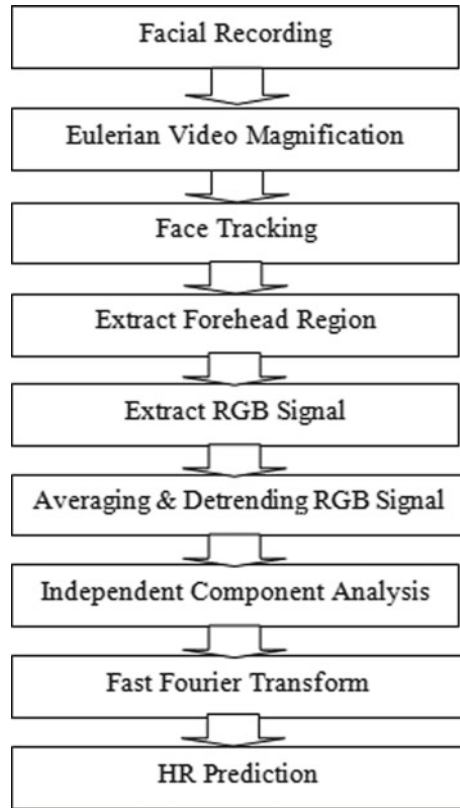
improves [9] the spatial motion which is not visible. This method has a multistage approach to amplify motion without facial tracking of feature or motion estimation.

3.1.3 Face Tracking and Extract Forehead Region

We have used MATLAB 2017a software for pre- and post-video processing for video analysis of physiological parameter. Our main aim is to recover the blood volume pulse from facial region. So, we use face tracker for detection of faces which are present in video frame. After tracking of face, we can find ROI from each video frame. We use OpenCV library which is free to find face location in video frame and collect coordinates of detected face location. This is free library, and it is also MATLAB-compatible. This OpenCV algorithm is also known as Viola and Jones algorithm [10]. This algorithm has cascade nature. Each cascade uses multiple classifiers which are applied for all ROI regions. For every stage, classifier is built with good boosting. Either all categories are transferred, which means that the region may contain faces, or the location may be rejected. To identify a good match of different sizes, the size of
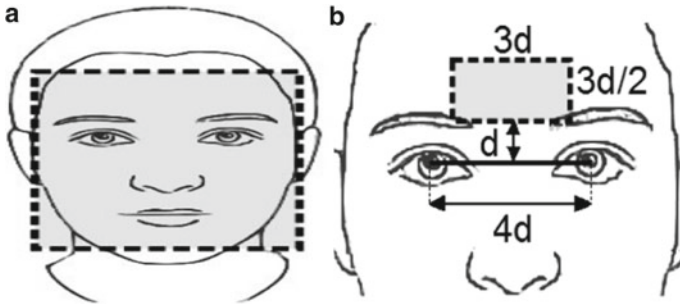
Fig. 3 a Whole face as ROI and **b** selected part of forehead as ROI

ROI is changed sequentially. The Viola and Jones algorithm gives x and y coordinate values of the detected surface. This algorithm also gives width and height of box which is around selected face. From this observed width, we can use 60% width and 100% height box as region of interest for further calculation. Face-to-face errors can be removed by taking face links to the previous frame and using them if no faces are found. When multiple faces are detected, then the algorithm selects face links that were very closest to the links from the previous image frame.

We use two ROI sizes (interesting regions) to analyse [11]. First, a rectangle of face region is selected. This rectangle is first frame of full video recording, which is shown in Fig. 3a. Throughout the sequence of images, the linking of the selected facial region remained constant. The second ROI (Fig. 3b) was a rectangular portion of the area on the forehead region. From pupils' coordinate, we can define forehead region. If $4d$ is distance between two pupils, forehead rectangle is at a distance of d. This rectangle has dimensions of $3d$ and $3d/2$.

3.1.4 Extract, Averaging and Detrending RGB Signal

The colour values of R, G and B are the basic elements of the R, G and B signals drawn from the ROI of the forehead region [12]. With 24-bit depth image, every pixel present in ROI image area has a 3×1 matrix. Then, three RGB signals are produced in two stages. First, from each frame the red, green and blue signals were separated. In the second stage, their averaging is carried out and the resulting image is represented in Fig. 4a.

For every image frame, the mean values of all pixels are calculated from forehead region. In this for i'th frame $y_{i,j}$ is the mean value of colour $j \in \{\text{red, green, blue}\}$ in the ROI.

For complete video, specific colour j signal can be given as $y_{j.}$ This original signal will vary because of multiple parameters. To compensate for this, the signal needs detrending [13]. We have
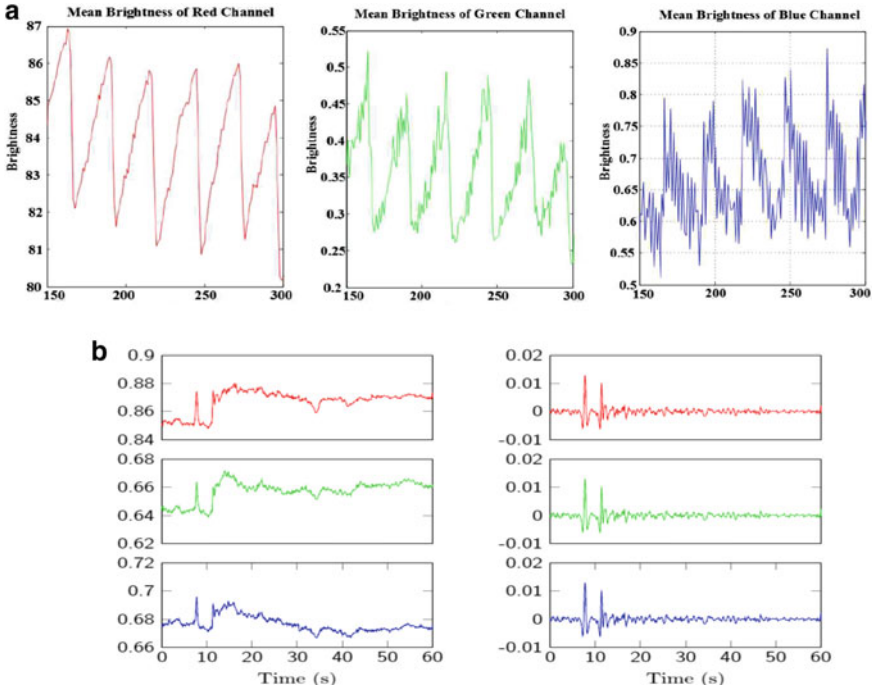
Fig. 4 a Different colour channel signals recorded by webcam, **b** average RGB signal and **c** detrended RGB signal

$$y'_{i,j} = y_{i,j} - \frac{1}{2n+1} \sum_{k=-n}^{n} y_{i+k,j} \tag{1}$$

where $y'_{i,j}$ is detrended signal of $y_{i,j}$ where the length of the moving average is $2n + 1$. Figure 4b shows average of RGB signal, and Fig. 4c shows RGB signal after detrending.

3.1.5 Independent Component Analysis (FastICA)

For blind source separation (BSS), we can use techniques of an independent component analysis. BSS works with the division of a set of integrated signals into a set of source signals without the slightest knowledge of the source signals. An example is a new situation where many people talk at a time in the same room and if someone records a sound in a same room with the help of more than one microphone available signals can be a mixture of multiple speech signals. The purpose of the BSS is to convert the signals into multiple set of signals containing each person's speech signal. Figure 5 shows the concept of BSS separation. For ICA model, we always

Fig. 5 BSS concept
illustration
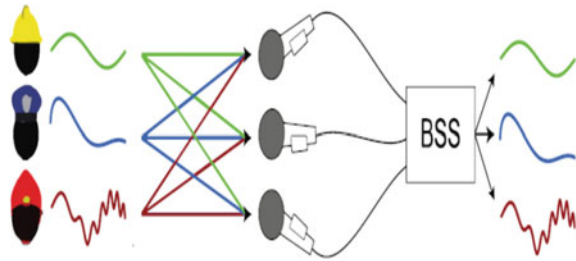
assume that source signal is statically independent and these signals have always non-Gaussian response.

For this, we assume original or source signal has linear mixture which is from observed signal, i.e.

$$x(t) = As(t) \tag{2}$$

where $x(t) = [x_1(t), x_2(t), \ldots, x_n(t)]^T$ is the observed signal, $s(t) = [s_1(t), s_2(t), \ldots s_m(t)]^T$ is the source signal and A is mixing matrix which has $n * m$ dimensions. The total number of recovered signal sources must be less than or equal to observed signal. In all applications, m should be equal to n. So, A is a matrix which has $n * m$ dimensions. ICA is mainly used to find inverse of matrix A which is denoted by W.

$$\tilde{s}(t) = Wx(t) \tag{3}$$

where $\tilde{s}(t) = [\tilde{s}_1(t), \tilde{s}_2(t), \ldots, \tilde{s}_n(t)]^T$ is an estimate signal of multiple source signals $s(t)$. As per central limit theorem, the addition of all independent components has more Gaussian response. Reducing the most visible signals and thus obtaining signal W source signals significantly increase the Gaussianity of every signal received. Since the sources are thought to be non-Gaussian, this is quite possible. Different algorithms use different non-Gaussianity measurement methods such as kurtosis. In our system, we use FastICA which is ICA algorithm for separation of blind source. Hyvarinen and Oja present idea of fast fixed point ICA algorithm [14]. This algorithm is mainly used to separate linear mixed signal which is from independent sources. The FastICA is computationally effective algorithm. This FastICA is mainly used for separation of blind source and analysis of independent components.

Mathematical Model

ICA model is defined by the equation

$$x(t) = As(t)$$

where $x(t)$ represents received signal which is a vector, A represents the mixing matrix and $s(t)$ represents the original source signal which is vector.

ICA algorithms such as JADE, Infomax, FastICA and SOBI focus to compute an un-mixing matrix W [12]. This matrix W is seen to be inverse of matrix A. So, we can redefine ICA model as:

$$W x(t) = y(t) \tag{4}$$

where $y(t)$ represents original signal which is approximate, and we can define $y(t)$ as:

$$y(t) = s(t) \tag{5}$$

All ICA algorithms use pre-processing step which is called as whitening. Whitened signals can be defined by $z(t)$. This whitening signal can be obtained by multiplying whitening matrix B with received signals:

$$z(t) = B x(t) \tag{6}$$

All above expressions are defined in matrix form. In almost all ICA algorithms, mathematical operations are performed on all received signals in the form of matrix, not in the vector form. FastICA is mainly used for parallel implementation. So, we can use FastICA in real time. This algorithm changes quickly as it seeks out each item individually. FastICA uses kurtosis of the scale of the independent material. Usually, whitening is performed on data prior to algorithm execution. The following process enables FastICA [14].

1. Set initial value for w_i (in random).
2. $w_i^+ = E\big(\emptyset'\big(w_i^T X\big)\big) w_i - E\big(x\emptyset\big(w_i^T X\big)\big)$
3. $w_i = \frac{w_i^+}{||w_i^+||}$
4. If $i = 1$, go to last step. Else go to next step.
5. $w_i^+ = w_i + \sum_{j=1}^{i-1}\big(w_i^T w_j w_j\big)$
6. $w_i = \frac{w_i^+}{||w_i^+||}$
7. If this is not converged, then go to step 2. If it converges, then go back to step 1 with $i = i + 1$ until all components are extracted.

3.1.6 Fast Fourier Transform

Finally, we used the fast Fourier transform (FFT) algorithm on the specified source signal to find the power spectrum. The pulse frequency was selected as the frequency corresponding to the high spectrum power within the active frequency band. In our experiment, we can set the range of frequency from 0.75 to 4 Hz. This range is

Fig. 6 FFT of ICA component
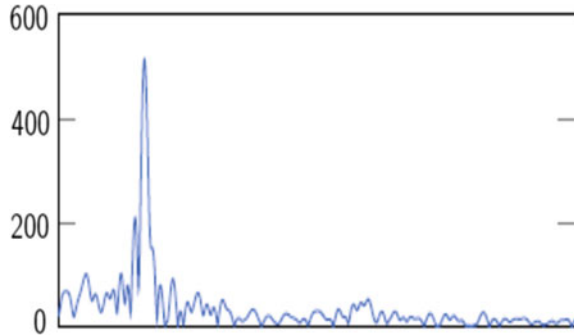
corresponding to heart beat from 45 to 240 bpm which is required for heart rate measurement. Figure 6 shows the FFT of the selected part of the ICA [9]. Similarly, we use finger probe sensor to obtain heart rate as a reference.

4 Result

4.1 Experimental Set-Up

Our main objective is to develop heart rate measurement system which should be low cost and easy to use, and it must have good accuracy. In this experiment, we have used webcam embedded in laptop. With the help of this webcam, we recorded videos for analysis purpose. All recorded videos have 24-bit depth with RGB information. We have recorded videos with 30 frames per second. All these videos have same resolution of 640×480 and AVI format. Twenty-four male participants from different age groups participated in this experiment. The readings are taken under doctor's observation. All participants are of varying skin colour. For all experiments, we used blood volume pulse (BVP) sensor for reference reading. This sensor is used with finger probe. This probe is used for validation at 256 Hz. The experiments were conducted in room which had only sunlight as source of light.

Experimental set-up is shown in Fig. 7. The participants were requested to sit in front of a laptop with approximate distance of 0.5 m from the built-in webcam. Videos were recorded for all participants. At the time of recording, participants were instructed to sit in front of webcam and to keep the hand wearing the BVP sensor still.

The photograph of the face was taken with a webcam. To ensure the accuracy of this real-time measurement system, finger probe sensor which is commercially available was used to measure a participant's heart rate. We used root-mean-square error as performance parameter. We have recorded the heart rate of different patients by proposed method and commercial method, and the result shows that there is a good correlation between the heart rates from the proposed route and the commercial route.

Fig. 7 Experimental set-up
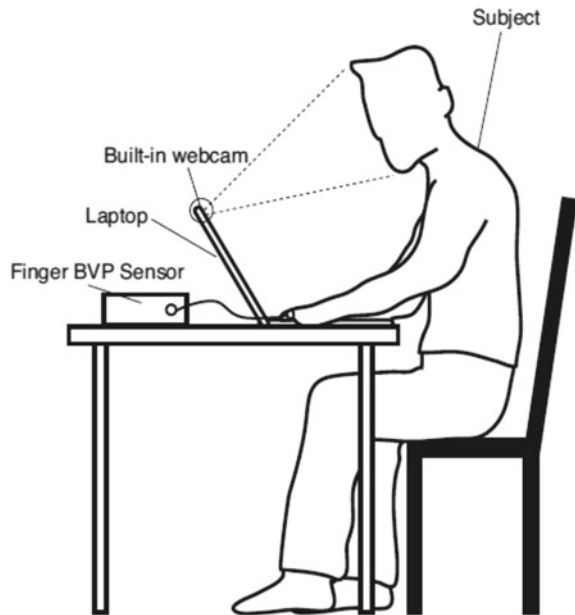
Moreover, heart rates are recorded in clinical rooms under the doctor's supervision. Table 1 shows the error percentage of the heart rate from commercial method and the heart rate from proposed method. The results show that proposed technique has 98.11% accuracy according to error formula. Earlier method required video recording of 1–2 min. But this proposed method required video recording of 30 s.

$$\text{Error} = \frac{\text{HR(clinical)} - \text{HR(proposed)}}{\text{HR(clinical)}} * 100 \tag{7}$$

The accuracy of any measurement technique can be determined by deviation of the readings from the mean value. Therefore, we have calculated the standard deviation of the proposed measuring technique. For this, as shown in Table 2, we had taken consecutively ten readings of the heart rate of the subject in a small interval of time, i.e. each reading at an interval of 5 minutes. The actual heart rate would be most probably very much closer to the mean value of the readings. Therefore, in this scenario standard deviation should be as small as possible. For the proposed method, the standard deviation comes to 1.344, which is lesser than that of other techniques [2].

Comparative study

The proposed method is tested with remote HR measurement for 24 participants from different age groups. The results of the method are compared with standard state of the art to define the robustness, accuracy and error rate of the proposed method. The results of our study are compared with Poh et al.'s [5] and Hamed Monkaresi's

Table 1 Error percentage for a different age male gender

S. no.	Age	Heart rate clinical	Heart rate proposed	Error (%)	Square error (%)
1	18	70	69.75	0.25	0.061
2	20	71	72.1	− 1.54	2.372
3	22	71	69.8	1.69	2.856
4	24	74	73.2	1.08	1.167
5	26	69	70.1	− 1.59	2.529
6	28	72	71.8	0.27	0.072
7	30	70	68.1	2.63	6.917
8	32	69	69.5	− 0.72	0.519
9	36	72	73.4	− 1.94	3.763
10	38	74	76.1	− 2.83	8.009
11	40	72	73.3	− 1.81	3.277
12	42	70	68.2	2.57	6.605
13	46	74	75.3	− 1.76	3.098
14	48	72	71.3	0.97	0.941
15	50	71	69.5	2.11	4.452
16	52	68	69.3	− 1.91	3.648
17	56	70	69.3	1	1
18	58	72	70.8	1.67	2.789
19	60	72	73.3	− 1.81	3.277
20	62	73	71.1	1.9	3.610
21	65	70	71.9	− 2.71	7.344
22	67	72	73.8	− 2.50	6.250
23	68	75	73.1	2.53	6.401
24	70	74	76.1	− 2.1	4.410
Total					85.367

Mean square error $= \frac{85.367}{24} = 3.56$

Root-mean-square error $= 1.89$

Accuracy $= (100 - 1.89) \% = 98.11\%$

method [2]. Poh et al.'s method [5] uses JADE ICA algorithm. Hamed Monkaresi has two different studies. First study of Hamed Monkaresi uses ICA (JADE) + KNN, and in second study, they use ICA (JADE) + Regression. This comparison is shown in Table 3. RMSE and SD of proposed work value are 1.89 and 1.344, respectively, which is lower than other methods. Hence, the proposed algorithm outperforms over other studies.

Table 2 Calculation of standard deviation

Reading	Heart rate	Difference with mean value	Square value
1	73.02	1.292	1.669264
2	71.76	0.032	0.001024
3	74.03	2.302	5.299204
4	72.34	0.612	0.374544
5	71.82	0.092	0.008464
6	72.11	0.382	0.145924
7	70.04	− 1.688	2.849344
8	72.44	0.712	0.506944
9	69.51	− 2.218	4.919524
10	70.21	− 1.518	2.304324
Total			18.07856

Mean square value $= \frac{18.07856}{10} = 1.807856$

Standard deviation (SD) $= 1.344$

Table 3 Comparison of different algorithm results with our study

S. no.	Parameters	Poh et al.'s study	Hamed first study	Hamed second study	Proposed method
1	Method	ICA (JADE)	ICA (JADE) + KNN	ICA (JADE) + regression	Eulerian + ICA (FastICA)
2	Recording rate	15	30	30	30
3	Experiment length (second)	60	60	60	30
4	Mean bias	− 0.05	0.86	0.65	0.32
5	Standard deviation (SD)	2.29	4.33	13.70	1.344
6	RMSE	2.29	4.33	13.69	1.89
7	Correlation coefficient	0.98	0.99	0.94	0.99

5   Conclusion

The contactless and real-time HR extraction method is described in this paper. For our experiment, we used facial recorded video. This method is easy to use, inexpensive and comfortable. The colour variation in forehead region is because of BVP. From this colour variation, we can extract HR. For this, we use integrated camera of laptop. Experiment is conducted in indoor natural environment with natural ambient light. According to experiment, values are shown in table and we have achieved highest closeness with standard measurement. This contactless heart rate measurement with

FastICA is a promising technology which helps to improve healthcare system. Due to the wide availability of webcams, it can be used for indoor applications.

References

1. Rahman, H. et al.: Real time heart rate monitoring from facial RGB color video using webcam. In: The 29th Annual Workshop of the Swedish Artificial Intelligence Society (SAIS), 2–3 June 2016, Malmö, Sweden. No. 129. Linköping University Electronic Press, 2016
2. Monkaresi, H., Calvo, R.A., Yan, H.: A machine learning approach to improve contactless heart rate monitoring using a webcam. IEEE J. Biomed. Health Inform. **18**(4), 1153–1160 (2013)
3. Sahonero, G., Calderon, H.: A comparison of SOBI, FastICA, JADE and Infomax algorithms. In: International Multi-conference on Complexity, Informatics and Cybernetics, Orlando, Florida, US , March 2017
4. van der Kooij, K.M., Naber, M.: An open-source remote heart rate imaging method with practical apparatus and algorithms. Behavior Res. Methods **51**, 2106–2119 (2019)
5. Poh, M.-Z., McDuff, D.J., Picard, R.W.: Advancements in noncontact, multiparameter physiological measurements using a webcam. IEEE Trans. Biomed. Eng. **58**(1), 7–11 (2010)
6. Lakens, D.: Using a smartphone to measure heart rate changes during relived happiness and anger. IEEE Trans. Affect. Comput. **4**(2), 238–241 (2013)
7. Wu, H.-Y., Rubinstein, M., Shih, E., Guttag, J., Durand, F., Freeman, W.T.: Eulerian video magnification for revealing subtle changes in the world. ACM Trans. Graph. **31**(4) (2012)
8. Liu, T.M., Zhang, H.J.: A novel video key frame extraction algorithm. In: IEEE International Symposium on Circuits and Systems, 2002. ISCAS 2002, vol. 4, pp. IV-149–IV-152
9. Buijs, H., Pomerleau, A., Fournier, M., Tam, W.: Implementation of a fast Fourier transform (FFT) for image processing applications. IEEE Trans. Acoust. Speech Signal Proc. **22**, 420–424 (1974)
10. Viola, P., Jones, M.: Rapid object detection using a boosted cascade of simple features. Proc. IEEE Conf. Comput. Vis. Pattern Recogn. I-511–I-518 (2001)
11. Deng-feng, Z., Shui-sheng, Y., Shaohua, H.: Research on application of region-of interest in face detection. In: 2010 Third International Symposium on Intelligent Information Technology and Security Informatics (IITSI), pp. 192–194 (2010)
12. Akti, G., Goularas, D.: Frequency component extraction from color images for specific sound transformation and analysis. In: 2012 3rd International Conference on Image Processing Theory, Tools and Applications (IPTA), pp. 253–258, 2012
13. Tarvainen, M.P., Ranta-aho, P.O., Karjalainen, P.A.: An advanced detrending method with application to HRV analysis. IEEE Trans. Biomed. Eng. **49**, 172–175 (2002)
14. Sahonero-Alvarez, G., Calderon, H.: A comparison of SOBI, FastICA, JADE and Infomax algorithms. In: Proceedings of the 8th International Multi-Conference on Complexity, Informatics and Cybernetics (IMCIC 2017)

Navigation Enabling Application for Blind People

Atindra Nath Sarkar, Jayita Saha, Pamela Das, Ritu Kumari, Tulika Chakraborty, and Naiwrita Dey

Abstract This paper proposes an assistive navigation application system to help visually impaired persons with independent travel in indoor. The proposed system is implemented in two parts: first, the obstacle detection is done by object identification using image processing and the images are stored in cloud further. You only look once (YOLO) version 3 which is a fully convolutional neural network (FCNN) is used for object identification. Twenty classes are considered with 2600 number of image samples. The application assembly is developed in android studio in Java platform. The application is named as "NETRA". The blind person has to be logged in to the application beforehand. Later with text-to-speech conversion, the blind individual will be navigated. In the present work, the object identification using image processing and the overall application assembly is shown and discussed.

Keywords Navigation · Image processing · YOLO · Cloud · Application

1 Introduction

According to WHO, the aggregate of visually disabled individuals is approximately 285 million worldwide, of whom 39 million are totally sightless. A large part of these people lives by themselves due to their children residing abroad for their jobs. Some of the major problem faced by them in their daily life is navigating alone, which may arise due to streets having heavy traffics, potholes and stairs in the path and collision with other pedestrians. The traditional solution for a long time was to use the white cane or walking with the guide dogs. With the advancement of technologies, many new methods are coming up every day, which are more reliable and less embarrassing. J. S. Sierra and J. S. R. Togores designed an application with special controls (buttons, sliders, tables, etc.) provided with Low Vision Mobile

A. N. Sarkar · Jayita Saha · P. Das · R. Kumari · T. Chakraborty
Department of AEIE, RCCIIT, Kolkata, India

N. Dey (✉)
Department of ECE, RCCIIT, Kolkata, India

App Portal for aged and visually impaired users to access mobile applications on their smartphones. Though this application would help the users to navigate on the smartphone, they will not be of any help in the real-world navigation [1]. A face detection framework has been developed by P. Viola and M. Jones, called robust real-time face detection, which is able to process images swiftly while gaining high detection rates [2]. Various algorithms such as AdaBoost and methods for merging succeeding more composite classifiers in a cascade form which enhances the pace of the detector by concentrating on optimistic areas of the image have also been used in this work. S. K. Chadalawada has done real-time object detection and recognition—using deep learning methods, which identifies, evaluates and compares suitable and highly efficient deep learning models for real-time object recognition and tracking, concluding YOLOv3 as the best algorithm [3]. Route tracking on Android device is done by J. Samualby building a monitoring Android application using object GPS devices to determine its present and previous locations at particular intervals. Unlike other tracking systems, this will facilitate its users to create bookmarks of present locations and to return back from anywhere using Google Maps APIs in case they forget the previous location [4]. In this work, text-to-speech and speech-to-text systems having various steps (speech recognition, feature extraction, language translation, etc.) have been used along with various analysis models and algorithms to process the data and produce the desired outputs [5]. Glass-type wearable terminal using an ultrasonic sensor with a pair of earphones has been designed by the authors which aids not only the user, but also the other pedestrians from collision. Multi agent simulation study has validated the efficiency of the proposed system [6]. A wearable electronic travel assistance for visually impaired persons using HC-SR04, Raspberry Pi 2 computer for controlling the ultrasonic sensors and translating the data from the output to instructions heard by the sightless user using Bluetooth headphone, has been developed in this project [7]. A smart cap for helping the sightless to navigate freely using real-time object detection and identification using Raspberry Pi-3 with a pre-trained convolutional neural network (CNN) model has been developed in this project using TensorFlow using NoIR camera [8]. The authors of this paper have studied and reviewed the ETAS for people who are visually impaired, and a new wearable system CASBliP has been described in this paper [9]. Object detection with R-CNN using category-independent region proposals, convolutional neural network that extracts a predetermined length feature vector from each area and set of class-specific linear SVMs, has been done in this project [10]. Real-time-based object detection, using SSD algorithms, mAP and FPS as standard parameters for object detection, has been done in this work [11]. Along with this study, a novel method of navigation assistance tools for blind people has been proposed in this work.

The paper is ordered as follows. In Sect. 2, the overall methodology of the work is explained. In Sect. 3, object detection and identification are discussed. Image storage in cloud is discussed in Sect. 4. In Sect. 5, the real-time application assembly is presented followed by a conclusive statement along with future extension of this work. References are defined at the end.
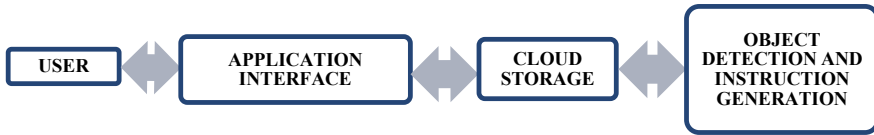
Fig. 1 Schematic overview of the methodology used

2 Methodology

The proposed system will include a mobile application that can interact with the user and send the data to the cloud storage where object detection is performed and required results are returned back to the user. At first, the user needs to enter the login credentials. Once the authentication is verified, the application, enabled with real-time location tracking, activates speech recognizer for converting speech to text. Then, the application can be used to capture images simultaneously and upload to the cloud storage. A fully convolutional neural network, called YOLOv3, is used to detect the obstacles or objects in the images. For this, a custom dataset comprising of 2600 images is created which is used to train the model. The images obtained from the mobile application are passed through the trained model, and output in the form of text is stored back to the cloud. This information is transferred to the mobile application which converts the text to speech and gives the required instruction to the user. Figure 1 shows the overall block diagram of the system.

3 Object Detection and Identification

Object detection is a computer technology that is associated with image processing and computer vision. Instances of the interpreted objects of a definite class present in a digital image or in videos are detected in this process. It comprises two parts—object classification (what objects?) and object localization (where are the objects located?). Well-researched fields of the object detection accommodate face detection in addition to pedestrian detection. The two major methods of object detection are machine learning construct and deep learning approaches.

In machine learning, it is necessary to define prior traits and then use a method like support vector machine (SVM) for the categorization. On the contrary, deep learning methods can detect entities without even explicitly defining features and are constructed on convolutional neural networks (CNNs). G. Shrestha et al. had earlier used CNN-based method for agricultural productivity through detection of plant diseases [12].

YOLOv3 is used in this proposed model for image processing. Figure 2 sums up the entire process.

```
┌──────────┐   ┌────────────┐   ┌────────────┐   ┌────────────┐
│ CREATING │   │  CLONING,  │   │CONFIGURING │   │  CREATING  │
│ DATABASE │⇒ │CONFIGURING │⇒ │YOLOV3_CUSTOM_│⇒│OBJECT NAMES│
│          │   │    AND     │   │ TRAIN.CFG  │   │FILEIN DATA │
│          │   │ COMPILING  │   │            │   │   FOLDER   │
│          │   │  DARKNET   │   │            │   │            │
└──────────┘   └────────────┘   └────────────┘   └────────────┘
                                                        ⇓
┌──────────┐   ┌────────────┐   ┌────────────┐   ┌────────────┐
│IMAGES ARE│   │  TRAINED   │   │TRAINING THE│   │  CREATING  │
│ OBTAINED │   │WEIGHTS ARE │   │   MODEL ON │   │FOLDER FOR  │
│   FROM   │⇐ │SAVED TO THE│⇐ │CUSTOM DATA │⇐ │  IMAGES,   │
│DISTRIBUTION│ │  BACKUP    │   │    SET     │   │TRAIN.TXT AND│
│  BUCKET  │   │  FOLDER    │   │            │   │  VAL.TXT   │
└──────────┘   └────────────┘   └────────────┘   └────────────┘
     ⇓
┌──────────┐   ┌────────────┐   ┌──────────────────────────────────┐
│IMAGES ARE│   │  OBJECTS   │   │FINAL INSTRUCTION TO BE SENT BACK,│
│RUN THROUGH│⇒│    ARE     │⇒ │   GENERATED IN TEXT FORMAT       │
│ TRAINED  │   │ DETECTED   │   │                                  │
│ DETECTOR │   │            │   │                                  │
└──────────┘   └────────────┘   └──────────────────────────────────┘
```
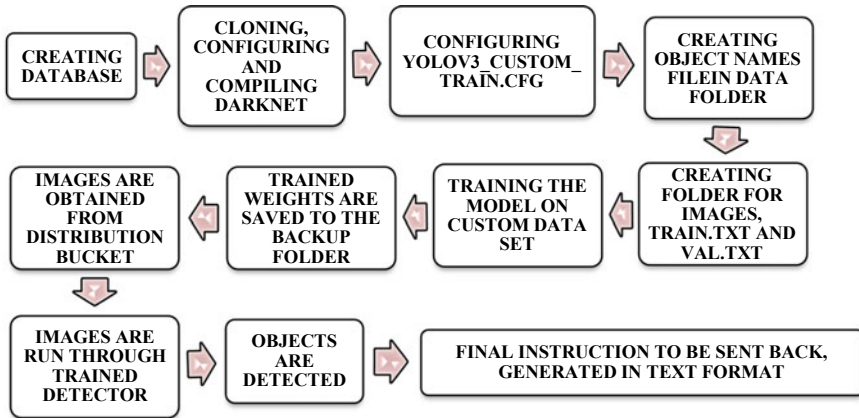
Fig. 2 Object detection process

3.1 YOLOv3

You only look once (YOLO) version 3 is an algorithm used for object detection. It is a fully convolutional neural network (FCNN) that can be used in real-time detection purposes without too much loss in accuracy. The whole image is being forwarded by YOLOv3 only once through the network. Features provided by YOLOv3:

- Ease to integrate with an OpenCV application.
- OpenCV CPU version is $9\times$ faster.
- Support**s** Python.

   Features of the model:

- It comprises 75 convolutional layers, including up-sampling and skip connection layers.
- It uses Darknet53 framework (the layers are shown in Table 1) to train neural networks. In detection process, another 53 layers are stacked onto the original 53 layers, making it a 106-layer fully convolutional network.
- Leaky ReLU is chosen as activation function. It is given by $f(x) = \max(0.01x, x)$.

- 1×1 detection kernels are applied on feature maps of three dissimilar sizes at three separate positions in the network. The detection kernel form is given by $1 \times 1 \times (B \times (5 + C))$ where B represents the count of bounding boxes a cell on the feature map can extract and C is the count of object classes. Figure 3 contains the details of the same.

   If anyone uses 1×1 convolutions, the dimensions of the prediction map will be completely the proportion of the feature map. In YOLOv3, prediction map is explicated for each cell to predict a definite number of bounding boxes. It can be

Table 1 Layers of Darknet53

|	Type	Filters	Size	Output
	Convolution	32	3 × 3	256 × 256
	Convolution	64	3 × 3/2	128 × 128
	Convolution	32	1 × 1	
1 ×	Convolution	64	3 × 3	
	Residual			128 × 128
	Convolution	128	3 × 3/2	64 × 64
	Convolution	64	1 × 1	
2 ×	Convolution	128	3 × 3	
	Residual			64 × 64
	Convolution	256	3 × 3/2	32 × 32
	Convolution	128	1 × 1	
8 ×	Convolution	265	3 × 3	
	Residual			32 × 32
	Convolution	512	3 × 3/2	16 × 16
	Convolution	256	1 × 1	
8 ×	Convolution	512	3 × 3	
	Residual			16 × 16
	Convolution	1024	3 × 3/2	8 × 8
	Convolution	512	1 × 1	
4 ×	Convolution	1024	3 × 3	
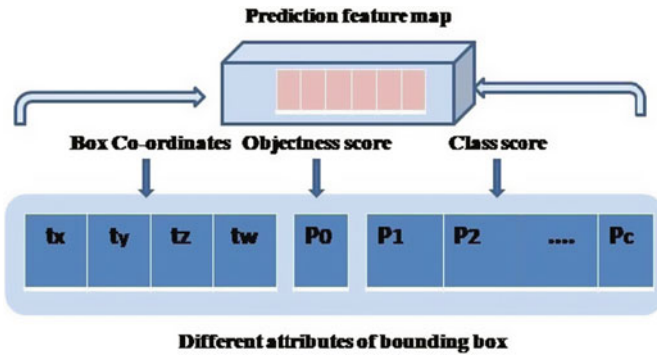
Fig. 3 Object detection process

assumed that depth-wise, there are (B x (5 + C)) appearances in a fixed feature map and the number of bounding boxes that every cell may predict is presented by *B*. Therefore, every one of these *B* bounding boxes will be restricted in determining a particular type of entity. Every bounding box has 5 + C traits, which are explained as the dimensions, centre coordinates, the objectness score and class confidences for each bounding box. Three bounding boxes for each cell will be prognosticated by YOLOv3. User can anticipate that every cell of that feature map will identify an entity with one of the bounding boxes supposing that the centre of that entity resides well in the area of the cell. For example, if the input image is of 416 × 416, with network stride 32, the feature map's dimensional size will be of 13 × 13. The inserted image can be split into cells of 13 × 13.

On the input image, the cell which accommodates the centre of the ground truth box of the object is accountable for predicting the object. User can allocate the 7th cell of 7th row on the feature map accountable for distinguishing the object. Now, by this cell three bounding boxes can be predicted.

- Pooling layers are not present; instead, a stride 2 convolutional layer is deployed to facilitate down-sampling.
- This aids in ceasing the low-level loss of features that arises due to pooling. In case of YOLO, the prediction is made by using a convolutional layer which uses 1 × 1 convolutions. It uses 3 anchor boxes for each scale, thus 9 in total. For example, for an image of size of 416 × 416, YOLOv3 predicts ((52 × 52) + (26 × 26) + (13 × 13)) = 10647 bounding boxes.

A group of preset default bounding boxes of a certain height and width are called anchor boxes, which can predict the height and width of a bounding box, whereas actually, during training, it can conduct to unstable gradients. In spite of that, log-space transforms are predicted by almost all modern object detectors. Later on, these transforms are put to the anchor boxes for acquiring the output. In YOLOv3, there are 3 anchors. Among them there are 3 bounding boxes per cell for outcome prediction purpose. The bounding box which will be accountable for detection of the required entity will have the highest IoU with respect to the ground truth box. The below-mentioned formulae explain how the output of the network is transfigured to acquire predictions of the bounding box.

$$b_x = \sigma(t_x) + c_x, by = \sigma(t_y) + c_y, b_z = \sigma(t_z) + c_z \tag{1}$$

$$b_w = p_w e^{tw}, b_h = p_h e^{th} \tag{2}$$

where b_x, b_y are the x, y centre coordinates, and b_w, b_h are the width and height of prediction. T_x, t_y, t_w, t_h are the results of the network output. c_x, c_y are the top-left grid coordinates. p_w, p_h are size of the anchors of the boxes. Generally, absolute entire coordinates of a bounding box's centre are not perceived by YOLOv3. Rather, offsets are predicted by it which:
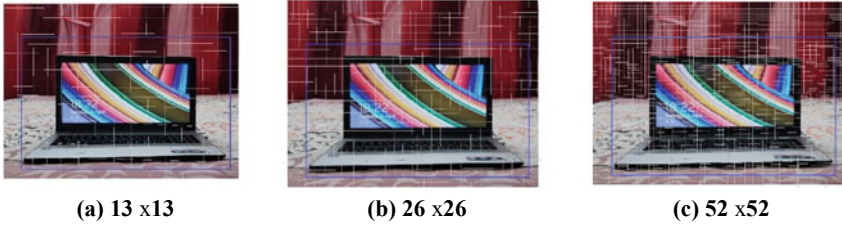
| (a) 13 x13 | (b) 26 x26 | (c) 52 x52 |

Fig. 4 Prediction feature maps using different scales

- are relative to the grid cell's top-left corner that predicts the entity.
- are normalized by the size of the feature map's cell, that is, 1.

For instance, if the prediction for centre in an image is (0.4, 0.7), as the top-left coordinates of the bounding cell are, is (6, 6), then the centre lies at (6.4, 6.7), on the 13 × 13 feature map. The expectation of an entity that is accommodated within a bounding box is represented by object score. It is mostly one for the centre and its neighbouring grids, but almost zero for those corner grids.

The objectness score then goes through the sigmoid, after which it is explicated as probability. The probabilities of the entities detected that belongs to definite classes (person, dog, car, plant, etc.) are represented by class confidences. Across three different scales, YOLOv3 can make prediction. Feature maps with strides of 32, 16 and 8 are chosen for making detection, which implies, for an input of 416 × 416, user can train to detect in order of 13 × 13, 26 × 26 and 52 × 52 (see Fig. 4).

Down-sampling is performed on the inserted image by the network till first detection layer. Here, stride 32 feature maps are used. Later on, up-sampling by an element of 2 is done on the layers and joined with feature maps of the preceding layers which have alike feature map magnitudes. Repetitions occur at layers with stride 16 and finally with stride 8. At every step, three bounding boxes are estimated by every cell with three anchors, so the entire number of anchors exerted is nine.

- The finest bounding box for an entity is determined by deploying non-max suppression.

3.2 Dataset Used

A custom image dataset is prepared. Dataset details has been listed in Table 2. The process of image annotation is shown in Fig. 5.

Table 2 Custom dataset details

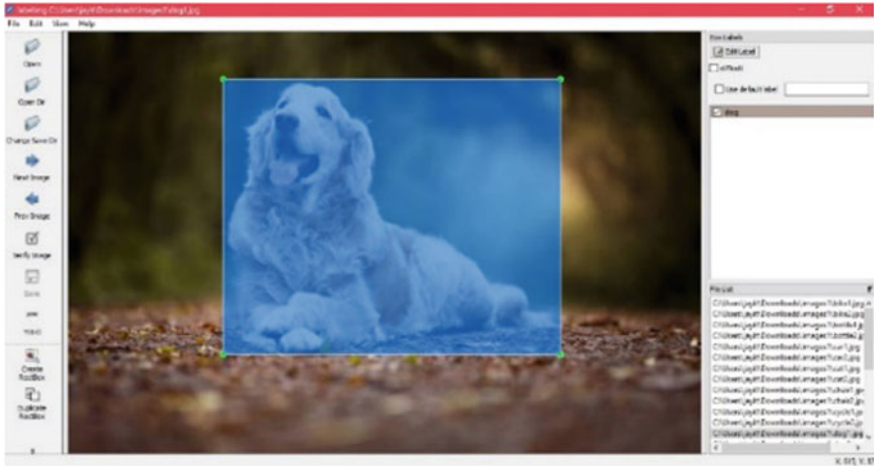|	
Number of object classes	20
Total number of images used	2600
Number of images in train.txt (70% of total images)	1820
Number of images in val.txt (30% of total images)	780

Fig. 5 Object marking using labelImg for annotation

The training steps for object detection are creating dataset, cloning, configuring and compiling Darknet, configuring Yolov3.cfg file, creating object.names file inside the data folder (it contains count of entities, the address of train.txt, test.txt, object.names files and the address where the YOLO weights are to be stored), creating folder for images and creating train.txt file in data folder. After the model is trained, it will be able to detect random objects. (A pre-trained COCO dataset can also be used instead, which contains 80 labels including people, cycles, dogs, etc.)

Generating instruction for navigation guidance. Based on the output of the depth estimation model, final text outputs such as "obstacle ahead" or "<detected object> is on your left" will be generated.

4 Image Storage Cloud

Cloud storage is used to reserve data, files, images, etc., in an external area which can be retrieved through the Internet. After receiving the request from the user, the images are uploaded to the specific area of cloud storage. The V4 signing process is used to create Cloud Storage RSA key signed URLs into the workflow of the app for uploading images to the Google Cloud. After validation, the image files is sent to the Google Colab for image processing. A service hosted is implemented on Google Cloud platform. Using this, a user can upload images constantly. In the present work, a serverless architecture is used. Using this architecture, an unspecified number of user can access cloud resources seamlessly. The requirements involved to implement this service are—managed service, authenticated users, validation of the contents. After receiving request from the user, a signed URL is generated. Signed URL allows
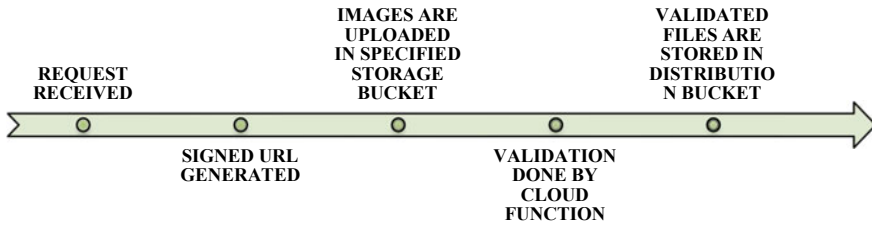
IMAGES ARE
UPLOADED
IN SPECIFIED
STORAGE
BUCKET

VALIDATED
FILES ARE
STORED IN
DISTRIBUTIO
N BUCKET

REQUEST
RECEIVED

SIGNED URL
GENERATED

VALIDATION
DONE BY
CLOUD
FUNCTION

Fig. 6 Cloud storage workflow

PUT request that can be executed for a specific cloud storage bucket. Images can be uploaded in the specific bucket. After uploading images, validation is done by cloud function. Next, the validated files are uploaded in the distribution bucket. Figure 6 shows the workflow.

The steps involved in generation of signed URL:

- At first, a new service account is created.
- Then, a necessary string is created for generating a signed URL.
- Next, PUT is chosen for cloud storage.
- At the end, the bucket and object are specified. Storage, buckets.get, storage.objects.create, storage.objects.has are granted for the same.

5 Application Assembly

Entire process of developing application can be summarized in certain steps that has been carried out, and it is given below. Figure 7 shows the block diagram of the same.

Step 1   Creating the app interface in Android studio using Java—In the Main Activity Page, "Intent" object is created and "setOnClickListener" method is used to move to the next page. For Login Activity Page, two "EditText

START
APPLICATION

VERIFICATION
OF LOGIN
CREDENTIALS

SPEECH RECOGNISER OBJECT
INITIALISED AND LISTENER
METHOD IS SET TO CONVERT
SPEECH TO TEXT

DEVICE CAMERA CAPTURES
IMAGES AND SIGNED URL
GENERATION REQUEST IS
SENT TO CLOUD

FINAL
INSTRUCTION
TEXT IS
CONVERTED TO
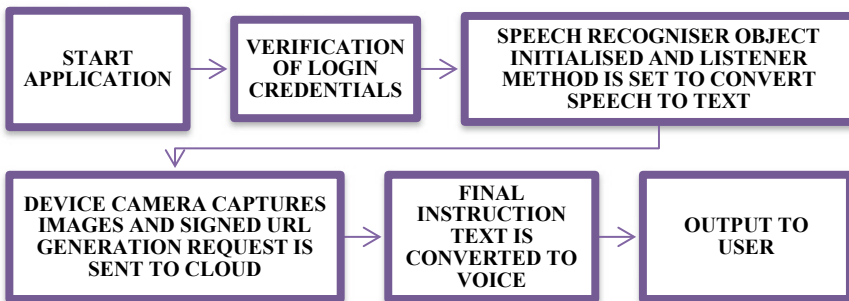VOICE

OUTPUT TO
USER

Fig. 7 Mobile application workflow

fields" (username and password) are sent to the cloud using Volley Library API. Authorization success/failure status is collected in JSON Parser file in XML format. The device camera is used to capture one image per second which is simultaneously uploaded to the cloud using the signed URL method.

Step 2 Taking voice commands (speech-to-text)—After initializing the speech recognizer object, the "Intent" object is created and language is evaluated. Next, the listener method is set to convert speech to text.
Step 3 Returning voice information (text-to-speech).
Step 4 Permissions are required for Google Maps, device camera, text, messaging, calls and device microphone.

6 Result

Figure 8 shows the application interface, and Figs. 9 and 10 show the object detection.

7 Conclusion

A mobile application is implemented to assist blind people to be used in indoor as presented here. Obstacle detection and identification are carried out with image processing. The effectiveness of the implemented system is experimented within the room with blindfolded, and the mobile application is worked properly in synchronization with object detection. Further work is to be done to test staircase identification and also for outside locations to make the system more robust and functional.
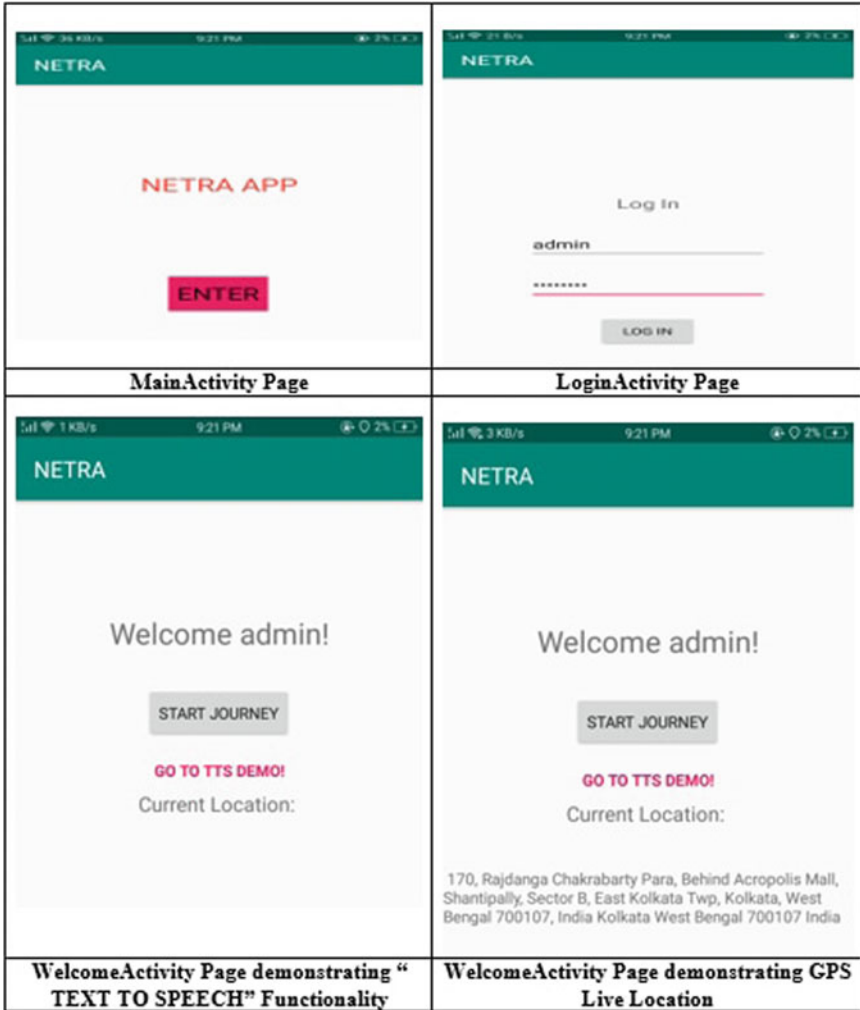
Fig. 8 Real-time application view

Fig. 9 Image before object detection

Fig. 10 Object detected by
the model

References

1. Sierra, J.S., Togores, J.S.R.: Designing mobile apps for visually impaired and blind users—using touch screen based mobile devices: iPhone/iPad". In: ACHI 2012: The Fifth International Conference on Advances in Computer-Human Interactions, Copyright (c) IARIA, 2012, pp. 47–52, ISBN: 978-1-61208-177-9
2. Viola, P., Jones, M.J.: Robust real-time face detection. Int. J. Comput. Vision **57**, 137–154 (2004). https://doi.org/10.1023/B:VISI.0000013087.49260.fb
3. Chadalawada, S.K.: Real Time Object Detection and Recognition—Using Deep Learning Methods, pp. 1–52 (2020)
4. Samual, J.: Implementation of GPS based object location and route tracking on android device. Int. J. Inf. Syst. Eng. **3**(2), 61–72 (2015). ISSN: 2289-7615. https://doi.org/10.24924/ijise/2015.11/v3.iss2/61.72
5. Trivedi, A., Pant, N., Shah, P., Sonik, S., Agarwal, S.: Speech to text and text to speech recognition systems a review. IOSR J. Comput. Eng. (IOSR-JCE) **20**(2), 36–43 (2018). e-ISSN: 2278-0661, p-ISSN: 2278-8727. https://doi.org/10.9790/0661-2002013643
6. Hiroto, K., Katsumi, H.: A Wearable Walking Support System to provide safe direction for the blind. In: 2019 34th International Technical Conference on Circuits/Systems, Computers and Communications (ITC-CSCC), pp. 1–4, 2019. Electronic ISBN: 978-1-7281-3271-6, USB ISBN: 978-1-7281-3270-9, ISBN: 978-1-7281-3272-3. https://doi.org/10.1109/ITC-CSCC.2019.8793305

7. Laubhan, K., Trent, M., Root, B., Abdelgawad, A., Yelamarthi, K.: A wearable portable electronic travel aid for blind. In: International Conference on Electrical, Electronics, and Optimization Techniques (ICEEOT), 2016, pp. 1999–2003. https://doi.org/10.1109/ICEEOT.2016.7755039

8. Nishajith, A., Nivedha, J., Nair, S.S., Shaffi, J.M.: Smart cap—wearable visual guidance system for blind. In: 2018 International Conference on Inventive Research in Computing Applications (ICIRCA), pp. 275–278, 2018, Electronic ISBN: 978-1-5386-2456-2. ISBN: 978-1-5386-2456-2. https://doi.org/10.1109/ICIRCA.2018.8597327

9. Dunai, L.D., Lengua, I.L., Tortajada, I., Simon, F.B.: Obstacle detectors for visually impaired people. In: 2014 International Conference on Optimization of Electrical and Electronic Equipment (OPTIM), pp. 809–816, 2014, Electronic ISBN: 978-1-4799-5183-3, Print ISSN: 1842-0133. https://doi.org/10.1109/OPTIM.2014.6850903

10. Girshick, R., Donahue, J.: Region-based convolution networks for accurate object detection and segmentation. IEEE Trans. Pattern Anal. Mach. Intell. 142–158 (2018). Print ISSN: 0162-8828, CD: 2160-9292, Electronic ISSN: 1939-3539. https://doi.org/10.1109/TPAMI.2015.2437384

11. Kumar, A., Zhang, Z.J., Lyu, H.: Object detection in real time based on improved single shot multi-box detector algorithm. EURASIP J. Wirel. Commun. Netw. **204**, 1–18 (2020). https://doi.org/10.1186/s13638-020-01826-x

12. Shrestha, G., Deepsikha, D.M., Dey, N.: Plant disease detection using CNN. In: 2020 IEEE Applied Signal Processing Conference (ASPCON), 2020, pp. 109–113. Electronic ISBN: 978-1-7281-6882-1, USB ISBN: 978-1-7281-6881-4, ISBN: 978-1-7281-6883-8. https://doi.org/10.1109/ASPCON49795.2020.927672

Futuristic Cloud Market—Game Theoretic Equilibrium

Avijit Bose, Pradyut Sarkar, and Jana Premananda

Abstract Recent development has initiated the importance of cloud computing platforms. Cloud is not merely used for data storage any more but computation platform has been an integral constituent of cloud systems. The day is not far away when there will be a futuristic cloud market where customers will have the provision of choosing among cloud providers. But then the question arises whether CP's will compromise on QoS for penetrating into the market. We try to answer this question with a double-bargaining game where cloud providers do not have to sacrifice their Cournot equilibrium and the incentives which are required for their survival. This is a new area which we are trying to put in the Cloudnomics domain. Here, one side the customer will be increasing the bidding value and CP's will reduce their incentive to an extent such that the successful negotiation can take place. Broker has to play a key role in the negotiation mechanism.

Keywords Cloud economy · Game theory · Nash equilibrium · Resource allocation

1 Introduction

Cloud pricing is an important topic in the area of Cloudnomics. The literatures covered so far indicates the parameters based on which cloud providers set their prices. Futuristic cloud market will force the cloud provider to reduce the cost under a perfect competitive environment. But under reduced price mechanism it is not possible to maintain the QoS level for the cloud providers. So it's always better to go for a market driven mechanism as mentioned in [6] and implement a bargaining

A. Bose (✉)
Computer Science and Engineering, MCKV Institute of Engineering, Howrah, West Bengal, India

P. Sarkar
Computer Science and Engineering, MAKAUT, Kolkata, West Bengal, India

J. Premananda
Netaji Subhash Open University, Kolkata, West Bengal, India

scheme where both the buyer and seller compromise a bit on price without compromising on QoS. We try to design a game theoretic proposition for the condition and check whether Nash Equilibrium is achieved under this bargaining algorithm.

- Previous works have pointed out pricing based on competitive environment.
- Special focus has been given previously on price determination but market dependent pricing scheme has been implemented in the paper which is a futuristic cloud market feature.
- Double-bargaining scheme has been implemented such that cloud providers do not have to sacrifice their price against QoS.

2   Previous Work

In [1], the author discusses about the inter-organizational economic theory. Whether in the long term the service provider will continue with the service depends upon the price it sets. High QoS level support basically attracts more and more customers.

If cloud providers go for successful estimation then resource wastage can be prevented up to a larger extent. In this paper, authors have focused on single-service scenario by multiple service providers. They have provided each cloud operators with a demand function with parameters such as QoS, price. They provide a non-cooperative game price. Authors have worked on multi-tier cloud architecture. They implement a M/M/1 queuing model and finds out the existing price. In [2], authors take a case study with AWS which is the leading cloud service provider across the globe. However, they express their concern over the continuous decreasing price. More is the market share the probability of reducing the competitive price is also more. General purpose instances and memory optimized instances have been taken care of in this paper. After analyzing, authors have found the cost of storage is a reduced step size plot over time. Authors have done an extensive time series analysis and found that though in terms of storage cost the price reduction is justifiable but other parameters like resource provisioning, QoS need also to be taken into consideration. In [3], there is a new concept of function as a service (FaaS). Such service is getting developed under the so called server less computing. According to the author, the cost charged by the cloud provider is the summation of a fixed cost and a variable cost. There is SM (Spot Market) concept where idle resources can be used. There is a threshold value to run the job or user; it is the maximum monetary sum the user is willing to pay to run the job. Authors say automatic scaling is one of the solutions. Authors have claimed three parameters (i) threshold that is the value user can purchase and (ii) time of resource allocation required for completion of the job and (iii) space occupied by job that is required by the user. Another parameter that will be of interest is the energy. The paper has discussed Spot market, Pay as you go, on demand costing model. In [4] discusses that different types of resources are being offered such as storage as a service and platform as a service. This paper also talks about the oligopoly market. In economic theory Cournot equilibrium comes into the picture. Cournot equilibrium is the price which already covers the

production cost. Based on the service type the costing may be offered. Thus, major parameters that are considered in AWS and Azure are prices for VM hours, GB of storage, and external bandwidth. Even more sophisticated services such as load balancing and database use are metered. Mobile telephony pricing may also play a key role though its direct dependency with cloud-economy is not clear. However, database monitoring and costing are still a challenge. Combined scheduling and pricing models are an active area of research. When all the parameters are bundled together they are called one-dimensional problem and parameters are considered individually they are called multidimensional. The paper then discusses pricing one-dimensional offerings by considering a hybrid market where there is pay as you go model and spot market modelling. This paper also focuses taking the time slice as a parameter and then discusses the market competition and fairness associated with it. Perhaps that's the advantage of oligopoly market. At last, the paper discusses about the cooperative game theory and speaks about the revenue sharing between service providers associated with the cooperative model. In [5] authors go for a literature review on the pricing model and the major pricing model that is discussed here are (i) Fixed pricing model which is not optimum for consumer but somewhat optimum for service provider. (ii) Dynamic pricing model which is not worth for run time entertainment procedures in cloud computing model. Based on the above mentioned primary differentiation, further sub division has taken place which are as follows (i) Subscription model: fixed and static and it is already running successfully, and this is not worthy for customers. (ii) Pay as you go model: static but faces the problem of under provisioning and over provisioning. (iii) Pay for resource model: static model and advantageous in terms of maximum utilization of resources but it's difficult to be implemented. There are dynamic models which are classified as (i) Dynamic resource pricing on federated clouds: it is dynamic in nature as name denotes and the cloud provider uses current level of supply/demand to determine resource/service prices but it suffers from the problem of scalability issue. (ii) Value based pricing: -it is dynamic in nature and resource/service prices are defined depending on the customer's point of view. But it is hard to implement. (iii) Competition based pricing: cloud providers are influenced by competitors pricing; however, this model suffers from customer perspective. (iv) Datacenter net profit optimization with individual job dead-lines: which takes into account job scheduling mechanisms to set resource/service prices but it does not take into consideration heterogeneous servers and is difficult to implement. (v) Genetic model for pricing in cloud computing markets: depending on the state of a real time market pricing is determined but suffers from scaling problem. But it is very difficult and very critical during dynamic demand requirement of customers. (vi) A novel financial economic model: A cloud provider sets prices between lower and upper boundary. But in this model, maintenance costs are not taken in consideration. (vii) Customer based pricing: cloud consumers define the current price but it is difficult to set price. (viii) Cost based pricing: cloud provider specifies the profit level to set resource/service prices but does not consider cloud consumers. (ix) Pricing algorithm for cloud computing resources: service providers set the price on market state but faces problem when supply/demand fluctuates. In [6] authors have explained about the pricing schemes in cloud computing. Every cloud provider has his own

pricing scheme; however, the aim is to provide better QoS for customers. Authors describe the model in general and have portrayed that for SaaS and PaaS services IaaS plays a major role. There are several costs associated with IaaS they are (i) cloud fixed cost and (ii) cloud utilization cost (iii) virtual machine cost (iv) server cost, and (v) rack cost. Server cost involves (a) maintenance cost (b) network cost (c) hardware cost (d) software cost. Rack cost involves (a) cooling cost (b) power cost (c) facilities cost and (d) real estate cost. Comparison of the model as depicted in [5] remains same in this paper also. Author describes fixed pricing which involves pay per use pricing which involves customers pay as per the usage. Subscription pricing involves users pay on a recurring basis to access software as an online service or to have profit from a service. Hybrid pricing model is a hybrid of pay per use and subscription. Then, there is dynamic pricing where price of the resources is determined according to demand and supply. There is market dependent pricing which includes (a) bargaining (b) yield management (c) auction theory (d) dynamic market. In [7] authors have analyzed the monopoly as well as duopoly case, while going for price mechanism in cloud. For monopoly case, the optimal base price, quality level, and customer demand function have been taken into consideration. It has been marked that as price increases the quality of service demand also increases, and there are certain customer bases that does not care about the pricing index but does not compromise on quality. It is also marked that as service provider demands increases they decrease the quality of product for low compatible services going against the ethics. In duopoly in order to reach to the Nash equilibrium, there are certain restrictions that have been made, i.e., both offer the single quality of service. Multiple quality of service cannot lead to a firm solution. However, rapid development in technology has helped for both customers and service provider to decrease the price. So this paper generally goes for competition based price determination. However, the focus is on IaaS market. The paper designs a numerical model and reaches the Nash equilibrium. So going through the literature survey, we can point out the brief analogy of literature mentioned in Table 1.

3 Proposed Work

In the futuristic cloud computing architecture, the major role will be played by broker or arbiter who will act as an interface between the customer and cloud service provider. The customer fixes a certain cost which he is ready to pay for a service or resource to the broker and the broker sends the request to all service providers with the cost and now the negotiation algorithm will start. Cloud provider will reduce the price and the user will increase the cost he has claimed till the game reaches the Nash Equilibrium. Almost all the service provider attains the equilibrium but one that reaches first may be chosen by the broker or the user/customer. However, the architecture has got a single disadvantage that is the service provider who will keep the price low compared to the other service providers reaches the Nash Equilibrium fast. According to [2], the major players are going to be benefited by the game.

Table 1 Brief analogy of literature

S. No.	Author name	Focused area	Non focused area
1	Pal et al. [1]	Non-cooperative game price of a multi-tier architecture cloud computing platform. Single service scenario by multiple service providers	There is no negotiation scheme implemented
2	Kicinski et al. [2]	Has focused on decreasing price trends of cloud operators. As far as memory is concerned it has become cheaper but other resource parameters like QoS, Resource provisioning needs to be taken into consideration	Not focused on competition among the cloud operators. Not exactly focusing on futuristic cloud market
3	Dimitri [3]	Has focused on pay as you go, spot market and on demand costing model. Detailed explanation of scaling, cost analysis is there	Exact market condition where tremendous competition among cloud providers will exist is the futuristic market and is not focused
4	Kash et al. [4]	Discusses about different pricing parameters and with case study explains Cournot pricing equilibrium	Market and consumer's behavior toward cloud platforms have not been covered in the paper
5	Ali et al. [5]	Literature survey paper and discusses about cloud providers mechanism to set prices	Bargaining methodology has not been covered. However, declares that demand supply fluctuation is a problem to set prices for the cloud platforms
6	Mazrekaj et al. [6]	Discusses about several pricing scheme especially about market dependent pricing. Here, bargaining is one of the method	Bargaining implementation has been inspired from this paper's idea which is an integral part of futuristic cloud market
7	Cinar et al. [7]	Speaks about the quality of service and competition based price determination and ultimately reaches Nash Equilibrium	Competition leads to reduction in price but the higher branded CP's can reduce the rate which is not possible for ordinary cloud providers so bargaining concept comes which is market driven

As seen in Fig. 1 user/consumer asks for the cloud resources to the broker. Broker then asks for bid from the service provider and while consumer also increments his/her price for the cloud prices service providers also diminishes its rate so a negotiation mechanism starts and when it reaches the equilibrium the one with minimum number of iterations is selected. So algorithm is as follows

Fig. 1 Proposed model architecture

3.1 Algorithm

/* equilibrium determination of cloud prices for n cloud providers single buyer*/
Print "How many players are there"

    Input n
    For i= 1 to n do
    Print "Enter the prices of service provider"
    Input p[i]
    End for
    Print "enter the buyer negotiation price"
    Input c
    Set max-price=max (p[i])
    While max-price > c
    c = c+Δc
    For i in n do
    p[i] = p[i]-Δp[i]
    End for
    Max-price =max-price $-$ Δmax-price
    If (c= = p[i])
    Print "equilibrium is achieved for ith service provider"
    End while
    Print "equilibrium cannot be achieved"
    End

4   Simulation and Result

The above algorithm was implemented with Python 3. X, and it was checked whether the algorithm reaches the equilibrium. Following interesting observations were noted. The simulation was carried out for Number of sellers was 5 and prices offered by the sellers were {3000, 4000, 5000, 6000, 7000} and the buyers' agreement price was {2000} and number of iterations were found to be 250 for all sellers to attain equilibrium but {Seller1} was the winner as he attained the equilibrium in less time.

When the number of sellers was 3 with prices offered by the sellers were {1000, 2000, and 3000} and the buyer's price offered was {900} it took 105 iterations to achieve the equilibrium. The figures of simulations are depicted in Figs. 2 and 3.

The broker now can take decisions based on the total equilibrium game. If we look at the game diagram it looks as Tables 2, 3 and 4. Now the broker has got following equilibrium points which he can submit to customer where service providers are likely to pay they are {950, 1460, 1950}. Now it's up to the customer to choose among the three service providers. Similarly, for the 5 players game, the return values are {2500, 3000, 3500, 4000, and 4500}, and the game theory figures will look like as

Fig. 2 Simulation result of 5 service provider game
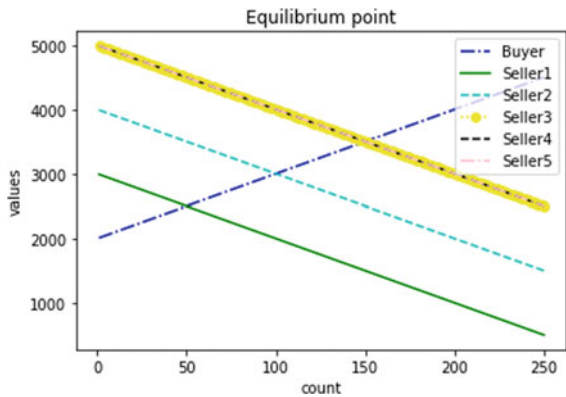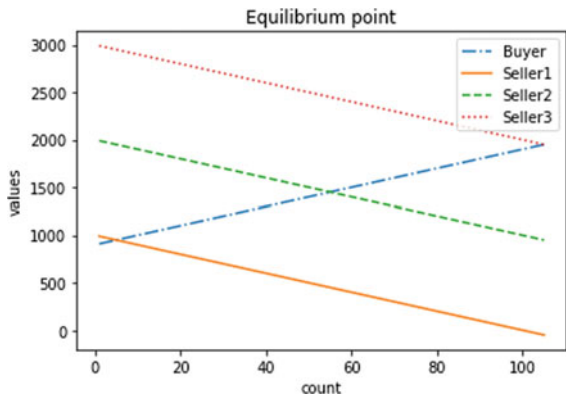

Fig. 3 Simulation result of 3 service provider's game

Table 2 Game for service provider1 with buyer in 3 player game

Buyer S.P.1 = 1000 S.P.1 = 950		
900	− 1, 1	− 1, 0.5
950	− 1,1	**1, 1 N.E.**

Bold which indicates that this is the Nash Equilibrium point

Table 3 Game for service provider 2 with buyer in 3 player game

Buyer S.P.2 = 2000 S.P2 = 1460		
900	− 1, 1	− 1, 0.5
1460	− 1, 1	**1, 1 N.E.**

Bold which indicates that this is the Nash Equilibrium point

Table 4 Game for service provider 3 with buyer in 3 player game

Buyer S.P.3 = 3000 S.P.3 = 1950		
900	− 1, 1	− 1, 0.5
1950	− 1, 1	**1, 1 N.E.**

Bold which indicates that this is the Nash Equilibrium point

Table 5 Game for service provider 1 with buyer in 5 player game

Buyer S.P.1 = 3000 S.P.1 = 2500		
2000	− 1, 1	− 1, 0.5
2500	− 1, 1	**1, 1 N.E.**

Bold which indicates that this is the Nash Equilibrium point

Table 6 Game for service provider 2 with buyer in 5 player game

Buyer S.P.2 = 4000 S.P.2 = 3000		
2000	− 1, 1	− 1, 0.5
3000	− 1, 1	**1, 1 N.E.**

Bold which indicates that this is the Nash Equilibrium point

Table 7 Game for service provider 3 with buyer in 5 player game

Buyer S.P.3 = 5000 S.P.3 = 3500		
2000	− 1, 1	− 1, 0.5
3500	− 1, 1	**1, 1 N.E.**

Bold which indicates that this is the Nash Equilibrium point

Table 8 Game for service provider 4 with buyer in 5 player game

Buyer S.P.4 = 6000 S.P4 = 4000		
2000	− 1, 1	− 1, 0.5
4000	− 1, 1	**1, 1 N.E.**

Bold which indicates that this is the Nash Equilibrium point

Table 9 Game for service provider 5 with buyer in 5 player game

Buyer S.P.5 = 7000 S.P.5 = 4500		
2000	− 1, 1	− 1, 0.5
4500	− 1, 1	**1, 1 N.E.**

Bold which indicates that this is the Nash Equilibrium point

Tables 5, 6, 7, 8 and 9. Here, the intermediate values have not been taken into account but exactly the equilibrium price has been taken into consideration.

5 Conclusion and Future Work

As mentioned above, the algorithm will converge for multiplayer but the decision has been left over to the customer whom to select if he selects the first one on first come first serve, i.e., the service provider which reaches the equilibrium first. But the algorithm will be refined based on parameters like QoS. One thing is certain that more reputed and large company will be able to keep the price low, so reaches the equilibrium fast. In that approach, the above algorithm works fine. In future parameters like QoS, spot market and scaling needs to be taken into consideration and further refinement will be undertaken.

References

1. Pal, R., Hui, P.: Economic models for cloud service markets: pricing and capacity planning. Theor. Comput. Sci. **496**, 113–124 (2013). https://doi.org/10.1016/j.tcs.2012.11.001
2. Kicinski, A., Souiri, H.: (2019) iceaaonline.com
3. Dimitri, N.: Pricing cloud IaaS computing services. J. Cloud Comput. **9**, 14 (2020)
4. Kash, I.A., Key, P.B.: Pricing the cloud. IEEE Internet Comput. **20**(1), 36–43 (2016). https://doi.org/10.1109/mic.2016.4
5. Ali, T.E.S.M., Ammar, H.H.: Pricing models for cloud computing services, a survey. Int. J. Comput. Appl. Technol. Res. **5**(3), 126–131 (2016). https://doi.org/10.7753/ijcatr0503.1002
6. Mazrekaj, A., Shabani, I., Sejdiu, B.: Pricing schemes in cloud computing: an overview. Int. J. Adv. Comput. Sci. Appl. **7**(2) (2016). https://doi.org/10.14569/ijacsa.2016.070211
7. Cinar, K., Justin, R.M.: Cloud computing international world wide web conference committee (iw3c2). iw3c2, www 2016. ACM (2016). https://doi.org/10.1145/2872427.2883043

Analytical and Deep Neural Network Based Hybrid Modelling of Single-Segment Continuum Robot

Saptak Bhattacherjee, Sudipta Chattopadhyay, Aparajita Sengupta, and Subhasis Bhaumik

Abstract Hyper-redundancy and ability to propagate through complex curvilinear pathways have made the continuum robots immensely popular in different fields of application. Precise control of continuum robot position relies on the accurate knowledge of the manipulator kinematics. However, the inverse kinematic model of continuum robots based on analytical modelling fails to include the unmodeled dynamics and effect of disturbances due to gravity and friction resulting in low accuracy in modelling and control. On the other hand, purely data driven continuum models require huge amount of data and time for training and suffer from high inaccuracy in modelling as well. Hybrid modelling in this scenario has been perceived to achieve better accuracy by combining the advantages of these two modelling approaches. Therefore, in the present work, we focus on the inverse kinematics of the single-segment continuum robot by using the analytical and deep neural network based hybrid modelling approach. Experimental results indicate that the proposed method increases the modelling accuracy and also at the same time it reduces the network training time significantly.

Keywords Continuum robot · Deep neural network · Hybrid modelling · Inverse kinematics

1 Introduction

Recent developments in the area of flexible robotics have revealed new technologies that offer enormous advantages in almost every sector ranging from subsea to space applications [1]. Continuum robots are no exception to be amongst one of the phenomenal developments in the field of flexible robotics [2]. Unlike rigid link robots,

S. Bhattacherjee (✉) · S. Bhaumik
School of Mechatronics and Robotics, Indian Institute of Engineering Science and Technology, Shibpur, Howrah, India

S. Chattopadhyay · A. Sengupta
Department of Electrical Engineering, Indian Institute of Engineering Science and Technology, Shibpur, Howrah, India

continuum robots have hyper-flexible structural bodies which allow them to mimic the motion of an elephant trunk, snake or octopus tentacle [3]. Owing to their intrinsic dexterity, these robots have the ability to propagate through tortuous pathways and can access areas which are inaccessible by rigid link. Due to these advantages, the continuum robots have become immensely popular in all branches of robotics gaining widespread applications in defencee, underwater, space and medical fields [4].

Highly accurate modelling of continuum robot seems to be very crucial for reliable and accurate control of these hyper-redundant robots in real time. However, precise modelling of continuum robots is very challenging due to their high inherent dexterity and hyper-redundant nature [5]. Therefore, in the recent years, inverse kinematic modelling of continuum robot has become an extremely important area of research. Several approaches have been made on the derivation related to analytical inverse kinematics model of continuum robots. Hirose et al. estimated the planer kinematics of snake like robots by using a serpentine curve approach; however, they did not address the 3D kinematic modelling of continuum robot [6]. Chirikjian et al. applied model decomposition method to find the inverse kinematics of a 30 DoF robot, yet the applicability of their model is limited only on specific continuum robot models [7]. An alternative approach has also been used by researchers to deduce the inverse kinematic model by considering the continuum robots as an assembly of rigid links and spherical joints and then applying the Denavit-Hartenberg (D-H) method [8]. However, this approach resulted in inaccurate modelling of actual continuum robots due to their continuous structure and absence of any prismatic or revolute joints in the robot structure.

On the other hand, in conventional robotics applications, neural networks have been widely employed for inverse kinematics modelling [9]. Researchers have also used several architectures of neural networks for modelling and control of continuum robots and compact bionic handling arms (CBHA) [10]. However, existing research on neural network based inverse kinematics modelling shows that purely data driven models are inefficient in modelling the manipulator kinematics with high accuracy [11].

Therefore, in the present work, we propose a strategy for solving the inverse kinematics of continuum robot using hybrid modelling approach based on analytical modelling and deep neural network model. In the proposed strategy, first the inverse kinematic solution is estimated using analytical model. The derived solution is then used to generate simulated data for training the deep neural network based solution of the continuum robot. The results obtained with hybrid model are compared to the results obtained using the analytical model to show the supremacy of the proposed approach over the analytical one.

The paper is organized in the following manner: Sect. 2 describes the structure and kinematic modelling of the continuum robot along with the scheme for training the deep neural network with pre-generated data based on analytical model. Section 3 illustrates the results of modelling followed by conclusion and future scope of work.

Fig. 1 Structure of the
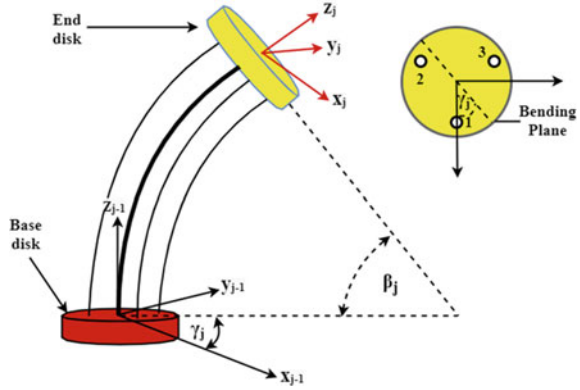single-segment continuum
robot
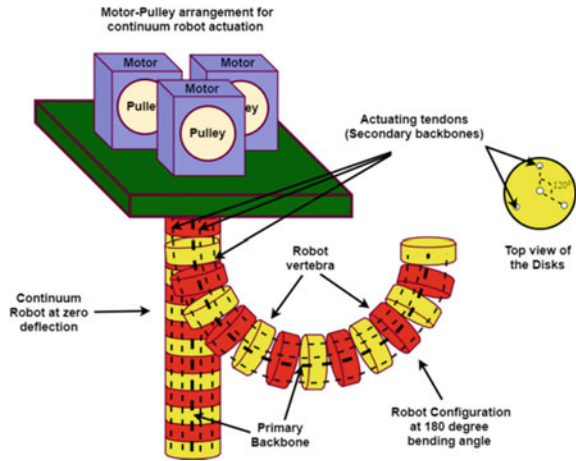
2 Methods

2.1 Continuum Robot Structure

The single-segment continuum robot consists of a hyper-flexible primary backbone
attached with equispaced circular discs acting as the robot vertebra which forms the
main skeleton of the continuum manipulator. Additionally, the robot also consists of
three secondary backbones placed 120 degree apart from each other for actuation.
Each of the secondary backbone passes through the circular discs and is connected
to the last disc at one end. The other end of the secondary backbone is connected to
motor-pulley actuator system. During actuation, the effective length of the secondary
backbone changes due to coiling. The strain generated at each of the secondary
backbone is then transferred to the primary backbone through the distal end disc of the
robot. Under this scenario, the primary backbone undergoes deflection in appropriate
direction according to the direction of the resultant strain. Both the primary and
secondary backbones of the continuum robot are made of superelastic Nitinol alloy
so that the robot can regain its initial configuration after each deflection. The entire
structure of the continuum robot has been shown in Fig. 1.

2.2 Kinematic Model of the Single Segment Continuum Robot

For analyzing the correlation between the robot configuration space, the task space
and the driven space, the inverse kinematic solution of the continuum robot is esti-
mated based on the notion of the constant curvature model. Generally, the kinematic

Fig. 2 Coordinate system
and notations of
single-segment continuum
robot

model of the single-segment continuum robot can be derived by utilizing the robot transformation matrices. The coordinate systems of the single-segment robot have been shown in Fig. 2.

Assuming the deflection of the continuum robot under constant curvature, the inverse kinematics model can be estimated by using the Euler transformation with two parameters $h_j = [\beta_j \gamma_j]^T$, where the position of the distal end for zero deflection can be defined as $g_j = [0, 0, d_0]$ and can be expressed as:

$$g_j^{j1} = \left[\frac{\cos \gamma_j (1 - \cos \beta_j) d}{\beta_j} \quad \frac{\sin \gamma_j (1 - \sin \beta_j) d}{\beta_j} \quad \frac{\sin \beta_j d}{\beta_j} \right]^T \tag{1}$$

where, the bending angle, the rotation angle and the arc length of the segment is denoted as β_j, γ_j, and d, respectively.

Therefore, the rotational transformation matrix of the bending segment can be estimated as:

$$R_j^{j-1} = \begin{bmatrix} \cos \beta_j \cos \gamma_j^2 + \sin \gamma_j^2 & \cos \gamma_j \sin \gamma_j (\cos \beta_j - 1) & \cos \gamma_j \sin \beta_j \\ \cos \gamma_j \sin \gamma_j \cos \beta_j & \sin \gamma_j^2 \cos \beta_j + \cos \gamma_j^2 & \sin \gamma_j \sin \beta_j \\ -\cos \gamma_j \sin \beta_j & -\sin \gamma_j \sin \beta_j & \cos \beta_j \end{bmatrix} \tag{2}$$

Hence, the transformation matrix of the distal end with respect to the base can be expressed as:

$$T_j^k = T_0^k \begin{bmatrix} R_j & G_j \\ 0 & 1 \end{bmatrix} = \begin{cases} R_j = R_j^{j-1}, & G_j = g_j^{j-1} (j = 1) \\ R_j = R_{j-1} R_j^{j-1}, & G_j = R_{j-1}^{j-1} g_j + G_{j-1} (j > 1) \end{cases} \tag{3}$$

where, T_0^k denotes the homogeneous transformation matrix between the actuation system and the base coordinate system. The forward kinematics model of the single-segment continuum robot is represented in Eq. 3.

Thus, the robot end effecter position and orientation can be expressed in terms of γ_j and β_j as follows:

$$\gamma_j = \arctan\left(\frac{g_y}{g_x}\right) \tag{4}$$

$$c = \frac{g_y^2}{g_z^2 \sin \gamma_j^2} \tag{5}$$

$$\beta_j = \arccos\left(\frac{1-c}{1+c}\right) \tag{6}$$

Based on the geometric association, the relationship amongst task space, driven space and configuration space can be estimated as:

$$d_{j1} = d - a\beta_j \cos(\gamma_j) \tag{7}$$

$$d_{j2} = d - a\cos\left(\gamma_j - \frac{2\pi}{3}\right) \tag{8}$$

$$d_{j3} = d - a\beta_j\cos\left(\gamma_j + \frac{2\pi}{3}\right) \tag{9}$$

where, $d_{j,k}(k = 1, 2, 3)$ denotes the k-th cable for the continuum segment, a represents the radius between the centre of each disc to each secondary backbone guide hole of the continuum robot. If the configuration parameters γ, β are known, the motion of the continuum robot can be controlled to accomplish the preferred configuration by estimating each length of driving cables based on the Eqs. (7), (8) and (9). The internal friction between the disc and the actuating tendons has not been considered for simplification of the kinematic model.

2.3 Pre-training the Deep Neural Network

The present work proposes deep neural network based architecture for inverse kinematics modelling of the continuum robot. The hyper-parameters of deep neural network, i.e. the number of neurons in a layer, number of hidden layers, activation function and learning rate are chosen by heuristic approach. The number of hidden layers is chosen to be 4 and the number of neurons on first two layers is set to be 25 and that of the last two layers are to be 20. The activation function used is a
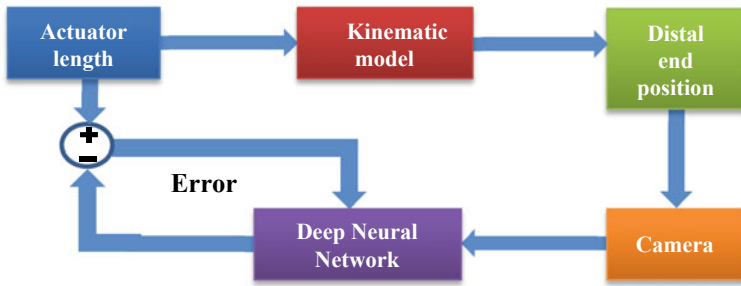
Fig. 3 Schematic for training the deep neural network using simulated data

sigmoid function for first three layers and that of last layer is a linear one. Standard normalization techniques are used at every layer. The proposed network is trained by using pre-generated dataset obtained from the analytical inverse kinematic model. The training dataset consists of actuator lengths and corresponding 3D position and orientation of the distal end. The block diagram for training the deep neural network has been shown in Fig. 3.

The training input consists of *x*, *y*, *z* position of the tip of continuum robot, and training output consist of the length of 4 strings. The training method is standard Backpropagation method with gradient descent algorithm. The weight updates are given by the following equation:

$$W_{\text{new}} = W_{\text{old}} + L_R.(\partial y/\partial x).W_{ij}.E_j.O_i \qquad (10)$$

where, L_R represents the learning rate, W_{ij} is the weight connecting *i*th neuron and *j*th neuron, E_j is the error at *j*th neuron and O_i is the prior output of the *i*th neuron.

2.4 Experimental Setup

The experimental setup for data collection and modelling performance evaluation has been shown in Fig. 4. The continuum robot is actuated using three actuating tendons which are in turn connected with three Dynamixel MX28 motor-pulley assemblies. The 3D position and orientation of the distal end is tracked using two webcams (Logitech C310 HD).

A red coloured object is placed in front of the continuum robot which acts as the target. The 3D position and orientation of the target is tracked by two webcams (Logitech C310HD) using colour thresholding and triangulation method. The target position and orientation are then fed to train deep neural network model running in MATLAB simulation tool in order to predict the actuator's length which is expressed in terms of motor actuation angles. The predicted motor angle is then compared with

Fig. 4 Experimental setup for data collection

the motor angle derived using the analytical model, and the error is then fed to deep neural network for predicting the motor angle with higher accuracy.

3 Results

The tracking capability of the hybrid model for predicting the inverse kinematic solution for different positions has been shown in Fig. 5.

Figure 6 illustrates the tracking accuracy of the hybrid model for a given trajectory along with the errors in x, y and z axis.

From Fig. 6, it can be observed that the deep neural network efficiently performed the trajectory tracking with minimal error in x, y and z axis. This is due to the architecture of the deep neural network and use sigmoid function as activation function. The similar experiment when performed with artificial neural network yielded an accuracy of 70.3%. Hence, the deep neural network has been proposed in the present
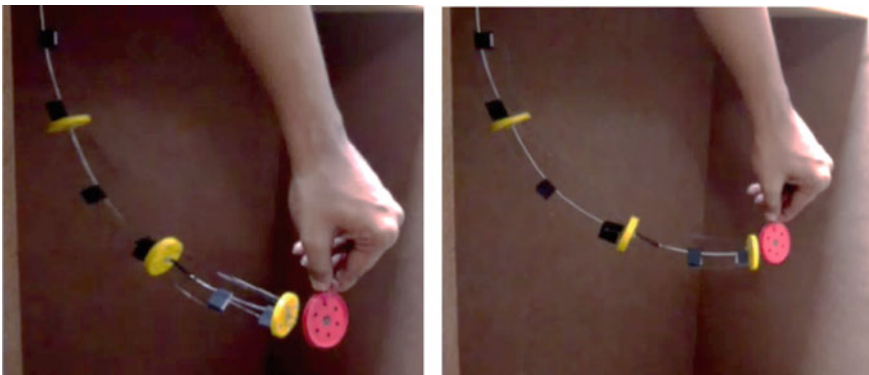
Fig. 5 Continuum robot tracking the object at different instances
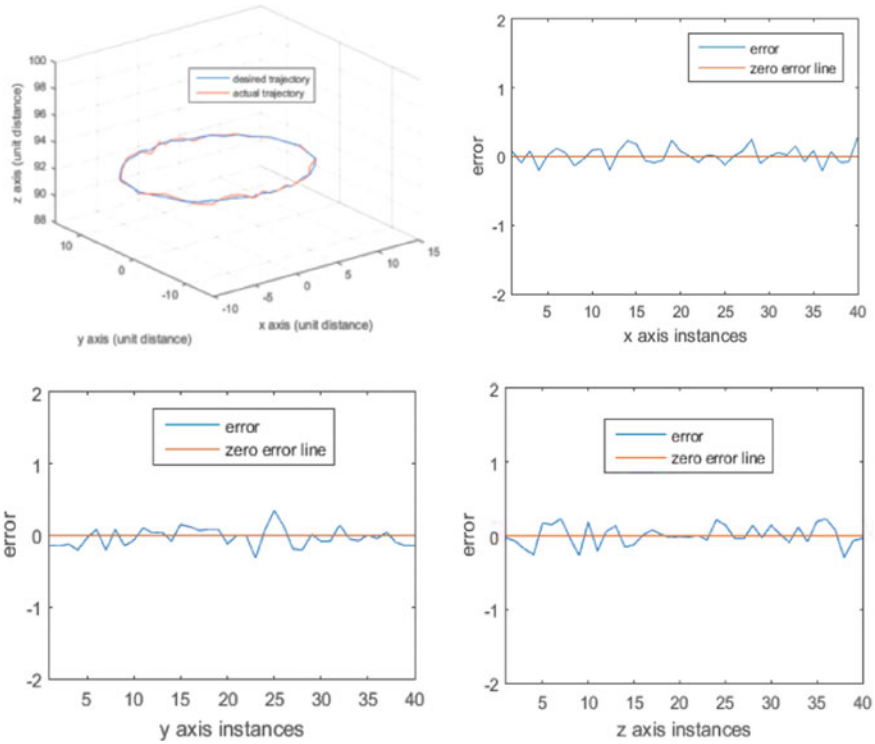
Fig. 6 Trajectory tracking performance of the continuum robot based on hybrid model

study. The performance evaluation of the hybrid model in comparison with analytical model and deep neural network (DNN) based model has been presented in Table 1.

From Table 1 it is evident that the proposed hybrid model performs much better in tracking the target's position in comparison with the analytical model and purely data driven models.

Table 1 Comparison of performances of different model architectures for tracking various target positions

Model	Accuracy (%)
DNN based model	78
Analytical model	83.75
Hybrid model	92.87
Hybrid model with online update	96.52

4   Conclusion

The present work explores the advantages of hybrid modelling over the conventional analytical models and purely data driven models. Results thus obtained provide the validation of hybrid data driven modelling for control of complex nonlinear systems such as continuum robots. The usage of hybrid data not only reduces the time required for training but also increases the efficiency, training accuracy and validation accuracy of the deep neural network. The proposed hybrid model seems to provide benefit for cases where data collection is costly and analytical model is not enough to drive the system due to modelling uncertainty and unmodeled dynamics.

References

1. Sayahkarajy, M., Mohamed, Z., Mohd Faudzi, A.A.: Review of modelling and control of flexible-link manipulators. Proc. Inst. Mech. Eng. Part I J. Syst. Control Eng. **230**(8), 861–873 (2016)
2. Kolachalama, S., Lakshmanan, S.: Continuum robots for manipulation applications: a survey. J. Robot. **2020** (2020)
3. Robinson, G., Bruce, J., Davies, C.: Continuum robots-a state of the art. In: Proceedings 1999 IEEE International Conference on Robotics and Automation, vol. 4, pp. 2849–2854. IEEE (1999)
4. Bhattacherjee, S., Chattopadhayay, S., Rao, V., Seth, S., Mukherjee, S., Sengupta, A., Bhaumik, S.: Kinematics and teleoperation of tendon driven continuum robot. Proc. Comput. Sci. **133**, 879–886 (2018)
5. Yip, M.C., Sganga, J.A., Camarillo, D.B.: Autonomous control of continuum robot manipulators for complex cardiac ablation tasks. J. Med. Robot. Res. **2**(01), 1750002 (2017)
6. Hirose, S.: Biologically Inspired Robots, pp. 147–155. Oxford University Press, Oxford, U.K. (1993)
7. Chirikjian, G.S., Burdick, J.W.: A modal approach to hyper-redundant manipulator kinematics. IEEE Trans. Robot. Autom. **10**(3), 343–354 (1994)
8. Wolf, A., Brown, H.B., Casciola, R., Costa, A., Schwerin, M., Shamas, E., Choset, H.: A mobile hyper redundant mechanism for search and rescue tasks. In: Proceedings of IEEE/RSJ International Conference on Intelligence Robots Systems, vol. 3, pp. 2889–2895. Taipei, Taiwan (2003)
9. Demby's, J., Gao, Y., DeSouza, G.N.: A study on solving the inverse kinematics of serial robots using artificial neural network and fuzzy neural network. In: 2019 IEEE International Conference on Fuzzy Systems (FUZZ-IEEE), pp. 1–6. IEEE (2019)
10. Shahabi, E., Kuo, C.-H.: Solving inverse kinematics of a planar dual-backbone continuum robot using neural network. In: European Conference on Mechanism Science, pp. 355–361. Springer, Cham (2018)
11. Jiang, H., Wang, Z., Liu, X., Chen, X., Jin, Y., You, X., Chen, X.: A two-level approach for solving the inverse kinematics of an extensible soft arm considering viscoelastic behavior. In: 2017 IEEE International Conference on Robotics and Automation (ICRA), pp. 6127–6133. IEEE (2017)

A Novel Control Strategy of PV Microgrid Using UPQC Under Nonlinear Load

Anagha Bhattachatrya, Debashis Chatterjee, and Swapan Kumar Goswami

Abstract A microgrid normally comprises of Renewable Energies hence owing two its fluctuation Power Quality is huge issue for microgrid operation and control. In this paper, a novel control topology to enhance power quality as well as to mitigate harmonics is proposed using Unified Power Quality Controller (UPQC). The microgrid comprises of two Solar Photovoltaic modules and battery energy storage system (BESS) as storage device. Detailed simulation study is done in MATLAB under nonlinear load and fault condition. It is observed that with the application of UPQC in the novel control scheme power quality is enhanced, and Total Harmonic Distortion (THD) is reduced as per IEEE norms.

Keywords Solar PV · BESS · UPQC · THD · VSI

1 Introduction

The increasing electricity demand has given rise to renewable energy sources for the generation of electric power. With the passage of time and the evolution of power electronic converters the grid size has become smaller and microgrid (MG) is introduced for supply of power to a local load [1]. Flexible AC Transmission System (FACTS) devices came into play and power delivery became more versatile with the introduction of unconventional methodologies. The major challenge of MG is to have a control topology to enhance power quality under varying load and generation and to mitigate harmonics. Solar energy is widely used as a source for MG operation [2]. The major limitation of solar PV is its intermittent nature which hinders its availability throughout the day. Unified Power Quality Controller (UPQC) is used

A. Bhattachatrya (✉)
Department of EEE, NIT Mizoram, Aizawl, Mizoram, India
e-mail: anagha.eee@nitmz.ac.in

D. Chatterjee · S. K. Goswami
Department of EE, Jadavpur University, Kolkata, West Bengal, India

off late for the above-mentioned purpose [3–5]. It has gained popularity to regulate harmonic current and to mitigate load voltage fluctuations with back to back connection of shunt and series Voltage Source Inverters (VSI) [6]. In this study, a UPQC is successfully designed and implanted to mitigate harmonics and enhance the power quality of the system. The simulation results in MATLAB/SIMULINK depicts the performance of UPQC under nonlinear loads, the performance is tested for symmetrical and unsymmetrical faults, and the proposed methodology is verified in hardware.

2 Microgrid Modelling

In this study, a microgrid system is considered of two Photovoltaic Source (PV) and a battery for backup during non-insolation period.

2.1 Solar PV System

The expression of current of a Solar PV array can be expressed as [7]

$$I_{pv} = \eta_p I_{ph} - \eta_p I_{rs} \left[\exp\left(\frac{q}{k\theta A} \frac{V_{PV}}{n_s} \right) - 1 \right] \tag{1}$$

and

$$I_{ph} = [I_{src} + k_\theta (\theta - \theta_r)] \frac{s}{100} \tag{2}$$

where I_{rs} and θ are the reverse saturation current and the temperature of p–n junction. I_{src} and I_{rs} are the short-circuit current of PV cell, n_s and η_p are the number of series and parallel cells attached to the string. The solar PV array is connected to the boost converter to generate the DC link voltage. The maximum power point (MPPT) of the PV array is generated by Perturb and Observation (P&O) Method which is extensively popular method for MPPT (Fig. 1).
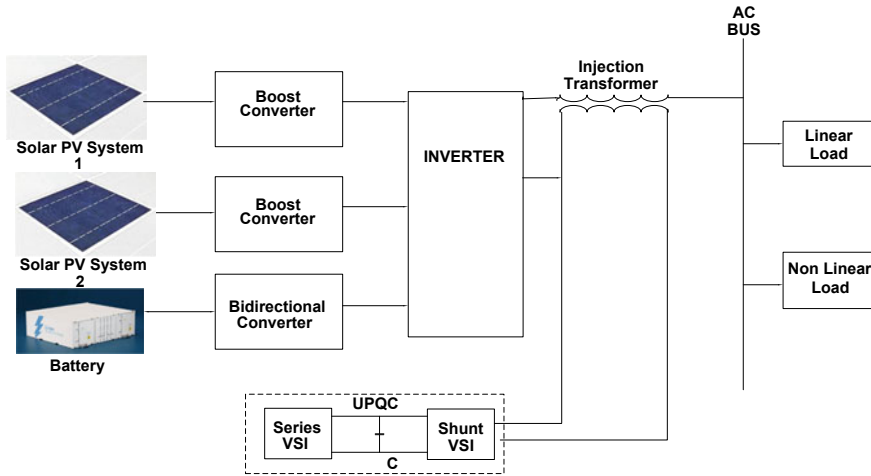
Fig. 1 Overall microgrid structure with UPQC

2.2 Battery Energy Storage System (BESS)

BESS forms the storage part of the system. A lithium–Ion battery module is considered for this proposed system. The main function of the BESS is to store energy when demand is less than generation and subsequently deliver power to the utility during non-insolation period and peak load demand. In general, a battery module comprises several units each where each unit maintains and monitors its State of Charge (SoC). The major objective is to maintain SoC during charging and discharging with respect to the utility.

The State of Charge (SOC) of battery is given by [8]

$$\text{SoC}(t) = \text{SoC}(t-1) - \frac{1}{C_{\text{nom}}} \int_{t_0}^{t} I_{\text{bat}}(t)\text{d}t \tag{3}$$

where C_{nom} and $I_{\text{bat}}(t)$ are the battery capacity (Ah) and the battery current (A), respectively.

2.3 Unified Power Quality Conditioner (UPQC)

Active filters are widely used for electric power transmission to mitigate harmonics as well as to improve power quality delivered to the utility. The shunt filters tackle the problems associated with current, whereas the series filter takes care of the voltage issues. Since connecting two devices simultaneously in the system increases the

complexity hence UPQC came into effect to provide both the series and shunt effect simultaneously. It gained popularity to minimize harmonics and to regulate load voltage with back to back voltage source inverter configuration.

The basic operation of a UPQC can be explained by the following equation [9].

$$i_{sh}(t) = i_s^*(t) - i_1(t) \qquad (4)$$

where i_{sh} i_s and i_1 represents the shunt inverter current, reference source current, and load current, respectively.

Similarly, series voltage control equation can be expressed as

$$v_{sr}(t) = v_1^*(t) - v_s(t) \qquad (5)$$

where v_{sr}, v_1 and v_s represent the series inverter voltage, reference load voltage, and actual source voltage, respectively.

3   Control Scheme

3.1   Droop Control Two Converter System

The PV modules are connected to two boost converters, and droop control is employed to control the flow of power to the load. The droop control is applied to each converter so that it measures its frequency which is measured using Phase Locked Loop (PLL) [10].

The dynamic equation of the converter in q–d frame is given by

$$V_{sq} = V_{lq} - L_s p I_{sq} - R_s I_{sq} - \omega_s L_s I_{sd} = M_q \frac{V_{dc}}{2} \qquad (6)$$

$$V_{sd} = V_{ld} - L_s p I_{sd} - R_s I_{sd} + \omega_s L_s I_{sq} = M_d \frac{V_{dc}}{2} \qquad (7)$$

where V_s and V_1 are the sources and load voltage, respectively. R_s, L_s are the resistance and inductance of the transmission line, respectively, M_d and M_q are the modulation index of the converter and ω_s is the frequency of the system and V_{dc} is the dc link voltage and $p = $ d/dt.

3.2 UPQC Control

Series Converter Control of UPQC
The reference source voltage is extracted from the distorted from the load side and is termed as V_s. A Unit Vector Template (UVT) is generated from the reference source voltage and is passed through PLL to generate the voltage at the fundamental frequency. The unbalance voltage is cancelled from the voltage signals generated from the UPQC which can be referred to as U_a, U_b and U_c.

$$\begin{bmatrix} V_a \\ V_b \\ V_c \end{bmatrix} = V_s^* \begin{bmatrix} U_a \\ U_b \\ U_c \end{bmatrix} \tag{8}$$

where V_s^* is the peak value of the reference voltage V_s.

The generated voltage signals are compared with the reference signal to generate the pulses for Series Compensation. This enables that the unbalance in the system voltage is balanced by the injection from the series compensator of the UPQC and mitigates the harmonics present in the system.

The detailed Series Compensating Control Scheme by UPQC is given in Fig. 2.

Shunt Converter Control of UPQC
For Shunt Compensation, the reference signal is generated from Clarkes Transformation of the source voltage also known as p–q theory.

The fundamental V_s^* is tracked from the inverter output of the PV module and then it is compared with the dc link voltage V_{dc} through a PI controller to obtain the power loss P_L. which will maintain the Dc link voltage. Since the UPQC supplies the fundamental active and reactive power demand hence the losses, $P_i + P_L$ associated for the DC link voltage is used for reference generate the reference current signal I_s^*.
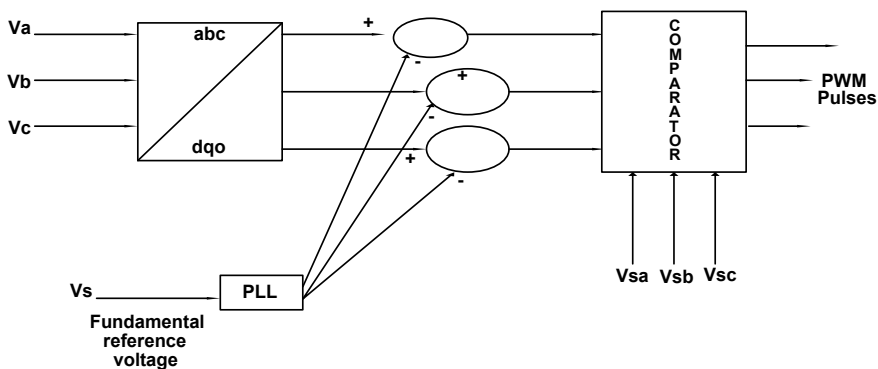
Fig. 2 Control scheme of series operation of UPQC

The mathematical expressions for calculation of real calculating real (p), reactive (q) and zero sequence (p_0) power can be given by

$$
\begin{bmatrix} p_0 \\ p \\ q \end{bmatrix} = \begin{bmatrix} V_o 0 0 \\ 0 V_\alpha V_\beta \\ 0 - V_\beta - V_\alpha \end{bmatrix} \begin{bmatrix} I_0 \\ I_\alpha \\ I_\beta \end{bmatrix} \tag{9}
$$

$$
\text{And} \quad \begin{bmatrix} V_0 \\ V_\alpha \\ V_\beta \end{bmatrix} = C \begin{bmatrix} V_{sa} \\ V_{sb} \\ V_{sc} \end{bmatrix} \quad \text{where } C = \begin{pmatrix} \frac{1}{\sqrt{2}} & \frac{1}{\sqrt{2}} & \frac{1}{\sqrt{2}} \\ 1 & \frac{-1}{2} & \frac{-1}{2} \\ 0 & \frac{\sqrt{3}}{2} & \frac{\sqrt{3}}{2} \end{pmatrix} \tag{10}
$$

Finally, three phase current reference is calculated as

$$
\begin{bmatrix} i_{s\alpha}^* \\ i_{s\beta}^* \end{bmatrix} = \frac{1}{V_\alpha^2 + V_\beta^2} \begin{bmatrix} V_\alpha & -V_\beta \\ V_\beta & V_\alpha \end{bmatrix} \begin{bmatrix} Pi + PL \\ -q \end{bmatrix} \tag{11}
$$

The resultant i_s^* is then converter by Clarkes Transformation and sent to PWM controller for generation of gate pulses.

The novelty of the proposed method is the ac component has both current and voltage harmonics. The introduction of instantaneous power based methodology overcomes both the harmonic problem, and UPQC is cancelling the harmonic components.

The overall control scheme of shunt control UPQC is given in Fig. 3.
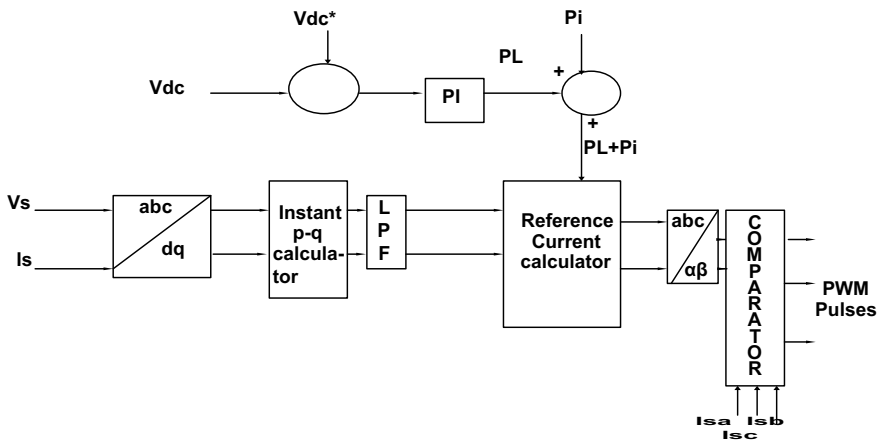
Fig. 3 Control scheme for shunt operation of UPQC
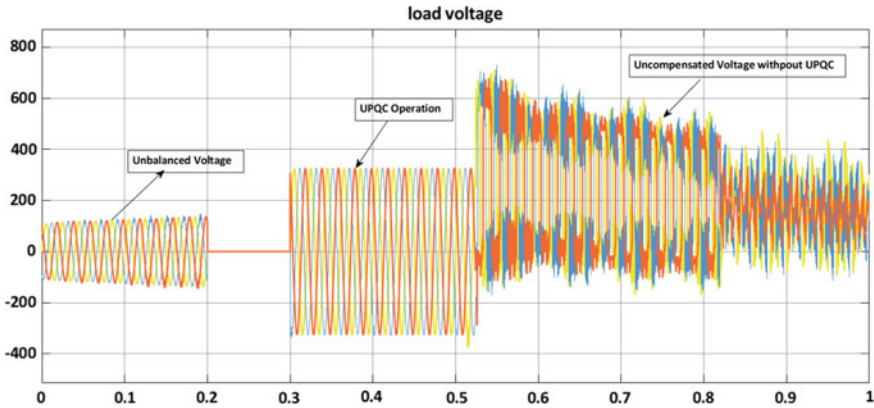
Fig. 4 Uncompensated and compensated load voltage with and without UPQC

4   Simulation Results and Discussions

The proposed system is implemented in MATLAB/SIMULINK and the system is studied for both compensation without UPQC and compensation with UPQC. In Fig. 4, the UPQC operation takes place from 0.3 to 05 s. Initially, the line was uncompensated. During 0.2 s a three phase fault occurs and power is reduced to zero. At 0.3 s, the UPQC operation starts and fault is cleared. We can observe that the voltage profile is balanced during UPQC operation. Subsequently when UPQC is switched off at 0.5 s, the voltage profile again becomes distorted with high harmonic content. Figure 6a depicts the harmonic content without UPQC, and from Fig. 6b, it is observed that harmonic content is reduced with the application of UPQC. The proposed scheme is developed in hardware, and Figure 7b has the hardware result which is similar to the simulation result of Fig. 7a (Fig. 5).

In Fig. 5, we can observe the load current variation with the injection of UPQC. The UPQC operates from 0.4 to 0.5 s, and we can observe balance load current. Beyond 0.5 s the load current becomes unbalanced.

5   Conclusion

In this paper, Voltage Current and Harmonic compensation are implemented in MATLAB, and it is observed that UPQC successfully delivers balanced voltage and current to the load. Further, the Total Harmonic Distortion (THD) is mitigated by UPQC which is observed from the simulation results. It is observed that the power quality is drastically improved with the application of UPQC. The proposed simulation results are implemented in hardware which establishes the simulation results with the hardware.
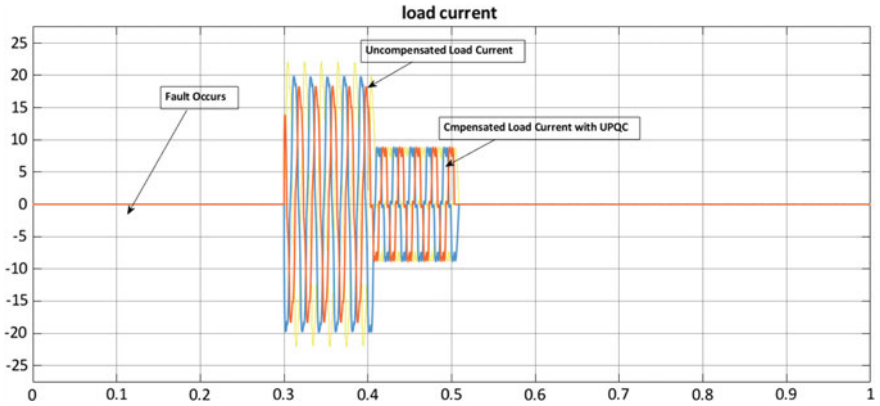
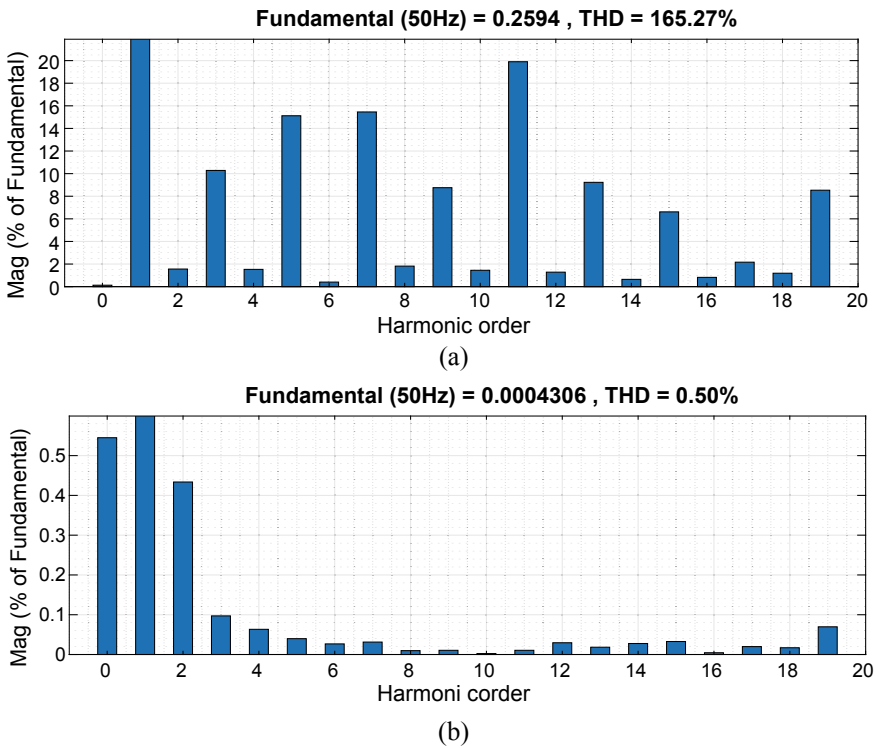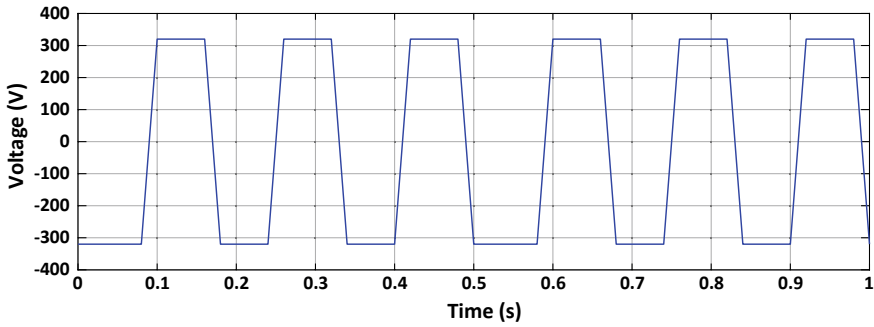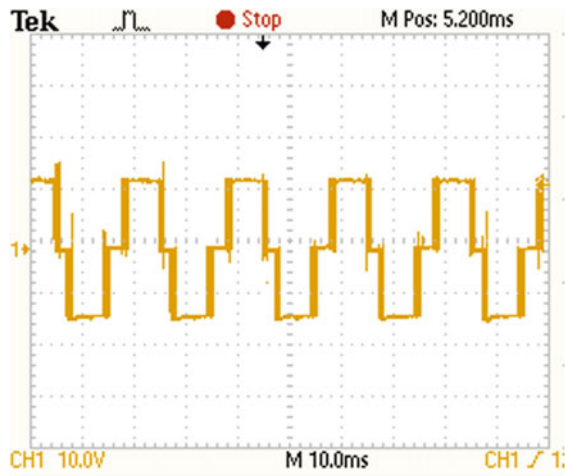**Fig. 5** Uncompensated and compensated load current with and without UPQC

(a)

(b)

Fig. 6 a THD without UPQC under nonlinear load. **b** THD with UPQC under nonlinear load

(a)

(b)

Fig. 7 **a** Voltage output from inverter. **b** Hardware result of inverter voltage output

References

1. Barker, P., Johnson, B., Maitra, A.: Investigation of the technical and economic feasibility of micro-grid based power systems. EPRI, Palo Alto, CA (2001)
2. Liserre, M., Sauter, T., Hung, J.Y.: Future energy systems: integrating renewable energy sources into the smart power grid through industrial electronics. IEEE Ind. Electron. Mag. **4**(1), 18–37 (2010)
3. Zheng, Z., Huan, Y., Shengqing, T., Rongxiang, Z.: Objective-oriented power quality compensation of multifunctional grid-tied inverters and its application in microgrids. IEEE Trans. Power Electron. **30**(3) (2015)
4. Khadkikar, V., Chandra, A.: UPQC-S: a novel concept of simultaneous voltage sag/swell and load reactive power compensations utilizing series inverter of UPQC. IEEE Trans. Power Electron. **26**(9), 2414–2425 (2011)
5. Devassy, S., Singh, B.: Modified p–q theory-based control of solar PV integrated UPQCS. IEEE Trans. Ind. Appl. **53**(5), 5031–5040 (2017)

6. De Araujo Ribeiro, R.L., de Azevedo, C.C., de Sousa, R.M.: A robust adaptive control strategy of active power filters for power-factor correction, harmonic compensation, and balancing of nonlinear loads. IEEE Trans. Power Electron. **27**(2), 718–730 (2012)

7. Yazdani, A., Dash, P.P.: A control methodology and characterization of dynamics for a photo-voltaic (PV) system interfaced with a distribution network. IEEE Trans. Power Delivery **24**(3), 1538–1551 (2009)

8. Mclennan, J.F.: Living building challenge standard 2.1, Seattle. International Living Future Institute, WA, USA (2012)

9. Strzelecki, R., Benysek, G., Rusinski, J., Debicki, H.: Modeling and experimental investigation of the small UPQC systems. In: Proceedings of Compatibility in Power Electronics, pp. 223–237 (2005)

10. Li, Y., Fan, L.: Stability analysis of two parallel converters with voltage–current droop control. IEEE Trans. Power Delivery **32**(6), 2389–2397 (2017). https://doi.org/10.1109/TPWRD.2017.2656062

Analysis of a Wind-PV Hybrid System with Smart Control for Grid-Secluded Critical Loads in Onshore Indian Area

Arunava Chatterjee (ID)

Abstract Wind and solar energy are extensively used as a generation source in the past few decades owing to its abundance in nature. This paper analyzes the prospective of a wind-photovoltaic (PV)-based hybrid generation scheme in a remote onshore location in eastern coastal India, intended to serve a rural health center. The scheme uses both wind turbine generator and PV panels for generation purpose. A laboratory-based experimental setup is used to study the proposed system. The system loads are automatically controlled via Internet of Things (IoT)-based smart controller, and a novel closed-loop control for the same is proposed in this paper. The system has capability to withstand single-phasing for short periods which also increases the consistency as regards availability of power. The system can be implemented for onshore grid-secluded area in grid-secluded region in India as validated by the simulation and experimental studies.

Keywords Wind-photovoltaic (PV) · Critical load · Hybrid generation · Smart control · Internet of Things (IoT)

1 Introduction

Constant upsurge in demand for energy with ever-increasing populace has led to diminution of natural fossil fuel assets. Thus, there is a continual need for development of a cost-effective, consistent, and inexhaustible source of energy for sustaining life. Among renewable energy sources, solar, wind, geothermal, tidal, and ocean wave are widely used for electricity generation [1]. However, all of the renewable energy sources are intermittent in nature and, hence, requires proper control measures and are costly to implement and also cannot be employed in most places. Amid all the renewable sources, wind and solar energies are chiefly used in grid-connected generation purpose. Sometimes, a hybrid source containing two or more energy sources

A. Chatterjee (✉)
Department of EE, Raghunathpur Government Polytechnic, Purulia, West Bengal 723121, India

is also recently used for electricity generation with better reliability as regards availability of power. For standalone mode of generation, such hybrid sources such as wind-PV [2] and hydro [3] are also being used to cater isolated and grid unreachable loads.

With the advent of various renewable energy sources, the need for supplying uninterruptable power to a critical load has become a source of utmost importance. It is observed that the hybrid generation sources are mostly useful for supplying grid-isolated loads efficiently [2]. Among the different renewable energy sources, wind is a confined, abundant, and a clean energy source but with an intermittent and uncontrollable nature. Also, it is an important source of energy especially in onshore and remote location. However, obtaining stable power from wind can be a challenging task and will require high-end control techniques. Wind along with solar-photovoltaic (PV) power as a hybrid source can be a possible solution to this problem as it is observed mostly that the wind and PV sources complement each other well [1].

In an emergent country like India, remote and country electrification is challenging to establish especially owing to the geographical barriers and economic considerations of transmission line costs and their associated losses. Therefore, a suitable standalone renewable source of generation for microgeneration-based application is essential. In the recent past, many studies are conducted which deal with large-scale electrification or electrification of a remote region in isolation from the grid [4–6]. In the recent past, ample research has been conducted regarding technical analysis and optimization of such hybrid systems [5, 7]. However, none of the studies report generation of power and its control for supplying critical loads such as a rural health center which is of an utmost importance in such a region.

Although most parts of India are electrically connected to grid, however, owing to geographical barriers, still major regions of eastern onshore India and some parts of sub-hilly Himalayan region are not connected to the grid. This makes it difficult for sustaining critical loads like a health center or hospitals which can be set up remotely and be helpful in pandemic situations and also in normal conditions. The paper aims at proposing a remotely controllable health center which can be viable to be set up in such conditions. The main focus is reliability as regards availability of power in varying operating conditions and easier control. The principal returns of the proposed scheme are:

- A novel closed-loop smart controller for the hybrid generation system with increased availability of power.
- Previously, no such technical analysis for the system is proposed including single-phasing fault ride through conditions for critical loads.

The hybrid system consists of a wind turbine and photovoltaic (PV) panel as major power sources. The system also has storage batteries connected as main storage and retrieval unit. A bidirectional converter is used to convert electricity from AC to DC and vice versa for storage and supplying loads. The block diagram of a hybrid generation system is shown in Fig. 1 with the proposed generation scheme shown in
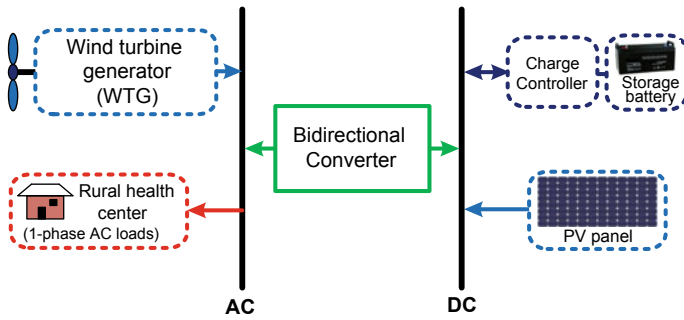
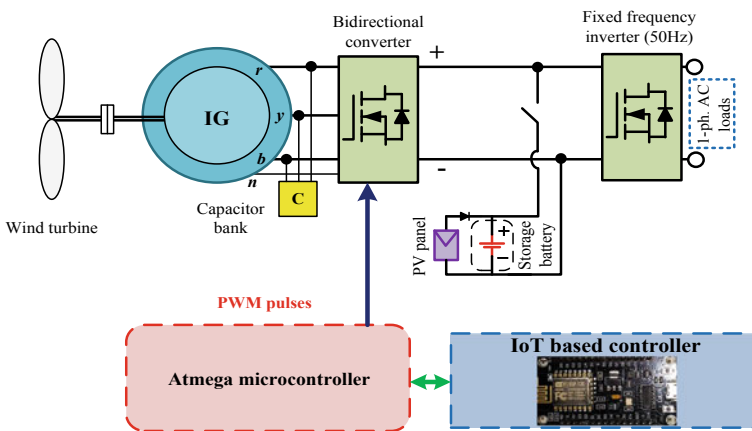**Fig. 1** Basic block diagram of the hybrid generation system

Fig. 2 Block diagram of proposed generation scheme

Fig. 2. The system is intended to be used for supplying a single setup which is not connected to the grid having a critical load setup of a rural health center.

Natural wind is highly variable, and thus, it is imperative to use some other sources with it. Moreover, this kind of hybrid source will help in making the system cost-effective by reducing the size of the storage batteries [8].

2 Control of the Proposed System

The proposed system stores the surplus power when the load demand is less than the generated power. The battery *SOC* will be calculated and updated for the purpose. If *SOC* is maximum (at 100% and indicated as 1), the excess power can be fed to a preset dummy load. If,

$$\left(P_{wtg} + P_{\mathrm{pv}}\right) > P_L \text{ and SOC}(t) < 1, \text{ then } P_{\mathrm{batt}} = (-)\text{ve,} \tag{1}$$

$$\text{else if } \left(P_{wtg} + P_{\mathrm{pv}}\right) > P_L \text{ and SOC}(t) = 1, \text{ then } P_{\mathrm{batt}} = 0 \tag{2}$$

where P_{wtg}, P_{pv}, P_L, and P_{batt} are the generated power from wind turbine generator, PV panel, load power, and power from the battery, respectively. Battery power is negative indicating charging mode of operation.

If the generated power is less than the load demand, the excess power required by the load will be fed from the storage battery. This will be possible only when battery *SOC* is sufficiently high (greater than 80%). Here, battery power becomes positive which indicates discharging mode of operation. If

$$\left(P_{wtg} + P_{\mathrm{pv}}\right) < P_L \text{ and SOC}(t) > 0.8, \text{ then } P_{\mathrm{batt}} = (+)\text{ve} \tag{3}$$

The system loads are turned ON/OFF remotely using Wi-Fi-enabled ESP8266 module via relay control. This is done to remotely control the loads based on availability of power. The entire control via ESP8266 is, thus, an application of Internet of Things (IoT). IoT has two layers which work concurrently for control. The physical layer consists of the hardware components like sensors, network hardware and the network layer, which is primarily used for communication with a device. A smartphone is used as Wi-Fi network provider which connects with the ESP8266 board for communication. Secure end-to-end data connectivity and control is ensured via Blynk software application installed in the smartphone which acts as dashboard for the IoT-based control. The dashboard is nothing but a graphical user interface for easy controlling the end user loads.

The DC bus voltage is sensed by a LV-25-P voltage sensor, and the sensed data are sent to an Atmega-based microcontroller for PWM generation for driving bidirectional converter and for controlling the speed of the DC motor prime mover. Inside the microcontroller, the sensed voltage is compared with a reference voltage, and the error is fed to programmed proportional-integral (PI) controller. The controlled output is compared with bus current which is sensed using LTS-25-NP sensor, and the error is fed to another PI controller for obtaining PWM pulses. The bidirectional converter also maintains the variable reactive power requirement of the IG during load and speed transients. The bulk excitation during the start of IG is provided using a conventional delta-connected capacitor bank.

3   Simulation and Experimental Results

A laboratory-based experimental prototype is chosen for validation of the proposed system along with simulation in *HOMER* environment. The system consists of a 2 kW, 415 V, 4-pole induction machine working as induction generator (IG). Capacitors of 36 μF, 400 V are connected in star for the capacitor bank. The IG system is

driven by a closed-loop-driven DC motor prime mover which emulates wind turbine characteristics. This is done with the help of a speed controller which is fed with wind turbine data. The controller adjusts the speed depending on the shaft speed through closed-loop control. The proposed system experimental setup and its block diagram are shown in Figs. 3a and b, respectively. The IoT components for the proposed system are shown in Fig. 3c.

In the present study, a typical AC load of 7.5 kWh/day is considered. The load consists of lighting in the health center during evening and night hours and emergency LED lights supporting first aid and minimal surgical procedures. It also consists of a single refrigerator for keeping vaccines, medicines, and running some basic laboratory equipment like an incubator and a centrifuge. The peak load is 560 W. The typical loads used in the facility are given in Table 1. In the study, monocrystalline PV panel is chosen at 500 W-peak (2 panels of 250 Wpk connected in series, 36 V) and has a mean output of around 130 Watts with a capacity factor of around 25.7%.

Higher rated PV panel is not considered as it increases the cost of the system, and it also increases the maintenance costs. The generator has a capacity factor of around 66.7%. Accordingly, the electricity production from it is 3273 kWh/yr, while that of PV panel is 705 kWh/yr. Thus, a combined value of 3979 kWh/yr electricity can be produced. The loads used are mostly lagging *p.f.* loads, but capacitors connected to IG can supply this VAr requirement quite effectively. The system is simulated in *HOMER* platform for a projection period of 25 years. The monthly generated average electricity production from the system is shown in Fig. 4.

The system is designed for supplying critical load, and thus, the system should reliably operate under faults. Provision is kept for the system to operate under phase fault by providing single-phase generation from the IG. In that case, an extra limb with switches is connected, and the IG is operated in single-phasing mode. The generated power is converted to DC and back to AC using a single-phase converter and fixed frequency inverter (operated at 50 Hz) connected at the output. The generator connection during such a fault is shown in Fig. 5. Maximum power generated in normal condition with v_L and i_L as line voltage and current is,

$$P_{\max} = \sqrt{3} v_L i_L \cos \phi \qquad (4)$$

During fault as shown in Fig. 5, if both windings generate with winding current not exceeding the safe limit, the generated power is,

$$P_{\max 1} = v_L i_L \cos \phi + \frac{v_L}{\sqrt{3}} i_L \cos \phi \qquad (5)$$

Thus, from (4) and (5), it is observed that almost 91% power can be generated with a phase fault [6]. Similar settings can be used to supply single-phase loads [9, 10].
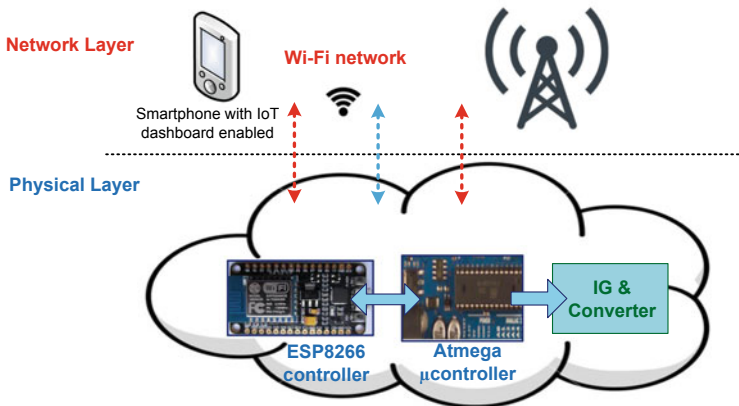
The system DC bus voltage and load voltage are shown in Fig. 6a with step change in load from half-rated to rated value shown in Fig. 6b. The DC bus voltage with changing turbine speed is shown in Fig. 6c. The voltage regulation is decent with
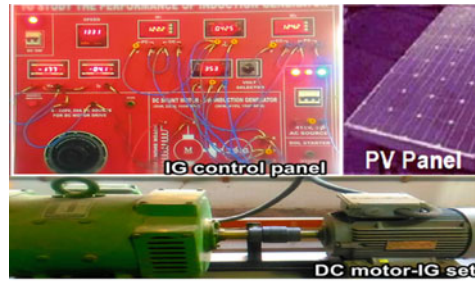
(a)
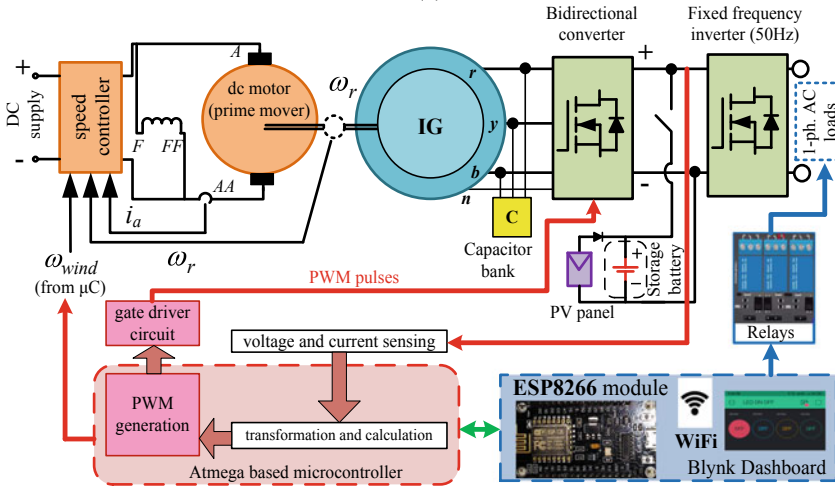
(b)

(c)

Fig. 3 **a** Experimental setup, **b** Block diagram, and **c** IoT components

Table 1 Loads used in the facility with their power consumption

Loads used		Power consumption (W)	Load type
LED bulb (3 nos.)		21	Base
Ceiling fan (2 nos.)		130	Base
Refrigerator		160	Base
Incubator		125	Peak
Centrifuge		120	Peak
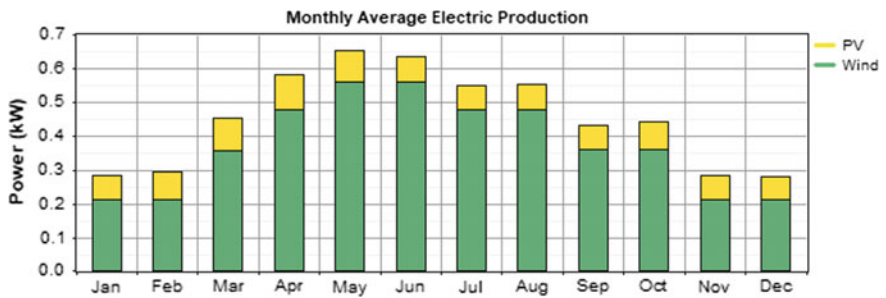
Fig. 4 Generated average electricity production from the simulated system

OC Generated
voltage across *rn* =
330V at 1145 r/min

Generated voltage 'Vg'
across *rn* with 1p.u.
load= 285V at 1035 r/min

Generated voltage
across *rn* with 1p.u.
load= 295V at 1060 r/min

OC Generated
voltage across *rn* =
300V at 1147 r/min

Generated voltage 'Vg'
across *rn* with 1p.u.
load= 245V at 1038 r/min

Generated voltage
across *rn* with 1p.u.
load= 270V at 1060 r/min
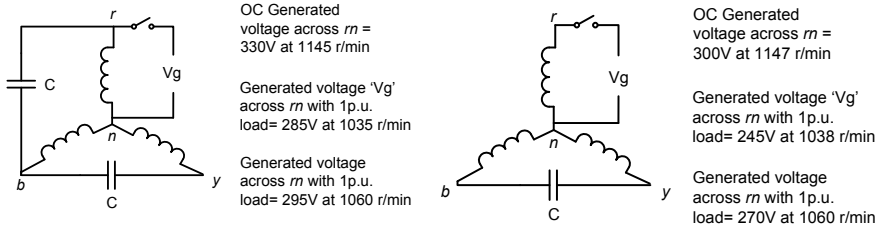
Fig. 5 Scheme of generator connection during phase faults

CH 1: Y-axis: 150V/div.
CH 2: Y-axis: 200V/div.

a)

CH 1: Y-axis: 2A/div.
CH 2: Y-axis: 200V/div.

b)

CH 1: Y-axis: 100 rpm/div.
CH 2: Y-axis: 100 V/div.

c)

CH 1: Y-axis: 2A/div.
CH 2: Y-axis: 200 V/div.

d)
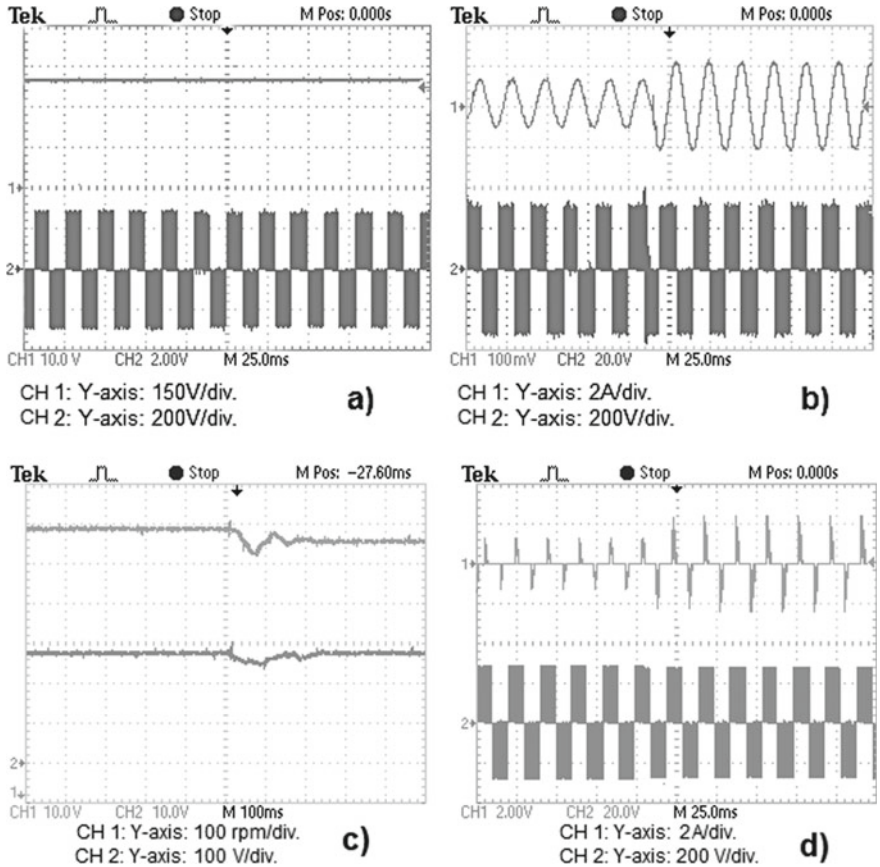
Fig. 6 **a** DC bus voltage and load voltage, **b** Load current variation with load voltage, **c** DC bus voltage with changing turbine speed, and **d** Load current variation with load voltage for nonlinear load like an incubator

stable output voltage as shown. When a nonlinear load is suddenly changed, the load voltage remains constant with proposed control as shown in Fig. 6d.

4   Conclusion

The paper extensively investigates the prospective of an onshore/remote hybrid generation scheme with smart control for supplying a critical load in a grid-isolated area. The system is shown to be reliable as regards availability of power. The system control is made through an IoT-based smart system for controlling the loads and Atmega microcontroller for controlling the variable excitation of the IG with the help of bidirectional converter. The durability also increases as it has a capability to fault override during single-phasing for some duration of time. The system is, thus, suitable for critical loads as validated by the proposed simulation and experimental study.

References

1. Patel, M.R.: Wind and solar power systems: Design, analysis and operation, 2nd edn. CRC Press, Boca Raton, USA (2006)
2. Roy, K., Chatterjee, A., Chatterjee, D., Ganguli, A.K.: A photovoltaic-based improved excitation control strategy of three-phase self-excited induction generator suitable for wind power generation. Electr. Power Compon. Syst. **43**(17), 1912–1920 (2015)
3. Reznicek, E., Braun, R.J.: Techno-economic and off-design analysis of stand-alone, distributed-scale reversible solid oxide cell energy storage systems. Energy Convers. Manage. **175**, 263–277 (2018)
4. Borowy, B.S., Salameh, Z.M.: Methodology for optimally sizing the combination of a battery bank and PV array in a wind/PV hybrid system. IEEE Trans. Energy. Convers. **11**(2), 367–375 (1996)
5. Chauhan, A., Saini, R.P.: Techno-economic optimization-based approach for energy management of a stand-alone integrated renewable energy system for remote areas of India. Energy **94**, 138–156 (2016)
6. Chatterjee, A., Chatterjee, D.: Analysis and control of photovoltaic-assisted three-phase induction machine operating as single-phase micro-wind generator. IET Gener. Transm. Distrib. **10**(9), 2165–2176 (2016)
7. Musa, I., Gadoue, S., Zahawi, B.: Integration of induction generator based distributed generation in power distribution networks using a discrete particle swarm optimization algorithm. Electr. Power Compon. Syst. **44**(3), 268–277 (2016)
8. Dalala, Z.M., Zahid, Z., Lai, J.S.: New overall control strategy for small-scale WECS in MPPT and stall regions with mode transfer control. IEEE Trans. Energy Convers. **28**(4), 1082–1092 (2013)
9. Chatterjee, A., Chatterjee, D.: PV-assisted microgeneration scheme with single-phase induction generator suitable for wide speed range application. IET Power Electron. **10**(14), 1859–1869 (2017)
10. Chatterjee, A., Chatterjee, D.: An improved current balancing technique of two-winding IG suitable for wind-PV-based grid-isolated hybrid generation system. IEEE Syst. J. **14**(4), 4874–4882 (2020)

Internet of Things for Fishery

Sourish Haldar , **Arvik Sain** , **Sk Suman** , **Linkan Biswas** ,
and **Kapataksha Biswas**

Abstract This article is presenting a robust solution for remotely monitoring the quality of water in fisheries in realtime. The parameters that will be monitored by the system are pH, turbidity, water level, and temperature. A waterproof camera is installed for visually checking the fishes. Also, a mechanism for regulating the water level is implemented. If the level falls below a certain predetermined threshold, a water supply pump would be turned ON. The system is built around Raspberry Pi 4. The Raspberry Pi minicomputer collects all the sensor data, does the processing, and sends it to cloud storage through the Internet. All cloud data are remotely accessible by a custom developed Android application.

1 Introduction

Pisciculture plays an important role in Indian culture and economy. It provides food for a major section of the population of India at any time. Today, the natural water bodies are severely affected by pollution from numerous sources. This article describes a method to monitor the water quality in regard of suitability for the fishery. The fish-farmers regularly face the challenge of ensuring that water of fishery is suitable for the type of fish being cultivated. The standard procedure is to present the collected samples to the laboratory for testing. This procedure takes time and the cost involved is significant. The laboratories are usually located in distant towns. The population of fishes is critically susceptible to variation of water parameters within a short span of time. Unfavorable changes result in poor yield and in the worst case death of the population. This work was done toward an automated system, which uses dedicated sensors, devices, and the Internet of things (IoT) technology

S. Haldar (✉) · A. Sain · Sk Suman · L. Biswas · K. Biswas
Department of Electronics and Communication Engineering, JIS College of Engineering,
Kalyani, West Bengal, India
e-mail: sourish.haldar@jisgroup.org

for the monitoring of the quality of the water in fisheries. The proposed system makes use of a turbidity sensor, pH sensor, temperature sensor, a water level sensor, and a dissolved oxygen sensor. There is a provision for an automatic feeding mechanism in the system. The feeder is started after a pre-programmed interval. The system will also be equipped with water-resistant AI cameras, which will record the data on the size of the fish. Fishermen will get all the valuable data on their phones with the help of an Android application along with appropriate charts. The user will also get real-time notifications.

2   Literature Survey

The work described in [1] detects the quality of aquaculture water with the help of microclimate. The solution is designed for culture of seaweed in salt water, as well as fish farming. The second article [2] is about monitoring and control of systems of aquaculture in the farming of seaweed and fish. The main feature of the system is a PCDuino microcontroller, which performs the function of control of data transmission and the working principle of an automatic sampling unit, which is based on the comparison of the values of the measured parameters with a particular threshold. Recirculation aquaculture system is integrated with the sensors and the CNS development of the filter system of measurement, control, and all of the parameters, variables. In the third article [3], a continuous water quality monitoring system is presented which consists of a sensor to measure dissolved oxygen, pH, and the collection of data on the basis of the PCDuino, microcontroller, a sampling device, and a PC-based graphical display. In [4], the data which have been measured can be displayed on a computer for more analysis. This is the prototype of the system is expected to find wide application in the field of the monitoring of the environment for the aquaculture industry. This article presents a method for monitoring and controlling the movement of the fluid direction. The Arduino microcontroller development board to read the rate from the flow meter and sends it to the Raspberry Pi, a microcomputer for controlling the solenoid valve, which is connected to the pipeline. The sixth article [5] gives an overview of popular methods for the measurement of dissolved oxygen (DO). The principal methods of measuring dissolved oxygen are optical and electrochemical. Electrochemical sensors can be divided into polar graphic, pulsed, and electroplating. The sensors can be designed to test for biochemical demand of oxygen, spot, sampling, and/or long-term monitoring. Temperature is typically measured by a thermistor in the sensor and recorded by a counter. The seventh article [6] shows an analog pH meter, specially designed for the Arduino controller, and it has a built-in simple, convenient, and practical connection and function.

3 Proposed Plan and Methodology

This system has several types of sensors such as Pi camera, dissolved oxygen sensor, pH sensor, turbidity sensor, temperature sensor, and water level sensor. These sensors will act accordingly to look into the environmental situation in the fishery. Depending on the temperature and level of the water, the automatic water pump system will be activated to restore nominal condition. The unit is equipped with an automatic feeding system. This device may be used to check the size of fishes on a regular basis, to ensure that they are growing in accordance with set criteria. This device is built with off-the-shelf modular components with affordability, simplicity, and ease of use in mind (Figs. 1 and 2).

3.1 Techniques and Features

I.   Turbidity sensor SKU_SEN0189 used in this project provides analog output depending on the number of suspended particles in the test liquid. The output voltage of the probe varies between 4.1 V and 0 V with a 5 V power supply. If the turbidity value of the sample is less than 1 NTU, the water will be transparent and the voltage output of the probe would be highest. As the number of suspended particles increases, the output voltage decreases and NTU increases. If the turbidity is higher than the 300 NTU, then the water body is not suitable for breeding of fish.
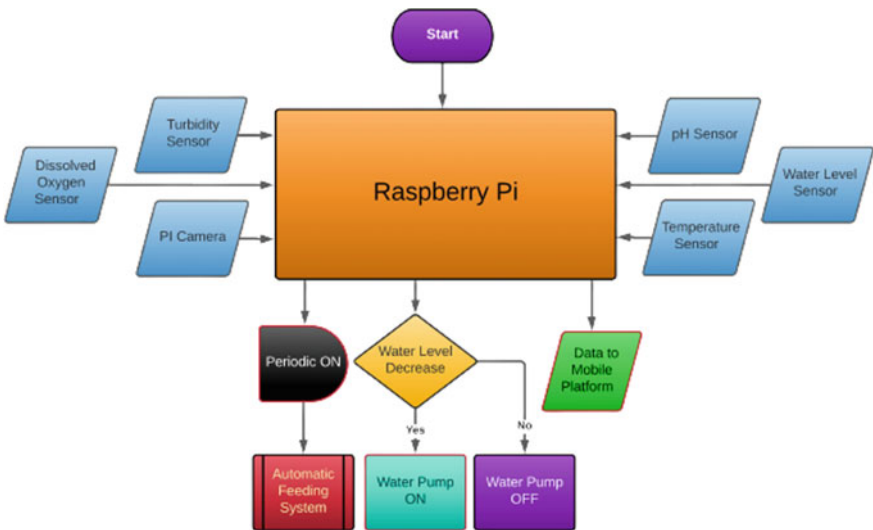

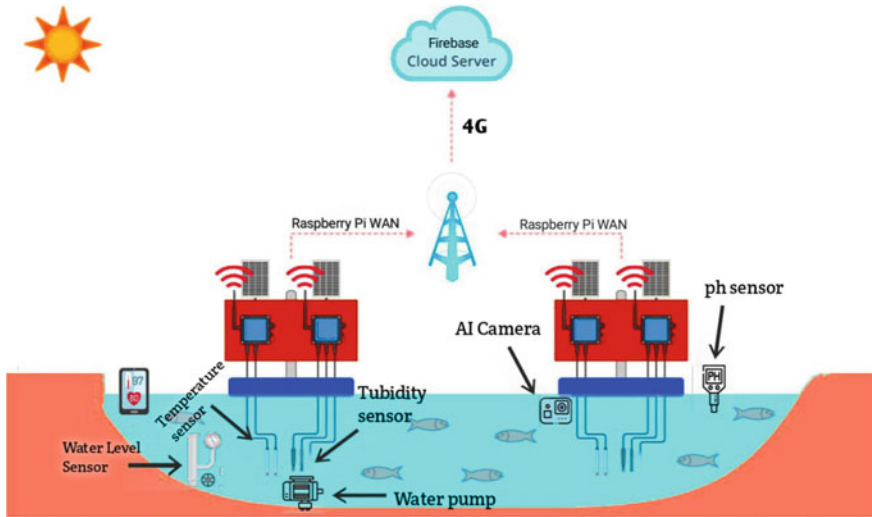**Fig. 1** Flowchart for IoT and mobile application development

Fig. 2 Functionality of the developed system

II. The pH sensor is used to find the pH and alkalinity of the water. The tolerable pH range is from 6.5 to 8.5.

III. The built-in temperature sensor allows a preset temperature of 25 °C. The range allowed in between 5 and 40 °C. When the temperature will be out the predefined value, an alarm will be started.

IV. A water level sensor has been implemented for real-time measurements. When the water height drops under the predefined value, the user would receive a message. An automatic water supply pump is installed, with manual override. The water pump is used to regulate temperature and level of water. When the temperature of the water increases over or the water level drops under the predefined value, the system will start the pump to increase the volume of water thereby nominally maintaining the level and temperature.

V. There is an auto feeding system integrated with this machine. The system turns the feeder ON for a certain time period at predetermined times of the day.

VI. A submersible Pi camera is installed that helps to identify the size of the fish in the pond. The OpenCV platform which is a classifier model is used in software for processing the images from the camera to get relevant data about the fishes and their size.

There is a mini-PC called Raspberry Pi. All the modules and the sensors will be connected to it. It has built in Wi-Fi system (Fig. 3). This system allows us to send all of the data from the peripheral devices to the cloud network. For that purpose, we use Google Firebase. The administrator will be able to see this information on any Android device as per convenience. Administrator would also receive alerts on their device as per programming. Due to use of cloud-based login authentication, all consumer data will be private and protected.
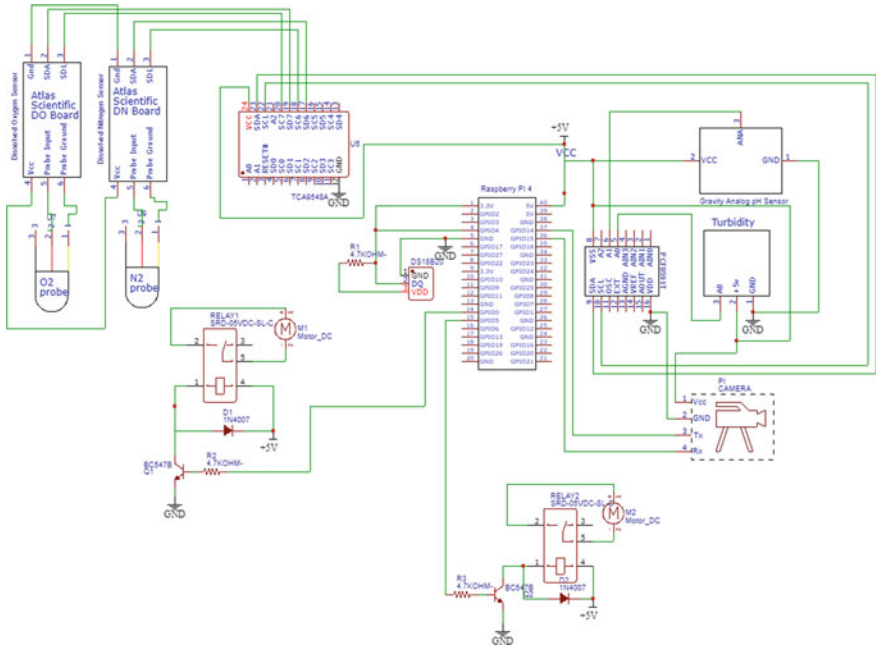
Fig. 3 Schematic of interconnection of modules

3.2 Algorithm for Estimating the Size of Fish

For identifying a fish and estimating its size, a cascade classifier algorithm has been used with deep learning which will measure the total number of the pixels of a known metric and then compare with image of fish. It is said the "pixels per metric" ratio that has been formally defined below. To get the nearly exact size of a particular fish in the image, firstly, it is necessary to perform a "calibration" by utilizing the object which will be called as an object of reference. The object which will be used as reference must have certain properties as below:

- Property 1: The measurements of the given object (in terms height and width) must be in a unit which can be measured (like centimeters, foot).
- Property 2: The reference object should be chosen in such a way that the image must have the properties that will be helpful to compare with the real-time image. The reference image should be placed in a way so that it can be easily identifiable. The reference image must have a distinguishable color, shape, and unique size from all other objects in the surrounding.

For this, python computer vision libraries like SciPy, Imutils, NumPy, and cv2 are imported. The image would be loaded from the storage device of the camera and converted to grayscale. Next, the image would be smoothened by using a Gaussian filter. After the above procedure, the edges in the image could be properly detected

which will be nearly in the middle of edge detection map. It is necessary to find the contours which are the outlines of the image. The contours are selected from the left to the right position of the value of pixel per static value. After this, all the contours should be stared for looping. In case, the contours are small, the algorithm will reject the particular region by assuming that it is the noise of the image which was not removed at the time of edge detection procedure. Next, the Euclidean distance is measured in the set of the middle points. At last, the pixel per metric value is compared with the size of original image.

Example for the algorithm:

Suppose, the fish has a width of 4 inches. Now, suppose that fish width is measured by 628 pixels. The pixels per metric is, therefore: 628 px/4 in = 157 pixels. Using this ratio, the size of a fish can be measured.

Drawback of the algorithm:

The fish reported as 4 inch × 7.5 inch. However, not all these results are perfect. The measurements of the object are not cent percent accurate. The reasons are given below:

- The camera frame does not have an accurate 90° angle on the object in the corners. Without a perfect 90°, the size of objects would be deformed.
- Calibration is not performed for every image. Ideally, before taking the picture of the object, an image of the reference should be taken for keeping all parameters ideal. Without calibration of these parameters, the images can be subject to the radial lens distortion.

4 Results

The whole setup was used to measure the different parameters of four water bodies in Memari area of Burdwan district of West Bengal.

The readings of the turbidity sensor SKU SEN0189 are listed in Table 1. Unit of turbidity is Nephelometric turbidity units (NTU). Water fit for human consumption has to have turbidity less than 5 NTU as per WHO. Clear ponds have reading less than 25 NTU, while moderate water bodies have a range from 25–100 NTU. If the reading is more than 100 NTU, the water is considered muddy and it affects the respiration mechanism of fishes. Also, high turbidity causes low growth of planktons, which are primary source of nutrition for fishes. The measured value is suitable for pisciculture.

Table 1 Turbidity sensor outputs

Water body	NTU reading
Pond 1	12.4
Pond 2	13.35
Pond 3	9.78
Pond 4	7.52

Table 2 pH sensor outputs

Water body	pH reading
Pond 1	7.5
Pond 2	9.26
Pond 3	7.4
Pond 4	6.4

Table 3 Dissolved oxygen sensor output

Water body	DO reading in (mg/L)
Pond 1	4.78
Pond 2	3.26
Pond 3	4.78
Pond 4	3.26

Before measuring pH of the water bodies, the pH probe was calibrated using standard pH solutions of pH 4.0 and 9.18. The readings of the pH measurement are shown in Table 2. The range of acceptable pH values for pisciculture is 6.5–8.5.

Dissolved oxygen (DO) requirement is greatly dependent on the species of fish, ambient temperature, time of the day, season, and several other factors. As such, there can be no absolute threshold for all species of fish. Being cold blooded animals, fish needs more DO at higher ambient temperatures. Studies have suggested that a minimum of 4–5 parts per million (ppm) of DO would support a large body of fish consisting of various species. The optimum DO level is over 9 ppm. Measurement methodology of [7] was followed for this work. Dissolved oxygen level below 3 ppm is fatal for almost all species. The measured dissolved oxygen levels are above the minimal limit but not optimum (Table 3).

Figures 4 and 5 are displaying the used temperature sensor DS18B20 [8] output. The graphs show that the used sensor is working in the predefined range which is 5–50 °C. Acceptable range depends on the species of the fish being cultured. For the
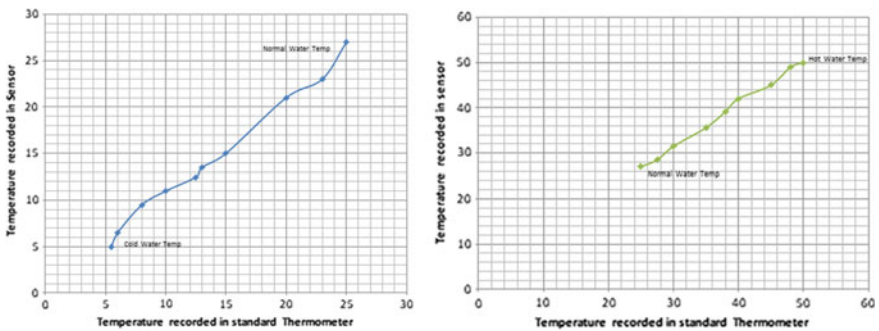

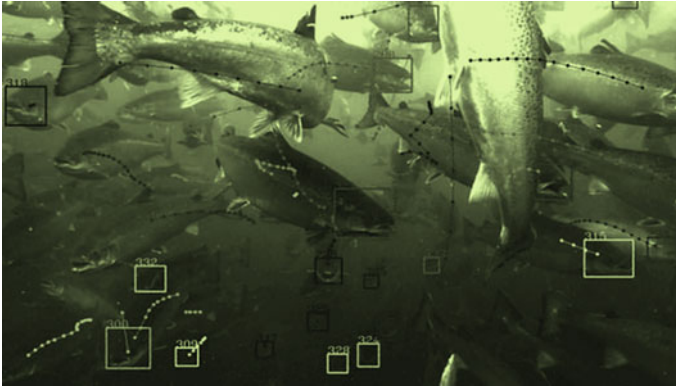**Fig. 4** Output of temperature sensor for increasing and decreasing temperatures

Fig. 5 Size of fish is indicated by AI camera

Burdwan area, the indigenous species cultured, the highest acceptable temperature would be around 40 °C. The temperature measurement of the ponds was not stressed on as the temperature varies diurnally as well as seasonally. Whenever measured, the temperatures were in acceptable range.

A waterproof camera has been used for detecting the fish size in real-time manner when the fishes will come near the camera. The user will get the notification about the fish size through Firebase system. This system is automatic and real-time monitoring procedure.

Nominally, the water level regulation system operates with the inputs from water level and temperature sensor. If the temperature increases or level decreases beyond use determined threshold, the pump starts working to fill the water body. User can override and operate the pump manually also. The automatic operating of the pump sends an alert to the user's mobile application. An Android application has been specifically developed for this system (Fig. 6).

5   Conclusion and Future Work

A prototype version of this system is used in inland water. The system is able to check the pH, temperature, dissolved oxygen, and fish size. The system was also able to start the automatic feeding machine and the water pump at a certain time period at the time of testing. The collected data were sent to the Android application in mobile phone with the Internet of things technology. Future work will focus on the demonstration of the integrated system. The installation of such a system was a challenging task as the system needs to be robust and weather resistant, as well as illegal interference resistant. In addition, the system must have security features in order to ensure authorized access. Along with the additional settings and features of the system, it can be a valuable tool for small-scale fisheries in rural areas.
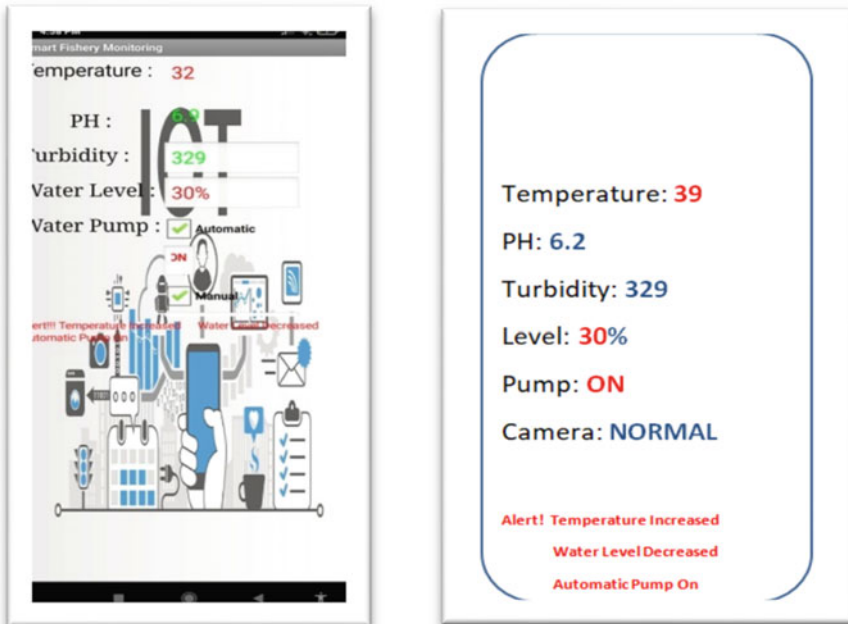
Fig. 6 Android platform application for monitoring real-time sensors outputs

References

1. Salim, T.I., Haiyunnisa, T., Alam, H.S.: Design and implementation of water quality monitoring for eel fish aquaculture. In: 2016 International Symposium on Electronics and Smart Devices (ISESD), IEEE (2016)
2. Mahalik, N.P., Kim, K.: Aquaculture monitoring and control systems for seaweed and fish farming. World J. Agric. Res. **2**(4), 176–182 (2014). http://pubs.sciepub.com/wjar/2/4/7
3. Wiranto, G.,Mambu, G.A., Hiskia, Hermida, I.D.P.,Widodo, S.: Design of online data measurement and automatic sampling system for continuous water quality monitoring. In: 2015 IEEE International Conference on Mechatronics and Automation (ICMA), IEEE, China (2015)
4. Suresh, N., Balaji, E., Ant3, K.J., Jenith, J.: Raspberry pi based liquid flow monitoring and control. IJRET: Int. J. Res. Eng. Technol. eISSN: 2319–1163 | pISSN: 2321–7308 (2014)
5. Parlaungan, Y.: Kualitas Air danHubungannyadenganPenyakitIkan Air Tawar, Carmudi (2016)
6. Suryono, T., Badjoeri, M.: Kualitas Air PadaUjiPembesaran Larva IkanSidat (Anguilla Spp.) DenganSistemPemeliharaan Yang Berbeda **20**(0854–8390), 169–177. Limnotek (2013)
7. Measuring Dissolved Oxygen. http://www.fondriest.com/environmental-measurements/equipment/measuring-water-quality/dissolved-oxygen-sensors-and-methods/ 2016, [online]
8. Temperature Sensor-Waterproof (DS18B20). https://www.sparkfun.com/products/11050 (2016)

Methods for Effective Speed Control of DC Shunt Motor-Part 2: Fuzzy Logic-Based PID Controller Tuning Method

Ramireddy Karthik, Harshit Harsh, and Y. V. Pavan Kumar

Abstract PID controller is used in applications like motor speed control, liquid level control, temperature control, etc. It works well in both closed-loop and open-loop system configurations. To set gain parameters in the PID controller, the main issue is with the computation of gain parameters in offline mode. So, the controller may not be adjusted itself when deployed online. The disturbance that occurs in a system is spontaneous, thereby the PID gain parameters should be adjusted in tune with the disturbance online. So, the online mode of controller tuning has become popular. Artificial intelligence (AI)-based logical techniques like fuzzy logic, neural networks, and genetic algorithm-based methods have gained prominence in the process of tuning the gain parameters of a PID controller. There is a provision to train the controller in presence of disturbance and hence a better disturbance rejection can be obtained. In the present work, the fuzzy logic is used for tuning the gain parameters of the PID controller adaptively to control a DC shunt motor. From the time domain characteristics, it can be concluded that the controller tuned using fuzzy logic which performs better when compared to a controller tuned using conventional tuning methods.

Keywords PID controller · Fuzzy logic · Speed control · Controller tuning · Time domain performance · DC shunt motor

1 Introduction

Direct current (DC) motors are used widely in general applications and across many industries. Further, the DC motors are used in the construction of servo motor, stepper

R. Karthik · H. Harsh · Y. V. Pavan Kumar (✉)
School of Electronics Engineering, VIT-AP University, Amaravati, Andhra Pradesh 522237, India
e-mail: pavankumar.yv@vitap.ac.in

R. Karthik
e-mail: karthik.18bev7028@vitap.ac.in

H. Harsh
e-mail: harshit.18bev7002@vitap.ac.in

motor, extruders drive motors, actuators for industrial robots, feed driver for CNC machine tools, etc. It is also used in common applications like fans, AC, mixer grinder, etc. DC motor speed can be controlled easily when compared to AC motor, and DC motor is more efficient when compared to AC motors. So, this paper mainly focuses on DC motor. There are different types of DC motors available, among them, series and shunt DC motors are widely used. Series DC motors have armature winding connected to field winding in a series manner, whereas, DC shunt motors have field winding which is connected in parallel to the armature winding. Normally, shunt DC motors are widely used because of ease of speed control. DC motors, by the way in which the speed is controlled, are classified into two types—armature-controlled and field-controlled motors. In field-controlled DC motors, speed is controlled by changing the field flux keeping the armature voltage constant; while in armature-controlled DC motor, speed is controlled by altering the armature voltage and fixing the field flux as constant. Normally, armature-controlled DC motors are used because of their less complex operation. When armature-controlled DC motors are used in series DC motor configuration, it gives good starting torque but the speed decreases as the load is increased. When armature control DC motor is used with shunt configuration, it gives less starting torque but its speed is constant irrespective of the weight of the load. Hence, armature control shunt DC motor is preferably used and has many applications.

There are several design methods available for tuning the controllers for various applications such as control of wind turbine [1] and speed control of motors using PID controllers [2–4]. As we know, PID controlling methods are offline methods that will be inactive when real-time errors are induced in the system. So, to reject the disturbance, the PID controller with fuzzy logic is required which is of the best artificial intelligence technique known by [5–15]. In this paper, various types of disturbances are injected into the DC motor system operation and the analysis is carried out to verify the efficiency of fuzzy logic PID controller fused DC motor system and a comparative analysis of time domain parameters is conducted between conventional PID and proposed fuzzy logic-based PID controller and discussed the results.

2   Description of PID Controlled DC Shunt Motor

In recent years, rigorous research is done for identifying an effective way of controlling the speed of DC motor through PID controller. DC motor is categorized into the electrical model and mechanical model. In the electrical model, the differential equation involving the quantities of armature circuit can be obtained as (1) whose Laplace transform is obtained as (2). Similarly, the differential equation representing the mechanical quantities of the motor is obtained as (3) whose Laplace transform is obtained as (4). Finally, the transfer function of electrical and mechanical models of DC motor is combined as (5). The design specifications of the DC motor were

Table 1 Specifications of shunt motor modeling

S. No.	Parameter	Specifications
1	L_a	0.23 H
2	R_a	1.35 Ω
3	K_T	1.41 N m/A
4	J_s	0.000052 kg m^2
5	B_o	0.01 N/(rad/sec)
6	K_b	0.235 V/(rad/sec)

shown in Table 1. Further, the transfer function given in (5) can be simplified as (6) by substituting the values of DC motor specifications given in Table 1.

$$L_a \frac{dI_a}{dt} + R_a I_a + E_b = V \tag{1}$$

$$(L_a s + R_a) I_a(s) = V(s) - E_b(s) \tag{2}$$

$$J \frac{d^2\theta}{dt^2} + B \frac{d\theta}{dt} = T_m = k_T I_a \tag{3}$$

$$\left(J s^2 + B s\right)\theta(s) = k_T I_a(s) = T_m(s) \tag{4}$$

$$\frac{\theta(s)}{V(s)} = \frac{K_T}{s[(Js + B)(L_a + R_a) + K_T K_b]} \tag{5}$$

$$\frac{\theta(s)}{V(s)} = \frac{1.41}{s[(0.000052s + 0.01)(0.23s + 1.35) + 0.33135]} \tag{6}$$

where $\theta(s)$ = angular displacement, $V(s)$ = terminal voltage, J = moment of inertia, B = viscous friction coefficient, L_a = armature inductance, and R_a = armature resistance.

3 Designing of Fuzzy Logic PID Controller

From the analysis of the conventional methods presented in [16], the WJC method is recommended as the best proportional integral derivative controller method for supervising the speed of the DC shunt motor. The main idea of the controller designing is to obtain better controlling responses with respect to stability and robustness for the set point changes and load disturbances. These disturbances can be intentional or unintentional. The controller is expected to provide superior performance in all such cases.

The artificial intelligent control structure is a combination of a higher-level simple logical controller and basic level classical controller. The higher-level logical controller gives the respective responses according to the disturbances and errors present in the system, whereas the basic level classical controller will deliver the outputs according to the situation. In the proposed architecture, a fuzzy controller is placed as a higher-level controller and a PID controller is placed as the basic level controller. The diagram representing the hybrid control architecture of the fuzzy logic PID controller which is visualized in Fig. 1. The membership functions of deviation, K_P, K_I, and K_D are displayed as the pictorial representation given in Fig. 2.

The fuzzy logic PID controller is trained though Mamdani ruled fuzzy trained interface by using membership functions. Finally, the PID gain parameters are trained into fuzzy logic PID controller and acquired the ability to change its values according
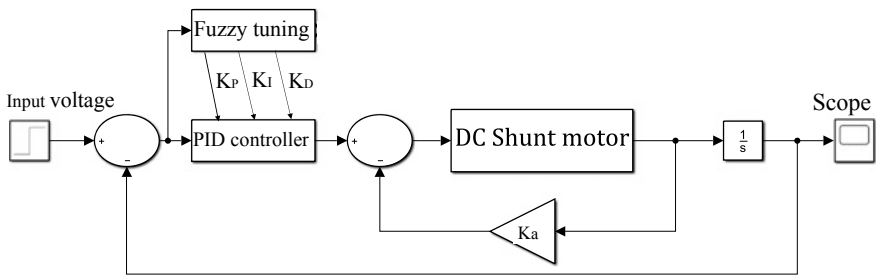

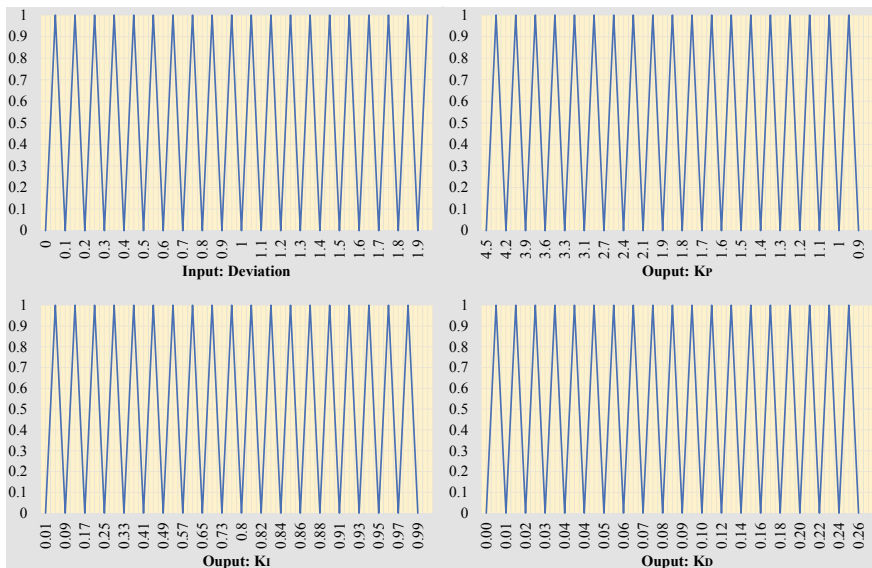Fig. 1 Hybrid controller architecture of fuzzy logic PID controller

Fig. 2 Membership functions of deviation, K_P, K_I, and K_D
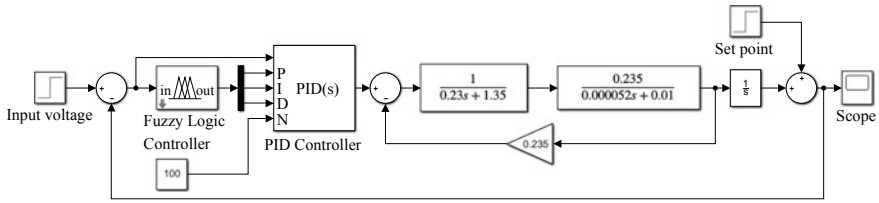
Fig. 3 Simulink model of the system having fuzzy logic trained PID controller

to the external disturbance that occurred to the system. The simulink diagram used in the simulation is shown in Fig. 3.

4 Simulation Results and Analysis

Extensive simulations have been carried out to persuade the importance of the proposed fuzzy logic tuned PID controller. The comparative time domain response of the conventional PID controller and the proposed fuzzy PID controller is plotted between the speed and run time of the DC motor. For this, various circumstances such as without disturbance, sinusoidal disturbance, ramp error disturbance, and chirp disturbance are realized and the system responses are plotted as shown in Figs. 4, 5, 6, and 7, respectively.

To classify the effective controller between the conventional PID controller and the proposed fuzzy logic PID controller, a various time-response indexes such as peak undershoot, peak overshoot, and settling time are taken into consideration and are computed using the standard procedure. This index is calculated under all test
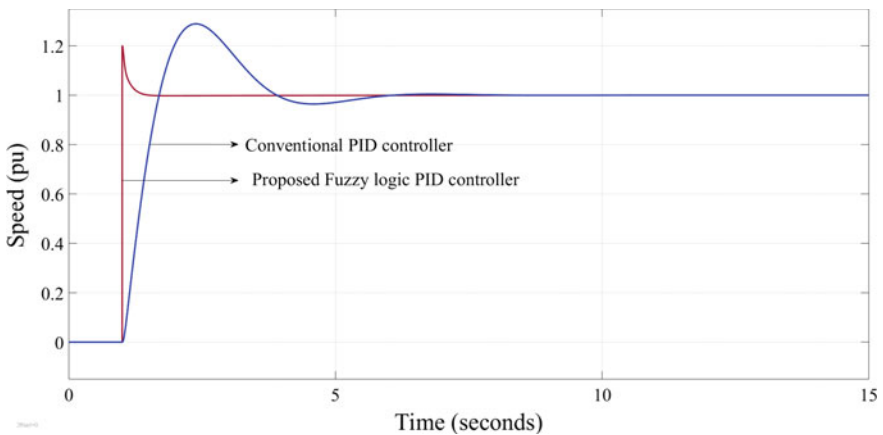

Fig. 4 System responses of both controllers without disturbance
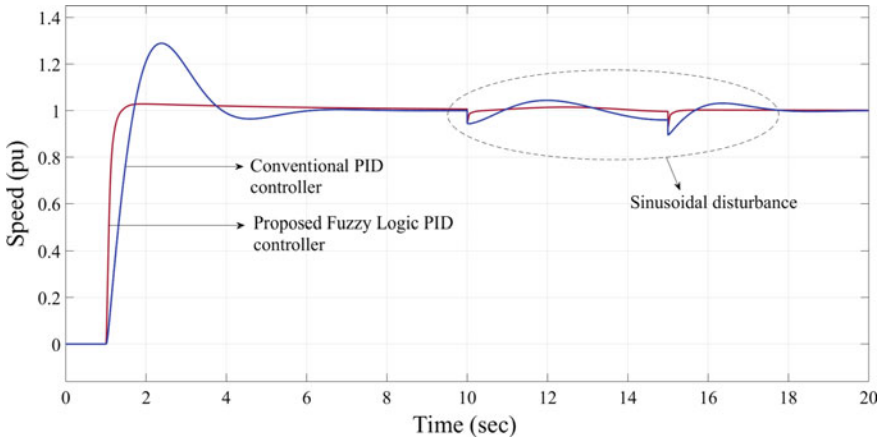
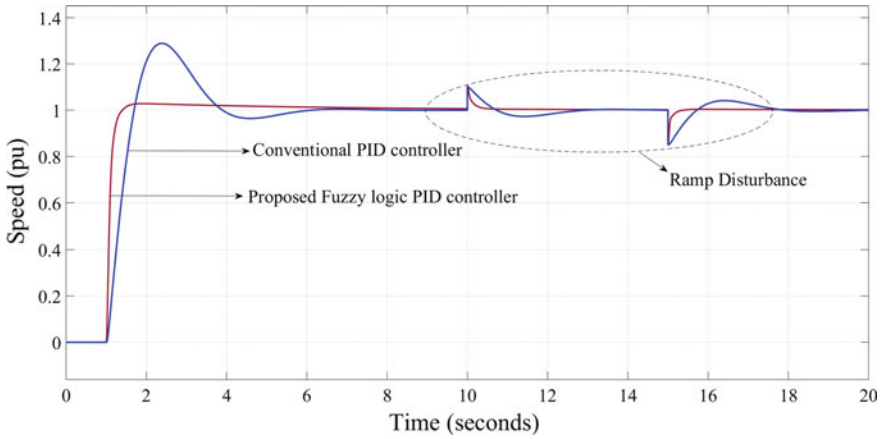Fig. 5   System responses of both controllers under sinusoidal disturbance

Fig. 6   System responses of both controllers under ramp signal disturbance

conditions that are described above. Using this index, the efficient controller can be decided in such a way that the controller exhibits lower time domain parameters in the majority of the specifications. All the quantitative computations of the time domain parameters are shown in Table 2.

5   Conclusion

Through this paper, an investigation on the performance of a DC shunt motor with a PID controller when tuned with both conventional tuning methods and proposed
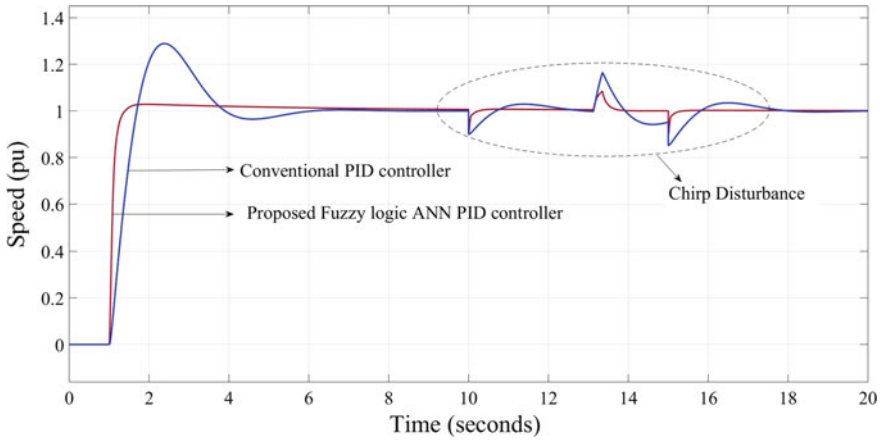
Fig. 7 System responses of both controllers under chirp signal disturbance

Table 2 Time domain parameters computed with the respective controllers

System model	Type of controller	Peak undershoot	Peak overshoot	Settling time
Without disturbance	Conventional PID	0.964	1.29	3.2
	Proposed fuzzy PID	0.998	1.2	6.7
Sinusoidal disturbance	Conventional ZNPI	0.89	1.045	20.6
	Proposed fuzzy PID	0.93	1.01	11.5
Ramp disturbance	Conventional ZNPI	0.85	1.105	13.5
	Proposed fuzzy PID	0.855	1.1	12
Chirp disturbance	Conventional ZNPI	0.85	1.16	14.7
	Proposed fuzzy PID	0.9	1.08	11.6

ANN-based tuning is presented. In both cases, some key disturbances were injected into the system and obtained the results were analyzed. From the comparative analysis projected in Table 2 and by analyzing the simulation results, it can be concluded that the proposed fuzzy logic PID control method is more effective than conventional PID tuning methods. From the results obtained, the proposed fuzzy-based PID controller is identified as well suited to minimize the effect of random disturbances that occur in DC shunt motor operation.

References

1. Karthik, R., Hari, A.S., Kumar, Y.V.P., Pradeep, D.J.: Modelling and control design for variable speed wind turbine energy system. In: 2020 International Conference on Artificial Intelligence and Signal Processing (AISP 2020), pp. 1–6. Amaravati, India (2020)
2. Sangamwar, A., Barapatre, N., Karekhar, S., Vairagade, D., Hardas, B.V.: Modelling and simulation of speed control of DC shunt motor using PID controller. Int. J. Innov. Res. Electr. Electron. Instrum. Control Eng **5**(3), 42–46 (2017)
3. Olvera, R.T., Carbajal, F.B., Mejia, O.A., Gonzalez, A.V.: An adaptive speed control approach for DC shunt motors. Energies **9**(11) (2016)
4. Girirajkumar, M.S., Kumar, A.A., Anantharaman, N.: Speed control of a real time D.C. shunt motor using SA based tuning of a PID controller. Int. J. Comput. Appl. **5**(11), 20–26 (2010)
5. Deepshikha, Kumar, R.: A fuzzy logic speed controller for separately excited DC motor and its comparison with PID speed controller. IOSR J. Electr. Electron. Eng. (IOSR-JEEE) **9**(4), 46–52 (2014)
6. Baidya, D., Roy, G.R.: Speed control of DC motor using fuzzy-based intelligent model reference adaptive control scheme. Adv. Commun. Devices Netw. **462**, 729–735 (2018)
7. Rai, J.N., Singhal, M., Nandwani, M.: Speed control of DC motor using fuzzy logic technique. IOSR J. Electr. Electron. Eng. **3**(6), 41–48 (2012)
8. Velmurugan, J., Sekar, M.R., Pushpavanam, B., Muthukumaran, S.: Design of an intelligent controller for armature controlled DC motor using fuzzy logic technique. Int. J. Recent Innov. Trends Comput. Commun. **4**(11), 203 (2016)
9. Salim, Ohri, J., Naveen.: Speed control of DC motor using fuzzy logic based on labVIEW. Int. J. Sci Res. Publ. **3**(6), 1–5 (2013)
10. El-kholy, E.E., Dabroom, A.M.: Adaptive fuzzy logic controllers for DC drives: a survey of the state of the art. J. Electr. Syst. **2**(3), 116–145 (2006)
11. Ahmad, A.M., Rai, P., Mahato, A., Mahapatra, M.: Speed control of a DC motor using fuzzy logic application. Int. J. Res. Eng. Technol. Sci. **7**, 1–11 (2017)
12. Sathya, T., Premalatha, R., Raja, G.B., Karthikeyan, N.: Performance comparison of conventional and fuzzy logic controller on DC motor. Int. J. Adv. Res. Comput. Commun. Eng. **5**(5), 190–196 (2016)
13. Dubey, S., Srivastava, S.K.: Speed control of using fuzzy logic controller. IJBSTR Res. Paper **1**(7), 34–38 (2013)
14. Tushir, M., Srivastava, S.: Type-2 fuzzy logic controller implementation for tracking control of DC motor. Int. J. Comput. Netw. Secur. (IJCNS) **3**(1), 34–41 (2015)
15. Shabbiruddin, R.A.: Speed control techniques using fuzzy logic and response surface methodology. Int. J. Adv. Soft Comput. Appl. **4**(2), 1–16 (2012)

Animal Human Conflict Resolution Mechanism by Machine Learning in Passive Optical Wireless Networks

Deepa Naik and Tanmay De

Abstract Increasing urbanization, cities stretching into their outskirts, and expansion in road-rail networks have resulted in encroachment of wildlife space wild animals frequent outside their habitat due to shrinkage in space as there is a scarcity of food, water, and shelter. Naturally, there is an uptrend in human-animal conflicts. This has resulted in a loss of valuable human and animal life, serious injury, traffic blockades, etc. In this paper, we demonstrate the integration of sensor networks with optical and wireless access networks to augment animal-human cohabitation. Sensor networks detect wild animals approaching near the road/speeding trains. Images of the animals are captured and preprocessed using a combination of a small global positioning-integrated computing edge device with a built-in camera. From the collected data only, the relevant information is transferred to the base station to minimize energy consumption. At the base station, data are classified using machine learning. Convolutional neural network (CNN) is used to predict the type of animals found in the area and generate alert messages to the authorized people. The base station which is enabled with machine learning algorithms to distinguish the latency-related traffic demands. The allocating bandwidth is done by the optical line terminal (OLT) and they are enabled with machine learning algorithms to predict the bandwidth demand. This will reduce the latency time related in bandwidth requests and bandwidth granted by OLT. The dynamic allocation of bandwidth depending on the traffic demand in the hybrid networks and data processing data at origin lower network congestion and source to destination node delay. For simulation purposes, we have considered only two animals (elephant, dear) that are more likely to frequent on roads/train tracks.
.

Keywords Hybrid networks · Base station · Edge computing devices · Machine learning · Wireless sensor networks (WSNs) · Convolutional neural network (CNN)

D. Naik (✉) · T. De
National Institute of Technology, Durgapur, India
e-mail: dn.12cse1103@phd.nitdgp.ac.in

1   Introduction

The wild animals roam around roads, villages, train tracks, and near water resources. As a result, human-animal conflict occurs, resulting in human deaths and accidental collisions between animals-vehicles/trains [1]. Although, today's technology developments in computers and networking are being employed to develop smart cities. These rail/road networks, for example, were not designed with animal coexistence in mind [2]. Electrically, controlled fences are part of a smart fault detection system in Sri Lanka [3]. Elephants in India are prevented from crossing railways via a wireless sensor network (WSN) consisting of passive nodes and infrasound sounds, according to [4]. In [5], implements the infrared and seismic sensors for detecting wild elephants entering townships. Similar work found in [6, 7] using wireless sensor networks to alerts the passing vehicle drivers about wildlife crossing the road. In [8], the author collects data and detects animals using a neural network-based animal classification algorithm. Some animals only leave the house at night. Infrared sensors can detect the animal's night vision, which results in a posture-adjusted image. In this case, machine learning is useful in detecting animals early on. The work in [9] focused on the drone-based cattle farming to detect the faming animals which are spread over large area.

For an early warning alert model, we suggest a cloud-based hybrid network (comprising passive optical and wireless networks). Sensors, passive optical networks, and AI-enabled base stations (BSs) form the foundation of this hybrid network. Using three cutting-edge technologies, we developed early warning systems. Cloud computing, artificial intelligence, and fiber-wireless networks will contribute to minimizing the latency time of the service requested. The most important parameter is the latency in the early identification of the animal and sending an out alert message to the respective authority. When traffic demands are too high, the edge device (base station) has provided minimum computing and processing power to process the data locally for crucial and latency-sensitive early warning systems. The use of raw data at the edge can aid in the reduction of network congestion.

In the proposed work, we first identify animal movements at the sensor nodes then send sensor data to the base station using wireless sensor aggregation networks. The enabled base station allowed for the processing of vital data and the request of bandwidth from the OLT based on traffic demands. The OLT enabled with a cloud services which can run the machine learning algorithms to pre-compute the bandwidth ahead from the historical traffic demands.

The main contributions of this paper are discussed below.

- A traffic management system with an early warning system for approaching animals.
- For data acquisition and processing, we use a hybrid networks with a convolutional neural network to predict animal detected.
- This technology is cost-effective and has a shorter delay in serving the delay sensitive application. Machine learning algorithms for early prediction of the traffic demands to minimize the time delay in serving the requests.

The remainder of this paper has Sect. 2 which briefly introduces hybrid networks and machine learning. Section 3 illustrates the role of machine learning algorithms as applied to human-animal cohabitation, for traffic prediction. In Sect. 4, it discusses role of machine learning in image prediction. An early warning system and performance through simulation in Sect. 5. Finally, in Sect. 6, we conclude the work and discuss the future scope of this work in Sect. 7.

2 Hybrid Network

The term "hybrid network" refers to a network that combines optical and wireless networks. This network provides universal Internet access at a reasonable cost, with comparable better capacity than traditional wireless networks. A base station connects nodes to an optical network unit (ONU). These nodes could be sensors, smartphones, hand-held devices, and computer machines that can be connected ONU with the wired line or wireless links. Optical line terminal (OLT) is positioned at the service provider's central office. OLT is responsible for allocating bandwidth to ONUs. The ONUs are used to connect end users. Heterogeneous traffic is handled by ONUs. This passive optical device manages wireless traffic between base stations as well as wired traffic from fiber-to-the-home (FTTH) subscribers.

We have used orthogonal frequency-division multiplexing (OFDM) with the PON technology. The WDM PON and TDM PON may be used instead of OFDM PON. The WDM PON wavelength channels may not be utilized efficiently due to the variation in the network traffic (during morning time and at night its high and mind day the network traffic may be low). The TDM PON may not able to cater the delay sensitive traffic. The most suitable technology is OFDM PON that is used as backend. OLT generates the OFDM spectrum and assigns a fraction of it to individual ONUs. This reduces latency and increases synchronization [10]. A central office (OLT) dynamically allocates spectrum in PON subsystems based on the traffic predicted at its ONUs. This improves bandwidth usage efficiency and decreases latency.

Figure 1 shows the wireless sensor nodes that have been deployed along the road/train tracks. Wireless links connect these sensors to the base station. When they detect an animal, they communicate the animal's image and location to the base station.

WSN gateways and base stations are enabled with AI-enabled machine learning algorithms to transfer only relevant data for further processing at the OLT. This leads to minimizing energy consumption and network congestion. But edge computing devices (base station and WSN gateways) suffer from limited processing and storage capability. Hence, a cloud-based infrastructure connected to the OLT accurately deduces information from the animal's raw data.
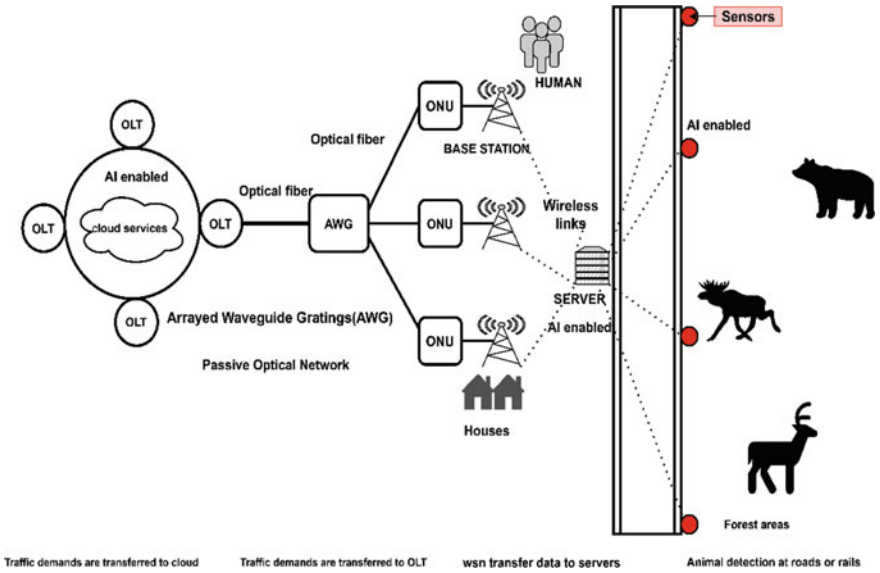
Fig. 1 Hybrid networks

3 The Role of Machine Learning in Serving Latency Aware Traffic Demands

The use of machine learning algorithms has enhanced the performance of hybrid networks. Machine learning is applied in our work to allocate bandwidth and object detection. For heterogeneous services, allocation is based on traffic forecast. Upstream data rates in PON are lower (e.g., 2.5 Gb/s), whereas downstream traffic at OLT is considerable. (For example, 10 Gb/s). As a result, upstream data are crucial. Because traffic patterns change throughout the day, allocating OFDM subcarriers and time slots at ONU are extremely difficult. In this case, ML-based traffic forecast aids in meeting traffic needs [11].

In 4G, the maximum delay rate is on the order of milliseconds. As a result, for latency-sensitive applications, specific frequency bands are required. To estimate traffic demands, the OLT uses AI-enabled cloud services. Latency is reduced using the long short-term memory (LSTM) network concept. It learns long-term dependencies and avoids vanishing gradients. LSTM networks mine out future traffic predictions using historical traffic patterns. Once bandwidth allocation from OLT to ONU is done, base station sends an early alert signal to passing vehicular and humans under the coverage area of the base station.

4 The Role of Machine Learning in Image Detection

Animal identification, here, is using passive infrared (PIR) sensor. ML algorithms are used for classifying images locally. Images may be captured and transferred instantaneously or it will be captured, processed, and then transferred to base stations. The base station has a pre-trained model based on a convolutional neural network (CNN) algorithm to classify the images.

The sensors at the road side are powered by renewable solar power so they are constrained by power. To optimize energy consumption, only a few sensors continuously sense the effects of animal crossing. These effects result in a change in, pressure, vibration, etc. False alarms may be triggered by wind disturbances and large birds. These are to be differentiated from actual crossings. Infrared sensors are mostly used for this. Once animals are detected, other sensors are activated to capture images. These images, when processed, give an idea of about animal's size, position, speed, numbers, and direction.

We are concerned with the only type of animals present. We capture images and classification algorithms are run. Different traffic patterns are used to train a machine learning algorithm. Convolutional neural network (CNN) classification models used for training. 2000 images of elephant and bear for training and validation and testing (1000) images of each type. Sampled and predicted data are used for training and testing MI models.

This model can recognize four image classes after retraining. They are the presence or the absence of an animal inside the captured image, if preset then what type of animal is found and the location of the animal and the average walking or running speed of the animals are computed.

Here, an early warning system, its implementation details, and its evaluation by a simulation are studied. Performance is analyzed by designing subsystems, the detection of animals founds during day and night time on roads/trail tracks. The steps involved are (i) animal detection; (ii) message transfer to base stations (BSs); (iii) send bandwidth requests to OLT; and (iv) alert message transmission to vehicles/humans. The flow of algorithm is depicted in Fig. 2.

5 Simulation Results

In the hybrid network, we used ONUs, a WSN network of five sensors connected to reach base station with the shortest routing path. The WSN topology is shown earlier in Fig. 1.

In order to train the model, we require the data sets for animal images and network traffic demands between the ONUs. We have downloaded the animal images using image downloader extension, which is chrome extension and the data preprocessing done on the acquired data set and for traffic prediction, the data set was generated using Python ID.
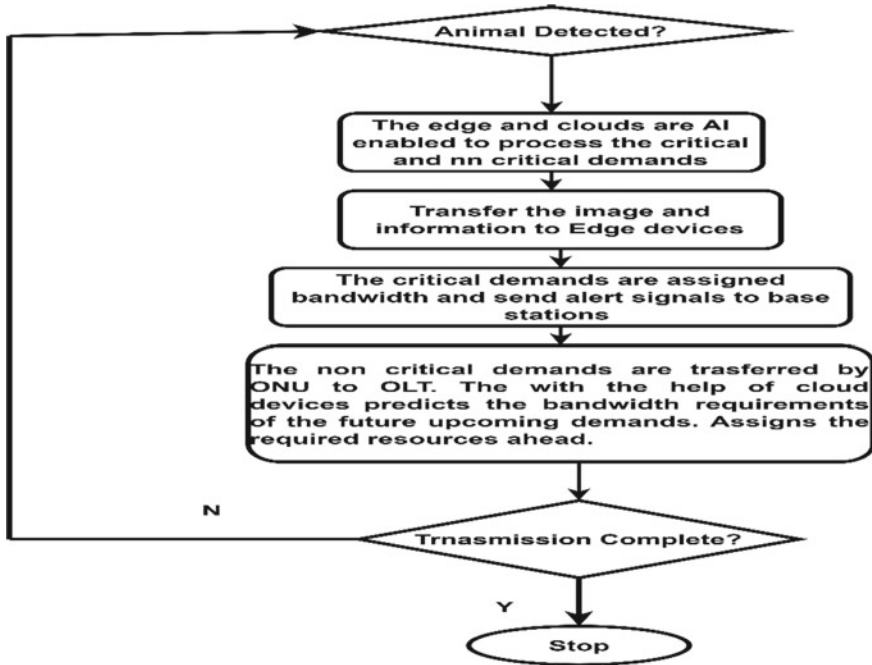
Fig. 2 Flow of the algorithm

The training accuracy is close to 100%, and the validation accuracy is in the 70–80% per range as depicted in Figs. 3 and 4. The trained model is overfitting as it does well with images it has seen before but not so well with images it has not seen before. In order to avoid over fitting, one simple method is to apply image augmentation. The ImageDataGenerator class in the Keras deep learning neural network library fits models using image data augmentation. Here, transformed versions of original images are created and a training data set is created. This transformation process involves a series of image manipulation techniques like shifts, flips, and zooms. Image data augmentation is applied to the training data set and not to the validation or test data set. After applying the image augmentation, this gave us training accuracy around 85% and validation accuracy around 81%after running the simulation for 100 epoch (as depicted in Figs. 5 and 6).

The normal scenario of the CNN model takes 8 s to detect, and depending on the captured images, the cameras are capable of identifying the average distance of the animal detected and send the alert message to passing vehicles and humans in the premises. The augmentation is applied to CNN model, the model takes 16 s to detect the objects (Table 1).

Our focus, here, is on upstream reservation. Hence, based on upstream reservation from edge devices to BSs to central office, results are derived. A sufficiently large fixed size queue is maintained to store data packets of animal class at each ONU.
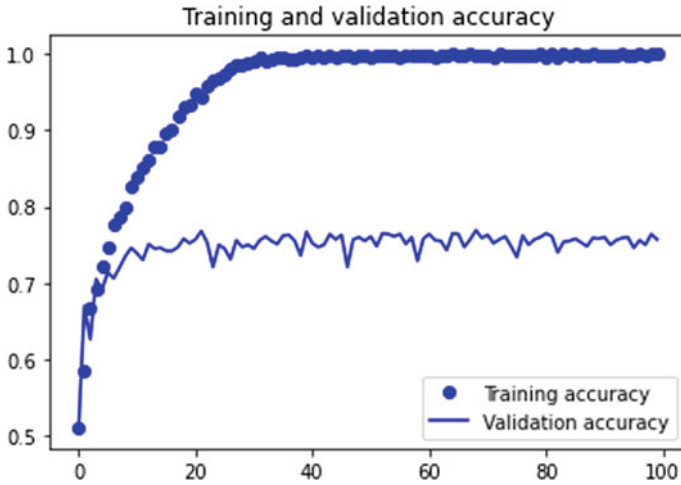
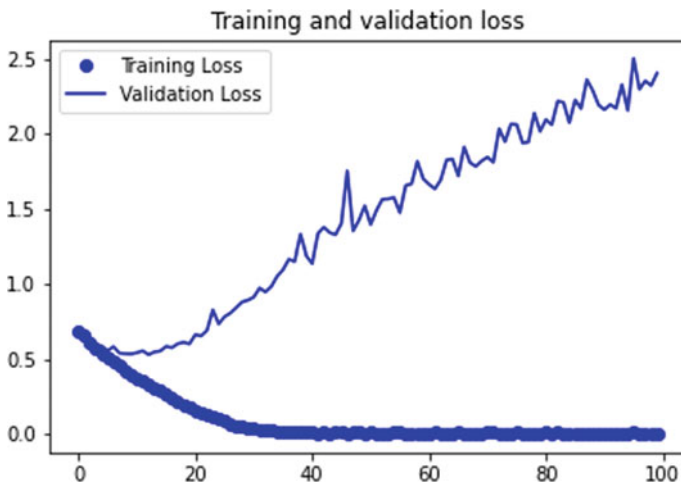**Fig. 3** The training and validation accuracy (normal)

Fig. 4 The training and validation loss (normal)

Different classes of service depending on their delay requirement are served differently. Delay non tolerant classes served immediately. The base station is AI enabled to classify the urgent traffic and send the traffic demands to OLT. The clouds are also capable of handling noncritical data packets. The clouds services are used to predict the bandwidth demands ahead and help in reducing the latency time associated with traffic demands.

During the training phase, train on all 2000 images of each class, for 100 epochs, and validate on all 1000 test images. Per epoch displays the loss, accuracy, validation
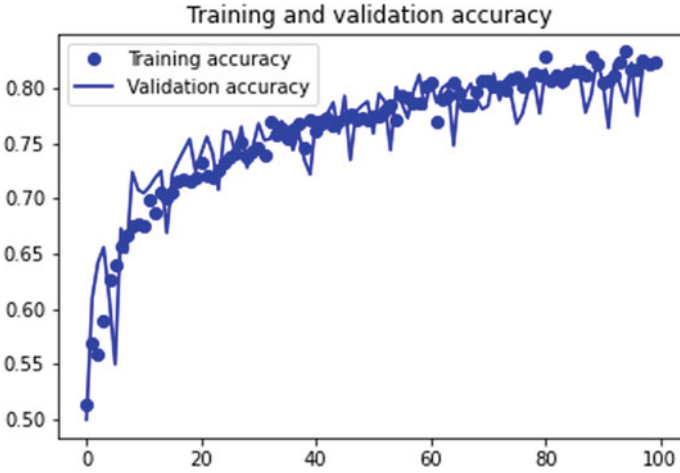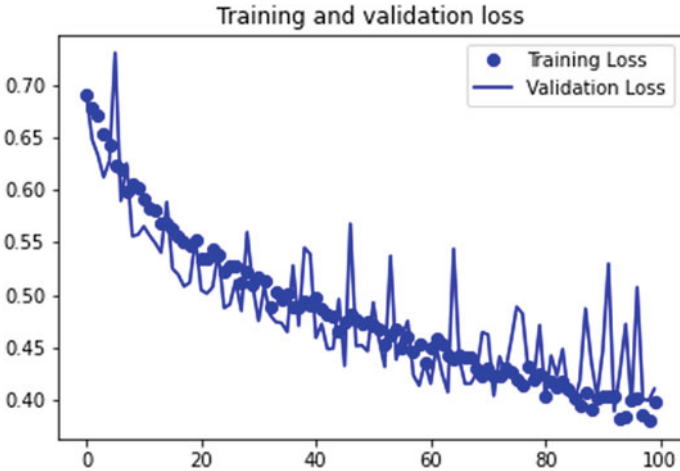
Fig. 5 The training and validation (augmented)

Fig. 6 The training and validation loss (augmented)

Table 1 The training and validation accuracy

Methods	Time	Training loss	Training accuracy	Validation accuracy	Validation loss
Normal	8 s	0.0181	0.9975	2.3321	0.7420
Augmentation	16 s	0.3442	0.8570	0.4282	0.8170
Dropout layers	16 s	0.3979	0.8235	0.4105	0.8210

Table 2 The bandwidth prediction accuracy

Methods	Training accuracy
Simple RNN	7.2349772453308105
LSTM	7.110543251037598
GRU	7.153998374938965

loss, and validation accuracy. The loss and accuracy are indicates the progress of training phase. The classification of the training data sets is then measuring it against the known label, calculating the result. Accuracy is indicating correct guesses.

The validation accuracy is the measurement with the data that have not been used in training. The loss: 0.0179, accuracy: 0:9945, validation loss: 2:0214, validation accuracy: 0:7020. This model got over-fitted. In order improve the image classification, the dropout layer is added. Then, the model achieved the loss: 0.4509, accuracy: 0:78,755, validation loss: 0:5123, and validation accuracy: 0:74,020. So, the proposed model able to classify the images. These images with the critical bandwidth requirements are severed by the base station. The alert signal message is sent to respective premises, where the animal is found. No critical traffic demands are forwarded to the OLT via ONU. The AI-enabled cloud services at the OLT can assign the pre-estimated bandwidth that is assigned to ONU. So, the critical traffic demands are served ahead to achieve the required goal in sending alert signals to the end devices.

The long short-term memory (LSTM) model is used for the time series traffic prediction. However, this algorithm is capable of learning long-term dependencies. The vanishing gradients which are a very common problem in ML learning algorithms where the gradient of error functions get reduced quickly without improving the learning process. To get a good prediction, a ML algorithm needs to be trained with many and different traffic patterns, and depending on the number of hidden layers, neurons per layer and training data sets, it predicts (also classify) the future events. In our approach, we first generate a time-varying traffic (real data). In order to predict the bandwidth demands of the future one hour, the previous seven hours traffic demands are learn by the LSTM algorithm. The "Adam" optimizer is used for all the models. The data set is split into 80:20 ratio for training and testing. We can see that the simple RNN, LSTM, and GRU models root mean square errors during training and testing are shown in Table 2. Thus, the spectrum is allocated depending on the network demands.

6 Conclusion

In this paper, to enhance animal-human cohabitation, we suggested a novel early warning system structure. The proposed system is fiber-wireless and could warn the nearby road/rail traffic management of approaching wild animals. This is extremely desired for a real-time warning system. The main criterion is whether the data should

be processed at the OLT or the BSs. This is subject to network congestion. In hybrid networks, dynamic bandwidth allocation improves bandwidth utilization efficiency. We believe that this type of system can be seamlessly integrated into an existing smart city and smart transportation infrastructure.

7   Future Scope

In future work, we will use 5G hybrid networks using for multi-objective detection. This technology has lower latency, higher capacity, and increased bandwidth compared to 4G networks. Greater speed in the transmissions will help in connecting a greater number of devices. In 5G, obstructions impair connectivity. Further, frequency waves can travel a short distance; and hence, 5G range is not great. 4G wavelengths have a range of about 10 miles, whereas 5G has a range of just 1000 feet. Due to this, 5G signals can be blocked by physical barriers like walls, barricades, trees, and hills. While implementing with 5G, we will examine the limitation aspect also.

References

1. Suman, P., Gupta, P., Kassey, P.B., Saxena, N., Choudhary, Y., Singh, V., Radhakrishna, M.: Identification of trespasser from the signatures of buried single mode fiber optic sensor cable. In: 2015 Annual IEEE India Conference (INDICON), pp. 1–6. IEEE (2015)
2. Jukan, A., Masip-Bruin, X., Amla, N.: Smart computing and sensing technologies for animal welfare: a systematic review. ACM Comput. Surv. (CSUR) **50**(1), 1–27 (2017)
3. Tennakoon, E., Madusanka, C., Zoysa, K.D., Keppitiyagama, C., Iyer, V., Hewage, K., Voigt, T.: Sensor-based breakage detection for electric fences. In: 2015 IEEE Sensors Applications Symposium (SAS), pp. 1–4. IEEE (2015)
4. Mathur, P., Nielsen, R.H., Prasad, N.R., Prasad, R.: Wildlife conservation and rail track monitoring using wireless sensor networks. In: 2014 4th International Conference on Wireless Communications, Vehicular Technology, Information Theory and Aerospace and Electronics Systems (VITAE), pp. 1–4. IEEE (2014)
5. Nakandala, M.S., Namasivayam, S.S, Chandima, D.P., Udawatta, L.: Detecting wild elephants via WSN for early warning system. In: 7th International Conference on Information and Automation for Sustainability, pp. 1–6. IEEE (2014)
6. Viani, F., Rocca, P., Lizzi, L., Rocca, M., Benedetti, G., Massa, A.: WSN-based early alert system for preventing wildlife-vehicle collisions in Alp's regions. In: 2011 IEEE-APS Topical Conference on Antennas and Propagation in Wireless Communications, pp. 106–109. IEEE (2011)
7. Viani, F., Polo, A., Giarola, E., Robol, F., Benedetti, G., Zanetti, S.: Performance assessment of a smart road management system for the wireless detection of wildlife road-crossing. In: 2016 IEEE International Smart Cities Conference (ISC2), pp. 1–6. IEEE (2016)
8. Dominguez-Morales, J.P., Rios-Navarro, A., Dominguez-Morales, M., Tapiador-Morales, R., Gutierrez-Galan, D., Cascado-Caballero, D., Jimenez-Fernandez, A., Linares-Barranco, A.: Wireless sensor network for wildlife tracking and behavior classification of animals in Doñana. IEEE Commun. Lett. **20**(12), 2534–2537 (2016)

9. Aburasain, R.Y., Edirisinghe, E.A., Albatay, A.: Drone-based cattle detection using deep neural networks. In: Proceedings of SAI Intelligent Systems Conference, pp. 598–611. Springer, Cham (2020)
10. Habel, K., Koepp, M., Weide, S., Fernandez, L., Kottke, C., Jungnickel, V.: 100G OFDM-PON for converged 5G networks: from concept to real-time prototype. In: Optical Fiber Communication Conference, pp. W1K-4. Optical Society of America (2017)
11. Singh, S.K., Jukan, A.: Machine-learning-based prediction for resource (re) allocation in optical data center networks. IEEE/OSA J. Opt. Commun. Netw. **10**(10), D12–D28 (2018)

Identifying Prognostic Markers of Non-small Cell Lung Carcinoma Using Bioinformatics

Siladitya Khan and **Debamitra Chakraborty**

Abstract We present a transcriptomics pipeline for performing the functional analysis of array expression profiling data of normal and adenocarcinoma lung tissue. Our aims are twofold, firstly to elucidate molecular processes that transform normal tissue, to a lung adenocarcinoma. Following this, we perform functional analysis to screen potential hub genes and demonstrate their value in cancer prognosis. Analysis was performed on a total of 500 differentially expressed genes (DEG), screened for their regulation and transcriptional modulation in a female population carrying non–small cell lung carcinoma (NSCLC). Key pathways like cytokine-cytokine receptors, ECM receptor interactions, and TNF signaling were identified suggesting a potential role in lung tumorigenesis.

Keywords Bioinformatics · NSCLC · Differential gene expression · Pathway analysis

1   Introduction

Lung cancer is a leading cause of cancer-related morbidity in the US. An estimated 235,760 new cases, amounting to a total of 12.4% of all new cancer detection in 2021, are accounted by some form of lung or bronchus cancer [1]. Non-small cell lung carcinoma (NSCLC) accounts for ~84% of all lung cancer diagnoses, with female non-smokers within the age of 40–80 years being more susceptible and about two-thirds of cases culminating in adenocarcinoma [2]. Lack of knowledge in molecular mechanisms of NSCLC progression can now be addressed by the rapid development

S. Khan (✉)
Department of Biomedical Engineering, University of Rochester, Rochester, NY 14627, USA
e-mail: skhan45@ur.rochester.edu

Goergen Institute for Data Science, University of Rochester, Rochester, NY 14627, USA

D. Chakraborty
Materials Science Graduate Program, University of Rochester, Rochester, NY 14627, USA

of high-throughput bioinformatic pipelines. Such expression profiling has oncological relevance, by being able to screen for potential disease-associated biomarkers of tumor progression and genesis. This article presents a transcriptome-level analysis of a standard micro-array dataset of a non-smoking female population, to identify the hub genes and key pathways of NSCLC progression.

2 Materials and Methods

2.1 Data Mining

The data consisted of transcriptional profiles of normal and lung carcinoma samples for non-smoking females obtained from a publicly available Gene Expression Omnibus (GEO) database by NCBI (*GSE19804,* PMID: 20,802,022). Affymetrix U133 Plus 2.0 expression arrays of 60 primary tumor samples alongside the 60 adjacent normal tissue collected in the study [3] were used for analysis. The workflow follows three broad stages, firstly data curation and preprocessing, followed by differential gene expression, followed by functional analysis.

2.2 Quality Control (QC) and Feature Engineering

The objective of this step was to perform quality control (QC) using bioconductor packages and data visualization. QC is an essential step to do an exploratory analysis on the data, in order to make sure that it can be made reliable before usage. It also helps in identifying the outliers which can be detrimental in deriving reliable insights from the results. The QC of the analysis was viewed in the AffyBatch-generated QC report. Relative log expression (RLE) and normalized unscaled standard error (NUSE) metrics were computed. Scatterplot of the mean and standard deviation of probe intensities is shown in Fig. 1, depicting the dependence of the standard deviation on mean. The red line represents the running median estimator.

2.3 Correction and Normalization

Removal of signals from non-specific hybridization sites was achieved using background correction. Systematic biases due to differential absorption rates, microarray spatial heterogeneity were corrected using the robust multi-array average array (rma) normalization [4]. Batch correction ironed out any batch effects that may have arisen due to combining several datasets for further downstream analysis. Background correcting the normalized data from the metadata using the model.matrix()

Fig. 1 Dependence of mean-SD probe intensities with red representing median
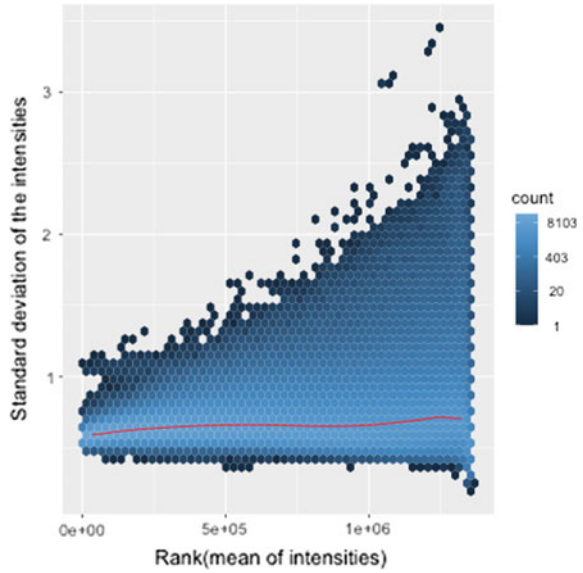
object retained the interesting features. Figures 2a, b represent the probe-level data before and after normalization, respectively.

Finally, visualization of the preprocessed datasets was achieved using boxplots and PCA scatter plots and correlation heatmaps to compare between the raw and preprocessed data and detect outliers. Figures 3a, b represent the gene expression profiles represented in the principal component (PC) plane. The dots represent the expression values of the significant genes, represented through the first two PC coordinates. The normalized data show clear delineation between the cancer and the control groups on the PC plane.

The heatmap in Fig. 4 shows the detailed expression patterns of the genes, after undergoing preprocessing in tumor and normal samples. Also annotated in the plot are the hierarchical clustering results based on a dissimilarity metric, in which a
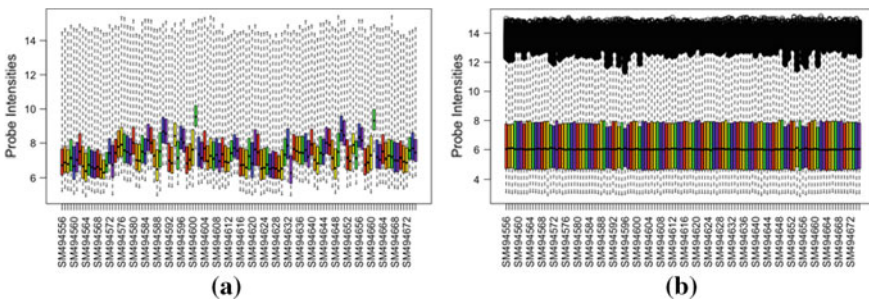

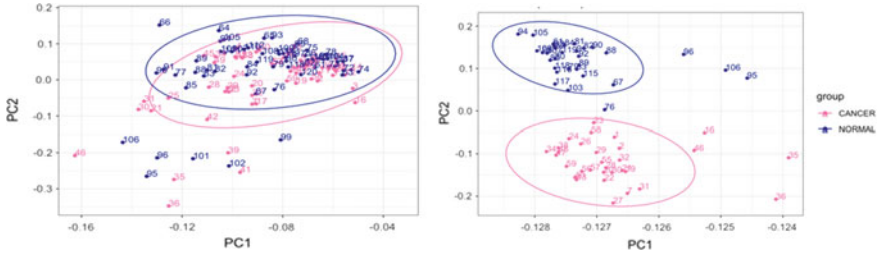**Fig. 2** Raw probe intensities without normalization (left) and with rma (right)

Fig. 3 Principal component analysis of expression data with normalization (left) and with RMA normalization (right)
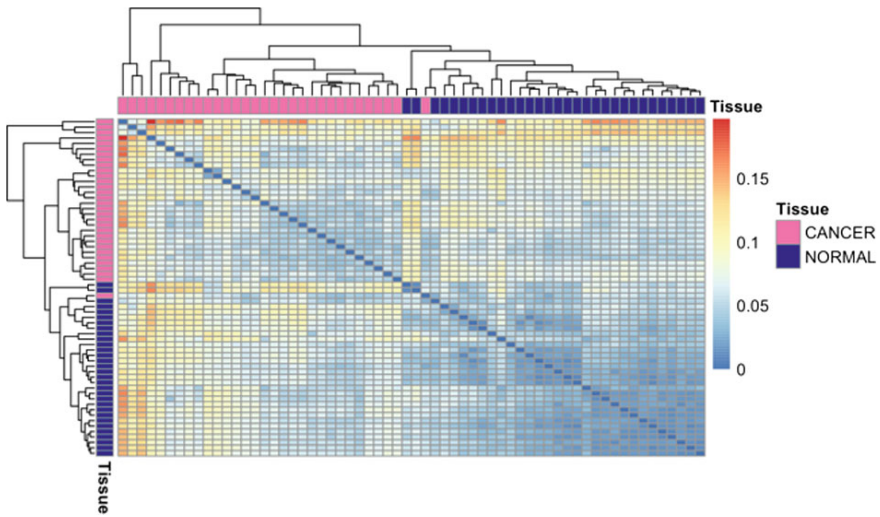

Fig. 4 Correlation heatmaps showing expression patterns in tumor and control samples

value of 0 depicting similar samples and a value closer to 1 for samples that are most dissimilar. Lower branches represent a closer relationship signifying higher similarity than those with further branches.

2.4 Differential Gene Expression

Once the outliers are removed from the data and the metadata, annotation is performed using a standard database hgu133plus.db with AnnotationDbi [5], to account for different databases with different probe IDs that correspond to different sequences. Duplicate probe ID's and extraneous entries are further removed in order to retain
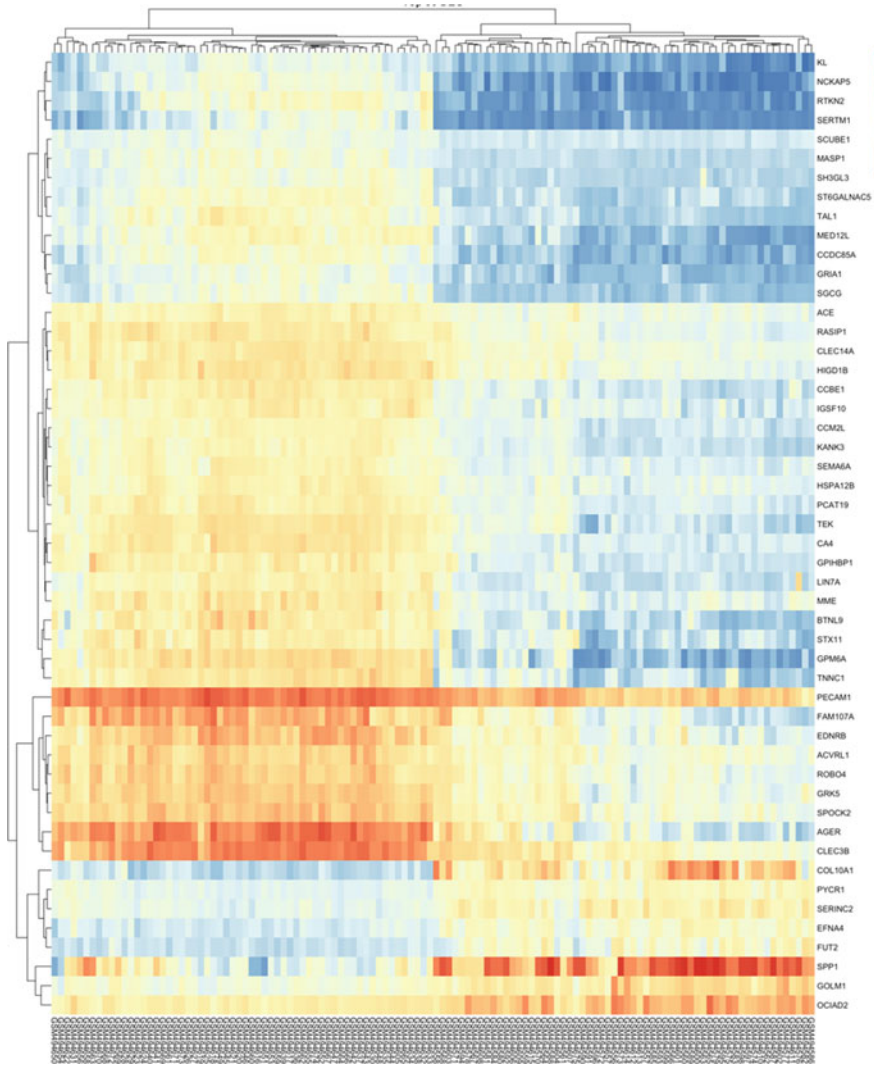
Fig. 5 Volcano plot as a
representation of differential
gene expression

unique occurrence. Gene filtering was performed as percentage of expression distribution of the entire dataset, and genes below the second percentile of the expression distribution were omitted. Differential expression results in increasing order of their p-values, and the significant genes with adjusted p-values < 0.05 were recorded, and a paired t-test was used to estimate the differences between cancel and control groups.

Volcano plots of log-fold change against negative log-p values, and heatmaps of top 50 DEG's were generated. Figure 5 shows x-axis with log-fold change and the negative log-p value on y-axis. Higher the absolute value of $\log_2$-fold changes, the more differentially expressed the corresponding gene is. The p-value indicates the level of statistical significance in the log-fold change in a Bayesian formalism. A higher-$\log_{10}$-p value indicates greater significance. By inspection, we observe that genes at the top right or top left of Fig. 5 are the most differentially expressed genes with the greatest significance. A total of 10,947 genes are visualized; the colored dots represent various degrees of significance; and the non-significant genes (NS) are represented in gray. The top 50 DEG analyzed genes based on the adjusted p-value are plotted with hierarchically clustered in Fig. 6.

2.5 Functional Analysis

Once the DEG vector is generated and the up-regulated genes are selected, gene ontology (GO) analysis was performed to segregate cellular components (CC), biological processes (BP), and molecular functions (MF). Potential functional implications can be unraveled using the GO and surveying the comprehensive gene distributions of the associated Kyoto Encyclopedia of Genes and Genomes (KEGG) pathways. Enrichment analysis was performed using the KEGG database, and top 5 enriched KEGG pathways were visualized. Global Gene Set Enrichment Analysis (GSEA) was performed using hallmarked genes from Molecular Signatures Database (MSigDB) [6]. Preliminary gene factor analysis was performed by visualizing the top 5 (t-5) signatures to form a gene concept network. The transcription factor (TF) analysis was done on similar lines as the GSEA, but now with the C3: regulatory target gene sets in MSigDB. The C3 set consisted of genes grouped by elements sharing their non-protein coding regions.

Fig. 6 Heat map of top 50 differentially expressed genes

3 Results

Among the BP group of significantly enriched GO terms in Figs. 7b and 8, significant terms were enriched suggesting potential roles in lung tumorigenesis. The BP terms revealed significant contributions angiogenic regulators, followed by development of vasculature and its permeability. Previous studies have shown them to be key promoters for development of pleural effusions in NSCLC [7]. The CC plot in Fig. 7c
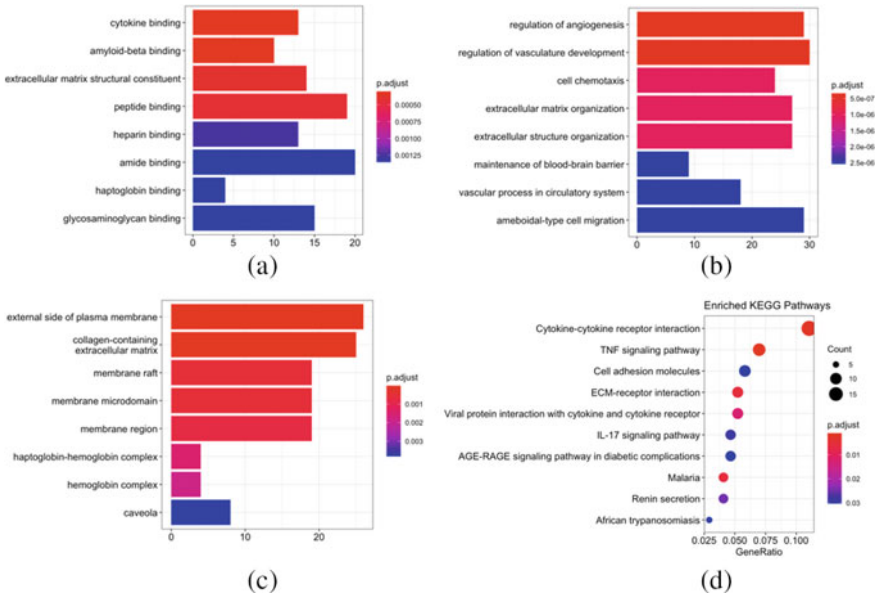
Fig. 7 Bar plots that show enriched GO terms for **a** Molecular functions (MF), **b** Biological processes (BP), and **c** Cellular components (CC) of up-regulated DEGs. **d** Shows significantly enriched KEGG pathways

revealed contributions of the pulmonary extracellular matrix revealing its potential-altered roles in chronic lung diseases. They are consistent with studies that have explored the roles of integrins and extracellular matrix proteins in NSLC [8]. The enriched KEGG pathways in Fig. 7c revealed 15 counts of cytokine-cytokine receptor interaction which was most common, followed by 10 counts of TNF signaling pathways. Cytokines in the lung, as in many organs, are responsible for maintenance of homeostasis and most commonly regulate the initiation and preservation of immune as well as inflammatory responses. The second significant term arising in the KEGG enrichment is the tumor necrosis factor (TNF) which has already a well-established role in inflammation-induced diseases and has been to be widely expressed in NSCLC [9]. Most notably, the disease malaria appeared in the KEGG analysis confirming previous studies on potential roles of antimalarial compounds as anticancer agents [10].

To ascertain the genes belonging across multiple annotation categories, a gene concept network is visualized that portrays the linkages of genes and biological concepts.

Figure 8 shows the gene concept networks of top 5 enriched KEGG pathways, the genes are represented as colored dots in orange, while the concepts in yellow, the linkages are shown in solid lines. Gene concept network in Fig. 8 shows cytokine-cytokine receptor pathway, ECM receptor interactions, malaria, and TNF signaling
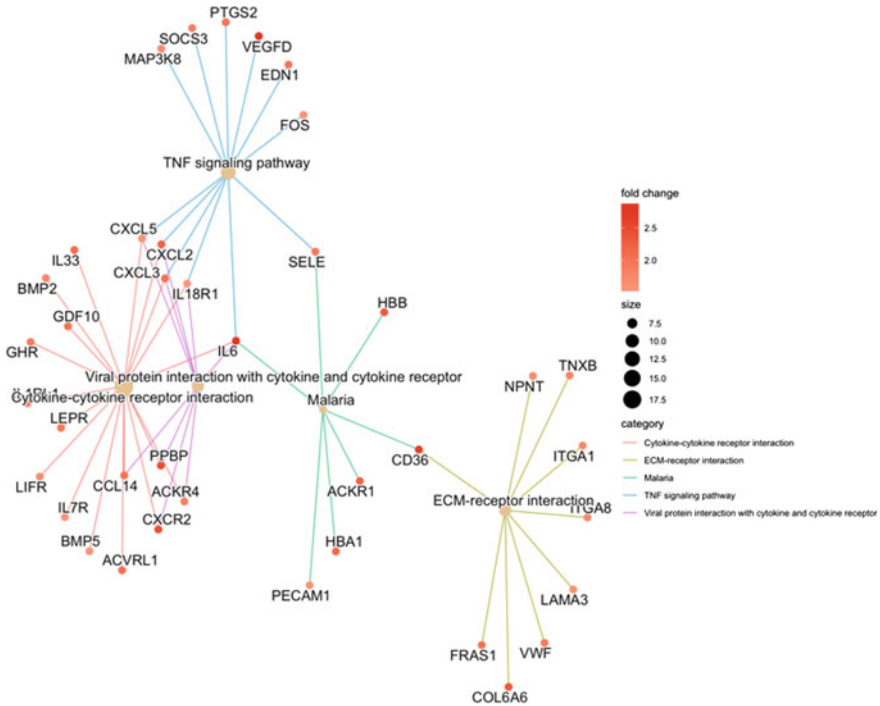
Fig. 8 Gene concept network of enriched KEGG pathways

pathways abnormal expression patterns of crucial genes, thereby implying an important role for them in the occurrence and genesis of lung carcinoma. Most of the analysis until now were concerted toward the up-regulated genes from DEG set, and a similar approach could have been taken for the down-regulated ones; however, to provide a comprehensive overview, we need to visualize and evaluate the data at the level of gene sets. The a-priori knowledge about the correlation of these gene sets to a particular phenotypic class enables us to define gene groups. We ascertain their roles based on respective contributions to hallmarks of cancer in MSigDB [6]. The GSEA plot in Fig. 9 shows the enrichment score as a representation of the degree to which genes are over presented at the top/bottom of the ranked list. The score is calculated by incrementing the sum-statistical value when the gene is present and penalizing when absent. The increment value depends on its correlation to the phenotype, and the bottom half of the plot shows the rank in the ordered gene set. The GSEA analysis allowed us to look at enriched and up-regulated genes in-depth, and we should now turn toward regulatory factors such as transcriptional factors (TF's), microRNAs, and lncRNAs. For most studies, TF networks across genome-wide studies' TF network structures are largely descriptive and obstruct us from drawing quantitative conclusions.
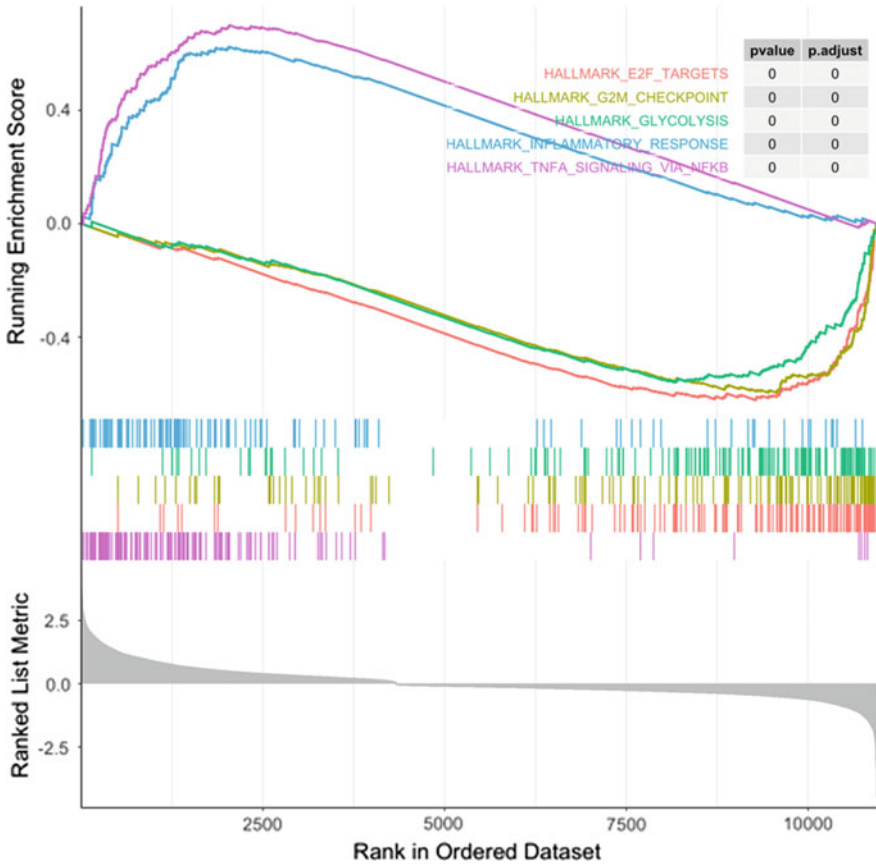
Fig. 9 Enrichment plot with running ES score and positions of gene set members

One should look at a TF analysis not only for drawing genes of interest but also for the way they are regulated as shown in Fig. 10.

The C3 gene set collection was analyzed following which the ENTREZIDs were converted to corresponding gene symbols followed by the visualization of the network. It shows the genome-wide screening to identify TFs that might be responsible for NSCLC cell proliferation.

4 Conclusion and Future Work

The work presented evidential support in finding prognostic biomarkers for NSCLC's and could be extended to other chronic lung illnesses in the future. We further hope to use such knowledge to explore therapeutic landscapes beyond chemoimmunotherapy.
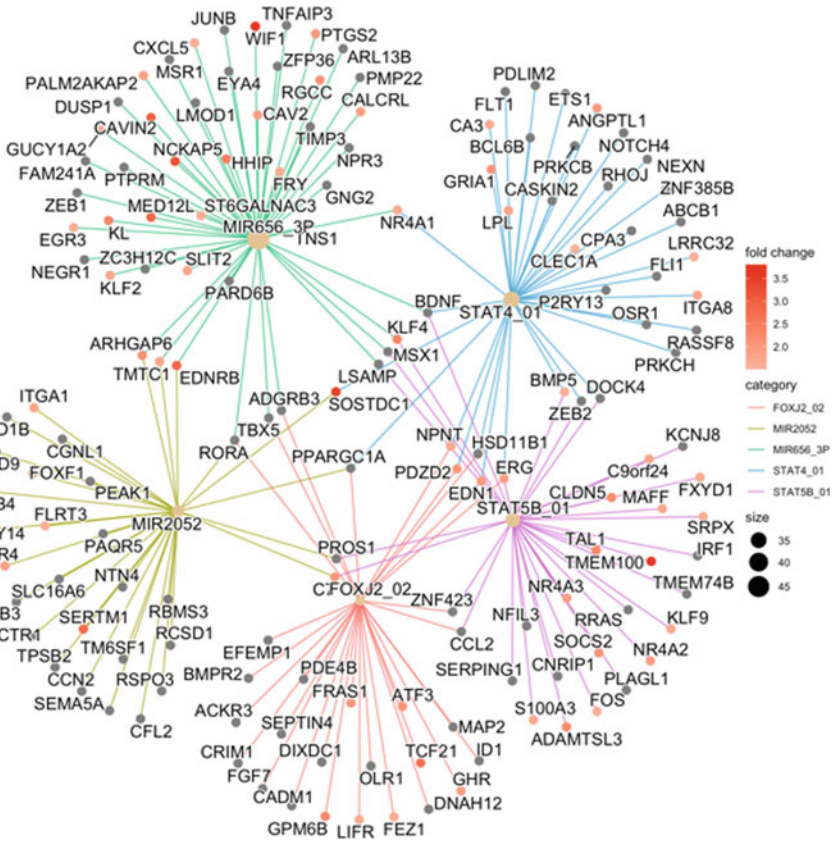
Fig. 10 Gene concept network of transcriptional factors (TF)

References

1. Lung-Statistics: https://www.cancer.org/cancer/lung-cancer. Last accessed 30 Apr 2021
2. Molina, J.R.: Non-small cell lung cancer: epidemiology, risk factors, treatment, and survivorship. Mayo Clinic Proc. **83**(5), (2008)
3. Lu, T.P.: Identification of a novel biomarker, SEMA5A, for non-small cell lung carcinoma in nonsmoking women. Cancer Epidemiol. Prevent. Biomark. **19**(10), 2590–2597 (2010)
4. Irizarry, R.A.: Exploration, normalization, and summaries of highdensity oligonucleotide array probe level data. Biostatistics **4**(2), 249–264 (2003)
5. Pages, H.: Package 'AnnotationDbi' (2013)
6. MSigDB: http://software.broadinstitute.org/gsea/msigdb/. Last accessed 30 Apr 2021

7. Yano, S.: Molecular mechanisms of angiogenesis in non-small cell lung cancer, and therapeutics targeting related molecules. Cancer Sci. **94**(6), 479–485 (2003)
8. Burgstaller, G.: The instructive extracellular matrix of the lung: basic composition and alterations in chronic lung disease. Eur. Respir. J. **50**(1), (2017)
9. Tumor necrosis factor in lung cancer: Complex roles in biology and resistance to treatment
10. Tang, Q.: Hub genes and key pathways of non-small lung cancer identified using bioinformatics. Oncol. Lett. **16**(2), 2344–2354 (2028)

Data-Based Tuning of PI Controller for First-order System

Abdul Wahid Nasir, Idamakanti Kasireddy, Rahul Tiwari, B. K. Imtiyaz Ahmed, and Abdullah Furquan

Abstract The present work aims at utilizing regression model for the tuning of proportional–integral (PI) controller for the first-order system. The dataset containing the tuning parameters, i.e., proportional gain (K_p) and integral gain (K_i), is generated optimally with the help of fmincon, a constrained optimization algorithm available in MATLAB, by minimizing an error-based objective function. Based on this data, regression model is obtained for controller parameters. Then, the performance evaluation and feasibility of controller parameters derived from controller regression model are investigated based on different performance indices.

Keywords PI controller · Regression model · First-order system · Fmincon

1 Introduction

Conventional PI/PID is still the most preferable industrial controller nowadays. Among PI and PID, majority of the control loop consist of PI controller, and in some cases where one needs to consider the change of error in controller design, PID is required. Thus, tuning of such controller is very important, and a good number of research articles are available for the same. In addition to well-established tuning rule, e.g., Ziegler-Nichols, Cohen-Coon, various optimization-based tuning have been reported in the recent past [1].

With the evolution of advanced and fast computing techniques, data science has found its application in almost every field of engineering. Control engineering is also no exception, and researchers are utilizing data science for the purpose of modeling and control design, but it needs more investigation and exploration [2, 3]. Therefore,

A. W. Nasir (✉) · R. Tiwari · B. K. I. Ahmed
CMR Institute of Technology, Bengaluru, India

I. Kasireddy
Vishnu Institute of Technology Bhimavaram, Kovvada, India

A. Furquan
Siemens Technology and Services Pvt. Ltd., Bengaluru, India

in this paper, a data-based approach for PI controller is presented for the first-order system. Here, datasets containing controller parameters are generated optimally using a nonlinear constrained optimization technique subject to minimization of error-based objective function by varying dynamics of the first-order system. Once dataset is obtained, then regression model is obtained for controller. Finally, the efficiency of controller based on such regression model is studied.

2 Data Generation

For problem formulation, a first-order system, $P(s)$ given by (1), has been considered, where K is gain and τ is time constant.

$$P(s) = \frac{K}{\tau s + 1} \tag{1}$$

$$\text{ISE} = \int_0^\infty \{y_{\text{sp}}(t) - y(t)\}^2 \mathrm{d}t = \int_0^\infty \{E(t)\}^2 \mathrm{d}t \tag{2}$$

For the above first-order system, optimal proportional gain (K_{p}) and integral gain (K_{i}) of PI controller are obtained using fmincon [4] as illustrated in Fig. 1. $y_{\text{sp}}(s)$ is set point, $y(s)$ is the actual output, $u(s)$ is control signal, and $E(s)$ is the error signal defined as the difference of $y_{\text{sp}}(s)$ and $y(s)$, i.e., $E(s) = y_{\text{sp}}(s) - y(s)$. This error is used to construct objective function, i.e., integral of squared error (ISE) [5], in present case as given in (2). The fmincon is the optimization tool available in the MATLAB used to find the minimum of constrained nonlinear multivariable function.

The value of K is fixed as unity, and the value of τ is varied from 0.1 to 1000 with the interval of 0.1. Hence, the generated dataset will be consisting of 10,000 of samples, which will be used to train regression model for the PI controller.

Fig. 1 Generation of dataset containing controller parameters
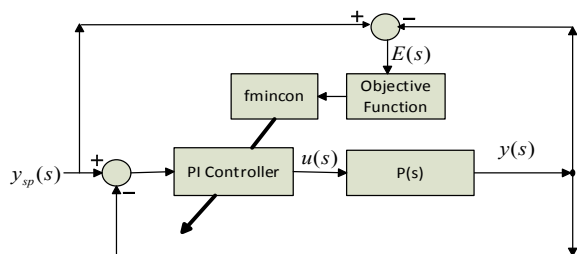
3 Regression

In statistics, regression analysis is used to determine the relation between dependent variable and independent variables [6, 7]. By using regression analysis, the value of dependent variable can be predicted on the basis of independent variables. It gives nature of the relation among dependent and independent variables. It also gives the information about impact of one variable on other variables. Therefore, it can be used in various domains such as business, economics, engineering [8]. Regression analysis has been segregated into simple and multiple regression analyses. In case of simple regression, two variables will be studied at a time. Out of two variables, one variable is dependent and other is independent. In case of multiple regression, more than two variables can be studied. In this, one variable is dependent variable and other variables are independent variables. Regression analysis is classified into linear regression and nonlinear regression. Depending upon the relation between input and output, one can choose any suitable regression model [9].

4 Training of Regression Model

First step toward training the model is to decide the nature of curve that will best fit the dataset. As mentioned, the value of system gain (K) is fixed and time constant (τ) is varied; therefore, τ is taken as feature for the model. Since there are two controller parameters K_p and K_i, so two models are required. First model is trained for the output K_p against the input τ; similarly, second model is trained for the output K_i against the input τ. The procedure for training both the models is discussed individually as follows.

4.1 Modeling of Kp

The scatter plot relating to input τ and output K_p is shown in Fig. 2.

From plot, it is clear that the relation between K_p and τ is not linear; hence, in the present case, nonlinear regression model is proposed given by Eq. (3).

$$K_\mathrm{p} = \alpha - \exp(-\beta * \tau) \tag{3}$$

where α and β are the parameters, whose values are found out optimally using nonlinear least squares regression.

Fig. 2 Plot of K_p against τ
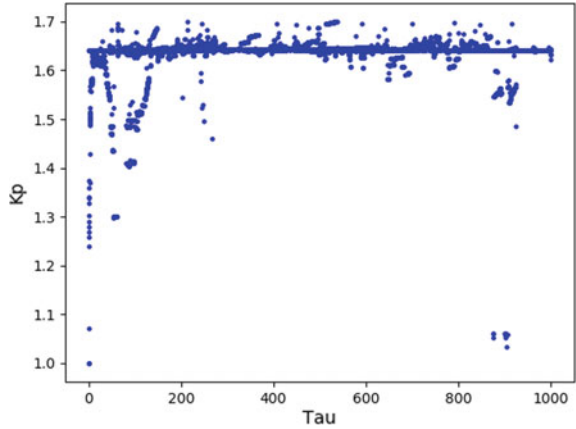

4.2 Modeling of K_i

The scatter plot relating to input τ and output K_i is shown in Fig. 3. The dataset is divided into three regions to bring accuracy and ease in modeling. It is evident from plot that the relation between K_p and τ is linear in Region 1, whereas it is nonlinear in Region 2 and Region 3.

Hence, in the present scenario, regression model proposed for Region 1, Region 2, and Region 3 is given by Eqs. (3), (4), and (5), respectively.

$$K_i = m * \tau + c \tag{4}$$

$$K_i = {\theta_1}/{\tau} \tag{5}$$

Fig. 3 Plot of K_i against τ
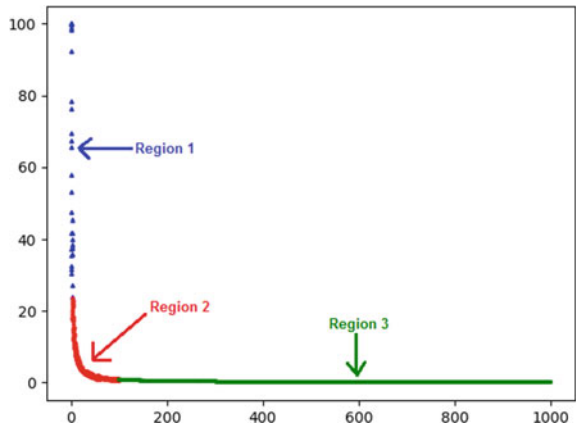
$$K_i = {\theta_2}/{\tau} \qquad (6)$$

where $m, c, \theta_1,$ and θ_2 are the parameters, whose values are again found out optimally using nonlinear least squares regression.

5   Results and Discussion

Table 1 gives the parameter value of the regression model of K_p, along with model evaluation metrics, i.e., mean absolute error (MAE) and mean squared error (MSE). Model fit for the same is illustrated in Fig. 4. Similarly, Table 2 gives the parameter value of the regression model for all the three regions of K_i, along with model evaluation metrics MAE and MSE. Model fit for the same is shown in Fig. 5.

By bringing random variation in τ, the first-order system defined in Eq. (1) will result in plant of different dynamics. PI control parameters, i.e., K_p and K_i for these randomly chosen plants are determined using their regression model, respectively. The performance of such regression-based controller is investigated by carrying comparative study of unit step response in term of rise time (tr), settling time (ts), maximum overshoot (Mp), peak time (tp), and ISE, with fmincon optimized PI controller. The performance indices for both type of PI controller are tabulated in Tables 3, 4, 5, and 6 for different values of τ, i.e., 0.5, 10, 100, and 500, respectively.

Table 1 Model parameters and evaluation metrics for K_p

Model parameters	Mean absolute error (MAE)	Mean squared error (MSE)
$\alpha = 1.636331$; $\beta = 1.287748$	0.02	0.001

Fig. 4 Model fit for K_p
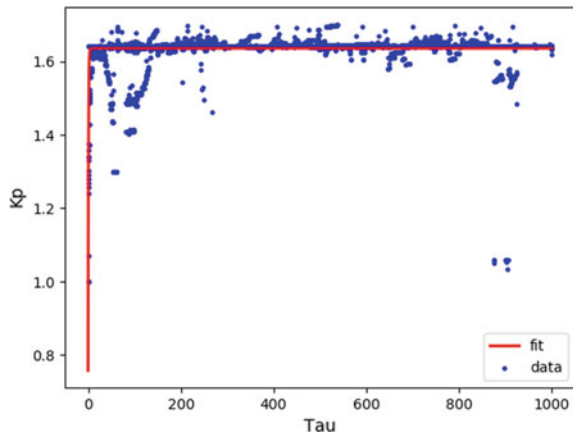
Table 2 Model parameters and evaluation metrics for K_i

Model parameters	Region-wise evaluation metrics	Overall evaluation metrics
Region 1	MAE = 9.31	
$m = -27.878175$	MSE = 93.11	
$c = 103.357690$		
Region 2	MAE = 0.24	MAE = 0.06
$\theta_1 = 80.818922$	MSE = 0.32	MSE = 0.46
Region 3	MAE = 0.01	
$\theta_2 = 81.670129$	MSE = 0.001	

Fig. 5 Model fit for K_i
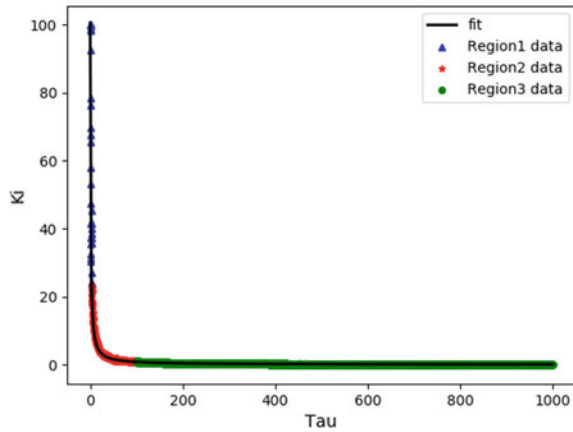
Table 3 Performance indices for system having $\tau = 0.5$

Controller based on	Controller parameter	ISE	tr	tp	ts	Mp (%)
Fmincon optimization	$K_p = 1.072$; $K_i = 99.846$	6.0453	0.09	0.220	2.5	63
Regression model	$K_p = 1.111$; $K_i = 89.418$	6.0582	0.10	0.245	2.5	61

Table 4 Performance indices for system having $\tau = 10$

Controller based on	Controller parameter	ISE	tr	tp	ts	Mp (%)
Fmincon optimization	$K_p = 1.6212$; $K_i = 7.9939$	6.006	1.4	3.15	40	63
Regression model	$K_p = 1.6363$; $K_i = 8.0818$	6.005	1.4	3.15	40	63

Table 5 Performance indices for system having $\tau = 100$

Controller based on	Controller Parameter	ISE	tr	tp	ts	Mp (%)
Fmincon optimization	$K_p = 1.6365$; $K_i = 0.8056$	6.005	12.4	32	400	63
Regression model	$K_p = 1.6363$; $K_i = 0.8082$	6.005	12.4	32	400	63

Table 6 Performance indices for system having $\tau = 500$

Controller based on	Controller Parameter	ISE	tr	tp	ts	Mp (%)
fmincon optimization	$K_p = 1.6365$; $K_i = 0.8056$	6.005	65	160	2000	63
Regression model	$K_p = 1.6363$; $K_i = 0.8082$	6.032	65	160	2000	63

Fig. 6 Closed-loop unit step response for $\tau = 0.5$
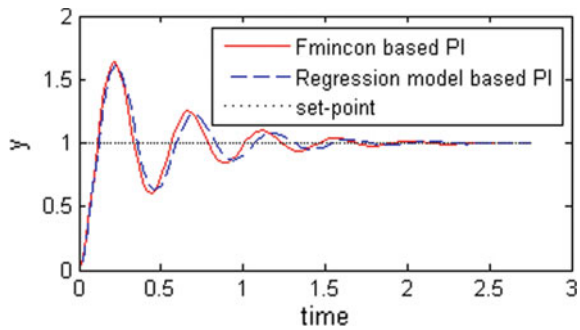
Similarly, for each different first-order system, unit step response for both the type controller is given in Figs. 6, 7, 8, and 9, respectively.

The value of MAE and MSE as calculated for K_p regression model is 0.02 and 0.001, indicating an effective fit. Same is the case with K_i regression model, whose MAE and MSE value for overall region is 0.06 and 0.46, respectively, which is also quite effective. Moving to controller side, it is evident from the performance indices tabulated in Tables 3, 4, 5, and 6 that the performance of regression-based PI controller satisfactorily matches with the optimized PI controller. Same can be inferred from the closed-loop unity step response illustrated in Figs. 6, 7, 8, and 9.

6 Conclusion

This paper has presented a data-based approach for the design of PI controller for the first-order system. Depending upon the data, both linear as well as nonlinear regression were used to find the models. The controller based on such models was

Fig. 7 Closed-loop unit step response for $\tau = 10$
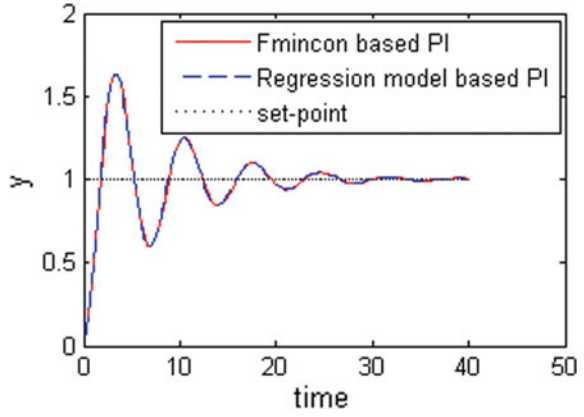
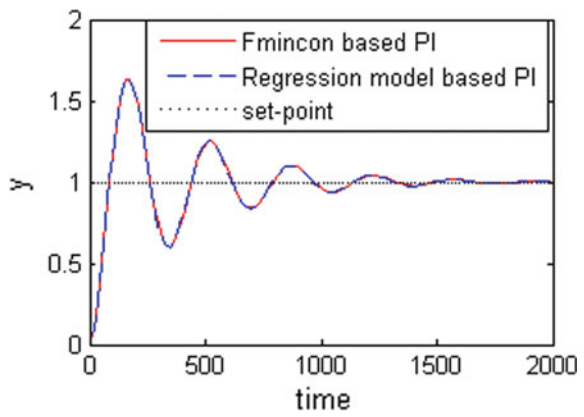**Fig. 8** Closed-loop unit step response for $\tau = 100$
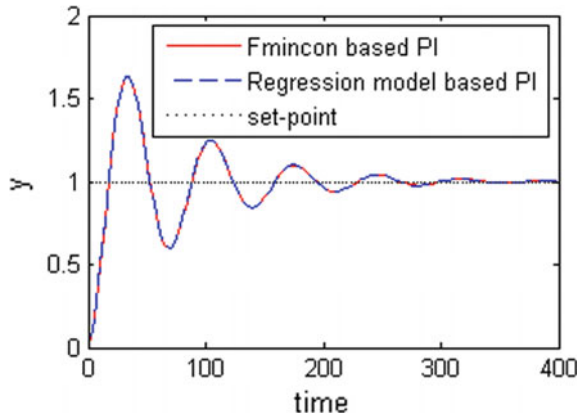
Fig. 9 Closed-loop unit step response for $\tau = 500$

performing equally well as original optimized controllers which is evident from results. Actually, the performance of such controller very much depends on the accuracy of regression model. Hence, it is very important to have good fit between model and data. This work has the potential to be extended in various way, viz., the same concept can be employed to find controller parameters of some other advanced controllers like internal model control (IMC), PID for the first- or second-order system.

References

1. Borase, R.P., Maghade, D.K., Sondkar, S.Y. et al.: A review of PID control, tuning methods and applications. Int. J. Dynam. Control (2020)
2. Shukor, N.S.A., Ahmad, M.A.: Data-driven PID tuning based on safe experimentation dynamics for control of double-pendulum-type overhead crane. In: Hassan, M. (ed.) Intelligent Manufacturing & Mechatronics. Lecture Notes in Mechanical Engineering. Springer, Singapore (2018)
3. Ghazali, M.R., Ahmad, M.A., Ismail, R.M.T.R.: Data-driven neuroendocrine-PID tuning based on safe experimentation dynamics for control of TITO coupled tank system with stochastic input delay. In: Kim, J.H., Myung, H., Lee, S.M. (eds.) Robot Intelligence Technology and Applications. RiTA 2018. Communications in Computer and Information Science, vol. 1015. Springer, Singapore (2019)
4. Fmincon: https://in.mathworks.com/help/optim/ug/fmincon.html. 28 Feb 2021
5. Das, S., Saha, S., Das, S., Gupta, A.: On the selection of tuning methodology of FOPID controllers for the control of higher order processes. ISA Trans. **50**(3), 376–388 (2011)
6. Herkenhoff, L., Fogli, J.: Non-linear regression. In: Applied Statistics for Business and Management using Microsoft Excel. Springer, New York (2013)
7. Xu, L., Chen, J., Zhang, X., Yeo, J.H., Jiang, L.: Improving noninvasive blood glucose measurement accuracy by applying genetic algorithm to partial least square regression model. In: Hinduja, S. (ed.) Proceedings of the 34th International MATADOR Conference. Springer, London (2004)
8. Kalantar, A.H.: "A distribution-free alternative to least-squares regression and its application to Rb/Sr isochron calculations" by R.G. Vugrinovich. Math. Geol. **22**, 145–146 (1990)
9. Virk, D.S., Virk, P.S., Mangat, B.K., et al.: Linear and non-linear regression analysis of genotype X environment interactions in pearl millet. Theoret. Appl. Genetics **75**, 736–740 (1988)

Smart Analysis and Measurement of Hysteresis Loss of an Inverter-fed Transformer for Renewable Energy Application

Arunava Chatterjee [ID]**, Sankar Das, and Debashis Chatterjee**

Abstract This paper studies the effect of source side harmonics on transformer operation and provides smart analysis and control. This type of source harmonics is present in power electronic sources like an inverter output which is commonly used in microgrid and in renewable applications. The prolonged effect of source side harmonics can be observed on the hysteresis curve of the transformer core. In this study, single-phase transformers are used to observe the effect of harmonics on magnetization and demagnetization cycle using an electronic operational amplifier-based integrator circuit. The study also proposes a modified hysteresis model for the transformer considering the effect of harmonics. A method is presented for plotting the hysteresis curve from the transformer terminal measured data. The proposed study can be an effective tool for easy measurement and analysis of harmonic effects on the transformer, and accordingly, safety measures can be taken for better operation of the transformer. The MATLAB/Simulink-based model and simulations backed by suitable experiments validate the proposed study.

Keywords Transformer · Harmonics · Hysteresis · Internet of Things (IoT) · Piecewise mixed model

1 Introduction

The effect of harmonics in source voltage and its effects in different electrical systems are a widely studied subject. In fact, the study of harmonics and their effect on transformer is also well-researched topic. Generally, the effect of harmonics is flow of harmonic currents which can cause increase in losses which leads to eventual rise

A. Chatterjee (✉)
EE Department, Raghunathpur Government Polytechnic, Purulia, WB 723121, India

S. Das
EE Department, Government College of Engineering and Textile Technology, Berhampore, India

D. Chatterjee
EE Department, Jadavpur University, Kolkata, India

in internal temperature of the transformer [1]. Previously, different studies are done regarding effect of harmonics in transformers. In [2], voltage harmonic effects on transformers are studied for high-power low-voltage motor cores. Effect of harmonic contamination for distribution transformers is studied using simple open and short circuit tests [3]. This is a simple way for studying the effects; however, they require the transformer to be out of operation for carrying out such tests. Also, measurement and required correction of core losses in transformer are studied [4]. In this paper, mainly distorted supply voltage is considered. Estimation of core loss when the flux has fundamental and a single odd harmonic component in it is studied classically. Different core sample materials are tested in the research with estimation of the core loss. Core loss prediction from low-frequency measurements is studied in [5] and is shown to be effective for transformer laminations. Finite element-based hysteresis loop is studied based on energetic hysteresis model. No-load loss prediction under sub-harmonics for power transformers is presented in [6] using two-dimensional finite element model analysis. Under non-sinusoidal or distorted voltage supply, the core or the iron losses can be predicted using modified formulae of core loss as devised in [7]. The same with some modifications can be used for pulsed waveforms also. Also, modified core loss for brushless DC machine drives is also predicted considering harmonics in [8]. It is quite evident that core loss needs some modifications when used for prediction of losses in case of supply with harmonics. In general, the transformer is not loaded at the rated value, or it is operated in derated mode [9]. Approach for measurement and correction of losses under no-load conditions for distorted supply is also offered for power transformers [10]. For distribution transformer, harmonic impact is studied for no-load losses [11]. New methods for measurements of no-load losses for transformers are also studied [12]. This type of modelling is also essential nowadays for specific applications like usage in fault current limiters as shown in [13].

In this paper, model-based analysis of effect of harmonics is made for single-phase transformers connected to power electronic source like an inverter. This configuration is quite commonly used in renewable applications for providing stable voltage and frequency output from a wind turbine generator as shown in Fig. 1a. The connected inverter produces non-sinusoidal voltage at output which will contain harmonics. This study provides a simple yet conclusive basis on transformer operation when the source side contains harmonics. In this study, the supply is having harmonics, and the effect for the same is shown on the hysteresis curve. By analysing and comparing the hysteresis loop using Internet of Things (IoT)-based controller, an idea about the core loss of the transformer is also made. A remedial measure is also proposed for transformer operation with source harmonics. The same study is extended to laboratory-based experimental setup for proper transformer operation.
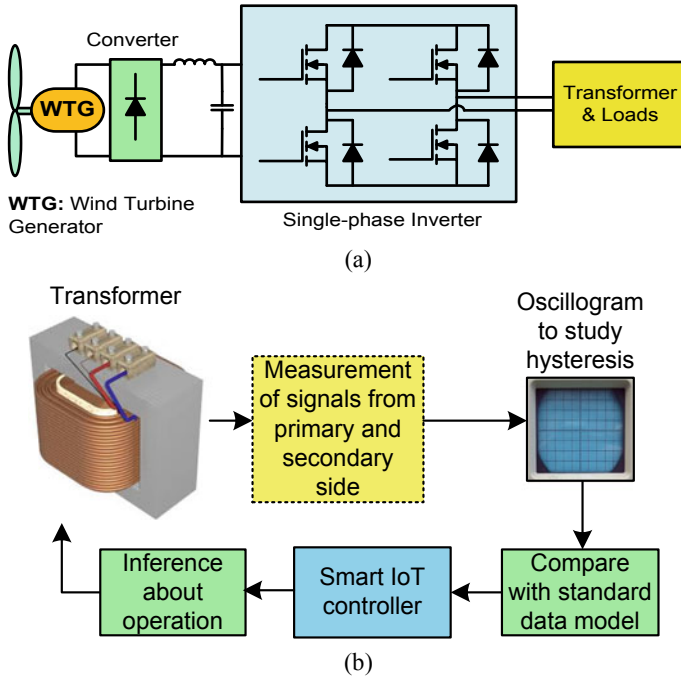
Fig. 1 **a** Wind turbine generator-based system and **b** Technique of analysis

2 Proposed Technique and Harmonic Model

The proposed technique is targeted at finding the transformer hysteresis plot or the B-H curve. Accordingly, some measurements are taken at different conditions. It is to be kept in mind that normally it is difficult to find the magnetic field intensity in the transformer core as well as the flux density. Thus, alternate method for measurement of different quantities is to be made for suitable analysis.

2.1 Proposed Technique

The system connection along with the block diagram of the proposed scheme is shown in Figs. 1a, b, respectively.

Accordingly, the transformer diagram for measurement is shown in Fig. 2. The transformer core material magnetic field strength H is given as,

$$H = (N I_m)/l \qquad (1)$$

Fig. 2 Proposed measurement technique
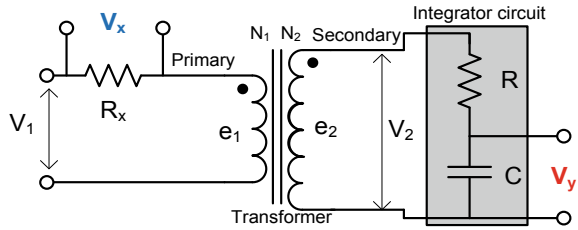
where N is number of turns and l is the length of the core. I_m is the magnetizing current. With N and l as constant values for a particular transformer with fixed core. For the accurate measurement of I_m, a resistance R_x is connected in series with the primary winding. Now, the voltage across the resistor is proportional to the magnetizing current value which is again proportional to the magnetic field strength of the core.

$$V_x = R_x I_m \tag{2}$$

Also, for plotting the hysteresis curve, the magnetic flux density is a required quantity. The quantity, B, is found popularly by,

$$B = \phi/A \tag{3}$$

where ϕ is the magnetic flux in Webers and A is the cross-sectional area of the magnetic core which is again constant. From Eq. (3), it can be observed that the magnetic flux density is directly proportional to the magnetic flux. The rate of change of flux is proportional to the induced emf. This is in turn proportional to the voltage at output. Thus, the magnitude of induced emf e_2 is written as,

$$e_2 = N_2 \frac{d\phi}{dt} \tag{4}$$

$$\frac{1}{N_2} e_2 dt = d\phi \tag{5}$$

Integrating both sides of Eq. (5),

$$\phi = \frac{1}{N_2} \int e_2 dt \tag{6}$$

Thus, flux is proportional to the integral of the secondary voltage. From Eq. (6), it is evident that time integration of the secondary voltage signal is required for determining the flux density. For this purpose, a RC-based integrator circuit is used.

The RC integrator will act as a passive low-pass filter circuit, and voltage across the capacitor can be measured as integrated output. From the integrator circuit,

$$V_y = \frac{1}{RC} \int V_2 \mathrm{d}t \qquad (7)$$

2.2 Parameter Selection

For choosing the resistors R_x, R and capacitor C, the following procedure is adapted where these circuit components are chosen on the basis of transformer physical quantities. For choosing the resistor R_x, let the number of primary turns be N_1. Length of wire for primary l with radius r,

$$l = 2\pi r N_1 \qquad (8)$$

Replacing value of l obtained from Eq. (8) in Eq. (1),

$$H = I_m/2\pi r \qquad (9)$$

or

$$H = I_m Z_1 \qquad (10)$$

where Z_1 $(=1/2\pi r)$ is a constant whose value depends on radius of primary wire. The value of H can be expressed using I_m from Eqs. (2) and (10) as,

$$H = V_x \frac{Z_1}{R_x} \qquad (11)$$

If $Z_1 = R_x$, then $H = V_x$.

Once the primary side resistor value is chosen, the secondary side resistor and capacitor values are to be selected using the following technique. For choosing resistor R and capacitor C in secondary side, from Eqs. (3) and (6),

$$B = \frac{1}{AN_2} \int e_2 \mathrm{d}t \qquad (12)$$

Taking Laplace transform on both sides of Eq. (12) with neglecting the initial condition,

$$B(s) = \frac{E_2(s)}{s} \left(\frac{1}{AN_2} \right) \qquad (13)$$

The transfer function of *RC* network,

$$\frac{V_y(s)}{E_2(s)} = -\frac{1/Cs}{R + 1/Cs} = \frac{1}{1 + RCs} \tag{14}$$

Thus,

$$B(s) = -\left(\frac{RC}{AN_2}\right)\left[1 + \frac{1}{RCs}\right]V_y(s) \tag{15}$$

If $RC \ll 1$, $(1/RC) \gg 1$. Thus, Eq. (15) becomes,

$$B(s) = \left(\frac{1}{AN_2}\right)\left[\frac{V_y(s)}{s}\right] \tag{16}$$

For the integrator, the chosen value of R is 1 kΩ and C is 160 μF.

2.3 Harmonic Model and Internet of Things (IoT)-based Control

Thus, magnetic flux density in core B is pure integral of V_y with a multiplying factor of $(1/AN_2)$. The core loss model of a magnetic material changes for presence of different harmonic frequencies as hysteresis curve depends on it. The core loss consists of hysteresis and eddy current losses. The hysteresis loss P_h in watts using Steinmetz equation,

$$P_h = kB_m^x f \tag{17}$$

where f is frequency of flux reversal and k is hysteresis loss coefficient. Considering the harmonic frequencies, Eq. (17) is modified [14] for single-phase system as,

$$P_h = k(B_{m1}^x f_1 + B_{m3}^x f_3 + B_{m5}^x f_5 + B_{m7}^x f_7 + ... + B_{mn}^x f_n) \tag{18}$$

where subscripts, 3, 5, 7, …, n correspond to odd harmonic order of frequencies. For symmetrical switching, even harmonic components are absent. Moreover, for three-phase system, the triplen harmonics will be absent in line, and thus, they are not considered. Although they may be present in phase and add in neutral, but it does not affect line quantities. For the single-phase system, as presented, the third-order harmonics are found to be dominant for the present system.

Due to the presence of odd harmonics in the supply, the hysteresis loss will change which will also be reflected in the hysteresis curve. The hysteresis curve can be compared for a healthy running transformer with no supply harmonics to understand the operating behaviour of a transformer.

For comparison of fault, an ESP8266-based Internet of Things (IoT) controller is used. This also supports Wi-Fi and works by comparing the data obtained from the transformer in operation with a standard data obtained from a transformer running free from harmonics. The IoT-based controller can control the operation of the transformer and take decision to turn ON/OFF the counter mechanism to reduce the effect of harmonics. Firstly, the harmonics are determined from the magnetization data. If it contains harmonics, then the IoT-based controller can be used to effectively send signals to turn on the harmonics counter mechanism. The automated control achieved is cost-effective using only a smart-controller supporting IoT-based bidirectional communication.

3   Results and Discussion

For the proposed technique, the simulations are done using *MATLAB/Simulink* environment for single-phase transformers. The rating of the transformer is chosen as 750 VA, 60/120 V, 50 Hz for simulation. The simulation waveform of supply voltage and the hysteresis curve are shown in Fig. 3a when the supply is free from harmonics.

When the supply contains harmonics of third and fifth orders, the hysteresis curves are shown in Fig. 3b; contrast to the supply without harmonics, when the supply contains harmonics, the hysteresis curve shows some curvatures unlike the smoother flux reversal of Fig. 3a.

It is clear than the hysteresis waveforms obtained have unusual curvatures than a normal hysteresis curve when the supply is strictly sinusoidal. This can be mathematically verified and analysed using standard data with modified curve fitting-based technique. The technique used in this paper for storage and curve fitting is piecewise mixed model [14]. In this technique, magnetization characteristics of the transformer
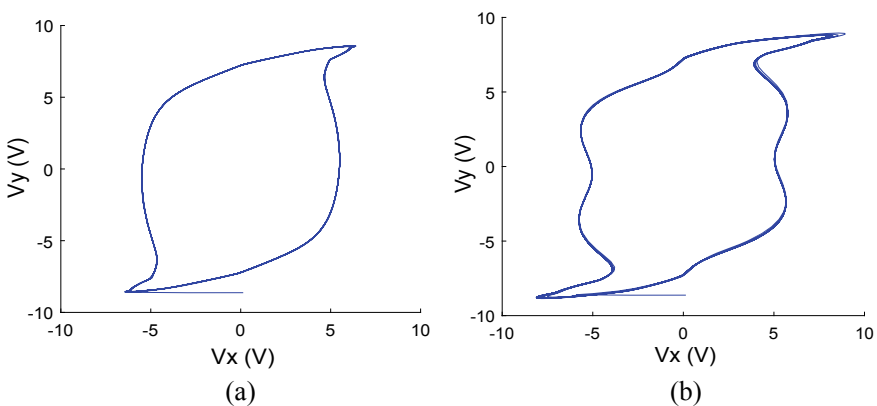
Fig. 3 Hysteresis curve **a** For sinusoidal supply **b** For supply with third- and fifth-order harmonics
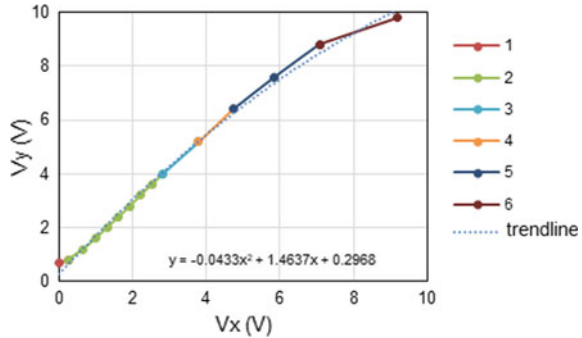
are found experimentally in laboratory. The curve is then broken into piecewise mixed model for storage. The data for the curve is then compared with standard data, and the inference about the operating condition is made for the difference data. For sinusoidal supply, the magnetization curve is shown in Fig. 4. From the figure, it is seen that the magnetization curve is linear up to some extent and nonlinear afterwards. It can be, thus, broken in to different small linear sections for storage. Afterwards, a mathematical analysis with the standard magnetization characteristics can be made using the aforementioned IoT-based control. The trendline for the characteristics follows a polynomial equation of order two. Figure 4 also indicates that the curve can be broken into small linear segments for storing purpose, and later, comparisons with a standard magnetization characteristic can be made later on. Similarly, the hysteresis plot can be stored as a whole.

This magnetization curve is stored offline in an *Atmega*-based microcontroller. This magnetization data is then compared with obtained magnetization data with source harmonics. For comparison purpose, a simple subroutine is used which tracks the changes in the obtained data for a high deviation. If the deviated data is greater than a tolerance value, then the transformer should be used in derated mode. The flowchart for comparison is shown in Fig. 5.

For the transformer to negate the source harmonic effect, some special connection is required at the supply side. A passive inductor–capacitor *LC* filter is used in parallel to the magnetizing branch. The *LC* filter used is tuned at fourth harmonic order of fundamental frequency (i.e. ~200 Hz) with 50 Hz supply, so that it can attenuate both third (=150 Hz) and fifth (=250 Hz) order of harmonic component of source. These harmonics can be suppressed effectively by the use of the filter circuit. From the expression of resonant frequency (in Hz), the value of *L* for the filter is calculated from Eq. (19), where *n* is order of harmonics.

$$L = \frac{1}{4\pi^2 f_r^2 n^2 C} \tag{19}$$

A capacitor value of 1 μF is used for choosing inductance as 630 mH. The switch S is solid-state switch which (IGBT) can be used to isolate the *LC* filter when source

Fig. 5 Flowchart for
comparison and operation
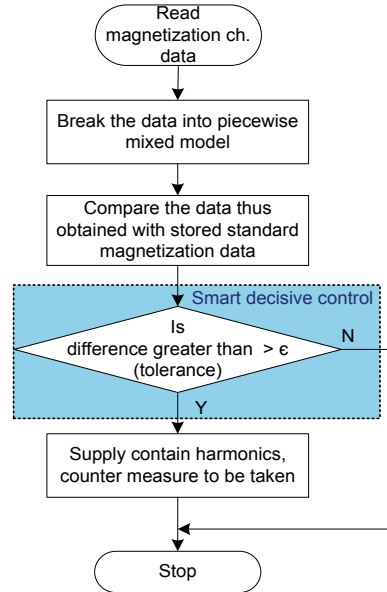
is free from harmonics with the smart control. Accordingly, *L* and *C* values can be
selected. This will reduce the effect of harmonics on the source side as shown in the
circuit of Fig. 6a with corresponding hysteresis curve shown in Fig. 6b.

The hysteresis plot shape is less distorted which again validates the reduced effect
of source harmonics on the transformer. Figure 7 shows the core current signal for
the transformer with reduction in source harmonics with the proposed technique as
shown in top trace. It is observed that the filter reduces the effect of harmonics with
as shown in the top trace of the figure than the current in core when transformer
supply contains third, fifth and seventh harmonics as shown in the bottom trace of
the figure.
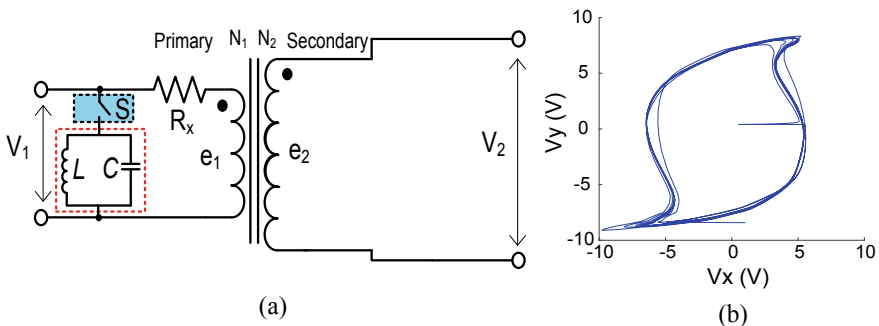
Fig. 6 a Proposed technique to counter the source harmonics and **b** Hysteresis curve
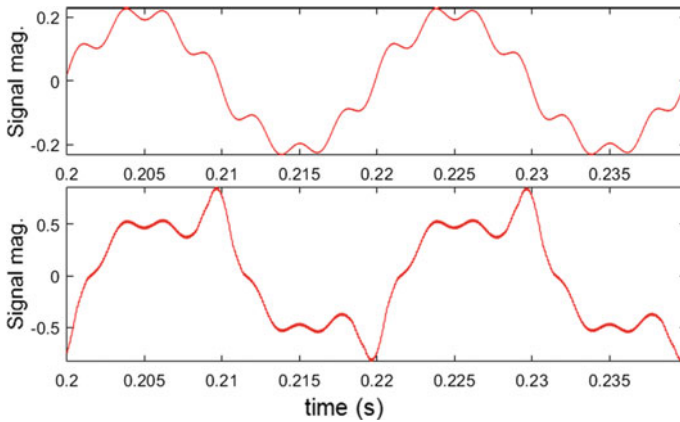
Fig. 7 Signal (p.u. core current) for the transformer with reduction in source harmonics with the proposed technique as shown in top trace

4 Conclusion

This paper presents an analytical study on the effect of source side harmonics on transformer operation. For this study, the effect of source side harmonics is observed on the hysteresis curve of the transformer core fitted at the output of an inverter. The study proposes a modified hysteresis loss model for the transformer considering the effect of harmonics. Also, a technique is presented for handy measurement of transformer internal parameters for plotting the hysteresis curve. The proposed study can be an effective tool for easy measurement and smart IoT-based analysis of harmonic effects on the transformer. A remedial technique for the transformer operation with source harmonics is also proposed. *MATLAB/Simulink*-based simulations backed by suitable experiments validate the proposed study.

References

1. Dao, T., Phung, B.T.: Effects of voltage harmonic on losses and temperature rise in distribution transformers. IET Gener. Transm. Distrib. **12**(2), 347–354 (2018)
2. Ioniţă, V., Cazacu, E., Petrescu, L.: Effect of voltage harmonics on iron losses in magnetic cores with hysteresis. In: Proceedings of 18th International Conference on Harmonics and Quality Power (ICHQP), Ljubljana, 1–5 (2018)
3. Dao, T., Halim, A., Liu, Z., Phung, B.T.: Voltage harmonic effect on losses in distribution transformers. In: Proceedings of International Conference on Smart Green Technology in Electrical and Information System, pp. 27–32 (2016)
4. So, E., Arsenau, R., Hanique, E.: No-load loss measurements of power transformers under distorted supply voltage waveform conditions. IEEE Trans. Instr. Meas. **52**(2), 429–432 (2003)
5. Zhang, Y., et al.: Magnetic characteristics and core losses in machine laminations: high-frequency loss prediction from low-frequency measurements. IEEE Trans. Ind. Appl. **48**(2), 623–629 (2012)

6. Arslan, E., Sakar, S., Balci, M.: On the no-load loss of power transformers under voltages with sub-harmonics. Proc. IEEE Int. Energy Conf. (ENERGYCON), Cavtat 228–233 (2014)
7. Amar, M., Kaczmarek, R.: A general formula for prediction of iron losses under nonsinusoidal voltage waveform. IEEE Trans. Mag. **31**(5), 2504–2509 (1995)
8. Nag, T., et al.: Fuzzy logic-based loss minimisation scheme for brushless DC motor drive system. IET Power Electron. **9**(8), 1581–1589 (2016)
9. Faiz, J., Ghazizadeh, M., Oraee, H.: Derating of transformers under non-linear load current and non-sinusoidal voltage—an overview. IET Electr. Power Appl. **9**(7), 486–495 (2015)
10. Arseneau, R., So, E., Hanique, E.: Measurements and correction of no-load losses of power transformers. IEEE Trans. Instr. Meas. **54**(2), 503–506 (2005)
11. Kefalas, T., Kladas, A.: Harmonic impact on distribution transformer no-load loss. IEEE Trans. Ind. Electron. **57**(1), 193–200 (2010)
12. Liu, X., et al.: Measurement of the no-load characteristics of single-phase transformer using an improved low-frequency method. IEEE Trans. Ind. Electron. **65**(5), 4347–4356 (2018)
13. Sarkar, D., Roy, D., Choudhury, A., Yamada, S.: Harmonic analysis of a saturated iron-core superconducting fault current limiter using Jiles-Atherton hysteresis model. Model. Meas. Cont. A. **89**(1), 101–117 (2016)
14. Chatterjee, D.: A novel magnetizing-curve identification and computer storage technique for induction machines suitable for online application. IEEE Trans. Ind. Electron. **58**(12), 5336–5343 (2011)

Potential Energy-Driven Stability Analysis of Tie Lines in Ring Network

Debopoma Kar Ray [ID]**, Tamal Roy** [ID]**, and Surajit Chattopadhyay** [ID]

Abstract Ring main system's stability analysis is of immense importance in recent years to retain the reliability of the lines and to maintain quality power at the consumer end. In this context, this work has been advanced wherein symmetrical fault-based stability analysis has been done in an interconnected power system. Firstly, a system has been built in software interface at harmonic environment, and symmetrical fault has been created at chosen buses. At this condition, potential energy of some connected tie lines has been assessed, and features have been extracted for stability analysis of the tie lines. At the end, algorithms have been developed for disintegrating symmetrical faults in the buses connected to tie lines.

Keywords Ring system · Potential energy · Stability zone · Symmetrical fault · Tie lines

1 Introduction

Power system analysis is usually performed to obtain stable operation of a power system. Line voltage stability indices-based stability analysis has been seen to be implemented on standard IEEE 14 and IEEE 118 bus systems for authentication [1]. Catastrophe theory-based stability analysis has been seen for islanded micro-grids [2, 3]. Proximity sensor-based voltage stability has been seen for network with 30 and 57 bus as per IEEE standard [4]. Generator over-excitation limiter-based voltage stability analysis has been seen [5]. Voltage stability analysis can also be done using phasor measurements in smart energy meters [6]. Loadability change-based voltage stability analysis has been seen for 16 bus system [7].

Voltage stability analysis using contingency screening and PV analysis has been seen [8]. PV-QV curve-based voltage stability assessment has been seen for a power

D. K. Ray · T. Roy (✉)
MCKV Institute of Engineering, Liluah, WB, India

S. Chattopadhyay
GKCIET, Malda, WB, India

system [9]. A comparative study among different index values of stability was seen in [10]. None of the analysis seen was found to carry out the analysis using potential energy analysis-based technique for the connected tie lines.

Thus, the motivation of this proposed approach is dealt with the analysis of tie lines stability, monitoring the line potential energy for the inception of short circuit faults that are symmetrical in nature and occur at generator bus in a ring main system. Firstly, a network has been built in software interface, and symmetrical fault has been created in the generator bus. At this condition, the potential energy of some connected and distant lines have been calculated both for normal and for the advent of symmetrical fault in the generator bus. Features have been extracted from the analysis, and an algorithm has been proposed at the end for determining the system stability.

2 Network Modeling

Mathematical modeling was developed by six bus and eight lines connected in ring structure as shown in Fig. 1 [11]. Line with bus specifications of the developed network is given in Tables 1 and 2. The normal and faulty condition Y-bus matrices have been provided in Table 3.
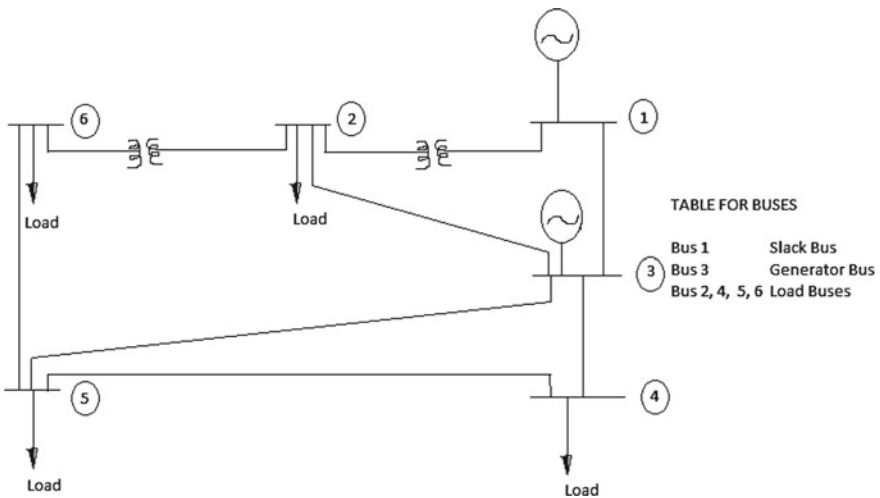
Fig. 1 Test system

Table 1 Network's line specifications	Bus orientation	Line impedance	Susceptance	Tap
	B_{1-3}	$0.041 + j0.29$	$j0.012$	–
	B_{2-3}	$0.028 + j0.21$	$j0.011$	–
	B_{3-4}	$0.042 + j0.18$	$j0.012$	–
	B_{3-5}	$0.041 + j0.21$	$j0.013$	–
	B_{4-5}	$0.028 + j0.16$	$j0.011$	–
	B_{5-6}	$0.061 + j0.28$	$j0.012$	–
	B_{1-2}	$j0.29$	–	1.04
	B_{2-6}	$j0.22$	–	1.03

Table 2 Network's bus specifications

Bus number	P_d	Q_d	P_g	Q_g	V
B_1	0	0	–	–	$1.03 \angle 0°$
B_2	0.9	0.11	0	0	$1.0 \angle 0°$
B_3	0	0	1.49	0.73	$1.0 \angle 0°$
B_4	0.43	0.26	0	0	$1.0 \angle 0°$
B_5	0.41	0.22	0	0	$1.0 \angle 0°$
B_6	0.34	0.12	0	0	$1.0 \angle 0°$

3   Gauss-Seidal Approach

Unknown bus voltage is found by using Gauss-Seidal [11] iterative approach. After finding voltages, power components are determined. Let us assume that bus is specified by K with maximum N possibility. Bus current may be written as follows:

$$I_K = \sum_{K=1}^{N} Y_K V_K \tag{1}$$

where Y_K is bus admittance matrix and V_K is bus voltage matrix. So,

$$I_K = V_{KK} V_K + \sum_{\substack{n=1 \\ n \neq k}}^{N} Y_{Kn} V_n \tag{2}$$

or

$$V_K = \frac{I_K}{Y_{KK}} - \frac{1}{Y_{KK}} \sum_{\substack{n=1 \\ n \neq K}}^{N} Y_{Kn} V_n \tag{3}$$

Table 3 Y-bus matrix at harmonic environment

[Y-bus] healthy

$$
\begin{bmatrix}
0.436 - 5.532i & 0 + 2.238i & -0.43 + 3.27i & 0 + 0i & 0 + 0i & 0 + 0i \\
0 + 2.238i & 0.733 - 12.18i & -0.73 + 4.88i & 0 + 0i & 0 + 0i & 0 + 4.901i \\
-0.44 + 3.27i & -0.73 + 4.88i & 3.093 - 17.74i & -0.96 + 4.807i & -0.959 + 4.807i & 0 + 0i \\
0 + 0i & 0 + 0i & -0.96 + 4.807i & 2.243 - 11.19i & 0 + 0i & 0 + 0i \\
0 + 0i & 0 + 0i & -0.961 + 4.807i & 0 + 0i & 2.88 - 14.2i & -0.641 + 3.205i \\
0 + 0i & 0 + 4.901i & 0 + 0i & 0 + 0i & -0.641 + 3.205i & 0.641 - 8.195i
\end{bmatrix}
$$

[Y-bus] faulty

$$
\begin{bmatrix}
0.017 - 1.109i & 0 + 0.47i & -0.017 + 0.66i & 0 + 0i & 0 + 0i & 0 + 0i \\
0 + 0.47i & 0.029 - 2.45i & -0.039 + 1.25i & 0 + 0i & 0 + 0i & 0 + 1.22i \\
-0.016 + 0.66i & -0.04 + 1.24i & 0.127 - 3.622i & -0.062 + 1.246i & -0.062 + 1.24i & 0 + 0i \\
0 + 0i & 0 + 0i & -0.061 + 1.245i & 0.093 - 2.309i & -0.08 + 1.65i & 0 + 0i \\
0 + 0i & 0 + 0i & -0.0621 + 1.24i & -0.08 + 1.66i & 0.11 - 2.96i & -0.041 + 0.83i \\
0 + 0i & 0 + 1.22i & 0 + 0i & 0 + 0i & -0.041 + 0.83i & 0.02 - 1.65i
\end{bmatrix}
$$

Table 4 Bus voltage in harmonic environment

Healthy bus voltages (p. u.)					
V_1	V_2	V_3	V_4	V_5	V_6
1.05	2.87	4.2	4.01	3.2	2.2
Bus voltages (p. u.) faulty					
V_1	V_2	V_3	V_4	V_5	V_6
2.1	1.4	0	2.13	1.89	2.31

However,

$$I_K = \frac{P_K - jQ_K}{V_K^*} \tag{4}$$

$$V_K = \frac{1}{Y_{KK}} \left[\frac{P_K - jQ_K}{V_K^*} - \sum_{\substack{n=1 \\ n \neq K}}^{N} V_{Kn} V_n \right] \tag{5}$$

for $K = 1, 2, 3, …, N$.

By multiple iteration, V_K is determined. Harmonic voltages are obtained by modifying frequency components of [Y-bus].

4 Determination of System Bus Voltages

Tables 1, 2, and 3 data are used to determine bus voltage for fundamental as well as few harmonics components. The computation output have been presented in Table 4. Both healthy conditions and faulty conditions were considered in determining bus voltages where fault refers to fault at generator bus.

5 Power Flow

After determination of bus voltage, considering harmonics at normal and fault conditions, flow of active power component from the ith bus to jth bus is determined in following approach.

$$S_{ij} = V_i \left(\frac{V_i - V_j}{z_{ij}} + V_i y_{ij0} \right)^* \tag{6}$$

$$\therefore P_{ij} = \text{Real}\left[V_i^*(V_i - V_j)y_{ij} + V_i^* V_i y_{ij0} \right]$$
$$Q_{ij} = -\text{Im}\left[V_i^*(V_i - V_j)y_{ij} + V_i^* V_i y_{ij} \right] \tag{7}$$

where y_{ij0} is charging impedance of line and z_{ij} is impedance of line.

Considering π-equivalent model of line with transformer.

$$\therefore P_{ij} = \text{Real}\left[V_i^*(V_i - V_j)yy_{ij} + V_i^*V_i\,yc1_{ij}\right]$$
$$Q_{ij} = -\text{Im}[V_i^*(V_i - V_j)yy_{ij} + V_i^*V_i\,yc1_{ij}] \tag{8}$$

where yy_{ij} is line series admittance, $yc1_{ij}$ is ith bus shunt admittance, and $yc2_{ij}$ is jth bus shunt admittance.

6 Flow of Complex Power

Table 5 represents flow of power found in complex form. It shows variation of magnitudes as well as angle of the complex form of power. Powers at both healthy and faulty conditions are determined.

$$\begin{bmatrix} S_{11} & S_{12} & S_{13} & S_{14} & S_{15} & S_{16} \\ S_{21} & S_{22} & S_{23} & S_{24} & S_{25} & S_{26} \\ S_{31} & S_{32} & S_{33} & S_{34} & S_{35} & S_{36} \\ S_{41} & S_{42} & S_{43} & S_{44} & S_{45} & S_{46} \\ S_{51} & S_{52} & S_{53} & S_{54} & S_{55} & S_{56} \\ S_{61} & S_{62} & S_{63} & S_{64} & S_{65} & S_{66} \end{bmatrix} \tag{9}$$

7 Stability Analysis Based on Tie Line Potential Energy

7.1 Stability Analysis Criterion

In this analysis technique, each tie line enclosed by two buses has been considered as two machines equivalent model [12] as shown in Fig. 2 for pre-fault condition and in Fig. 3 for post-fault condition.

Potential energy of each tie line under has been calculated both at healthy condition and also at faulty condition where symmetrical fault is occurred at generator bus.

For this analysis, the swing equation has been considered, wherein a frequency-dependent energy function has been considered, dependent on which the chosen feeder stability has been assessed.

$$M\frac{\mathrm{d}^2\delta}{\mathrm{d}t^2} = P_a = P_m - P_e \tag{10}$$

Table 5 Power flow at harmonic environment

Complex power flow (healthy)

$$
\begin{bmatrix}
0 & -2.64 + 1.26i & -0.175 - 0.102i & 0 & 0 & 0 \\
2.67 + 1.07i & 0 & 0.49 - 0.075i & 0 & 0 & -0.117 + 0.43i \\
0.175 + 0.179i & -0.48 + 0.41i & 0 & 2.74 - 0.29i & 0.77 + 0.087i & 0 \\
0 & 0 & -2.59 + 6.67i & 0 & -1.95 + 6.67i & 0 \\
0 & 0 & -0.76 + 0.41i & 2.091 - 2.15i & 0 & -0.38 + 1.51i \\
0 & 0.117 - 0.152i & 0 & 0 & 0.45 + 0.112i & 0
\end{bmatrix}
$$

Complex power flow (faulty)

$$
\begin{bmatrix}
0 & -0.472 - 0.0799i & -0.85 - 0.14i & 0 & 0 & 0 \\
0.47 + 0.195i & 0 & -1.18 - 0.48i & 0 & 0 & -0.083 - 0.435i \\
0.881 + 2.838i & 1.218 + 3.91i & 0 & 0.21 + 1.204i & -1.131 + 1.095i & 0 \\
0 & 0 & -0.236 - 0.89i & 0 & -1.41 - 0.021i & 0 \\
0 & 0 & 1.13 - 0.59i & 1.39 + 0.53i & 0 & 2.17 + 2.065i \\
0 & 0.083 + 0.85i & 0 & 0 & -2.11 + 0.704i & 0
\end{bmatrix}
$$

Fig. 2 Pre-fault network and its two machine equivalent
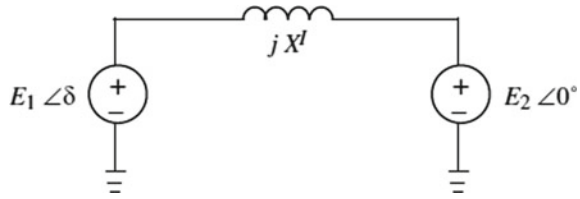
Fig. 3 Post-fault network and its two machine equivalent
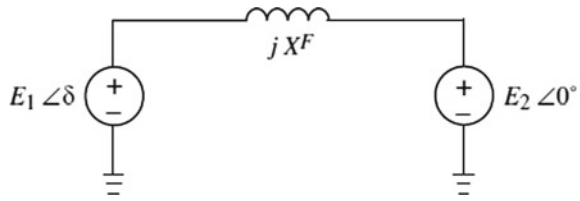
where denotes the angular momentum of the machine, is the accelerating power, and are the mechanical and electrical powers respectively and

$$P_e = \frac{|E_1||E_2|}{X} \sin \delta = P_{max} \sin \delta \tag{11}$$

This is the swing equation of an alternator which has been considered at fault condition. Now, let us consider that there is a difference in angular velocity between rotor and air-gap field due to small disturbance at fault in the system, and a damping torque gradually dies out the oscillation, and the system gradually stables down.

$$M \frac{d^2\delta}{dt^2} + D \frac{d\delta}{dt} = P_m - P_{max} \sin \delta = \frac{-\partial V_n}{\partial \delta} \tag{12}$$

$$\text{or } V_n(\delta) = -P_m\delta - P_{max} \cos \delta \tag{13}$$

where corresponds to fundamental frequency. Now, multiplying Eq. (3), we get,

$$\left[M \frac{d^2\delta}{dt^2} + D \frac{d\delta}{dt} + \frac{\partial V_n}{\partial \delta} \right] \frac{d\delta}{dt} = 0 \tag{14}$$

where $\frac{d}{dt}[V(\delta, \omega)]_n = 0$ is the frequency variable energy function which has been used in a variable frequency scenario to calculate the normal and fault potential energies. From the concept of potential well, the variation of potential energies in presence of various harmonic frequencies has been assessed with respect to load angle, and stability of the feeder under study has been determined. The calculated bus voltages at normal and at fault, in presence of various harmonic frequencies in the system, have been compared with the aforesaid energy function to ascertain the

Table 6 Potential energy calculation-based steady-state stability analysis

Line	V_{PEn}		E_n		Remarks at fault
	Healthy	Fault in generator bus	Healthy	Fault in generator bus	
2–3	15	6.7	0.62	−2.92	Stable (2.92 < 6.7)
2–6	12	4.7	0.4	−3.5	Stable (3.5 < 4.7)
4–5	13.5	7.5	0.56	8.4	Unstable (8.4 > 7.5)
3–5	12.8	6.9	0.4	7.3	Unstable (7.3 > 6.9)

stability of each feeder under study. For fault in either generator or load buses of the network,

i. If $E_n < V_n$, the feeder is considered to be stable.
ii. If $E_n > V_n$, the feeder is considered to be unstable.

7.2 Work Contribution

Potential energies were determined during healthy and generator bus fault conditions. The results have been shown in Table 6 for mixed frequencies. The novelty of this work is that, here, the whole stability analysis has been done in variable frequency scenario considering some noted frequencies in the network as per [13]. Also, the whole analysis has been done using frequency variable program with very small time of execution.

7.3 Algorithm

Thus it is clear that if potential energy of tie lines can be monitored, steady-state stability of lines can be assessed. Thus, depending on the extracted features, an algorithm has been developed as listed below:

Step 1: Acquire system data.

Step 2: Perform load flow studies to calculate complex V, P.

Step 3: Observe change of magnitude as well as change of angles.

Step 4: Predict stability.

8 Conclusion

Steady-state stability of tie lines was judged for an interconnected grid system monitoring the tie line potential energy. A system has been built in software interface at harmonic infiltrated condition, and normal and symmetrical fault (at generator bus)-based load flow study was carried out and power flow in the tie lines. Thereafter, potential energy of tie lines has been calculated, and depending on the variation in the line, potential energies at fault form normal stability of lines have been assessed. At last, an algorithm has been proposed for ascertaining steady-state stability of tie lines in the network. The future proposition of the work aspires to acquire field data for analyzing effectiveness of the algorithm in real time for the advent of real-time faults using others frequencies in the network.

References

1. Althowibi, F.A., Mustafa, M.W.: Power system voltage stability: indications, allocations and voltage collapse predictions. Int. J. Adv. Res. Electr. Electron. Instrum. Eng. **2**(7). ISSN (print): 2320–3765, ISSN (online): 2278–8875, pp. 3138–3152 (2013)
2. Hemmatpour, M.H., Mohammadian, M., Gharaveisi, A.-A.: Simple and efficient method for steady-state voltage stability analysis of islanded microgrids with considering wind turbine generation and frequency deviation. IET Gener. Transm. Distrib. **10**(7), 1691–1702 (2016)
3. Mahmoud, G.A.: Voltage stability analysis of radial distribution networks using catastrophe theory. IET Gener. Transm. Distrib. **6**(7), 612–618 (2012)
4. Zabaiou, T., Dessaint, L.-A., Kamwa, I.: "Preventive control approach for voltage stability improvement using voltage stability constrained optimal power flow based on static line voltage stability indices. IET Gener. Transm. Distrib. **8**(5), 924–934 (2014). ISSN:1751-8687. https://doi.org/10.1049/iet-gtd.2013.0724
5. Chen, Y., Zhang, Y., Zhang, J., Zhang, Y., Song, L.: A Full dynamic voltage stability research based on time-domain simulation. Energy Power Eng. (2013). https://doi.org/10.4236/epe.2013.54B148
6. Hazarika, D., Talukdar, B.K., Gupta, B.M.: Identification of voltage stability condition of a power system using measurements of bus variables. J. Eng. (2014). https://doi.org/10.1049/joe.2014.0263
7. Jahan, S., Mannan, Md.A.: Voltage stability analysis of a 16-bus distribution network based on voltage sensitivity factor. Int. J. Multidiscip. Sci. Eng. **5**(4). ISSN: 2045-7057, pp. 1–5
8. Yang, Z., Rajagopalan, S., Conto, J.: Practical voltage stability analysis. Power Energy Soc. Gener. Meet. IEEE. 1–7 (2010). https://doi.org/10.1109/PES.2010.5589892
9. Bujal, N.R., Hasan, A.E., Sulaiman, M.: Analysis of voltage stability problems in power system. ICE2T 278–283 (2014). https://doi.org/10.1109/ICE2T.2014
10. Cupelli, M., Cardet, C.D., Monti, A.: Comparison of line voltage stability indices using dynamic real time simulation. Innov. Smart Grid Technol. (2012). https://doi.org/10.1109/ISGTEurope.2012.6465625,p.1-8
11. Chakrabarti, A., Halder, S.: Power System Analysis Operation and Control. PHI Learning Private Limited (2008). ISBN-978-81-203-3585-1
12. Sauer, P.W., Pai, M.A.: Power System Dynamics and Stability. Stipes Publishing Co., pp. 287–294. ISBN-10:1588746739, ISBN-13:978-1588746733
13. IEEE Standard Definitions for Measurement of Electric Power Quantities under Sinusoidal, Non-Sinusoidal, Balanced or Unbalanced Conditions, IEEE Std. 1459-2010

I-Fresh: An IoT-Based System for Predicting the Freshness of Vegetables and Flower

Amiya Karmakar, Nayan Sengupta, and Partha Sarathi Banerjee

Abstract Identifying freshness by color is crucial for the evaluation of vegetables, fruits, or flowers. In this proposed work, an IoT-based framework has been developed which can evaluate the freshness of the object by sensing and analyzing its color. The system can predict the life of the flower or the fruit depending on the evaluated threshold. The fuzzy normal distribution is used to calculate the threshold. Output visualization has been carried out using web-based applications that work on real-time data. A color sensor is used to get the color code of the object. Color of the object depends on ambient temperature and humidity. Temperature and humidity sensor has been incorporated in the model to enhance the accuracy of the obtained result. I-fresh outperforms other state-of-the-art techniques with respect to the accuracy of result, cost-efficiency, and power efficiency.

Keywords IoT · Color sensor · Freshness

1 Introduction

Vegetables, flowers, and fruits are the by-products of plants having short-time availability. When we buy vegetables, fruits, or flowers, we always tend to check the freshness criteria. However, there is no such thing as finding out the freshness criteria. People inspect virtually. We cannot detect the actual freshness. So here, we have come up with an approach that will predict the freshness by using color sensors, temperature, and humidity sensors. Nowadays, due to an excessive rise in air pollution, agriculture is adversely affected. Ozone precursor emissions (nitrogen oxides and volatile organic compounds) are a particular concern for global food security as these compounds react to form ground-level ozone [1]. This in turn penetrates into plant structure and impairs its ability to develop. So, farmers use some chemicals

---

A. Karmakar · N. Sengupta (✉) · P. S. Banerjee
Kalyani Government Engineering College, Kalyani, West Bengal, India

A. Karmakar
e-mail: amiya.karmakar@kgec.edu.in

to get rid of these problems. But, those chemicals have adverse effects on human health. And, nowadays, people selling vegetables in market places use to store them in cold storages so that they seem to look fresh [2]. In this proposed work, freshness is predicted by the amalgamation of color, temperature, and humidity sensors. This will not only detect the color, but it will also detect the freshness depending upon temperature and humidity. With the increase in storage temperature, the deterioration in color is quite faster. This is because temperature affects the metabolism and respiration rate. Low temperature and high humidity increase the commercial lifespan of vegetables and fruits [3]. Considering these two inputs (temperature and humidity), freshness can be easily predicted. So, in our research work, we have seen that with the increase in temperature, freshness decreases, and with the increase in humidity, freshness increases.

Major contribution:

- In this proposed work, freshness of flowers and vegetables is identified by using a color sensor, humidity, and temperature sensors. All these sensors consume very little power, and their cost is very low. Hence, we made a power-efficient as well as a cost-efficient model for identifying the freshness of vegetables and flowers.
- Sensors often produce noisy data, and to remove the noise from the data and making the data more usable, we applied fuzzy normal distribution. It gives more weightage near the mean value and discards noisy data.
- We developed an interactive user interface for the output where the user can see all the required details about the product, and the user interface is remotely accessible by using the Internet.

2   Background and Related Works

Juliano et al. [4] used TCS 3200 to identify the maturity stages of strawberries. Strawberries are costly, so they proposed this model to identify the maturity stages. In this work, TCS 3200 is used to sense the RGB color values from the strawberry, and based on the value, maturity is calculated. This device is capable of approving and applying the maturity stages of strawberries. Damayanti et al. [5] introduced a non-invasive method that can identify the maturity of tomatoes. In their proposed work, they used RGB digital image and vitamin C content to make their work more efficient. Putra et al. [6] introduced color sensor to predict the ripeness of tomato, and they also introduced sorting tools to sort the ripped fruit. Toro et al. [7] used a color sensor to identify the ripeness in Hass avocado, and they made the model cost-efficient by using only one sensor.

3 System Architecture

The architecture of the proposed model is elaborated in this section. Figure 1 represents the full architecture of the proposed model.

Full architecture is divided into the following three parts.

3.1 Sensing Layer

This is the most important layer of the model. In this layer, all sensors are present. DH11 sensor is used to sense both the temperature and humidity of the environment. The color sensor is the brain of the model, and it senses the RGB values from the object. All sensors are connected with Arduino UNO [8]

3.2 Remote Processing Layer

This layer helps to make a bridge between the application layer and the sensor layer. ESP8266_01 module is used to send this data to the remote server using TCP/IP
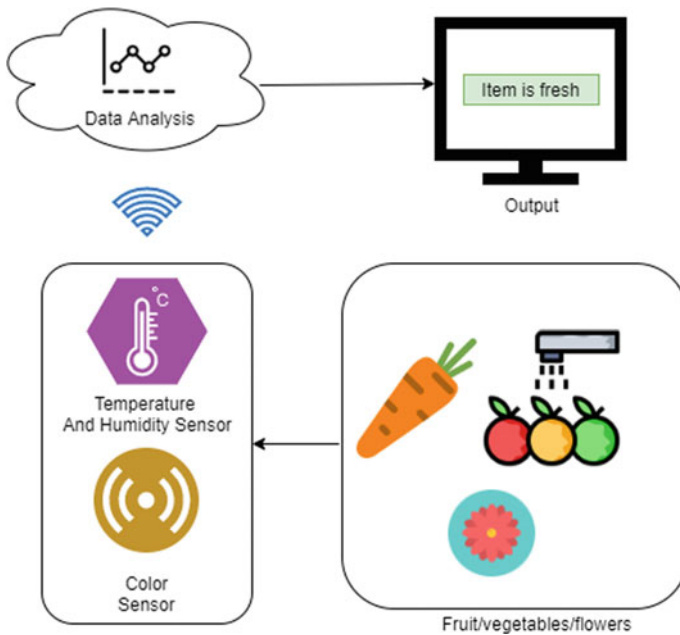
Fig. 1 Conceptual architecture of the proposed model

protocol as described in [9]. In this proposed model, we used ThingSpeak to receive the data remotely. ESP8266_01 module sends the data to ThingSpeak. All the data will be sent to the remote server for further calculation.

3.3 Application Layer

From the remote processing layer, this layer will retrieve the data through API [10] calls which are communicating with a remote server through hibernate mappings. This in turn will populate frontend Web UI, and depending upon the data, it will be displayed on UI whether the item is fresh or not.

4 Design of I-Fresh

In this section, both hardware and software designs are elaborated. The motivations behind using these designs are all sensors and hardware are economical, and Arduino is a low-powered microcontroller.

4.1 Integrated Design of the Sensors Node

In I-fresh, DTH11 and TCS 3200 are used. Both the sensors are connected with Arduino UNO, and ESP 8266_01 is used to send the received data from mentioned sensors to the cloud; for further, I-fresh model is configured based on the following condition:

Color sensors will continue sensing when the system will get power. If a color sensor finds any predefined color, other sensors will continue sensing. The full circuit diagram is presented in Fig. 2. The process flow of the proposed model is presented in Fig. 3.

4.2 Integrated Design of the Sensor

In this proposed work, two sensors are mainly used:

- DTH 11: DTH11 is used to measure the temperature and humidity of the environment [11]. It converts the environmental humidity and temperature into an electrical signal. The freshness of vegetables and flowers depends on both humidity and temperature. To find the relation between them, this sensor is used.

Fig. 2 Circuit diagram of the proposed model
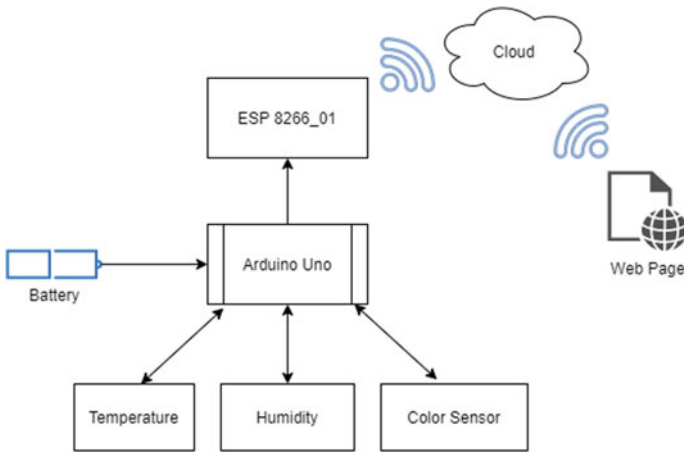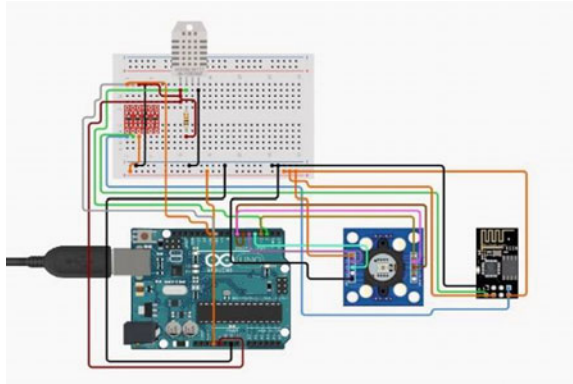
Fig. 3 Block diagram of the proposed model

- TCS 3200: This sensor is used to identify the color of the object in RGB [5] form. TCS 3200 is a type of photoelectric sensor which detects color by using reflected light [12].

ESP 8266_01 [13] is used to send the data into the remote server using TCP/IP protocol. All sensors are connected to the Arduino as represented in Fig. 2. The flow of the system is presented in Fig. 3.

4.3 Design of Gateway

IoT gateway always plays a major role in any IoT-based technological environment. This mainly creates a connection or we can say a communication bridge so that

the sensors get connected to the Internet, Bluetooth devices, and so on. Here, ESP 8266_01 is used to send the data to the remote server using TCP/IP protocols. There is also a Web site designed as well which will receive the data from RestApi generated in backend by pulling the data from the server. For each request, we are generating a unique user ID for differentiating the data. In Web UI, it will be displayed whether the item is fresh or not.

4.4 Implementation of the Remote Server

Here, we will use Heroku [14] server for the deployment of our microservice. Our Microservice is going to pull the data from an Excel sheet and is going to store the data in the remote server. As our service is running on top of the Heroku cloud platform, it will dynamically load the data received from the IoT module, and in the backend, the result will be calculated and a RestApi [15] will be generated. This RestApi will reflect on Web UI with our final outcome.

5 Implementation Framework

5.1 Data Sensing and Data Aggregation

In this proposed model, all the data are processed with the help of fuzzy normal distribution [16]. A fuzzy normal distribution curve was plotted using the dataset, and we found in a constant time frame in which ranges the data are more congested. To find the congested area, we make the threshold 90%. Values of RGB will be congested near the mean. In order to give more weightage near the mean, one triangular function is used with a normal distribution as represented in Fig. 4. In this work, we tried to find out how many days passed after the harvesting. The color of vegetables and flowers changes with respect to time. We calculated the range of RGB values for a particular day. We also introduced the temperature and humidity coefficient in order to find the ranges. If models find a match with predefined ranges generated using fuzzy normal distribution with the test data, it will send the output to the Web site.
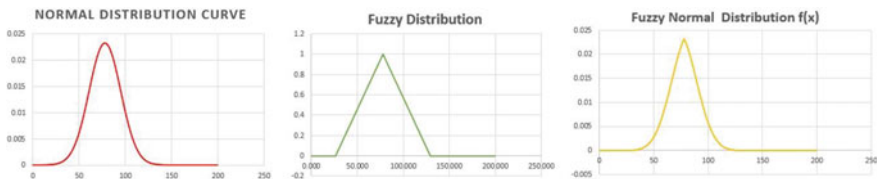
Fig. 4 Distribution curve

Table 1 Comparative analysis

Features	I-fresh	[4]		[5]	[6]	[17]
Usages of multiple sensors	Yes	No		No	No	Yes
Remote monitoring	Yes	No		No	No	No
Text to voice approach for blind and aged person	Yes	No		No	No	No
Sensor noise reduction	Yes	No		No	No	No
Application on different fruit and flowers if the database is present	Yes	No		No	No	No
Consideration of output dependency on different parameters	Yes	No		No	No	Yes

5.2 Data Transmission

Data communication is done by using the following methods:

Humidity and color sensor communicates with Arduino UNO, by using ESP8266_01 module. All the data are transferred to the remote server by using TCP/IP protocol. In this proposed work, two servers are used.

I. Repository server: In this proposed work, Google sheets are used for the repository server. Data collected from sensors are shared to the repository server for storing and analyzing data. ThingSpeak acts like middleware between sensor and repository servers. By using the IFTTT protocol, repository server catches the data.

II. Web server: Web server is used to host the Web site. In this server, all the user data are stored, and it manages the Web site's backend.

6 Comparison

See Table 1.

7 Application of Proposed Model—A Case Study

7.1 Data Creation

We have collected 25 Hibiscus Rosasinensis and created a database for RGB values of every petal of those flowers. We sensed the values after every four hours for three days.

Table 2 Findings of Day 1, Day 2, Day 3

Day 1			Day2		Day 3	
Channel	Range	Percentage of data belongs to this range (%)	Range	Percentage of data belongs to this range (%)	Range	Percentage of data belongs to this range (%)
Red	140–168	90.21	55–110	90.54	33–47	90.001
Green	3–21	90.07	15–50	90.06	17–29	90.00
Blue	5–27	90.00	19–49	90.86	16–30	90.04

7.2   Data Analysis

Ranges for each red, green, blue channel are calculated by using the fuzzy normal distribution. During the collection of data, the temperature was in the range of 57–76 °F. The below tables contain the result that we got after applying the fuzzy normal distribution.

$$\text{Normal distribution} f(x) = \frac{1}{\sqrt{2\pi\sigma^2}} e^{-\frac{(x-\mu)^2}{2\sigma^2}} \tag{1}$$

$$\text{Membership function } g(x) = \begin{cases} 0 (x \leq a) \\ \frac{x-a}{\mu-a}(a \leq x < \mu) \\ \frac{b-x}{b-u}(\mu < x < b) \\ 0 (x \geq b) \end{cases} \tag{2}$$

$$\text{Area under the curve } A = \int_{h_1}^{h_2} f(x)g(x)\mathrm{d}x \tag{3}$$

Based on the above Eq. (3), Table 2 is calculated.

7.3   Result

We took 27 flowers for range calculation, and for testing purposes, we used four flowers. The result is mentioned in Table 3.

Model achieved 75% accuracy.

Table 3 Expected output versus original output

Sample	RGB value	Expected output	output	Sample	RGB value	Expected output	output
Sample 1	(145,20,7)	Day 1	Day 1	Sample 2	(56,42,20)	Day 2	Day 2
Sample 3	(120,4,6)	Day 1	Day 2	Sample 4	(33,18,20)	Day 3	Day 3

8 Conclusion

Due to a smaller number of data, this model is now in the initial stage, and we are creating a strong database to make the model more accurate. We are also planning to add sleep mode to all the sensors to optimize the power. We are working to make the model compatible with solar energy. In the future scope, a camera module can be introduced to identify the shape of the object to automate the object selection.

References

1. Air Pollution and Food Production. (n.d.). Retrieved March 09, 2021, from https://unece.org/air-pollution-and-food-production#:~:text=There%20is%20a%20two%20way,pollution%20can%20impact%20food%20production.&text=Conversely%2C%20there%20is%20increasing%20evidence,also%20threatened%20by%20air%20pollution
2. Kumar, K.: Cold Preservation and Processing (2020)
3. http://www.foodandnutritionjournal.org/vol04nospl-issue-conf-october-2016/effect-of-temperature-in-color-changes-of-green-vegetables/
4. Juliano, A., Hendrawan, A.H., Ritzkal, R.: Information system prototyping of strawberry maturity stages using Arduino Uno and TCS3200. J. Robot. Control (JRC) **1**(3), 86–91 (2020)
5. Damayanti, R., et al., Prediction of tomatoes maturity using TCS3200 color sensor. In: IOP Conference Series: Earth and Environmental Science, vol. 475. No. 1. IOP Publishing (2020).
6. .Putra, F., Rizaldi, T.: Application of color sensor in the determination of tomato fruit ripeness (Solanum Lycopersicum, L) in gravitation type fruit sorting tool (gravitation type). Indonesian J. Agric. Res. **2**(1), 13–20 (2019)
7. Toro, J., et al.: Portable equipment for determining ripeness in Hass avocado using a low-cost color sensor. In: SPECKLE 2015: VI International Conference on Speckle Metrology. Vol. 9660. International Society for Optics and Photonics (2015)
8. Louis, L.: Working principle of Arduino and using it as a tool for study and research. Int. J. Control Autom. Commun. Syst. (2018). https://doi.org/10.5121/ijcacs.2016.1203
9. Sujin, J.S., et al.: IoT based patient monitoring system using TCP/IP protocol. In: 2021 7th International Conference on Advanced Computing and Communication Systems (ICACCS), vol. 1. IEEE (2021)
10. Adamczyk, P., et al.: Rest and Web Services: In Theory and in Practice. REST: From Research to Practice, 35–57. Springer, New York (2011)
11. DHT11—Temperature and humidity sensor module. (n.d.). Retrieved March 09, 2021. from https://www.electronicscomp.com/dht11-temprature-humidity-sensor-module-india
12. Li, Q., et al.: Study on color analyzer based on the multiplexing of TCS3200 color sensor and microcontroller. Int. J. Hybrid Inform. Technol. **7**(5), 167–174 (2014)
13. Schwartz, M.: Internet of Things with ESP8266. Packt Publishing Ltd. (2016)
14. Heroku Security. (n.d.). Retrieved March 15, 2021, from https://www.heroku.com/policy/security
15. Neumann, A., Laranjeiro, N., Bernardino, J.: An analysis of public REST web service APIs. IEEE Trans. Serv. Comput. 1–1 (2018). https://doi.org/10.1109/TSC.2018.2847344
16. Liu, H., Guan, J.: A model of fuzzy normal distribution. Open J. Stat. **6**, 749–755 (2016). https://doi.org/10.4236/ojs.2016.65061
17. Jayasankar, K., et al.: Fruit freshness detection using raspberry PI. Int. J. Pure Appl. Math. **119**, 1685–1691 (2018)

Estimation of Cascaded Wireless Channel and Configuration Selection of RIS-Assisted Communication Systems

C. H. T. Krishna Teja Yadav, Rahul Tiwari, and K. Venkateswaran

Abstract Reconfigurable intelligent surfaces (RISs) are recommended to be used in beyond 5G wireless communication systems to control the propagation environment so as to achieve higher data rate, spectrum efficiency, and increased throughput. In RIS-aided wireless communication, the interaction of radio waves on the surface of RIS plane can be controlled by tuning the impedance over the surface which results in the changes of amplitude and phase shift associated with each element. In this work, an attempt is made to estimate the base station (BS)-RIS-user cascaded channel coefficients based on the $4N$ received signals at the user end using OFDM system model. In this paper, signal processing cup (SP CUP 2021) dataset1 is used to configure the surface in MATLAB to identify the configuration that achieves maximum data rate.

Keywords Reconfigurable intelligent surfaces · Orthogonal frequency division multiplexing · Pilot signal · Metamaterials · Cascaded channel matrix · Configuration selection

1 Introduction

In wireless communication systems, radio waves travel from the transmitter to receiver through many propagation paths. These paths exhibit fading like phenomenon which possess a constant behavior. Hence, current technology does not have complete control over the propagation environment [1]. The communication system must provide higher data rates, improved spectral efficiency, large coverage, and continuous connectivity to the user equipment. The 5G systems employ the multiple-input and multiple-output (MIMO), and massive MIMO technologies to

C. H. T. Krishna Teja Yadav (✉) · R. Tiwari · K. Venkateswaran
CMR Institute of Technology, Bengaluru, India
e-mail: krishna.t@cmrit.ac.in

R. Tiwari
e-mail: rahul.t@cmrit.ac.in

support these requirements. The problem of achieving them comes at the increased cost of hardware, and complicated signal processing operations are involved. In recent times, a reconfigurable intelligent surface (RIS) is used for beyond 5G systems whose features are more advanced than current technology, and it is considered for smart radio environment.

RIS is a thin layer of engineered meta-surface whose properties are not found in the naturally occurring materials having conformal structure with light weight, and it is controlled electronically with a software controller. RIS is a two-dimensional meta-surface containing large number of elements acting as scatterers. The sub-wavelength $\lambda/5$- or $\lambda/10$-sized elements are placed all along the surface either in a continuous or in a discrete manner. The RIS surfaces can be deployed in the indoor environment such as within the buildings, ceilings, mounting on walls, and on the rooftops [2].

The electromagnetic waves impinging on them can be controlled to direct them toward the intended receiver. These elements reflect the incident wave by adjusting the amplitude and phase shift of the reflected signals [3]. The reflected radio waves from the RIS are shaped by the elements either individually or as a group according to generalized Snell's law where the angles of reflection and incidence are not same anymore. The RIS is also referred to as intelligent reflecting surfaces (IRSs), software controlled meta-surfaces in the literature. The rest of the paper is organized as follows: Section 2 discusses about the differences between RIS and conventional relay system. Section 3 gives the detail about the system model used. Section 4 describes the protocol used for estimating coefficients of cascaded BS-RIS-user channel. Finally, the simulation results are shown in Sect. 5.

2   RIS Versus Relay Systems

The performance of the communication system is improved by placing the RIS in the intermediate location which is normally far from the transmitter and receiver. When the direct path between the base station and user is severely attenuated by walls of large building, RIS can be deployed on in such situations by leveraging the walls and edges of those buildings. The RIS collects the signal from the transmitter and beam form it toward the receiver in a passive manner. The individual elements of RIS act as a passive antennas which do not have any signal processing capability. This means RIS can neither transmit nor receive on its own, but they can only reflect the signals reaching them in a diffuse manner. Hence, the propagation environment (wireless channel) can be controlled by this passive operation of RIS unlike conventional systems which consumes power.

In conventional systems, relays are placed along the communication path to amplify the signal from the transmitter. These relays can operate in both half-duplex and full-duplex modes, whereas RIS can operate only in full-duplex mode. The relay systems achieve better signal-to-noise ratio (SNR) compared with RIS of large surface area due to lack of amplification performed at the RIS. There is also

large power requirement in large surface RIS because of reconfiguration done on a continuous manner. At the same time, RIS provides less-complex hardware structure compared with the traditional relay systems. The N discrete number of elements on a RIS re-radiates the signal toward the receiver following the square law principle, thereby increasing the SNR proportional to N^2. The end-to-end SNR does not show the linear relationship with the surface area of the RIS which makes it more suitable whenever high spectral efficiency is required. RIS can synthesize an object such as a parabolic reflector producing time delay at each point on the surface such that the reflected wave is more directed toward the receiver. This results in RIS controlling both the shape and angle of the reflected beam from the surface [4].

The RIS can be operated in various configurations for aiding user communication in wireless systems to increase the quality of service. Each element of an RIS can be operated in a way that results in the change of impedance over the surface. The impedance variation is tunable which is controlled using a switch having two states resulting in the changes of reflection coefficient. Based on the control signal received from either the base station or user, the best RIS configuration will be employed for rest of the communication setup. Since the elements N in RIS is very large, a total number of 2^N configurations considered grows exponentially to a large extent and is close to infinity. This makes it a very difficult task to search for a best RIS configuration within this large set that can be used to achieve the maximum data rate. Hence, an algorithm will be developed representing a linear relationship based on N received signals at the user location to select the best RIS configurations.

3   System Model

The system model is developed by adopting the orthogonal frequency division multiplexing (OFDM) over the communication channel [5]. The set of transmitted symbols are represented as $\{x[n]\}$ in the complex base band domain at the base station. Since the channel behaves as a linear filter, its finite impulse response $\{h_\theta[l] : l = 0, 1...M - 1\}$ will be estimated based on the set of received signals at the user. In order to estimate the frequency response $\overline{h_\theta}[\nu]$ of the channel, a known pilot signal is transmitted initially within one frame of OFDM symbol. The noise at the receiver $\{w[k]\}$ is of additive nature which is circularly symmetric complex Gaussian (CSCG) in both the time and frequency domains. Let $\{z[k]\}$ represent the received signal in the complex base band domain which is given as (1).

$$z[k] = \sum_{l=0}^{M-1} h_\theta[l]x[k - l] + w[k] \qquad (1)$$

To transform this representation to OFDM system model, we prefix a cyclic code as the last $(M - 1)$ samples of the transmitted signal and increase its length to K. The number of subcarriers represented by K is higher than the length of the impulse

response M. We represent one OFDM block that allows transmission of a known pilot signal using K parallel subcarriers as [1]:

$$\overline{z}[v] = \overline{h_\theta}[v]\overline{x}[v] + \overline{w}[v], \quad v = 0, 1 \ldots K - 1 \tag{2}$$

This model can be represented by using K-dimensional vectors in matrix form as:

$$
\begin{bmatrix} \overline{z}[0] \\ . \\ . \\ . \\ \overline{z}[K-1] \end{bmatrix} = \begin{bmatrix} \overline{h_\theta}[0] \\ . \\ . \\ . \\ \overline{h_\theta}[K-1] \end{bmatrix} \odot \begin{bmatrix} \overline{x}[0] \\ . \\ . \\ . \\ \overline{x}[K-1] \end{bmatrix} + \begin{bmatrix} \overline{w}[0] \\ . \\ . \\ . \\ \overline{w}[K-1] \end{bmatrix} \tag{3}
$$

It can be described in compact form as $\overline{Z} = \overline{h_\theta} \odot \overline{x} + \overline{w}$ with $\odot$ operator representing the element-wise (Hadamard) product. The channel matrix $h_\theta[k]$ is a $M-$tap FIR filter contains two parts, namely the uncontrollable channel decided by nature and the controllable part representing the reflection coefficients (amplitude and phase shifts) of each element in the IRS.

4   Channel Estimation

A known pilot signal is transmitted over K subcarriers with various RIS configurations. A set of multiple noisy received signals $\overline{z}$ is obtained at the receiver for N different configurations [6–8]. The channel impulse response $h_\theta[k]$ is given by [1]:

$$h_\theta[k] = V^T \omega_\theta, k = 0, 1 \ldots M - 1 \tag{4}$$

V is a $N \times M$ matrix with each element representing the BS-RIS-user cascaded channel coefficients, and ω_θ is $N \times 1$ column matrix representing the controllable channel parameter (reflection coefficient) for each RIS element. The frequency response can be computed as:

$$
\begin{bmatrix} \overline{h_\theta}[0] \\ . \\ . \\ . \\ \overline{h_\theta}[K-1] \end{bmatrix} = FV^T \omega_\theta \tag{5}
$$

where F is a $K \times M$ DFT matrix with the value of (i, j) the element is given by $e^{-j\frac{2\pi}{K}ij}$.

To compute the frequency response $\overline{h}_\theta$, it is required to estimate the cascaded channel matrix V to determine the MN parameters. Consider a sequence of N configurations represented by a pilot matrix $\Omega = \begin{bmatrix} \omega_{\theta_1}, \ldots, \omega_{\theta_N} \end{bmatrix}$ which is invertible. A set of N OFDM signal blocks are received at all the K subcarriers for each

configuration in the matrix Ω. The received signal for all the configurations can be written using (2) as:

$$\underbrace{\left[\overline{z}[1],\,...\,,\overline{z}[N]\right]}_{\overline{Z}} = F_M V^T \Omega x + \underbrace{\left[\overline{w}[1],\,...\,,\overline{w}[N]\right]}_{\overline{W}} \tag{6}$$

From (6), it can be seen that the term $\overline{Z}$ is known for all the configurations. The receiver noise and its power spectral density N_0 will be estimated based on these signals. The cascaded channel matrix V^T is calculated from (6) as:

$$V^T = \underbrace{\frac{1}{x} F_M^{-1} \overline{Z} \Omega^{-1}}_{\text{Signal}} - \underbrace{\frac{1}{x} F_M^{-1} \overline{W} \Omega^{-1}}_{\text{Noise}} \tag{7}$$

5 Results and Discussion

The dataset1 used for the simulation studies is obtained from SP CUP 2021 [9]. The simulation is carried out in MATLAB. The dataset1 contains a user connected in line-of-sight channel to RIS, whereas the base station and RIS have a direct path between them. RIS is a two-dimensional surface of $N = 4096$ elements whose geometry can either be 64×64 or 32×128. Each element is operated in either ON (+1) or OFF (−1) states. These states create a phase difference of π which can be 0 and π or $+\frac{\pi}{2}$ and $-\frac{\pi}{2}$.

A total number of $4N$ configurations are tried out in dataset1 which gives an opportunity to estimate noise power spectral density and other parameters. The noise in frequency domain is additive in nature. This is found by taking the difference between the received signals obtained using the same configuration. For example, configurations 1 and 8183 are exactly the same. Hence, the difference between the received signals obtained using these configurations represents noise which is CSCG. From this estimated noise, power spectral density $N_0 = 3.0673 \times 10^{-23}$ W/Hz is calculated. The noise variable $\overline{W}$ is used to determine the propagation channel V^T as indicated by (7). This channel remains constant during the transmission of pilot signals. The RIS configuration and the noise are the parameters that vary when there are multiple users connected to RIS in either line-of-sight or in non-line-of-sight channels.

In dataset1, we have the pilotMatrix4N variable denoting the $4N$ different configurations used for transmitting the pilot signal over all $K = 500$ subcarriers. The received signal 4N represents the OFDM signal block received using all $4N$ configurations. The $M = 20$ tap FIR filter is used for representing the impulse response of the wireless channel. After obtaining the propagation channel or the BS-RIS-user cascaded channel coefficients associated with all the elements of RIS, the frequency

response of the channel is computed using (5). Using this channel frequency response, the estimate of the received signal is found using (3) for N configurations in the pilotMatrix4N. Using $\overline{h}_\theta[v]$, the rate of user is calculated for each configuration as:

$$R = \frac{B}{K + M - 1} \sum_{v=0}^{K-1} \log_2 \left(1 + \frac{P|\overline{h}_\theta[v]|^2}{BN_0}\right) \text{ bps} \qquad (8)$$

The maximum rate of 114.672 Mbps is achieved for configuration 26, and the signal power in dBW is plotted in Fig. 1 for both the dataset and the estimated received signal calculated using (3). It can be seen from Fig. 1 that both these signal power overlap with each other over all the subcarriers indicating the confidence of estimated channel for the best configuration. Similarly, the minimum data rate of 14.077 Mbps is achieved for configuration 2065, and the signal power is shown for both the dataset and estimated signal using this configuration in Fig. 2.

For LOS channels, the data rate of approximately 100 Mbps is achieved, and for NLOS channels, the data rate is approximately 50 Mbps. The carrier frequency of 4 GHz with transmit power of $P = 1$ W and a bandwidth of $B = 10$ MHz is used for transmission of pilot signals.
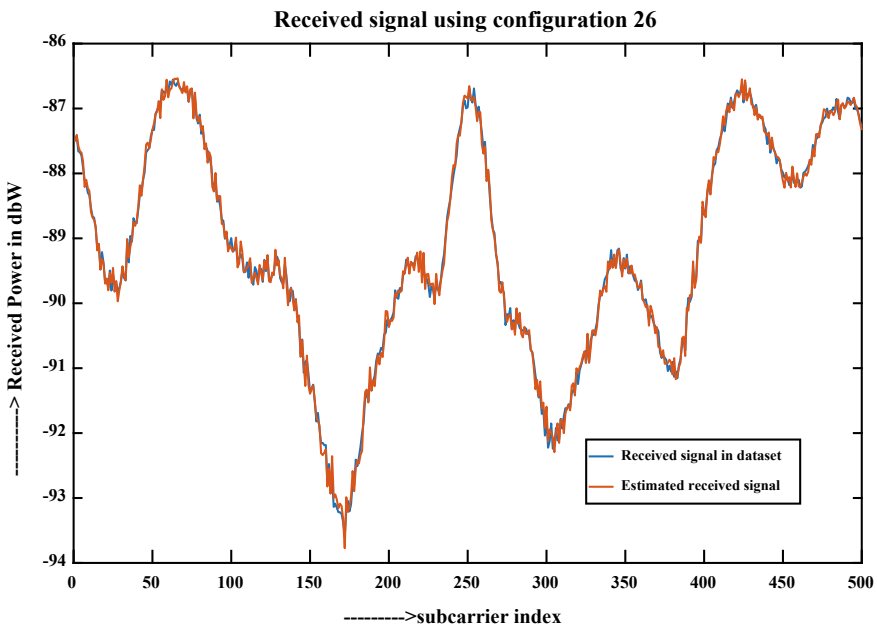
Fig. 1 Received signal power in dBW using configuration 26
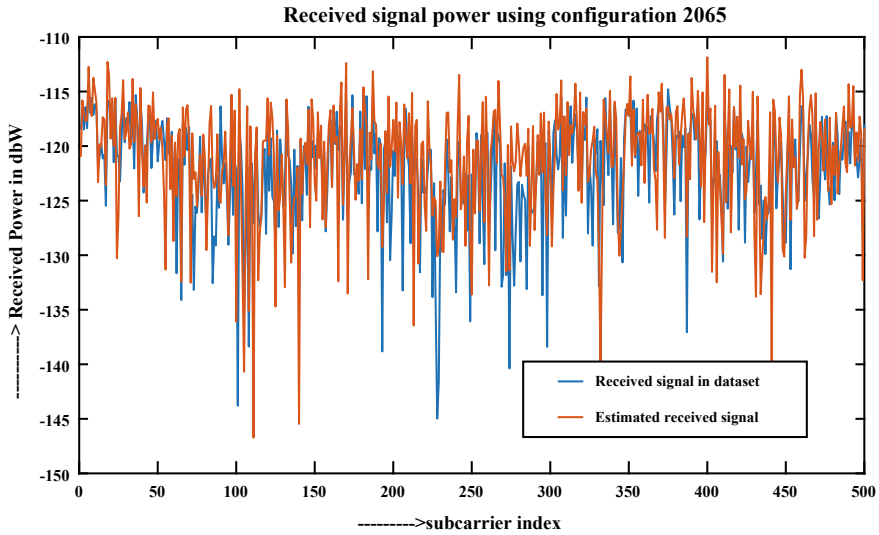
Fig. 2 Received signal power in dBW using configuration 2065

6 Conclusion

In this paper, the dataset1 from SP CUP 2021 is used to estimate the cascaded BS-RIS-user channel coefficients based on the received signals obtained using $4N$ different RIS configurations. The $4N$ configurations are formed by using Hadamard matrix representations which have repeated configurations. Using these repeated configurations, we have estimated the CSCG noise and the noise power spectral density. After the computation of frequency response of the propagation channels, it is found that the configuration number 26 is selected for the single user based on the maximum data rate of 114.672 Mbps. This work can be extended to identify the geometrical shape of the array by exploiting the sparsity in the propagation channels to obtain an effective selection algorithm.

References

1. Björnson, E., Wymeersch, H., de Carvalho, E.: Reconfigurable Intelligent Surfaces: A Signal Processing Perspective with Wireless Applications. arXiv:2102.00742 [eess.SP]
2. Lin, S., Zheng, B.: Adaptive transmission for reconfigurable intelligent surface-assisted OFDM wireless communications. IEEE J. Sel. Areas Commun. **38**(11), 2653–2665 (2020). https://doi.org/10.1109/JSAC.2020.3007038
3. You, C., Zheng, B., Zhang, R.: Intelligent reflecting surface with discrete phase shifts: channel estimation and passive beamforming. In: ICC 2020—2020 IEEE International Conference on Communications (ICC)

4. Björnson, E., Özdogan, Ö., Larsson, E.G.: Reconfigurable intelligent surfaces: three myths and two critical questions. IEEE Commun. Mag. **58**(12), 90–96 (2020). https://doi.org/10.1109/MCOM.001.2000407
5. Zheng, B., Zhang, R.: Intelligent reflecting surface-enhanced OFDM: channel estimation and reflection optimization. IEEE Wirel. Commun. Lett. **9**(4), 518–522 (2020). https://doi.org/10.1109/LWC.2019.2961357
6. Wei, X., Shen, D., Dai, L.: Channel estimation for RIS assisted wireless communications—Part I: fundamentals, solutions, and future opportunities. IEEE Commun. Lett. **25**(5), 1398–1402 (2021). https://doi.org/10.1109/LCOMM.2021.3052822
7. Özdogan, Ö., Björnson, E.: Deep Learning-Based Phase Reconfiguration for Intelligent Reflecting Surfaces. arXiv:2009.13988 [eess.SP]
8. Alexandropoulos, G.C., Samarakoon, S., Bennis, M., Debbah, M.: Phase configuration learning in wireless networks with multiple reconfigurable intelligent surfaces. In: 2020 IEEE Globecom Workshops
9. https://kth.app.box.com/v/spcup2021-dataset1

Intelligent Control-Based Boost Converter Interfaced with Three-Level Diode Clamped Inverter

Vikas Kumar, Punithavathi Duraiswamy ⓘ**, and S. Nagaraja Rao**ⓘ

Abstract This paper presents simulation and analysis of intelligent control-based boost converter interfaced with three-level-diode clamped inverter (TL-DCI) for renewable energy and AC motor drive applications. The main objective of a DC–DC boost converter is to maintain a constant output voltage with an optimum duty cycle despite variations in input voltage or load current using an intelligent control, i.e., fuzzy logic control (FLC) approach. Further, better conversion efficiency with reduced ripple can be obtained by keeping optimum range of output voltage. To achieve the desired results from a DC–DC converter, an intelligent controller is required. The open loop and conventional proportional integral (PI) controllers have certain limitations to improve dynamic performance due to variation of parasitic into components. The FLC uses voltage output as feedback for significantly improving the dynamic performance of boost DC–DC converter. In addition, an intelligent control-based boost converter interfaced with TL-DCI using sine pulse width modulation (PWM) to apply for AC motor drive applications. This paper shows an improved dynamic performance of boost converter using FLC compared to open loop and conventional PI controllers using MATLAB or Simulink. The performance of TL-DCI using sine PWM integrated with FLC-based boost converter has been analyzed in terms power quality with respect to voltage and current waveforms.

Keywords Boost converter · PI control · Intelligent control · TL-DCI · Sine PWM

1 Introduction

DC–DC converters are one of the important applications in industry, domestic appliances, renewable energy conversion, electric vehicle, and space power system [1,

V. Kumar · P. Duraiswamy · S. Nagaraja Rao (✉)
M.S. Ramaiah University of Applied Sciences, Bangalore, India
e-mail: nagarajarao.ee.et@msruas.ac.in

P. Duraiswamy
e-mail: punithavathi.ec.et@msruas.ac.in

2]. All users need regulator output voltage despite of variation in load and inputs or components [3, 4]. Apart from regulated output, DC–DC design must have excellent transient, steady-state response [5], and EMI or EMC performance with minimum cost and size. DC–DC converters have different topology buck, boost and buck boost no isolated and many isolated topology (flyback, forward, push, pull, etc.) to achieve the regulated outputs. To improve dynamic response various controllers are available in analog domain like proportional controller and PID controller similarly in digital domain fuzzy logic and adaptive fuzzy logic or ANN-based controller [6].

Nowadays, inverters have many applications such as AC motor drive, solar renewable energy, industry, home appliances, and many more [7, 8]. Basically, inverter converts DC to AC with the help of different switch control mechanisms [9]. Conventional inverter has limitations like more harmonic distortion and high switching losses which affect the overall performance [10]. Therefore, multilevel inverters (MLIs) are preferred due to several advantages such as less harmonic distortion, low switching loss, and more efficient [11]. MLIs are classified into three basic types: diode clamped [12], capacitor clamped, and cascaded H-bridge [13]. Under these basic different levels, inverters are available. In this paper, TL-DCI using sine PWM fed RL-load is integrated with intelligent control-based boost converter to validate the performance by considering variable step voltages or duty cycles.

2 Proposed FLC-Based Boost Converter Interfaced with TL-DCI

The circuit configuration of FLC-based boost converter interfaced with TL-DCI is shown in Fig. 1. The FLC-based boost converter topology doubles the voltage gain with reduced voltage or current ripple in comparison with the conventional controllers, which makes it a better configuration for PV integration. The TL-DCI configuration provides improved power quality with low harmonic distortion in the load current which makes it suitable for AC motor drives and a lesser amount of electromagnetic interference (EMI) which makes it a better configuration for PV integration.

2.1 Boost Converter with State Space Model

The boost converter circuit which doubles the voltage gain with an optimum duty ratio of 0.5 using MOSFET 'M' is shown in Fig. 2 [5]. When the MOSFET 'M' is turned on, the inductor 'L' is connected to 'V_{dc}' and stores the energy. When the 'M' is off, an accumulated energy is delivered to the load.

From the fundamentals, output voltage (V_o) in terms of duty cycle (D) is arrived as given in Eq. (1).
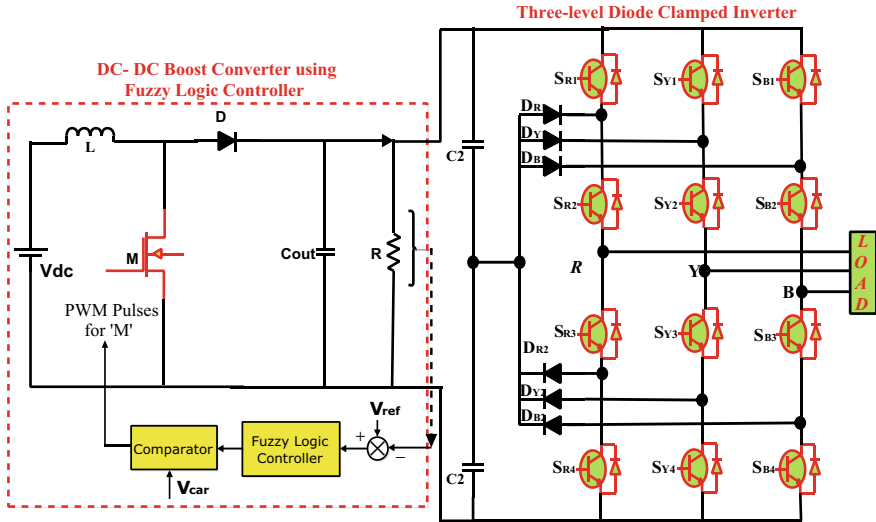
Fig. 1 Configuration of three-phase TL-DCI integrated with FLC-based boost converter

Fig. 2 Boost converter
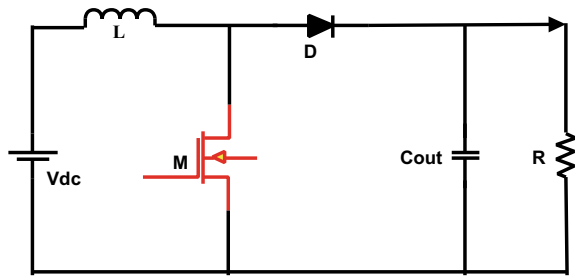
$$\frac{V_{\text{O}}}{V_{\text{dc}}} = \frac{1}{1-D} \tag{1}$$

The state space model of boost converter can be attained with on and off states of MOSFET 'M' are represented in Eqs. (2) and (3), respectively.

$$L\frac{di_{\text{L}}}{dt} = -(1-D)V_{\text{o}} + V_{\text{dc}} \tag{2}$$

$$C\frac{dV_{\text{c}}}{dt} = (1-D)i_{\text{L}} - \left(\frac{1}{R}\right)V_{\text{o}} \tag{3}$$

The state space model of boost converter can be represented by considering inductor current and output voltage as state variables in terms of input variables 'D' and 'V_{dc}' is given in Eqs. (3) and (4).

$$\frac{\mathrm{d}}{\mathrm{d}t}\begin{bmatrix} i_{\mathrm{L}} \\ V_{\mathrm{c}} \end{bmatrix} = \begin{bmatrix} 0 & -\left(\frac{1}{L}\right) \\ \frac{1}{C} & -\left(\frac{1}{RC}\right) \end{bmatrix}\begin{bmatrix} i_{\mathrm{L}} \\ V_{\mathrm{c}} \end{bmatrix} + \begin{bmatrix} \left(\frac{1}{L}\right)V_{\mathrm{O}} & \frac{1}{L} \\ -\left(\frac{1}{C}\right)i_{\mathrm{L}} & 0 \end{bmatrix}\begin{bmatrix} D \\ V_{\mathrm{dc}} \end{bmatrix} \qquad (4)$$

2.2 Configuration of Three-Phase TL-DCI

Figure 3 shows the three-phase TL-DCI configuration. For m-level, it requires '6(m-1)' switches and main diodes, '(m-1)' DC bus capacitors, and '3(m-1)(m-2)' clamping diodes to generate '(2 m-1)' levels across the load. Therefore, three-phase TL-DCI requires twelve switches and diodes, two DC bus capacitors, and six clamping diodes to generate five levels between any two line-to-line voltages. The operation of TL-DCI is explained in the form of switching states represented in Table 1 [13, 14].
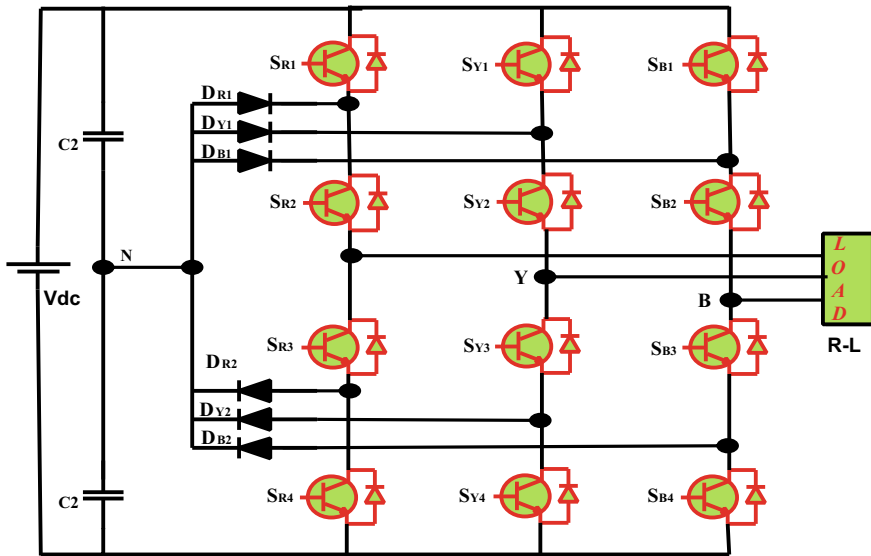
Fig. 3 Three-phase TL-DCI configuration fed R-L load

Table 1 Three-phase TL-DCI switching sequence

Sl. No.	Conducting switches in each phase	Clamping diodes in each phase	Voltage
1	S_{R1}, S_{R2} / S_{Y1}, S_{Y2} / S_{B1}, S_{B2}	–	$+V_{\mathrm{dc}}/2$
2	S_{R2}, S_{R3} / S_{Y2}, S_{Y3} / S_{B2}, S_{B3}	D_{R1}, D_{R2} / D_{Y1}, D_{Y2} / D_{B1}, D_{B2}	0
3	S_{R3}, S_{R4} / S_{Y3}, S_{Y4} / S_{B3}, S_{B4}	–	$-V_{\mathrm{dc}}/2$

3   Control of Boost Converter and TL-DCI

This section shows boost converter results using open loop and PI control along with execution of intelligent control using FLC approach. Further, the control of TL-DCI using three-phase sine PWM is explained to generate pulses for the respective switches used in TL-DCI.

3.1   Open Loop and PI Control

The simulation results of boost converter using open loop and PI control methods are analyzed by considering an optimum operating point or duty cycle of 0.5, with an desired input voltage (V_{dc}) of 50 V. In a closed loop system, the controller circuit is important for both steady-state and transient output. The boost regulator control circuit senses the output and compares it to the reference voltage to produce error signal. Using PWM, a duty cycle 'D' is generated corresponding to error signal. The 'D' determines the output voltage. The 'D' of the converter varies depending on the error signal, resulting in regulated output.

3.2   Boost Converter Using Intelligent Control

FLC approach is one of the intelligent digital controllers which is built with set of rule based on system behavior and human knowledge. FLC gives advantages of system dynamics improvement even for nonlinear system which is not possible in conventional controller. The process of FLC involves four components, namely fuzzification, interface mechanism, rule base, and defuzzification. Fuzzification interface converts input into linguistic values. Set of rule creation and making decision based on inputs are done in interface block. Defuzzification do reverse process of fuzzification, i.e., linguistic variable to control action outputs. FLC has designed to regulate the output of boost regulator by varying 'D' with respect to reference voltages. In the simulation process, sensed output voltage subtracts from reference set voltage and error signal is generated. During the simulation process, the sensed output voltage is subtracted from the reference set voltage, and an error signal is produced. Both error and change in error signal are divided into five sets known as NB: negative big, NS: negative small, Z: zero, PS: positive small, and PB: positive big. Fuzzy base rules are shown in Table 2. FLC implementation process with generation of input error, change in error, output duty cycle, and rule surface view is represented in Fig. 4a–d, respectively.

Table 2 Fuzzy rules for boost converter

e ce	NB	NS	Z	PS	PB
NB	NB	NB	NB	NS	Z
NS	NB	NB	NS	Z	PB
Z	NB	NS	Z	PS	PB
PS	NB	Z	PS	PB	PB
PB	Z	PS	PB	PB	PB
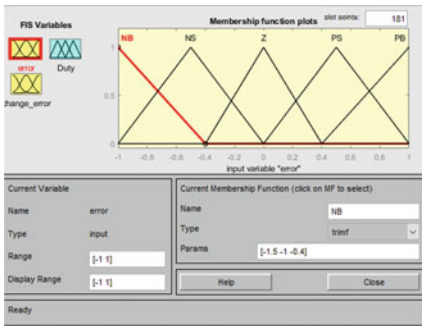
(a)
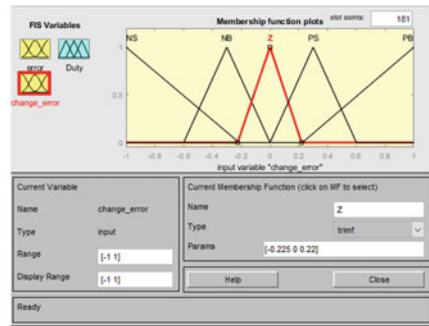
(b)
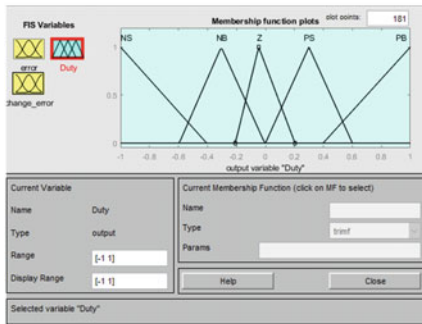
(c)
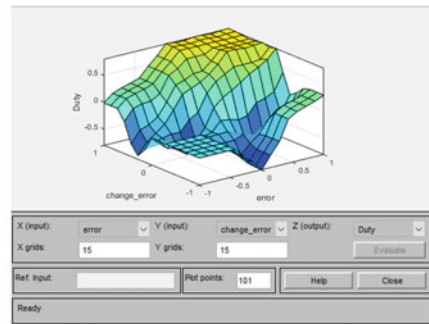
(d)

Fig. 4 FLC implementation process for the boost converter. **a** Input error. **b** Change in error. **c** Output duty cycle. **d** Rule surface view

3.3 TL-DCI Using Sine PWM

The output of intelligent control-based boost converter is interfaced with TL-DCI in place of DC source as shown in Fig. 1. The pulses for TL-DCI switches are generated using three-phase sine PWM as shown in Fig. 5. The control circuit of TL-DCI uses two triangular carriers (V_{tri1} and V_{tri2}) displaced in same phase and three sine waves
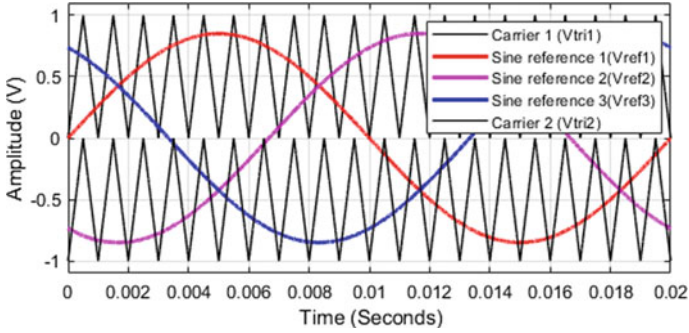
Fig. 5 Sine PWM for three-phase TL-DCI

($V_{\text{ref}1}$, $V_{\text{ref}1}$ and $V_{\text{ref}3}$) with a displacement of 120° with each other. Two triangular waves are compared with each sine wave to generate pulses for the switches in TL-DCI.

4 Simulation Results and Readings of Boost Converter Interfaced with TL-DCI Fed R-L Load

This section describes the simulation results and readings of boost converter interfaced with TL-DCI-fed R-L load using open loop, PI control, and intelligent control approach using FLC. The MATLAB or Simulink parameters are listed in Table 3.

Figure 6. shows the boost converter output under open loop with a variable duty ratios by considering 0.4, 0.5, and 0.6 values, and the respective simulation output voltage readings are 82.41, 97.47, and 122.8 V, but the actual theoretical values should be 83.33, 100, and 125 V for the duty ratios of 0.4, 0.5, and 0.6, respectively, as per Eq. (1). Therefore, the output voltage consists deviations with respect to input voltages. In addition, the simulation readings of peak time, rise time, overshoot, settling time, and % voltage deviations are shown in Table 4.

Table 3 Simulation parameters of TL-DCI integrated with boost converter

Parameters	Value/range
Input voltage of each HG-qZSN	50 V
MOSFET operating frequency	25 kHz
L and C_{out} of boost converter	1 mH and 200 μF
Input voltage applied to TL-DCI	100 V
C_1 and C_2 of TL-DCI	1 μF
Modulation index of sine wave	0–1
R' and 'L' values of three-phase load	10 Ω and 20 mH
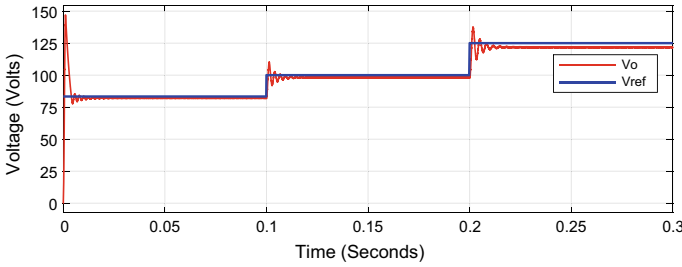
Fig. 6 Variable step output of boost converter using open loop

Table 4 Simulation readings of open loop boost converter

S. No.	V_{dc} (V)	Expected voltage V_{ref} (V)	Rise time (t_s in mS)	Peak time (t_p mS)	Peak overshoot (M_p in %)	Settling time (t_s mS)	V_{out}	Voltage deviation (V)
1	50	83.33	0.86	1.146	71.8	34.36	82.41	0.92
2	50	100	1.22	1.36	42.39	30.32	97.47	2.53
3	50	125	1.06	1.18	14.96	29.76	122.8	2.2

Figure 7 shows the boost converter output under PI control with a variable reference voltages (V_{ref}) by considering 82.25, 98.23, and 123.47 V values, and the duty cycles are adjusted automatically according to the 'V_{ref}' values. The simulation readings of peak time, rise time, overshoot, settling time, and % voltage deviations are shown in Table 5.

Figure 8 shows the fuzzy controller-based boost converter output with a variable reference voltages (V_{ref}) by considering 83.33, 100, and 125 V values. The simulation readings of peak time, rise time, overshoot, settling time, and % voltage deviations are shown in Table 6.
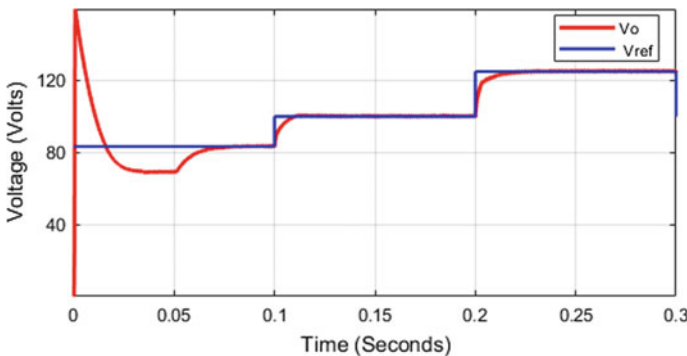
Fig. 7 Variable step output of boost converter using PI control

Table 5 Simulation readings of boost converter with PI control

S. No.	V_{dc} (V)	V_{ref} (V)	Rise time (t_s in mS)	Peak time (t_p mS)	Peak overshoot (M_p in %)	Settling time (t_s mS)	V_{out}	Voltage deviation (V)
1	50	83.33	0.73	0.1	70.48	65	83.31	0.02
2	50	100	0.85	0.1	65.28	64	99.64	0.36
3	50	125	0.78	0.1	45.23	63	124.6	0.4
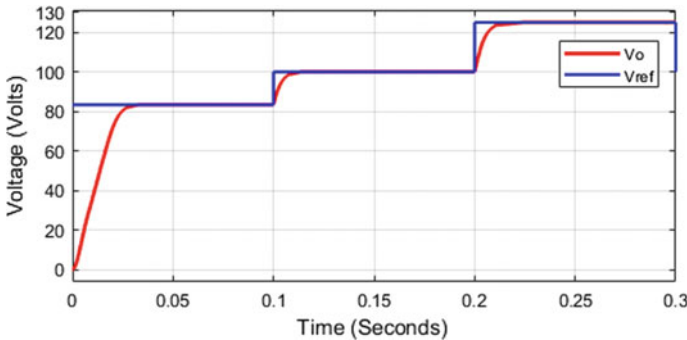
Fig. 8 Variable step output of boost converter using FLC control

Table 6 Simulation readings of boost converter with fuzzy control

S. No.	V_{dc} (V)	V_{ref} (V)	Rise time (t_s in mS)	Peak time and overshoot	Settling time (t_s mS)	V_{out}	Voltage deviation (V)
1	50	83.33	20	–	28	83.32	0.01
2	50	100	26	–	36	99.98	0.02
3	50	125	40	–	41	124.9	0.1

From Tables 4, 5, and 6 simulation readings, it is noticed that FLC-based boost converter has good dynamic performances, fast settling time (< 50 ms), no peak overshoot, and less voltage deviation (< 0.02%) compared to conventional PI controller (< 65 ms) peak overshoot (< 70.8%) and voltage deviation (0.4%) with reference to various reference voltages. Further, the output of FLC-based boost converter has been interfaced with three-phase TL-DCI using sine PWM.

Figures 9 and 10 show the line-to-line voltages (V_{RY}, V_{YB}, and V_{BR}) and THD of three-phase TL-DCI-fed RL-load integrated with FLC-based boost converter, respectively, and it can be observed that voltage THD is 35.28%. Figure 11 shows the corresponding line current waveform with THD. It can be observed that 2.36% THD is occurred in line current through 'I_R' which is acceptable as per IEEE 519 standards.
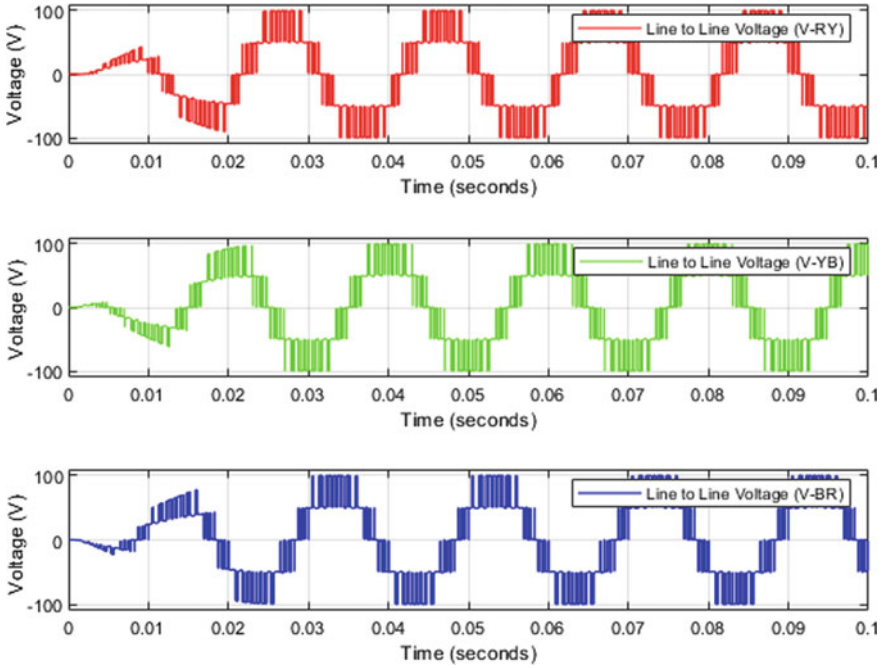
Fig. 9 Three-phase TL-DCI line-to-line voltages (V_{RY}, V_{YB} and V_{BR}) integrated with FLC-based boost converter
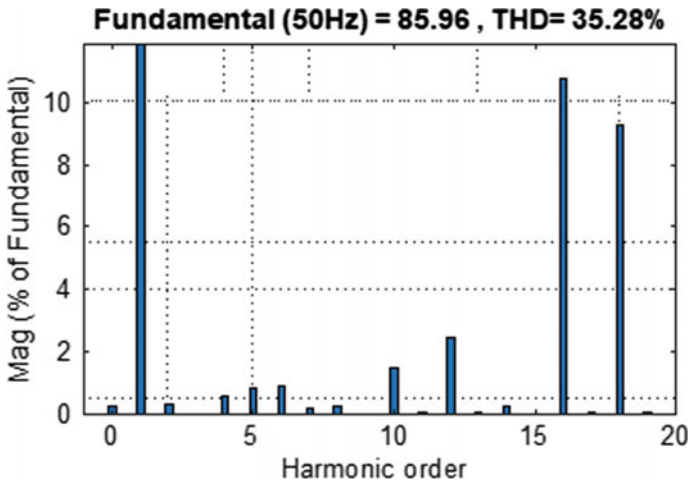
Fig. 10 Three-phase TL-DCI line-to-line voltage THD across V_{RY}
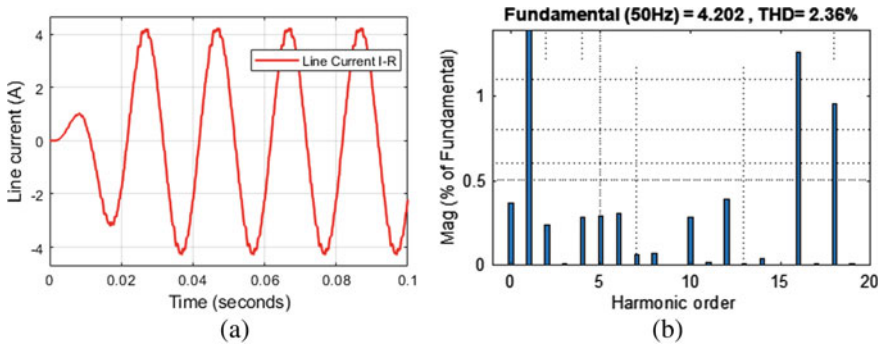
Fig. 11 Three-phase TL-DCI. **a** line current (I_R). **b** THD through I_R

Hence, the designed TL-DCI interfaced with FLC-based boost converter is suitable for AC motor drive applications.

5 Conclusion

In the presented work, open loop, conventional PI, and FLC-based controllers for boost converter are simulated in MATLAB or Simulink with variable reference voltages with respect to duty ratios in open loop control. From the simulation readings, it can be noticed that the FLC-based boost converter has good dynamic response with negligible voltage deviations. Further, the output of FLC-based boost converter interfaced with three-phase TL-DCI using sine PWM fed RL-load to improve the power quality as per IEEE standards. Therefore, the proposed FLC-based boost converter interfaced with three-phase TL-DCI has been recommended renewable energy and AC motor drive applications.

References

1. Tofoli, F.L., de Castro Pereira, D., de Paula, W.J., Júnior, D.D.S.O.: Survey on non-isolated high-voltage step-up dc–dc topologies based on the boost converter. IET Power Electron. **8**(10), 2044–2057 (2015)
2. Venkateswarlu, K.: Renewable energy fed bidirectional converter based on grid application using fuzzy logic-PID controller. Turkish J. Comput. Math. Educ. (TURCOMAT) **12**(6), 275–280 (2021)
3. Ganeswari, J.A., Kiranmayi, R.: Performance improvement for DC boost converter with fuzzy controller. In: 2018 2nd International Conference on Inventive Systems and Control (ICISC), pp. 358–362, IEEE (2018)

4. Kiran Kumar, B.M., Indira, M.S., Nagaraja Rao, S.: Performance Evaluation of Solar PV Us-ing Multiple Level Voltage Gain Boost Converter with C-L-C Cell. In: Mekhilef, S., Favorskaya, M., Pandey, R.K., Shaw, R.N. (eds,) Innovations in Electrical and Electronic Engineering. Lecture Notes in Electrical Engineering, vol. 756. Springer, Singapore (2021)
5. Ismail, N., Musirin, I., Baharom, R., Johari, D.: Fuzzy logic controller on DC/DC boost converter. In: 2010, IEEE International Conference on Power and Energy, pp. 661–666 (2010)
6. Fudoli, F.H., Vechia, D.D., Bonaldo, J.P., Bertogna, E.G.: Design, simulation and comparative evaluation of both a classic and a fuzzy logic PI controller applied to a DC-DC converter. Przeglad Elektrotechniczny **94**(5), 27–31 (2018)
7. Rao, S.N., Kumar, D.A., Babu, C.S.: New multilevel inverter topology with reduced number of switches using advanced modulation strategies. In: International Conference on Power, Energy and Control (ICPEC), pp. 693–699. IEEE (2013)
8. Rao, S.N., Kumar, P., Veerabhadra: Performance analysis of Z-source inverter topologies for renewable energy sources and fuel cell applications. In: 2020 IEEE International Conference on Distributed Computing, VLSI, Electrical Circuits and Robotics (DISCOVER), pp. 165–170, IEEE (2020)
9. Gupta, K.K., Ranjan, A., Bhatnagar, P., Sahu, L.K., Jain, S.: Multilevel inverter topologies with reduced device count: a review. IEEE Trans. Power Electron. **31**(1), 135–151 (2015)
10. Rao, S.N., Pranupa, S., Kiran Kumar, B.: Three phase diode clamped multilevel DC link inverter with multi reference modulation techniques. J. Adv. Res. Dyn. Control Syst. **10**(8), 1793–1804 (2018)
11. Vijeh, M., Rezanejad, M., Samadaei, E., Bertilsson, K.: A general review of multilevel inverters based on main submodules: structural point of view. IEEE Trans. Power Electron. **34**(10), 9479–9502 (2019)
12. Shi, S., Wang, X., Zheng, S., Zhang, Y., Lu, D.: A new diode-clamped multilevel inverter with balance voltages of DC capacitors. IEEE Trans. Energy Convers. **33**(4), 2220–2228 (2018)
13. Sulake, N.R., Devarasetty Venkata, A.K., Choppavarapu, S.B.: FPGA implementation of a three-level boost converter-fed seven-level dc-link cascade H-bridge inverter for photovoltaic applications. Electronics **7**(11), 282 (2018)
14. Rao, S.N., Kumar B.M., Swathy, N.: Three-level modified capacitor assisted extended boost Z-source multilevel inverter for photovoltaic applications. In: Advances in Energy Technology, Lecture Notes in Electrical Engineering, vol. 766. Springer, Singapore. 978-981-16-1475-0, 500101_1_50 (2021)

Peculiar Effectual Approach: Q-Routing in Opportunistic Network

Renu Dalal and Manju Khari

Abstract Extraordinary class of mobile ad-hoc network and delay tolerant network (DTN) is known as opportunistic network, which includes diverse range of applications in today's scenario. This network works in many applications like animal evacuee tracking, intelligent transportation, connectivity in rural area, and mobile social networking (MSN), etc. Routing in opportunistic network is a crucial task due to its onerous characteristics. As many routing protocols has been already proposed in earlier, each protocol have their own advantages and disadvantages. In this paper, novel routing protocol named QRP is proposed to enhance the best selection of relay node in the opportunistic network. Reinforcement-based deep-q-learning approach is used to find the Q-value of the node. This Q-value of the node decides that either the packet is disseminated in the network.

Keywords Machine learning · Nature-inspired algorithm · Optimization · Opportunistic network · Routing protocol · ONE tool · Q-learning

1 Introduction

Dynamic network topology, frequent movement of nodes, no existence of source to receiver route, and many more peculiarity are included by opportunistic network. Store-carry-forward approach of broadcasting the messages is utilized by the opportunistic nodes in the network [10]. This approach enables opportunistic network being different from traditional networks like mobile ad-hoc network (MANET), vehicular ad-hoc network (VANET), etc. [3–5]. MANET is different from opportunistic network like MANET includes multi-hop communication, connectivity among nodes, no higher delay, no buffer, no store-carry-forward approach, etc. [6]. Integrity of nodes, data confidentiality of packets, privacy of nodes, trust

R. Dalal (✉)
Guru Gobind Singh Indraprastha University, Delhi, India

M. Khari
Jawaharlal Nehru University, Delhi, India

among nodes, and authenticity of nodes are various security challenges are faced by opportunistic network.

Diverse routing protocols like HSR, ACTP, LKH, etc., are already introduced for ad-hoc network, due to acceptable cost of MANET [7]. Forwarding based and flooding based are two basic categories of routing in opportunistic network. Opportunistic network confronts various issues like duplicate copies of message, message dropping, delay in message transmission, reliable relay node, etc. To overcome these problems, new routing protocol based on Q-value of Q-learning algorithm [21] is proposed in this paper. According to global and local trust value of the node with the integration of Q-value, it is the decision parameter of selection of relay node in the network. This paper is organized as follows. Section 2 describes the overview of various routing protocols of opportunistic network. Flowchart of proposed protocol is summarized in Sect. 3. At the end, Sect. 4 concludes the paper.

2 Literature Survey

This section illustrates two types of routing and details of some existing routing protocol of opportunistic network. (a) content-based (or flooding, or infrastructure-less) and (b) context-based (or forwarding, or infrastructure-based) are types of routing in DTN. Figure 1 presents various existing protocol for infrastructure-less based and infrastructure-based protocol.
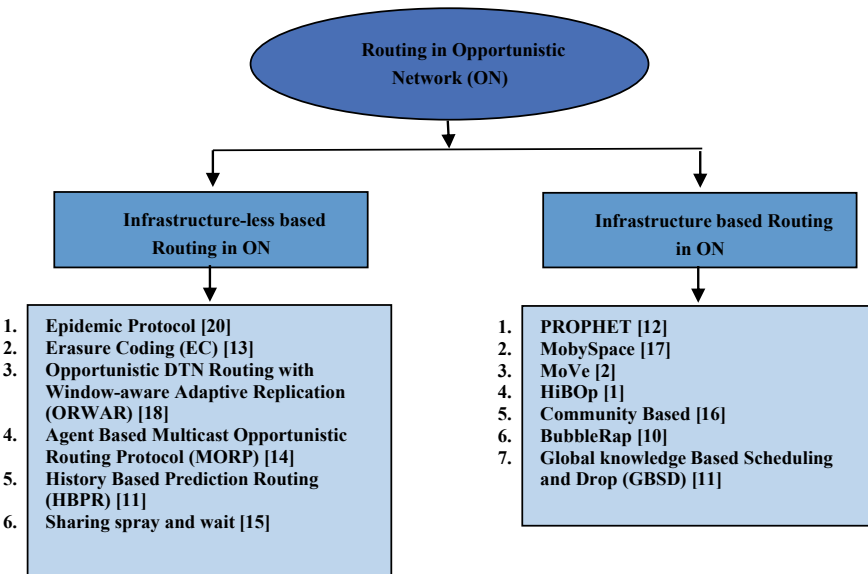
Fig. 1 Basic types of routing in opportunistic network

Vahadat et al. [22] have introduced the routing protocol named epidemic, flooding-based protocol for ON in 2000. This protocol minimizes the delivery delay of messages from sender to receiver node. It needs higher requirement of buffer size and bandwidth for communication in network. In 2005, Lin et al. have proposed erasure coding (EC) for opportunistic network [15]. This protocol is not suitable for highly dynamic network. It includes the advantages of having infinite buffer occupancy and works efficiently for dense network. This protocol is implemented on DTNSIM-Java-based simulator. Opportunistic DTN routing with Window-aware adaptive replication (ORWAR) protocol has proposed by Sandulescu et al. in 2008 [20]. This protocol has limited replication of messages with multicopy routing and based on quota replication. ORWAR woks adequately with the factors, delivery ratio, overhead ratio, and average latency.

Probabilistic routing protocol using history of encounters and transitivity (PROPHET) protocol has introduced by Lindgren et al. in 2003 [14]. Probabilistic metric has used by this protocol to estimate the probability of transmitting the message to destination node. Delivery probability is directly proportional to the no. of times the nodes encountered to each other. Motion vector (MoVe) protocol has proposed by LeBurn et al. in 2005 [2]. To estimate the minimum distance between nodes, information of neighboring nodes and corresponding velocity of nodes are used. This protocol has lesser buffer usage and overhead ratio. Boldrini et al. have proposed history-based routing protocol (HiBOp) in 2007 [1]. Present context information has used to select appropriate relay node. Identity table has used by each node for keeping the context information. In 2019, knowledge-based multiplayer collaborative (KBMC) approach was proposed [9]. Utility function is estimated by considering the factors like velocity of node, message carrying time, and number of copies. Intelligent water drop neural network (IWDNN) approach was introduced in 2020. It was used three phases; feed forward, weight update, and operation [13].

3 Proposed Protocol for Opportunistic Network

In this section, Q-value-based routing protocol (QRP) for opportunistic network is proposed. Figure 2 presents the basic work flow of proposed QRP routing methodology for opportunistic network. Various parameters are used to train the nodes in opportunistic network like success ratio, probability, buffer capacity, current hop-count, etc. From Fig. 2, it is very obvious that after training of nodes, each and every node in network is capable of performing their operation. Node's Q-value is used to decide that whether the node will perform their function. Each node in network is having their packet format; this format contains various field like present node-id, relay node-id, message id, Q-value, local trust value, global trust value, action, and destination node-id. $Q(X_t, A)$ defines the current Q-value of node at time (t) on performing action (A). Increasing or decreasing of Q-value depends on the action performed by that node and reward value received by neighboring node in the network. The procedure used for designing the QRP protocol is briefed as:
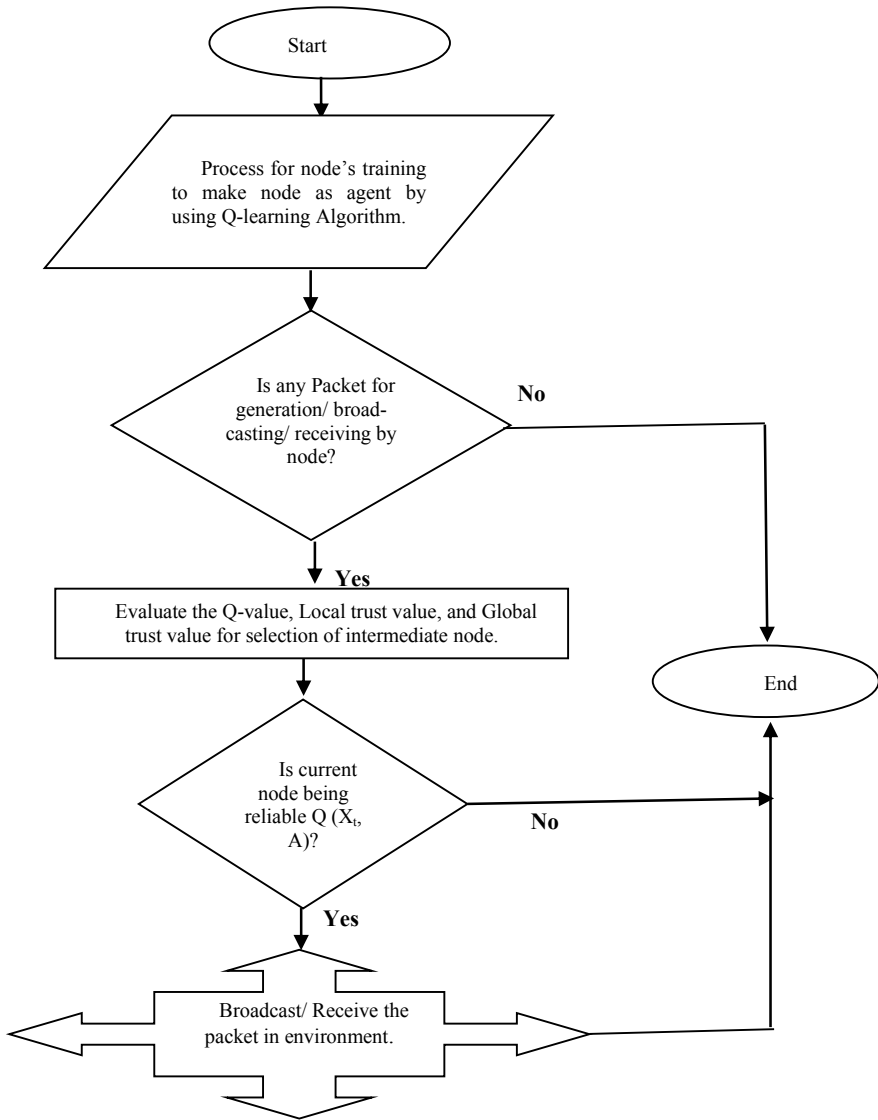
Fig. 2 Flowchart for QRP routing methodology

A. Training Environment Phase: By using Weka tool, each and every node in opportunistic network is trained. Various learning parameters are used for this purpose like node's speed, energy, distance among nodes, current hop-count, success ratio, probability, etc. Existing routing parameters available for epidemic protocol are used for training procedure. Procedure for Q-learning: Reinforcement learning-based evolutionary machine learning algorithm named

Q-learning is used for the appropriate selection of intermediate node in the network. Markov decision process (MDP) is used for each action performed in opportunistic network. Deep neural network is first initialized by trained nodes in the network. Each node in the network is having their packet header, which includes their Q-value. This Q-value is primarily used for the selection of relay node.

B.   Selection of Intermediate Node: After the successful use of Q-learning algorithm in network; set of nodes are ranked according to their reliability. Q-value is calculated by using node's past Q-value and current action done by particular node. The Q-value for each node is updated periodically. If no one node does not found with reliable Q-value, the message will not be forwarded to that node.

C.   Message Dissemination Phase: In this phase; message transmits to reliable relay node in the network, and this node forwards the packet to destination node. The Q-learning process is repeated for another transmission in the network, if required.

D.   Q-value Updating Phase: Q-value for each node is calculated and updated in the Q-routing table for reliable selection of intermediate node in the network. After this phase, procedure for QRP is terminated.

$$Q(X_t, A) = R(X_t, A) + \Upsilon * \max\big[Q(X_{t+1}, A)\big] \qquad (1)$$

The background of Q-learning approach is Markov decision processes (MDP). It can be defined by using (X, A, R, T, π) these five tuples. Set of definite actions at state X is known as 'A'. Transition function 'T' is used from state X_t to X_{t+1}. 'R' is the reward function used to give reward value to the node, and π is the policy. At initial period, exploration method is utilized for learning, and after this exploitation approach is used for selection of relay node in network. Equation (1) is used to calculate the Q-value for each pair (X, A). Υ, it is known as learning factor during simulation of network.

Calculation of Local and Global Trust: Each node in network maintains the trust list of all its neighboring nodes according to past communication between them; 0, 1, and -1 are the valid trust value for trust list. Here, 0 indicates no interaction with node, 1 shows complete trust, and -1 presents distrust. Local node (LN) keeps local trust value in the list, and global node (GN) estimates the global trust value according to the information provided by local node. For example, opportunistic network contains source node (Sn), destination node (Dn), GN1, and LN set (1, 2, 3, 4, 5). Here, network nodes are trained by using machine learning algorithm with using Weka tool. Now, Sn selects the reliable relay node from the LN set. On the basis of communication, each LN keeps the trust value of their neighboring node. By using Eq. (1), trust values of LN is modified. GN maintains the trust value of each LN in their region.

4   Conclusion and Future Work

This paper proposed the new protocol named Q-value-based routing protocol (QRP). It utilized the reinforcement-based machine learning algorithm to calculate the Q-value of the intermediate node in the opportunistic network. Opportunistic node/relay node/candidate node in the network works on the principle of store-carry-forward. Diverse protocols and their characteristics are summarized in this paper. Description of QRP protocol and election of best relay node by using Q-learning algorithm are also briefed in this paper. In future work, this protocol will be simulated by using ONE tool. Diverse parameters like overhead ratio, delivery probability, average buffer time, and average hop-count, etc., will be considered to evaluate the performance of QRP. This protocol is also compared by other existing routing protocols.

References

1. Boldrini, C., Conti, M., Jacopini, J., Passarella, A.: HiBOp: a history based routing protocol for opportunistic network. In: IEEE Conference (2007)
2. Burns, B., Brock, O., Levine, B.N.: MoVe routing and capacity building in disruption tolerant network. In: Proceedings of IEEE INFOCOM, vol. 1, pp. 398–408 (2005)
3. Dalal, R., Singh, Y., Khari, M.: A review on key management schemes in MANET. Int. J. Distrib. Paral. Syst. **3**(4), 165 (2012)
4. Dalal, R., Khari, M., Singh, Y.: Different ways to achieve trust in MANET. Int. J. AdHoc Netw. Syst. (IJANS) **2**(2), 53–64 (2012)
5. Dalal, R., Khari, M., Singh, Y.: Survey of trust schemes on ad-hoc network. In: International Conference on Computer Science and Information Technology, pp. 170–180. Springer, Berlin, Heidelberg (2012)
6. Dalal, R., Khari, M., Singh, Y.: Authenticity check to provide trusted platform in MANET (ACTP). In: Proceedings of the Second International Conference on Computational Science, Engineering and Information Technology, pp. 647–655 (2012)
7. Dalal, R., Khari, M., Singh, Y.: The New Approach to Provide Trusted Platform in MANET (2012)
8. Dhurandher, S.K., Sharma, D.K., Woungang, I., Bhati, S.: HBPR: history-based prediction for routing in infrastructure-less opportunistic networks. In: 2013 IEEE 27th International Conference on Advanced Information Networking and Applications (AINA), pp. 931–936. IEEE (2013)
9. Deng, X., Chen, H., Cai, R., Zeng, F., Xu, G., Zhang, H.: A knowledge–based multi-player collaborative routing in opportunistic networks. In: 2019 IEEE International Conference on Dependable, Autonomic and Secure Computing, International Conference on Pervasive Intelligence and Computing, International Conference on Cloud and Big Data Computing, International Conference on Cyber Science and Technology Congress (DASC/PiCom/CBDCom/CyberSciTech). IEEE; Fukuoka, Japan (2019)
10. Huang, C.-M., Lan, K.-C., Tsai, C.-Z.: A survey of opportunistic networks. In: International Conference on Advanced Information Networking and Applications Workshops, pp. 1672–1677 (2008)
11. Hui, P., Crowcroft, J., Yoneki, E.: Bubble rap: social-based forwarding in delay-tolerant networks. IEEE Trans. Mob. Comput. **10**(11), 1576–1589 (2010)
12. Krifa, A., Barakat, C., Spyropoulos, T.: An optimal joint scheduling and drop policy for delay tolerant networks. In: 2008 International Symposium on a World of Wireless, Mobile and Multimedia Networks, pp. 1–6. IEEE (2008)

13. Kumaram, S., Srivastava, S., Sharma, D.K.: Neural network-based routing protocol for opportunistic networks with intelligent water drop optimization. Int. J. Commun. Syst. **33**(8), e4368 (2020)
14. Lindgren, A., Doria, A., Schelén, O.: Probabilistic routing in intermittently connected network. ACM SIGMOBILE Mob. Comput. Commun. Rev. **7**, 19–20 (2003)
15. Lin, Y., Liang, B., Li, B.: Performance modeling of network coding in epidemic routing. (2007). https://doi.org/10.1145/1247694.1247709
16. Maddali, B.K., Barman, D.K.: Agent-based multicast opportunistic routing protocol for wireless networks. In: Proceedings of the 2nd ACM Workshop on High Performance Mobile Opportunistic Systems, pp. 1–8 (2013)
17. Nahideh, D., Sabaei, M., Rahmani, A.M.: Sharing spray and wait routing algorithm inopportunistic networks. Wirel. Netw. **22**(7), 2403–2414 (2016)
18. Niu, J., Zhou, X., Wang, K., Ma, J.: A data transmission scheme for community based opportunistic network. In: Proceedings of IEEE (2009)
19. Poonguzharselvi, B., Vetriselvi, V.: Survey on routing algorithms in opportunistic network. In: International Conference on Computer Communication and Informatics, Coimbatore, pp. 1–5 (2013), https://doi.org/10.1109/ICCCI.2013.6466129
20. Sandulescu, G., Nadjm-Tehrani, S.: Opportunistic DTN routing with window-aware adaptive replication. In: Proceedings of the 4th Asian Conference on Internet Engineering, pp. 103–112 (2008)
21. Sutton, R.S., Barto, A.G.: Reinforcement Learning: An Introduction (2011)
22. Vahdat, A., Becker, D.: Epidemic Routing for Partially Connected Ad Hoc Networks (2000)

A Study on the Development and Deployment of IoT Based Remote Health Monitoring System Utilizing ECG Signal

Arijita Das and Ujjwal Mondal

Abstract In this work, the emphasis has been given on this real-time monitoring of ECG signal, and for this purpose, the platform used over here is LabVIEW. The abnormality which has been the focus of this work is myocardial infarction. When this abnormality is detected, the database is being monitored on real-time basis. The other part of the present work is to notify the doctor who is not present near the patient about this abnormality (Yang et al., IEEE Sens J 16(12):4669–4670 [1], Weiping et al., EURASIP J Wirel Commun Netw 2018:176 [2]). The moment when this abnormality is detected, the notification automatically goes to the doctor as a message through email. The ECG database is also mailed to the doctor through LabVIEW as a .lvm file. This .lvm file is nothing but .csv file which can be opened and worked upon like any other Excel file.

Keywords Myocardial infarction · QRS complex · Internet of Things · Mail · LabVIEW

1 Introduction

In recent times, the health monitoring procedure from a remote location has been predominantly emerging. The main reason behind it is that a patient in a severe condition may need immediate treatment which is not possible by a doctor who is far away from that patient. There should be a method of bringing the present condition of the patient into the knowledge of the doctor by some means, so that some immediate effective measures can be suggested from the doctor's end.

ECG signal analysis has been playing a very important role in the detection and analysis if arrhythmic diseases of the heart [3, 4]. Myocardial infarction is another feature extracted from the ECG signal to detect the heart muscle related diseases.

A. Das (✉)
Institute of Engineering and Management, Kolkata, India

U. Mondal
University of Calcutta, Kolkata, India

QRS is part of the ECG signal which is mainly used to extract the RR interval and duration of the peaks [5]. Since almost all the abnormalities related to the heart functioning are detected through the analysis of the QRS complex, the different common algorithms used for such extraction are like Hamilton-mean algorithm, Hamilton-median algorithm, RS slope algorithm, etc.

In the diagnosis of acute myocardial infarction, a rise and a fall of troponin are essential. The ECG plays a very pivotal role in the diagnosis of MI and should be frequently repeated, especially if the initial ECG is not able to diagnose myocardial Infarction.

LabVIEW is a designing software where the total hardware design can be represented in a virtual platform. LabVIEW is also referred to as the backbone of virtual instrumentation. It also helps in real-time data acquisition, monitoring, and transmission.

Internet of Things is an integral part of the latest trend of remote monitoring of data [6–8]. Data can be acquired, processed, sent, and stored using the concept of Internet of Things. It forms a platform where number of ends can work on same data set without being in the same geographical location.

2 Methodology

In this paper, at first, the ECG signal is acquired from a subject. Then this acquired signal is passed through a high pass filter to remove baseline wandering [9]. The cut-off frequency assigned is 0.15 Hz. Then this filtered signal is passed through a low pass filter to remove power line interference. The cut-off frequency was set to 40 Hz. This artifact-less signal is the passed through a band pass filter (lower cut-off frequency—10 Hz and higher cut-off frequency—255 Hz). This band pass filter functions in extracting the QRS complex from the ECG signal. Then, the amplitude of that QRS complex is measured by passing the signal through at one measurement block of LabVIEW. This is done because the detection of myocardial infarction is based on the amplitude value of the QRS complex and also on its duration. This checks whether there is any presence of lower amplitude or negative amplitude. If this amplitude value goes below the threshold value, then it is considered to be the presence of myocardial infarction. Let the positive amplitude value to be A and the positive threshold value be A_{TP}, then

If $A > A_{TP}$, and persist for a certain duration, then there is certain presence of myocardial infarction.

If $A < A_T$, then the patient is considered to be okay.

Let the negative amplitude value to be A and the negative threshold value be A_{NH}, then.

If $A > A_{TN}$, then the patient is okay.
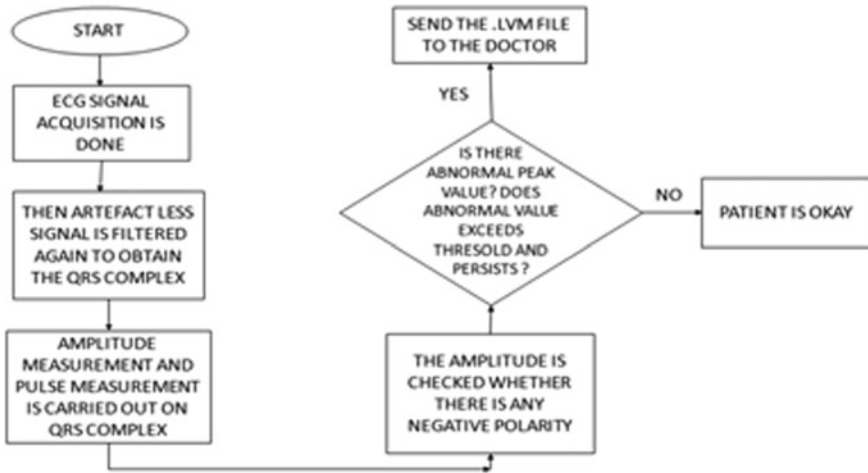
Fig. 1 Flow diagram to show the sequential flow of the work and illustrate the logic

If A < A_{TN}, and persist for a certain duration, then there is certain presence of myocardial infarction.

The duration of the detected pulse is also checked. After this checking if myocardial infarction is detected, then that signal database is saved and sent to the corresponding doctor for further proceedings. This sending of signal database is done through email ID of the doctor which is already fed to the VI block for mailing. The signal is sent to the doctor in .lvm format which can be further processed to convert it into Excel format. The complete flowchart of the work procedure is shown in Fig. 1.

2.1 Acquisition of the ECG Signal

This part shows how the raw ECG signal is acquired from the patient body. The block name is read bio-signal. This block reads the signal in .lvm format. The output of this block is passed through a high pass filter to remove baseline wandering, the cut-off frequency here is 0.15 Hz, and also passed through a low pass filter to remove power line interference, the cut-off frequency here is 40 Hz (Fig. 2).
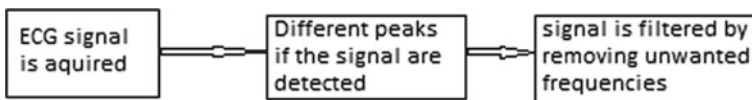
Fig. 2 Part of the block diagram which shows the acquisition of the ECG signal

620   A. Das and U. Mondal

Fig. 3 Part of the block diagram shows the selection of a band pass filter to extract QRS complex
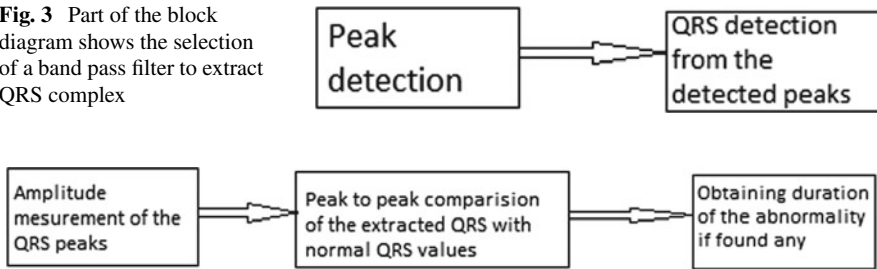
Fig. 4 The part of the block diagram shows the different parameters which are determined from the extracted QRS complex

2.2 Extraction of QRS Complex

This part of the block diagram shows the signal is further passed through a band pass signal. The main objective of the band pass filter is to extract the QRS complex [10]. The lower and the upper cut-off frequency of this filter is taken to be 10 and 255 Hz, respectively. The configuration of the filter is chosen to be Kaiser Window. From this QRS complex which is extracted, the monitoring on the positive and negative peak values is done (Fig. 3).

2.3 Comparison of the Features Extracted from the QRS Complex

Here in this part of the block diagram, different parameters are determined. The parameters are like negative peak value of the amplitude, positive peak value of the amplitude, peak-to-peak value, duty cycle, high state pulse duration, and low state pulse duration [11]. The positive and the negative peak values are passed through negative and positive threshold values, respectively. The block used over here is amplitude level measurement. The amplitude measurement can also be done by the block named tone measurement. But this block only gives the value of the amplitude but cannot determine the different aspects related with the amplitude values (Fig. 4).

2.4 The Mailing Part

As soon as the peak values of the QRS complex exceed the threshold values, a notification is obtained. The mail ID of the concerned doctor is fed to the required block of the VI. This mail sending VI has two parts; one is to send a notification to the doctor's mail ID as a message notification, second the database of the obtained
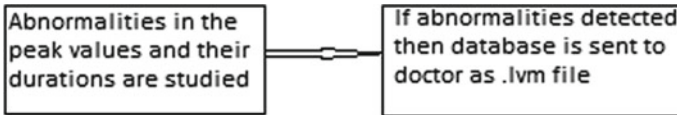
Fig. 5 Part of the block diagram shows the mailing part where the detected signal is mailed

(a)

(b)

(c)
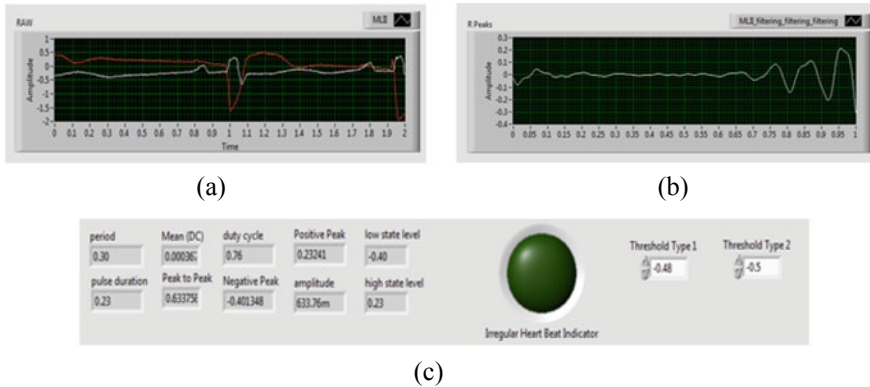
Fig. 6 **a** Raw signal is shown on a normal ECG signal. **b** The filtered signal is shown with detected R peak. **c** The front panel which shows that the LED is not glowing when peak values are within threshold

signal with myocardial infarction is also send to the doctor's mail as .lvm file as an attachment with the message (Fig. 5).

3 Results and Analysis

This front panel shows that the LED is not glowing when the peak values obtained from the QRS complex are within the threshold values. The threshold values are − 0.47 and 0.5 (Figs. 6 and 7).

In the above snapshot, it is shown the mail id which is assigned in the VI receives the mail. Figure 8 shows that both the message as well as the database of the ECG signal is received. The signal is received in .lvm format.

4 Conclusion

In this paper, focus has been given on the real-time monitoring of the health system. Thus, when the patient is not in the vicinity of the doctor, still his/her health condition can be monitored by the doctor. Not only the notification of the illness goes to the

(a)

(b)

(c)
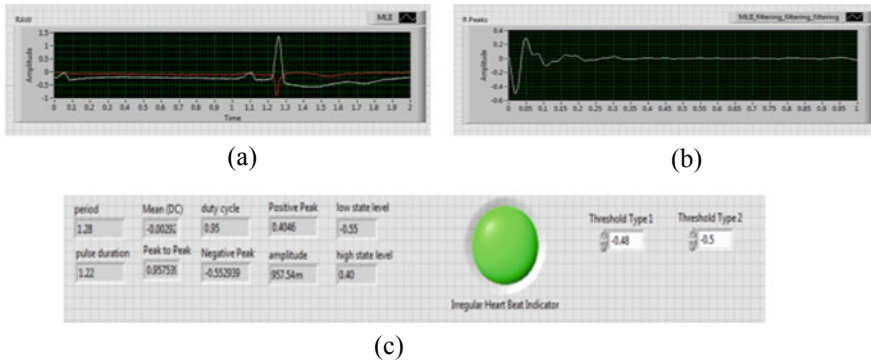
Fig. 7 **a** Raw signal is shown on a normal ECG signal. **b** The filtered signal is shown with detected R peak. **c** The Front Panel which shows that the LED is glowing when peak values are beyond threshold
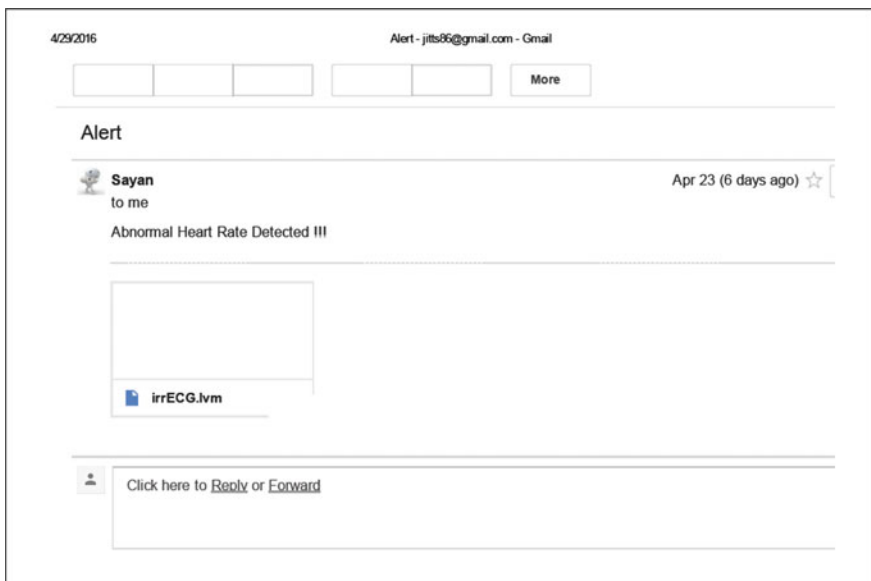
Fig. 8 Snapshot of the Gmail page where notification and the database are both received

doctor, but also the database of the signal reaches the doctor. The doctor can prescribe the required measures remotely and monitor the patient. This work can be further used for many other diseases which can be detected from signal database. More experimentation scopes are possible for human being with different diseases by applying this algorithm for various bio-potential signals. Later on, this transfer of data can be done using GSM concept by utilizing the concept of Internet of Things.

References

1. Yang, Y., Xi, Z., Ke, M., Roy, B.V.B., Simorangkir, Nimai C.K., Karu, P.E.: Development of wireless transducer for real-time remote patient monitoring. IEEE Sens. J. **16**(12), 4669–4670 (2016)
2. Weiping, Z., Mohit, K., Junfeng, Y., Jingzhi, Y.: Medical long-distance monitoring system based on internet of things. EURASIP J. Wirel. Commun. Netw. **2018**, 176 (2018)
3. William, S., David, J.H., Pablo, L., Cohen, M.: Advances in electrocardiogram signal processing and analysis. EURASIP J. Adv. Signal Proces. **2007**(1), 5 pages (2007), Article ID 69169
4. Quiroz-Juarez, M.A., Jimenez-Ramirez, O., Vazquez-Medina, R., Ryzhii, E., Ryzhii, M., Aragon, J.L.: Cardiac conduction model for generating 12 lead ECG signals with realistic heart rate dynamics. IEEE Trans. NanoBiosci. 1–1 (2018)
5. Liu, C., Zhang, X., Zhao L., Liu, F., Chen, X., Yao, Y., Li, J.: Signal quality assessment and lightweight QRS detection for wearable ECG smart vest system. IEEE Internet Things J. **6**, 1363–1374 (2019)
6. Banu, C., Uslu, Ertug, O., Erkan, D.: Analysis of factors affecting IoT-based smart hospital design. J. Cloud Comput. Adv. Syst. Appl. (2020)
7. Jiaming, C., Ali, V., Abolfazl, R.: Smart heart monitoring: early prediction of heart problems through predictive analysis of ECG signals. IEEE Access **7**, 120831–120839 (2019)
8. Khairul, A.S., Ibrahim, K., Herbert, F.J.: ECG biometric with abnormal cardiac conditions in remote monitoring system. IEEE Trans. Syst. Man Cybern. Syst. **44**, 1498–1509 (2014)
9. Udit, S., Barathram, R., Sabarimalai, M.: Automated ECG noise detection and classification system for unsupervised healthcare monitoring. IEEE J. Biomed. Health Inform. 722–732 (2018)
10. Liu, C., Zhang, X., Zhao, L., Liu, F., Chen, X., Yao, Y., Li, J.: Signal quality assessment and lightweight QRS detection for wearable ECG smart vest system. IEEE Internet Things J. **6**, 1363–1374 (2019)
11. Mohammad, A.D., Hamza, D., Christos, K., Elena, P., Abbes, A., Faycal, B., George, D., Guillaume, A.: ECG signal reconstruction on the IoT-gateway and efficacy of compressive sensing under real-time constraints. IEEE Access **6**, 69130–69140 (2018)

Author Index